frontiers | Research Topics

Hydrodynamics and water environment characteristics in coastal areas under the influences of climate change and human activities

Edited by
Sha Lou, Gangfeng Ma and Yi Pan

Published in
Frontiers in Marine Science

ISSN 1664-8714
ISBN 978-2-8325-2302-5
DOI 10.3389/978-2-8325-2302-5

About Frontiers

Frontiers is more than just an open access publisher of scholarly articles: it is a pioneering approach to the world of academia, radically improving the way scholarly research is managed. The grand vision of Frontiers is a world where all people have an equal opportunity to seek, share and generate knowledge. Frontiers provides immediate and permanent online open access to all its publications, but this alone is not enough to realize our grand goals.

Frontiers journal series

The Frontiers journal series is a multi-tier and interdisciplinary set of open-access, online journals, promising a paradigm shift from the current review, selection and dissemination processes in academic publishing. All Frontiers journals are driven by researchers for researchers; therefore, they constitute a service to the scholarly community. At the same time, the *Frontiers journal series* operates on a revolutionary invention, the tiered publishing system, initially addressing specific communities of scholars, and gradually climbing up to broader public understanding, thus serving the interests of the lay society, too.

Dedication to quality

Each Frontiers article is a landmark of the highest quality, thanks to genuinely collaborative interactions between authors and review editors, who include some of the world's best academicians. Research must be certified by peers before entering a stream of knowledge that may eventually reach the public - and shape society; therefore, Frontiers only applies the most rigorous and unbiased reviews. Frontiers revolutionizes research publishing by freely delivering the most outstanding research, evaluated with no bias from both the academic and social point of view. By applying the most advanced information technologies, Frontiers is catapulting scholarly publishing into a new generation.

What are Frontiers Research Topics?

Frontiers Research Topics are very popular trademarks of the *Frontiers journals series*: they are collections of at least ten articles, all centered on a particular subject. With their unique mix of varied contributions from Original Research to Review Articles, Frontiers Research Topics unify the most influential researchers, the latest key findings and historical advances in a hot research area.

Find out more on how to host your own Frontiers Research Topic or contribute to one as an author by contacting the Frontiers editorial office: frontiersin.org/about/contact

Hydrodynamics and water environment characteristics in coastal areas under the influences of climate change and human activities

Topic editors

Sha Lou — Tongji University, China

Gangfeng Ma — Old Dominion University, United States

Yi Pan — Hohai University, China

Citation

Lou, S., Ma, G., Pan, Y., eds. (2023). *Hydrodynamics and water environment characteristics in coastal areas under the influences of climate change and human activities*. Lausanne: Frontiers Media SA. doi: 10.3389/978-2-8325-2302-5

Table of contents

frontiers | Frontiers in Marine Science

TYPE Editorial
PUBLISHED 17 April 2023
DOI 10.3389/fmars.2023.1199807

OPEN ACCESS

EDITED AND REVIEWED BY
Marta Marcos,
University of the Balearic Islands, Spain

*CORRESPONDENCE
Yi Pan
panyi@hhu.edu.cn
Sha Lou
lousha@tongji.edu.cn

SPECIALTY SECTION
This article was submitted to Coastal Ocean Processes, a section of the journal Frontiers in Marine Science

RECEIVED 04 April 2023
ACCEPTED 06 April 2023
PUBLISHED 17 April 2023

CITATION
Pan Y and Lou S (2023) Editorial: Hydrodynamics and water environment characteristics in coastal areas under the influences of climate change and human activities.
Front. Mar. Sci. 10:1199807.
doi: 10.3389/fmars.2023.1199807

Editorial: Hydrodynamics and water environment characteristics in coastal areas under the influences of climate change and human activities

Yi Pan[1]* and Sha Lou[2]*

[1]College of Harbor, Coastal and Offshore Engineering, Hohai University, Nanjing, Jiangsu, China, [2]Department of Hydraulic Engineering, Tongji University, Shanghai, China

KEYWORDS

storm surge, coastal hydrodynamics, coastline evolution, river plume, aquatic vegetation

Editorial on the Research Topic
Hydrodynamics and water environment characteristics in coastal areas under the influences of climate change and human activities

The global apprehension regarding the effects of climate change and human activities on coastal regions has been extensively documented. Researchers worldwide have investigated the precise repercussions on extreme water level, coastal structures, coastal evolution, sediment, water exchange, and water quality (e.g., Weatherdon et al., 2016; Almar et al., 2021; Pan et al., 2022). However, the impact of climate change and human activities is systematic and intricate, and it is evident that more investigation is needed to further understand its ramifications. This Research Topic aims to provide a comprehensive understanding of the effects of climate change and human activities on coastal areas, specifically in terms of storm surge, coastal hydrodynamics, coastline evolution, river plume, and related topics.

The intensities of storm surges are highly likely to increase in the context of global climate change (IPCC, 2021), posing significant threats to coastal structures such as sea levees (e.g., Pan et al., 2020). Wu et al. conducted a comparative analysis of the performances of parametric wind models through numerical simulations of waves induced by tropical cyclones in the East China Sea. The study found that the asymmetric wind model exhibited superior performance in this region. Pan et al. used a numerical study scheme to investigate the effects of increasing maximum wind speed of tropical cyclones on the return periods of water levels in the Yangtze River Delta. The numerical study scheme involved 154 storm surges under historical and enhanced scenarios. It was found that the inner areas of the estuaries were more sensitive to the increasing maximum wind speed of tropical cyclones than the outer areas in terms of extreme water levels and corresponding return periods. Zhou et al. examined the combined effects of wave and surge overtopping on sea levees and proposed an empirical distribution to describe the distribution of normal stress on the levee induced by the combined wave and surge overtopping.

Coastal hydrodynamics can be significantly affected by both climate change and human activities. Wu et al. conducted a numerical simulation study to investigate the impact of Bohai Sea coastline changes on hydrodynamics and water exchange. The results indicated that coastline changes had a more significant effect on the semi-diurnal tide amplitude than the diurnal tide amplitude, causing a shift of the amphidromic point towards the offshore direction. Similarly, Zhang et al. used a numerical simulation approach to explore the hydrodynamic and sedimentary effects of tidal flat reclamation on adjacent areas. The study found that reclamation led to a decrease in intertidal area, a shift of the M4 shallow water tidal line towards the shore, a weakening of the flood tide advantage, and a reduction in suspended sediment concentration. However, the impact on net sediment transport was limited. Moreover, the construction of guide dikes in the estuarine area interfered with suspended sediment circulation and strengthened landward sediment transport. Kwak and Cho employed a three-dimensional numerical model to investigate water exchange between two neighboring bays, considering factors such as river flow, wind stress, sea surface heat flux, and tides. The study showed that river flow was the primary factor influencing water exchange between the bays during the summer. Wang et al. studied the effects of river runoff on coastal water quality after heavy rainfall, taking into account a complex coastline with two artificial islands. It is found that dissolved inorganic nitrogen (DIN) and nitrate-nitrogen (NO_3-N) concentrations in the study area remained high after the flooding process, while ammonium-nitrogen (NH_4-N) and orthophosphate (PO_4-P) showed a response with an ephemeral correspondence with the flooding process. Concentration recovery took approximately 5.5 days for DIN and NO_3-N and only approximately 1 day for NH_4-N and PO_4-P. Luo et al. used a numerical model to investigate the impacts of human activities on the coastal hydrodynamics surround Liyashan oyster reefs, based on which the impacts on oyster reefs were discussed.

Coastlines and tidal flats are experiencing a general eroding trend due to sea level rise and human activities. In Gao et al., the authors utilized field data and remote sensing images to investigate the impacts of climate change and sea level rise on the evolution of the coastline in the Shandong Peninsula between 2007 and 2020. They found that the coastline retreat was primarily driven by sea level rise due to global climate change. In Zhang et al., the authors used four phases of Sentinel-2 multispectral images and field data to investigate the spatial and temporal distributions of tidal flat surface sediment in the Doulonggang tidal flat in Jiangsu Province, China. Their study demonstrated that the sediment composition of the tidal flat coarsened over time, with an increase in sand content and a decrease in clay and silt contents. Shen et al. surveyed the sedimentation of cohesive sediments at the subtidal flat based on an 11-day field study at the subtidal region of the Hengsha Shoal adjacent to the turbidity maximum zone of the Yangtze Estuary. They concluded that the deposition process of cohesive sediments could be better explained by the simultaneous deposition paradigm compared to the exclusive deposition paradigm based on the direct data-model comparison of the bed level changes. Fu et al. utilized the coastal erosion vulnerability index (CVI) method to investigate the coastal erosion vulnerability of typical coasts on Hainan Island. Their study found that coral reef coasts were the least vulnerable areas to coastal erosion, while estuary coasts were identified as the most vulnerable areas.

The phenomenon of river plume and its associated effects on salinity have garnered significant attention in estuarine studies. In Xu et al., the movement characteristics of the river plume were analyzed using the particle image velocimetry (PIV) technique and the dye tracing method. The results revealed that the horizontal velocity of the plume could be effectively described by a 1/2 Gaussian distribution curve. It was also found that the turbulent kinetic energy increased with an increase in flow rate or density difference. In Matsoukis et al., the impact of river flow regimes on river delta salinization was explored using an idealized model. The study revealed that the magnitude of peak flow, time of occurrence, and the length of a hydrograph's tails could be vital parameters affecting stratification, freshwater residence, and renewal times. Cho et al. analyzed the variation in salinity gradient along the entire Sumjin River estuary and its effect on the exchange flow over fortnightly tidal cycles using observations and numerical model experiments. The study demonstrated the significance of salinity gradient variation in estuarine dynamics and its impact on water exchange.

The flow structure and sediment transport in estuaries can be impacted by aquatic vegetation. In Wu et al., laboratory experiments were conducted to study the effects of submerged vegetation with different flexibility on the flow structure and turbulence characteristics under unidirectional flow. Based on the experimental results, a turbulent kinetic energy model (TKE model) was established, which can be used to predict the turbulent kinetic energy and its shear production term within the vegetation canopy. Lou et al. proposed an improved model for incipient sediment suspension considering the effect of cylinder density to simulate the bottom sediment flux in the flow with cylinders. It is proved that the proposed model is capable of simulating sediment suspension under both unidirectional and combined wave–current flows reasonably well with the average the coefficients of determination and model skills greater than 0.8 and 0.64.

Author contributions

All authors listed have made a substantial, direct, and intellectual contribution to the work and approved it for publication.

Funding

The National Natural Science Foundation of China (51979098), the Major Scientific and Technological Project of the Ministry of Water Resources (SKS-2022025) and the Natural Science Foundation of Zhejiang Province (LZ22E090003).

Conflict of interest

The authors declare that the research was conducted in the absence of any commercial or financial relationships that could be construed as a potential conflict of interest.

Publisher's note

References

Almar, R., Ranasinghe, R., Bergsma, E. W., Diaz, H., Melet, A., Papa, F., et al. (2021). A global analysis of extreme coastal water levels with implications for potential coastal overtopping. *Nat. Commun.* 12 (1), 3775. doi: 10.1038/s41467-021-24008-9

IPCC (2021). "Summary for policymakers," in *Climate change 2021: the physical science basis. contribution of working group I to the sixth assessment report of the intergovernmental panel on climate change*. Eds. V. Masson-Delmotte, P. Zhai, A. Pirani, S. L. Connors, C. Péan, S. Berger, N. Caud, Y. Chen, L. Goldfarb, M. I. Gomis, M. Huang, K. Leitzell, E. Lonnoy, J. B. R. Matthews, T. K. Maycock, T. Waterfield, O. Yelekçi, R. Yu and B. Zhou (Cambridge, United Kingdom and New York, NY, USA: Cambridge University Press). doi: 10.1017/9781009157896.001

Pan, Y., Yin, S., Chen, Y. P., Yang, Y. B., Xu, C. Y., and Xu, Z. S. (2022). An experimental study on the evolution of a submerged berm under the effects of regular waves in low-energy conditions. *Coast. Eng* 176, 104169. doi: 10.1016/j.coastaleng.2022.104169

Pan, Y., Zhou, Z. J., and Chen, Y. P. (2020). An analysis of the downward-flushing flow on the crest of a levee under combined wave and surge overtopping. *Coast. Eng* 158, 103701. doi: 10.1016/j.coastaleng.2020.103701

Weatherdon, L. V., Magnan, A. K., Rogers, A. D., Sumaila, U. R., and Cheung, W. W. (2016). Observed and projected impacts of climate change on marine fisheries, aquaculture, coastal tourism, and human health: an update. *Front. Mar. Sci.* 3. doi: 10.3389/fmars.2016.00048

frontiers | Frontiers in Marine Science

TYPE Original Research
PUBLISHED 14 November 2022
DOI 10.3389/fmars.2022.1051868

OPEN ACCESS

EDITED BY
Sha Lou,
Tongji University, China

REVIEWED BY
Ya Ping Wang,
East China Normal University, China
Houjie Wang,
Ocean University of China, China

*CORRESPONDENCE
Feng Luo
fluo@hhu.edu.cn
Zhipeng Chen
zpchen@hhu.edu.cn

SPECIALTY SECTION
This article was submitted to Coastal Ocean Processes, a section of the journal Frontiers in Marine Science

RECEIVED 23 September 2022
ACCEPTED 28 October 2022
PUBLISHED 14 November 2022

CITATION
Luo F, Chen Z, Wu H, Zhu F, Zeng J and Quan W (2022) Hydrodynamic and sediment dynamic impact of human engineering activity on Liyashan oyster reefs, China. *Front. Mar. Sci.* 9:1051868. doi: 10.3389/fmars.2022.1051868

Hydrodynamic and sediment dynamic impact of human engineering activity on Liyashan oyster reefs, China

Feng Luo[1,2,3]*, Zhipeng Chen[1]*, Hongbo Wu[1], Fei Zhu[1], Jingwei Zeng[1] and Weimin Quan[4]

[1]College of Harbour, Coastal and Offshore Engineering, Hohai University, Nanjing, Jiangsu, China, [2]Nantong Ocean and Coastal Engineering Research Institute, Hohai University, Nantong, China, [3]Key Laboratory of Coastal Disaster and Defence, Ministry of Education, Nanjing, China, [4]East China Sea Fisheries Research Institute, Chinese Academy of Fishery Sciences, Shanghai, China

As human activity increases, coastal ecosystems are becoming increasingly vulnerable to a range of challenges. Oyster reefs are coastal ecosystems that provide habitats for a diverse range of marine species while also purifying water and providing natural coastal defense. However, because of human activity, global oyster reef areas have drastically diminished and are in grave danger. Simultaneously, it is impossible to determine the negative impact of human engineering activity on oyster reefs, due to the lack of intuitive and quantitative study methodologies. To address this issue, we applied a hydrodynamic model to analyze the impact on oyster reefs. First, we considered that human engineering activity, that is, coastal engineering, mainly affects the development of Liyashan Oyster Reefs by influencing hydrodynamics, sediment concentration, and bed-level evolution. We then applied MIKE3 to establish and validate a 3D hydrodynamic model of the southern part of the Yellow Sea around oyster reefs. Results showed that regional variations in flow velocity and suspended sediment concentration occurred in oyster reef waters, but the magnitude of these variations was limited. However, seabed elevation increased substantially in the Center Protection Area, which had a negative impact on oyster reefs. In general, our study provided a paradigm for analyzing the degree of impact on oyster reefs, showed the advantages of hydrodynamic models in quantitatively analyzing impact factors, and had reliable results.

KEYWORDS

oyster reefs, human activities, hydrodynamic model, sediment transport, coastal engineering, MIKE3

1 Introduction

An oyster reef is a biological reef formed by the long-term attachment and growth of oysters (Beck et al., 2011), and is widely distributed in coastal temperate and subtropical estuarine areas (Airoldi and Beck, 2007). As filter-feeding shellfish, oysters can effectively filter detritus and suspended sediment in water, which can considerably improve water quality and increase water clarity (Nelson et al., 2004; Newell, 2004; Dame et al., 2006). Simultaneously, oysters can absorb nutrients such as nitrogen and phosphorus from the water and promote denitrification to avoid harmful algal blooms and eutrophication outbreaks (Hoellein et al., 2014). Furthermore, oysters have a strong enrichment effect on Pb, Cd, and other heavy metals, which can effectively reduce heavy metal pollution in water (Chakraborty, 2017). In addition to purifying waters, oyster reefs perform more diverse ecosystem service functions (Peterson et al., 2003; Coen et al., 2007; Scyphers et al., 2011; Smaal et al., 2019). Similar to tropical coral reef systems, the complex three-dimensional reef structure of oyster reefs provides a habitat for a wide range of marine organisms, including benthic invertebrates, fish, and crustaceans (Rodney and Paynter, 2006). Oyster reefs are gaining increasing attention as a form of natural coastal defense (Morris et al., 2018), and a specific scale of oyster reefs can reduce wave energy, stabilize sediments, and thus reduce coastal erosion (Grabowski and Peterson, 2007; Scyphers et al., 2011).

Estuarine coastal areas are among the most densely populated and economically developed areas for human activity, with approximately 60% of the world's population living in them (Morris et al., 2018), within which oyster reefs are also distributed. Owing to the global acceleration of coastal urbanization, human intervention and modification of coastal areas are becoming more intensive (Heath, 2008; Rockström et al., 2009). However, while meeting social and economic development needs, human activity has also altered the natural characteristics of coastal areas, causing severe damage to oyster reefs worldwide. Oyster reefs globally have been severely degraded for nearly 100 years due to overfishing, pollution discharge, and coastal area development (Airoldi and Beck, 2007; Richardson et al., 2022), and 85% of oyster reefs have been extirpated (Jackson et al., 2001), making them one of the most endangered marine ecosystems (Beck et al., 2011). The Liyashan Oyster Reef is the largest living oyster reef in China, which not only has economic benefit but also plays a crucial role in the conservation of marine biological resources and ecological protection and has great scientific value. However, owing to the combined effect of the natural environment and human activity, the Liyashan Oyster Reef has been in continuous degradation for almost half a century, which has caused widespread concern among relevant departments and researchers. According to the results of the 2013 survey, the reef area decreased by approximately 38.8% compared to that in 2003 (Quan et al., 2016).

With the acceleration of urbanization, the population and infrastructure of coastal areas has increased dramatically, and changes in traditional fishing practices and engineering activities have severely affected oyster reef survival and development. Some engineered structures may cause changes to the nearshore seabed, further altering the coastal dynamic environment (Pan et al., 2022). Therefore, current research on the effect of human activity on oyster reefs has focused on direct damage to reefs from fishing and engineering projects. As coastal settlement populations have grown rapidly, overfishing has severely damaged the living environment of oyster reefs, resulting in the collapse and even extinction of local oysters (Jackson et al., 2001; Alleway and Connell, 2015). Waves generated by the stern of a ship during sailing can affect the attachment of oysters, and thus reduce their survival rate (Wall et al., 2005). The spatial structure of oyster reefs can be severely damaged by dredging, which leads to a drastic reduction in oyster production and oyster reef area (Rothschild et al., 1994). Simultaneously, sediment resuspension caused by dredging projects inundates oyster beds, generating high sediment loads and directly causing decline in oyster populations (Volety et al., 2009; Wilber and Clarke, 2010; Lin et al., 2021). All these human activities have a direct or indirect effect on the development of oyster reefs.

At present, studies on oyster reefs mainly focus on current status assessment, growth characteristics, impact of human activity, and reef structure. Studies on the systematic impact of changes in the hydrodynamic environment and bed level caused by coastal engineering on oyster reefs are limited. Oyster reef development is affected by a combination of environmental factors such as flow velocity, suspended sediment concentration, and bed level. Coastal engineering affects these environmental factors, which in turn has a substantial impact on the development of oyster reefs. Therefore, it is necessary to study the effects of changes in marine environmental factors on oyster reefs owing to coastal engineering.

Meanwhile, oysters, as benthic shellfish, live on the bottom of the water long-term and grow attached to the surface of the reef, mainly constrained by environmental conditions of the bottom waters. The two-dimensional model calculates the vertical average flow velocity and suspended sediment concentration. However, when the hydrodynamic environment of the water changes drastically, the distribution of these two physical quantities in the vertical direction becomes irregular, and the simulated values obtained by the two-dimensional model cannot reflect the vertical hydrodynamic characteristics of the sea well at this time.

The categories of impact studied in this paper are hydrodynamics and sediment dynamics. Specifically, we analyzed the current velocity, sediment concentration and bed level evolution. And the impact of human activity on oyster reefs discussed in this paper is mainly caused by coastal engineering,

including reclamation projects, port and dike construction, and channel construction. Based on the analysis results of oyster reef growth impact factors, a conceptual model was constructed to characterize the impact of human engineering activity on oyster reefs, as shown in Figure 1. Human engineering activity affects oyster reef development in many ways; coastal engineering mainly influences hydrodynamics, suspended sediment concentration, and bed-level evolution, which are also the basic influences considered in our modeling. First, flow velocity can affect the grazing rate of oysters (Beisel et al., 1998), and when the flow velocity is too high, oysters may not be able to feed (Lenihan et al., 1996). In addition, if the distribution of the vertical flow velocity is disturbed, oysters need to consume more energy to maintain their spatial position (Hart and Finelli, 1999). Second, high suspended sediment concentrations can damage the gill filaments of oysters and affect their filter feeding rates (La Peyre et al., 2020). It may also carry a greater load of contaminants, causing serious oyster poisoning (Edge et al., 2015). Third, oysters at the bottom are at risk of suffocation and death if the bed level is raised. Related studies have found that oysters die when the sediment layers exceed 40 and 60 mm in thickness (Comeau, 2014), and only a few millimeters of sediment can inhibit oyster larvae from colonizing the reef (Thomsen and McGlathery, 2006).

Therefore, to study the influence of changes in regional hydrodynamics and sediment dynamics characteristics caused by coastal engineering on oyster reefs, and to compensate for the shortcomings of the two-dimensional model, we used MIKE3 numerical simulation software to construct a three-dimensional hydrodynamic model. By calculating the vertical distribution of flow velocity and suspended sediment concentration before and after the project, as well as the variation of bed bottom, and combining it with the change in sea level in the oyster reef area, the impact of coastal engineering on Liyashan Oyster Reefs was comprehensively analyzed.

2 Materials and methods

2.1 Study area and study content

2.1.1 Study area

The Liyashan Oyster Reef is located in the intertidal zone on the southern side of the western section of the Xiaomiaohong Channel, Nantong, Jiangsu Province, China, as shown in Figure 2. The Xiaomiaohong Channel is located on the southern flank of the submarine radial sand ridges southwest of the Yellow Sea. The study area is characterized by irregular semidiurnal tides and a large tidal range, with neap tides reaching 2.5 m and spring tides reaching 6 m (Lin et al., 2021). Shielded by the wide Yaosha Shoal extending from east to west, the waves of the Xiaomiaohong Channel are small, and the multi-year average wave height is only 0.3 m (Zhang, 2004). In addition, the number of days without waves is approximately 50%, the average wave height when there are waves is 0.53 m, and the measured maximum wave height is 3.8 m (Zhang, 2004). The tidal flats adjacent to the oyster reefs are the transition zone from siltation to strong erosion on the southern part of the Jiangsu coast; therefore, the overall geological activity of the oyster reefs is relatively weak (Zhang, 2004).

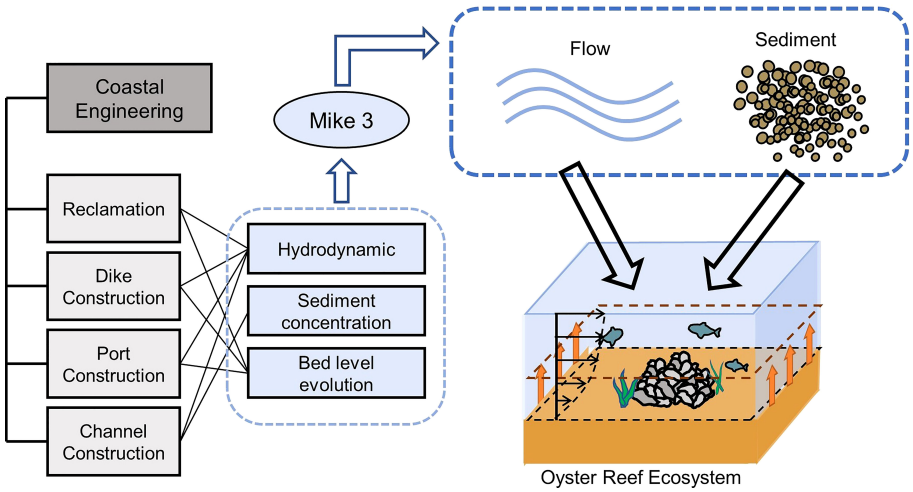

FIGURE 1
The framework of this study. The effects of the four main forms of coastal engineering on the three natural properties of waters and their relative relationships are shown. We abstracted these three natural properties as flow and sediment through the MIKE3 model and studied their variation at the three-dimensional scale to assess the impact of coastal engineering on oyster reefs.

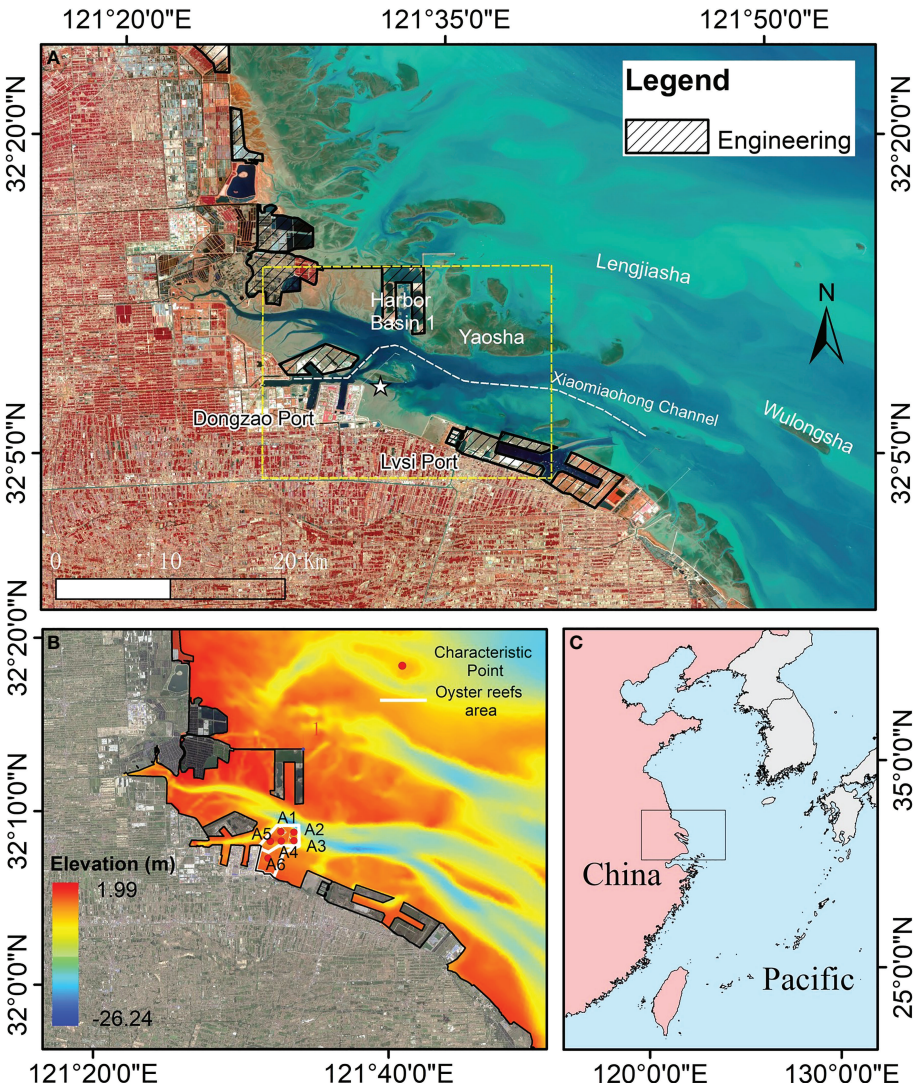

FIGURE 2
Location map of Liyashan Oyster Reefs. **(A)** Remote sensing image of the engineering area and oyster reefs (represented by a pentagram). **(B)** Selection of characteristic points in the oyster reef waters (A1 to A6). The elevation selection is National Vertical Datum 1985. **(C)** General location map of oyster reef area.

An important change in the depositional environment occurred in the study area approximately 5630 years ago, resulting in coarser sediment grain size, lower salinity of seawater, and lower concentration of suspended sediment, which created conditions suitable for oyster growth and oyster reef development (Wang et al., 2009). However, the high salinity of the study area currently is not suitable for the survival of the dominant species of local oysters; the low temperature in winter and high temperature in summer inhibit the growth of oysters to a certain extent, and the high concentration of sediment suspended in seawater is not suitable for the reproduction and development of oysters (Wang et al., 2009). In this context, human engineering activity may accelerate the deterioration of prospects for development of the Liyashan Oyster Reefs.

The reef area was divided into three functional areas: the center protection area (CPA), resource restoration area (RRA), and moderate utilization area (MUA), as shown in Figure 3. Oyster reefs and their biological resources are mainly concentrated in the CPA and RRA on the north side, whereas the reefs in the MUA near the shore on the south side are relatively sparsely distributed. The CPA is divided into two major blocks of dense oyster reef areas in the southeast and

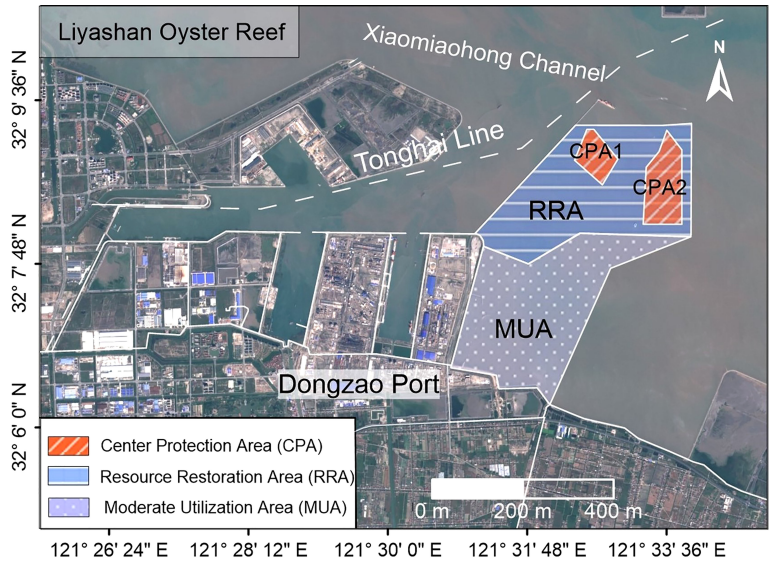

FIGURE 3
Relative position of the Liyashan Oyster Reefs to the coast and surrounding engineering. The Liyashan Oyster Reefs are divided into three types of functional areas, of which the Centre Protection Area is divided into two blocks.

northwest of the Liyashan Oyster Reefs, which are the key protection zones in the reef area.

2.1.2 Introduction to human engineering activity

In early 2012, Nantong City planned to conduct a series of coastal projects in Tongzhou Bay to promote the implementation of related development strategies. The main types of coastal engineering are mudflat reclamation and construction of guide dikes, as well as port and channel construction. It includes the formation of Harbor Basin 1 through the reclamation of Yaosha Shoal, the construction of an east-west guide dike to connect Harbor Basin 1 to the shoreline, the reclamation of Dongzao Port and Lvsi Port, and the construction of the channel connecting the Xiaomiaohong channel with Harbor Basin 1 and Dongzao Port. All the above construction areas are shaded in Figure 2A, except for the channel construction. The model considered the impact of channel construction in changing the seabed elevation in the channel area. The connections between the various types of engineering and environmental factors are shown in Figure 1.

The reclamation of the three coastal blocks northwest of Yaosha Shoal, the reclamation of Dongzao Port, and the construction of Lvsi Port were completed by 2013, whereas the construction of Harbor Basin 1 was completed by 2015. Therefore, in this paper, 2015 is considered as the dividing year, and all construction after 2015 is considered as completed in order to analyze the impact of the construction of coastal engineering through the model.

Considering human engineering activity, the impact of reclamation on oyster reefs is relatively important and should be discussed under the following two conditions. When the flow velocity is greater than 0.6 m/s or the suspended sediment concentration is higher than 0.5 kg/m^3 (Li and Shen, 2013), the increase in flow velocity and suspended sediment concentration will cause stress to the growth of oysters and interfere with the development of the reef, while a decrease in flow velocity and suspended sediment concentration will be beneficial to its further development. In contrast, when the flow velocity was less than 0.6 m/s or the suspended sediment concentration was less than 0.5 kg/m^3, the changes in flow velocity and suspended sediment concentration had no effect on oyster reefs. In addition, oyster reefs can be affected under three other conditions. First, since oyster growth requires calm water flow conditions, oyster growth is stressed when the distribution of water flow velocity in the vertical direction is disturbed and irregular (Figure 1) (Hart and Finelli, 1999). Second, when the vertical growth rate of oyster reefs was less than the sediment deposition rate, oyster reefs were at risk of degradation by the sediment cover (Figure 1) (Colden and Lipcius, 2015). At this time, enhanced siltation would considerably increase the risk of oyster reef degradation, whereas weakened siltation would be beneficial for reef development. Third, when slight scouring occurs, reef development is not affected, but when scouring is enhanced, the reef is at risk of erosion retreat (Gangnery et al., 2003; Soletchnik et al., 2007).

The construction of ports and dikes has almost the same impact as the reclamation project. The difference, however, is that ports and dikes have a smaller impact on the water, usually confined to the vicinity of the project area, and do not affect the natural properties of the water overall. Channel construction will not only change the hydrodynamic and siltation environments in the sea, but more importantly, the suspended materials generated by dredging during waterway construction will cause great harm to the organs of oysters, which will interfere with the normal development of oyster reefs.

To compare the effects of human engineering activities on the hydrodynamic environment and the bed-level change in the oyster reef area, A1–A3 were taken from the CPA, A4–A5 from the RRA, and A6 from the MUA (Figure 2B) for quantitative analysis of the effect of human engineering activity on tidal flow velocity, suspended sediment concentration, and siltation distribution in the oyster reef area.

2.2 Model setup

2.2.1 Model description

The MIKE3 Flow Model FM is based on a flexible mesh approach and it has been developed for applications in oceanographic, coastal and estuarine environments. The system is based on the numerical solution of the three-dimensional incompressible Reynolds averaged Navier-Stokes equations invoking the assumptions of Boussinesq and of hydrostatic pressure. At the same time, the free surface is taken into account using a sigma coordinate transformation approach. The main equations involved include equations (1) to (8) (DHI, 2012), and the parameters used in the MIKE3 model are listed in Table 1.

Among them, equations (1) to (5) are basic equations of water flow.

TABLE 1 Model parameters.

Parameter	Value	Definition
g	9.81 N kg^{-1}	Gravitational acceleration
ρ	1027 kg m^{-3}	Density of water
ρ_{sed}	2650 kg m^{-3}	Specific density sediment
f	0	Coriolis parameter
A	0.001 N s m^{-2}	Viscosity coefficient
n	0.014 s m$^{-1/3}$	Friction coefficient (Manning)
α	5.5 m s^{-1}	Settling coefficient
ω_s	0.0005 m s^{-1}	Sediment settling velocity
τ_d	0.2 N m^{-2}	Critical bed shear stress of deposition
τ_e	0.5 N m^{-2}	Critical bed shear stress of erosion
M	5*10^{-5} kg m^{-3} s^{-1}	Erosion coefficient
γ_d	550 kg m^{-3}	Dry capacity of bed sediment

The continuous equation is characterized as:

$$\frac{\partial \mathbf{u}}{\partial \mathbf{x}} + \frac{\partial \mathbf{v}}{\partial \mathbf{y}} + \frac{\partial \boldsymbol{\omega}}{\partial \mathbf{z}} = \mathbf{0} \tag{1}$$

The momentum equation is characterized as:

$$\begin{aligned} &\frac{\partial \mathbf{u}}{\partial \mathbf{t}} + \frac{\partial \mathbf{u}^2}{\partial \mathbf{x}} + \frac{\partial \mathbf{vu}}{\partial \mathbf{y}} + \frac{\partial \boldsymbol{\omega}\mathbf{u}}{\partial \mathbf{z}} \\ &= -\mathbf{g}\frac{\partial \boldsymbol{\eta}}{\partial \mathbf{x}} - \frac{\mathbf{1}}{\boldsymbol{\rho}_0}\frac{\partial \mathbf{P_a}}{\partial \mathbf{x}} \\ &- \frac{\mathbf{g}}{\boldsymbol{\rho}_0}\int_{\mathbf{z}}^{\boldsymbol{\eta}} \frac{\partial \boldsymbol{\rho}}{\partial \mathbf{x}} \mathbf{dz} - \frac{1}{\boldsymbol{\rho}_0 \mathbf{h}}\left(\frac{\partial \mathbf{S_{xx}}}{\partial \mathbf{x}} + \frac{\partial \mathbf{S_{xy}}}{\partial \mathbf{x}}\right) \\ &+ \frac{\partial}{\partial \mathbf{z}}\left(\mathbf{u_t}\frac{\partial \mathbf{u}}{\partial \mathbf{z}}\right) + \mathbf{F_u} + \mathbf{fv} \end{aligned} \tag{2}$$

$$\begin{aligned} &\frac{\partial \mathbf{v}}{\partial \mathbf{t}} + \frac{\partial \mathbf{v}^2}{\partial \mathbf{y}} + \frac{\partial \mathbf{uv}}{\partial \mathbf{x}} + \frac{\partial \boldsymbol{\omega}\mathbf{v}}{\partial \mathbf{z}} \\ &= -\mathbf{g}\frac{\partial \boldsymbol{\eta}}{\partial \mathbf{y}} - \frac{1}{\boldsymbol{\rho}_0}\frac{\partial \mathbf{P_a}}{\partial \mathbf{y}} \\ &- \frac{\mathbf{g}}{\boldsymbol{\rho}_0}\int_{\mathbf{z}}^{\boldsymbol{\eta}} \frac{\partial \boldsymbol{\rho}}{\partial \mathbf{y}} \mathbf{dz} - \frac{1}{\boldsymbol{\rho}_0 \mathbf{h}}\left(\frac{\partial \mathbf{S_{yx}}}{\partial \mathbf{x}} + \frac{\partial \mathbf{S_{yy}}}{\partial \mathbf{y}}\right) \\ &+ \frac{\partial}{\partial \mathbf{z}}\left(\mathbf{u_t}\frac{\partial \mathbf{v}}{\partial \mathbf{z}}\right) + \mathbf{F_v} + \mathbf{fu} \end{aligned} \tag{3}$$

In equations (2) and (3):

$$\mathbf{F_u} = \frac{\partial}{\partial \mathbf{y}}\left(\mathbf{A}\left(\frac{\partial \mathbf{u}}{\partial \mathbf{y}} + \frac{\partial \mathbf{v}}{\partial \mathbf{x}}\right)\right) + \frac{\partial}{\partial \mathbf{x}}\left(2\mathbf{A}\frac{\partial \mathbf{u}}{\partial \mathbf{x}}\right) \tag{4}$$

$$\mathbf{F_v} = \frac{\partial}{\partial \mathbf{x}}\left(\mathbf{A}\left(\frac{\partial \mathbf{u}}{\partial \mathbf{y}} + \frac{\partial \mathbf{v}}{\partial \mathbf{x}}\right)\right) + \frac{\partial}{\partial \mathbf{y}}\left(2\mathbf{A}\frac{\partial \mathbf{v}}{\partial \mathbf{y}}\right) \tag{5}$$

Where, t is time; η is water surface fluctuation; d is still water depth; h is total water depth ($h = d + \eta$); u, v, ω are flow velocity vectors along x, y, z direction respectively; g is gravitational acceleration; f is Coriolis parameter ($f = 2\omega sin\varphi$, ω is the angle of earth rotation, φ is local latitude); S_{xx}, S_{xy}, S_{yx}, S_{yy} are the wave radiation stresses; u_t is the vertical turbulence coefficient; P_α is the atmospheric pressure; ρ is the density of water; ρ_0 is the relative density of water; F_u, F_v are the stress terms in x and y directions; A is the viscosity coefficient.

The remaining equations (6) to (8) are sediment transportation equations (DHI, 2014).

Convective diffusion equation is characterized as:

$$\begin{aligned} &\frac{\partial \mathbf{S}}{\partial \mathbf{t}} + \frac{\partial \mathbf{uS}}{\partial \mathbf{x}} + \frac{\partial \mathbf{vS}}{\partial \mathbf{y}} + \frac{\partial \boldsymbol{\omega}\mathbf{S}}{\partial \mathbf{z}} \\ &= \frac{\partial}{\partial \mathbf{x}}\left(\boldsymbol{\epsilon}_\mathbf{x}\frac{\partial \mathbf{S}}{\partial \mathbf{x}}\right) + \frac{\partial}{\partial \mathbf{y}}\left(\boldsymbol{\epsilon}_\mathbf{y}\frac{\partial \mathbf{S}}{\partial \mathbf{y}}\right) + \frac{\partial}{\partial \mathbf{z}}\left(\boldsymbol{\epsilon}_\mathbf{z}\frac{\partial \mathbf{S}}{\partial \mathbf{z}}\right) + \frac{\mathbf{F_s}}{\mathbf{h} + \boldsymbol{\zeta}} \end{aligned} \tag{6}$$

Where, ϵ_x, ϵ_y, and ϵ_z are the sediment diffusion coefficients in the x, y, and z directions, respectively; S is the sediment concentration of water; F_s is the sediment source and sink function or bed level change function, also known as near-bottom sediment flux, given by equation (7).

$$F_s\left\{\alpha\omega_s S\left(\frac{\tau_b}{\tau_d}-1\right),\ \tau_b \le \tau_d \quad 0,\ \tau_d < \tau_b < \tau_e \quad M\left(\frac{\tau_b}{\tau_d}-1\right),\tau_b \ge \tau_e\right. \tag{7}$$

In equation (7), α is the settling coefficient; ω_s is the sediment settling velocity; τ_b is the shear stress at the bottom of bed; τ_d is the critical siltation shear stress, determined by experiments or field data; τ_e is the critical scouring shear stress, and is related to the bed sand dry bulk weight, porosity and other parameters; M is the scouring coefficient.

Equation of bed level change is characterized as:

$$\gamma_d \frac{\partial \eta_b}{\partial t} + F_S = 0 \tag{8}$$

In Eq. (8), γ_d is the dry capacity of bed sediment; η_b is the bed level.

2.2.2 Mesh and model parameters

The calculation domain of the hydrodynamic model is shown in Figure 4. The model area was set to approximately 3770 km^2, with a non-structural triangular grid for dissection. Furthermore, local refinements were conducted in the near-shore area. The minimum grid resolution of the model was 30 m, the number of grid cells was 43 640, and the number of grid nodes was 22 162. Three outer sea open boundaries were set in the model, including south, east, and north, all of which were provided by the tide model of the offshore waters of Jiangsu Province for tidal level boundary conditions.

2.3 Model validation

In order to verify the accuracy of the model, the measured data of tide level, flow velocity and suspended sediment concentration from December 22, 2018 to January 22, 2019 were applied. And the distribution of the validation points is shown in Figure 4.

The actual measurement data used in the paper were acquired from the hydrodynamic and sediment measurements conducted by the CCCC Third Harbor Consultants Co., LTD. in the waters of Tongzhou Bay from December 2018 to January 2019. Tidal level measuring stations A and B used the AQUAlogger 520p tide gauge from AQUATEC, which automatically records water level values every 10 minutes and uses 40 sets of water level values spaced 1 second apart each time for wave abatement operations. Each tidal current measurement station uses NORTEK's Acoustic Doppler Current Profiler (ADCP) for vertical tidal current velocity measurement. Finally, water samples were collected in six layers using a horizontal water collector on six tidal current measuring stations, with a sampling volume of 500 ml each. The suspended sediment concentration at the measurement points was obtained by filtering, drying and weighing operations.

During the measurement period, the average wind speed was between 6.9 m/s and 8.1 m/s, and the maximum wind speed was within 14.2 m/s. The wind direction was mainly northwest to north, and the sea state was below level 4. Hydrodynamic measurements were carried out in strict accordance with technical requirements and specifications, and all measuring instruments were calibrated before the measurements to ensure the reliability of the original data.

According to the measured data to determine the tide level validation period from December 23, 2018 00:00 to January 22,

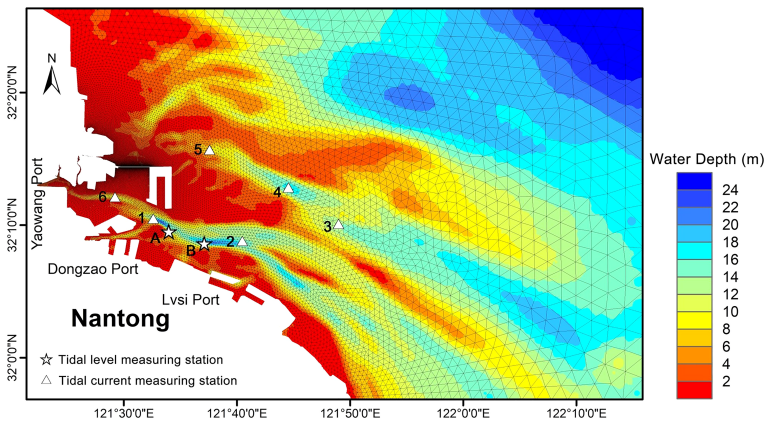

FIGURE 4
Model grid of study area, and locations of two tidal level measuring stations **(A, B)** and six tidal current measuring stations (1–6). The model grid is refined in the nearshore waters, and the water depth in the surrounding waters is represented by a gradual change from red to blue. The map also identifies the names of adjacent ports and cities. In addition, the water depth corresponds to the National Vertical Datum 1985.

2019 23:00, the flow velocity and sediment concentration validation period from December 22, 2018 16:00 to December 23, 2018 18:00. Among them, the tide level validation stations were the tidal level measuring station A and tidal level measuring station B, and the flow velocity and sediment validation stations were points 1-6 as shown in Figure 4. In view of the limitation of space, only the tidal level validation results of tidal level measuring station A and tidal level measuring station B, along with the flow velocity and sediment concentration validation results of station 1 are listed in this paper, as shown in Figures 5–7. The validation results show that the difference between the calculated value and the actual measurement is slight, and the process is in good agreement, indicating that the model can be relatively accurate to simulate the hydrodynamic conditions of coastal area. Due to space limitations, the validation of flow velocity, flow direction and sediment concentration at the station 1-6 in the surface and bottom layer is shown in the Supplementary Figures 1-3.

Also, to quantitatively show the results of the model validation, we evaluated the differences between the measured and simulated values of flow velocity, flow direction, and sediment concentration, which are shown in Supplementary Tables 2, 3. We use Pearson correlation coefficient to evaluate the correlation between flow velocity and flow direction, the higher the result tends to 1, the better the model simulation results. Supplementary Table 2 shows that the Pearson correlation coefficient for 87.5 percent of the flow velocity exceeds 0.9, indicating that the model simulated flow velocity distribution is very close to the actual situation. Supplementary Table 2 also shows that the Pearson correlation coefficient for 83.3 percent of the flow direction exceeds 0.8, indicating that the model simulated flow distribution is also quite close to the actual situation. In addition, considering the relatively large difference in simulation accuracy of sediment concentration in the mathematical model, we use Mean Absolute Percentage Error (MAPE) to evaluate, as shown in Supplementary Table 3. The results show that the MAPE of 75 percent sediment concentration is less than 0.1, and the maximum MAPE is 0.152. Considering the difference of sediment concentration distribution in Figure 8, the error of the model is acceptable and basically does not affect the analysis of sediment concentration distribution.

3 Results

Although the Liyashan Oyster Reefs are in a state of degradation due to high salinity, low winter temperature, and high summer temperature, as well as high suspended sediment concentration of seawater (Wang et al., 2009), disturbance to the oyster reefs by human engineering activity still cannot be ignored. As benthic shellfish, oysters always live on the seabed and grow on the surface of the reef, which is mainly affected by the environment of the bottom waters. Human engineering

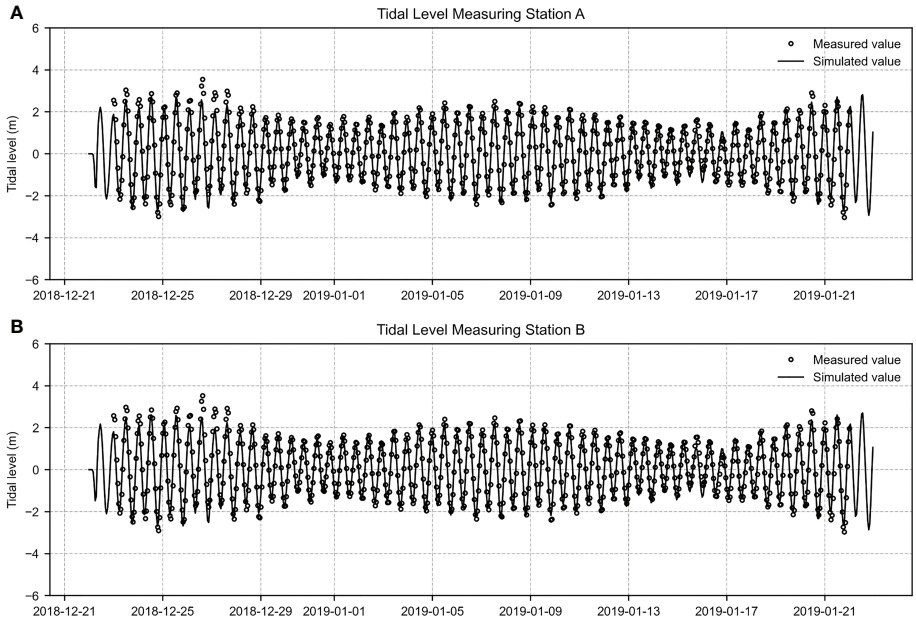

FIGURE 5
Comparison of tidal level measurement data points with model simulated tidal level fit curves for **(A)** Tidal Level Measuring Station A and **(B)** Tidal Level Measuring Station B from December 22, 2018 to January 22, 2019.

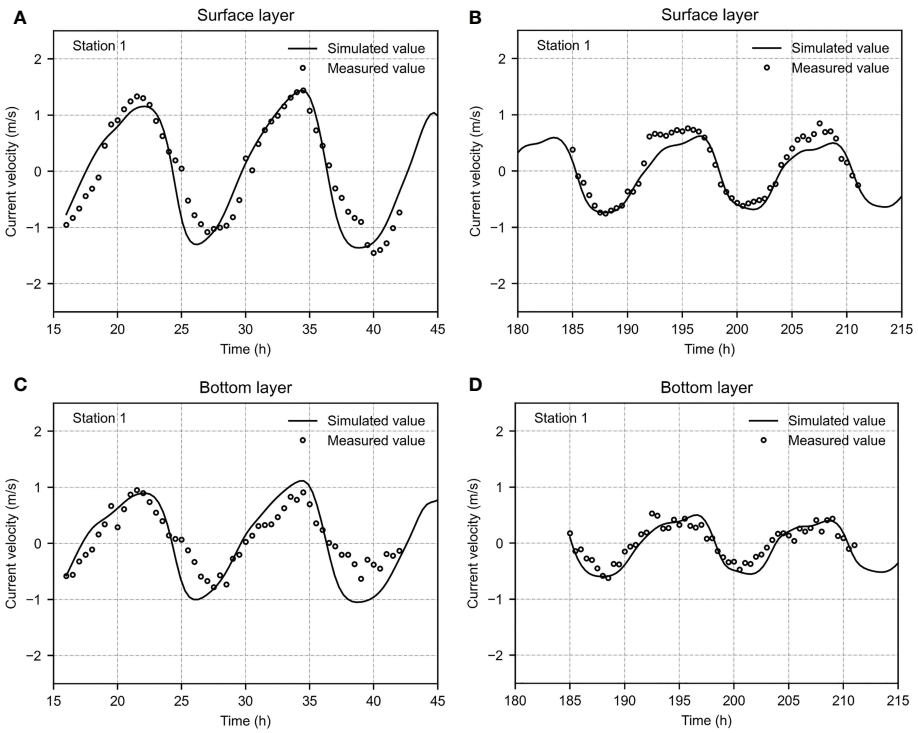

FIGURE 6
Validation of surface & bottom flow velocity during spring & neap tide at Station 1. **(A)** Surface current velocity at Station 1 during spring tide. **(B)** Surface current velocity at Station 1 during neap tide. **(C)** Bottom current velocity at Station 1 during spring tide. **(D)** Bottom current velocity at Station 1 during neap tide.

activity affects oyster growth by influencing the environmental factors of the water column, which in turn hinders the development of oyster reefs. However, human engineering activity directly leads to the degradation of reef cover by promoting sediment deposition, which is also the most important reef stress factor.

3.1 Analysis of the impact of the flow velocity

The dynamic environment of the Liyashan Oyster Reefs is mainly controlled by progressive waves in the East China Sea. Tidal waves are in the form of standing waves, and the currents reciprocate. The distribution of bottom flow velocity changes in the oyster reef waters before and after human engineering activity (Figure 9) showed that bottom flow velocity in the reef area generally decreased due to human engineering activity. The decrease in flow velocity is most obvious in the CPA and RRA, and largest in the area near the inlet channel of Dongzao Port and the side of Xiaomiaohong Channel, with the largest decrease of 0.15 m/s. The decrease in flow velocity in the near-shore MUA was smaller, and in the reef area showed a trend of increasing offshore. In addition, a comparison of the surface and bottom flow fields during spring and neap tides in the oyster reef area before and after human engineering activity is shown in Supplementary Figure 4. It can be seen that the flow direction in the oyster reef waters, which is our concern, remained stable.

To further study the influence of human engineering activity on the vertical distribution of tidal flow velocity in the oyster reef area, a logarithmic distribution fit was conducted to further determine whether the vertical distribution of flow velocity is stable and whether stable current conditions can have a positive effect on the growth of oyster reefs. The simulated values of the vertical flow velocity at the characteristic points before and after human engineering activity were plotted and fitted with a logarithmic distribution, as shown in Figure 10. In this study, the coefficient of determination R and root mean square error (RMSE) were used to evaluate the fitting effect of the vertical flow distribution to the logarithmic distribution. The values of R range from [0, 1]; the closer R is to 1, the better the fit to the logarithmic distribution. Similarly, the closer the RMSE is to 0, the more effective the fit to the logarithmic distribution.

The coefficient of determination R and RMSE for the fit to logarithmic distribution of flow velocity at each characteristic point is listed in Supplementary Table 1. By combining Figure 9

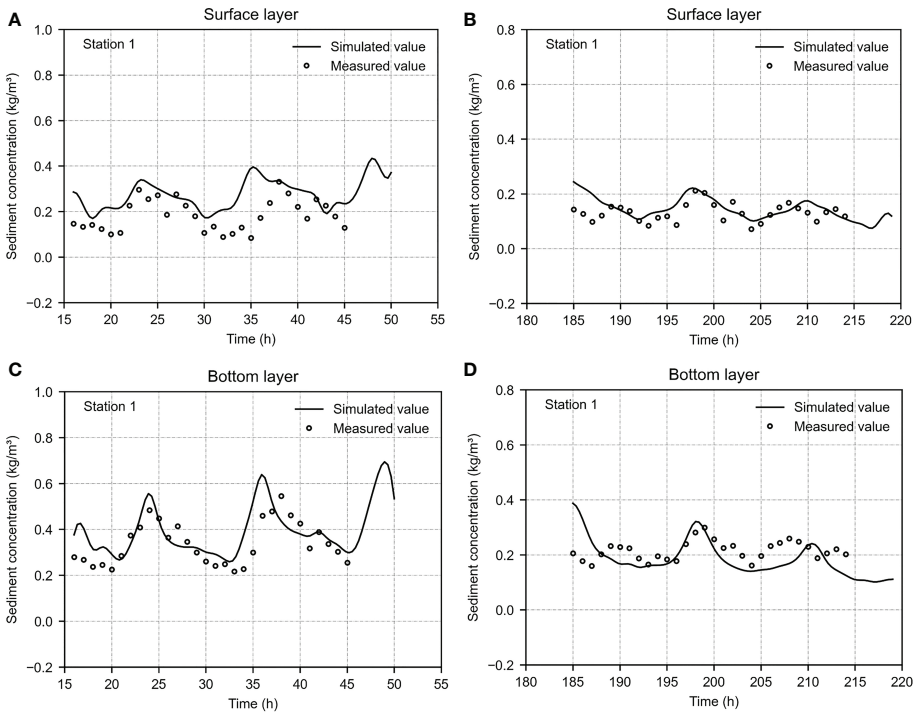

FIGURE 7
Validation of surface & bottom sediment concentration during spring & neap tide at Station 1. **(A)** Surface sediment concentration at Station 1 during spring tide. **(B)** Surface sediment concentration at Station 1 during neap tide. **(C)** Bottom sediment concentration at Station 1 during spring tide. **(D)** Bottom sediment concentration at Station 1 during neap tide.

with Supplementary Figure 5, it can be seen that before human engineering activity, the flow velocities in CPA1 (A2), RRA (A4, A5), and MUA (A6) basically conformed to the logarithmic distribution in the vertical direction, and CPA2 (A2, A3) was close to the Xiaomiaohong Channel, which had a slightly poorer fit to the logarithmic distribution of flow velocity. The positions of A1–A6 are shown in Figure 1. The overall flow pattern in the oyster reef area was stable, surface flow velocity was greater than bottom flow velocity, vertical flow velocity was in line with the logarithmic distribution, and the flow velocity in the CPA was the largest. Flow velocity in the reef area decreased owing to human engineering activity; however, the law that the vertical flow velocity conforms to the logarithmic distribution remains unchanged, and the water flow remains stable.

3.2 Analysis of changes in the suspended sediment

The implementation of human engineering activity will lead to simultaneous changes in the suspended sediment environment in oyster reef areas. Unlike the changes in flow velocity, the changes in suspended sediment concentration in the vertical direction were not consistent, and human engineering activity led to an overall decreasing trend in the surface suspended sediment concentration in the reef areas, whereas changes in the bottom suspended sediment concentration were distributed regionally (Figure 11 and Supplementary Figure 6).

For the bottom suspended sediment concentration, the southwest side of the RRA showed the greatest change during spring tide. The concentration of suspended sediment in the CPA remained at 0.30–0.40 kg/m^3 (basically unchanged); in the southwest side of the RRA a clear change was noted, from 0.20–0.40 kg/m^3 to 0.17–0.35 kg/m^3, with the largest reduction value of 0.15 kg/m^3, while the rest of the zone showed less change. In MUA, the concentration of suspended sediment increased nearshore and decreased offshore, and the change value was within 0.05 kg/m^3. During neap tide, the change in suspended sediment concentration was smaller than that during spring tide, and was most obvious in the MUA. The concentration of suspended sediment in CPA of oyster reefs had decreased, from 0.12–0.18 kg/m^3 to 0.1–0.16 kg/m^3, with a maximum reduction of 0.03 kg/m^3; in the southeast and southwest sides of the RRA it decreased significantly, from 0.15–0.18 kg/m^3 to 0.13–0.15 kg/m^3 in the southeast side, with a maximum reduction of 0.02 kg/m^3; in the southwest side it decreased from 0.10–0.13 kg/m^3 to 0.08–0.11 kg/m^3, with a maximum reduction of 0.02 kg/m^3; the remaining areas had basically no

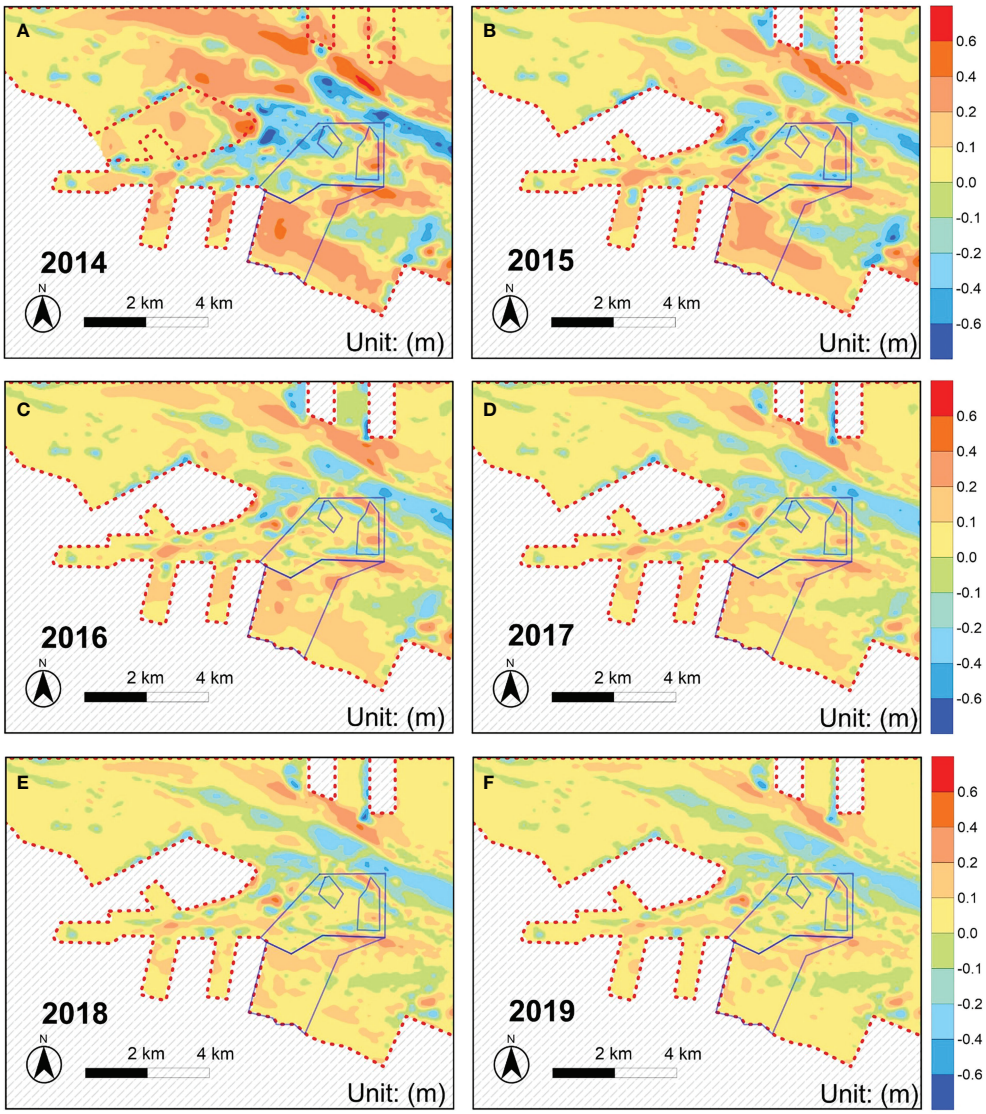

FIGURE 8
Distribution of bed level in oyster reef waters before (2014) and after (2015–2019) human engineering activity. The locations of oyster reefs and their subdivisions are marked on the figures with solid blue lines. **(A–F)** 2014–2019.

change; in the MUA it was increasing nearshore and decreasing offshore, and the variation was within 0.04 kg/m^3.

3.3 Analysis of the impact of bed level

Changes in the hydrodynamic environment caused by human engineering activity inevitably led to changes in the intertidal bed level. Figures 8, 12, 13 show bed-level distribution and its variation from the model simulation. As the model does not consider the effect of natural sedimentation, the results shown in the figure can be regarded as being caused by engineering alone. As shown in Figures 8 and 12, human engineering activity did not change the overall trend of siltation pattern in oyster reefs, but the local siltation pattern in the CPA and RRA changed significantly, and the rate of bed-level change in the reef areas varied from −0.20 m/a to 0.40 m/a.

Figure 13 shows the annual variation in bed-level change intensity at characteristic points before and after human engineering activity, where 2014 and 2015–2019 show the bed-level change before and after human engineering activity. From Figures 8, 12, 13, it can be seen that after human engineering activity, the siltation in CPA1 is clearly enhanced, from the combination of scouring and siltation to overall siltation, and

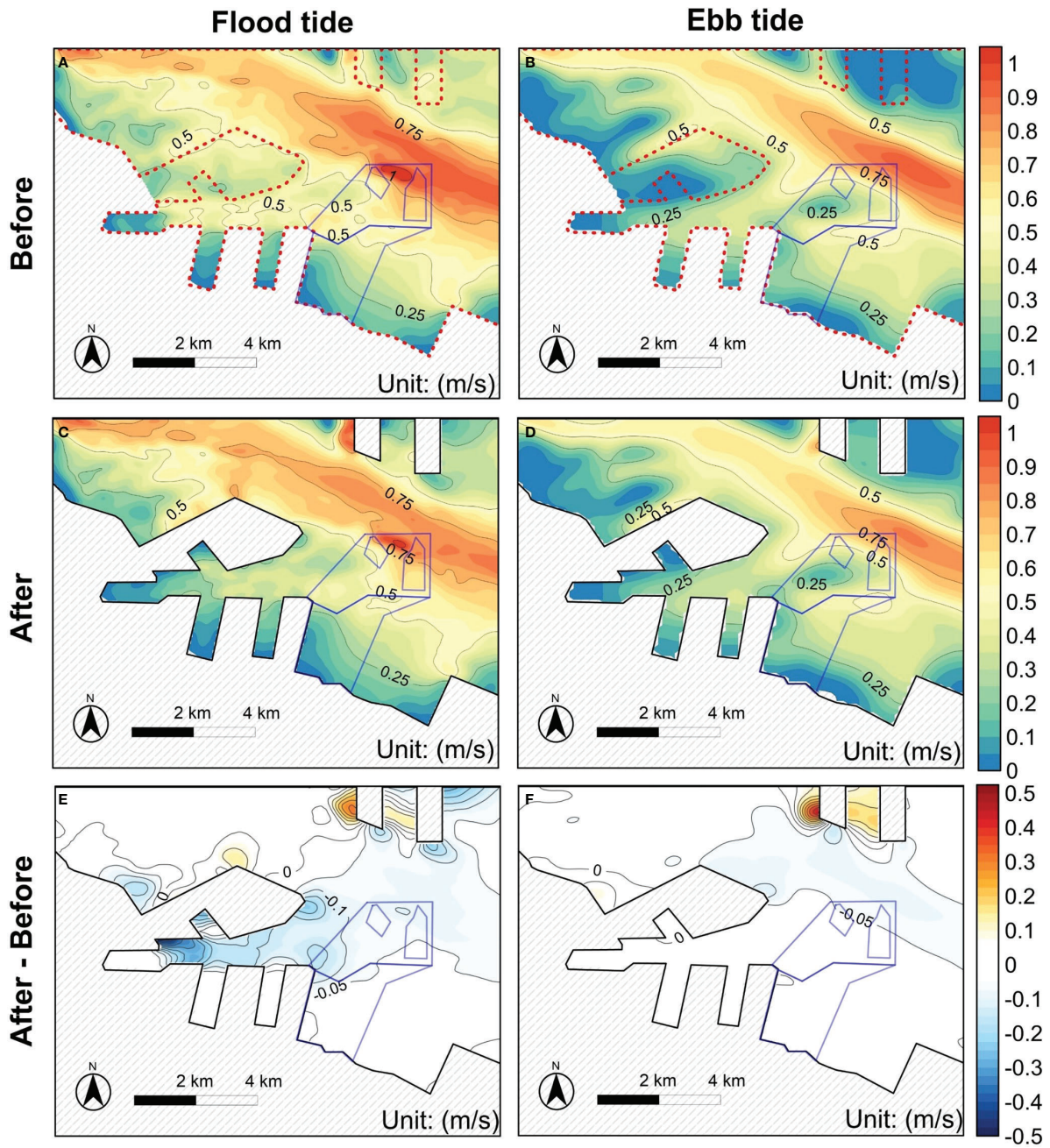

FIGURE 9
Comparison of bottom flow velocity during spring tide before and after construction of the project. The locations of oyster reefs and their subdivisions are marked on the figures with solid blue lines. Bottom flow velocity distribution during **(A)** peak flood tide and **(B)** peak ebb tide of the spring tide before construction of the project. Bottom flow velocity distribution during **(C)** peak flood tide and **(D)** peak ebb tide of the spring tide after construction of the project. Difference in bottom flow velocity distribution during **(E)** peak flood tide and **(F)** peak ebb tide of the spring tide before and after construction (flow velocity before construction minus flow velocity after construction).

annual siltation increased to 0.03–0.15 m, with a maximum increase value of 0.3 m, and then decreased annually, and tended to balance scouring and siltation. At the northeast corner of CPA2, annual bed-level change was altered from scouring to siltation, and maximum annual siltation was 0.2 m, with an average increase of 0.2 m, while the siltation in the rest of the area was weakened, with a maximum decrease of 0.15 m. The central local area favored scouring and maximum annual scouring volume was 0.1 m, the siltation on the south side had weakened, however, maximum annual siltation volume still maintained

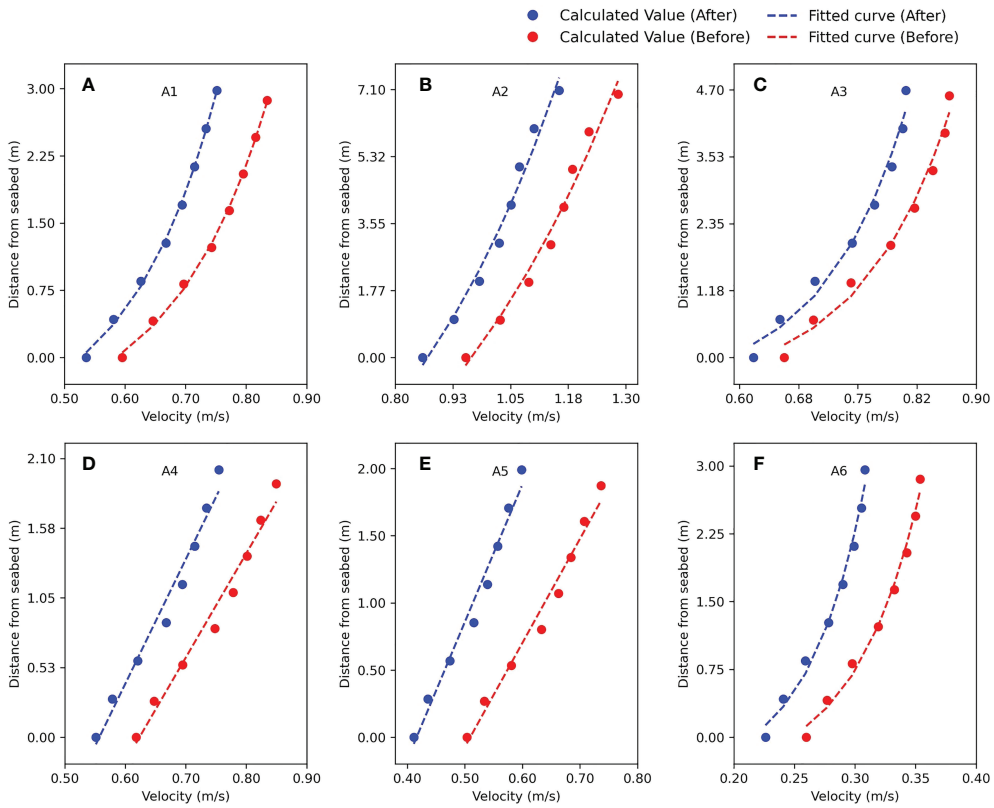

FIGURE 10
Calculated values and fitted curves of vertical flow velocity at characteristic points of peak flood tide of spring tide before and after human engineering activity. **(A–F)** Characteristic points A1 to A6.

around 0.3 m annually. The overall siltation in the RRA was enhanced, and the area near the inlet channel of Dongzao Port changed from scouring to siltation, average annual siltation was 0.1 m, the rest of the area was slightly weakened, the deep trough on the south side of the boundary still maintained the trend of scouring, and the RRA tended towards slight scouring or slight siltation with the evolution. The MUA still maintained overall siltation, however, annual siltation volume generally decreased by about 0.05 m, and siltation intensity gradually decreased as the evolution proceeded, and finally, annual siltation volume stabilized at approximately 0.07 m.

4 Discussion

4.1 Analysis of the impact of human engineering activity on oyster reefs

Human engineering activity affects the growth of oysters and thus the growth of reefs indirectly by changing the flow velocity and suspended sediment concentration in the water column on the one hand, and directly affects the evolution of reefs by changing the bed level on the other hand.

4.1.1 Flow velocity stress

Both excessively fast and turbulent flow velocities are detrimental to oyster attachment growth. According to related specifications, flow velocity during the oyster breeding period should be no more than 0.6 m/s, so the evaluation standard for flow velocity is 0.6 m/s. Human engineering activity did not change the logarithmic distribution law of the vertical flow velocity. During spring tide, the flow velocity was high and exceeded 0.6 m/s in some areas, which was conducive to oyster attachment and reproduction due to the decrease in flow velocity caused by human engineering activity. In the rest of the area, the flow velocity was low, and the decrease in flow velocity had no effect on oyster growth. During neap tide, the flow velocity was below 0.6 m/s, and the decrease in flow velocity had no effect on the growth of oysters. In general, changes in the hydrodynamic conditions of the Liyashan Oyster Reef waters caused by human engineering activity would not have a significant effect on oyster reef development.

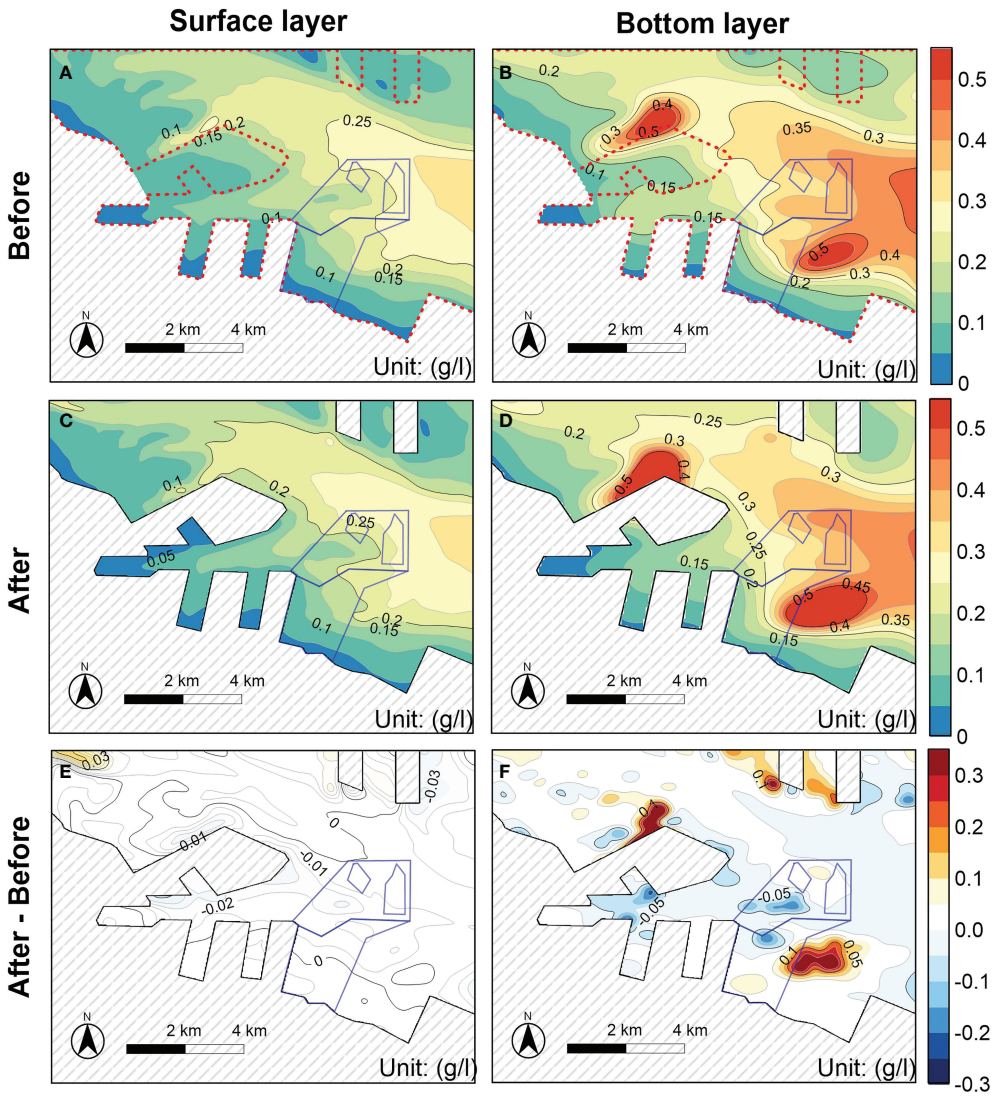

FIGURE 11
Comparison of surface and bottom sediment concentrations before and after human engineering activity. The locations of oyster reefs and their subdivisions are marked on the figures with solid blue lines. **(A)** Surface and **(B)** bottom sediment concentration distribution during the flood tide of spring tide before construction of the project. **(C)** Surface and **(D)** bottom sediment concentration distribution during the flood tide of spring tide after construction of the project. Difference in **(E)** surface and **(F)** bottom sediment concentration distribution during the flood tide of spring tide before and after construction (sediment concentration before construction minus sediment concentration after construction).

4.1.2 Suspended sediment stress

The survival rate of oysters was not affected by low concentrations of suspended sediments. However, when concentration of suspended sediment exceeds 0.5 kg/m^3, the growth of Kumamoto Oysters, which is the dominant species, will be inhibited, so 0.5 kg/m^3 is used as the evaluation standard of suspended sediment concentration. When the concentration of suspended sediment is greater than 0.5 kg/m^3, the increase will harm oyster development; however, when the concentration of suspended sediment is less than 0.5 kg/m^3, the effect of suspended sediment concentration on oysters can be ignored.

After human engineering activity, the bottom suspended sediment concentration in the reef areas showed regional changes. The suspended sediment concentration on the nearshore side of the MUA increased locally, while in other areas it generally decreased. The bottom suspended sediment concentration remained below 0.5 kg/m^3, and the change in suspended sediment concentration under such a concentration

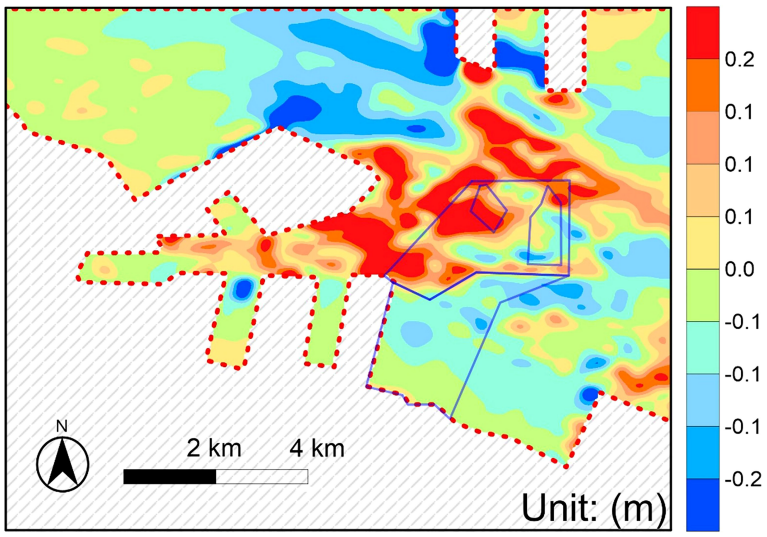

FIGURE 12
Difference in the distribution of bed-level change in oyster reef waters before (2014) and after (2019) human engineering activity. The locations of oyster reefs and their subdivisions are marked on the figures with solid blue lines. .

range would not affect the growth of oysters. Therefore, changes in the bottom suspended sediment concentration caused by human engineering activity would not have significant effect on the growth of oysters and the development of reefs in the Liyashan Oyster Reef waters.

4.1.3 Impact of bed-level change

Sediment deposition is the most important cause of oyster reef degradation in the Liyashan Oyster Reefs. Sediment covering the surface of the reefs directly leads to oyster

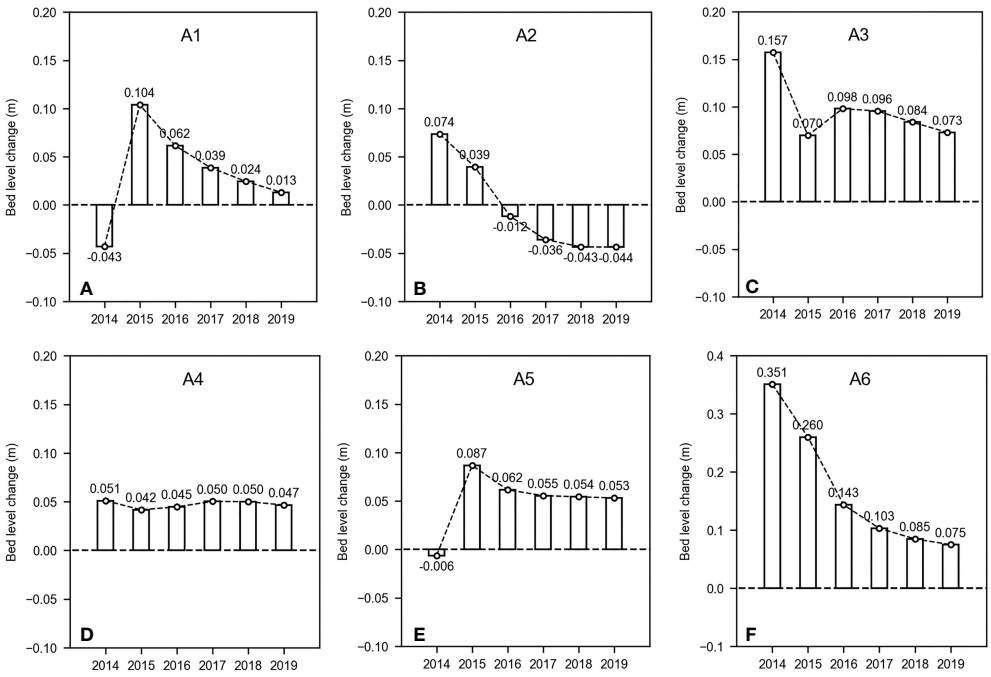

FIGURE 13
Annual variation of bed-level change intensity at characteristic points before and after human engineering activity. **(A–F)** Characteristic points A1 to A6.

suffocation or even death, resulting in a reduction in the reef area.

After human engineering activity, the siltation of CPA1 was enhanced, the northeast corner of CPA2 changed from scouring to siltation, scouring of the central area was enhanced, and siltation of the southern area was weakened; however, the intensity of siltation remained at a high level. The CPA is the most densely populated area for oysters. The enhanced siltation in CPA1 led to an increased risk of degradation of oyster reefs covered by sediment, whereas scouring in the central area of CPA 2 was slightly enhanced, and the intensity of siltation on the south side decreased, which was favorable for reef growth and development. However, the high intensity of sediment deposition on the southern side of the reefs should not be neglected. The RRA changed from a combination of scouring and siltation, to siltation, and the risk of degradation of oyster reefs on the side of the inlet channel of Dongzao Port greatly increased. The scouring intensity at the northeast corner near Xiaomiaohong Channel weakened but remained at a high value, and the reefs were still in danger of receding from erosion. The overall siltation in the RRA was enhanced, and human engineering activity was generally more detrimental than beneficial to reefs in the area. However, siltation intensity of the MUA decreased less after human engineering activity, and the reefs in this area were sparsely distributed; therefore, human engineering activity would have no effect on oyster reefs in this area. In general, the impact of human engineering activity on bed-level in the Liyashan Oyster Reef waters was significant, especially in CPA.

4.2 Application of the model to oyster reefs conservation

In this study, a hydrodynamic model was constructed using MIKE3 (Figure 4), which was validated by tide level, flow velocity, flow direction, and suspended sediment concentration (Figures 5–7, Supplementary Figures 1–3). The difference between the measured data and the model-simulated data is slight, which shows that the model meets the accuracy requirements for simulating nearshore hydrodynamic conditions, especially the waters around the Liyashan Oyster Reefs. Previous studies using hydrodynamic models have tended to analyze the effects of individual factors, such as salinity, on oyster reefs (Wang et al., 2008; Kaplan et al., 2016); however, a comprehensive quantification of the various influences is lacking. Results of the model simulation include the changes in flow velocity (Figure 11), suspended sediment concentration (Figure 11), and bed level (Figures 8–11), as well as the changes in flow velocity (Figure 10) and bed level (Figure 13) at characteristic points in the oyster reef waters before and after construction. Results of the model simulations provide intuitive data and, with strict test criteria, a comprehensive analysis of the impact of human engineering activity on oyster reefs.

The unique advantage of applying hydrodynamic modeling to oyster reef conservation lies in its generalizability and quantification. In response to different events, such as coastal engineering mentioned in this study, sea level rise, storm surge, etc., the dominant factors affecting oyster reefs can change or even produce completely different factors. Fortunately, the model can adapt to varying research needs, study scales (both temporal and spatial), and analyze quantitative simulation results to obtain reliable conclusions for assessing the future state of oyster reef development. If an engineering project has a considerable adverse impact on oyster reefs, it is necessary to reconsider the site and scale of the project to reduce damage. The model can also simulate the expected effects of various oyster reef protection projects and simultaneously consider environmental protection and resource conservation to select the best engineering strategy, which is conducive to the long-term protection of oyster reefs.

In this study, the developed model considers several main influencing factors determined by engineering, as shown in Figure 1. Undeniably, if we want to fully analyze the impact on oyster reefs, we also need to consider the changes in temperature, salinity, chlorophyll, dissolved nutrients, dissolved oxygen, heavy metal pollutant concentrations, etc. of the waters (Hoellein et al., 2014). However, too comprehensive a consideration can greatly increase the difficulty of modeling and discussion because of complex interaction between the various factors. Therefore, for different research subjects, we believe that it is necessary to properly select the important influencing factors before modeling, which is beneficial for completing the study in a cost-effective way.

4.3 Overall results and suggestions for restoration

In conclusion, changes in the hydrodynamics of oyster reef waters due to human engineering activity would not affect the development of oyster reefs, but changes in the distribution of bed level would cause some stress to the local reef body. The risk of degradation of oyster reefs by sediment cover increased with enhanced siltation in CPA1 and most of RRA. The overall siltation in CPA2 was weakened; however, the southern reef was still stressed by high-intensity sediment deposition. The northeast side of the RRA was weakened by scouring but still at risk of erosion and degradation, and the MUA was unaffected by human engineering activity due to the sparse distribution of reefs and weakened siltation.

Most areas of oyster reefs are currently under duress of sediment deposition and some areas are severely scoured; therefore, the oyster population would be in decline, so the following suggestions are made.

(1) Replenishment of oyster populations

Oyster reef development is directly related to the number of oyster populations. To maintain the development of oyster reefs, it is recommended to place adult oysters of local species or larvae on the surface of the reef at neap tide to enhance the replenishment of oyster resources and maintain them at the level of the self-sustaining population.

(2) Oyster reef dredging and restoration

The areas south of CPA1 and CPA2 were seriously silted. Experimental dredging measures are suggested to expose the reef beach surface with a certain vertical structure, which is conducive to the attachment and growth of oyster larvae, and allow the reef to recover naturally.

(3) Protective restoration of eroded oyster reefs

The northeast corner of the RRA was seriously eroded by tidal waves. It is suggested that a large concrete ecological protective oyster reef be placed in front of the reef (seaward side) to protect the natural oyster reef, on the one hand, and increase the oyster attachment area on the other.

5 Conclusion

In this study, a three-dimensional hydrodynamic model of the southern part of the Yellow Sea around oyster reefs was established using MIKE3 numerical simulation software. After the accuracy of the model was verified, we quantitatively analyzed the impact of human engineering activity on the hydrodynamics and the sediment dynamic of the Liyashan oyster reef waters, and then discussed the contribution of this study to ecological protection. The following conclusions were obtained.

Human engineering activity has effectively changed the water environment of the Liyashan Oyster Reefs. First, the water flow pattern was stable after the completion of engineering; however, the overall flow velocity decreased. While surface concentrations of suspended sediment remained basically unaffected and concentrations of suspended sediment remained stable at the bottom of CPA, there was a slight variation in concentrations of suspended sediment in other areas, ranging from −0.2 to 0.1 kg/m^3 during spring tides. This indicates that the impact on the hydrodynamic environment is relatively minor and does not necessitate serious warning indicators. Secondly, CPA and RRA show obvious siltation trends after engineering, while MUA shows a slight scouring trend, and the annual variation of bed level in the oyster reef waters ranges from 0.2 to 0.35 m. This indicates that the bed level in priority protection areas is increasing, which is harmful for oyster reef development.

The changes in hydrodynamic and bed levels were regional. In particular, we must pay sufficient attention to the siltation of CPA and RRA by organizing regional measures to reduce silt and avoid oyster reef cover degradation. Some of the measures mentioned in this study may be applied to protect oyster reefs. Moreover, hydrodynamic modeling requires attention for oyster reef conservation. As the model has universal applicability and quantification ability, it can be adapted to a wide range of scenarios to obtain reliable conclusions to assess the impact of human engineering activity and finally facilitate the adoption of optimal engineering and environmental protection measures.

Data availability statement

The original contributions presented in the study are included in the article/Supplementary Material. Further inquiries can be directed to the corresponding authors.

Author contributions

FL: Conceptualization, Methodology, Validation, Supervision. ZC: Methodology, Software, Writing - Review & Editing. HW: Data Curation, Writing - Original Draft. FZ: Formal analysis, Investigation. JZ: Visualization. WQ: Writing - Review & Editing. All authors contributed to the article and approved the submitted version.

Funding

This study is supported by the Marine Science and Technology Innovation Project of Jiangsu Province (Grant No. JSZRHYKJ202105), the National Key Research and Development Program of China (Grant No. 2020YFD0900703), the National Natural Science Foundation of China (Grant 51909100), and the Nantong Science and Technology Bureau (Grant No. MS12022009, No. MS22022082, No. MS22022083).

Conflict of interest

The authors declare that the research was conducted in the absence of any commercial or financial relationships that could be construed as a potential conflict of interest.

Publisher's note

Supplementary material

The Supplementary Material for this article can be found online at: https://www.frontiersin.org/articles/10.3389/fmars.2022.1051868/full#supplementary-material

References

Airoldi, L., and Beck, M. W. (2007). "Loss, status and trends for coastal marine habitats of Europe," in *Oceanography and marine biology*, vol. 45 . Eds. R. N. Gibson, R. J. A. Atkinson and J. D. M. Gordon (Boca Raton: Crc Press-Taylor & Francis Group), 345–405.

Alleway, H. K., and Connell, S. D. (2015). Loss of an ecological baseline through the eradication of oyster reefs from coastal ecosystems and human memory. *Conserv. Biol.* 29, 795–804. doi: 10.1111/cobi.12452

Beck, M. W., Brumbaugh, R. D., Airoldi, L., Carranza, A., Coen, L. D., Crawford, C., et al. (2011). Oyster reefs at risk and recommendations for conservation, restoration, and management. *BioScience* 61, 107–116. doi: 10.1525/bio.2011.61.2.5

Beisel, J.-N., Usseglio-Polatera, P., Thomas, S., and Moreteau, J.-C. (1998). Stream community structure in relation to spatial variation: the influence of mesohabitat characteristics 16. *Hydrobiol.* 389, 73–88. doi: 10.1023/A:1003519429979

Chakraborty, P. (2017). Oyster reef restoration in controlling coastal pollution around India: A viewpoint. *Mar. pollut. Bull.* 115, 190–193. doi: 10.1016/j.marpolbul.2016.11.059

Coen, L., Brumbaugh, R., Bushek, D., Grizzle, R., Luckenbach, M., Posey, M., et al. (2007). Ecosystem services related to oyster restoration. *Mar. Ecol. Prog. Ser.* 341, 303–307. doi: 10.3354/meps341303

Colden, A. M., and Lipcius, R. N. (2015). Lethal and sublethal effects of sediment burial on the eastern oyster crassostrea virginica. *Mar. Ecol. Prog. Ser.* 527, 105–117. doi: 10.3354/meps11244

Comeau, L. A. (2014). Spring awakening temperature and survival of sediment-covered eastern oysters crassostrea virginica. *Aquaculture* 430, 188–194. doi: 10.1016/j.aquaculture.2014.04.009

Dame, R. F., Zingmark, R. G., and Haskin, E. (2006). Oyster reefs as processors of estuarine materials. *J. Exp. Mar. Biol. Ecol.* 83, 239–247. doi: 10.1016/S0022-0981(84)80003-9

DHI (2012). *MIKE 3 flow model user guide and scientific documentation* (Hørsholm, Denmark: Danish Hydraulic Institute).

DHI (2014). *MIKE21 & MIKE 3 flow model FM mud transport module scientific documentation* (Hørsholm, Denmark: Danish Hydraulic Institute).

Edge, K. J., Dafforn, K. A., Simpson, S. L., Ringwood, A. H., and Johnston, E. L. (2015). Resuspended contaminated sediments cause sublethal stress to oysters: A biomarker differentiates total suspended solids and contaminant effects: Resuspended contaminated sediment effects. *Environ. Toxicol. Chem.* 34, 1345–1353. doi: 10.1002/etc.2929

Gangnery, A., Chabirand, J.-M., Lagarde, F., Le Gall, P., Oheix, J., Bacher, C., et al. (2003). Growth model of the pacific oyster, crassostrea gigas, cultured in thau lagoon (Méditerranée, France). *Aquaculture* 215, 267–290. doi: 10.1016/S0044-8486(02)00351-4

Grabowski, J. H., and Peterson, C. H. (2007). Restoring oyster reefs to recover ecosystem services. *Ecosyst. Eng. Plants Protists* 4, 281–298. doi: 10.1016/S1875-306X(07)80017-7

Hart, D. D., and Finelli, C. M. (1999). Physical-biological coupling in streams: The pervasive effects of flow on benthic organisms. *Annu. Rev. Ecol. Syst.* 30, 363–395. doi: 10.1146/annurev.ecolsys.30.1.363

Heath, M. R. (2008). Comment on "A global map of human impact on marine ecosystems." *Science* 321, 1446–1446. doi: 10.1126/science.1157390

Hoellein, T. J., Zarnoch, C. B., and Grizzle, R. E. (2014). Eastern Oyster (Crassostrea virginica) filtration, biodeposition, and sediment nitrogen cycling at two oyster reefs with contrasting water quality in great bay estuary (New Hampshire, USA). *Biogeochemistry* 122, 113–129. doi: 10.1007/s10533-014-0034-7

Jackson, J. B. C., Kirby, M. X., Berger, W. H., Bjorndal, K. A., Botsford, L. W., Bourque, B. J., et al. (2001). Historical overfishing and the recent collapse of coastal ecosystems. *Science* 293, 629–637. doi: 10.1126/science.1059199

Kaplan, D. A., Olabarrieta, M., Frederick, P., and Valle-Levinson, A. (2016). Freshwater detention by oyster reefs: Quantifying a keystone ecosystem service. *PLoS One* 11, e0167694. doi: 10.1371/journal.pone.0167694

La Peyre, M. K., Bernasconi, S. K., Lavaud, R., Casas, S. M., and La Peyre, J. F. (2020). Eastern Oyster clearance and respiration rates in response to acute and chronic exposure to suspended sediment loads. *J. Sea Res.* 157, 101831. doi: 10.1016/j.seares.2019.101831

Lenihan, H. S., Peterson, C. H., and Allen, J. M. (1996). Does flow speed also have a direct effect on growth of active suspension-feeders: An experimental test on oysters. *Limnol. Oceanogr.* 41, 1359–1366. doi: 10.4319/lo.1996.41.6.1359

Lin, H., Yu, Q., Du, Z., Fan, Y., Wang, Y., and Gao, S. (2021). Geomorphology and sediment dynamics of the liyashan oyster reefs, jiangsu coast, China. *Acta Oceanol. Sin.* 40, 118–128. doi: 10.1007/s13131-021-1866-3

Li, Y., and Shen, A. (2013). Damage and recovery in the kumamoto oyster crassostrea sikamea stressed by suspended solids: Damage and recovery in the kumamoto oyster crassostrea sikamea stressed by suspended solids. *J. Fish. Sci. China* 19, 138–144. doi: 10.3724/SP.J.1118.2012.00138

Morris, R. L., Konlechner, T. M., Ghisalberti, M., and Swearer, S. E. (2018). From grey to green: Efficacy of eco-engineering solutions for nature-based coastal defence. *Glob. Change Biol.* 24, 1827–1842. doi: 10.1111/gcb.14063

Nelson, K. A., Leonard, L. A., Posey, M. H., Alphin, T. D., and Mallin, M. A. (2004). Using transplanted oyster (Crassostrea virginica) beds to improve water quality in small tidal creeks: a pilot study. *J. Exp. Mar. Biol. Ecol. Anthropogenic Influences Ecol. Tidal Creeks Canals* 298, 347–368. doi: 10.1016/S0022-0981(03)00367-8

Newell, R. I. (2004). Ecosystem influences of natural and cultivated populations of suspension-feeding bivalve molluscs: a review. *J. Shellfish Res.* 23, 51–62.

Pan, Y., Yin, S., Chen, Y. P., Yang, Y. B., Xu, C. Y., and Xu, Z. S. (2022). An experimental study on the evolution of a submerged berm under the effects of regular waves in low-energy conditions. *Coast. Eng.* 176, 104169. doi: 10.1016/j.coastaleng.2022.104169

Peterson, C. H., Grabowski, J. H., and Powers, S. P. (2003). Estimated enhancement of fish production resulting from restoring oyster reef habitat: quantitative valuation. *Mar. Ecol. Prog. Ser.* 264, 249–264. doi: 10.3354/meps264249

Quan, W., Zhou, W., Ma, C., Feng, M., Zhou, Z., Tang, F., et al. (2016). Ecological status of a natural intertidal oyster reef in haimen county. *Acta Eeologica Sin.* 36, 7749–7757.

Richardson, M. A., Zhang, Y., Connolly, R. M., Gillies, C. L., and McDougall, C. (2022). Some like it hot: The ecology, ecosystem benefits and restoration potential of oyster reefs in tropical waters. *Front. Mar. Sci.* 9. doi: 10.3389/fmars.2022.873768

Rockström, J., Steffen, W., Noone, K., Persson, Å., Chapin, F. S., Lambin, E. F., et al. (2009). A safe operating space for humanity. *Nature* 461, 472–475. doi: 10.1038/461472a

Rodney, W. S., and Paynter, K. T. (2006). Comparisons of macrofaunal assemblages on restored and non-restored oyster reefs in mesohaline regions of Chesapeake bay in Maryland. *J. Exp. Mar. Biol. Ecol.* 335, 39–51. doi: 10.1016/j.jembe.2006.02.017

Rothschild, B. J., Ault, J. S., Goulletquer, P., and Héral, M. (1994). Decline of the Chesapeake bay oyster population: a century of habitat destruction and overfishing. *Mar. Ecol. Prog. Ser.*, 111:29–39. doi: 10.3354/meps111029

Scyphers, S. B., Powers, S. P., Heck, K. L., and Byron, D. (2011). Oyster reefs as natural breakwaters mitigate shoreline loss and facilitate fisheries. *PLoS One* 6, e22396. doi: 10.1371/journal.pone.0022396

Smaal, A. C., Ferreira, J. G., Grant, J., Petersen, J. K., and Strand, Ø. (Eds.) (2019). *Goods and services of marine bivalves* (Cham: Springer International Publishing). doi: 10.1007/978-3-319-96776-9

Soletchnik, P., Ropert, M., Mazurié, J., Gildas Fleury, P., and Le Coz, F. (2007). Relationships between oyster mortality patterns and environmental data from monitoring databases along the coasts of France. *Aquaculture* 271, 384–400. doi: 10.1016/j.aquaculture.2007.02.049

Thomsen, M. S., and McGlathery, K. (2006). Effects of accumulations of sediments and drift algae on recruitment of sessile organisms associated with oyster reefs. *J. Exp. Mar. Biol. Ecol.* 328, 22–34. doi: 10.1016/j.jembe.2005.06.016

Volety, A. K., Savarese, M., Hoye, B., and Loh, A. N. (2009). *Landscape pattern: present and past distribution of oysters in south Florida coastal complex (Whitewater Bay/Oyster Bay/Shark to robert's rivers)* (Fort Myers: Fla. Gulf Coast Univ).

Wall, L. M., Walters, L. J., Grizzle, R. E., and Sacks, P. E. (2005). Recreational boating activity and its impact on the recruitment and survival of the oyster crassostrea virginica on intertidal reefs in mosquito lagoon, florida. J. *Shellfish Res.* 24, 965–973. doi: 10.2983/0730-8000(2005)24[965:RBAAII]2.0.CO;2

Wang, H., Huang, W., Harwell, M. A., Edmiston, L., Johnson, E., Hsieh, P., et al. (2008). Modeling oyster growth rate by coupling oyster population and hydrodynamic models for Apalachicola bay, Florida, USA. *Ecol. Model.* 211, 77–89. doi: 10.1016/j.ecolmodel.2007.08.018

Wang, J., Zhao, M., Bai, S., Gong, X., Zhang, M., Wu, Y., et al. (2009). Environmental background of oyster reef development in near-shore haimen of southern yellow Sea. *Geogr. Res.* 28, 1170–1178.

Wilber, D., and Clarke, D. (2010). "Dredging activities and the potential impacts of sediment resuspension and sedimentation on oyster reefs," in *Proceedings of the Western Dredging Association Thirtieth Technical Conference*. (San Juan, Puerto Rico, USA: WEDA). 61–69jmn

Zhang, R. (2004). The gromorphology-sedimentology character of oyster reef in xiaomiaohong tidal channel, jiangsu province. *Oceanol. Limnol. Sin.* 35, 1–7.

frontiers | Frontiers in Marine Science

TYPE Original Research
PUBLISHED 13 December 2022
DOI 10.3389/fmars.2022.1077004

OPEN ACCESS

EDITED BY
Gangfeng Ma,
Old Dominion University, United States

REVIEWED BY
Henry Bokuniewicz,
(SUNY), United States
Longhuan Zhu,
Michigan Technological University,
United States

*CORRESPONDENCE
Yong-Jin Tak
yjtak@gwnu.ac.kr

SPECIALTY SECTION
This article was submitted to Coastal Ocean Processes, a section of the journal Frontiers in Marine Science

RECEIVED 22 October 2022
ACCEPTED 28 November 2022
PUBLISHED 13 December 2022

CITATION
Cho E-B, Tak Y-J, Cho Y-K and Na H (2022) Fortnightly variability of horizontal salinity gradient affects exchange flow in the Sumjin River estuary. *Front. Mar. Sci.* 9:1077004. doi: 10.3389/fmars.2022.1077004

Fortnightly variability of horizontal salinity gradient affects exchange flow in the Sumjin River estuary

Eun-Byeol Cho[1,2], Yong-Jin Tak[3]*, Yang-Ki Cho[1,2] and Hanna Na[1,2]

[1]School of Earth and Environmental Sciences, Seoul National University, Seoul, Republic of Korea, [2]Research Institute of Oceanography, Seoul National University, Seoul, Republic of Korea, [3]Department of Marine Ecology and Environment, Gangneung-Wonju National University, Gangneung, Republic of Korea

The horizontal salinity gradient has been reported to play a crucial role in fortnightly variability of estuarine exchange flow in short estuaries. However, spatiotemporal variations in the salinity gradient and exchange flow have not been examined over an entire short estuary, as only data observed only at specific points was available. We analyzed the variation in salinity gradient along the entire Sumjin River estuary and its effect on the exchange flow over fortnightly tidal cycles based on observations and numerical model experiments. The salinity gradient and exchange flow were in different phases between the lower and upper estuaries by 6–7 days. The maximum salinity gradient periodically reciprocated along the channel as a result of salt flux changes determined by vertical mixing. The stronger exchange flow (> 0.04 m s^{-1}) changed location from mouth to head of estuary while the tidal range decreased, resulting from variability of the salinity gradient. The horizontal salinity gradient is large enough to overwhelm the vertical mixing effect on the exchange flow. The spatiotemporal changes of strong exchange flow correspond well with the horizontal Richardson number value (> 3). This study suggests that for the health of estuarine ecosystems, it is important to determine the spatiotemporal variation in exchange flow throughout the estuary.

KEYWORDS

horizontal salinity gradient, exchange flow, fortnightly tidal cycle, short and narrow estuary, salt flux

Introduction

The transport and behavior of substances, such as pollutant sediments, organisms, and nutrients, largely depend on the strength of estuarine exchange flow. The exchange flow is the tidally averaged along-channel velocity through an estuarine cross-section (Stacey et al., 2001; Valle-Levinson, 2010; Geyer and MacCready, 2014) and is also referred to as estuarine circulation (Geyer and MacCready, 2014; Dijkstra et al., 2017). The vertical shear of the exchange flow is mainly determined by competition between vertical mixing and the horizontal salinity gradient (Uncles and Stephens, 1990; Park and Kuo, 1996; Stacey et al., 2001; Mantovanelli et al., 2004; Valle-Levinson, 2010; Garel and Ferreira, 2013). Increased vertical mixing enhances the vertical momentum flux, which weakens the vertical shear of exchange flow, whereas an increased salinity gradient strengthens the vertical shear. The intensity of vertical mixing and salinity gradient can vary depending on the tidal range, and the contention results of these two factors change fortnightly; in turn, this determines exchange flow (Park and Kuo, 1996).

Previous studies have proposed that fortnightly variation in the vertical shear of exchange flow is determined by turbulent mixing owing to the tide. During spring tides, vertical momentum exchange is active owing to strong vertical mixing, and exchange flow is weakened; during the neap tide, exchange flow is strong owing to decreased vertical mixing, as observed in many estuaries, such as the Hudson River estuary (Geyer et al., 2000; Bowen and Geyer, 2003; Scully et al., 2009; MacCready and Geyer, 2010), Modaomen estuary (Gong et al., 2014), Peruípe River estuary (Andutta et al., 2013), and Curimatau River estuary (de Miranda et al., 2005). On the other hand, recent studies of short estuaries (i.e., those that are shorter than the dominant tidal wavelength) have reported that the salinity gradient plays a major role in the exchange flow variation, which is stronger during the spring tide (Becker et al., 2009; Cho et al., 2020). In the Cape Fear River estuary, stronger tidal forcing and associated mixing contribute to increased estuarine circulation due to a greater near-bottom horizontal salinity gradient during the high tidal range (Becker et al., 2009). In the Sumjin River estuary, the effect of the horizontal salinity gradient, which is six times higher during the spring tide compared with the neap tide, overwhelms the effect of vertical mixing, resulting in stronger exchange flow during the spring tide (Cho et al., 2020). However, as these studies were conducted only at specific points, the fortnightly variation of exchange flow over the whole short estuary remains unclear. In the study of the short Blackwater estuary, a semi-analytical approach was used and the analysis focused on lateral changes in residual circulation, but did not examine spring–neap variation (Wei et al., 2022). Therefore, fortnightly variation of the vertical shear of exchange flow in the entire estuary is still poorly understood as the analysis has received little attention.

In this study, the variability of the horizontal salinity gradient and exchange flow during the fortnightly tidal cycle was analyzed for the entire short and narrow estuary, based on observations and numerical model experiments. The estuary was simulated using a numerical model by simplifying the geometry of the Sumjin River estuary. The mechanism underlying periodic salinity gradient change and its effect on the exchange flow were investigated. A numerical experiment with realistic topography was conducted to examine its applicability to the Sumjin River estuary.

Materials and methods

Study area

The Sumjin River estuary is located in the central part of the southern coast of Korea (Figure 1A). The Sumjin River discharges into Gwangyang Bay (Figure 1B). The Sumjin River discharges into Gwangyang Bay. The length of the estuary is estimated to be approximately 25 km based on the salinity distribution suggested by Pritchard (1967). The scale of the estuary can be classified by a non-dimensional length parameter (δ), which is the ratio between the length of the estuary (L) and one-quarter of the tidal wavelength (λ/4), according to the definition of Li and O'Donnell (2005) as follows:

$$\delta = \frac{4L}{\lambda} \left(\lambda = \frac{\sqrt{gh}}{f} \right), \quad (1)$$

where g is the acceleration of gravity, h is the depth, and f is the tidal frequency (2.23×10^{-5} s^{-1}). An estuary with a δ value smaller (or larger) than 0.6–0.7 is defined as a short (or long) estuary. The Sumjin River estuary, has a δ value of 0.27 and can therefore be classified as a short estuary. The estuary is relatively a narrow and shallow estuary; the width and depth at the mouth are 1 km and 15 m, respectively, decreasing to 300 m and 2 m at the head. There are tributaries on the lower estuary side. However, based on data from Conductivity–Temperature–Depth (CTD) station 7, the east tributary has minimal effect on the salinity distribution of the main channel. A tributary on the west from station 4 has flow mainly out of the estuary, with hardly any flow into the estuary.

The tides are mainly mixed semi-diurnal, and the main tidal constituents are M_2 and S_2, with amplitudes of ~1 and ~0.46 m, respectively. These two tidal components were used as forcing in the model. The tidal range is approximately 3.1 m during the spring tide and 1.0 m during the neap tide. Estuary stratification is partially to well mixed during spring tides and becomes stratified during neap tides (Shaha and Cho, 2009), and it is periodically strongly stratified. Tidal data were collected from the Gwangyang tidal gauge station, which is

operated by the Korea Hydrographic and Oceanographic Agency (http://www.khoa.go.kr). The 20-year mean discharge rate of the Sumjin River from 2001 to 2020 was 78 m^3 s^{-1}. The river discharge rate was obtained from the Songjung gauge station, which is located approximately 35 km upstream of the estuary mouth and is operated by the Ministry of Construction and Transportation (http://www.wamis.go.kr).

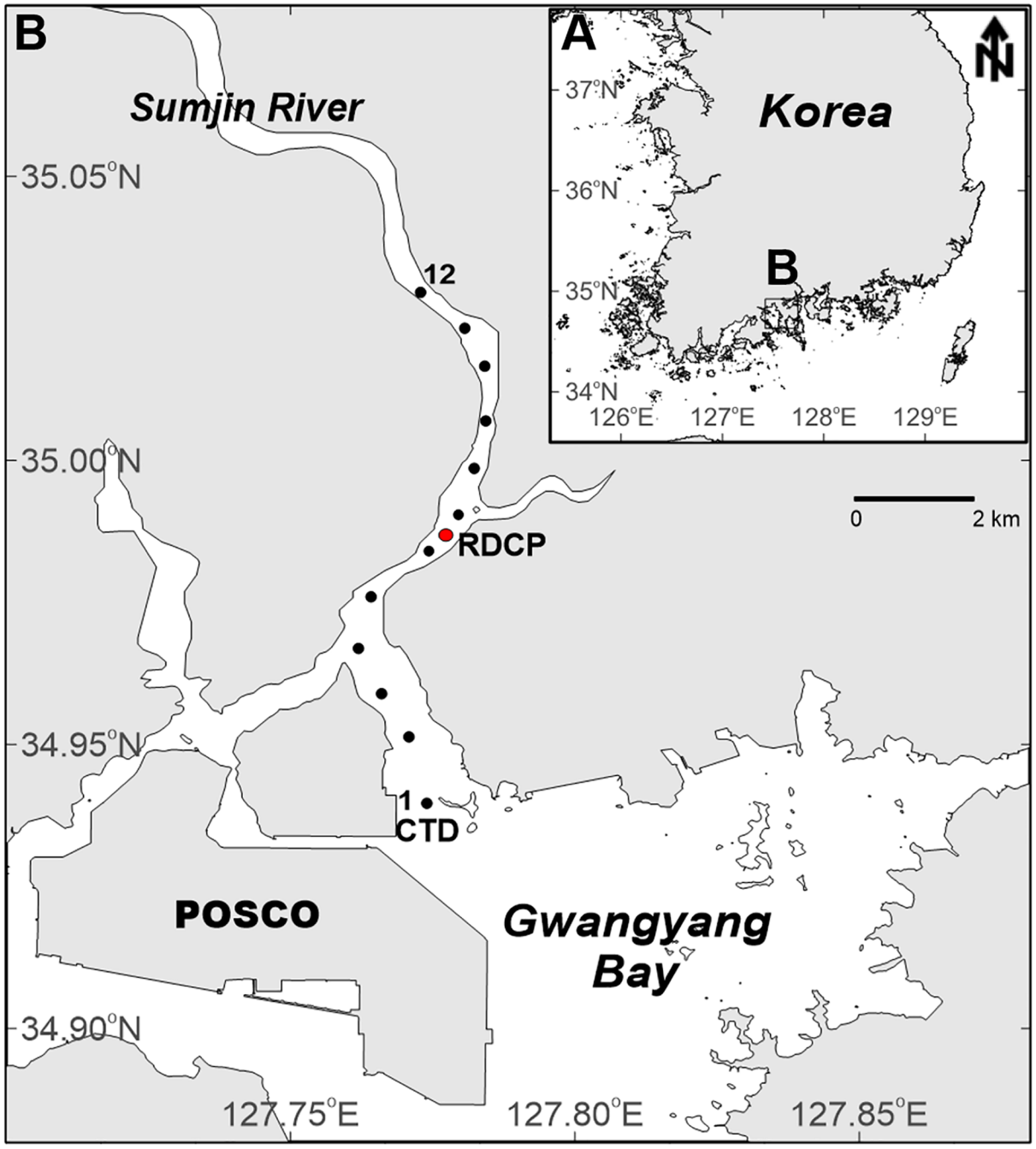

FIGURE 1
Study area and observation stations: **(A)** Overview map of Korea; **(B)** the Sumjin River estuary, including the Conductivity–Temperature–Depth (CTD) stations 1–12 (black circles), the current mooring station (red circle), and the Gwangyang tidal gauge (triangle).

Observations

We observed the current velocity at one point and salinity at 12 stations along the channel up to 12 km upstream from the mouth of estuary. The velocity was observed by upward-looking Recording Doppler Current Profiler (RDCP 600 kHz; Aanderaa Data Instruments AS, https://www.aanderaa.com/) for 23 days at 7 km upstream from the mouth of estuary (Figure 1B; RDCP). The upward-looking RDCP was installed at the deepest point (12 m) in the section to obtain vertical velocity profiles from October 19 to November 10, 2013. The velocity data were obtained at 10-min intervals with a vertical resolution of 1 m from 3 m above the bottom to the surface layer. The upper and lower most bins were excluded to avoid boundary interference. The north and east components of the velocities were decomposed to obtain along- and cross-channel velocities; the along-channel velocity was analyzed in this study.

The YSI Castaway Conductivity–Temperature–Depth (CTD) (https://www.sontek.com/castaway-ctd) was used during shipboard surveys conducted on a neap tide (October 30, 2013) and spring tide (November 5, 2013). Hydrological data were acquired along the estuary from stations 1–12 (Figure 1B), with an accuracy of 0.1 g kg^{-1} for salinity and 0.05°C for temperature. The distance between the stations was approximately 1 km. The CTD observations started from station 1, 30 min before the peaks of the flood and ebb tides. The observations up to station 12 usually took less than 50 min to minimize the total casting time to maintain the concurrence of the tidal phase along the estuary. The subtidal salinity was calculated by averaging the flood and ebb observations. More detailed information regarding these observations is described in Cho et al. (2020).

Model description

We assumed a simplified Sumjin River estuary system that is well mixed or periodically stratified, forced with a steady river flow rate and two tidal constituents (M_2, S_2), resulting in fortnightly tidal variation. This particular configuration was designed to be as simple as possible in order to reproduce the spring–neap tidal variation observed in the Sumjin River estuary. The simulation was performed using the Regional Ocean Modeling System (ROMS), which solves the hydrostatic, incompressible, Reynolds-averaged momentum and tracer conservation equations with a terrain-following vertical coordinate and free surface (Shchepetkin and McWilliams, 2005).

The idealized model domain includes a bay between the open boundary and estuary mouth (Figure 2A). To match the observations, we assumed that the estuary mouth was located 7 km from the boundary. The estuary was implemented in a straight line to exclude the effect of meandering. The cross-section was rectangular in shape, and the water depth and width followed a linear trend based on the actual change (Figures 2B, C). This simplification minimizes the nonlinear effect caused by complex topography and focuses only on the fortnightly variation. However, since these settings are different from the friction effect in real geometry, the mixing parameterization

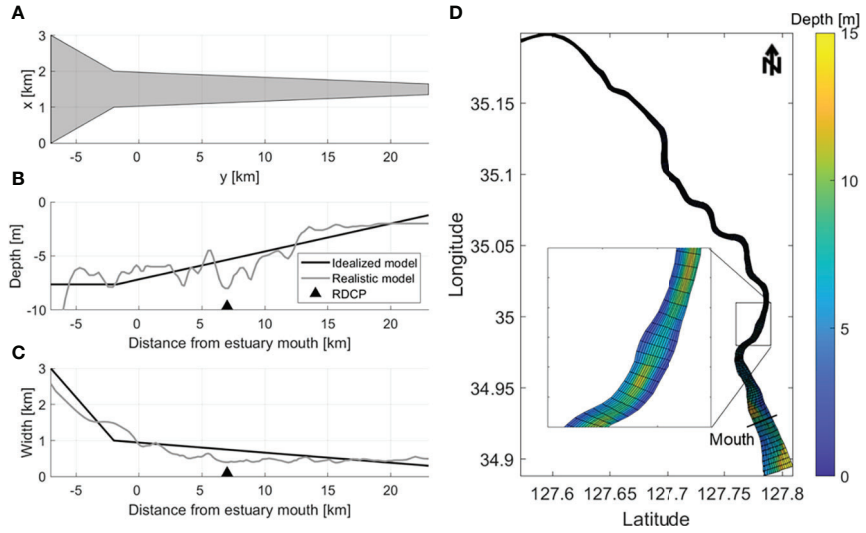

FIGURE 2
Idealized model domain information. **(A)** Idealized estuary model domain and the along-channel variations of **(B)** depth and **(C)** width for the model (black lines) and observations (grey lines) in the Sumjin River estuary. The observation depth is laterally averaged. The black triangles indicate the velocity observation station in Figure 1B RDCP. **(D)** Realistic model domain with depth (m); the estuary mouth is indicated by the black line.

should be elaborately tuned using a proper vertical mixing scheme and forcing. The vertical mixing was parameterized using the K-Profile Parameterization scheme (KPP; Large et al., 1994). In the Mellor–Yamada and GLS (k-kl, k-e, k-w) mixing schemes, the thickness of the thermocline was thinner than that of the KPP during the neap tide, and the length of inflow of the high salinity (> 28) water mass to the bottom layer was longer by 1–5 km. During the spring tide, all schemes similarly implemented strong vertical mixing, but in all schemes other than KPP, the inflow of the high salinity water mass was longer by 1–4 km. The vertically averaged salinity reduction rate along the channel and the inflow length of high salinity water were most similar to the observation in the KPP.

The idealized model was constructed with 110 (along-channel, y-direction) × 17 (cross-channel, x-direction) grids and 10 (vertical, z-direction) vertical layers. The along-channel grid size (Δy) was 340 m, the cross-channel grid size (Δx) was 34–190 m, and the 10 vertical layers were uniformly discretized. The model was forced by river flow at the northern end of the estuarine channel, and two tidal components were imposed at the southern boundary. The inflowing river discharge rate was 60 m^3 s^{-1}, with a salinity of 0 g kg^{-1}, which was suitable for an idealized model. The salinity at the ocean boundary was 35 g kg^{-1}, and the initial salinity was set to 20 g kg^{-1}. The temperatures at the open boundary and river inflow were set to 20°C, the same as the background temperature set throughout the entire domain. The open boundary was treated with the Champman condition for surface elevation, Flather condition for barotropic velocity, and Clamped boundary conditions for open-ocean salinity. The other forcing was a tidal sea surface height variation on the open boundaries at the M_2 and S_2 frequencies. The idealized model was integrated for 100 days with a baroclinic time step of 10 s. The idealized model presented a steady spring–neap tidal cycle in the salinity field after a spin-up period of 30 days, after which it was run for another 70 days to capture several fortnightly tidal cycles.

The realistic model was constructed with 158 (along-channel, y-direction) × 14 (cross-channel, x-direction) grids and 10 (vertical, z-direction) vertical layers (Figure 2D). The along-channel grid size (Δy) was 10–540 m, the cross-channel grid size (Δx) was 6–240 m, and the 10 vertical layers were uniformly discretized. Like the idealized model, the realistic model was forced by river flow and the two tidal components at the northern and southern boundary, respectively. The initial and boundary values of salinity and water temperature were also the same as in the idealized model. The realistic model was integrated for 100 days with a baroclinic time step of 2 s. The realistic model presented a steady spring–neap tidal cycle in the salinity field after a spin-up period of 30 days, after it had been

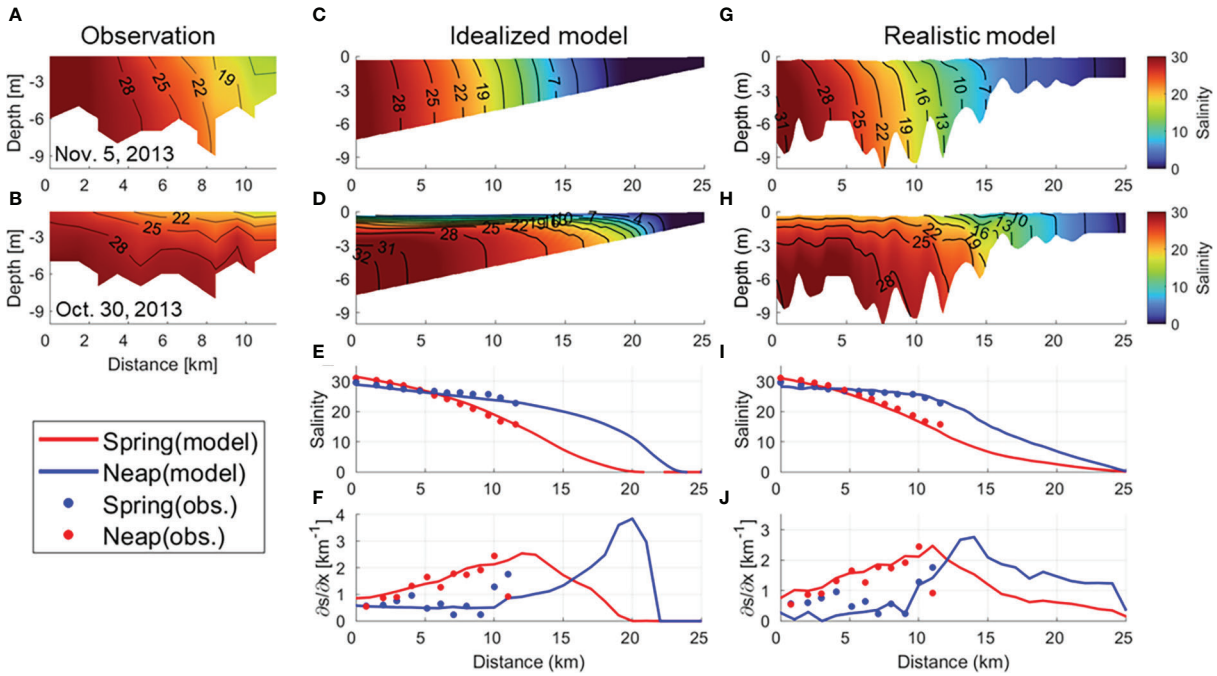

FIGURE 3
Comparisons of salinity among observations, an idealized model, and a realistic model. Vertical sections of the along-channel salinity during **(A, C, G)** the spring tide and **(B, D, H)** neap tide in **(A, B)** observations, **(C, D)** the idealized model and **(G, H)**, and the realistic model. Variations in depth-averaged **(E, I)** salinity and **(F, J)** horizontal salinity gradient from mouth to head during spring (red) and neap tides (blue). Dots and lines denote observations and model outputs, respectively.

run for another 70 days to capture several fortnightly tidal cycles.

Comparison of salinity and current between observations and models

The model was designed to simulate the fortnightly variability of salt distribution in the Sumjin River estuary, and the results were compared with the observations. The salinity in the model was in good agreement with that observed at most stations (Figure 3). The root-mean-square error for all the stations in idealized (realistic) model was 0.68 (3.4) and 0.48 (1.68) g kg^{-1} for depth-averaged salinity along the channel and 0.51 (0.46) and 0.35 (0.48) km^{-1} for the horizontal salinity gradient during the spring and neap tides, respectively. Model salinity sections were vertically mixed as observed during the spring tide, but stratified more strongly than observed during the neap tide. However, both models reproduced accurately that the salinity gradient was up to 7 times greater during the spring than the neap tide, which was a major feature in observation.

The horizontal salinity gradient may vary depending on the horizontal length scale (Geyer et al., 2000) and the depth to be used. Therefore, we needed to check whether there was a change in the fortnightly variation of the salinity gradient. So, when calculating the salinity gradient with the observed salinity, the horizontal length was changed to 1–10 km intervals. When the salinity was averaged vertically, the water depth from the surface layer was also applied differently. As the horizontal interval increased, the horizontal salinity difference also increased, and the salinity gradient decreased only slightly. Even when the salinity gradient was estimated by averaging the salinity at various water depths, there was almost no change. In the analytical model using the balance equation of pressure gradient and friction (Cho et al., 2020), the observed exchange flow was well realized when the horizontal length scale was set at a 1 km interval when calculating the salinity gradient. Therefore, we used the salinity from the surface layer to the bottom and set the horizontal length to 1 km to calculate the salinity gradient.

A comparison of the depth-averaged along-channel velocity between the model and the observations indicated that the phase was properly simulated; however, the magnitude was overpredicted in the model (Figure 4A). When the tidal range was small, the difference in magnitude was approximately 15 cm s^{-1}, which decreased to 7 cm s^{-1} at a large tidal range. The exchange flow in observations and the model was compared (Figure 4B). The exchange flow was calculated using a 25-hour low pass filter (MATLAB R2021b function: all subsequent low pass filter used this tool) for the observation results at a 10 min interval, and for the model at a 1-hour interval to suppress semi-diurnal tidal variability. We tried different timeframes (25 – 72 h) for the low pass filters, and the results were all similar. The vertical shear of the exchange flow observed at the lower estuary was greater during spring tides than during neap tides (Figure 4B). The model captured the difference in the vertical velocity profile between the two periods well.

Decomposition of salt flux

The salinity distribution and the horizontal salinity gradient was estimated based on the salt flux. The along-channel salt flux was divided into seaward and landward fluxes (Fischer, 1972; Hunkins, 1981; MacCready, 2007). The driving mechanisms of the salt flux were examined by applying the flux decomposition method proposed by Lerczak et al. (2006).

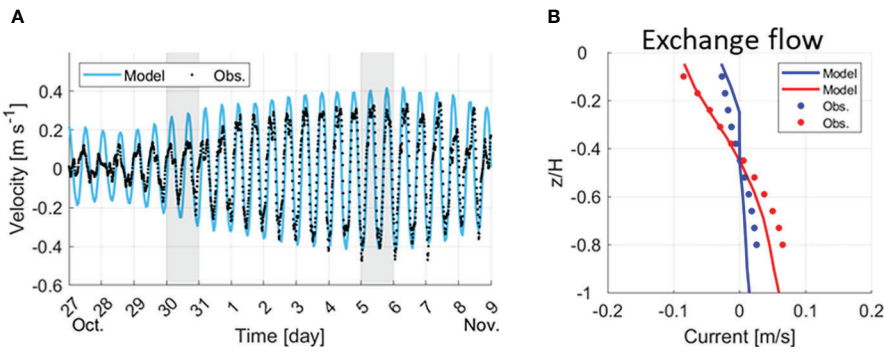

FIGURE 4
Comparison of flow rates between observations and the idealized model. **(A)** Time series of the depth-averaged velocity in observations (black dots) and the model (cyan line), with grey shading indicating Conductivity–Temperature–Depth (CTD) observation dates. **(B)** Vertical velocity profile of the observations (dots) and model (lines) during spring (red) and neap (blue) tides denoted by CTD observation data (grey shading boxes) in **(A)**.

The area-integrated, total along-channel salt flux was calculated as:

$$F = \iint vsdA, \tag{2}$$

where the angled bracket denotes the tidal average; dA denotes the cross-sectional area of the individual grid cells estimated by multiplying dx and dz, where dx and dz are determined by the horizontal and vertical sizes of the individual grid cells in the cross-sectional areas. Note that dz is time-dependent owing to the changes in surface height, while v and s are the temporal along-channel velocity and salinity, respectively.

The cross-sectional area A at a particular along-channel location is divided into a constant number of differential element dA that constrict and expand with the tidal rise and fall of the free surface, respectively. The tidally averaged area (A_0) property is defined as follows:

$$dA_0 = dA, \; A_0 = \iint dA, \tag{3}$$

where ∫∫ indicates the cross-sectional integral. Assessment of the contribution of the different processes to the salt fluxes requires decomposing the along-channel velocity and salinity fields into three components, which is the same as proposed by Lerczak et al. (2006): both tidally averaged over a tidal period and the area of cross-section component (v_0,s_0), tidally averaged and a cross-sectionally varying component (v_E, s_E), and tidally and cross-sectionally varying component (v_T,s_T):

$$v_0 = \frac{\iint vdA}{A_0} \tag{4}$$

$$v_E = \frac{vdA}{dA_0} - v_0 \tag{5}$$

$$v_T = v - v_E - v_0, \tag{6}$$

There is a corresponding set of equations for the salinity. The variable v_0 is related to the river flow volume flux Q_0[=–v_0A_0, v_E is the estuarine exchange flow, and v_T represents tidal current. The tidal varying components v_T and s_T satisfy $\langle v_T dA\rangle$ =0 and $\langle s_T dA\rangle$ =0 .Then, the total along-channel salt flux can be calculated as:

$$F = \iint (v_0 + v_E + v_T)(s_0 + s_E + s_T)dA$$

$$= \iint (v_0 + v_E)(s_0 + s_E)dA_0 + \iint \langle v_T s_T dA \rangle + cross \;\; terms$$

$$= \underbrace{-Q_0 S_0}_{F_R} + \underbrace{\iint v_E s_E dA_0}_{F_E} + \underbrace{\iint \langle v_T s_T dA \rangle}_{F_T} \tag{7}$$

where the cross terms have been dropped because the results are negligible and uncorrelated by definition. Under this decomposition, F_R is the advective salt flux due to the river outflow, which is always a seaward salt flux; F_E is the salt flux resulting from steady shear dispersion, which is the spatial correlation of tidally averaged velocity and salinity; and F_T is the cross-sectionally integrated tidal oscillatory salt flux due to the correlation among tidal variations in velocity, salinity, and depth. Here, we use the low pass filter with 25 h to obtain the tidally averaged values.

Results and discussion

We primarily analyzed the results of the idealized model to exclude nonlinear effects caused by complex topography and focus on spring-neap variations. The realistic model results in 3.4 were referred to confirm that our main findings are applicable to the real estuary.

Periodic propagation of the horizontal salinity gradient

First, the spatiotemporal variability of the salinity distribution, which determines the horizontal salinity gradient, was investigated. In order to focus on the fortnightly variation of the salinity distribution, salinity at a 1-hour interval from the model was low pass filtered (25-hour) and sectionally averaged (Figure 5). The salinity distribution varied periodically (Figure 5B). During spring tides, the salt intrusion length was the shortest, the vertical salinity difference was less than 2, and it was vertically well-mixed (Figure 5C), and so the horizontal difference of salinity was large. During neap tides, the salt intrusion length was the longest and stratification was strong, and so the horizontal difference of salinity was small.

The variability of salt transport determines the variation of the length of the salt intrusion. Based on the commonly used subtidal salt flux decomposition for estuaries, the seaward salt flux due to river outflow is balanced by the landward salt flux due to the upstream dispersive mechanism (Ralston and Stacey, 2005; Lerczak et al., 2006; MacCready, 2007; Garcia et al., 2022). The composition of each salt flux was estimated using the decomposition method (Lerczak et al., 2006; MacCready, 2011; Chen et al., 2012). The total horizontal salt flux (F)

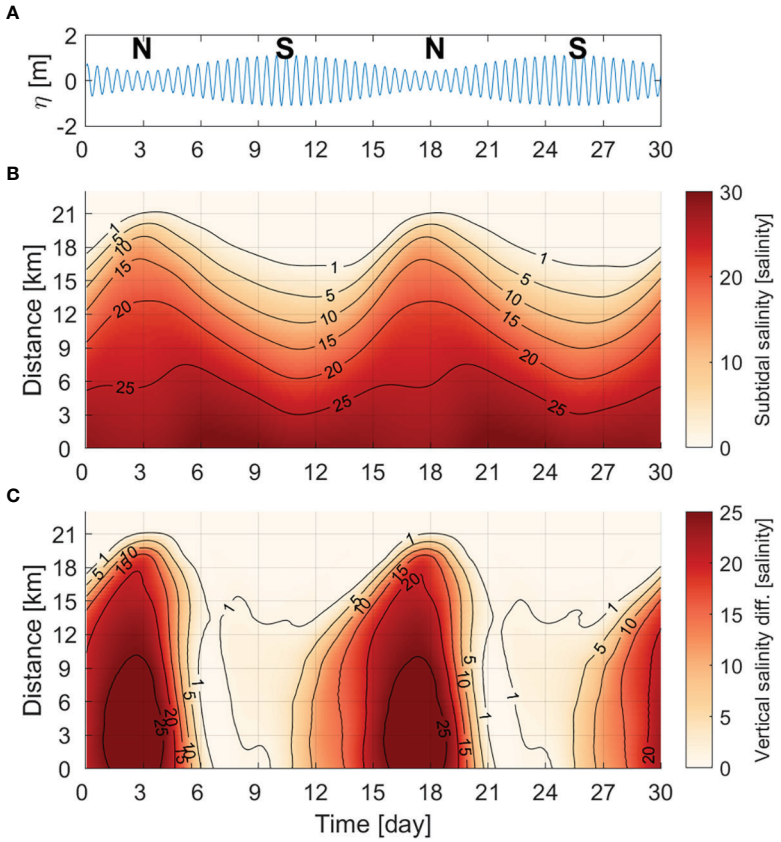

FIGURE 5
(A) Time series of sea-level height at the mouth of the idealized estuary and the N and S stand for neap tide and spring tide, respectively. Hovmöller diagram of **(B)** sectionally averaged subtidal salinity (unit: g kg^{-1}) and **(C)** the difference in salinity between the surface and bottom layer.

exhibited marked fortnightly variability (Figure 6A). The fluctuation in F implies that the estuary gains salt when the tidal range decreases but loses salt when the tidal range increases. As the landward of the salt flux continues, the salt intrusion becomes longer, and as the seaward salt flux continues, the salt intrusion becomes shorter. Salt was imported by F_E and F_T, and F_E contributed approximately 80% of the total landward salt flux, on average, during the fortnightly tidal cycle (Figure 6B). The diffusive fraction of landward salt flux ($\nu = F_T/(F_T+F_E)$) after Hansen and Rattray (1966) was generally less than 0.5 when the total salt flux is landward. It also proves that the steady shear dispersion salt flux (F_E) is dominant in the landward salt flux.

The horizontal salinity gradient along the channel also exhibited distinct fortnightly variation (Figure 7A). During spring tides, the salinity gradient was relatively high from the mouth and was the highest (> 2.0km^{-1}) around the middle estuary (~10 km from the mouth). While the tidal range was decreasing, the maximum salinity gradient propagated to the head of estuary, becoming larger and reaching at least 5.0 km^{-1} during neap tides. Then, while the tidal range increased, the maximum salinity gradient retreated from the head. Thus, the fortnightly variation of the maximum salinity gradient was out of phase between the lower and upper estuary (Figure 7B). The time-varying maximum salinity gradient is similar to the results from the Hudson River estuary (Ralston et al., 2008; Geyer and Ralston, 2015). However, the maximum salinity gradient was maintained at the head without changing the position until the next spring tide in the Hudson River estuary, which differs from the Sumjin River estuary. Owing to its long length, the salinity distribution in the Hudson River estuary cannot immediately respond to the tidal cycle in the upper estuary (Park and Kuo, 1996; Lerczak et al., 2009). Therefore, the maximum salinity gradient in the upper estuary may persist.

In the estuary considered in this study, the continuous movement of a high salinity gradient along channel is related to the convergence of the salt flux, ($\partial F/\partial x$) The stronger the convergence becomes, the greater the horizontal difference in salinity and a salinity gradient occurs. As the convergence decreases, the horizontal difference in salinity decreases. That is, the movement of the maximum salinity gradient zone can be

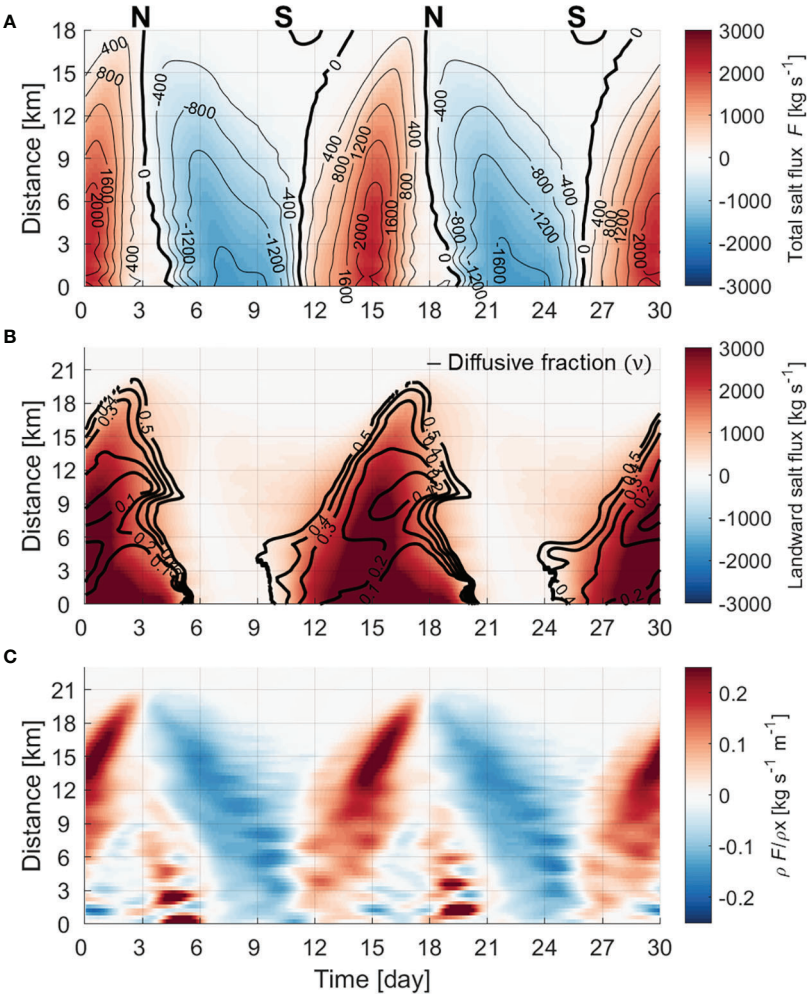

FIGURE 6
Hovmöller diagrams of the **(A)** total horizontal salt flux **(F)**, **(B)** landward salt flux (color shading: steady shear dispersion salt flux [F_E] + tidal oscillatory salt flux [F_T]; unit: kgs^{-1}) and diffusive fraction (ν; black contour lines), and **(C)** convergence of total salt flux (unit: kgs^{-1}m^{-1}).

determined by the convergence of the salt flux. Figure 6C shows the spatiotemporal change of the convergence of the salt flux. When the total salt flux is landward (seaward), the greater the positive (negative) value, the stronger the convergence. While the tidal range decreases after a spring tide, salt is imported into the estuary owing to the steady shear dispersion salt flux. As the salt intrusion length becomes longer, the high salinity gradient propagates toward the head of the estuary. The convergence of the salt flux also becomes stronger as it moves toward the estuary head, especially from 12 km to the head. Therefore, the salinity gradient increases from 2 to 6 km^{-1} from the middle estuary to the head. While the tidal range increases after the neap tide, salt is exported out of the estuary owing to the advective salt flux, and as the salt intrusion length is shortened, the salinity gradient also moves toward the mouth. Owing to constant convergence in the seaward direction, a salinity gradient of 2 km^{-1} or more moves toward the mouth. As such, the salinity gradients in the lower and upper estuary have different time changes (Figure 7B), which has a major effect on the exchange flow.

Fortnightly variation in exchange flow and its cause

To analyze the fortnightly variation of exchange flow in the entire estuary, we calculated the intensity of exchange flow by averaging the absolute values with depth (Burchard et al., 2011). If the intensity is 0.04 or more (unit: ms^{-1}), the exchange flow can be set as strong, because at this intensity, F_E due to the exchange flow can induce the total salt flux landward. Uniquely, the exchange flow was strong (> 0.04 ms^{-1}) in the lower and middle estuary around the spring tide and was generally weak

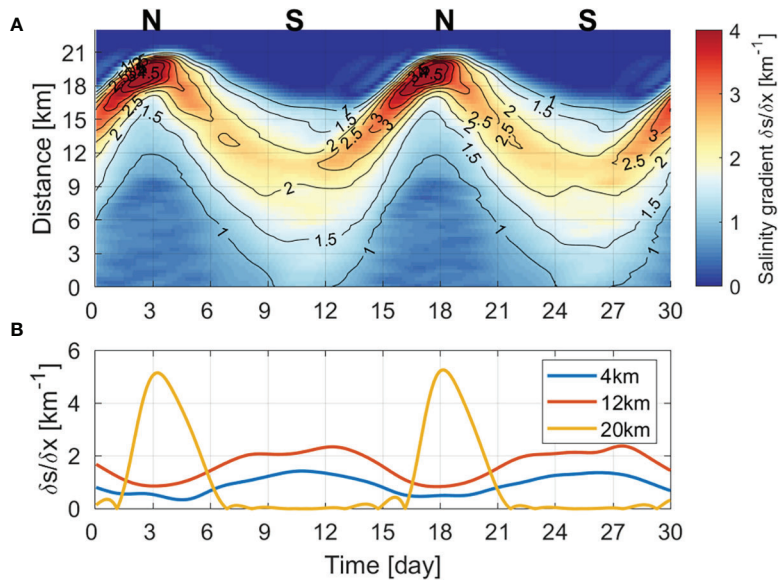

FIGURE 7
Hovmöller diagram of **(A)** horizontal salinity gradient along the channel (unit: km^{-1}) and **(B)** time series of salinity gradient at 4, 12, and 20 km.

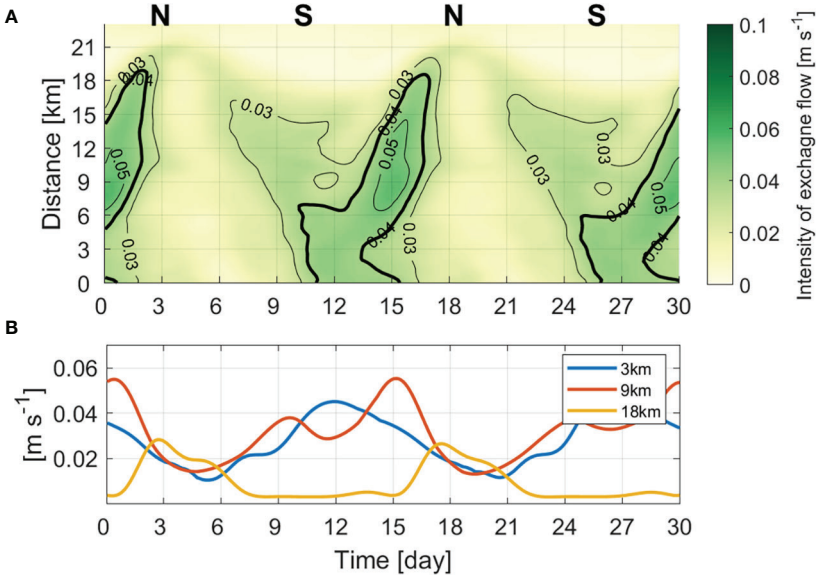

FIGURE 8
(A) Hovmöller diagram of the depth-averaged absolute value of the exchange flow and **(B)** timeseries of the intensity of the exchange flow at 3, 9, and 18 km from the estuary mouth (unit: ms^{-1}).

during increasing tidal range, but strong during decreasing tidal range (Figure 8A). Therefore, there was a phase difference depending on the location (Figure 8B). In the lower estuary, it was at a maximum around the spring tide and a minimum after 2–3 days of the peak neap tide. In the upper estuary, it was strongest before and after the neap tide and weakest during the spring tide.

In a previous study of the Sumjin River estuary, the salinity gradient was the main determinant in the fortnightly variation of exchange flow in the lower estuary (Cho et al., 2020). To

determine what mechanism caused the variation in the intensity of the exchange flow in the entire estuary, we compared the salinity gradient and vertical mixing effect, which are the main factors that determine the vertical shear of the exchange flow. The horizontal Richardson number (Ri_x), also referred as the Simpson number, has been used to provide a diagnostic balance between baroclinic forcing and vertical mixing due to tidal friction (Stanev et al., 2015; Li et al., 2018). We calculated Ri_x according to previous studies (MacCready and Geyer, 2010; Rayson et al., 2017) to identify the main factor that determines the exchange flow:

$$Ri_x = \frac{g\beta H^2(\partial s/\partial x)}{C_d u_b^2}, \quad (8)$$

where β is the saline contraction coefficient of 7.7 $\times 10^{-4}$ proposed by Wang et al. (2015), g is the acceleration due to gravity, $\partial s/\partial x$ is the horizontal salinity gradient, H is the local water depth, $C_d(4.0 \times 10^{-3})$ is the drag coefficient (used in the model setting), and u_b is the amplitude of the bottom tidal velocity (Stacey et al., 2001). There is considerable variation in the estimate of the critical value for Ri_x (MacCready and Geyer, 2010); it is less than 1 or set to 3 (Stacey et al., 2001; MacCready and Geyer, 2010; Li et al., 2018). Since we use the bottom tidal velocity, vertical mixing is weaker than when using the depth-mean tidal velocity (Pein et al., 2014; Schulz et al., 2015; Stanev et al., 2015; Li et al., 2018) and the salinity gradient is large; therefore, the Ri_x is generally higher than 1. As such, we set the critical value to 3 in order to identify the main factor that strengthens the vertical shear of the exchange flow.

The baroclinic forcing and vertical mixing, which determine Ri_x, differ in the timing and location of their strong appearance (Figures 9A, B). Between lower and

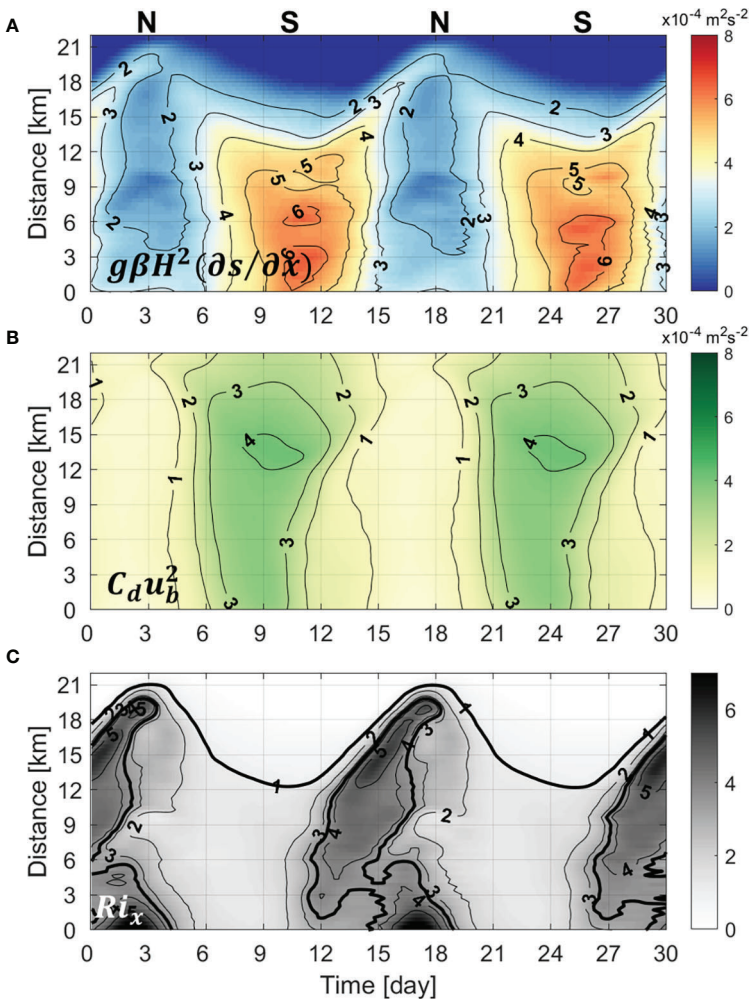

FIGURE 9
Hovmöller diagram of the **(A)** baroclinic forcing (unit: × 10^4 m^2 s^{-2}), **(B)** bottom stress (unit: × 10^4 m^2 s^{-2}), and **(C)** nondimensional horizontal Richardson number.

upper estuaries, baroclinic forcing has out-of-phase variability but vertical mixing exhibits relatively in-phase variability. According to Eq. (8), baroclinic forcing is mainly determined by the horizontal salinity gradient. Therefore, the subtidal variation in baroclinic forcing was nearly consistent with the horizontal salinity gradient (Figure 7A). During tidal range decreases, the exchange flow became stronger toward the head of the estuary because vertical mixing gradually decreased, but the baroclinic forcing effect became predominant as the maximum salinity gradient moved to the head (Ri_x>3 > 3; Figure 9C). After the neap tide, as the tidal range increased, vertical mixing became stronger throughout the estuary, the baroclinic forcing effect became insignificant ($Ri_x \approx 1$) , and the vertical shear of exchange flow weakened. The spatiotemporal changes with high Ri_x (> 3) and strong exchange flow (> 0.04 m s^{-1}) agree relatively well. Therefore, the determinant of the fortnightly variation of exchange flow not only in the lower estuary but also in the entire estuary is the salinity gradient, and the phase difference occurs in the lower and upper estuaries because the salinity gradient is out of phase between lower and upper estuaries.

Restriction of salt intrusion by vertical mixing

Unlike many estuaries, in the Sumjin River estuary, the exchange was stronger during spring tide than during neap tide in the lower estuary. This was also confirmed through the idealized model experiment, and it was quantitatively proved with Ri_x that the salinity gradient effect was large enough to overwhelm the vertical mixing effect. In order for the salinity gradient to be sufficiently large during the spring tide, the

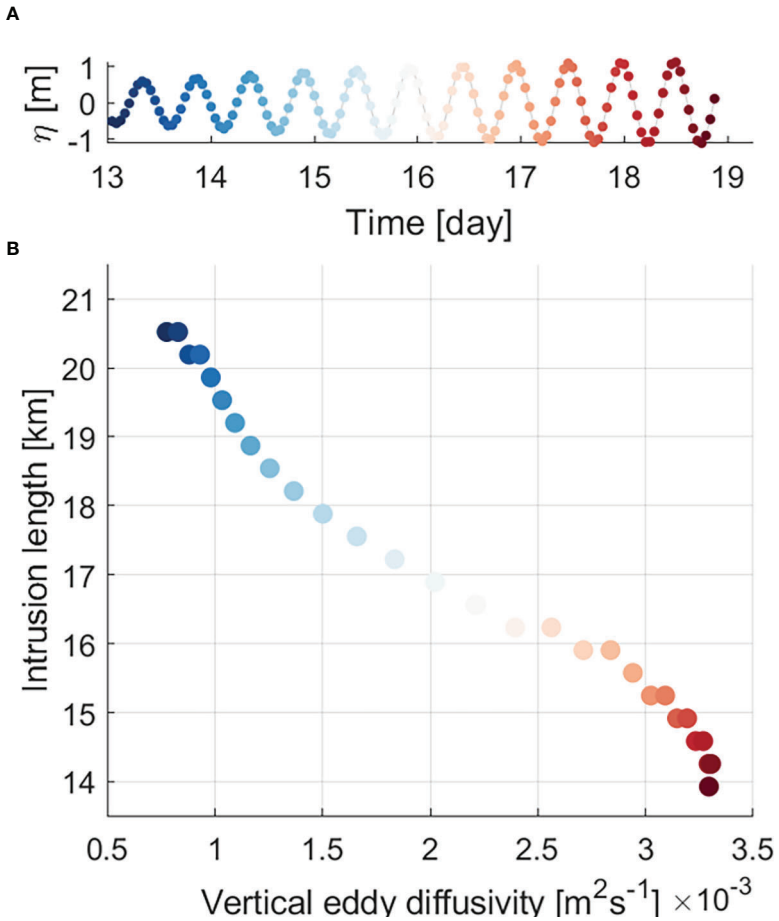

FIGURE 10
(A) Time series of sea-surface height (unit: m) and **(B)** scatter plot of intrusion length (unit: km) of the 5 gkg^{-1} isohaline versus cross-sectionally averaged vertical eddy diffusivity K_s (unit: m^2 s^{-1}) from the model results. Each colored dot in **(B)** indicates each timing denoted by the same colored dot in **(A)**.

response time of salinity distribution must coincide with the timescale of variation in vertical mixing (Park and Kuo, 1996). As vertical mixing increases, the salinity gradient increases, which can be the maximum during spring tides. In particular, this phenomenon occurs in short estuaries rather than long estuaries where the timescale of mass response is long (Park and Kuo, 1996). We estimated the vertical eddy diffusivity of salt (K_s) to examine the intensity of vertical mixing, which is the most common approach for quantification of the mixing in estuaries (Fischer, 1972; MacCready, 2007). We selected the 5 g kg^{-1} isohaline of bottom salinity to represent the salt intrusion length (Figure 10). A scatter plot of the salt intrusion distinctly shows an inverse linear relationship between the isohaline length and K_s. During the spring tide, when vertical mixing was strongest, the salinity gradient was at its maximum because the salt intrusion was at its minimum.

The relationship between exchange flow and salinity gradient with respect to vertical mixing can be summarized as follows. As vertical mixing increases, the vertical shear of exchange flow decreases and stratification weakens. As a result, F_E driving the landward salt flux decreases, and the total salt flux becomes seaward, resulting in salt intrusion that is shortened but vertically homogenous. During the spring tide, salt intrusion is minimal, and the salinity gradient in the lower estuary is large (~ 2.3 km^{-1}); we found that it was 2–4 times larger than that of other longer estuaries (e.g., 1 km^{-1} in the Modaomen estuary [~ 63 km] and 0.6 km^{-1} in the Hudson River estuary [> 100 km]). The salinity gradient was large enough to overwhelm the vertical mixing effect, which intensifies the vertical shear of exchange flow, resulting in the development of stratification. Therefore, as F_E increases, the total salt flux becomes landward. As the tidal range decreases, salt is imported into the estuary and salt intrusion becomes longer. The

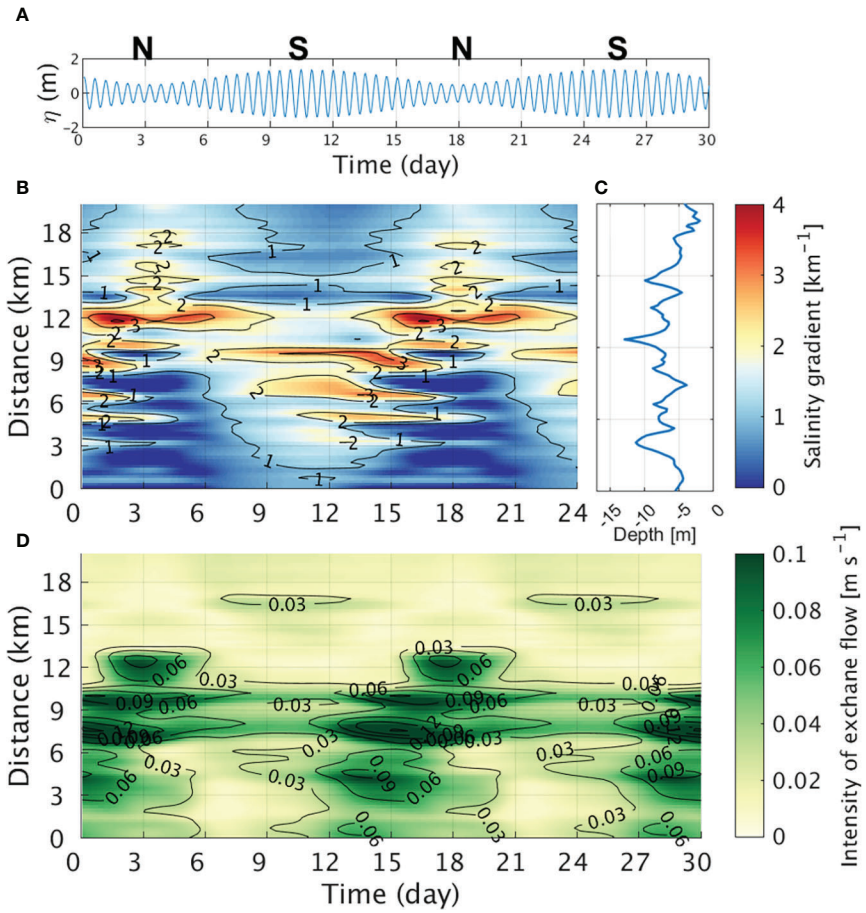

FIGURE 11
(A) Time series of sea-level height at the mouth of the real case and the N and S stand for neap tide and spring tide, respectively. Hovmöller diagram of **(B)** horizontal salinity gradient along the channel (unit: km^{-1}). **(C)** Depth variation in the Sumjin River estuary toward upstream, which is averaged across the channel (unit: m). **(D)** Hovmöller diagram of the depth-averaged absolute value of the exchange flow (unit: ms^{-1}).

strengthening of the convergence of the landward salt flux during this period induces the maximum salinity gradient to proceed further into the estuary. This process is repeated while the tidal range decreases, such that the maximum salinity gradient at the head enhances the exchange flow during the neap tide.

Model application to realistic topography in the Sumjin River estuary

The idealized model clearly showed the variations of salinity gradient in the entire short estuary and its effect on the exchange flow over fortnightly tidal cycles. However, the idealized model did not consider the effect of complicated topography on variations in the salinity gradient and exchange flow. A numerical experiment with realistic topography was conducted to confirm the spatiotemporal variations of the salinity gradient and exchange flow in the Sumjin River estuary. For the realistic model, the river discharge rate (30 m^3s^{-1}) in 2013 was applied. Other model settings were the same as those used in the idealized model experiment.

The realistic model appropriately simulated the fortnightly variation in the depth-averaged salinity and the horizontal salinity gradient (Figures 3E–J). The horizontal salinity gradient changed periodically over fortnightly tidal cycles as in the idealized model experiment, although its large value appeared sparsely owing to an uneven depth distribution (Figure 11). Occurrence of large horizontal salinity gradients may be attributed to the saline waters which persist for a few days due to irregular depth. The spatiotemporal change of exchange flow corresponds well with that of the horizontal salinity gradient, which shows out of phase between lower and upper estuaries, as in the idealized model experiment.

Both idealized and realistic models showed the larger salinity gradient and the stronger exchange flow variation during the spring tide, which is consistent with the observations of Cho et al. (2020) in the lower estuary. However, the model results suggest that the salinity gradient is smaller and the exchange flow is weaker in the upper estuary during the spring tide, but it is opposite to that in the lower estuary.

Summary and conclusions

Fortnightly variation of horizontal salinity gradient and exchange flow, and their mechanism, were investigated in an estuary with a short length and narrow width (i.e., the Sumjin River estuary). The fortnightly variation of the exchange flow had a different phase in the lower and upper estuary: in the lower estuary, it was strong during spring tides, but in the upper estuary, it was strong during neap tides.

During transitions from spring to neap tides, vertical mixing becomes weaker and baroclinic forcing dominates owing to the maximum salinity gradient moving from the mouth to the head. This intensifies the vertical shear of exchange flow and develops stratification, increasing the steady shear dispersion salt flux. Therefore, the total salt flux is landward and the salt intrusion becomes longer. Where convergence is strong while the salt flux is landward, the salinity gradient is at a maximum, making the exchange flow stronger toward the inside of the estuary. The salt intrusion continues to lengthen, and the salinity gradient at the head of estuary is maximized and the exchange flow is also strong during neap tides. While the tidal range increases, vertical mixing becomes stronger throughout the estuary and more dominant than the baroclinic forcing effect, resulting in weaker exchange flow and decreased landward salt flux. The total salt flux is seaward by the advective salt flux. As salt is exported out of the estuary, salt intrusion continues to be shortened. Owing to the minimum salt intrusion during the spring tide, the salinity gradient increases in the lower estuary.

As vertical mixing decreases after the peak spring tide, baroclinic forcing becomes dominant, and the exchange flow begins to intensify again. The determinant of the fortnightly variation of exchange flow in the entire estuary is the salinity gradient. The spatiotemporal change of strong exchange flow (> 0.04 m s^{-1}) corresponds well with that of high Simpson number ($Ri_x > 3$). Owing to the change in the salt intrusion determined by vertical mixing, the maximum salinity gradient periodically reciprocates, while the tidal range decreases; this dominates the vertical mixing effect, enhancing the exchange flow. Since the maximum salinity gradient is out of phase between the lower and upper estuaries, the phase of the exchange flow also varies depending on the location of the estuary.

Fortnightly variation in the salinity gradient and exchange flow also appeared in the model using realistic topography for the Sumjin River estuary although the non-linear topographic effects disturbed the fortnightly oscillation of the maximum salinity gradient zone and the exchange flow. This study proposes that the observations at a specific point cannot represent the fortnightly variation in the horizontal salinity gradient and exchange flow. The spatiotemporal variation over the entire estuary should be investigated to understand the estuarine circulation in a short and narrow estuary like the Sumjin River estuary.

Data availability statement

The raw data supporting the conclusions of this article will be made available by the authors, without undue reservation.

Author contributions

Conceptualization, E-BC and Y-KC. Methodology, E-BC and Y-KC. writing draft, E-BC. review and editing, Y-KC, Y-JT, and HN. visualization, E-BC. supervision, Y-KC and Y-JT. All authors contributed to the article and approved the submitted version.

Funding

This research was supported by the Korea Institute of Marine Science & Technology Promotion(KIMST) funded by the Ministry of Oceans and Fisheries (20220541) and the National Research Foundation (NRF) funded by the Korean government (NRF-2022M3I6A1085573).

Conflict of interest

The authors declare that the research was conducted in the absence of any commercial or financial relationships that could be construed as a potential conflict of interest.

Publisher's note

All claims expressed in this article are solely those of the authors and do not necessarily represent those of their affiliated organizations, or those of the publisher, the editors and the reviewers. Any product that may be evaluated in this article, or claim that may be made by its manufacturer, is not guaranteed or endorsed by the publisher.

References

Andutta, F. P., de Miranda, L. B., Franca Schettini, C. A., Siegle, E., da Silva, M. P., Izumi, V. M., et al. (2013). Temporal variations of temperature, salinity and circulation in the peruipe river estuary (nova vicosa, ba). *Contin. Shelf Res.* 70, 36–45. doi: 10.1016/j.csr.2013.03.013

Becker, M. L., Luettich, R. A., and Seim, H. (2009). Effects of intratidal and tidal range variability on circulation and salinity structure in the cape fear river estuary, north carolina. *J. Geophys. Res.* 114, (C4). doi: 10.1029/2008JC004972

Bowen, M. M., and Geyer, W. R. (2003). Salt transport and the time-dependent salt balance of a partially stratified estuary. *J. Geophys. Res. Oceans* 108, (C5). doi: 10.1029/2001JC001231

Burchard, H., Hetland, R. D., Schulz, E., and Schuttelaars, H. M. (2011). Drivers of residual estuarine circulation in tidally energetic estuaries: Straight and irrotational channels with parabolic cross section. *J. Phys. Oceanogr.* 41, 548–570. doi: 10.1175/2010JPO4453.1

Chen, S.-N., Geyer, W. R., Ralston, D. K., and Lerczak, J. A. (2012). Estuarine exchange flow quantified with isohaline coordinates: Contrasting long and short estuaries. *J. Phys. Oceanogr.* 42, 748–763. doi: 10.1175/JPO-D-11-086.1

Cho, E.-B., Cho, Y.-K., and Kim, J. (2020). Enhanced exchange flow during spring tide and its cause in the sumjin river estuary, korea. *Estuaries Coasts.* 43, 525–534. doi: 10.1007/s12237-019-00636-9

de Miranda, L. B., Bérgamo, A. L., and de Castro, B. M. (2005). Interactions of river discharge and tidal modulation in a tropical estuary, ne brazil. *Ocean Dyn.* 55, 430–440. doi: 10.1007/s10236-005-0028-z

Dijkstra, Y. M., Schuttelaars, H. M., and Burchard, H. (2017). Generation of exchange flows in estuaries by tidal and gravitational eddy viscosity-shear covariance (esco). *J. Geophys. Res. Oceans.* 122, 4217–4237. doi: 10.1002/2016JC012379

Fischer, H. (1972). Mass transport mechanisms in partially stratified estuaries. *J. Fluid Mech.* 53, 671–687. doi: 10.1017/S0022112072000412

Garcia, A. M. P., Geyer, W. R., and Randall, N. J. E. (2022). Exchange flows in tributary creeks enhance dispersion by tidal trapping. *Estuaries Coasts.* 45, 363–381. doi: 10.1007/s12237-021-00969-4

Garel, E., and Ferreira, Ó. (2013). Fortnightly changes in water transport direction across the mouth of a narrow estuary. *Estuaries Coasts.* 36, 286–299. doi: 10.1007/s12237-012-9566-z

Geyer, W. R., and MacCready, P. (2014). The estuarine circulation. *Annu. Rev. Fluid Mech.* 46, 175–197. doi: 10.1146/annurev-fluid-010313-141302

Geyer, W. R., and Ralston, D. K. (2015). Estuarine frontogenesis. *J. Phys. Oceanogr.* 45, 546–561. doi: 10.1175/JPO-D-14-0082.1

Geyer, W. R., Trowbridge, J. H., and Bowen, M. M. (2000). The dynamics of a partially mixed estuary. *J. Phys. Oceanogr.* 30, 2035–2048. doi: 10.1175/1520-0485(2000)030<2035:TDOAPM>2.0.CO;2

Gong, W. P., Maa, J. P.-Y., Hong, B., and Shen, J. (2014). Salt transport during a dry season in the modaomen estuary, pearl river delta, china. *Ocean Coast. Management.* 100, 139–150. doi: 10.1016/j.ocecoaman.2014.03.024

Hansen, D. V., and Rattray, J. M. (1966). New dimensions in estuary classification 1. *Limnology Oceanography.* 11 (3), 319–326. doi: 10.4319/lo.1966.11.3.0319

Hunkins, K. (1981). Salt dispersion in the hudson estuary. *J. Phys. Oceanogr.* 11, 729–738. doi: 10.1175/1520-0485(1981)011<0729:SDITHE>2.0.CO;2

Large, W. G., McWilliams, J. C., and Doney, S. C. (1994). Oceanic vertical mixing: A review and a model with a nonlocal boundary layer parameterization. *Rev. Geophys.* 32, 363–403. doi: 10.1029/94RG01872

Lerczak, J. A., Geyer, W. R., and Chant, R. J. (2006). Mechanisms driving the time-dependent salt flux in a partially stratified estuary. *J. Phys. Oceanogr.* 36, 2296–2311. doi: 10.1175/JPO2959.1

Lerczak, J. A., Geyer, W. R., and Ralston, D. K. (2009). The temporal response of the length of a partially stratified estuary to changes in river flow and tidal amplitude. *J. Phys. Oceanogr.* 39 (4), 915–933. doi: 10.1175/2008jpo3933.1

Li, X., Geyer, W. R., Zhu, J., and Wu, H. (2018). The transformation of salinity variance: A new approach to quantifying the influence of straining and mixing on estuarine stratification. *J. Phys. Oceanogr.* 48, 607–623. doi: 10.1175/JPO-D-17-0189.1

Li, C., and O'Donnell, J. (2005). The effect of channel length on the residual circulation in tidally dominated channels. *J. Phys. Oceanogr.* 35, 1826–1840. doi: 10.1175/JPO2804.1

MacCready, P. (2007). Estuarine adjustment. *J. Phys. Oceanogr.* 37, 2133–2145. doi: 10.1175/JPO3082.1

MacCready, P. (2011). Calculating estuarine exchange flow using isohaline coordinates. *J. Phys. Oceanogr.* 41, 1116–1124. doi: 10.1175/2011JPO4517.1

MacCready, P., and Geyer, W. R. (2010). Advances in estuarine physics. *Annu. Rev. Mar. Sci.* 2, 35–58. doi: 10.1146/annurev-marine-120308-081015

Mantovanelli, A., Marone, E., da Silva, E. T., Lautert, L. F., Klingenfuss, M. S., Prata, V. P., et al. (2004). Combined tidal velocity and duration asymmetries as a determinant of water transport and residual flow in paranagua bay estuary. *Estuar. Coast. Shelf Sci.* 59, 523–537. doi: 10.1016/j.ecss.2003.09.001

Park, K., and Kuo, A. Y. (1996). Effect of variation in vertical mixing on residual circulation in narrow, weakly nonlinear estuaries. *Coast. Estuar. Stud.* 53, 301–317. doi: 10.1029/CE053p0301

Pein, J. U., Stanev, E. V., and Zhang, Y. J. (2014). The tidal asymmetries and residual flows in ems estuary. *Ocean Dyn.* 64, 1719–1741. doi: 10.1007/s10236-014-0772-z

Pritchard, D. W. (1967). *What Is an Estuary: Physical Viewpoint* (Washington. D.C: American Association for the Advancement of Science, Washington Publications).

Ralston, D. K., Geyer, W. R., and Lerczak, J. A. (2008). Subtidal salinity and velocity in the hudson river estuary: Observations and modeling. *J. Phys. Oceanogr.* 38, 753–770. doi: 10.1175/2007JPO3808.1

Ralston, D. K., and Stacey, M. T. (2005). Longitudinal dispersion and lateral circulation in the intertidal zone. *J. Geophys. Res. Oceans* 110, (C7). doi: 10.1029/2005JC002888

Rayson, M. D., Gross, E. S., Hetland, R. D., and Fringer, O. B. (2017). Using an isohaline flux analysis to predict the salt content in an unsteady estuary. *J. Phys. Oceanogr.* 47, 2811–2828. doi: 10.1175/JPO-D-16-0134.1

Schulz, E., Schuttelaars, H. M., Gräwe, U., and Burchard, H. (2015). Impact of the depth-to-width ratio of periodically stratified tidal channels on the estuarine circulation. *J. Phys. Oceanogr.* 45, 2048–2069. doi: 10.1175/JPO-D-14-0084.1

Scully, M. E., Geyer, W. R., and Lerczak, J. A. (2009). The influence of lateral advection on the residual estuarine circulation: A numerical modeling study of the hudson river estuary. *J. Phys. Oceanogr.* 39, 107–124. doi: 10.1175/2008JPO3952.1

Shaha, D. C., and Cho, Y.-K. (2009). Comparison of empirical models with intensively observed data for prediction of salt intrusion in the sumjin river estuary, korea. *Hydrol. Earth Syst. Sci.* 13, 923–933. doi: 10.5194/hess-13-923-2009

Shchepetkin, A. F., and McWilliams, J. C. (2005). The regional oceanic modeling system (roms): A split-explicit, free-surface, topography-following-coordinate oceanic model. *Ocean Modell.* 9, 347–404. doi: 10.1016/j.ocemod.2004.08.002

Stacey, M. T., Burau, J. R., and Monismith, S. G. (2001). Creation of residual flows in a partially stratified estuary. *J. Geophys. Res.* 106, 17013–17037. doi: 10.1029/2000JC000576

Stanev, E. V., Al-Nadhairi, R., and Valle-Levinson, A. (2015). The role of density gradients on tidal asymmetries in the German bight. *Ocean Dyn.* 65, 77–92. doi: 10.1007/s10236-014-0784-8

Uncles, R. J., and Stephens, J. A. (1990). The structure of vertical current profiles in a macrotidal, partly-mixed estuary. *Estuaries.* 13, 349–361. doi: 10.2307/1351780

Valle-Levinson, A. (2010). *Contemporary issues in estuarine physics* (Cambridge, UK: Cambridge University Press).

Wang, T., Geyer, W. R., Engel, P., Jiang, W. S., and Feng, S. Z. (2015). Mechanisms of tidal oscillatory salt transport in a partially stratified estuary. *J. Phys. Oceanogr.* 45 (11), 2773–2789. doi: 10.1175/jpo-d-15-0031.1

Wei, X., Williams, M. E., Brown, J. M., Thorne, P. D., and Amoudry, L. O. (2022). Salt intrusion as a function of estuary length in periodically weakly stratified estuaries. *Geophys. Res. Lett.* 49 (15). doi: 10.1029/2022GL099082

frontiers | Frontiers in Marine Science

TYPE Original Research
PUBLISHED 20 December 2022
DOI 10.3389/fmars.2022.1061769

OPEN ACCESS

EDITED BY
Yi Pan,
Hohai University, China

REVIEWED BY
Ping Wang,
University of South Florida, United States
Zhiqiang Li,
Guangdong Ocean University, China

*CORRESPONDENCE
Chao Cao
caochao@tio.org.cn
KaiZhe Fu
fukaizhe@mail.cgs.gov.cn

SPECIALTY SECTION
This article was submitted to Coastal Ocean Processes, a section of the journal Frontiers in Marine Science

RECEIVED 05 October 2022
ACCEPTED 15 November 2022
PUBLISHED 20 December 2022

CITATION
Fu G, Cao C, Fu K, Song Y, Yuan K, Wan X, Zhu Z, Wang Z and Huang Z (2022) Characteristics and evaluation of coastal erosion vulnerability of typical coast on Hainan Island. *Front. Mar. Sci.* 9:1061769. doi: 10.3389/fmars.2022.1061769

Characteristics and evaluation of coastal erosion vulnerability of typical coast on Hainan Island

GuoWei Fu[1], Chao Cao[2,3,4]*, KaiZhe Fu[1]*, YanWei Song[1], Kun Yuan[1], XiaoMing Wan[1], ZiAng Zhu[1], ZhaoFan Wang[1] and ZanHui Huang[1]

[1]Haikou Research Center of Marine Geology, China Geological Survey, Haikou, China, [2]Third Institute of Oceanography, Ministry of Natural Resources, Xiamen, China, [3]Fujian Provincial Key Laboratory of Marine Ecological Conservation and Restoration, Xiamen, China, [4]Key Laboratory of Marine Ecological Conservation and Restoration, Ministry of Natural Resources, Xiamen, China

Coastal erosion vulnerability assessment is widely used to assess the loss degree of coastal zone caused by erosion, and plays an important role in coastal natural resources protection, planning, management and decision-making. Based on the natural and social characteristics of the east coast of Qiongdong and the coastal erosion vulnerability index (CVI) method, this study selected 8 assessment indicators, such as shoreline change rate (U1). The Delphi method and the entropy weight method were used to calculate the comprehensive index weight, combined with CVI method and geographic information system (GIS) technology, to quantitatively evaluate the temporal and spatial distribution characteristics of typical coastal erosion vulnerability such as coral reefs in the east of Hainan Island. The study area was divided into 5 grades: very low (31%), low (10%), moderate (28%), high (24%) and high vulnerability (7%), and the overall performance was moderate erosion vulnerability. The research showed that the interannual downward rate erosion of beach (U3) and the rate of change of the isobath (U2) of the beach were the main controlling factors affecting the vulnerability of coastal erosion in the study area, and the coastal dynamic factor had a greater impact than the other two factors. As a natural barrier, the coral reefs in the study area had good wave absorption and energy reduction, and the coral reef coasts showed low coastal erosion vulnerability, due to the complex hydrodynamic characteristics, estuary coasts is the most vulnerable areas. The verification results of the ROC-AUC method showed that the accuracy of erosion vulnerability was 68.9%, which provided an important reference for the ecological restoration of tropical coral reef biological coasts and the development and management of the Hainan Qiongdong coastal zone.

KEYWORDS

Hainan Island, coral reef coast, human activities, index method, coastal erosion vulnerability

1 Introduction

The coastal zone is the interaction zone between the ocean and land, and it is also the zone where human activities are concentrated (Barragan and Andreis, 2015). In recent years, with global warming, rapid sea level rise, frequent extreme climate events and intensified human production activities, the coastal zone has been experiencing increasingly serious coastal erosion risks, posing a very large threat to coastal zone engineering, natural ecological coastlines and ecosystems. (Jones and Phillips, 2011; Shi and Kasperson, 2015). Coastal erosion is a process of loss caused by the imbalance of sediments in a certain bank section. The main manifestations include shoreline retreat, downward erosion of beaches, high beach stability and low beach erosion, sediment coarsening, etc. (Mangor et al., 2017). Many scholars have studied coastal erosion processes and mechanisms (Bruun, 1962; Chen et al., 1988; Chen et al., 2004; Thampanya et al., 2006), erosion methods (Cai et al., 2008; Cai et al., 2022) and model research (Mohamed et al., 2021), erosion hazard evaluation (Liu, 2015), erosion protection management (Pan et al., 2022), and the quantitative relationship between economics and erosion has been systematically studied (Annelies et al., 2021; Hagedoorn et al., 2021).

With the in-depth study of coastal erosion, coastal erosion vulnerability assessment is widely used to assess the degree of loss caused by coastal erosion, and it plays an important role in coastal natural resource protection, planning and management decision-making (Kumar and Kunte, 2012; Andrade et al., 2019). There are certain differences in the scope, indicators and methods selected by different scholars in the assessment of coastal erosion vulnerability due to differences in coastal regional characteristics. Among them, the evaluation methods include the index method, numerical model method, fuzzy decision method, etc. (Chu et al., 2005). The earliest and most widely used is the coastal vulnerability index (CVI) method proposed by Gronitz (Gornitz, 1991), which comprehensively considers the risk levels of multiple factors, The evaluation index system is established from the aspects of vulnerability characteristics and causes, and the vulnerability index is formed by using mathematical methods to represent the vulnerability degree of the evaluation unit, compared with other methods, This method is simple and easy to operate, and it considers the superposition effect of different index factors, so it is highly scientific. Many scholars use CVI to conduct evaluation research at different levels and scales (Thieler and Hammar-Klose, 2000; Boruff et al., 2005; Dominguez et al., 2005).

In recent years, scholars have used various additional means to carry out coastal erosion vulnerability assessments, and thus, there has been rapid development and application of coastal erosion vulnerability assessments. Wang et al. (2021) used the percentile ranking method to comprehensively evaluate the physical and social vulnerability of the urban scale in the Yangtze River Delta region, and used bathymetric changes and independent evaluation to verify the reliability of the evaluation results. This method of verifying the results of the assessment is more credible and scientific, and is also the most commonly used method for vulnerability assessments at this stage. Yoo et al. (2014) proposed the environmental vulnerability index (EVI) to evaluate the coastal vulnerability of Jakarta, Indonesia, based on historical disasters and socioeconomic statistics, which were more affected by the vulnerability caused by land-based factors than was the CVI. In addition, some scholars have combined vulnerability, exposure, adaptability and hazard to assess coastal erosion risk (Merlotto et al., 2016; Narra et al., 2017; Roy et al., 2021; Swami and Parthasarathy, 2021). Based on vulnerability research, Swami and Parthasarathy proposed that system vulnerability includes three main factors: exposure, sensitivity and adaptability, which can comprehensively explain and evaluate the inherent characteristics of various coasts. Roy et al., (2021) and others selected 19 indicators, such as physical, environmental and socioeconomic geography, in the Mekhna River estuary area in Bangladesh and used the analytic hierarchy process (AHP) to evaluate the hazard, vulnerability and exposure indices. The area under the curve (AUC) has been used to verify the reliability of evaluating the degree of erosion risk. This research covers 19 index factors and considers almost all the influencing factors that can be involved, making it a more comprehensive assessment of the vulnerability of the Meghna Estuary. Cao Chao (Cao et al., 2022a; Cao et al., 2022b) used different methods to assess the vulnerability of coastal erosion from two scales, the national scale and the small scale of the Pearl River Estuary Greater Bay Area. Furthermore, the innovative introduction of cloud model theory at the national scale to construct a coastal erosion vulnerability assessment system for a comprehensive assessment of vulnerability showed that the cloud model theoretical index system and method were suitable for the assessment of coastal erosion vulnerability in mainland China. Second, on the small scale, a PRE - PRE coastal erosion vulnerability assessment system was established by comprehensively using the AHP, ideal solution similarity ranking technology (TOPSIS), independent weight method, Jenks natural discontinuity method (Jenks), exposure-sensitivity-adaptation (ESA) model and obstacle degree methods. Different evaluation methods were used at two different scales, and good research results were obtained, which made improved the development of research on coastal erosion vulnerability.

At present, scholars have made more assessments of coastal erosion vulnerability, and the vulnerability index factors have mainly selected generalized influencing factors. There is little research on regional typical shore sections, and the individualized and refined considerations of influencing factors are also relatively limited. The differences in the erosion vulnerability of different types of shore sections have not been

studied and analyzed. For example, the typical tropical coral reef-type coast, cape bay coast, et al. has not been evaluated for coastal erosion vulnerability, and the difference between different types of coastal erosion vulnerability has not been studied. Based on the tropical coral reef coast, cape bay coast and estuary coast et al. of Hainan Qiongdong, this paper selected the typical coast of Qionghai-Wanning in Hainan Qiongdong. Eight small-scale and typical influencing factors, such as shoreline change rate and shoreline erosion rate, were comprehensively selected from the aspects of coastal morphological characteristics, coastal dynamic characteristics, and socioeconomic and human activities, such as coastline change rate and interannual downward rate erosion. The weight of each evaluation index was determined by the AHP method, Delphi method (DM) and entropy method (TEM). The CVI of the study area was calculated, and the coastal erosion was divided by the vulnerability rating, and a comprehensive assessment of the vulnerability of typical coastal erosion was conducted.

2 Study area

The Qionghai-Wanning coast is located on eastern Hainan Island, China Figure 1A, and is one of the most important coastal development zones for tropical coral reef organisms in China (110°00′~110°40′E, 18°35′~19°29′N) (Figure 1B). Its coral reefs are mainly distributed in the nearshore sea area north of Qionghai Tanmen Port, and the type of reefs is fringing reef parallel to the coast. The length of the fringing reef is about 15km from south to north, and the width of the reef flat is about 2km, water depth is about 2m (Figure 1C). Quaternary and Cambrian strata are mainly exposed in the coastal zone of the study area (Tian et al., 2016). The climate type is a tropical marine monsoon climate, the tide is an irregular diurnal tide, the wind direction is mainly southerly wind in summer and northeasterly wind in winter, and the waves are mainly mixed waves, among which the mixed waves dominated by swell have the highest frequency, followed by the wind waves, and the pure swell has the lowest frequency. Marine disasters are mainly storm surges caused by tropical cyclones. From 1964 to 2018, a total of 34 typhoons made landfall in the study area, accounting for 35.4% of the total, making the area have the most landed typhoons in Hainan (Tropical et al., 2021).

In the 1970s and 1980s, the coastal erosion of Hainan Island already affected approximately 53% of the coastline (Xia et al., 1993), and in the 1990s, the eroded coast of Hainan increased to 71.9%, and there were 64 eroded coasts on the whole island, and erosion was strong. There were 7 shore sections, of which 3 were located in the strongly eroded section of the study area, accounting for approximately 42.8%. Coastal erosion has become the most important disaster problem on the coast of

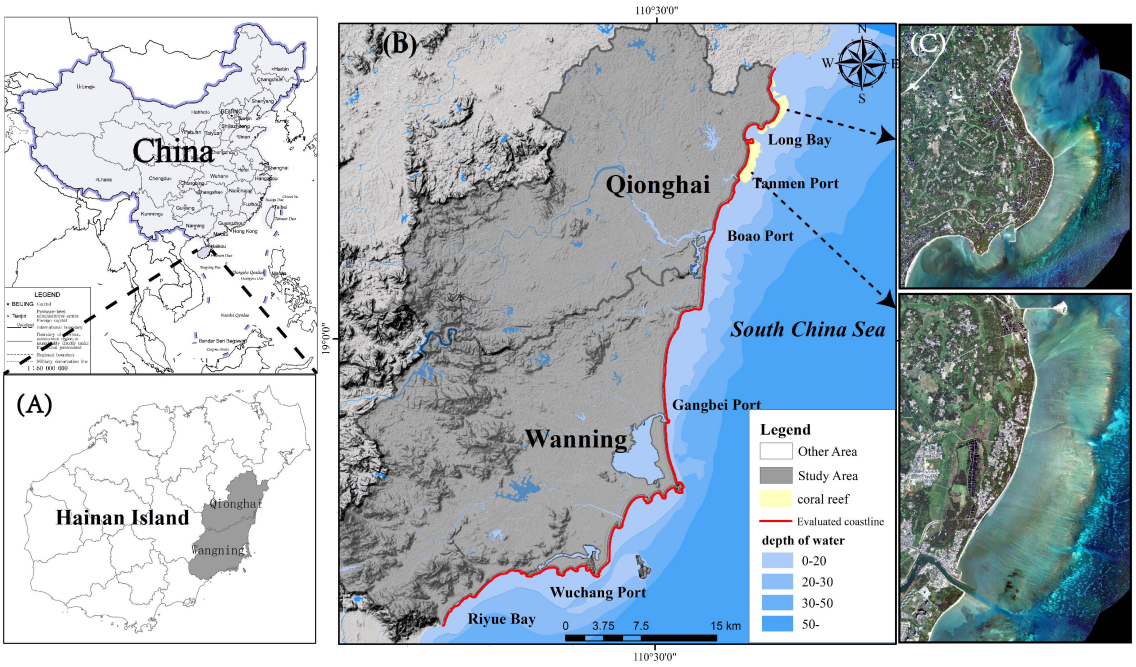

FIGURE 1
(A) Study area located on the Qionghai-Wanning coast of eastern Hainan **(B)** Images based on satellite images from China, The assessed coastline is the outer coastline of Qionghai-Wanning. **(C)** High-resolution remote sensing images of coral fringing reef with a resolution of 0.68 m.

Hainan Island, and the study area is the hardest hit area of coastal erosion (Chen et al., 2010b). Research analysis has shown that intensified human activities, such as the construction of reservoirs in the upper reaches of the river, the dredging of riverbeds and coasts, the mining of coral reefs and beach rocks, and various coastal projects, combined with frequent typhoons and other severe marine weather scouring the coast, are the main reasons causing the increasing coastal erosion on Hainan Island (Ji et al., 2007). According to the survey and statistics, the coverage rate of live coral in the study area declined from 32.2% in 2004 to 6.67% in 2018 (Huang et al., 2019), resulting in a great change in the structure of the biological community. Thus, the coast of Qiongdong, Hainan, is suffering from severe coastal erosion.

3 Materials and methods

3.1 Establishment of the evaluation index system

The construction of the evaluation index system comprehensively considers the principles of special regionality, coastal erosion correlation and data extractability and is mainly selected from coastal morphology, coastal dynamics, and socioeconomic and human activity factors. Coastal morphology is the direct bearer of the impact of erosion and is an internal characteristic of the coast, while the dynamic changes in the ocean are the direct external manifestation of the impact of erosion, which is an external featureMattei (Mattei et al., 2018), and socioeconomic and human activities are the driving factors for the occurrence of erosion.

The coastal dynamic characteristics of the coast are reflected from the beach in the supratidal zone, the shoreline in the intertidal zone, and the nearshore waters in the subtidal zone. Intuitive factors, such as the change rate of the shoreline (U1) and the interannual downward rate erosion of the beach (U3), are the most intuitive factors that can be used to characterize the dynamic evolution of the coast. Additionally, the construction of breakwaters, ports and erosion protection walls have prevented the further erosion and retreat of the shoreline to a certain extent, and coastal erosion has shifted into the downward erosion of the underwater bank slope, causing the erosion of the isobath line to approach the shore. Therefore, the rate of change of the isobath (U2) can be used to characterize the erosion of the underwater bank slope. Coastal morphological characteristics are the characteristics of the current state of the coast. Different coastal morphological characteristics bear different degrees of coastal erosion. Coast type (U4), beach width (U5), and beach slope (U6) are the basic components of coastal morphology. Socioeconomic and human activities have a greater impact on the change in coastal appearance, which in turn affects the degree of coastal erosion. Coastal socioeconomics is directly reflected by the degree of coastal development (U7), and the density of human activities (U8), which can indirectly indicate human activities. The evaluation system was constructed by obtaining the index values of each factor from each evaluation unit c1-c29 (Figure 2A) (Cai et al., 2019).

(1) U1

Multispectral remote sensing images are widely used in coastal resource surveys and dynamic evolution studies, and for coastline extraction, they have the advantages of large-scale and rich spectral features (Boak and Turner, 2005). To reduce the interpretation errors caused by remote sensing images of different resolutions and different time periods, this paper adopted Google Earth satellite images with the same resolution and the same season and selected the years 1985, 1990, 1995, 2000, 2005, 2010 and 2015, for a total of 7 time periods of remote sensing image data (Figure 2B), with a resolution of 16.8 m. Visual interpretation was used to extract the coastlines of each year based on the waterline (Alberico et al., 2012; Yang, 2013). The shoreline change rate adopted the LRR method provided by the digital coastline analysis system DSAS4.3 (http://woodshole.er.usgs.gov/project-pages/dsas/) (Deepika et al., 2013), starting from the northernmost part of the Qionghai administrative boundary. At the starting point (110°40'15" E, 19°21'32" N), a section was generated every 50 m, and a total of 2,910 cross-sections were used to analyze the changes in the Qionghai-Wanning coastline. The calculated value was negative, indicating that the coast was eroded, while a positive value would indicate that the coast was silted up (Table 1).

(2) U2

We compared and analyzed the erosion and deposition of the shallow seabed by collecting multiple periods of charts or isobath data in topographic maps. This paper used the 2005 nautical chart and the 2019 1:50,000 topographic map isobath 2 data (Figure 2B), additionally, the LRR method in the DSAS plug-in was used to calculate the 20-m isobath changes from 2005-2019 (Table 1).

(3) U3

The direct manifestation of coastal erosion is that in addition to shoreline retreat, downward rate erosion of beaches is an important manifestation and a critical factor in vulnerability assessment. However, at present, many scholars have not considered and analyzed the vertical erosion and siltation changes of the beach due to the large assessment scope and the lack of long-term continuous monitoring, which makes the vulnerability assessment results unrepresentative. In this paper, the monitoring data of 44 beaches in the Qionghai-Wanning coastal zone were used to calculate the interannual erosion and silting rate of each beach through interannual monitoring. If there was no beach, such as bedrock and artificial shoreline, the erosion rate of the beach was 0. This is the first assessment to incorporate the interannual downward rate erosion of beaches into the vulnerability assessment system, making the assessment results more scientific and representative (Table 1).

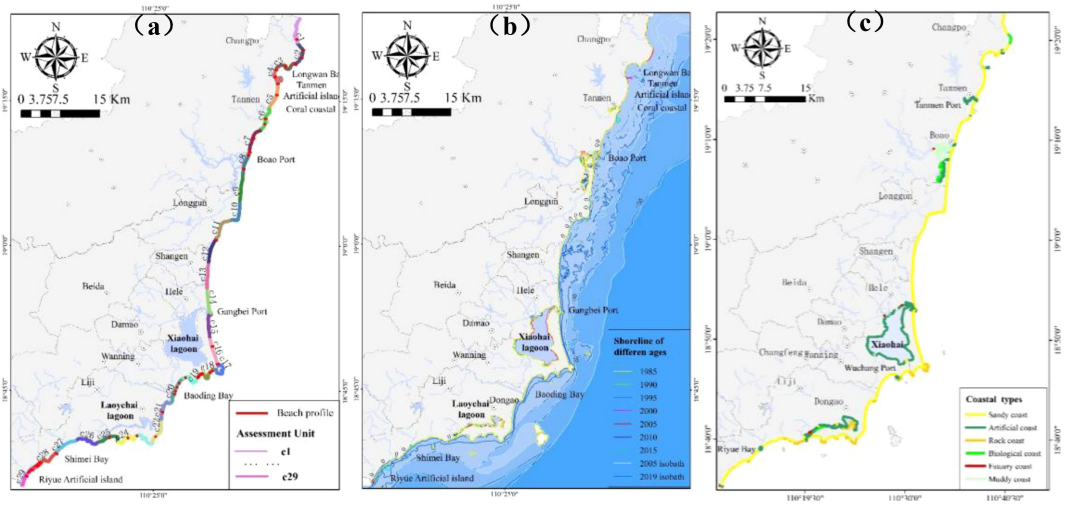

FIGURE 2
Evaluation factor index element distribution map. **(A)** Qionghai-Wanning vulnerability assessment unit division map. **(B)** Distribution map of coastlines in 7 periods from 1985 to 2015 and isobath distribution map from 2005-2019. **(C)** Qionghai-Wanning 2021 coastline type.

(4) U4

The coast itself is the direct bearer of coastal erosion, the study area has typical coral reef coast, cape bay coast, estuary coast, artificial island coast, etc. and different coast types have different degrees of erosion vulnerability. Such as coral reef coast, A large amount of coral reef debris is washed and deposited on the bank by the tide to form a coral reef beach (Figure 3A), which can dissipate wave energy and protect the beach from erosion. At the same time, the length, width, coarse rate and water depth of the fringing reef also have a great effect on wave energy dissipation, therefore, the coral reef coast has a low degree of vulnerability. In addition, the corresponding erosion vulnerability of coastal types, such as estuaries, artificial islands, and ports, presents different states (Figures 3B, C). The coast type data come from the field survey measurement data of the study area in 2021 (Figure 2C). Since the coastline type is dimensionless, the weights of erosion and siltation effects are assigned according to different coastline types (Table 1).

(5) U5

The beach width is characterized by the distance between the water edge and the grass edge or the shelterbelt; the smaller the width of the beach is, the greater the energy of tidal water scouring the beach, the higher the degree of erosion and retreat of the corresponding shoreline, and the higher the vulnerability. Wider beaches often fail to scour vegetation slopes and have a larger distance for buffering and releasing energy, so their vulnerability is relatively low. The beach width data in this paper were obtained from a field survey of the field research area in 2021 (Table 1).

(6) U6

The greater the slope value of the beach is, the stronger the scouring ability of the waves to increase water and climb the slope, and the corresponding erosion vulnerability is larger and vice versa. The beach slope data were derived from field survey measurement data in the study area in 2021. If there were several survey points in a unit, the average value of the beach slope recorded at each survey point was taken as the slope value of the section (Table 1).

(7) U7

The socioeconomic development and construction of coastal areas also enhances the degree of vulnerability to coastal disasters, making the degree of coastal development an indispensable factor in vulnerability assessment (Dolan and Walker, 2006; Bathi and Das, 2016; Hoque et al., 2019; Alam et al., 2020). The degree of coastal development mainly refers to the status quo of coastal utilization and development, including tourism development, aquaculture development, port and dam construction, man-made engineering construction and development. The higher the degree of development is, the higher the corresponding vulnerability index (Table 1).

(8) U8

The density of human activities is represented by the density of human activities on different coasts in the same time period or in a specific time period. The rapid growth of coastal populations and changes in natural habitats have brought greater pressure on coastal land, and the degree of vulnerability has gradually increased; in contrast, natural coasts with less human activities have better coastal beaches and environments, and their vulnerability is lower (Parvin et al., 2008; Appeaning, 2013; Narra et al., 2019). There are different anthropogenic activities, such as fishing activities, tourism, and resident population activities, along the coast of the study area. The data were obtained through the Baidu population heatmap to obtain the relative activity data of the Qionghai-Wanning coastal

TABLE 1 Assessment indicator vulnerability grading scale.

Indicators	Vulnerability level					Data sources
	Very high	High	Moderate	Low	Very low	
(1) Change rate of the shoreline U1 (m/a)	-4.22--1.27	-1.27-1.68	1.68-4.63	4.63-7.58	7.58-10.52	1985-2015Google Earth remote sensing images
(2) Rate of change of isobath U2 (m/a)	-31.21--23.45	-23.45--15.69	-15.69--7.93	-7.93~-0.17	-0.17-7.59	2015 chart, 2019 topographic map
(3) Interannual downward rate erosion of the beach U3(cm/a)	-12.80--7.00	-7.00--1.20	-1.20-4.60	4.60-10.40	10.40-16.20	Field survey monitoring 2020-2021
(4) Coast type U4	Artificial island coast, Headland bay coast	Estuary coast	Sandy coast	Muddy coast、Biological coast	Bedrock coast, Artificial coast, Coral coast	Field survey 2021
(5) Beach width U5(m)	5.00-16.00	16.00-27.00	27.00-38.00	38.00-49.00	49.00-60.00	Field survey 2021
(6) Beach slope U6(°)	17.80-14.44	14.44-11.08	11.08-7.72	7.72-4.36	4.36-1.00	Field survey 2021
(7) Degree of coastal development U7	Artificial island construction, Enclosing sea and cultivating, Mining Sand of beach	Engineering Construction, Tourism development, port	Nearshore marine aquaculture	Fishing、Agricultural Production	Undeveloped natural coast	Field survey 2021
(8) Population density U8	More densely	Densely	Medium	Sparsely	More sparsely	Baidu population heat map2021

U4、U7 and U8 are dimensionless, The vulnerability is assigned 5 - 1 from high to low.

population in the same time period to characterize the anthropogenic activity density (accuracy is 1 km) and assign values to different personnel densities (Table 1).

3.2 Index weights and evaluation methods

In a multi-indicator evaluation decision, it is necessary to prioritize indicators and find the advantage or weight level of each indicator relative to other indicators to achieve a more accurate evaluation goal. Various commonly used methods in verifying effectiveness include the AHP (Mosadeghi et al., 2015; Cabrera and Lee, 2019; Saffaria et al., 2020), maximum entropy model (MAXENT) (Cabrera and Lee, 2020), rank weight method (Alam et al., 2020), proportional weight method (Dou et al., 2017), fuzzy analytic hierarchy process method (Wijitkosum and Sriburi, 2019), and fuzzy logic method (Hoque et al., 2021a), and Cabrera and Lee showed that the AHP method was a reliable method in vulnerability assessment research based on multiple indicators. In this study, a combination of DM and TEM methods was used to analyze and calculate the index weights.

(i) In the DM method, the consistency ratio (*CR*) was introduced as a reliable index for judging the consistency of the matrix to overcome the randomness in the index judgment process (Saaty, 1980). The *CR* represents the comparison between the consistency index (*CI*) and the random consistency index (*RI*). When CR<0.1, the corresponding judgment matrix is acceptable for the AHP method, and if *CR*>0.1, the judgment matrix is readjusted.

The calculation formula of DM is as follows:

$$CI = \frac{\lambda_{max} - n}{n - 1} \tag{1}$$

$$RI = \frac{\bar{\lambda}_{max} - n}{n - 1} \tag{2}$$

$$CR = \frac{CI}{RI} \tag{3}$$

(1) where λ_{max} is the largest eigenvalue of the *n*-order judgment matrix, *n* is the number of evaluation indicators. (2) where $\bar{\lambda}_{max}$ is the average value of the maximum eigenvalues of the *n*-order random positive and negative square matrix.

The TEM calculation formula is as follows:

$$H_i = -k\sum_{j=1}^{n} U_{ij} \ln U_{ij} \ (\mathrm{i} = 1, 2 \ldots \mathrm{m}; \mathrm{j} = 1, 2, \ldots \mathrm{n}) \tag{4}$$

$$hi = 1 - Hi \tag{5}$$

$$a_i = \frac{h_i}{m - \sum_{i=1}^{m} H_i} \qquad (\mathrm{i} = 1, 2 \ldots \mathrm{m}) \tag{6}$$

Where constant k=1/ln(n) in (4), m is the number of factor indicators, n is the number of evaluation units. $0 \le a_i \le 1$, $\sum_{i=1}^{m} a_i = 1$.

The comprehensive weight values of the indicators calculated based on the DM and TEM are shown in Table 2.

FIGURE 3
(A) In coral reef shores, coral detritus is washed ashore and deposited to form a reef beach. **(B)** Coastal erosion scarps on artificial island coast. **(C)** Straight shore erosion.

The CVI has two mathematical calculation methods: one is to find the square root of the "product", and the other is to weight the "sum". When the weight of each indicator can be determined, the weighted summation method is adopted (Liu et al., 2013), and the formula is as follows:

$$CVI_{sum} = \sum_{i=1}^{n} P_i C_i \tag{7}$$

In the (7), P_i is the quantitative grading value of each evaluation index, and C_i is the weight value corresponding to the index.

4 Results

4.1 Temporal and spatial distribution characteristics of erosion and siltation

4.1.1 Spatial distribution characteristics of erosion and siltation

In 2021, there were 37 eroded shore sections and 5 silted shore sections in the study area. The longest eroded section was located in Baoding Bay, south of Wanning Wuchang Port, with a length of 3.5 km, and the shortest was 37 m (Figure 4). The cumulative length of the eroded section in Qionghai-Wanning was approximately 26.12 km, accounting for approximately 17.96% of the total shore section. The accumulative length of the silted section was approximately 4.95 km, accounting for approximately 3.40% of the total shore section, and the stable section accounted for approximately 78.64% of the total shore section. The eroded shores were widely distributed and mostly occurred on the northern and southern coasts of the artificial island, as well as in headland bays, both sides of the estuary, and seaward protruding shores. Among them, erosion must occur on the coasts of headlands and artificial islands, and the degree of erosion was significantly stronger than that of the straight coast. The siltation section was less distributed and occurred in the inner side of artificial islands, in the angle between the harbor and the dam, and on the floodplain position of the estuary.

The monitoring results of the beach profile showed that most of the beaches are in a state of erosion, and the shore sections with relatively large downward erosion were mainly distributed in artificial islands, headlands and estuaries, such as Qionghai Longwan, Tanmen Artificial Island, Coral Island, and Riyue Island in Wanning. The maximum downward erosion rate was located at the jade belt beach of Wanquan Estuary, with a

value of approximately -12.8 cm/a, followed by that in Riyue Bay in Wanning, showing a rate of decline of -10 cm/a.

4.1.2 Temporal distribution characteristics of erosion and siltation

The most direct characterization of coastal erosion and siltation is the advance and retreat of the coastline. From 1985 to 2015, 7 periods of remote sensing images were used to monitor the rate of change of the coastline and showed that (Figure 5), the Qionghai-Wanning coastal was in a state of weak siltation and erosion as a whole, and it was distributed throughout the northern and southern coasts of Qionghai-Wanning. Among them, the siltation rate of 0-6.29 m/a accounted for the largest proportion, approximately 50.15%, and was mainly distributed in the relatively straight sandy section, such as Gangbei port in the north section and the Wanquan River mouth in the north and south sections. Second, the weakest erosion rate was -0.99-0 m/a, accounting for approximately 39.54%, and these areas were mainly distributed along the coast of Shimei Bay, Riyue Bay and other cape bays in Wanning. The maximum erosion rate was -1.00~-7.58 m/a, accounting for approximately 6.77%, and these areas were mainly distributed in the Wanquan River estuary and the Tanmen artificial island section. The maximum rate of siltation on the coastline was 20.74-39.49 m/a, accounting for approximately 0.65%, and these sites were mainly north of Longwan Port. From the 1990s to the early 2000s, villagers reclaimed and built ponds in the shallow coral reef area and continuously reclaimed them to the sea, making the coastline advance to the sea at an increasing rate. Moreover, the construction of impervious roads connecting the artificial islands to the islands increased the artificial coastline, which also had a significant impact on coastal erosion and siltation.

4.2 Characteristics of coastal erosion vulnerability

4.2.1 Spatial distribution characteristics of coastal erosion vulnerability

The erosion vulnerability assessment results are shown in Figure 6. Most of the coastal erosion in Qionghai-Wanning is in a state of moderate vulnerability or above, accounting for approximately 59% of the total shore section, of which the vulnerability of high and above exceeds 31%, including 2 with very high vulnerability and 7 with high vulnerability. The very high vulnerability was distributed in the Wanquan Estuary of Qionghai and the nearby coasts to the south. The high vulnerability was distributed in some capes and estuaries, such as to the south of the Wanquan estuary and on the nearby shores of Wanning Shimei Bay, while a small part of the straight coasts had a higher vulnerability status. 8 locations had moderate vulnerability, accounting for approximately 28%, and the sites were relatively scattered, mainly distributed in some inner bays of the headlands, such as Wanning Dongwo Bay and Shimei Bay. There were 12 places with low vulnerability and below, including 3 places with low vulnerability and 9 places with very low vulnerability, accounting for approximately 41% of the Qionghai-Wanning coast, and these sites were mainly distributed in the coral reef area to the north of Tanmen Port, the headlands formed by various bedrocks, such as Wanning Dahuajiao, Shimeiwan headland, and the coasts where bedrock and sand alternately appear. Areas with hard engineering, such as port terminals and damp-proof gates also had a lower vulnerability.

4.2.2 Vulnerability level characteristics

4.2.2.1 Very high vulnerability

The very high vulnerability of Qionghai-Wanning coastal erosion occurred in the C8 and C10 sections, located in the Wanquan River mouth and adjacent coasts, which corresponded to the erosion intensity of the Wanquan Estuary. The interannual downward erosion rate U3 of the beach in this section was approximately -12.8 cm/a, which was the maximum value in the study area (Figure 7A. U3). This was related to the complex and strong hydrodynamic effects of the estuary. In addition, the beach slope (U6) of this section was generally higher than that of the other sections, and anthropogenic activity (U8) had a higher value due to the influence of intensive human activities such as Boao tourism and boat navigation. In general, the very high vulnerability was due to the dominant influence of a higher interannual downward erosion rate, steeper beach slope and denser anthropogenic activities.

4.2.2.2 High vulnerability

The areas with higher vulnerability were mainly distributed along some coasts, such as the headland bays and estuaries of northern and southern Wanquan estuary (C7) and the coastal sections near Shimei Bay (C27) in Wanning. The section with a high vulnerability distribution was accompanied by an obvious erosion phenomenon, and the beach slope (U6) of the high vulnerability c14 section had a maximum slope of approximately 65° (Figure 7B. U6). The overall slope range was generally 7-11°, and the interannual downward erosion rate (U3) of the beach was between 0 and 1.2 cm. It had obvious characteristics, such as more human activities; in addition, the coasts with high vulnerability had the characteristics of wider beaches, and the other factors had no obvious common characteristics. In summary, high vulnerability was characterized by a certain width of beach, and the slope and human activities had a greater impact.

4.2.2.3 Moderate vulnerability

The Qionghai-Wanning moderate vulnerability distribution was relatively scattered, and it was moderately vulnerable in the straight shore section, some headland coasts, and coral reef coasts.

TABLE 2 Index weight value of coastal erosion vulnerability assessment.

Evaluation Index	DM	TEM	Comprehensive weight *Ci*	Weights ordering
Change rate of shoreline U1	0.2821	0.0531	0.1676	1
Rate of change of isobath U2	0.1936	0.0544	0.1240	5
Interannual downward rate erosion of beach U3	0.1827	0.0845	0.1336	4
Coast type U4	0.0764	0.0584	0.0674	8
Beach width U5	0.0732	0.2487	0.1609	2
Beach slope U6	0.0594	0.0900	0.0747	7
Degree of coastal development U7	0.0938	0.1406	0.1172	6
Population density U8	0.0388	0.2703	0.1545	3

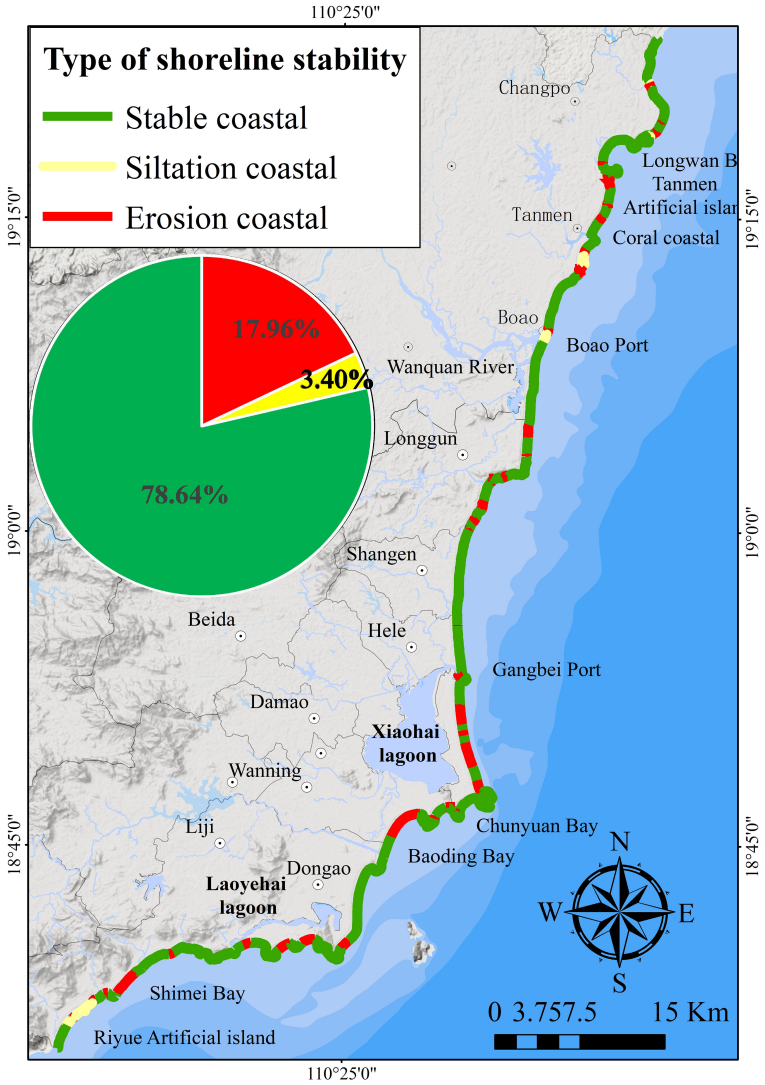

FIGURE 4
Spatial distribution map of coastal erosion and deposition in Qionghai-Wanning in 2021.

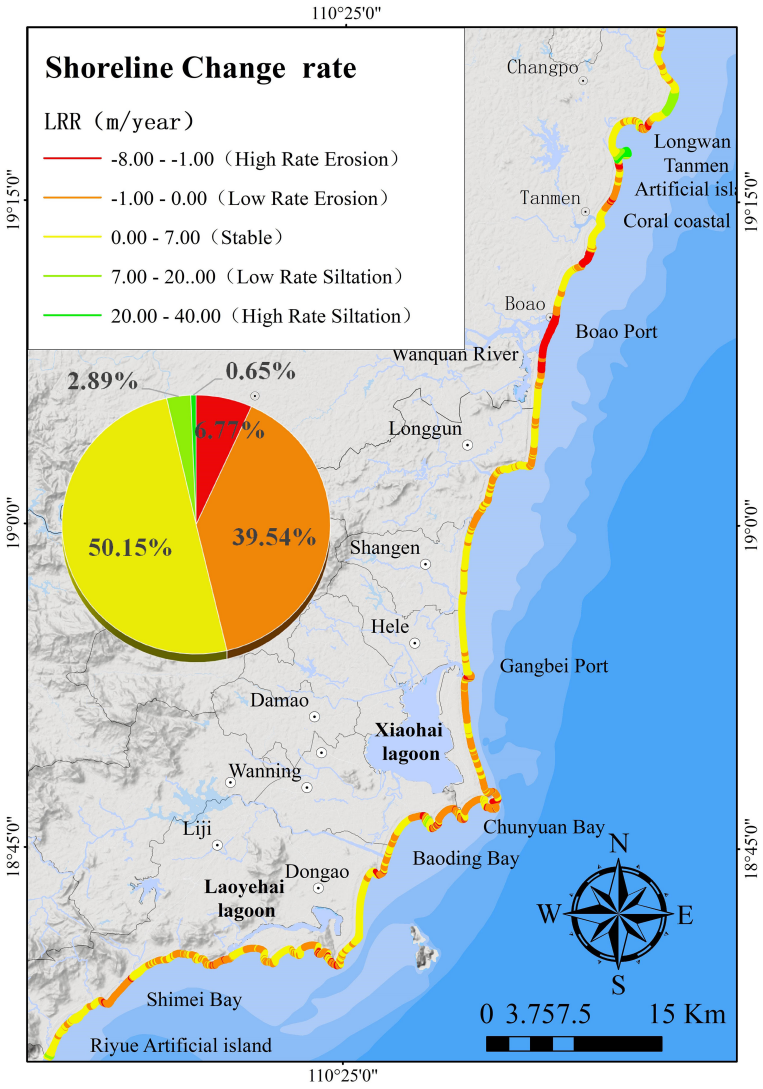

FIGURE 5
Distribution characteristics and proportion of Qionghai-Wanning coastline change rate from 1985 to 2015.

Additionally, we found that under the protection of coral reefs, the degree of vulnerability was generally low, but under the combined influence of artificial islands and coral reefs, the degree of vulnerability increased on artificial island coasts. For example, section c5 in the Tanmen artificial island area was moderately vulnerable. The common feature of moderate vulnerability was that the isobath change rate (U2) was between -15.69 and -7.93 m/a, and the rest had no obvious features.

4.2.2.4 Low and very low vulnerability

Except for the low vulnerability of some coral reef shore sections, bedrock shorelines, hard artificial shorelines, etc., the remaining low-vulnerability sections had obvious common characteristics, such as relatively gentle bank slopes, lower shoreline change rates, smaller isobath change rates, and interannual siltation states of beaches (Figure 7). Furthermore, some beaches had better protection under the action of alternate bedrocks and showed lower vulnerability; therefore, the hard coast type played a leading role in lower vulnerability.

5 Discussion

5.1 Variation in coastal erosion vulnerability

Through the Spearman correlation coefficient method (Rodgers and Nicewander, 1988), statistical analysis was carried out on the correlation between the raw data of each

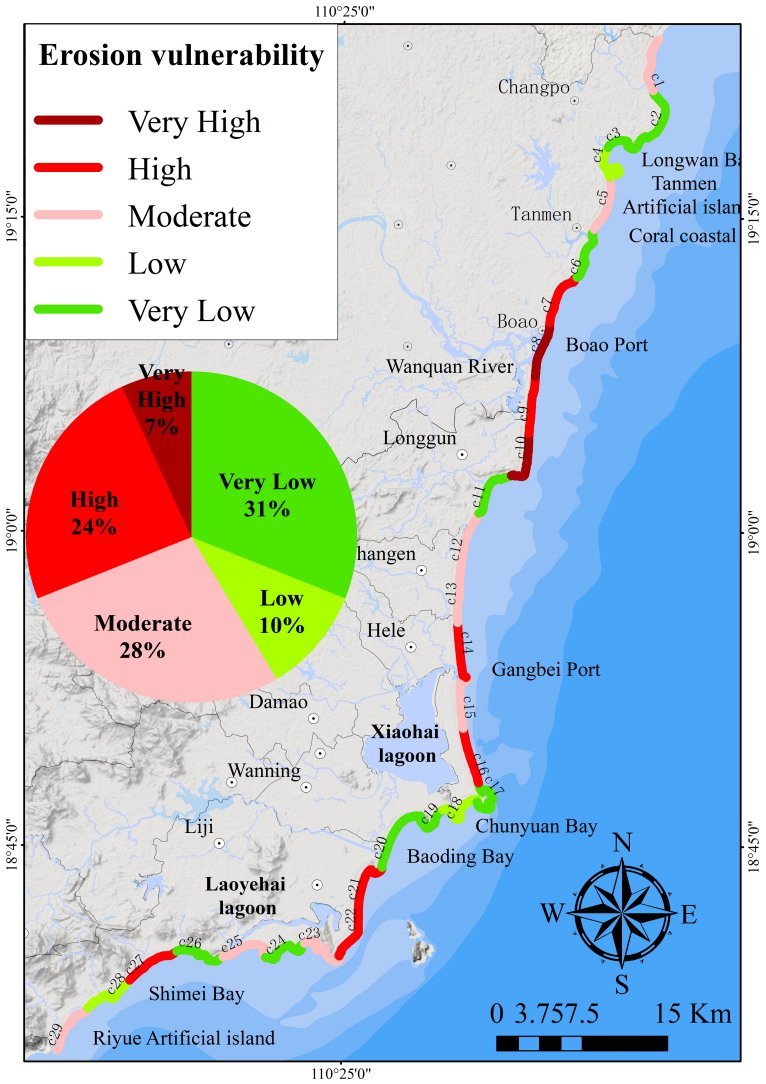

FIGURE 6
Spatial distribution characteristics and proportion of coastal erosion vulnerability in Qionghai-Wanning.

evaluation factor and the vulnerability index, and the results are shown in Table 3.

It was assumed that there was no mutual influence between the indicators; that is, in the absence of control variables, the interannual downward rate of erosion of beaches (U3) was moderately negatively correlated with the CVI (r=-0.48, p<0.01), which showed that the greater the rate of downward erosion was, the greater the degree of vulnerability. The beach width (U5) was strongly correlated with the CVI (r=0.79, p<0.01) (Figure 8), which indicated that the beach wider had a greater degree of vulnerability. The other indicators were not significantly correlated with the CVI ($|r|$<0.3, p>0.05).

In practical research, coastal vulnerability is the degree of vulnerability based on the morphological characteristics of the coast itself, and the characteristics are affected by conditions such as coastal dynamics and human activities. Therefore, based on the state of coastal morphological factors, we conducted a partial correlation analysis between the vulnerability and the vulnerability of the remaining index factors. The results showed that the rate of change of the isobath (U2) was significantly negatively correlated with coastal vulnerability (r=-0.58, p< 0.01), indicating that the greater the rate of change of the isobath was, the greater the degree of coastal vulnerability. The interannual downward rate of erosion of the beach (U3) was strongly negatively correlated with the degree of coastal vulnerability (r=-0.75, p< 0.01); that is, the greater the interannual beach downward erosion rate was, the greater the vulnerability of the coast. The remaining indicators and the CVI

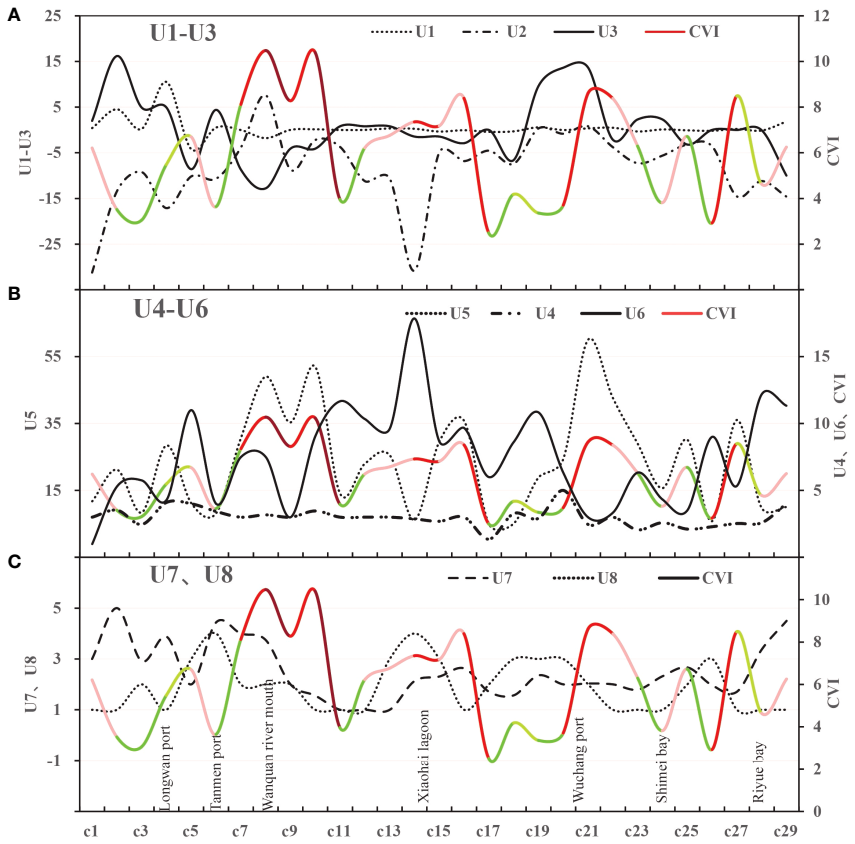

FIGURE 7
Vulnerability index and evaluation factor curve (The color of CVI curve corresponds to its vulnerability degree). **(A)** The relationship between U1-U3 index and CVI curve. **(B)** The relationship between U4-U6 index and CVI curve. **(C)** The relationship between U7, U8 index and CVI curve.

were not obviously linearly related (Figure 8). Therefore, the interannual downward erosion rate and isobath change rate of the beach were the main controlling factors in the vulnerability of coastal erosion, and the other factors were secondary factors.

5.1.1 Coastal morphological factors

Coastal morphological factors are important indicators reflecting the intrinsic characteristics of the coast. The width and slope of the beach can determine the reflection ability of waves, and the reflection ability of waves reflects the characteristics of erosion; that is, the erosion intensity of waves on the beach increasesWangYonghong (Wang 2018) and results in a higher erosion vulnerability. In contrast, a gentler slope and a wider beach result in lower vulnerability.

Figure 7B shows that the CVI curve was similar to the beach width U5 curve but had an opposite relationship with the slope; that is, a larger slope corresponds to a narrower beach width, which corresponds to a relatively lower vulnerability. In contrast, for flat and wider beaches, the slope was mostly gentle, and the vulnerability was relatively higher. There was a certain gap in the evaluation of individual factors because vulnerability was not presented according to the relationship of a single factor under the superimposed influence of the comprehensive factor indicators, which was consistent with the results of Wang (2018) in their assessment of erosion vulnerability along the Yangtze River Delta. Figure 9 shows that the proportion of coastal morphological factors in each segment was different to a certain extent; in general, coastal morphological factors played a secondary role in the vulnerability of each segment.

5.1.2 Coastal dynamic factors

The coastal dynamic factors reflect the dynamic change characteristics of the external factors affecting the performance of the coast itself. In this assessment, the coastal vulnerability was characterized by erosion and siltation changes in the position of the supratidal beach, intertidal shoreline and subtidal nearshore sea floor and could better and more comprehensively reflect the vulnerability of the coast itself under the influence of the external environment. The assessment results showed that the coastal dynamic factors in the vulnerability of each segment were the main controlling effects overall (Figure 9). Compared with coastal morphological

TABLE 3 Correlation between CVI and each evaluation factor based on Spearson method.

Control variables	Index	coefficient	CVI	U1	U2	U3	U4	U5	U6	U7	U8
Nothing	CVI	r	1	-0.170	0.079	-0.478	0.067	0.785	-0.016	-0.078	-0.205
		p		0.377	0.685	0.009	0.730	<0.001	0.936	0.688	0.286
	U1	r	-0.170	1	-0.296	0.393	0.266	0.042	-0.231	0.425	-0.299
		p	0.377		0.118	0.035	0.162	0.829	0.228	0.022	0.115
	U2	r	0.079	-0.296	1	-0.040	-0.098	0.454	-0.129	-0.157	0.025
		p	0.685	0.118		0.835	0.611	0.013	0.505	0.417	0.896
	U3	r	-0.478	0.393	-0.040	1	0.059	0.001	-0.285	0.033	0.020
		p	0.009	0.035	0.835		0.761	0.995	0.133	0.865	0.917
	U4	r	0.067	0.266	-0.098	0.059	1	0.035	0.105	0.282	0.096
		p	0.730	0.162	0.611	0.761		0.859	0.588	0.138	0.620
	U5	r	0.785	0.042	0.454	0.001	0.035	1	-0.336	-0.090	-0.316
		p	<0.001	0.829	0.013	0.995	0.859		0.075	0.644	0.095
	U6	r	-0.016	-0.231	-0.129	-0.285	0.105		1	-0.192	0.279
		p	0.936	0.228	0.505	0.133	0.588	0.075		0.320	0.143
	U7	r	-0.078	0.425	-0.157	0.033	0.282	-0.090	-0.192	1	-0.080
		p	0.688	0.022	0.417	0.865	0.138	0.644	0.320		0.680
	U8	r	-0.205	-0.299	0.025	0.020	0.096	-0.316	0.279	-0.080	1
		p	0.286	0.115	0.896	0.917	0.620	0.095	0.143	0.680	
u4 & u5 & u6	CVI	r	1.000	-0.279	-0.573	-0.754	0.102	-0.012			
		p		0.168	0.002	<0.001	0.620	0.954			
	U1	r	-0.279	1.000	-0.336	0.336	0.332	-0.313			
		p	0.168		0.093	0.094	0.098	0.119			
	U2	r	-0.573	-0.336	1.000	-0.026	-0.090	0.213			
		p	0.002	0.093		0.899	0.663	0.297			
	U3	r	-0.754	0.336	-0.026	1.000	-0.080	0.077			
		p	<0.001	0.094	0.899		0.699	0.708			
	U7	r	0.102	0.332	-0.090	-0.080	1.000	-0.109			
		p	0.620	0.098	0.663	0.699		0.598			
	U8	r	-0.012	-0.313	0.213	0.077	-0.109	1.000			
		p	0.954	0.119	0.297	0.708	0.598				

factors and socioeconomic and human activity factors, they had a greater impact, which was consistent with the research by Hoque et al. (2019), Sarwar (2013), and Roy and Mahmood (2016) and most of the studies believe that coastal dynamic factors such as shoreline change rate are the key factors of coastal vulnerability.

Figure 7A shows that the interannual downward rate erosion of the beach (U3) was inversely proportional to the CVI curve; in addition, there was no obvious corresponding relationship under the influence of other comprehensive superposition. Our previous index weight evaluation showed that the coastal dynamic factor had a higher weight; in particular, the change rate of the shoreline (U1) had the highest weight value, but it did not have a dominant position in the comprehensive impact of vulnerability. This result was related to the evaluation under the condition of synthesizing various indicators and factors and reflected the comprehensive scientific nature of the CVI method.

5.1.3 Socioeconomic and human activity factors

The integration of socioeconomic and human activity factors enhances the reliability and scientificity of previous erosion vulnerability models that considered only coastal shape or coastal dynamic components (Jana and Bhattacharya, 2013; Ahmed et al., 2018). The socioeconomic and human activity factors accounted for the smallest proportions in each evaluation unit and had the smallest impact value overall. The population density (U8) was generally inversely related to the CVI (Figure 7C), which indicated that in anthropogenic activities, the more developed tourism and frequent fishing activities are, the greater the vulnerability of the coast. However, the construction of coastal engineering, such as artificial islands, has had a greater impact on vulnerability than the straight section without engineering construction, which showed a state of moderate vulnerability; therefore, socioeconomic and human activity can increase the degree of coastal vulnerability.

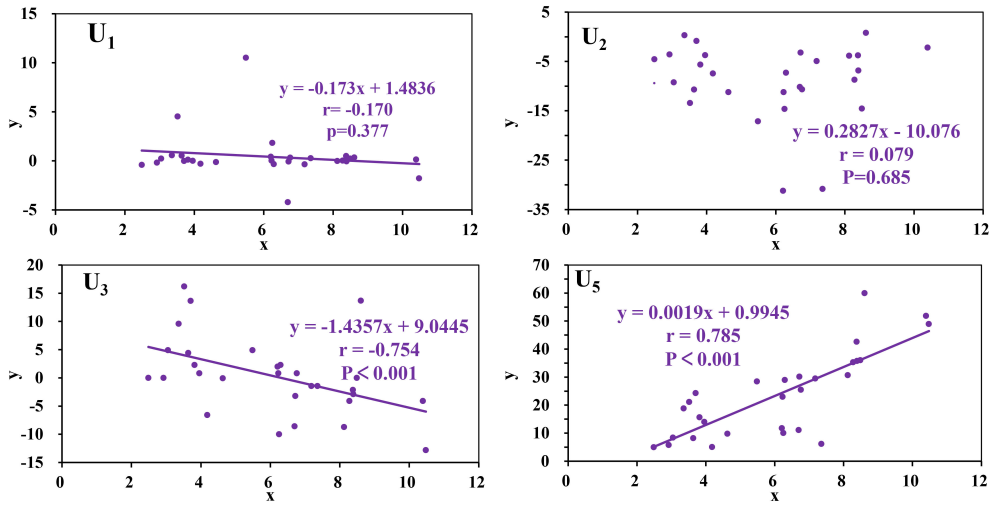

FIGURE 8
Correlation diagram of comprehensive evaluation vulnerability results and single factor index *Ui* linear regression (x in the figure is the comprehensive evaluation erosion vulnerability index, y is the original data of the factor index).

5.2 Coastal types and the CVI

Different types of coastal areas have different erosion vulnerabilities, and even the same type of coastal area will show different results under the combined effect of different factors. There were large ranges of coral reefs (c2-c5) on the coast north of Tanmen Port in Qionghai. The multiyear coastline change rate and vulnerability curve are shown in Figure 10. The c2-c4 section progressed with siltation overall, and the corresponding vulnerabilities were all below the low level, which had a certain relationship with the length of the reef flat in the coral reef disk, the roughness of the reef surface, and the reef crown on the wave propagation deformation. When the waves moved to the reef crown position, the wave energy was reduced due to its water blocking effect, causing the wave to increase water. When moving to the reef flat section, the water depth of the reef flat section was shallow, the existence of the large roughness of the reef surface reduced the wave water value, and the wave energy was further reduced. Therefore, the existence of coral reefs has a great energy dissipation effect on wave waterChaoShao (Shao, 2016). It is a natural revetment barrier, reducing wave scour and erosion, and the coast was protected to a certain extent and showed low vulnerability.

The multiyear average rate of change in the c5 section was eroded, and the corresponding vulnerability was moderate vulnerability, which was related to the distribution of 2 artificial islands and the Tanmen port in the c5 coral reef section. Affected by the construction of artificial islands and the fishing activities in the port, the hydrodynamic environment in this area has become complicated, the coral reefs have been degraded, the natural barrier protection of the coral reefs has been reduced, erosion has occurred, and vulnerability has become moderate. In general, the presence of coral reefs has a protective effect on the coast, leaving the adjacent coast with relatively low vulnerability.

The estuarine segment (c8-c10) is the place with the highest degree of vulnerability in the study area, and distributed on both sides of the estuary, which is positively correlated with its erosion intensity. There is a two-way interaction between river runoff and tidal current at the estuary. The flow direction is opposite at high tide and same direction at low tide, forming a complex hydrodynamic environment, indicating that the hydrodynamic interaction at the estuary of the river under natural conditions is the main reason for the high vulnerability of the adjacent coast, which is consistent with the results of Roy et al (2021) study.

5.3 Vulnerability verification

In many vulnerability assessment studies, the reliability of the assessment results is verified by the area under the curve (AUC) under the receiver operating characteristic (ROC) curve, which has been widely used and verified by scholars (Hoque et al., 2021b; Rahman et al., 2019; Cao et al., 2022a). By calculating the true positive rate (TPR) and the false positive rate (FPR) as the y axis to draw the characteristic curve, the size of the AUC can be calculated as the probability of verification.

$$TPR = \frac{TP}{TP + FN} \tag{8}$$

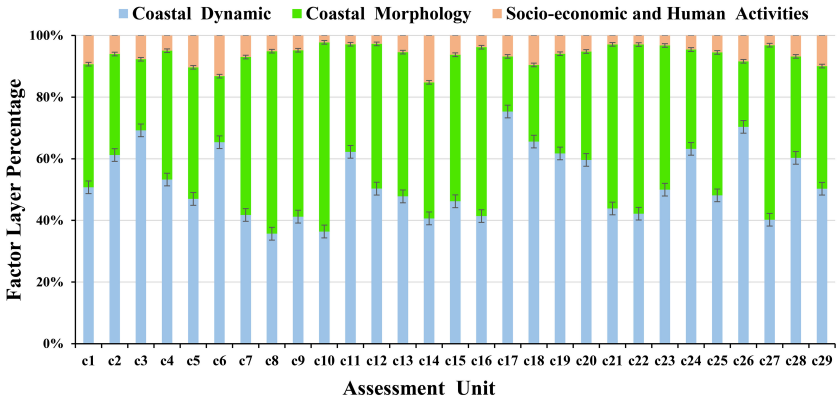

FIGURE 9
Map of the proportion of coastal morphology, coastal dynamics, and socioeconomic and human activity factors in each assessment unit.

$$FPR = \frac{FP}{FP + TN} \tag{9}$$

where TP (true positives): the number of observed erosion locations accurately identified; FP (false positives): the number of erroneously identified erosion locations in non-eroded regions; TN (true negatives): correctly identified non-erosion locations number of; FN (false negatives): the number of misidentified non-eroded locations in eroded regions (Roy et al., 2021).

We used the erosion points and non-erosion points determined by 390 observation points (Figure 11A) in the field survey as the validation dataset and the ROC curve in IBM SPSS Statistics 27 software to generate the prediction rate curve. The AUC of the prediction rate was 0.689, namely, the vulnerability assessment reached an accuracy of 68.9% (Figure 11B). The assessment results can provide important references for the development and management of the Hainan Qiongdong coastal zone and the ecological restoration of tropical coral reef biological coasts.

6 Conclusion

In this paper, 8 small-scale typical indicators, such as the change rate of the shoreline (U1) and the rate of change of the isobath (U2), were comprehensively selected, and the combination of DM and TEM was used to calculate the weight of comprehensive evaluation indicators, combined with GIS and the CVI to quantitatively evaluate the temporal and spatial distribution characteristics of coastal erosion vulnerability in Qionghai-Wanning, Qiongdong, Hainan.

(1) Most of the coastal erosion was in the state of moderate vulnerability or above, accounting for approximately 59% of the total shore section, of which the high-vulnerability section exceeded 31%. The coasts with higher vulnerability were mainly distributed in the Wanquan Estuary of Qionghai and some coasts of Cape Bay, and a few straight coasts also showed a state of higher vulnerability. The moderately vulnerable coasts were scattered, mainly in the inner bays of some headlands. The lower vulnerability areas accounted for approximately 41% of the Qionghai-Wanning coast, and they mainly distributed in coral reefs, headlands formed by bedrock, hard engineering and other locations.

(2) Under the influence of no control variables, the interannual downward rate erosion of the beach (U3) was negatively correlated with vulnerability, the beach width (U5) was highly positively correlated with vulnerability, and the rest showed an insignificant linear relationship with the CVI. Under the control variables, coastal vulnerability was based on the comprehensive influence of coastal morphological factors, showing that the rate of change of the isobath (U2) and the interannual downward erosion rate of the beach (U3) were highly negatively correlated with vulnerability. Therefore, the interannual downward erosion rate of the beach and the rate of change of the isobath were the main factors affecting the vulnerability to coastal erosion, and the other indicators were secondary factors. In addition, there were large coral reefs distributed north of Qionghai Tanmen as a natural barrier for revetment. The reason is that the length of the reef flat in the coral reef plate, the roughness of the reef surface and the reef crown can reduce the wave erosion and reduce the erosion of the coral reef coast, resulting in lower vulnerability, and the complex hydrodynamic environment, the estuarine coast presents a state of high vulnerability.

(3) The vulnerability was verified by the AUC value under the ROC curve, and the vulnerability assessment reached an accuracy of 68.9%. The assessment results provide a scientific basis for the restoration of coral reef biological coastal ecology

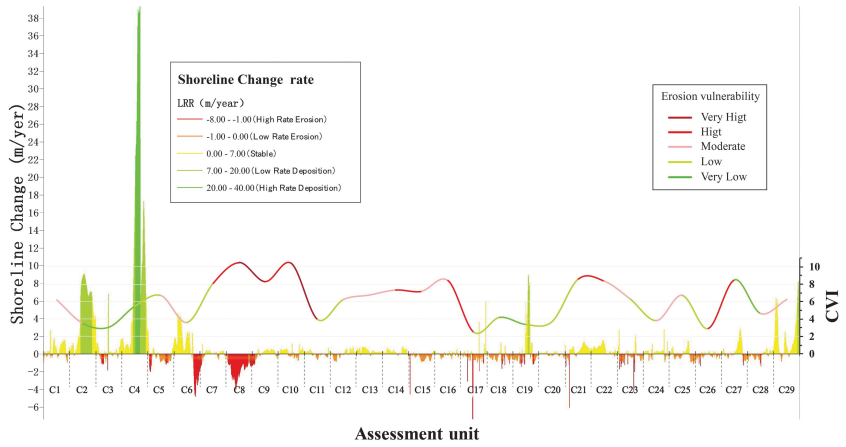

FIGURE 10
Shoreline change rate and vulnerability curve of different typical coasts (The left side is the legend of Change rate of shoreline, and the right side is the vulnerability index curve of the corresponding section).

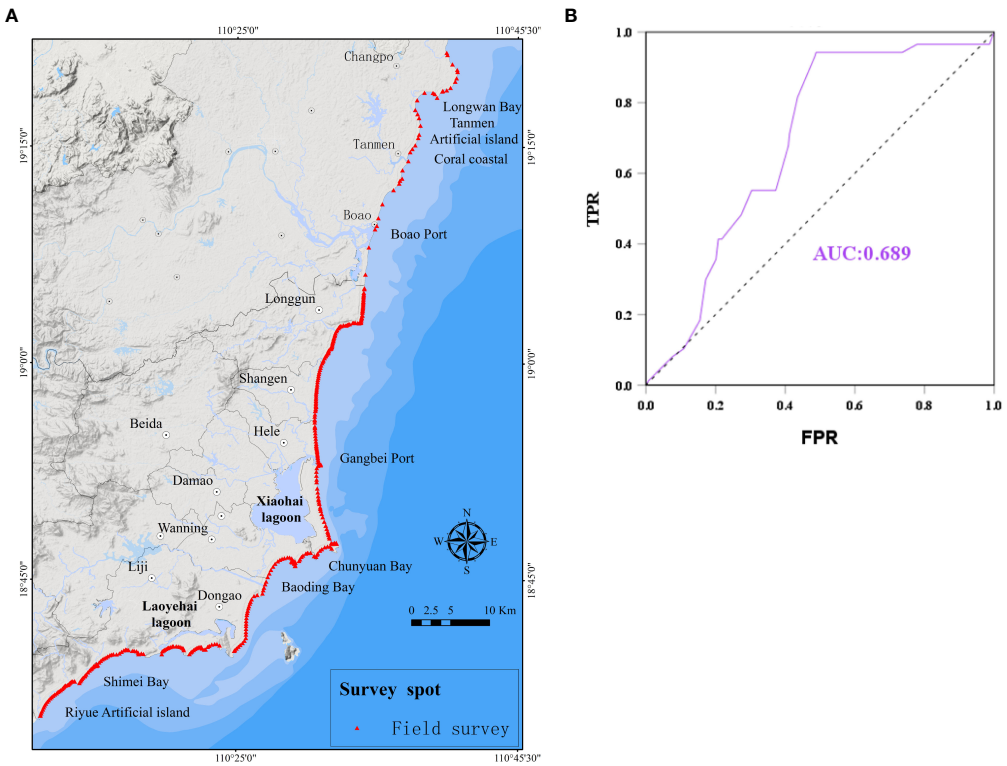

FIGURE 11
(A) Spatial distribution of field survey sites in 2021; **(B)** ROC curve and AUC = 0.689.

and the development and management of the Qiongdong coastal zone.

Data availability statement

The original contributions presented in the study are included in the article/Supplementary Material. Further inquiries can be directed to the corresponding authors.

Author contributions

Designed the study, wrote the main manuscript and prepared all figures: GF; contributed to the improvement of the manuscript: CC and KF; investigate: YS and KY; figure and software: GF, YS, and KY; all authors reviewed the manuscript. All authors contributed to the article and approved the submitted version.

Funding

This research was funded by the China Geological Survey Project: Qionghai-wanning Coastal Zone Comprehensive geological survey Project (Grant Nos. ZD20220608), the National Natural Science Foundation of China (Grant No. 42076058, 41930538), the Scientific Research Foundation of Third Institute of Oceanography, MNR (Grant No. 2019006).

Acknowledgments

The authors would like to express their sincere thanks to Huilong Xu, Fei Tan who have offered support.

Conflict of interest

The authors declare that the research was conducted in the absence of any commercial or financial relationships that could be construed as a potential conflict of interest.

Publisher's note

All claims expressed in this article are solely those of the authors and do not necessarily represent those of their affiliated organizations, or those of the publisher, the editors and the reviewers. Any product that may be evaluated in this article, or claim that may be made by its manufacturer, is not guaranteed or endorsed by the publisher.

Supplementary material

The Supplementary Material for this article can be found online at: https://www.frontiersin.org/articles/10.3389/fmars.2022.1061769/full#supplementary-material

References

Ahmed, A., Nawaz, R., Drake, F., and Woulds, C. (2018). Modelling land susceptibility to erosion in the coastal area of Bangladesh: A geospatial approach. *Geomorphol.* 320, 82–97. doi: 10.1016/j.geomorph.2018.08.004

Alam, A., Sammonds, P., and Ahmed, B. (2020). Cyclone risk assessment of the cox's bazar district and rohingya refugee camps in southeast Bangladesh. *Sci. Total Environ.* 704, 135360. doi: 10.1016/j.scitotenv.2019.135360

Alberico, I., Amato, V., Aucelli, P., D'Argenio, B., Di Paola, G., and Pappone, G. (2012). Historical shoreline changes of the sele plain (southern italy): the 1870-2009 time window. *J. Coast. Res.* 28 (6), 1638–1647. doi: 10.2112/J.COASTRES-D-10-00197.1

Andrade, T. S., Oliveira Sousa, P. H. G., and Siegle, E. (2019). Vulnerability to beach erosion based on a coastal processes approach. *Appl. Geogr.* 102, 12–19. doi: 10.1016/j.apgeog.2018.11.003

Annelies, B., das Neves, L., de Nocker, L., Ali, D., and Koen, C.. (2021). A methodological framework of quantifying the cost of environmental degradation driven by coastal flooding and erosion: A case study in West Africa. *J. Disaster Risk Reduction.* 01 (54), 2212–4209. doi: 10.1016/j.ijdrr.2020.102022

Appeaning, A. K. (2013). Shoreline morphological changes and the human factor, case study of Accra Ghana. *J. Coast. Conserv.* 17, 85–91. doi: 10.1007/s11852-012-0220-5

Compiled by China Meteorological Administration (2021). *Tropical of cyclone yearbook* Vol. 08 (China Meteorological Press), 15–193.

Barragan, J. M., and Andreis, M. (2015). Analysis and trends of the world's coastal cities and agglomerations. *Ocean Coast. Manage.* 114, 11–20. doi: 10.1016/j.ocecoaman.2015.06.004

Bathi, J. R., and Das, H. S. (2016). Vulnerability of coastal communities from storm surge and flood disasters. *Int. J. Environ. Res. Publ. Health* 13 (2), 239. doi: 10.3390/ijerph13020239

Boak, E. H., and Turner, I. L. (2005). Shoreline definition and detection: A review. *J. Coast. Res.* 21 (4), 688–703. doi: 10.2112/03-0071.1

Boruff, B. J., Emrich, C., and Cutter, S. L. (2005). Erosion hazard vulnerability of US coastal counties. *J. Coast. Res.* 21 (5), 932–942. doi: 10.2112/04-0172.1

Bruun, P. (1962). Sea-Level rise as a cause of shore erosion. *J. Waterways Harbours Divisions.* 88, 117–130. doi: 10.1061/JWHEAU.0000252

Cabrera, J. S., and Lee, H. S. (2019). Flood-prone area assessment using GIS-based multi-criteria analysis: A case study in davao oriental, Philippines. *Water.* 11, 2203. doi: 10.3390/w11112203

Cabrera, J. S., and Lee, H. S. (2020). Flood risk assessment for davao oriental in the Philippines using geographic information system-based multi-criteria analysis and the maximum entropy model. *J. Flood Risk Management.* 13, e12607. doi: 10.1111/jfr3.12607

Cai, F., Cao, C., Qi, H. S., Lei, G., Liu, JH., Zhu, K., et al. (2022). Rapid migration of Chinese mainland coastal erosion vulnerability due to anthropogenic changes. *J. Environ. Management.* 319, 115632. doi: 10.1016/j.jenvman.2022.115632 1–15

Cai, F., Su, X. Z., Cao, C., Lei, G., Liu, JH., Qi, HS., et al. (2019). China Coastal erosion vulnerability assessment and demonstration application. *Beijing Ocean Press* 08, 241–247.

Cai, F., Su, X. Z., Liu, J. H., Li, B., and Lei, G. (2008). Coastal erosion problems and preventive countermeasures in my country under the background of global climate change. *Prog. Natural Sci.* 10), 1093–1103.

Cao, C., Cai, F., Qi, H., Liu, JH., Lei, G., Zhu, K., et al. (2022a). Coastal erosion vulnerability in mainland China based on fuzzy evaluation of cloud models. *Front. Mar. Sci.* 8. doi: 10.3389/fmars.2021.790664

Cao, C., Zhu, K., Cai, F., Qi, H. S., Liu, J. H., Lei, G., et al. (2022b). Vulnerability evolution of coastal erosion in the pearl river estuary great bay

area due to the influence of human activities in the past forty years. *Front. Mar. Sci.* 9, 847655. doi: 10.3389/fmars.2022.847655

Chen, J. Y., Xia, D. X., Yu, Z. Y., and Cai, F. (2010). *Summary of coastal erosion in China* (Beijing: Beijing China Ocean Press), 320–324.

Chen, J. Y., Shen, H. T., and Yun, C. X. (1988). *Dynamic process and geomorphological evolution of the Yangtze estuary* (Shanghai: Shanghai Science and Technology Press), 158–189.

Chen, S. L., Zhang, G. A., Yang, S. L., and Yu, Z. Y. (2004). Temporal and spatial variation of suspended sediment concentration and sediment resuspension in the waters of the Yangtze estuary. *Chin. J. Geography.* 02, 260–266. doi: 10.11821/xb200402012

Chu, J. L., Gao, S., and Xu, J. G. (2005). Risk and safety evaluation methodologies for coastal systems: A review. *Mar. Sci. Bulletin.* 24 (3), 80–87. doi: 10.1111/j.1745-7254.2005.00209

Deepika, B., Avinash, K., and Jayappa, K. S. (2013). Shoreline change rate estimation and its forecast: remote sensing, geographical information system and statistics-based approach. *Int. J. Environ. Sci. Technol* 11 (2) , 395–416. doi: 10.1007/s13762-013-0196-11-22

Dolan, A. H., and Walker, I. J. (2006). Understanding vulnerability of coastal communities to climate change related risks. *J. Coast. Res.* 39, 1316–1323. doi: 10.2307/25742967

Dominguez, L., Anfuso, G., and Gracia, F. J. (2005). Vulnerability assessment of a retreating coast in SW Spain. *Environ. Geology.* 47 (8), 1037–1044. doi: 10.1007/s00254-005-1235-0

Dou, X., Song, J., Wang, L., Tang, B., Xu, S., Kong, F., et al. (2017). Flood risk assessment and mapping based on a modified multi-parameter flood hazard index model in the guanzhong urban area, China. *Stoch. Environ. Res. Risk Assess.* 32, 1131–1146. doi: 10.1007/s00477-017-1429-5

Gornitz, V. (1991). Global coastal hazards from future sea level rise. *Global Planetary Change.* 89 (4), 379–398. doi: 10.1016/0921-8181(91)90118-G

Hagedoorn, L. C., Appeaning, A. K., Koetse, M. J., Kinney, K., and van Beukering, P. J. H.. (2021). Angry waves that eat the coast: An economic analysis of nature-based and engineering solutions to coastal erosion. *Ocean Coast. Management.* 11, 0964–5691. doi: 10.1016/j.ocecoaman.2021.105945

Hoque, M. A. A., Pradhan, B., Ahmed, N., Ahmed, B., and Alamri, A. M. (2021a). Cyclone vulnerability assessment of the western coast of Bangladesh, geomatics, nat. *Hazards Risk.* 12 (1), 198–221. doi: 10.1080/19475705.2020.1867652

Hoque, M. A. A., Pradhan, B., Ahmed, N., and Roy, S. (2019). Tropical cyclone risk assessment using geospatial techniques for the eastern coastal region of Bangladesh. *Sci. Total Environ.* 692, 10–22. doi: 10.1016/j.scitotenv.2019.07.1320048-9697

Hoque, M. A. A., Pradhna, B., Ahmed, N., and Sohel, M. S. I. (2021b). Agriculturla drought risk assessment of northern new south Wales, Australia using geospatial techniques. *Sci. Total Environ.* 756, 143600. doi: 10.1016/j.scitotenv.2020.143600

Huang, H., Chen, Z., Huang, L. D., Wang, X., Niu, W. T., Tian, J. J., et al. (2019). China Coral reef status report. *Coral Reef Branch China Pacific Soc.*, 32–37.

Jana, A., and Bhattacharya, A. K. (2013). Assessment of coastal erosion vulnerability around midnapur-balasore coast, Eastern India using integrated remote sensing and GIS techniques. *J. Indian Soc. Remote Sensing.* 41 (3), 675–686. doi: 10.1007/s12524-012-0251-2

Ji, R. Y., Luo, X. L., Lu, Y. J., and Luo, Z. R. (2007). Analysis of coastal erosion characteristics and main causes of hainan island. *Proc. 13th China Ocean (Coastal) Eng. Symposium.* 09, 374–377.

Jones, A., and Phillips, M. (2011). Disappearing destinations: Climate change and the future challenges for coastal tourism. cabi, London. *Publications review/ Annals Tourism Res.* 39, 2220–2226. doi: 10.1016/j.annals.2012.07.014

Kumar, A. A., and Kunte, P. D. (2012). Coastal vulnerability assessment for chennai, east coast of India using geospatial techniques. *Natural Hazards.* 64 (1), 853–872. doi: 10.1007/s11069-012-0276-4

Liu, X. X. (2015). Coastal evolution and intrusion vulnerability assessment of abandoned yellow river delta [Master's thesis]. *Shanghai East China Normal University* 06, 2–4.

Liu, H. W., Sun, X. M., Wen, D. G., Fang, C., Hu, Y. Z., Ma, Z., et al. (2013). Vulnerability evaluation of the caofeidian coastal area based on coastal vulnerability index method. *Hydrogeology Eng. Geology.* 40 (3), 105–109. doi: 10.16030/j.cnki.issn.1000-3665.2013.03.013

Mangor, K., Dronen, N. K., Kaergaard, K. H., and Kristensen, S. E. (2017). Shoreline management guidelines. Netherlands. *DHI Water Environment.* 294, 153–154.

Mattei, G., Troisi, S., Aucelli, P. P., Pappone, G., Peluso, F., and Stefanile, M. (2018). Sensing the submerged landscape of nisida roman harbour in the gulf of naples from integrated measurements on a USV. *Water.* 10, 1686. doi: 10.3390/w10111686

Merlotto, A., B´ertola, G. R., and Piccolo, M. C. (2016). Hazard vulnerability and coastal erosion risk assessment in necochea municipality, buenos aires province. *Argentina. J. Coast. Conserv.* 20 (5), 351–362. doi: 10.1007/s11852-016-0447-7

Mohamed, E-S. E-M., Ali, S., Moursy, F. E., Sharaky, A., and Saleh, N.. (2021). Coastal erosion risk assessment and applied mitigation measures at ezbet elborg village, Egyptian delta. *Ain Shams Eng. J* 13 (3), 3–6. doi: 10.10.1016/j.asej.2021.10.016

Mosadeghi, R., Warnken, J., Tomlinson, R., and Mirfenderesk, H.. (2019). Comparison of FuzzyAHP and AHP in a spatial multi-criteria decision making model for urban land-use planning. *Comput. Environ. Urban Syst.* 49, 54–65. doi: 10.1016/j.compenvurbsys.2014.10.001

Narra, P., Coelho, C., Sancho, F., Escudero, M., and Silva, R. (2019). Coastal hazard assessments for sandy coasts: Appraisal of five methodologies. *J. Coast. Res.* 35 (3), 574–589. doi: 10.2112/JCOASTRES-D-18-00083.1

Narra, P., Coelho, C., Sancho, F., and Palalane, J. (2017). CERA: An open-source tool for coastal erosion risk assessment. *Ocean Coast. Manage.* 142, 1–14. doi: 10.1016/j.ocecoaman.2017.03.013

Pan, Y., Yin, S., Chen, Y. P., Yang, Y. B., Xu, C. Y., and Xu, Z. S. (2022). An experimental study on the evolution of a submerged berm under the effects of regular waves in low-energy conditions. *Coast. Eng.* 176, 104169. doi: 10.1016/j.coastaleng.2022.104169

Parvin, G. A., Takahashi, F., and Shaw, R. (2008). Coastal hazards and community-coping methods in Bangladesh. *J. Coast. Conserv.* 12 (4), 181–193. doi: 10.1007/s11852-009-0044-0

Rahman, M., Chen, N. S., Islam, M. M., Dewan, A., Iqbal, J., Muhammad, R., et al. (2019). Flood susceptibility assessment in Bangladesh using machine learning and multi-criteria decision analysis. *Earth Syst. Environment.* 3, 585–601. doi: 10.1007/s41748-019-00123-y

Rodgers, J. L., and Nicewander, W. A. (1988). Thirteen ways to look at the correlation coefficient. *Am. Statis tician.* 42 (1), 59–64. doi: 10.1080/00031305.1988.10475524

Roy, S., and Mahmood, R. (2016). Monitoring shoreline dynamics using landsat and hydrological data: A case study of sandwip island of Bangladesh. *Pennsylvania Geographer* 54 (2), 20–41.

Roy, S., Pandit, S., Papia, M., Rahman, M. M., Ocampo, J. C. O. R., Razi, M. A., et al. (2021). Coastal erosion risk assessment in the dynamic estuary: The meghna estuary case of Bangladesh coast. *Int. J. Disaster Risk Reduction.* 07-14, 2212–4209. doi: 10.1016/j.ijdrr.2021.102364

Saaty, T. L. (1980). *The analytical hierarchy process* (Great Britain: Mcgraw-Hill), 52–58.

Saffaria, S., Mahmoudi, A., Shafiee, M., Jasemi, M., and Hashemi, L. (2020). Measuring the effectiveness of AHP and fuzzy AHP models in environmental risk assessment of a gas power plant. *Hum. Ecol. Risk Assess.* 27 (5), 1227–1238. doi: 10.1080/10807039.2020.1816809

Sarwar, M. G. M. (2013). "Sea-Level rise along the coast of Bangladesh," in *Disaster risk reduction approaches in Bangladesh*. Eds. R. Shaw, F. Mallick and A. Islam (Tokyo: Springer), 217–231.

Shao, C. (2016). Study on coastal erosion and adaptive management of beach-coral reef. [Master's thesis]. *Third Institute Oceanography State Oceanic Administration.* 50–63. Available at: https://kns.cnki.net/KCMS/detail/detail.aspx?dbname=CMFD201701&filename=1016256149.nh

Shi, P., and Kasperson, R. (2015). *World atlas of natural disaster risk* (Berlin: Springer-Verlag), 10–15.

Swami, D., and Parthasarathy, D. (2021). Dynamics of exposure, sensitivity, adaptive capacity and agricultural vulnerability at district scale for maharashtra. *India Ecol. Indic.* 121, 107206. doi: 10.1016/j.ecolind.2020.107206

Thampanya, U., Vermaat, J. E., Sinsakul, S., and Panapitukkuld, N.. (2006). Coastal erosion and mangrove progradation of southern Thailand. *Estuarine Coast. Shelf Sci.* 68 (1), 75–85. doi: 10.1016/j.ecss.2006.01.011

Thieler, E. R., and Hammar-Klose, E. S. (2000). National assessment of coastal vulnerability to sea-level rise, preliminary results for the US Atlantic coast. *Survey USGS.* 28–35. doi: /10.9774/GLEAF.978-1-909493-38-4_2

Tian, H. B., Yin, P., and Yang, F. L. (2016). An analysis of erosional characteristics of the sandy coast in the eastern part of wanning, hainan. *Mar. Geology Quaternary Geology.* 38 (4), 44–55. doi: 10.16562/j.cnki.0256-1492.2018.04.004

Wang, Y. H.. (2018). Coastal dynamic geomorphology. *Beijing Sci. Press* 05, 99–103.

Wang, X. T., Zhang, W. G., Yin, J., Wang, J., Ge, J. Z., Wu, J. P., et al. (2021). Assessment of coastal erosion vulnerability and socio-economic impact along the Yangtze river delta. *Ocean Coast. Management.* 201, 164–191. doi: 10.1016/j.ocecoaman.2021.105953

Wijitkosum, S., and Sriburi, T. (2019). Fuzzy AHP integrated with GIS analyses for drought risk assessment: A case study from upper phetchaburi river basin, Thailand. *Water.* 11 (5), 939. doi: 10.3390/w11050939

Xia, D. X., Wang, W. H., Wu, G. Q., Cui, J. Q., Li, F. L., et al. (1993). Coastal erosion in China. *Acta Geographica Sinica.* 48 (5), 468–475. doi: 10.11821/xb199305010

Yang, Z. X. (2013). Monitoring coastline changes and tidal flat reclamation in jiangsu using remote sensing technology. *Yellow River.* 1), 85–87. doi: 10.3969/j.issn.1000-1379.2013.01.027

Yoo, G., Kim, A. R., and Hadi, S. (2014). A methodology to assess environmental vulnerability in a coastal city: Application to Jakarta, Indonesia. *Ocean Coast. Management.* 102, 169–177. doi: 10.1016/j.ocecoaman.2014.09.018

Zou, Z. H., Yun, Y., and Sun, J. N. (2006). Entropy method for determination of weight of evaluating indicators in fuzzy synthetic evaluation for water quality assessment. *J. Environ. Sci.* 18 (5), 1020–1023. doi: 10.1016/S1001-0742(06)60032-6

frontiers | Frontiers in Marine Science

TYPE Original Research
PUBLISHED 09 January 2023
DOI 10.3389/fmars.2022.1061189

OPEN ACCESS

EDITED BY
Yi Pan,
Hohai University, China

REVIEWED BY
Hidekatsu Yamazaki,
Shanghai Ocean University, China
Peng Zhan,
Southern University of Science and Technology, China

*CORRESPONDENCE
Yang-Ki Cho
choyk@snu.ac.kr

SPECIALTY SECTION
This article was submitted to Coastal Ocean Processes, a section of the journal Frontiers in Marine Science

RECEIVED 04 October 2022
ACCEPTED 20 December 2022
PUBLISHED 09 January 2023

CITATION
Kwak M-T and Cho Y-K (2023) Impact of dynamic factors on the exchange flow between two neighboring bays with contrasting topography during summer: A numerical study. *Front. Mar. Sci.* 9:1061189. doi: 10.3389/fmars.2022.1061189

Impact of dynamic factors on the exchange flow between two neighboring bays with contrasting topography during summer: A numerical study

Myeong-Taek Kwak[1] and Yang-Ki Cho[2]*

[1]Fishery Resource Management Research Institute based on Information and Communication Technology (ICT), Chonnam National University, Yeosu, South Korea, [2]School of Earth and Environmental Sciences/Research Institute of Oceanography, Seoul National University, Seoul, South Korea

A high-resolution, three-dimensional numerical ocean model was employed to understand the exchange flow through Noryang Channel, which connects Gwangyang Bay and Jinju Bay. These two bays exhibit contrasting topographies, with Gwangyang Bay connected to the open ocean through a broad and deep channel, whereas Jinju Bay is relatively isolated from the open ocean by a narrow and shallow channel. Numerical experiments were conducted to determine the contribution of river discharge, wind stress, surface heat flux, and tides to the exchange flow between the two bays during summer. The results suggested that river discharge was the dominant factor affecting the exchange flow along Noryang Channel. Particularly, a high river discharge during summer increased the sea level in Jinju Bay, creating a barotropic flow toward Gwangyang Bay. However, the dense water entering Gwangyang Bay through the wide and deep channel generated a baroclinic flow toward Jinju Bay along the lower layer of Noryang Channel. An analytical model supported the conclusion that river discharge is the main driver of the exchange flow in Noryang Channel.

KEYWORDS

Gwangyang Bay, Jinju Bay, Noryang Channel, FVCOM, exchange flow, river discharge, density gradient, surface elevation

1 Introduction

The southern coast of the Korean Peninsula is characterized by the presence of numerous bays enclosed by capes and islands, two of which are the semi-enclosed Gwangyang and Jinju Bays. Gwangyang and Jinju Bays have an area of 259 and 168 km^2, an average depth of 12 and 5 m, and a volume of 3.05 and 0.83 km^3, respectively.

Gwangyang Bay is connected to the open ocean through the broad and deep Yeosu Channel, whereas Jinju Bay is more isolated, being connected to the open ocean only through Changseon and Daebang Channels, which are narrow and shallow and contain a number of small islands. These two bays are interconnected by the narrow and deep Noryang Channel, which is approximately 500 m wide and 30 m deep (Figure 1).

The study area is characterized by semidiurnal tides, with an average range of approximately 3 and 1 m during spring and neap tides, respectively (Choo et al., 2002). Because Jinju Bay is affected by the presence of islands, the tidal current in Noryang Channel is mainly governed by tidal waves propagating through Gwangyang Bay. Additionally, the Tsushima Current to the south of the two bays exhibits an eastward flow all year round (Cho et al., 2009; Cho et al., 2013).

Gwangyang and Jinju Bays are influenced by freshwater discharge from Sumjin and Gahwa Rivers, respectively. During period of heavy precipitation, the discharge from these rivers can exceed 2000 m^3/s. High-volume freshwater discharge mainly occurs during the summer monsoon season, with more than 80% of the annual discharge occurring during summer (Kwak and Cho, 2020).

Coastal development in and around Gwangyang Bay, such as the construction of industrial complexes and channel dredging, has increased the pollution levels in this bay (Park et al., 2005). In contrast, there are several oyster and fish farms in Jinju Bay (Ro et al., 2007), occupying approximately 33% of the total area of the bay. Thus, it is crucial to evaluate the potential pollution risk posed by the pollutants originating in Gwangyang Bay on Jinju Bay, particularly during summer when the exchange flow is highest (Kwak and Cho, 2020). Moreover, oil spill accidents frequently occur in Gwangyang Bay (Lee, 2001), with 250 accidents spilling a total of 9080 kl into the bay from 1991 to 2000 (Lee, 2001).

Therefore, understanding the hydrographic responses in Gwangyang and Jinju Bays to various external factors during summer, and the resulting exchange flow between the two bays is crucial. The most likely drivers of circulation in most coastal bays are river discharge, surface heat flux, wind stress, and tides (Valle-Levinson et al., 1998; Guo and Valle-Levinson, 2007; Ralston et al., 2008). Particularly, stratification due to freshwater inflow plays a crucial role in determining the hydrography and flow of most coastal bays in summer. Additionally, the exchange flow in Noryang Channel can be driven by differences in the surface elevation and horizontal density between the two bays.

Thus, this study conducted three-dimensional numerical experiments to evaluate the contribution of potential drivers to the exchange flow between the two bays during summer. Numerical models that employ a fine grid system to resolve the exchange flow in narrow channels are necessary to clearly understand the dynamics in real channels with a complex topography. Accordingly, the model employed in this study controlled the river discharge, wind stress, surface heat flux, and tides to determine their effect on the exchange flow between Gwangyang and Jinju Bays.

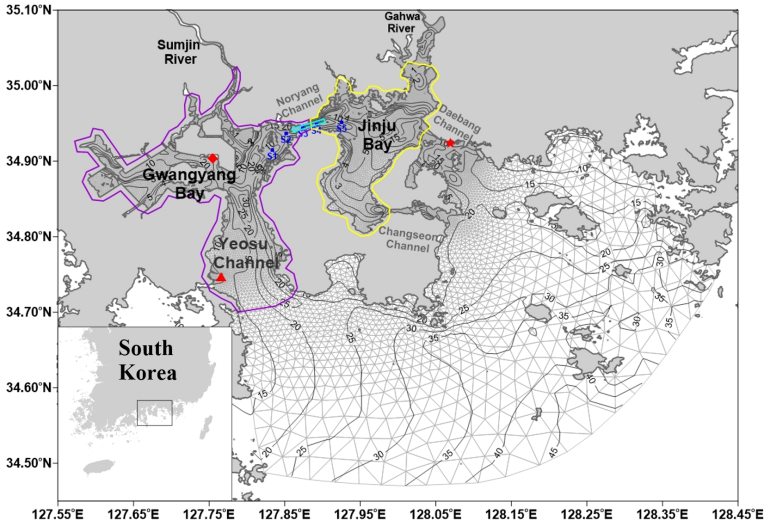

FIGURE 1
Study area, including Gwangyang and Jinju Bays. The red diamond, triangle, and star indicate the location of the tidal stations at Gwangyang, Yeosu, and Samcheonpo, respectively. The cyan rectangle denotes the location of the vertical profiles for the temperature, salinity, density, sea level, and density gradient. The blue circles represent CTD observation stations. The solid black lines indicate the water depth in meters. The gray triangles represent the model grid. The solid purple and yellow lines represent the initial concentration areas for dye experiment in Gwangyang and Jinju Bays, respectively.

2 Experimental model design

For the numerical experiments, this study adopted the Finite Volume Community Ocean Model (FVCOM) developed by Chen and Beardsley, (2006) to reproduce the exchange flow in Noryang Channel during a period of significant discharge in 2003. The FVCOM utilized an unstructured triangular grid system to precisely fit the shoreline and imposed a sigma-coordinate system for the vertical layers. The level 2.5 turbulence closure scheme developed by Mellor and Yamada (1982) was employed for vertical eddy mixing, and Smagorinsky (1963) formula was employed for horizontal eddy viscosity and diffusivity. Further details on the FVCOM are available in the study by Chen and Beardsley (2006).

The area covered by the model included Gwangyang and Jinju Bays and the nearby open ocean (Figure 1). The grid size in the study area ranged horizontally from a minimum of 60 m in the Sumjin River estuary to a maximum of 5000 m in the open boundary, with 10 vertical sigma layers. The temperature and salinity of the open boundary and initial conditions were calculated for the model grid using observed data from the National Institute of Fisheries Science of Korea (www.nifs.go.kr) for 2003. Interim data for 2003, including shortwave radiation, longwave radiation, wind speed, air pressure, and relative humidity, were obtained from the European Centre for Medium-Range Weather Forecasts (ECMWF) to establish the surface atmospheric conditions. The average wind speed during summer for the experiment period was 3.8 m/s. NAO.99Jb regional tide model data (Matsumoto et al., 2000) were employed along the open boundary using eight tidal components (M2, S2, K1, O1, N2, K2, P1, and Q1). The freshwater discharge from Sumjin and Gahwa Rivers was modeled using daily data from Korea Water Resources Corporation (www.kwater.or.kr).

The weather in 2003 exhibited typical seasonal variation (Chung et al., 2004). The river discharge from the Sumjin and Gahwa Rivers from 25 June to 29 July was set at 656.7 and 559.1 m^3/s, respectively. The river temperature was based on conductivity, temperature, and pressure (i.e., CTD) data observed in 2006 (Shaha et al., 2012) owing to the lack of water temperature data from 2003. Observational data suggest that the difference in the water temperature of the rivers between 2003 and 2006 was not significant (Kwak and Cho, 2020).

Four additional sensitivity experiments that excluded either wind stress, river discharge, surface heat flux, or tides from the control experiment were conducted (Table 1). The differences between the control experiment and sensitivity experiments were calculated to examine the effects of the factors on the exchange flow in Noryang Channel from 26 June to 24 July 2003. The difference (i.e., Control – Sensitivity) between the control experiment and the sensitivity experiments may represent the effect of each factor on the hydrography of both bays and the exchange flow in Noryang Channel.

3 Model validation

To verify the performance of the model, the tidal components from the control experiment and from observations at Yeosu, Gwangyang, and Samcheonpo tidal stations were compared (Figure 2) because the tidal elevation is a major factor governing the tidal current in both bays. Semidiurnal waves are dominant in the study area, with an average tide range of ~3 and ~1 m during spring and neap tides, respectively (Choo et al., 2002). The amplitude and phase at the Yeosu tidal station calculated in the control experiment were consistent with the observations (Figure 2). The differences in the tidal components at the Yeosu tidal station calculated using the control model and the observations were slightly lower than that at the Gwangyang tidal station. The root mean squared error (RMSE) for the amplitude observed at the Gwangyang, Yeosu, and Samcheonpo tidal stations was 3.0, 1.2, and 4.3 cm, respectively, and the RMSE for the phase was 15.2, 1.4, and 12.0°, respectively. The RMSE between the experimental and observed data was calculated using Eq. (1):

$$RMSEs = \sqrt{\frac{1}{8}\sum_{i=1}^{8}(Observation_i - Model_i)^2} \quad (1)$$

where i is a specific tidal component.

TABLE 1 External factors considered in each experiment.

Experiments	River discharge	Wind stress	Heat flux	Tide
Control	○	○	○	○
River	×	○	○	○
Wind	○	×	○	○
Heat	○	○	×	○
Tide	○	○	○	×

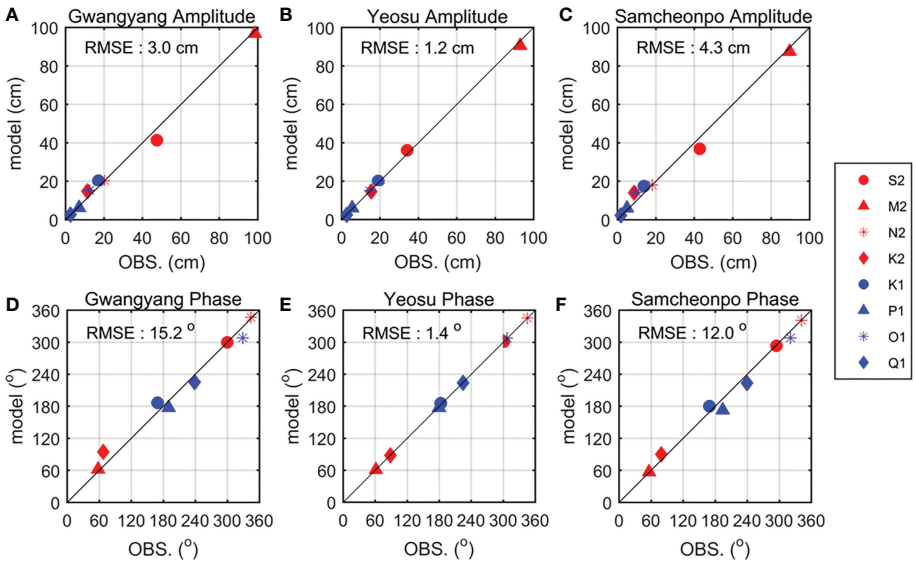

FIGURE 2
Comparison of the tidal amplitude and phases of the model and observations at: **(A)** and **(D)** Gwangyang, **(B)** and **(E)** Yeosu, and **(C)** and **(F)** Samcheonpo tidal stations (see Figure 1 for the locations).

Observations and the model predictions of the seawater temperature and salinity from stations S1 to S5 in Noryang Channel were compared (Figure 3). The observations revealed relatively light water (T: >20.8 °C; S<20) in the upper layer of Jinju Bay and dense water in the lower layer of Gwangyang Bay. The water temperature predicted by the model was consistent with the observations, with a difference of less than 0.5 °C. In addition, the salinity calculated by the model exhibited a stratified structure, which is consistent with the observations.

4 Results

4.1 Horizontal distribution of temperature, salinity, and surface elevation

The horizontal surface temperature, salinity, and surface elevation obtained from the control experiment were averaged over the 28.5 days from 26 June to 24 July (Figure 4). The results revealed that the mean sea surface temperature was high at the head

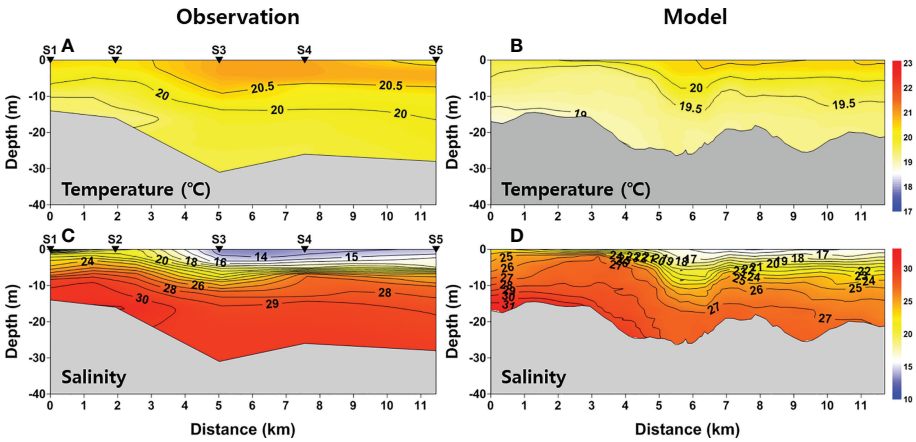

FIGURE 3
Comparison of **(A)** and **(C)** observed and **(B)** and **(D)** modeled vertical profiles from stations S1 to S5 for **(A)** and **(B)** temperature and **(C)** and **(D)** salinity on 13 July 2003.

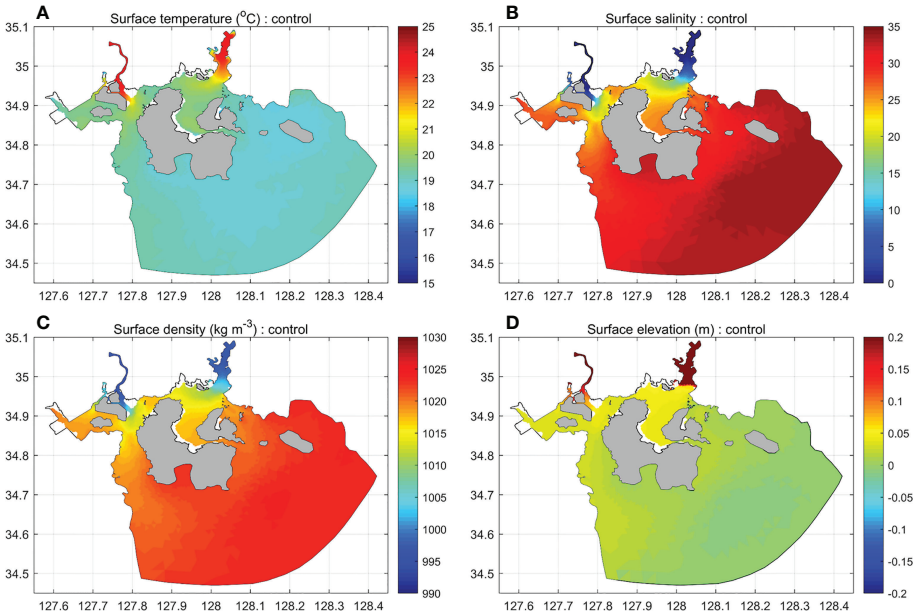

FIGURE 4
Averaged surface: **(A)** temperature, **(B)** salinity, **(C)** density, and **(D)** elevation results for the control model from 26 June to 24 July.

of the river estuaries and decreased toward the mouth, whereas it was lower in the two bays than in the rivers and decreased at distances closer to the open sea (Figure 4A). In contrast, the surface salinity exhibited the opposite trend: it was low at the head of the river estuaries, increased toward the bay, and was highest near the open sea (Figure 4B). The surface density was more strongly affected by the salinity than the water temperature, so it exhibited a similar trend to that of the surface salinity (Figure 4C). The mean surface elevation in Jinju Bay was approximately 2 cm higher than that of Gwangyang Bay (Figure 4D). In the Sumjin and the Gahwa River estuaries, the surface elevation was above 20 cm owing to the high river discharge. The surface elevation near the open sea was close to zero.

In the river experiment, the surface temperature was 2.3 °C higher in Sumjin and Gahwa Rivers and 0.9 °C higher in Gwangyang and Jinju Bays than in the control experiment, and it increased slightly near the open sea (Figure 5A). The wind stress contributed to a 0.5 °C decrease in the surface temperature near the open sea (Figure 5B), whereas the surface heat flux caused an increase in the surface temperature except in Sumjin and Gahwa Rivers, with an increase of 1 °C in Gwangyang and Jinju Bays and 2 °C near the open sea (Figure 5C). Additionally, the tides decreased the surface temperature in the central part of Gwangyang Bay and the mouth of the Gahwa River estuary owing to vertical mixing (Figure 5D).

The surface salinity of both bays was mostly affected by the river discharge, which significantly reduced their salinity (Figure 6A). The wind stress and surface heat flux exerted only a slight effect on the surface salinity (Figures 6B and C), whereas the tides increased the surface salinity in the central part of Gwangyang Bay and downstream of Gahwa River, which are relatively shallow and experience strong tidal currents (Figure 6D). In each sensitivity model (i.e., Control – Sensitivity), the distribution of the surface density was similar to that of the salinity.

The surface elevation of Jinju Bay was approximately 2 cm higher than that of Gwangyang Bay in the river experiment (Figure 7A). Despite the similarity in the river discharge from Sumjin and Gahwa Rivers affecting the two bays, the surface elevation of Jinju Bay was higher owing to its isolation, whereas Gwangyang Bay is connected to the open sea through the broad and deep Yeosu Channel. The wind stress, surface heat flux, and tides did not significantly contribute to the mean surface elevation in either bay (Figures 7B, C, and D). However, the tides resulted in a higher surface elevation in shallow coastal areas where tidal flats were present (Figure 7D).

In summary, these results collectively indicated that river discharge was the primary contributor to the differences in the surface elevation and horizontal density of the two bays. Particularly, the structure produced by the control model was similar to that of the river experiment in terms of the distribution of the surface elevation.

4.2 Vertical temperature, salinity, and density profiles along the channel

According to the control experiment, the distribution of the seawater temperature along the Noryang Channel exhibited a

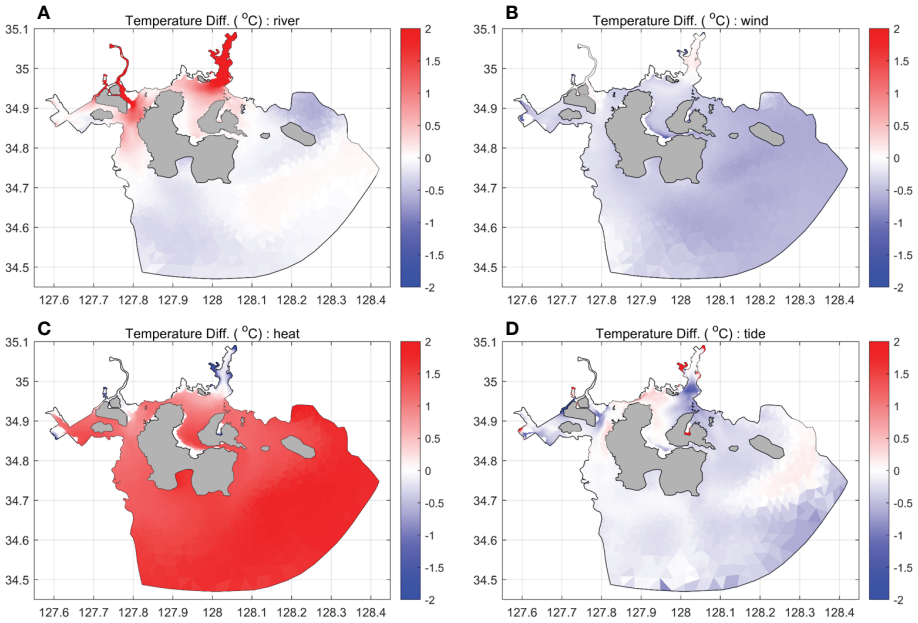

FIGURE 5
Contribution of river discharge, wind, heat flux, and tide to the surface temperature. The surface temperature represents the difference between the control experiment and the: **(A)** river discharge, **(B)** wind, **(C)** heat flux, and **(D)** tide experiments averaged from 26 June to 24 July.

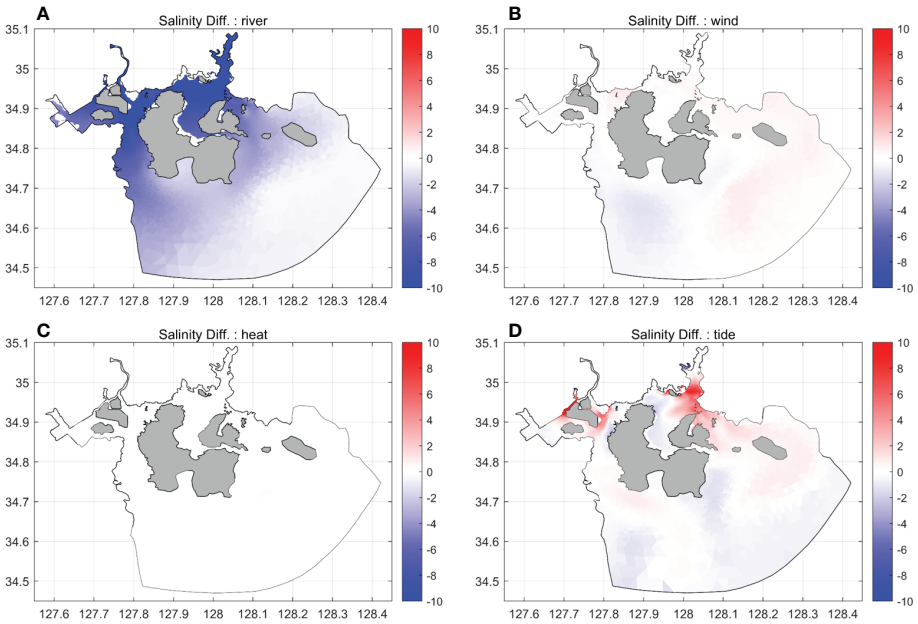

FIGURE 6
Same as Figure 5, but with surface salinity.

stratified structure with a temperature of approximately 19.5 °C in the surface layer and less than 19 °C in the lower layer (Figure 8A). In addition, the salinity was lower than 25 in the surface layer, but above 29 in the bottom layer (Figure 8B). Consequently, the density also exhibited a stratified distribution due to the difference between the surface layer and the lower layer in terms of temperature and salinity. The density was less than 1017 kg m^{-3} in the surface layer and more than 1020 kg m^{-3} in the lower layer (Figure 8C). Denser water (T<19 °C, S >30) was observed in the lower layer of Gwangyang Bay, whereas less

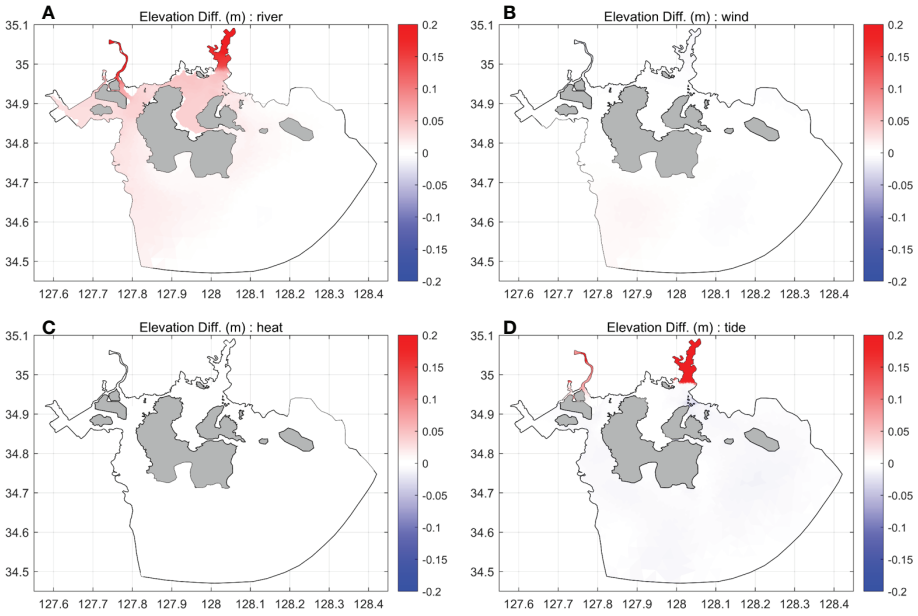

FIGURE 7
Same as Figure 5, but with surface elevation.

dense water (T >19.5 °C, S<23) was observed in the surface layer of Jinju Bay. The dissipation rate (ϵ) was calculated using the following equation (Chen and Beardsley, 1998; Chen and Beardsley, 2006):

$$\epsilon = q^3/B_1 l \quad (2)$$

$q^2=(u^2+v^2)/2$ represents the turbulent kinetic energy, B_1 is a constant equal to 16.6, l is the turbulent length scale. The dissipation rate was higher in the surface layer of both bays. The dissipation rate in the bottom layer of Jinju Bay was higher than that of Gwangyang Bay (Figure 8D).

The comparison of the control and river experiments (Control – Sensitivity) revealed an increase in temperature and a decrease in salinity owing to the river discharge. The maximum difference in the temperature and salinity in the surface layer was approximately 0.8 °C and 9, respectively (Figures 9A and 9B). The decrease in the density in the lower layer and surface layer was approximately 2.5 and 7 kg m^{-3}, respectively (Figure 9C). The increase in temperature may be attributed to the relatively warm river water during summer, and the reduced salinity could be attributed to the freshwater discharge from the two rivers.

Additionally, the comparison of the control and wind experiments revealed that there was only a slight change in the temperature, whereas the salinity increased due to wind stress (Figures 9D and 9E). Further, the maximum salinity increased slightly in the surface layer owing to vertical mixing *via* wind stress. The difference in density was less than 1 kg m^{-3} (Figure 9F).

The heat flux experiment revealed an increase of approximately 1 °C in the temperature compared to the control experiment, which could be attributed to surface heat flux (Figure 9G). The difference in the salinity and density was very small (Figures 9H and 9I).

In the tide experiment, although there was no significant change in the water temperature, the salinity in the surface layer increased, while that in the lower layer decreased due to active vertical mixing by the tidal currents (Figures 9J and 9K). The maximum change in the salinity was higher than 2 in the lower layer. Consequently, the density increased by approximately 2 kg m^{-3} in the lower layer, but decreased by approximately 1 kg m^{-3} in the surface layer (Figure 9L).

These experimental results suggest that river discharge was the primary factor influencing the spatial variation in the temperature, salinity, and density within the study area. The wind stress slightly increased the salinity in the surface layer, whereas heat only increased the water temperature by approximately 1 °C. The tides changed both the water temperature and salinity, while they weakened the stratification *via* vertical mixing.

5 Discussion

5.1 Differences in the surface elevation and density along the channel

The mean flow in Noryang Channel may be driven by differences in the surface elevation and horizontal density gradient between the two bays. This study examined the

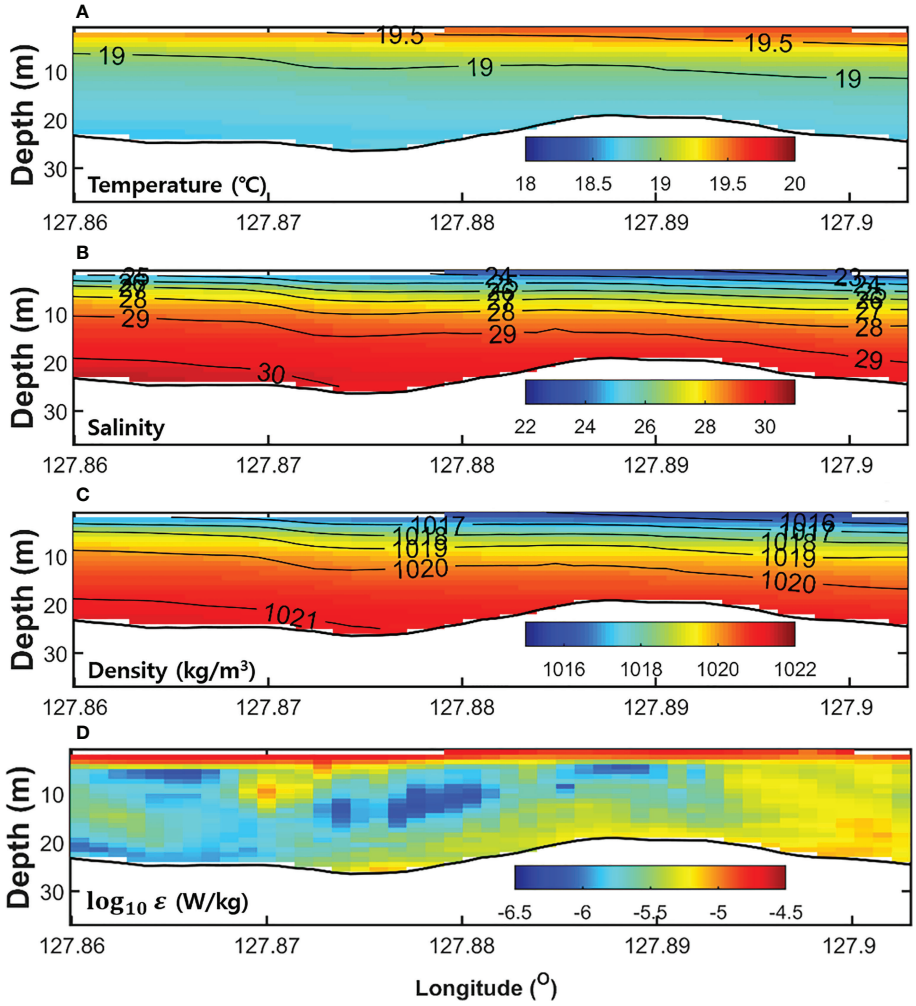

FIGURE 8
Vertical profiles of **(A)** temperature, **(B)** salinity, **(C)** density, and **(D)** dissipation rates in the control experiment along Noryang Channel (the cyan line in Figure 1) averaged from 26 June to 24 July.

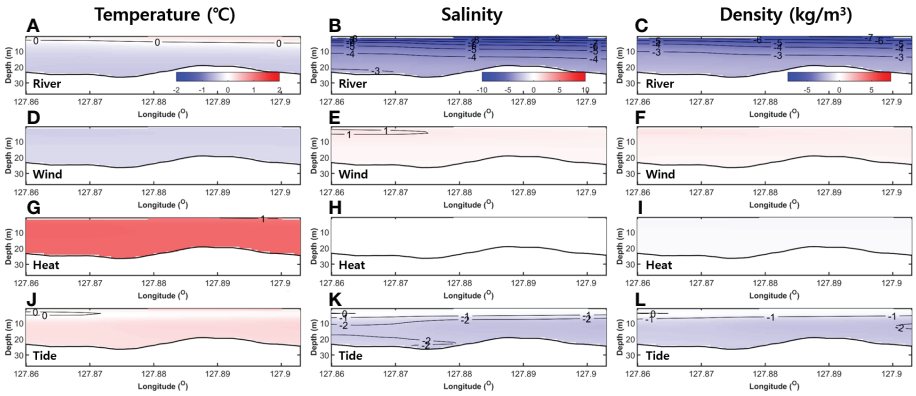

FIGURE 9
Differences in the [**(A)**, **(D)**, **(G)**, **(J)**] temperature, [**(B)**, **(E)**, **(H)**, **(K)**] salinity, and [**(C)**, **(F)**, **(I)**, **(L)**] density of the control experiment and the [**(A)**, **(B)**, **(C)**] river, [**(D)**, **(E)**, **(F)**] wind, [**(G)**, **(H)**, **(I)**] heat, and [**(J)**, **(K)**, **(L)**] tide experiments along Noryang Channel averaged from 26 June to 24 July.

vertical profiles for the surface elevation, horizontal density gradient, and residual current derived from the control experiment to determine the spatial change along Noryang Channel (Figure 10). Positive and negative residual currents indicated an eastward flow to Jinju Bay and a westward flow to Gwangyang Bay, respectively.

The control experiment revealed that the surface elevation near Jinju Bay was approximately 1 cm higher than that near Gwangyang Bay (Figure 10A). The eastward flow in the Noryang Channel was driven by the horizontal density gradient (0.01 kg/m^3/m) (Figure 10B), whereas the westward residual flow in the surface layer was driven by the difference in the surface elevation (Figure 10C).

The results of dye concentration experiments in the Noryang Channel were analyzed to figure out exchange flow. Figures 10D, E show the result of two experiments with the initial dye concentration of 1.0 only in Gwangyang Bay and Jinju Bay, respectively. Further detailed numerical design can be found in

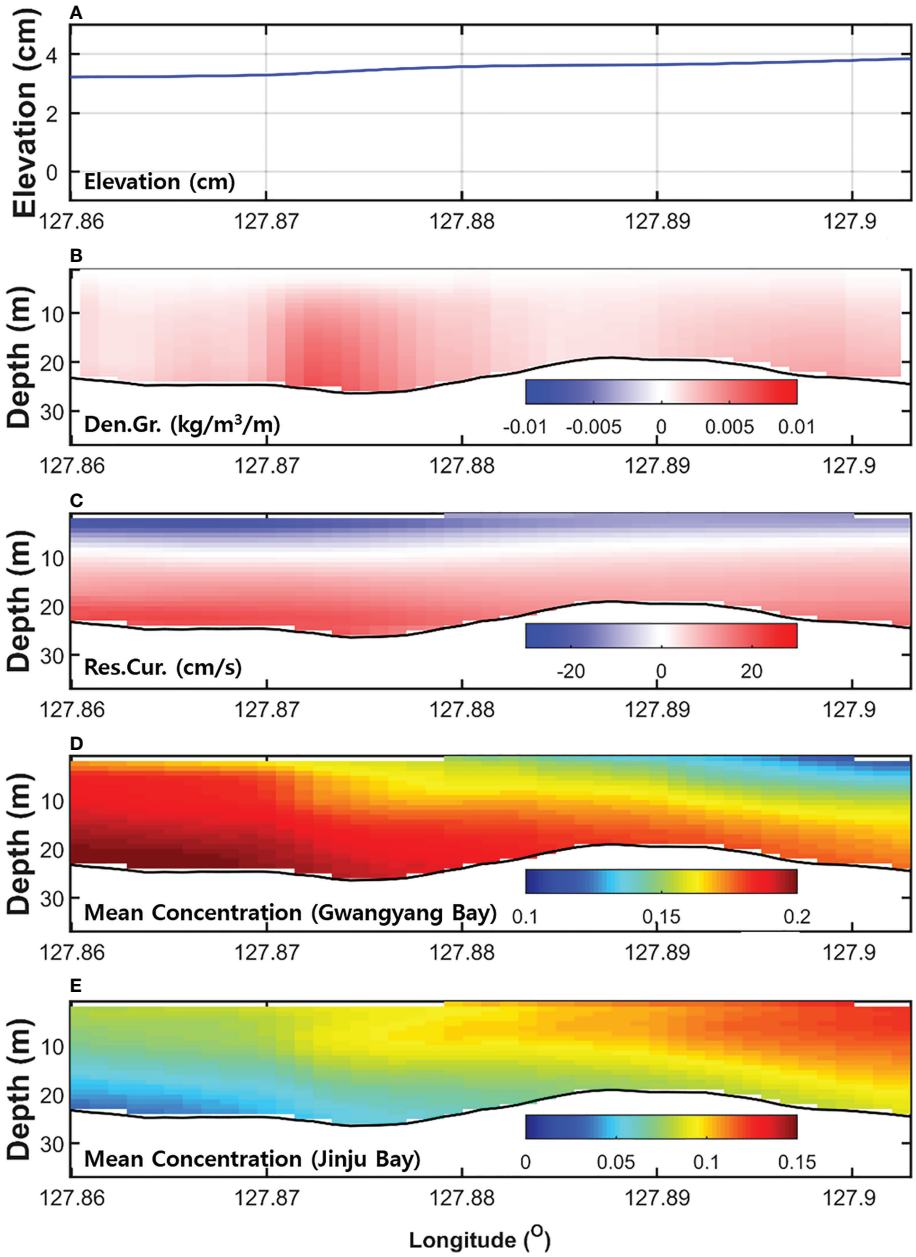

FIGURE 10
Vertical profiles of the **(A)** surface elevation, **(B)** density gradient, and **(C)** residual current from the control experiment along the Noryang Channel averaged from 26 June to 24 July. **(D)** Distribution of dye originating from Gwangyang Bay and **(E)** distribution of dye originating from Jinju Bay. The positive and negative residual currents represent eastward and westward flows, respectively.

previous study (Kwak and Cho, 2020). The high concentration in the lower layer originates from Gwangyang Bay, whereas that in the surface layer originates from Jinju Bay. The results of dye distribution distinctly show that the exchange flow is westward in the surface layer but eastward in the lower layer.In the river experiment, the difference in the surface elevation between Gwangyang and Jinju Bays was approximately 1.0 cm (Figure 11A). Additionally, the horizontal density gradient was positive, with a maximum gradient of 0.0061 kg/m^3/m at the bottom (Figure 11B). The residual current flowed westward in the surface layer, but eastward in the middle and lower layers, as in the control experiment (Figure 11C).

There was only a slight change in the surface elevation and density gradient in the wind experiment (Figures 11D, E). The residual current weakly flowed to Gwangyang Bay in the surface layer, but the opposite direction in the subsurface (Figure 11F). There were no differences between these parameters of the two bays in the heat experiment (Figures 11G and 11H), and the residual current was close to zero in the whole section (Figure 11I). Additionally, the surface elevation was mostly unchanged in the tide experiment, but the density gradient increased in the lower layer (Figures 11J, K). The residual current showed a complex structure. The residual current of the surface layer flowed westward in the west but eastward in the bottom layer (Figure 11L).

5.2 Barotropic and baroclinic forces along the channel

The horizontal pressure gradient force along the channel ($-\frac{1}{\rho}\frac{\partial P}{\partial x}$) can be decomposed into barotropic and baroclinic forces as follows:

$$-\frac{1}{\rho}\frac{\partial P}{\partial x} = -g\frac{\partial \eta}{\partial x} - \frac{g}{\rho_0}\int \frac{\partial \rho}{\partial x}dz \qquad (3)$$

where $-g\frac{\partial \eta}{\partial x}$ and $-\frac{g}{\rho_0}\int \frac{\partial \rho}{\partial x}dz$ represent the barotropic and baroclinic forces, respectively, P, ρ, and ρ_0 are the pressure, density, and depth-averaged density, respectively, g is the gravitational acceleration, and x and z are the eastward direction and depth, respectively. These forces result from differences in the surface elevation and density gradient, respectively.

The control experiment revealed that the barotropic force was driven westward along Noryang Channel across the entire column (Figure 12A). However, the baroclinic force was driven eastward and increased from the surface to the lower layer (Figure 12B). The sum of the two forces resulted in a westward flow in the surface layer and an eastward flow in the lower layer (Figure 12C).

The freshwater from Sumjin River mixed with saline water from the open ocean through the wide and deep Yeosu Channel, thus increasing the salinity in Gwangyang Bay. However, the mixing between the fresh water from the Gahwa River and the saline water from the open ocean was limited owing to the narrow and shallow Changseon and Daebang Channels, which retained the fresh water within Jinju Bay. The exchange flow in the channel was caused by the baroclinic force driven by the differences in the salinity of Gwangyang and Jinju Bays.

The tidal effect was smaller than that of the river, but was locally significant. The tidal effects on the residual current are quite complicated owing to nonlinear effects in tide-dominant shallow seas (Kim and Cho, 2017). Therefore, the distribution of the water temperature, salinity, and density in the channel can be affected by vertical mixing due to the tidal current. Uneven vertical mixing by the spatially varying tidal current might result in a horizontal density gradient in stratified seas. The model results revealed significant spatial variation in the tidal current within the study area. The maximum observed tidal current in Noryang Channel was approximately 1.3 m/s (Kwak et al., 2014).

The effect of the river discharge was significant for both the barotropic and baroclinic forces considering their surface

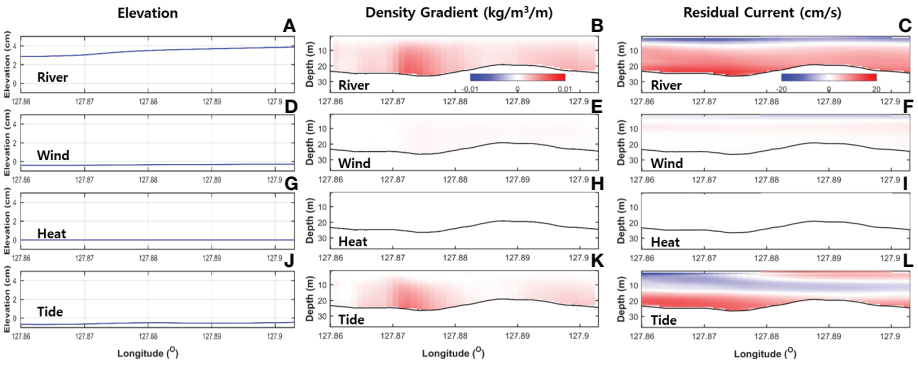

FIGURE 11
Differences (Control – Sensitivity) in the surface elevation, density gradient (kg/m^3/m), and residual current of the control experiment and the **(A–C)** river, **(D–F)** wind, **(G–I)** heat, and **(J–L)** tide experiments for the vertical profile along Noryang Channel averaged from 26 June to 24 July.

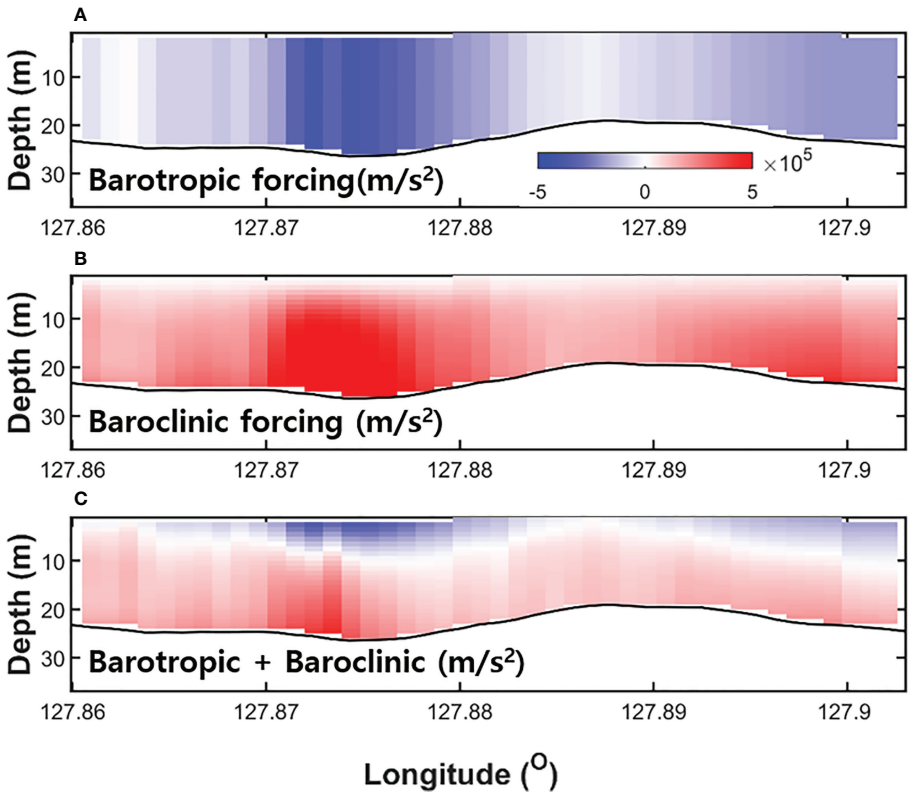

FIGURE 12
Vertical profiles of the **(A)** barotropic, **(B)** baroclinic, and **(C)** barotropic + baroclinic forces from the control experiment along Noryang Channel averaged from 26 June to 24 July.

elevation and horizontal density gradient (Figures 12A and 12B), whereas the effects of the wind stress and surface heating on both forces were very small.

5.3 Comparison of the analytical velocity profiles based on the densities obtained from the numerical experiments

The results from the numerical model regarding the main cause of the exchange flow are consistent with those of a previous study (Kwak et al., 2014). Based on limited observations of Noryang Channel, this previous study suggested that the exchange flow may be mainly driven by differences in the horizontal density owing to the river discharge. The horizontal density distribution, which drives the exchange flow in Noryang Channel, can also be potentially affected by wind stress, surface heat flux, and tides. Therefore, the results from each model were employed in an analytical model to quantitatively evaluate the contribution of each force to the development of the exchange flow in Noryang Channel. The analytical velocity profile that balances the vertical shear stress and pressure gradients along the channel (Officer, 1976) can be expressed using Eq. (4):

$$u(z) = \frac{gH^3}{24\rho_0 A_z}\frac{\partial \rho}{\partial x}\left[1 - 4\frac{z^3}{H^3} - 6\frac{z^2}{H^2}\right] \quad (4)$$

where u is the channel velocity, g and H are the gravitational acceleration and water depth, respectively, ρ_0 is the depth-averaged density, x and z are the eastward and upward directions, respectively, A_z is the eddy viscosity, and $\partial\rho/\partial x$ is the depth-averaged horizontal density gradient along the channel.

The analytical velocity profile obtained using Eq. (4) was calculated based on the density distribution obtained from the numerical experiments. The analytical model revealed that the flow in the channel was driven by the density gradient (Figure 13). The eddy viscosity in Noryang Channel was set to 0.015 m^2/s, which has been demonstrated to produce the best results for the study area (Kwak et al., 2014).

The analytical velocity profile based on the density from the control experiment was close to the observed velocity (the triangles at depths of 7 and 15 m in Figure 13). The analytical velocity profile obtained using the observed density (the dotted

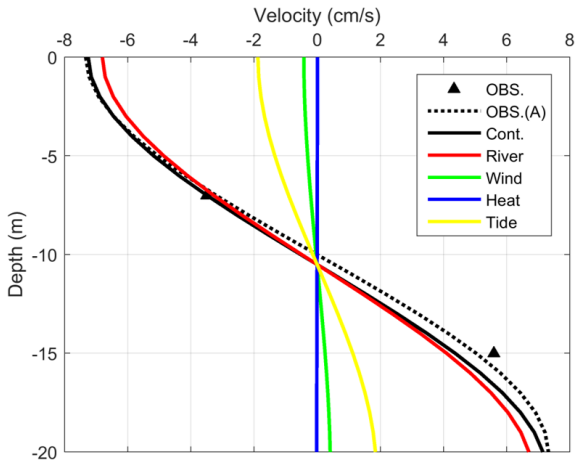

FIGURE 13
Along-channel velocity of the observed (triangles) and predicted velocity profile using Eq. (2) based on densities obtained from observations (dotted black line) and the control (solid black line), river (solid red line), wind (solid green line), heat (solid blue line), and tide experiments (solid yellow line).

black line) was also similar to the observed velocity. The velocity profile obtained using the density from the difference between the control and the river experiments (the solid red line) was similar to the results from the control experiment with a difference of –0.22 and 0.27 cm/s at 7 and 15 m, respectively. The velocity based on the densities from the wind and the heat experiments was less than 0.5 cm/s at both depths. The velocity obtained using the density from the tide experiment was approximately –1 and 1 cm/s at 7 and 15 m, respectively. These analytical model results support the interpretation that river discharge is the primary driver of the exchange flow in Noryang Channel during summer.

6 Conclusion

This study employed a three-dimensional numerical model to examine the major causes of the exchange flow in Noryang Channel, which connects two bays with contrasting topographies, during summer. A control experiment considering river discharge, wind stress, surface heat flux, and tides was conducted. In addition, sensitivity experiments considering river discharge, wind stress, surface heat flux, and tides were also conducted to evaluate the individual effects of the drivers on the exchange flow, and the results were compared to those obtained from the control experiment.

The control experiment revealed that the surface elevation of Jinju Bay was approximately 2 cm higher than that of Gwangyang Bay owing to the high river discharge during summer. The river experiment suggested that this difference in surface elevation was mainly caused by the river discharge; however, the other sensitivity experiments predicted only a slight difference in the surface elevation of the two bays.

The high river discharge resulted in large differences in the salinity and density of the two bays. In addition, the wind stress slightly decreased the surface temperature, but exerted no effect on the difference in the density of the two bays. The surface heat flux increased the water temperature by 1 °C, but there was only a slight change in the spatial density. Additionally, although the tides increased the surface salinity and decreased the lower-layer salinity owing to vertical mixing, they exerted no significant effect on the difference in the density of the two bays.

The control experiment suggested that the surface elevation and horizontal density gradient were the key drivers of the surface flow to Gwangyang Bay and the lower-layer flow to Jinju Bay, respectively. The results from the river experiment indicated that this exchange flow was mainly driven by the river discharge. The freshwater from Gahwa River generally has a high residence time in Jinju Bay owing to its isolation from the open sea, whereas the freshwater from Sumjin River mixes with saline seawater through the broad and deep Yeosu Channel in Gwangyang Bay.

The analytical model results supported the conclusion that river discharge plays the most important role among the potential drivers within the study area. The different responses to the high river discharge in terms of salinity and surface elevation in Gwangyang and Jinju Bay, which could be attributed to their contrasting topographies, resulted in the exchange flow between the two bays. The barotropic pressure gradient caused by the surface elevation resulted in a surface layer flow from Jinju Bay to Gwangyang Bay, whereas the baroclinic pressure gradient caused by the density gradient resulted in an opposite flow in the lower layer.

The exchange flow from Gwangyang Bay, where an industrial complex is located, may deliver pollutants to aquaculture in Jinju Bay. The numerous oyster and fish farms in Jinju Bay are highly susceptible to pollution *via* Noryang Channel owing to this exchange flow during summer. These findings from the numerical experiments were derived from typical weather conditions in 2003; however, greater river discharge may result in more severe pollution in Jinju Bay.

Data availability statement

The original contributions presented in the study are included in the article/Supplementary Material. Further inquiries can be directed to the corresponding author.

Author contributions

Conceptualization, Y-KC and M-TK. Methodology, M-TK and Y-KC. Writing draft, M-TK. Review and editing, Y-KC. Visualization M-TK. Supervision, Y-KC. Project administration, Y-KC. All authors contributed to the article and approved the submitted version.

Funding

This research was partly supported by the Korea Institute of Marine Science & Technology Promotion (KIMST) funded by the Ministry of Oceans and Fisheries (20220033) and the National Research Foundation (NRF) funded by the Korean government (NRF-2022M3I6A1085698). This research was a part of the project titled "Research center for fishery resource management based on the information and communication technology" (2023, grant number 20180384), funded by the Ministry of Oceans and Fisheries, Korea.

Conflict of interest

The authors declare that the research was conducted in the absence of any commercial or financial relationships that could be construed as a potential conflict of interest

Publisher's note

All claims expressed in this article are solely those of the authors and do not necessarily represent those of their affiliated organizations, or those of the publisher, the editors and the reviewers. Any product that may be evaluated in this article, or claim that may be made by its manufacturer, is not guaranteed or endorsed by the publisher.

Supplementary material

The Supplementary Material for this article can be found online at: https://www.frontiersin.org/articles/10.3389/fmars.2022.1061189/full#supplementary-material

References

Chen, C., and Beardsley, R. C. (1998). Tidal mixing and cross-frontal particle exchange over a finite amplitude asymmertric bank: A model study with application to georges bank. *J. Mar. Res.* 56, 1163–1201. doi: 10.1357/002224098765093607

Chen, C., and Beardsley, R. C. (2006). *An unstructured grid, finite-volume coastal ocean model: FVCOM user manual* (New Bedford: University of Massachusetts Dartmouth).

Choo, H. S., Lee, B. G., and Lee, G. H. (2002). Numerical simulation of residual currents by diagnostic multilevel model in kwangyang bay. *Korean Bull. Korean Environ. Sci. Soc* 11, 637–650. doi: 10.5322/jes.2002.11.1.041

Cho, Y.-K., Seo, G.-H., Choi, B.-J., Kim, S., Kim, Y.-G., Youn, Y.-H., et al. (2009). Connectivity among straits of the northwest pacific marginal seas. *J. Geophys. Res.* 114, C06018. doi: 10.1029/2008JC005218

Cho, Y.-K., Seo, G. H., Kim, C.-S., Choi, B.-J., and Shaha, D. C. (2013). Role of wind stress in causing maximum transport through the Korea strait in autumn. *J. Mar. Syst.* 115-116, 33–39. doi: 10.1016/j.jmarsys.2013.02.002

Chung, Y. S., Yoon, M. B., and Kim, H. S. (2004). On climate variations and changes observed in south Korea. *Climatic Change* 66, 151–161. doi: 10.1023/B:CLIM.0000043141.54763.f8

Guo, X., and Valle-Levinson, A. (2007). Tidal effects on estuarine circulation and outflow plume in the Chesapeake bay. *Cont. Shelf Res.* 27, 20–42. doi: 10.1016/j.csr.2006.08.009

Kim, B. G., and Cho, Y. K. (2017). Tide induced residual circulation in a bay with asymmetric lateral depth variation. *J. Geophys. Res.* 122, 4040–4050. doi: 10.1002/2016JC012473

Kwak, M.-T., and Cho, Y.-K. (2020). Seasonal variation in residence times of two neighboring bays with contrasting topography. *Estuar. Coast.*, 43, 512–524. doi: 10.1007/s12237-019-00644-9

Kwak, M. T., Seo, G. H., Cho, Y. K., Cho, C. W., Choo, H. S., Yoon, Y. H., et al. (2014). Baroclinic two-layer flow induced by extreme discharge from a dam in a narrow channel. *Estuar. Coast. Shelf Sci.* 151, 331–335. doi: 10.1016/j.ecss.2014.07.015

Lee, B. G. (2001). Status of oil spill accidents and prevention measures in gwangyang bay. *J. Korean Soc Mar. Environ. Energy* 5, 119–129.

Matsumoto, K., Takanezawa, T., and Ooe., M. (2000). Ocean tide models developed by assimilating TOPEX/POSEIDON altimeter data into hydrodynamical model: A global model and a regional model around Japan. *J. Oceanogr.* 56, 567–581. doi: 10.1023/A:1011157212596

Mellor, G. L., and Yamada, T. (1982). Development of a turbulence closure model for geophysical fluid problem. *Rev. Geophys.* 20, 851–875. doi: 10.1029/RG020i004p00851

Officer, C.B., 1976. *Physical Oceanography of Estuaries*. (New York: John Wiley & Sons Inc.), p. 465.

Park, K., Jung, H.-S., Kim, H.-S., and Ahn, S.-M. (2005). Threedimensional hydrodynamic-eutrophication model (HEM-3D): Application to kwang-yang bay, Korea. *Mar. Environ. Res.* 60, 171–193. doi: 10.1016/j.marenvres.2004.10.003

Ralston, D. A., Geyer, W. R., and Lerczak, J. A. (2008). Subtidal salinity and velocity in the Hudson river estuary: Observations and modeling. *J. Phys. Oceanogr.* 38, 753–770. doi: 10.1175/2007JPO3808.1

Ro, Y. J., Jun, W. S., Jung, K. Y., and Eom, H. M. (2007). Numerical modeling of tide and tidal current in the kangjin bay, south sea. Korea. *Ocean Sci. J.* 42 (3), 153–163. doi: 10.1007/BF03020919

Shaha, D. C., Cho, Y. K., Kim, T. W., and Valle-Levinson, A. (2012). Spatio-temporal variation of flushing time in the sumjin river estuary. terr. atmos. *Ocean. Sci.* 23 (1), 119–130. doi: 10.3319/TAO.2011.08.22.01(Hy)

Smagorinsky, J. (1963). General circulation experiments with the primitive equations. i. the basic experiment. *Mon. Weather Rev.* 91 (3), 99–164. doi: 10.1175/1520-0493(1963)091<0099:GCEWTP>2.3.CO;2

Valle-Levinson, A., Li, C., Royer, T. C., and Atkinson, L. P. (1998). Flow patterns at the Chesapeake bay entrance. *Cont. Shelf Res.* 18, 1157–1177. doi: 10.1016/S0278-4343(98)00036-3

frontiers | Frontiers in Marine Science

TYPE Original Research
PUBLISHED 10 January 2023
DOI 10.3389/fmars.2022.1041351

OPEN ACCESS

EDITED BY
Yi Pan,
Hohai University, China

REVIEWED BY
Alessandro Stocchino,
Hong Kong Polytechnic University,
Hong Kong SAR, China
Zhonghua Yang,
Wuhan University, China

*CORRESPONDENCE
Shiqiang Wu
sqwu@nhri.cn
Xiufeng Wu
xfwu@nhri.cn
Yu Zhang
yuzhang@nhri.cn

SPECIALTY SECTION
This article was submitted to Coastal Ocean Processes, a section of the journal Frontiers in Marine Science

RECEIVED 10 September 2022
ACCEPTED 06 December 2022
PUBLISHED 10 January 2023

CITATION
Wu C, Wu S, Wu X, Zhang Y, Feng K, Zhang W and Zhao Y (2023) Hydrodynamics affected by submerged vegetation with different flexibility under unidirectional flow. *Front. Mar. Sci.* 9:1041351. doi: 10.3389/fmars.2022.1041351

Hydrodynamics affected by submerged vegetation with different flexibility under unidirectional flow

Chenhui Wu[1,2], Shiqiang Wu[1]*, Xiufeng Wu[1]*, Yu Zhang[1]*, Kedong Feng[1,3], Weile Zhang[1,4] and Yuhang Zhao[1]

[1]State Key Laboratory of Hydrology-Water Resources and Hydraulic Engineering, Nanjing Hydraulic Research Institute, Nanjing, China, [2]College of Water Conservancy and Hydropower Engineering, Hohai University, Nanjing, China, [3]State Key Laboratory of Water Resources and Hydropower Engineering Science, Wuhan University, Wuhan, China, [4]State Key Laboratory of Hydraulic Engineering Simulation and Safety, Tianjin University, Tianjin, China

Submerged vegetation changes the hydrodynamic characteristics of rivers, lakes, wetlands, and coastal zones. However, only a few studies have focused on the effect of flexible submerged vegetation on hydrodynamic characteristics under unidirectional flow. Therefore, laboratory experiments were conducted to study the effects of submerged vegetation with different flexibility on the flow structure and turbulence characteristics under unidirectional flow. The results showed that the reconfiguration and coordination of wave motion of flexible submerged vegetation redistribute flow velocity, Reynolds stress, and turbulent kinetic energy inside and outside of the vegetation canopy. With a gradual decrease in the deflection height of vegetation, the differences in dimensionless velocity, dimensionless mixed layer thickness, bulk drag coefficient, averaged turbulent kinetic energy, and the averaged contribution rate of its shear production term for the vegetation canopy also decrease; the trend of the penetration depth of Reynolds stress is opposite. Based on the turbulent kinetic energy budget equation, a turbulent kinetic energy model (TKE model) was established, which can be used to predict the turbulent kinetic energy and its shear production term within the vegetation canopy. Here, the scaling factor was determined by the vegetation canopy Cauchy number. The TKE model can be applied under unidirectional flow conditions for submerged vegetation with different flexibilities with high accuracy. It is a simple method to predict vegetation-induced turbulence and the characteristics of sediment and material transport under the influence of submerged vegetation with different flexibility.

KEYWORDS

vegetation with different flexibility, vegetated flow, velocity, turbulent kinetic energy, TKE prediction model

1 Introduction

As an essential part of the ecosystems comprising rivers, lakes, wetlands, and coastal zones, aquatic vegetation canopy not only intercepts exogenous pollution and purifies water quality (Wilcock et al., 1999; Nepf, 2012; Wang et al., 2022) but also promotes sedimentation and provides a habitat to fish (Neumeier, 2007). They have thus high environmental and economic value (Liu et al., 2017). In addition, aquatic canopies can also provide resistance by raising the local water levels in rivers and reducing the flow velocity. Therefore, investigating the turbulence structure in water bodies under the influence of vegetation canopy can help further the understanding of pollutant and sediment transport (Nepf, 2011; Park and Hwang, 2019; Zhang et al., 2019; Abdolahpour et al., 2020). It can also shed light on the water transport and flooding capacity of the river, which has important implications for ecological restoration projects (Waycott et al., 2009).

Scholars have shown that turbulence generated by vegetation canopy enhances its nutrient uptake (Hu et al., 2018; Tang et al., 2021). It also promotes sediment resuspension and transport of nudged material by increasing the turbulent diffusion coefficient within the vegetation canopy (Morris et al., 2008) and changes the distribution characteristics, as well as the transport patterns of suspended sediments, along the vertical direction (López and García, 1998; Vargas-Luna et al., 2015; Tinoco and Coco, 2016; Huai et al., 2021). In recent years (Liu et al., 2022), some studies have shown that as compared to bed shear stress, turbulent kinetic energy can be used to better predict sediment initiation, nudge mass transport, and reveal sediment resuspension characteristics in areas where aquatic vegetation canopy is distributed in the river (Yang et al., 2016; Yang and Nepf, 2019). These studies highlight the importance of studying turbulence generated by the vegetation canopy to protect ecosystems and dynamic systems.

Many models were constructed recently to predict turbulent kinetic energy within the vegetation canopy (King et al., 2012; Beudin et al., 2017). For instance, Tanino and Nepf (2008b) developed a model suitable for predicting the turbulent kinetic energy in a rigid emerged cylindrical array; this model and its modified version were subsequently shown to be useful for predicting turbulent kinetic energy in submerged and emerged canopies under unidirectional flow (Tang et al., 2019; Zhang et al., 2020a; Liu et al., 2021), submerged canopies under oscillatory flow (Zhang et al., 2018), submerged canopies under combined wave-flow conditions (Chen et al., 2020), and emergent canopies with natural plant morphology (Xu and Nepf, 2020). Most of these studies used rigid materials to simulate the vegetation canopy; i.e., the canopy was assumed to not bend and deform with water flow. However, many types of natural vegetation canopy in rivers, lakes, wetlands, and coastal zones are flexible, such as seagrass meadows and kelp forests (Rominger and Nepf, 2014; Lei and Nepf, 2019). The phenomenon of flexible canopies being pushed and morphologically altered by flow is called reconfiguration (Albayrak et al., 2011; Nepf, 2012). The reconfiguration of the vegetation canopy not only helps enhance the solar energy utilization but also reduces the resistance of the vegetation canopy to the water flow by two mechanisms: reduction in the frontal area of the vegetation canopy and deflected height (Zimmerman, 2003; Li et al., 2014; Veelen et al., 2020). Li et al. (2018) reported that when the influence of the Reynolds number of the vegetation canopy is negligible, the bulk resistance coefficient establishes a logarithmic relationship with the Cauchy number of the vegetation canopy. Under the same environmental flow conditions, a flexible vegetation canopy has different effects on local hydrodynamic characteristics than a rigid vegetation canopy, and its ability to generate turbulence is different as well (Kouwen and Moghadam, 2000). Currently, most of the studies on vegetation canopy flow focus on rigid vegetation canopy, and there are fewer studies on the influence of vegetation canopy flexibility levels on turbulent kinetic energy. Consequently, there is a lack of models to predict the turbulent kinetic energy within diverse submerged vegetation canopies.

To investigate the turbulence characteristics of unidirectional flow under the influence of vegetation canopy with different flexibilities, we measured the streamwise velocity, bulk drag coefficient, and turbulent kinetic energy characteristics using strip-like submerged vegetation canopy models with different flexibilities. The effects of different vegetation canopy flexibility on the hydrodynamic characteristics were also analyzed. Finally, a model was constructed to predict the turbulent kinetic energy within the vegetation canopy with different flexibility. The results of this study can provide a basis for studies on more accurate prediction of vegetation canopy-generated turbulence. Section 2 of this paper discusses the method to calculate the drag coefficient of flexible vegetation canopy and the theory behind the model to predict turbulent energy generated by the vegetation canopy. Section 3 presents a discussion on the selection of flexible vegetation and the experimental setup. Section 4 analyzes the effects of vegetation canopy flexibility on streamwise velocity, Reynolds stress, bulk drag coefficient, and turbulent kinetic energy. Section 5 discusses the impact of vegetation flexibility on the shear layer, shear production, and wake production, and correlates the scaling factor with the Cauchy number of the vegetation canopy to develop a model for the prediction of the turbulent kinetic energy within the vegetation canopy. A brief conclusion is presented in Section 6.

2 The theoretical background of the model

The local drag coefficient, C_{dl}, varies along the vertical direction in submerged canopies with unidirectional flow. To calculate the vertical distribution of C_{dl} (Nezu and Sanjou, 2008), the following equation was derived:

$$\frac{\partial}{\partial z}\left(\langle -\overline{u'w'}\rangle\right) = 0.5C_{dl}a\langle \bar{u}\rangle^2 - gS \tag{1}$$

where $\langle\ \rangle$ characterizes spatially averaged variables (Raupach and Shaw, 1982). For the scalar parameter, ψ (e.g., velocity, pressure, etc.), its fluctuation in time, ψ', fluctuation in space, $\bar{\psi}''$, time-averaged $\bar{\psi}$, and spatially averaged $\langle\bar{\psi}\rangle$ can be expressed as $\psi = \bar{\psi} + \psi'$ and $\bar{\psi} = \langle\bar{\psi}\rangle + \bar{\psi}''$. The term $-\overline{u'w'}$ is the time-averaged Reynolds stress, and $\bar{u}$ is the time-averaged streamwise velocity; a is the vegetation frontal area per unit volume, and g is the gravitational acceleration; S is the energy slope. The bulk drag coefficient of the vegetation canopy, C_d, shows the following relationship with C_{dl}:

$$C_d = \frac{1}{U_\infty^2 h_e}\int_0^{h_e} C_{dl}\langle\bar{u}\rangle^2\, dz \tag{2}$$

where U_∞ is the average flow velocity of the incoming flow section and h_e is the time-averaged deflected height of the modeled vegetation canopy. The Reynolds number of the vegetation canopy is defined as $Re_d = u_1 b/\nu$, where b is the waterward width, u_1 is the canopy-averaged velocity, and ν is the kinematic viscosity of water. For a strip-like vegetation canopy, the reconfiguration of the vegetation canopy affected by flow is mainly reflected in the reduction of h_e, and this change impacts the size of the drag coefficient, C_d, of the bulk vegetation canopy bulk. Luhar and Nepf (2011) introduced the Cauchy number, Ca, of the vegetation canopy and the buoyancy parameter, B, to consider vegetation stiffness and buoyancy in model development. For a vegetation canopy group with the initial height of h_v, thickness of t, and density of ρ_v, under conditions of average flow velocity within the vegetation canopy of u_1, Ca and B can be written as:

$$Ca = 0.5\frac{\rho b t u_1^2 h_v^3}{EI} \tag{3}$$

$$B = \frac{(\rho - \rho_v)gbth_v^3}{EI} \tag{4}$$

where ρ is the density of water, E is the modulus of elasticity of the vegetation, and I is the moment of inertia of the cross-section, $I = bt^3/12$. When stiffness dominates the restoring force, the deflected height of the flexible vegetation reduces with an increase in Ca, decreasing the vegetation canopy bulk drag coefficient.

Upon doubling of averaging in time and space (Wilson, 1988), the turbulent kinetic energy budget equation within the vegetation canopy under conditions of steady and fully developed flow can be written as (Finnigan, 2000):

$$\frac{\partial k}{\partial t} = P_s + P_w - \langle\epsilon\rangle + T = 0 \tag{5}$$

The terms in Eq. 5 can be written as:

$$P_s = \langle -\overline{u'w'}\rangle\frac{\partial\langle\bar{u}\rangle}{\partial z} \tag{6}$$

$$P_w = \langle -\overline{u_i'u_j'}^{''}\frac{\partial\overline{u_i}^{''}}{\partial x_j}\rangle \tag{7}$$

$$T = \frac{\partial}{\partial z}\left[-\frac{\langle u_i'u_i'w'\rangle}{2} - \frac{\langle p'w'\rangle}{\rho} + \nu\overline{\langle u_i'\left(\frac{\partial u_i'}{\partial z} + \frac{\partial w'}{\partial x_i}\right)\rangle} - \frac{\langle \overline{u_i'u_i'}^{''}\bar{w}^{''}\rangle}{2}\right] \tag{8}$$

where i and j are Cartesian coordinates and k is the turbulent kinetic energy: $k = 0.5(\overline{u'}^2 + \overline{v'}^2 + \overline{w'}^2)$. When 2D-PIV is used for velocity measurement (Yang and Nepf, 2019; Tseng and Tinoco, 2020), k can be estimated by the following equation: $k = 0.5(2\overline{u'}^2 + \overline{w'}^2)$. The approximation, $\overline{u'} \approx \overline{v'}$, has been justified by previous velocity measurements (Tanino and Nepf, 2007). P_s is the shear production term for turbulent kinetic energy, P_w is its wake production term, and ϵ is the turbulent dissipation rate after spatial averaging. T is the transport term for turbulent kinetic energy, where transports due to diffusion, dispersion, pressure, and viscosity are described from left to right (Nikora et al., 2007). The P_w of turbulent kinetic energy is difficult to calculate directly; Brunet et al. (1994) assumed that the value of P_w is the same as the magnitude of turbulent energy that converts to mean flow while resisting the total vegetation canopy drag. As the total vegetation canopy drag contains both formation and viscous drag forces, and the latter drag is smaller, P_w can be simplified by neglecting the viscous drag of the vegetation canopy:

$$P_w \approx \frac{0.5C_d a\langle\bar{u}\rangle^3}{1-\phi} \tag{9}$$

where φ is the vegetation volume fraction. Tanino and Nepf (2008b) and Zhang et al. (2018) argued that T is negligible as compared to the other terms. Therefore, after spatially averaging within the vegetation canopy, Eq. 5 can be reduced to a balance between P_w of turbulent kinetic energy, its P_s, and the spatially averaged turbulent dissipation rate $\langle\epsilon\rangle$.

$$P_w + P_s - \langle\varepsilon\rangle = 0 \tag{10}$$

Tennekes and Lumley (1972) defined the characteristic eddy length scale, L_t; they showed the following relationship between the turbulent kinetic energy, k, and the turbulent dissipation rate

, $\langle \epsilon \rangle$:

$$\langle \varepsilon \rangle \sim \frac{k^{1.5}}{L_t} \tag{11}$$

A study by Tanino and Nepf (2008b) suggested that the characteristic eddy length scale, L_t, has a linear relationship with the ratio of turbulent kinetic energy and turbulent dissipation rate; therefore, a scaling factor, ξ, is introduced, producing the following:

$$L_t = \xi \frac{k^{1.5}}{\epsilon} \tag{12}$$

Averaging Eq. 12 along the depth from the top of the vegetation canopy to the bottom gives the relationship between the canopy-averaged wake production, P_{wc}, the canopy-averaged shear production, P_{sc}, the canopy-averaged characteristic eddy length scale, L_{tc}, the scaling factor, ξ, and the canopy-averaged turbulent kinetic energy, k_c, as follows:

$$k_c = \xi[(P_{sc} + P_{wc})L_{tc}]^{2/3} \tag{13}$$

Tanino and Nepf (2008b) considered that for emergent vegetation, the shear production is negligible relative to the wake production. It can thus be concluded that:

$$k_c = \xi\left[C_d u_1 \frac{a}{2(1-\varphi)} L_{tc}\right]^{2/3} \tag{14}$$

Equation 14 and its modified version have been successfully applied for the prediction of turbulent kinetic energy within the canopy (Tanino and Nepf, 2008b; Zhang et al., 2018; Tang et al., 2019; Zhang et al., 2020a; Lei and Nepf, 2021; Liu et al., 2022); C_d can be determined by different equations (Ellington, 1991; Tanino and Nepf, 2008a; Etminan et al., 2017; Xu and Nepf, 2020). For the characteristic eddy length scale, L_t, Tanino and Nepf (2008b) developed a method of calculation based on the relative magnitudes of the maximum distance between vegetation stems, S_{max}, and the vegetation diameter, d. If $S_{max} > 2d$, then $L_t = d$; if $S_{max} < 2d$, $L_t = S_{max}$. If the time-averaged streamwise velocity at each point within the vegetation canopy $\bar{u}$ is known and we assume a constant scaling factor, ξ, at any point within the vegetation canopy with the local eddy length scale, $L_t(z)$, being equal to, L_t, then the turbulent kinetic energy at any point within the vegetation canopy can be solved by the following equation:

$$\langle k(z) \rangle = \xi[(P_s(z) + P_w(z))L_t(z)]^{2/3} \tag{14}$$

3 Experimental setup

The experiments were conducted in an experimental flume in the Hydraulics Laboratory of Nanjing Hydraulic Research Institute (NHRI), China, with a length of 15 m and an effective experimental section of 12 m. The flume section was rectangular with a cross-sectional width of $W = 0.4$ m and a height of $T_w = 0.4$ m. The sides were made of transparent glass to facilitate observation of the reconfiguration of model vegetation. The upstream and downstream regions of the experimental flume were connected to the reservoir, and four invertible submersible pumps were installed in the upstream reservoir to drive water flow.

The vegetation was simulated using different materials, and its cross-section in the model was rectangular. Kouwen and Li (1980) measured the modulus of elasticity of natural vegetation and recorded distributions ranging from the order of MPa to GPa. This paper selected three materials, LDPE, polyurethane, and silicon (Jamali and Sehat, 2020). Young's modulus of the three materials ranges from 0.0018 to 3 GPa, and the densities range from 1,007 to 1,180 kg/m^3. Two thicknesses, t, of 1 and 2 mm were selected for each material, and the streamwise stiffness, EI, of the material ranged from 0.000001 to 0.0025 N·m^2. The undeflected height, h_v, of the model vegetation was 0.1 m, and the width, b, was 0.01 m. The flow spacing, L_x, and spreading spacing, L_y, between the linearly arranged model vegetation were 0.06 and 0.04 m, respectively. The vegetation density, N_v, was 425 stems/m^2. The physical parameters of the model vegetation are shown in Table 1.

A submersible pump controlled the inlet flow, which was measured using an electromagnetic flowmeter. A steel rectification grid was installed at the tank inlet to provide a smooth and uniform inlet flow. Water depth was measured by four water gauges arranged along the course. For all the

TABLE 1 Physical parameters of the model vegetation.

Material	Abbreviation	t (mm)	E (GPa)	ρ_v (kg/m^3)	I (m^4)	EI (N·m^2)
LDPE	PVC-1	1	3	1,180	8.3×10^{-13}	0.0025
LDPE	PVC-2	2	3	1,180	6.7×10^{-12}	0.02
Polyurethane	PU-1	1	0.01	1,050	8.3×10^{-13}	8.3×10^{-6}
Polyurethane	PU-2	2	0.01	1,050	6.7×10^{-12}	6.7×10^{-5}
Silicon	SC-1	1	0.0014	1,007	8.3×10^{-13}	1.2×10^{-6}
Silicon	SC-2	2	0.0014	1,007	6.7×10^{-12}	9.3×10^{-6}

experimental test conditions, the flow in the experimental layer reached a quasi-steady and uniform status. The test was configured with six planted forms (see Table 1), each with five inlet bulk flow velocities of 0.06, 0.084, 0.11, 0.14, and 0.17 m/s. The corresponding flow was 5.5, 8.4, 11.3, 14.1, and 17.0 L/s, respectively. A small uncertainty of 4% in the electromagnetic flowmeter reading was caused by the small fluctuation of pump flow. For all the experimental conditions, a constant water depth of 0.25 m was chosen to compare the effects of the different flexible vegetation on the hydrodynamics and turbulence characteristics along the vertical direction (Li et al., 2018). The *Ca* of vegetation canopy under natural environmental settings ranges from 0.001 to 1,000; in this paper, it ranged from 0.002 to 73.009 for all experimental conditions. As seen in Table 2, the buoyancy parameter, *B*, of the model vegetation under all working conditions was less than 1 because the difference between the densities of the three materials used was much smaller than the difference between their elastic moduli. It can be

TABLE 2 Vegetation and flow parameters for each test.

Test	Materials	Q (L/s)	Re_d	Ca	φ ($\times 10^3$)	B	h_e/h_v
A1-1	SC-1	5.5	379	7.687	4.25	0.687	0.86
A1-2	SC-2	5.5	281	0.836	8.5	0.172	0.87
A1-3	PU-1	5.5	271	0.573	4.25	0.453	0.9
A1-4	PU-2	5.5	268	0.07	8.5	0.113	0.93
A1-5	PVC-1	5.5	243	0.02	4.25	0.071	1
A1-6	PVC-2	5.5	216	0.002	8.5	0.018	1
B1-1	SC-1	8.4	412	21.137	4.25	0.687	0.83
B1-2	SC-2	8.4	344	2.445	8.5	0.172	0.87
B1-3	PU-1	8.4	341	1.692	4.25	0.453	0.9
B1-4	PU-2	8.4	324	0.198	8.5	0.113	0.93
B1-5	PVC-1	8.4	299	0.065	4.25	0.071	1
B1-6	PVC-2	8.4	250	0.007	8.5	0.018	1
C1-1	SC-1	11.3	551	31.277	4.25	0.687	0.73
C1-2	SC-2	11.3	522	3.788	8.5	0.172	0.81
C1-3	PU-1	11.3	503	2.642	4.25	0.453	0.83
C1-4	PU-2	11.3	463	0.304	8.5	0.113	0.85
C1-5	PVC-1	11.3	369	0.103	4.25	0.071	1
C1-6	PVC-2	11.3	310	0.012	8.5	0.018	1
D1-1	SC-1	14.1	741	50.144	4.25	0.687	0.68
D1-2	SC-2	14.1	681	5.854	8.5	0.172	0.74
D1-3	PU-1	14.1	641	3.705	4.25	0.453	0.8
D1-4	PU-2	14.1	574	0.421	8.5	0.113	0.83
D1-5	PVC-1	14.1	486	0.121	4.25	0.071	1
D1-6	PVC-2	14.1	376	0.013	8.5	0.018	1
E1-1	SC-1	17.0	838	73.009	4.25	0.687	0.65
E1-2	SC-2	17.0	777	8.711	8.5	0.172	0.69
E1-3	PU-1	17.0	751	6.226	4.25	0.453	0.77
E1-4	PU-2	17.0	743	0.725	8.5	0.113	0.85
E1-5	PVC-1	17.0	611	0.242	4.25	0.071	1
E1-6	PVC-2	17.0	507	0.03	8.5	0.018	1

assumed that the vegetation stiffness dominated the restorative force relative to the buoyancy experienced by the vegetation in the experiments (Zhang et al., 2020b). Therefore, the effect of the buoyancy of the vegetation on the deflected height of the vegetation, h_e, is not considered in this study.

Two-dimensional particle image velocimetry (2D-PIV) was used to measure the flow field in the longitudinal profile (x–z plane), and a sheet laser emitter was mounted below the bottom wall of the unidirectional flume with a maximum laser power of 10 W. The sheet laser illuminated the flow vertically from the bottom, parallel to the side wall of the unidirectional flume, with a thickness of 1.5 mm. A high-speed camera (MindVision, MV-XG4701C/M/T) was mounted on the side of the unidirectional flume and aligned vertically with the sheet laser. The camera had a maximum effective pixel count of 47 million and a maximum resolution of 8,240 × 5,628. The exposure time was set to 120 µs, considering the image contrast and particle trailing. Due to the computer hardware configuration, the camera's low frame rate at the highest pixel, and the transmission speed, the camera could operate only in the low pixel-high frame rate mode; therefore, after testing and comparison, 6,600 snapshots were taken for each condition with an image size of 1,280 × 960 pixels and a sampling frequency of 333 Hz. After testing and selection, polyamide resin particles (PSP) with a diameter of 10 µm, a density of ~1.03 g/cm^3, and a refractive index of 1.2 were used as tracers. Referring to a study by Okamoto et al. (2016), we positioned the irradiating sheet laser on the side of the model canopies as detailed in Figure 1. The FOV was located at the end of the vegetation patch to ensure that the flow was fully developed (Lei and Nepf, 2021). PIVlab was used to acquire the snapshots for processing (Thielicke and Stamhuis, 2014). After removing the background, the snapshots were preprocessed using a contrast-constrained adaptive histogram equalization technique. The intensity capping technique was used to minimize the error. The PIV snapshot pairs were analyzed using the FFT-based multi-pass algorithm with multiple grid iteration methods using an interrogation window size of 40 × 40, a minimum first-level window size of 20 × 20, and a 50% spatial overlap in both directions. The Gauss 2 × 3-point method was used for the sub-pixel estimator, providing a vector grid spacing of Δx = 2.13 mm and Δz = 2.13 mm. The initial flow vector field was subsequently post-processed to remove and replace bad vectors by using standard deviations and median filters with predefined thresholds. The flow field timing file consisting of all snapshots was saved in.dat format, and the turbulence statistical variables were computed by a post-processing program written in Python. We fixed the camera outside the glass window of the flume with the lens facing perpendicular to the center of the slice laser. During each sampling period, the motion of the model vegetation under the sheet laser irradiation was recorded by the camera. The camera sampling time was 2 min for each sampling. Time-averaged deflected height of the model vegetation canopy was obtained by analyzing the motion sequence with computer vision software.

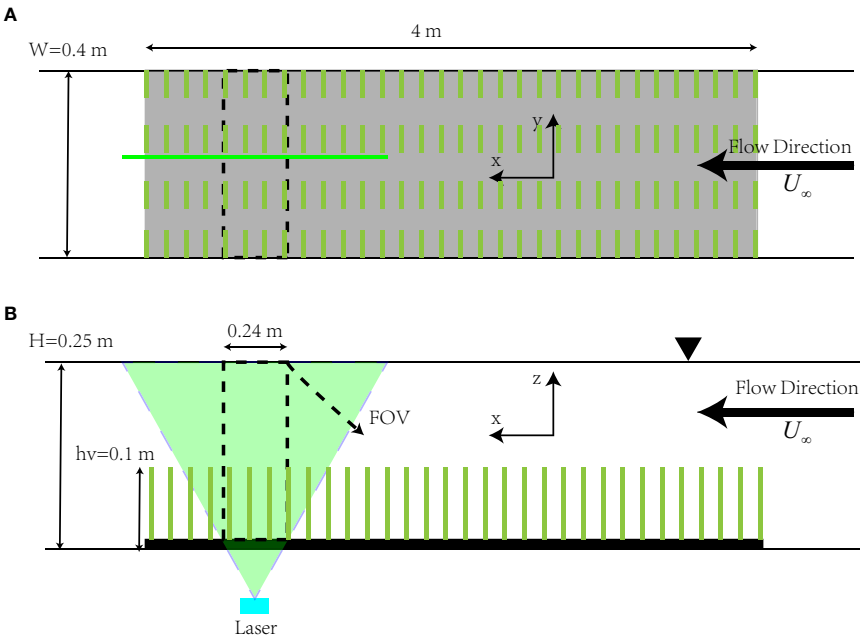

FIGURE 1
Views of the experimental section (not to scale), where the black dashed line in the figure is the PIV acquisition area (FOV): **(A)** top view; **(B)** side view.

4 Results

4.1 Velocity

Figure 2 shows the distribution of dimensionless time-average streamwise velocity, $\bar{u}/U_\infty$, and dimensionless double-averaged streamwise velocities, $\langle\bar{u}\rangle/U_\infty$, under different tests. The vertical coordinate, z, was dimensionless with respect to the undeflected height of vegetation, h_v, where $z/h_v = 0$ corresponds to the bed; $z/h_v = 1$ corresponds to the undeflected height of the vegetation position (green dashed line), and $z/h_v = 2.5$ corresponds to the free surface. As compared with the rigid vegetation, reconfiguration of the flexible vegetation stems significantly reduces the turbulence around the canopy top, leading to a flatter mean shear. It also reduces the local velocity gradient. At the same time, the "Monami" phenomenon of flexible vegetation greatly promotes the efficiency of momentum transmission from outside the canopy to the inside of it. Therefore, under the same flow rate, the canopy-averaged velocity for flexible vegetation is higher than that for rigid vegetation. As can be seen in Figures 2C, D, the $\langle\bar{u}\rangle/U_\infty$ trend for both rigid and flexible submerged vegetation showed an inverted "S" shape distribution along the vertical direction. From the bed, along the vertical direction, $\langle\bar{u}\rangle/U_\infty$ gradually increased; the velocity variation near the bed was small, and the velocity gradient, $\mathrm{d}(\langle\bar{u}\rangle/U_\infty)/\mathrm{dz}$, near the top of the vegetation canopy was larger. There was an obvious shear point around the vegetation canopy top as $\langle\bar{u}\rangle/U_\infty$ reached its maximum value at a certain distance below the free surface and then maintained this value until the free surface. For the same vegetation volume, as the vegetation thickness t increased, its volume fraction, φ, increased accordingly. The submerged vegetation had a greater ability to block the flow; therefore, $\langle\bar{u}\rangle/U_\infty$ within the vegetation canopy decreased and increased outside of it, while $\mathrm{d}(\langle\bar{u}\rangle/U_\infty)/\mathrm{dz}$ near the top of the vegetation canopy also increased. When comparing PVC-1 with PU-2 (tests A1-5 with A1-4 or tests E1-5 with E1-4), the model vegetation corresponding to PU-2 presented a higher vegetation volume fraction, φ, due to lower modulus of elasticity, but the model vegetation underwent reconfiguration under the

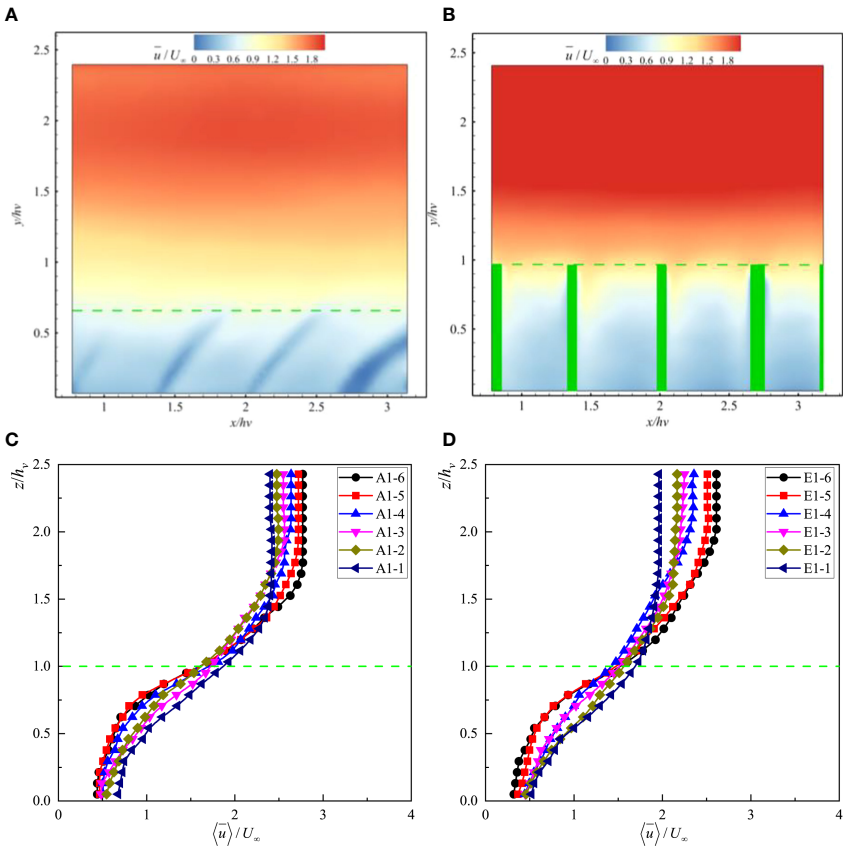

FIGURE 2
Distribution of the dimensionless time-averaged streamwise velocity $\langle\bar{u}\rangle/U_\infty$ under **(A)** E1-1 and **(B)** E1-5 and the distribution of the dimensionless double averaged streamwise velocity $\langle\bar{u}\rangle/U_\infty$ under **(C)** Test A and **(D)** Test E.

flow due to which its deflected height ratio, h_e/h_v, decreased, thus making PU-2 less capable of blocking flow than PVC-1. A similar phenomenon was observed upon a comparison of PU-1 with SC-2. As the Reynolds number, Re_d, of the vegetation canopy increased, the vertical distribution of the dimensionless velocity, $\langle\bar{u}\rangle/U_\infty$, did not change significantly for rigid submerged vegetation. Contrarily, the distribution of $\langle\bar{u}\rangle/U_\infty$ along the vertical direction presented a decrease in $h_e/h_v$for flexible submerged vegetation. The opposing trends of $\langle\bar{u}\rangle/U_\infty$ and d($\langle\bar{u}\rangle/U_\infty$)/dz with h_e/h_v above and within the vegetation canopy were particularly evident in modeled submerged vegetation with very low modulus of elasticity, such as SC-1. We found that in the test E1-1, the h_e/h_v was reduced to 0.63, while the "Monami" phenomenon occurred with a large oscillation, which greatly facilitated the transfer of first- and second-order momentum from the area outside the vegetation canopy to the area inside the vegetation canopy by bidirectional fluid–structure interaction. This also led to the distribution of $\langle\bar{u}\rangle/U_\infty$ along the vertical direction being different from the other test conditions, but it was similar to the distribution for test V3-9 in a study by Li et al. (2018). Overall, when the vegetation volume fraction was the same, $\langle\bar{u}\rangle/U_\infty$ and d($\langle\bar{u}\rangle/U_\infty$)/dz increased as h_e/h_v decreased within the vegetation canopy; they decreased as h_e/h_v decreased outside the vegetation canopy. These patterns suggest that the reconfiguration of flexible submerged vegetation affects the efficiency of momentum transfer along the vertical direction and also reduces the ability of the vegetation to block water flow.

4.2 Reynolds stress

Figure 3 shows the distribution of dimensionless time-average Reynolds stresses $-\overline{u'w'}/U_\infty^2$ and the dimensionless

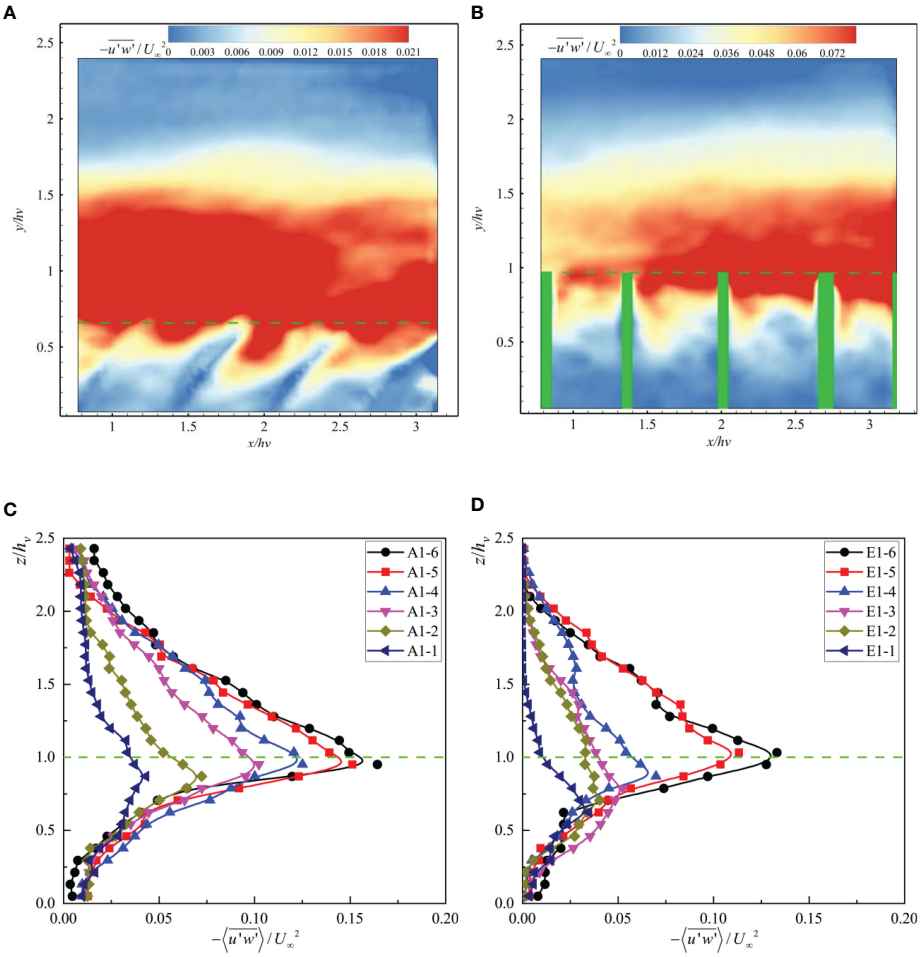

FIGURE 3
Distribution of the dimensionless time-averaged Reynolds stress $-\langle\overline{u'w'}\rangle/U_\infty^2$ under **(A)** E1-1 and **(B)** E1-5 and the distribution of the dimensionless double-averaged Reynolds stress $-\langle\overline{u'w'}\rangle/U_\infty^2$ under **(C)** Test A and **(D)** Test E.

space-time averaged Reynolds stresses $-\langle\overline{u'w'}\rangle/U_\infty^2$ under different tests. It can be seen from the figure that the reconfiguration (bending and streamlining) of flexible vegetation is more conducive to the transfer of turbulent energy from the outside of the canopy to its inside for rigid vegetation, which significantly reduces the peak $-\overline{u'w'}/U_\infty^2$ near the canopy top. Therefore, the coherent structure of turbulence can be more readily extended to the deeper part of the canopy in the flexible vegetation compared to the rigid vegetation (Li et al., 2018). It can be seen from Figures 3C, D that the Reynolds stress, $-\langle\overline{u'w'}\rangle/U_\infty^2$, gradually increased from the free surface vertically, reaching a maximum value near the top of the vegetation canopy. It then decreased rapidly along the vertical direction and remained constant near the bed. A similar pattern was presented by $\langle\bar{u}\rangle/U_\infty$, for the same vegetation material, whereby with an increase in vegetation thickness, t, the vegetation fraction, φ, increased. The blockage effect of the vegetation canopy was also more substantial; therefore, $-\langle\overline{u'w'}\rangle/U_\infty^2$ and its maximum value also increased along the vertical direction. When the vegetation fraction, φ, was the same, with a gradual decrease in h_e/h_v, the peak value of Reynolds stress near the top of the vegetation canopy gradually decreased. The position, where the Reynolds stress reached a minimum outside the vegetation canopy, was closer to the top of the vegetation canopy, while the position where it reached the minimum value within the vegetation canopy was closer to the bed; i.e., the vertical distribution of $-\langle\overline{u'w'}\rangle/U_\infty^2$ was closer to that without submerged vegetation (Dijkstra and Uittenbogaard, 2010). The double-averaged Reynolds stress distribution within the vegetation canopy of the flexible submerged vegetation was more uniform than that of the rigid submerged vegetation, indicating that the flexible submerged vegetation transfers a part of the turbulent energy from the outside of the vegetation canopy to its inside through reconfiguration.

As can be seen in Figure 3, the Reynolds stress decreased rapidly in the vertical direction after entering the vegetation canopy due to the blockage effect of vegetation stems hindering the efficiency of momentum transfer from the outside to the inside of the vegetation canopy. Many scholars have also observed this phenomenon in experiments. Nepf and Vivoni (2000) equated the measurement of the exchange momentum region inside and outside the vegetation canopy with the distance that the Reynolds stress, $-\langle\overline{u'w'}\rangle$, penetrates through the vegetation canopy; they proposed the penetration depth of the Reynolds stress, δ_e, which is defined as the distance required to reduce the Reynolds stress from the maximum near the top of the vegetation canopy to a value that is 10% of the maximum. The relationships between the dimensionless penetration depth, δ_e/h_e, and the Reynolds number of the vegetation canopy, Re_d, under different test conditions are given in Figure 4, where the uncertainty caused by this spatial change was 6%. For the same vegetation material, the larger the vegetation fraction, the greater the vegetation resistance within the canopy. It was also more difficult for the Reynolds stress caused by KH instability vortex and shear near the top of the vegetation canopy to penetrate the whole vegetation canopy, and thus, the dimensionless penetration depth, δ_e/h_e, was smaller. Due to the reconfiguration, swaying, and the "Monami" phenomenon of flexible submerged vegetation, the bulk resistance within the vegetation canopy was smaller, making it easier for the shear vortex to penetrate the whole vegetation canopy (Okamoto and Nezu, 2010). In contrast, rigid submerged vegetation is expected to be more effective in destroying the coherent eddy structure near the top of the vegetation canopy than the flexible submerged vegetation, thus reducing the penetration capacity of Reynolds stress. Overall, the dimensionless penetration depth, δ_e/h_e, increases with increasing Re_d, while δ_e/h_e increases with increasing Ca for the same Re_d.

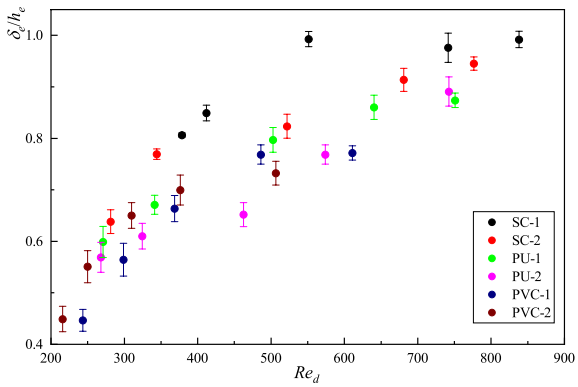

FIGURE 4
The relationship between dimensionless penetration depth, δ_e/h_e, and vegetation canopy Reynolds number, Re_d, under different test conditions.

4.3 Drag coefficient

Figures 5A, B show the vertical distribution characteristics of the local drag coefficient, C_{dl}, calculated by Eq. 1 under different test conditions. At the position near the bed, due to the influence of wake and resistance of vegetation stems, the vertical flow velocity was almost constant, and the Reynolds stress gradient in this area was also small. Therefore, the change in C_{dl} in this area was relatively small, which is similar to the local drag coefficient distribution of emergent vegetation (Nepf and Vivoni, 2000). In the area near the top of the vegetation canopy, C_{dl} decreased rapidly with an increase in z/h_v. Similar phenomena were observed by Li et al. (2018) and Tang et al. (2014), especially when the relative submergence was large. This phenomenon may be caused by the relaxation of the shape resistance caused by the bleeding behavior of the flow near the top of the model vegetation leaves (Ghisalberti and Nepf, 2006). With the same vegetation material, the local drag coefficient, C_{dl}, along the vertical direction increased as φ increased. As the modulus of elasticity of the vegetation decreased, the vegetation began to undergo reconfiguration, h_e/h_v decreased, and the maximum value of C_{dl} along the vertical direction decreased. For rigid submerged vegetation, the position, where the maximum value of C_{dl} appeared consistently, was located near z/h_e = 0.8. For flexible vegetation with a small elastic modulus, such as SC-1, when the bulk flow was large and the hydrodynamic force on the vegetation was far greater than the restorative force caused by the stiffness, the vegetation underwent strong reconfiguration; in such a case, the position, where the maximum value of C_{dl} appeared, decreased to h_e/h_v= 0.54. Under all working conditions, the position of the maximum value of C_{dl} along the vertical direction was between $0.7h_e$ and $0.8h_e$, which is consistent with the studies of Tang et al. (2014) and Ghisalberti and Nepf (2004b). For the same z/h_e position, with a gradual decrease in h_e/h_v, the local drag coefficient, C_{dl}, also gradually decreased, indicating that the reconfiguration of vegetation reduced the blockage of vegetation within the canopy.

The bulk drag coefficient, C_d, can be obtained by averaging the bulk drag coefficient, C_{dl}, within the deflected height, h_e, of the vegetation. Figures 5C, D, respectively, show the relationship between the bulk drag coefficient, C_d, Re_d, and Ca under different test conditions. With an increase in Re_d, C_d gradually decreased.

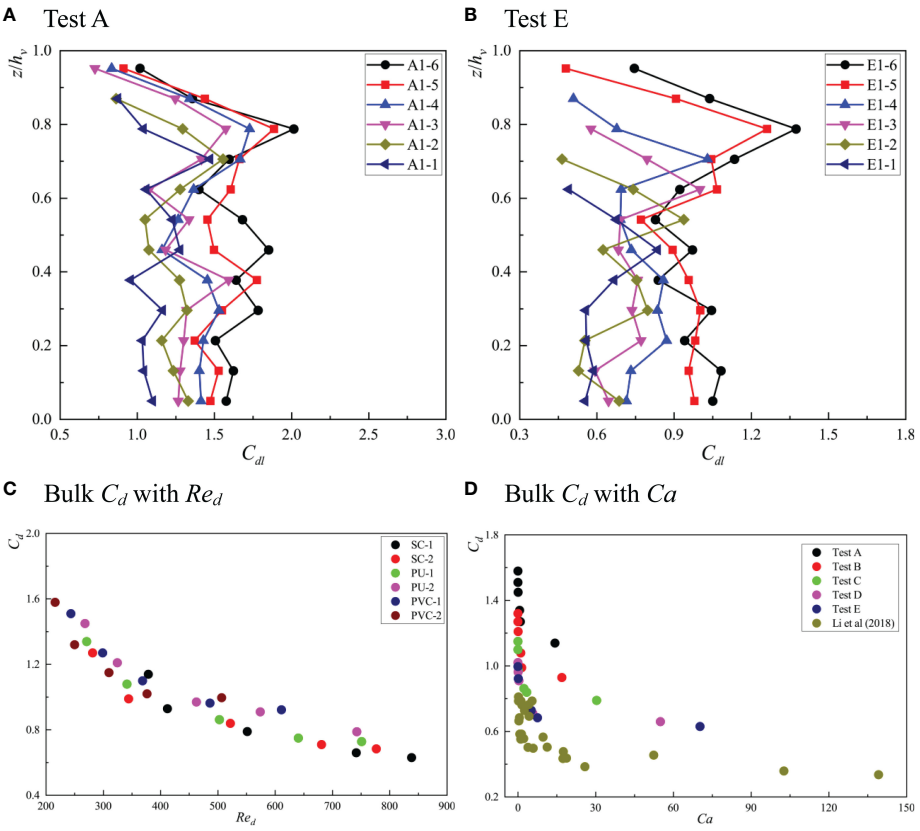

FIGURE 5
The vertical distribution of local drag coefficient, C_{dl} under **(A)** Test A and **(B)** Test E and the relationship between C_d and Re_d **(C)** and between C_d and Ca **(D)**.

When Re_d increased to 700, C_d tended to gradually stabilize. At the same time, with the same Re_d, C_d decreased with an increase in Ca. It can also be seen from the figure that there was a regular exponential relationship between the bulk drag coefficient and the Cauchy number of the vegetation canopy. In addition, C_d was positively correlated with φ, which is consistent with the report of Li et al. (2018), indicating that it is feasible to predict the bulk drag coefficient using Ca. Luhar and Nepf (2011) proposed a scaling law to correlate the effective length, drag force, and $Ca^{-1/3}$ based on the force balance between resistance and the restorative force caused by stem stiffness. Based on the above description and other relevant research (Sonnenwald et al., 2018), we believe that the relationship between the bulk drag coefficient, C_d, the Reynolds number of the canopy, Re_d, the Cauchy number of the canopy, Ca, and the vegetation fraction, φ, can be described by the following formula:

$$C_d = \frac{a1}{Re_d} + a2Ca^{-1/3} + a3\varphi + a4 \tag{15}$$

Among these, $a1$–$a4$ are the coefficients to be determined. The general global optimization method and quasi-Newton method were used to conduct nonlinear regression analyses on the relationship between C_d, Re_d, Ca, and φ, and finally, the fitting Eq. 16 was obtained:

$$C_d = \frac{238}{Re_d} + 0.01Ca^{-1/3} + 6.2\varphi + 0.38 \tag{16}$$

From Eq. 16, it can be seen that C_d was negatively correlated to Re_d and Ca, but positively correlated to φ, which is consistent with a previous study (Liu et al., 2020). In addition, Figure 6 shows a comparison between the predicted value of the bulk drag coefficient, C_d, and the measured value. It can be seen that the data were distributed on both sides of the perfect agreement line, and the determination coefficient, R^2, was 0.858. Therefore, in the turbulent kinetic energy model (TKE model) within the vegetation canopy, the determination of the bulk drag coefficient adopted Eq. 16.

4.4 Turbulent kinetic energy

The turbulent kinetic energy characterizes the degree of local turbulence. Figures 7A, B shows the spatial distribution of k/U_∞^2 for two test conditions and Figures 7C, D presents the spatially averaged turbulent kinetic energy, k/U_∞^2 , for the different test conditions. As can be seen from the figure, the distribution of k/U_∞^2 is similar to that of $-\overline{u'w'}/U_\infty^2$. The reconfiguration of flexible vegetation enhanced the efficiency of turbulent energy transport along the vertical direction, leading to lowered k/U_∞^2 near the top of the canopy as compared to the rigid vegetation. The maximum value of $\langle k \rangle/U_\infty^2$ along the vertical direction occurred near the top of the vegetation canopy and gradually decreased along the free surface and the bed. The average vertical gradient of turbulent kinetic energy, $d\langle k \rangle/U_\infty^2/dz$, in the area within the vegetation canopy was greater than the average vertical gradient in the area outside the vegetation canopy. For the same vegetation material, the spatially averaged turbulent kinetic energy, $\langle k \rangle/U_\infty^2$, along the vertical direction increased with an increase in φ. Overall, when the vegetation fraction, φ, was the same, the turbulent kinetic energy along the water depth gradually decreased with a gradual decrease in h_e/h_v. At the same time, with a decrease in h_e/h_v, the location of the maximum $\langle k \rangle /U_\infty^2$ also decreased. In general, the reconfiguration of vegetation reduced the turbulence under unidirectional flow.

The canopy-averaged turbulent kinetic energy, k_c, can be obtained by averaging the spatially averaged turbulent kinetic energy, $\langle k \rangle$, within the deflected height, h_e, of the vegetation. Figure 8 shows the relationship between the canopy-averaged

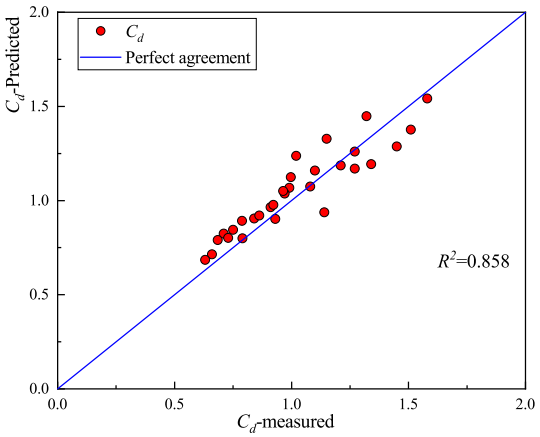

FIGURE 6
A comparison of the predicted and measured values of bulk drag coefficient, C_d, under different test conditions.

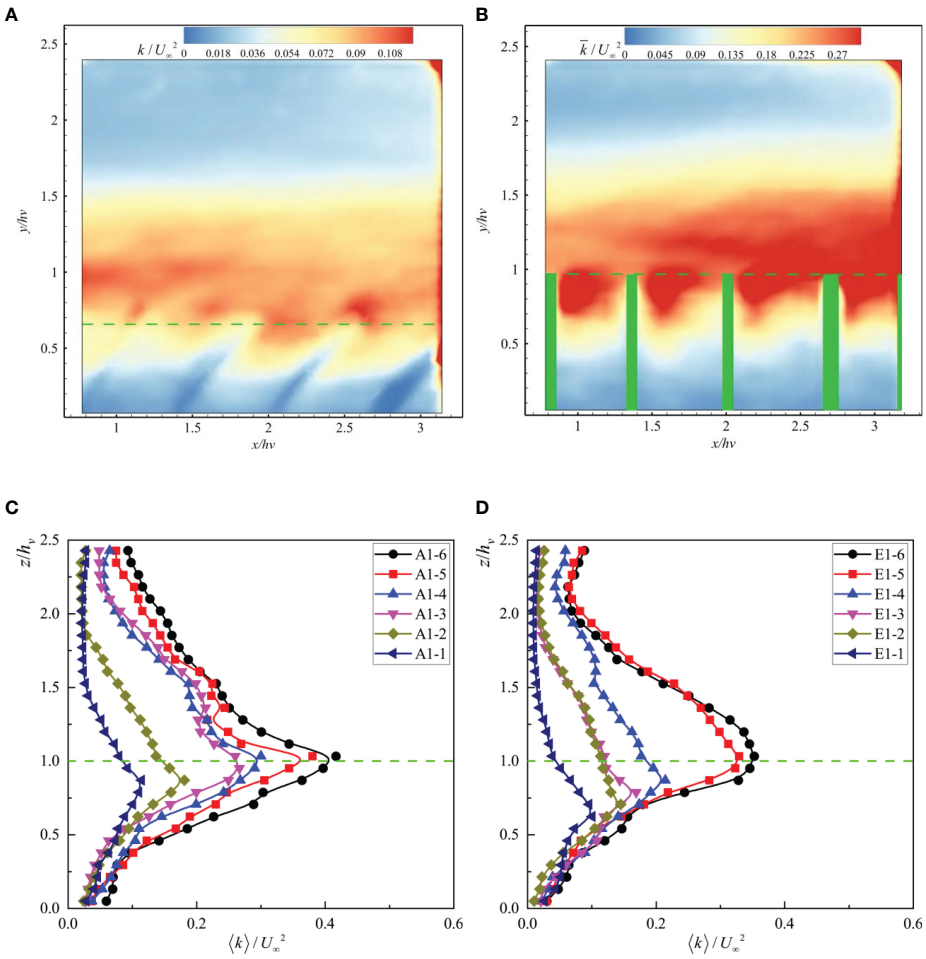

FIGURE 7
The distribution of dimensionless time-averaged turbulent kinetic energy k/U_∞^2 under **(A)** E1-1 and **(B)** E1-5 and the dimensionless double-averaged turbulent kinetic energy, $\langle k\rangle/U_\infty^2$, under **(C)** Test A and **(D)** Test E.

turbulent kinetic energy, k_c/U_∞^2, with the Cauchy number of the vegetation canopy, *Ca*, under different test conditions. Due to the reconfiguration of the flexible submerged vegetation, h_e/h_v decreased, making the blocking effect of the flexible submerged vegetation lower than that of the rigid submerged vegetation. Therefore, k_c/U_∞^2 decreased with an increase in the canopy Cauchy number, *Ca*.

5 Discussion

5.1 The characteristics of the shear layer

To study the influence of vegetation flexibility on the structure of vegetation around the canopy top (Bailey and Stoll, 2016), we calculated the time-averaged vorticity under four conditions; the results of these test conditions are compiled in Figure 9. It can be seen from the figure that there is a peak value of $\overline{\omega_y}$ near the canopy top, and the overall distribution is similar to k/U_∞^2 and $-\overline{u'w'}/U_\infty^2$. In the case of rigid vegetation, the maximum $\overline{\omega_y}$ near the canopy top and the area affected by high vortices were larger than those recorded for flexible vegetation, indicating that the average shear near the top of rigid vegetation canopy is stronger (Nezu and Sanjou, 2008). This phenomenon could be attributed to the fact that with an increase in Re_d, the stems of flexible vegetation begin to wave and h_e/h_v decreases accordingly, leading to less blockage compared to rigid vegetation. Therefore, the intensity of the coherent structure caused by Kelvin–Helmholtz instability and the range of its influence are also weaker than those for rigid vegetation (Li et al., 2018). This phenomenon can also be explained by the relationship between the dimensionless velocity difference, the dimensionless mixing layer thickness, and the Cauchy number of the canopy.

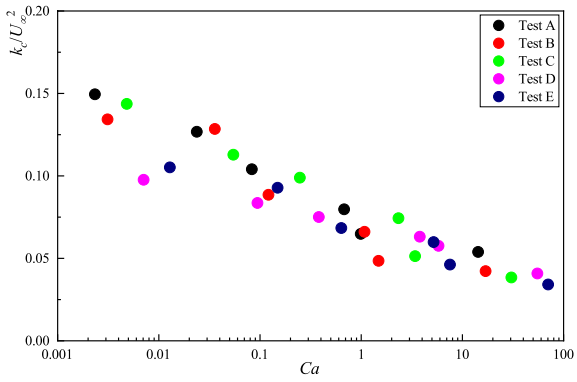

FIGURE 8
The relationship between canopy-averaged turbulent kinetic energy, k_c/U_∞^2, and the Cauchy number of the vegetation canopy, *Ca*.

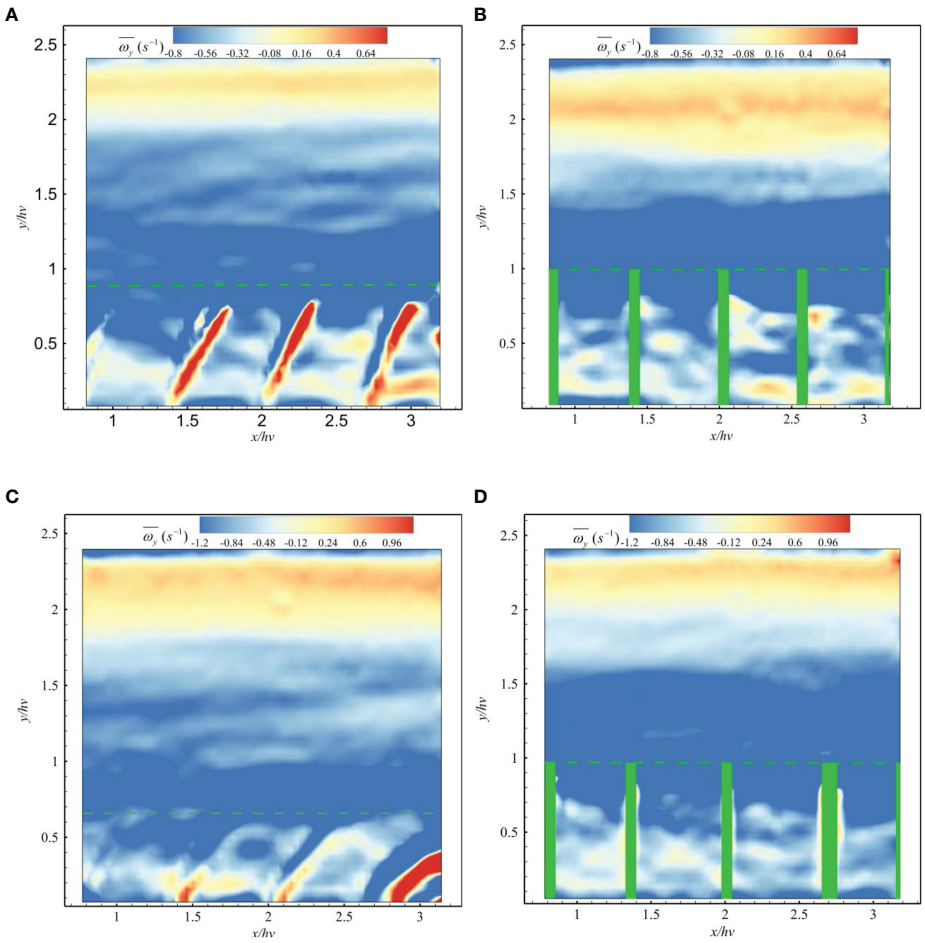

FIGURE 9
The distribution of the time-averaged vorticity $\overline{\omega_y}$ under **(A)** A1-1, **(B)** A1-5, **(C)** E1-1, and **(D)** E1-5.

Figure 10A presents the relationship between the dimensionless velocity difference, $\Delta u/U_\infty$, between the interior and exterior of the vegetation canopy, as well as the Ca for different test conditions; here, the x-axis is in log scale because the uncertainty caused by spatial change is 3%. For the same vegetation material and U_∞, $\Delta u/U_\infty$ increased with φ and gradually decreased with Ca. As Re_d increased, $\Delta u/U_\infty$ changed less for the rigid submerged vegetation, while it decreased with an increase in Re_d for the flexible submerged vegetation. This phenomenon is attributed to the increase in Re_d causing a gradual decrease in the h_e/h_v of the flexible submerged vegetation; it is also associated with the profile of $\bar{u}/U_\infty$ along the vertical direction tending to be more similar to the distribution seen with the classical unidirectional flow. Figure 10B depicts the relationship between the dimensionless mixed layer thickness, T_{ml}/H, and the Reynolds number, Re_d, of the vegetation canopy. Here, T_{ml}/H is defined as the distance between $z_{0.9}$ and $z_{0.1}$, where $z_{0.1}$ corresponds to the height of U_1 +0.1ΔU and $z_{0.9}$ corresponds to the height of U_1+0.9ΔU; the definitions of U_1 and ΔU can be found in Ghisalberti and Nepf (2004a). The uncertainty caused by this spatial change was 5%. T_{ml}/H increased with increasing Re_d in both rigid and flexible submerged vegetation within the error range. The increase in T_{ml}/H with increasing Re_d was lower for flexible submerged vegetation than for rigid submerged vegetation. For the former, h_e/h_v gradually decreased with increasing Re_d, resulting in a smaller increase in the strength and extent of the influence of coherent eddies near the top of the vegetation canopy. Overall, the dimensionless mixed layer thickness, T_{ml}/H, was positively correlated with Re_d and negatively correlated with Ca.

5.2 Shear and wake production terms

The elevated turbulent kinetic energy within the canopies under unidirectional flow can be attributed to two aspects. Firstly, turbulence can be generated in the wake area behind the vegetation stems. Secondly, the shear eddies caused by Kelvin–Helmholtz instability can occur near the top of the vegetation canopy, thus causing an increase in turbulent kinetic energy. Figure 11 shows the distribution of the shear production term, P_s, the wake production term, P_w, and the total production terms of turbulent kinetic energy, P_t, along the vertical direction under different test conditions; P_s was estimated using Eq. 2 and P_w was estimated by Eq. 5. As the wake production is only generated behind the vegetation stems, the calculation range is within the vegetation canopy, and P_t is the sum of the first two terms. As can be seen from the figure, P_s reached a maximum value at the top of the vegetation canopy due to the largest velocity gradient in this region, which is consistent with studies by Devi and Kumar (2016) and Termini (2019). P_s decreased rapidly as it entered the vegetation canopy and tended to become zero near the bed due to the blocking effect of the vegetation canopy. P_w reached a maximum value near the top of the vegetation canopy, while, upon entering it, local P_w was always greater than P_s. For the same flow rate, P_s, P_w, and P_t were greater for rigid submerged vegetation than for flexible submerged vegetation along the vertical direction, suggesting that a reduction in h_e/h_v significantly reduces the degree of turbulence within the vegetation canopy.

To compare the average contribution of the shear production term, P_s, to the turbulent kinetic energy within the vegetation canopy, we defined $R_{s/t}$ as follows:

$$R_{s/t} = \frac{100}{h_e}\int_0^{h_e}(P_s/P_t)dz \tag{17}$$

A larger value of $R_{s/t}$ indicates a larger ratio of the shear production term, P_s, to the total production term, P_t. Figure 12 shows the relationships between the vegetation canopy-averaged contribution of shear production term, $R_{s/t}$, and Ca under different test conditions.

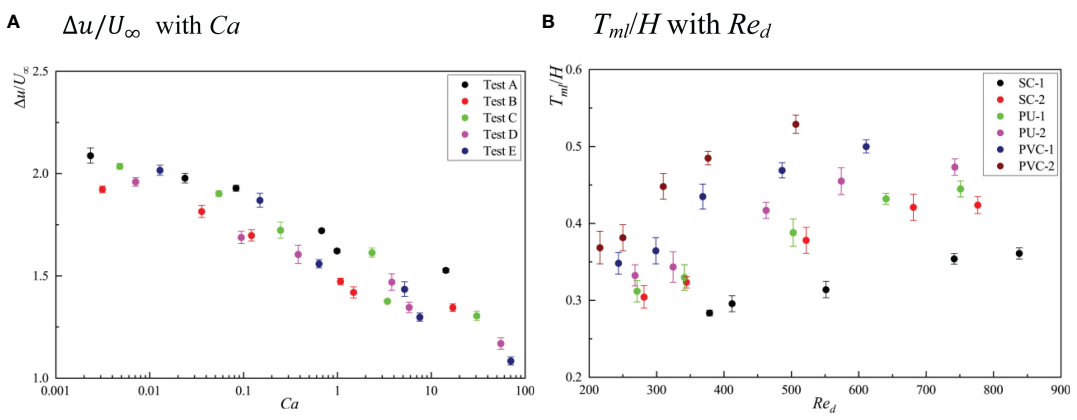

FIGURE 10
Relationships of $\Delta u/U_\infty$ and T_{ml}/H with Ca **(A)** and Re_d **(B)**.

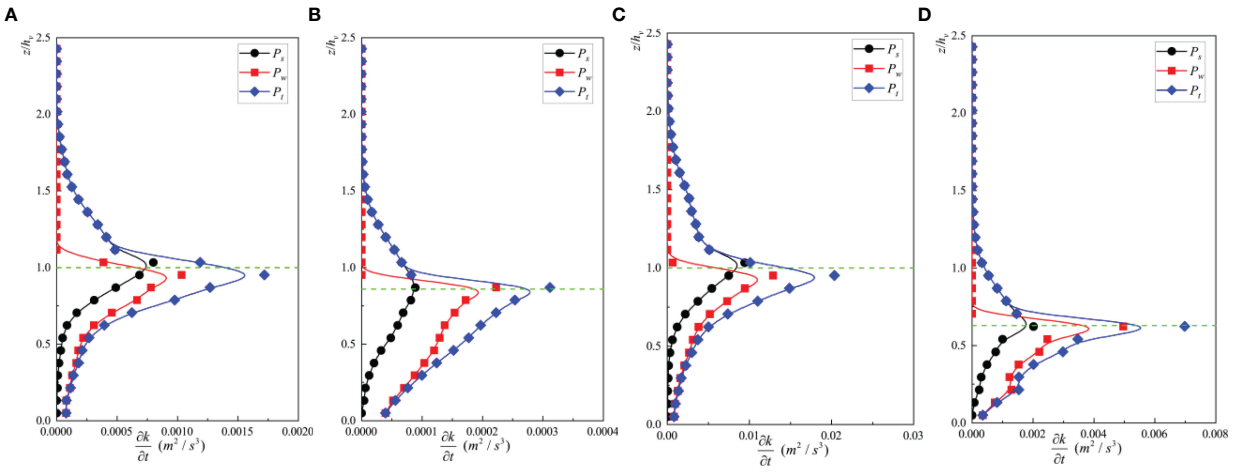

FIGURE 11
Vertical distributions of the shear production term, P_s, the wake production term, P_w, and the total production term, P_t, of turbulent kinetic energy under **(A)** A1-5, **(B)** A1-1, **(C)** E1-5, and **(D)** E1-1.

Figure 10 depicts that with an increase in *Ca*, the $R_{s/t}$ gradually decreased.

The shear production of turbulent kinetic energy is mainly controlled by the large-scale coherent structure near the canopy top induced by the Kelvin–Helmholtz instability (Ghisalberti and Nepf, 2001). As compared to rigid vegetation, flexible vegetation reduces P_s through two mechanisms. First, h_e/h_v gradually decreases with an increase in *Ca*, weakening the blockage effect and reducing the relative coherent structure strength near the canopy top (see *Section 5.1*). Second, the "Monami" phenomenon of flexible vegetation enhances the vertical transportation of turbulent energy, which may transport more turbulent energy to the interior of the canopy than the rigid vegetation, thus reducing P_s. The results from a study by Zhang et al. (2020a) demonstrated that the mean P_s within the vegetation canopy increased with $a{\cdot}h_e$, while P_w decreased with $a{\cdot}h_e$. In addition, the value of $R_{s/T}$ gradually increases and converges to 50% as $a{\cdot}h_e$ increases. Corresponding to the present experiment, for constant flow rate, as *Ca* increases, h_e gradually decreases, corresponding to $a{\cdot}h_e$, which also gradually decreases, so that $R_{s/T}$ decreases with increasing *Ca*. In addition, under all test conditions investigated here, $R_{s/t}$ ranged between 24% and 48%, indicating that the importance of shear production should not be ignored.

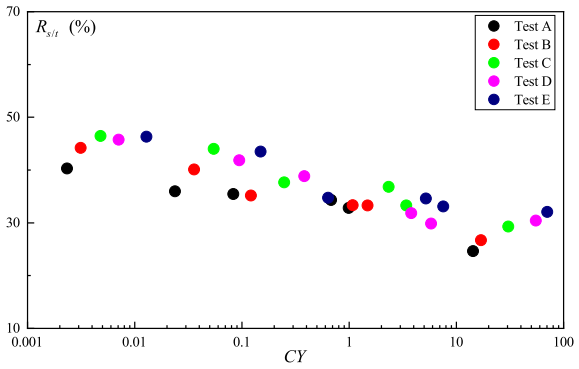

FIGURE 12
The relationship between $R_{s/t}$ and the Cauchy number *Ca*.

5.3 Prediction of turbulent kinetic energy within the vegetation canopy

To apply the TKE model, we first built alternative models for P_s, considering that it is relatively difficult to obtain. Chen et al. (2013) proposed that when the relative submergence is greater than 2, L_s can be estimated by Eq. 18:

$$L_s = \frac{\bar{u}_{h_e}}{\partial \bar{u}_{h_e} / \partial z} = \frac{0.4}{C_d a} \tag{18}$$

Ghisalberti (2009) found that the difference between the time-averaged velocity, $\overline{u_{h_e}}$, at the top of the vegetation canopy and vegetation canopy-averaged velocity, u_1, had a linear relationship with the friction velocity, u_*, which is:

$$\bar{u}_{h_e} - u_1 \approx 2.6 u_* \tag{19}$$

Substituting Eq. 19 into Eq. 18 gives:

$$\frac{\partial \bar{u}_{h_e}}{\partial z} = \frac{\bar{u}_{h_e}}{L_s} = \frac{C_d \cdot a \cdot \bar{u}_{h_e}}{0.4} = \frac{\left[2.6 u_* + u_1\right] + C_d \cdot a}{0.4} \tag{20}$$

The Reynolds stress at the top of the vegetation canopy, $-\overline{u'w'}_{h_e}$, can be calculated by the following equation (Chen et al., 2013):

$$-\overline{u'w'}_{h_e} = u_*^2 = C(u_2 - u_1) \tag{21}$$

where u_2 is the averaged velocity outside the vegetation canopy, and C is an empirical fitting factor characterizing this Reynolds stress. It can be calculated by the following equation:

$$C = K_c \left(\frac{h_p}{H}\right)^{1/3} \tag{22}$$

where K_c is an empirical coefficient with values ranging from 0.04 to 0.11. In this study, K_c was assumed to be 0.075. The penetration depth of Reynolds stress, δ_e, can be calculated by the following equation:

$$h_p = \min\left(\frac{0.23}{C_d \cdot a}, H - h_e, h_e\right) \tag{23}$$

Substituting Eq. 21 into Eq. 20 gives:

$$\frac{\partial \bar{u}_{h_e}}{\partial z} = \frac{\left[2.6\sqrt{C(u_2 - u_1)} + u_1\right] C_d \cdot a}{0.4} \tag{24}$$

Combining Eq. 24 and Eq. 21 gives the vegetation canopy-averaged shear production term, P_{sh}:

$$P_{sh} = -\overline{u'w'}_{h_e} \frac{\partial \bar{u}_{h_e}}{\partial z} = \frac{\left[2.6\sqrt{C(u_2 - u_1)} + u_1\right] C_d \cdot a}{0.4} C(u_2 - u_1) \tag{25}$$

The magnitude of the shear production term, P_s, tends to increase and then decrease along the free surface towards the penetration depth within the vegetation canopy, with maximum values observed near the top. Therefore, assuming in this paper that P_s decreased linearly from the top of the vegetation canopy to the penetration depth, δ_e, and became zero between the penetration depth and the bed, it can be averaged along $z = 0$ to $z = \delta_e$ to calculate the vegetation canopy-averaged shear production term, P_{sc}, as follows:

$$P_{sc} = \frac{h_p}{2h_e} P_{sh} \tag{26}$$

Therefore, only the vegetation canopy-averaged velocity, u_1, the average flow velocity outside the vegetation canopy, u_2, and the bulk drag coefficient, C_d, were needed to predict the vegetation canopy-averaged shear production term, P_{sc}. For the vegetation canopy-averaged characteristic eddy length, we substituted the vegetation width, b, for the cylindrical diameter, d, to characterize the characteristic eddy length scale, considering that we used strips to simulate submerged vegetation and also because $S_{\max} > 2b$ and $L_t = b$.

Before applying the TKE model, we verified the prediction accuracy of the intermediate variables. Figure 13 presents the predicted values of shear length scale, L_s, penetration depth, δ_e, vegetation canopy-averaged wake production term, P_{wc}, and vegetation canopy-averaged shear production term, P_{sc}, as compared with the measured values under test conditions. Except for δ_e, the predicted values of L_s, P_{wc}, and P_{sc} were in good agreement with the measured values, with a minimum R^2 of 0.9175. For δ_e, the calculated intrusion depth deviated from the calculated intrusion depth under some conditions with an R^2 of 0.7533. The prediction model accurately predicted the shear length scale, L_s, the penetration depth, δ_e, the vegetation canopy-averaged wake production term, P_{wc}, and the vegetation canopy-averaged shear production term, P_{sc}.

After obtaining P_{sc} and P_{wc}, we need to find the equation for the scaling factor ξ. In general, the scaling factor, ξ, is determined based on a linear fit to the left- and right-hand side of the turbulent kinetic energy budget equation at an intercept of zero (Xu and Nepf, 2020). We used $[(P_{wc}+P_{sc})L_{tc}]^{2/3}$ to perform linear fitting with k_c according to Eq. 13. Figure 14A shows the comparison between $[(P_{wc}+P_{sc})L_{tc}]^{2/3}$ and k_c under different test conditions. It can be seen from the figure that $[(P_{wc}+P_{sc})L_{tc}]^{2/3}$ and k_c increase with an increase in the bulk velocity, U_∞, for each vegetation material. For rigid submerged vegetation like PVC-2 and PVC-1, $[(P_{wc}+P_{sc})L_{tc}]^{2/3}$ showed a linear increase with k_c and no significant change in the slope (i.e., the scaling factor, ξ), suggesting that ξ does not vary with a. These observations are in line with the study of Zhang et al. (2018). For the flexible submerged vegetation, with an increase in vegetation flexibility, the slope corresponding to k_c and $[(P_{wc}+P_{sc})L_{tc}]^{2/3}$ gradually decreased, and the linear

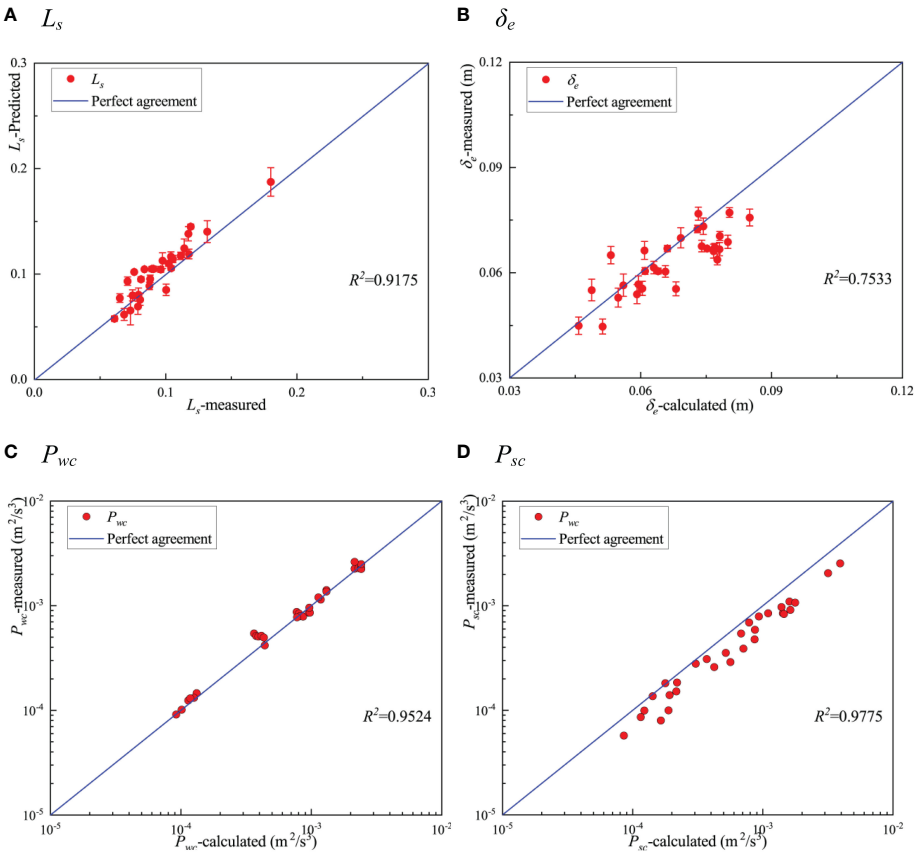

FIGURE 13
A comparison of predicted and measured values of shear length scale L_s **(A)**, the penetration depth δ_e **(B)**, vegetation canopy-averaged wake production term P_{wc} **(C)**, and the vegetation canopy-averaged shear production term P_{sc} **(D)** under different test conditions.

relationship was less evident than that for the rigid submerged vegetation. At the same time, when U_∞ was large, we observed some significant deviations from the fitted line (e.g., the point corresponding to E1-1), which was due to the reduction in the h_e/h_v of the vegetation at higher bulk flow velocities and a reduction in the intensity of the coherent eddies near the top of the vegetation canopy. These effects reduced the efficiency of turbulent kinetic energy production, making the increase in k_c with U_∞ smaller than the increase in $[(P_{wc}+P_{sc})L_{tc}]^{2/3}$. The occurrence of this phenomenon lowers the accuracy of fitting ξ for flexible submerged vegetation using a linear formulation as compared to the accuracy of fitting it for rigid submerged vegetation. In Figure 14A, we used a linear fit to derive $\xi = 0.95 \pm 0.26$, but the R^2 was only 0.66, indicating a lower accuracy of the fit.

Considering the possible relationship between the scaling factor, ξ, and Ca, we calculated the ξ corresponding to $[(P_{wc}+P_{sc})L_{tc}]^{2/3}$ and k_c under each of the 30 test conditions in this experiment. We sorted out the relationships in Figure 14B. Among these relationships, the ξ corresponding to rigid submerged vegetation is shown in red, and ξ corresponding to the flexible submerged vegetation is shown in blue. The figure shows that for the rigid submerged vegetation, ξ did not change with Ca, and its value remained stable at around 1.15. For flexible submerged vegetation, ξ tended to decrease with increasing Ca, and the decrease leveled off, which is consistent with the report of Chen et al. (2020). There are two possible reasons for this. The first reason was the simplified prediction of the characteristic eddy length scale. We assumed that $L_t = L_{tc} = b$, which was applied to the lower part of the canopy. However, the vortex scale in the upper part of the canopy was affected not only by the wake scale turbulence but also by the coherent structure near the canopy top (Zhang et al., 2020a). Therefore, the characteristic vortex scale of rigid vegetation was higher than that of flexible vegetation (Okamoto and Nezu, 2010). This part of the prediction required a larger scaling factor to be offset. The second reason was that the model ignored the vertical

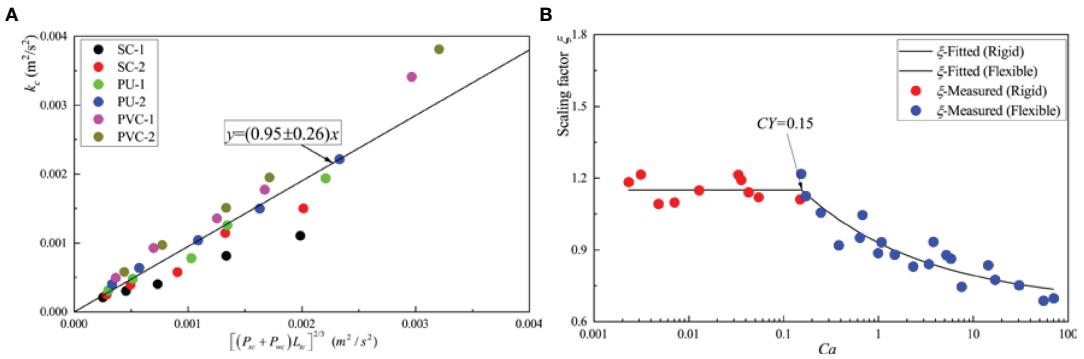

FIGURE 14
(A) Comparison between the vegetation canopy-averaged turbulent kinetic energy, k_c, and $[(P_{sc}+P_{wc})L_{tc}]^{2/3}$. The solid black line in the figure characterizes the best fit with an intercept of 0, corresponding to a scaling factor $\xi = 0.95 \pm 0.26$ ($R^2 = 0.62$). **(B)** Relationships between the scaling factor, ξ, and the Cauchy number of the vegetation canopy, Ca, under different test conditions ($R^2 = 0.91$).

transport of turbulent kinetic energy. Although many research studies have demonstrated that the vertical transport of turbulent kinetic energy is negligible as compared with wake and shear production terms, the impact of turbulent kinetic energy transport on the model still needs to be compensated by a scaling factor. This may thus be the reason why the scaling factor of rigid vegetation was greater than that of flexible vegetation.

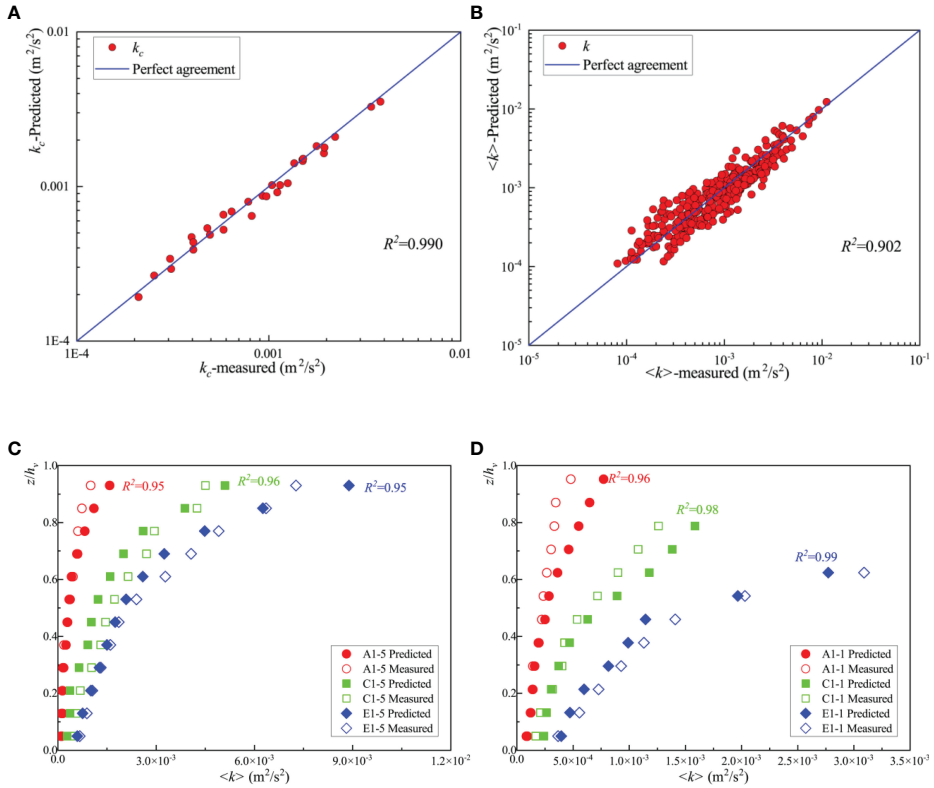

FIGURE 15
(A) Comparison of predicted and measured values of the vegetation canopy-averaged turbulent kinetic energy k_c; **(B)** comparison of the predicted and measured values of the local turbulent kinetic energy $\langle k \rangle$ within the vegetation canopy for all 30 test conditions; **(C, D)** comparison of predicted and measured values of the local turbulent kinetic energy $\langle k \rangle$ within vegetation canopy along the vertical direction under different tests.

Therefore, we took $Ca = 0.15$ as the Cauchy number of the critical vegetation canopy. When $Ca \leqq 0.15$ for rigid submerged vegetation, h_e/h_v does not change with Re_d, and produces a constant as the fitting form; when $Ca \geqq 0.15$ for flexible submerged vegetation, h_e/h_v changes with Re_d. Based on the fitting method for the bulk drag coefficient of flexible submerged vegetation, we used a natural exponential relationship as the fitting form. Finally, we used the least squares method to fit the relationship between ξ and Ca, yielding the following equation:

$$\begin{cases} \xi = 1.15, & Ca \leq 0.15 \\ \xi = 0.255Ca^{-\frac{1}{3}} + 0.67, & Ca \geq 0.15 \end{cases} \quad (27)$$

The coefficient of determination in Eq. 27 is $R^2 = 0.91$, which is higher than $R^2 = 0.62$ for the linear fitting approach. After obtaining the equation to determine the scaling factor, ξ, we substituted Eq. 27 into Eq. 13 to calculate the predicted values of the vegetation canopy-averaged turbulent kinetic energy k_c. Figure 15A presents the predicted values of the vegetation canopy-averaged turbulent kinetic energy, k_c, as compared with the measured values. Overall, the coefficient, $R^2 = 0.990$, for the 30 test conditions indicated high prediction accuracy, indicating that the combination of Eq. 27 and Eq. 13 can be used to reliably predict the vegetation canopy-averaged turbulent kinetic energy, k_c, under unidirectional flow with rigid or flexible submerged vegetation.

To predict the local turbulent kinetic energy within the vegetation canopy, k , we assumed that the scaling factor, ξ, remains constant along the vertical direction for the same type of vegetation. We also assumed that the distribution of the local turbulent kinetic energy along the vertical direction within the vegetation canopy can be predicted by the local turbulent energy shear production term, P_s, the wake production term, P_w, and the characteristic eddy length scale, L_t. The comparison of the predicted and measured values of the local turbulent kinetic energy within the vegetation canopy for all 30 sets of test conditions is presented in Figure 15B; here, $R^2 = 0.911$, indicating high accuracy of prediction.

Figures 15C, D show the predicted distribution of local turbulent kinetic energy within the vegetation canopy under six typical test conditions. The largest error along the vertical direction is located near the vegetation canopy top. Overall, the minimum coefficient of determination for the six characteristic working conditions was 0.92, indicating that the combination of Eq. 27 and Eq. 14 can be used to predict the vertical distribution of the local turbulent kinetic energy within the rigid or flexible submerged vegetation canopy under unidirectional flow.

However, the prediction model has some limitations. The first is the method of determining the characteristic eddy length scale, L_t, and the vegetation canopy-averaged characteristic eddy length scale, L_{tc} (Tanino and Nepf, 2008b). This method applies to vegetation, where the frontal area of vegetation remains constant along the vertical direction, but not to natural vegetation with complex morphology. The latter type of vegetation may correspond to a gradual change in L_t along the vertical direction due to complex body variations (Caroppi et al., 2019). The second limitation is that since the buoyancy parameter, B, is less than 1 for all test conditions, its effect on the resilience of the model vegetation was neglected in this experiment. For vegetation with low stiffness and density relative to pure water, B can have a significant effect on the deflected height ratio, h_e/h_v, hydrodynamic properties, and turbulence characteristics (Zhang et al., 2020b). In such cases, the bulk drag coefficient, C_d, and scaling factor, ξ, may be related not only to Ca but also to B. In addition, since the 2D-PIV was used for measurements in this experiment, the radial (y-direction) velocity was not considered, and thus, the calculated turbulent kinetic energy is expected to be different from the turbulent kinetic energy calculated using three-dimensional instruments, such as ADV, which may also introduce error.

6 Conclusion

In this paper, the vertical distributions of velocity, Reynolds stress, drag coefficient, and turbulent kinetic energy of strip-like model vegetation with different flexibilities were measured experimentally under unidirectional flow. The research shows that with the gradual decrease in the deflection height of vegetation, the dimensionless velocity difference, $\Delta u/U_\infty$, the dimensionless mixed layer thickness, T_{ml}/H, the bulk drag coefficient, C_d, the vegetation canopy-averaged turbulent kinetic energy, k_c, and the vegetation canopy-averaged contribution rate of shear production term of turbulent kinetic energy, $R_{s/T}$, also decrease. The trend of penetration depth of Reynolds stress, δ_e/h_e, is the opposite. Based on the turbulent kinetic energy budget equation, a TKE model was established in this study that can be used to predict the shear production term of turbulent kinetic energy, as well as the turbulent kinetic energy within the vegetation canopy. Here, the scaling factor, ξ, is determined by the Cauchy number of the vegetation canopy, Ca. The TKE model can accurately predict the vegetation canopy-averaged and local turbulent kinetic energy within the vegetation canopy under unidirectional flow, where we are dealing with submerged vegetation of different flexibilities. Therefore, the model can be used as a simple method to predict vegetation-induced turbulence, as well as the characteristics of sediment and material transport, under the influence of submerged vegetation with different flexibility.

Data availability statement

The original contributions presented in the study are included in the article, further inquiries can be directed to the corresponding authors.

Author contributions

All authors listed have made a substantial, direct, and intellectual contribution to the work, and approved it for publication.

Funding

This work was supported by the National Natural Science Foundation of China (Grant No. 52209032) and the Natural Science Foundation of Jiangsu Province, China (Grant No. BK20200160).

Conflict of interest

The authors declare that the research was conducted in the absence of any commercial or financial relationships that could be construed as a potential conflict of interest.

Publisher's note

All claims expressed in this article are solely those of the authors and do not necessarily represent those of their affiliated organizations, or those of the publisher, the editors and the reviewers. Any product that may be evaluated in this article, or claim that may be made by its manufacturer, is not guaranteed or endorsed by the publisher.

References

Abdolahpour, M., Ghisalberti, M., Mcmahon, K., and Lavery, P. (2020). Material residence time in marine canopies under wave-driven flows. *Front. Mar. Sci.* 7, 574. doi: 10.3389/fmars.2020.00574

Albayrak, I., Nikora, V., Miler, O., and O'Hare, M. (2011). Flow-plant interactions at a leaf scale: Effects of leaf shape, serration, roughness and flexural rigidity. *Aquat. Sci.* 74 (2), 267–286. 10.1007/s00027-011-0220-9

Bailey, B. N., and Stoll, R. (2016). The creation and evolution of coherent structures in plant canopy ows and their role in turbulent transport. *J. Fluid Mechanics* 789, 425–460. doi: 10.1017/jfm.2015.749

Beudin, A., Kalra, T., Ganju, N., and Warner, J. C. (2017). Development of a coupled wave-flow-vegetation interaction model. *Comput. Geosciences* 100 (2017), 76–86. doi: 10.1016/j.cageo.2016.12.010

Brunet, Y., Finnigan, J., and Raupach, M. R. (1994). A wind tunnel study of air flow in waving wheat: Single-point velocity statistics. *Boundary-Layer Meteorology* 70 (1), 95–132. doi: 10.1007/BF00712525

Caroppi, G., Västilä, K., Järvelä, J., Rowiński, P. M., and Giugni, M. (2019). Turbulence at water-vegetation interface in open channel flow: Experiments with natural-like plants. *Adv. Water Resour.* 127, 180–191. doi: 10.1016/j.advwatres.2019.03.013

Chen, Z., Jiang, C., and Nepf, H. (2013). Flow adjustment at the leading edge of a submerged aquatic canopy. *Water Resour. Res.* 49 (9), 5537–5551. doi: 10.1002/wrcr.20403

Chen, M., Lou, S., Liu, S., Ma, G., Liu, H., Zhong, G., et al. (2020). Velocity and turbulence affected by submerged rigid vegetation under waves, currents and combined wave–current flows. *Coast. Eng.* 159 (5), 103727. doi: 10.1016/j.coastaleng.2020.103727

Devi, T. B., and Kumar, B. (2016). Channel hydrodynamics of submerged, flexible vegetation with seepage. *J. Hydraulic Eng.* 142 (11), 04016053. doi: 10.1061/(ASCE)HY.1943-7900.0001180

Dijkstra, J., and Uittenbogaard, R. (2010). Modeling the interaction between flow and highly flexible aquatic vegetation. *Water Resour. Res.* 46 (12), 1–12. doi: 10.1029/2010WR009246

Ellington, C. P. (1991). Aerodynamics and the origin of insect flight. *Adv. Insect Physiol.* 23, 171–210. doi: 10.1016/S0065-2806(08)60094-6

Etminan, V., Lowe, R., and Ghisalberti, M. (2017). A new model for predicting the drag exerted by vegetation canopies. *Water Resour. Res.* 53 (4), 3179-3196. doi: 10.1002/2016WR020090

Finnigan, J. (2000). Turbulence in plant canopies. *Annu. Rev. Fluid Mechanics* 32, 519–571. doi: 10.1146/annurev.fluid.32.1.519

Ghisalberti, M. (2009). Obstructed shear flows: Similarities across systems and scales. *J. Fluid Mechanics* 641, 51–61. doi: 10.1017/S0022112009992175

Ghisalberti, M., and Nepf, H. M. (2001). Mixing layers and coherent structures in vegetated aquatic flows. *J. Geophysical Res.* 107 (C2), 1–11. doi: 10.1029/2001JC000871

Ghisalberti, M., and Nepf, H. M. (2004a). The limited growth of vegetated shear layers. *Water Resour. Res.* 40 (W07502), 1-12. doi: 10.1029/2003WR002776

Ghisalberti, M., and Nepf, H. M. (2004b). The limited growth of vegetated shear layers. *Water Resour. Res.* 40 (7), 1–12. doi: 10.1029/2003WR002776

Ghisalberti, M., and Nepf, H. (2006). The structure of the shear layer in flows over rigid and flexible canopies. *Environ. Fluid Mechanics* 6 (3), 277–301. doi: 10.1007/s10652-006-0002-4

Huai, W.-x., Li, S., Katul, G. G., Liu, M.-Y., and Yang, Z.-H. (2021). Flow dynamics and sediment transport in vegetated rivers: A review. *J. Hydrodynamics* 33 (3), 400–420. doi: 10.1007/s42241-021-0043-7

Hu, Z., Lei, J., Liu, C., and Nepf, H. M. (2018). Wake structure and sediment deposition behind models of submerged vegetation with and without flexible leaves. *Adv. Water Resour.* 118 (8), 28–38. doi: 10.1016/j.advwatres.2018.06.001

Jamali, M., and Sehat, H. (2020). Experimental study of lateral dispersion in flexible aquatic canopy with emergent blade-like stems. *Phys. Fluids* 32 (6), 067116. doi: 10.1063/5.0010665

King, A. T., Tinoco, R. O., and Cowen, E. A. (2012). A k-epsilon turbulence model based on the scales of vertical shear and stem wakes valid for emergent and submerged vegetated flows. *J. Fluid Mechanics* 701, 1–39. doi: 10.1017/jfm.2012.113

Kouwen, N., and Li, R.-M. (1980). Biomechanics of vegetative channel linings. *Am. Soc. Civil Engineers* 106 (6), 1085–1103. doi: 10.1061/JYCEAJ.0005444

Kouwen, N., and Moghadam, M. F. (2000). Friction factors for coniferous trees along rivers. *J. Hydraulic Eng.* 126 (10), 732–740. doi: 10.1061/(ASCE)0733-9429(2000)126:10(732)

Lei, J., and Nepf, H. M. (2019). Blade dynamics in combined waves and current. *J. Fluids Structures* 87, 137–149. doi: 10.1016/j.jfluidstructs.2019.03.020

Lei, J., and Nepf, H. M. (2021). Evolution of flow velocity from the leading edge of 2-d and 3-d submerged canopies. *J. Fluid Mechanics* 916, 1-27. doi: 10.1017/jfm.2021.197

Liu, M.-Y., Huai, W.-X., and Zhong-Hua Yang and Zeng, Y.-H. (2020). A genetic programming-based model for drag coefficient of emergent vegetation in open channel flows. *Adv. Water Resour.* 140 1–10. doi: 10.1016/j.advwatres.2020.103582

Liu, C., Shan, Y., and Heidi M, N. (2021). Impact of stem size on turbulence and sediment resuspension under unidirectional flow. *Water Resour. Res.* 57, e2020WR028620. doi: 10.1029/2020WR028620

Liu, C., Yan, C., Sun, S., Lei, J., Nepf, H., and Shan, Y. (2022). Velocity, turbulence and sediment deposition in a channel partially filled with a phragmites australis canopy. *Water Resour. Res* 58, 1-21. doi: 10.1029/2022WR032381

Liu, J., Zhang, Z., Yu, Z., Liang, Y., Li, X., and Ren, L. (2017). The structure and flexural properties of typha leaves. *Appl. Bionics Biomechanics*, 1–9. doi: 10.1155/2017/1249870

Li, Y., Wang, Y., Anim, D. O., Tang, C., Du, W., Ni, L., et al. (2014). Flow characteristics in different densities of submerged flexible vegetation from an open-channel flume study of artificial plants. *Geomorphology* 2014, 314–324. doi: 10.1016/j.geomorph.2013.08.015

Li, Y.-H., Xie, L., and Su, T.-C. (2018). Resistance of open-channel flow under the effect of bending deformation of submerged flexible vegetation. *J. Hydraulic Eng.* 144 (3), 04017072. doi: 10.1061/(ASCE)HY.1943-7900.0001419

López, F., and García, M. H. (1998). Open-channel flow through simulated vegetation: Suspended sediment transport modeling. *Water Resour. Res.* 34 (9), 2341–2352. doi: 10.1029/98WR01922

Luhar, M., and Nepf, H. M. (2011). Flow-induced reconfiguration of buoyant and flexible aquatic vegetation. *Limnology Oceanography* 56, 2003–2017. doi: 10.4319/lo.2011.56.6.2003

Morris, E. P., Peralta, G., Brun, F. G., Duren, L., Bouma, T. J., and Pérez-Lloréns, J. L. (2008). Interaction between hydrodynamics and seagrass canopy structure: Spatially explicit effects on ammonium uptake rates. *Limnology Oceanography* 53 (4), 1531–1539. doi: 10.4319/lo.2008.53.4.1531

Nepf, H. M. (2011). Flow and transport in regions with aquatic vegetation. *Annu. Rev. Fluid Mechanics* 44, 123–142. doi: 10.1146/annurev-fluid-120710-101048

Nepf, H. M. (2012). Hydrodynamics of vegetated channels. *J. Hydraulic Res.* 50 (3), 262–279. doi: 10.1080/00221686.2012.696559

Nepf, H. M., and Vivoni, E. (2000). Flow structure in depth-limited, vegetated flow. *J. Geophysical Res.* 105 (C12), 28547–28557. doi: 10.1029/2000JC900145

Neumeier, U. (2007). Velocity and turbulence variations at the edge of saltmarshes. *Continental Shelf Res.* 27 (8), 1046–1059. doi: 10.1016/j.csr.2005.07.009

Nezu, I., and Sanjou, M. (2008). Turburence structure and coherent motion in vegetated canopy open-channel flows. *J. Hydro-environment Res.* 2 (2), 62–90. doi: 10.1016/j.jher.2008.05.003

Nikora, V., McEwan, I., Mclean, S. R., Coleman, S., Pokrajac, D., and Walters, R. A. (2007). Double-averaging concept for rough-bed open-channel and overland flows: Theoretical background. *J. Hydraulic Eng.* 133 (8), 873–883. doi: 10.1061/(ASCE)0733-9429(2007)133:8(873)

Okamoto, T.-A., and Nezu, I. (2010). Turbulence structure and "Monami" phenomena in flexible vegetated open-channel flows. *J. Hydraulic Res.* 47 (6), 798–810. doi: 10.3826/jhr.2009.3536

Okamoto, T., Nezu, I., and Sanjou, M. (2016). Flow–vegetation interactions: Length-scale of the "monami" phenomenon. *J. Hydraulic Res.* 54 (3), 251–262. doi: 10.1080/00221686.2016.1146803

Park, H., and Hwang, J. H. (2019). Quantification of vegetation arrangement and its effects on longitudinal dispersion in a channel. *Water Resour. Res.* 55, 1–11. doi: 10.1029/2019WR024807

Raupach, M. R., and Shaw, R. H. (1982). Averaging procedures for flow within vegetation canopies. *Boundary-Layer Meteorology* 22 (1), 79–90. doi: 10.1007/BF00128057

Rominger, J. T., and Nepf, H. M. (2014). Effects of blade flexural rigidity on drag force and mass transfer rates in model blades. *Limnology Oceanography* 59 (6), 2028–2041. doi: 10.4319/lo.2014.59.6.2028

Sonnenwald, F., Stovin, V., and Guymer, I. (2018). Estimating drag coefficient for arrays of rigid cylinders representing emergent vegetation. *J. Hydraulic Res.* 57, 1–7. doi: 10.1080/00221686.2018.1494050

Tang, C., Lei, J., and Nepf, H. M. (2019). Impact of vegetation-generated turbulence on the critical, near-bed, wave-velocity for sediment resuspension. *Water Resour. Res.* 55, 1-14. doi: 10.1029/2018WR024335

Tang, X., Lin, P., Liu, P. L.-F., and Zhang, X. (2021). Numerical and experimental studies of turbulence in vegetated open-channel flows. *Environ. Fluid Mechanics* 21 (2), 1–27. doi: 10.1007/s10652-021-09812-7

Tang, H., Tian, Z., Yan, J., and Yuan, S. (2014). Determining drag coefficients and their application in modelling of turbulent flow with submerged vegetation. *Adv. Water Resour.* 69, 134–145. doi: 10.1016/j.advwatres.2014.04.006

Tanino, Y., and Nepf, H. (2007). *Experimental investigation of lateral dispersion in aquatic canopies* (Venice, Italy: 32nd International Association of Hydraulic Engineering & Research (IAHR)), 152.

Tanino, Y., and Nepf, H. M. (2008a). Laboratory investigation of mean drag in a random array of rigid, emergent cylinders. *J. Hydraulic Eng.* 134, 34–41. doi: 10.1061/(ASCE)0733-9429(2008)134:1(34)

Tanino, Y., and Nepf, H. M. (2008b). Lateral dispersion in random cylinder arrays at high reynolds number. *J. Fluid Mechanics* 600, 339–371. doi: 10.1017/S0022112008000505

Tennekes, H. H., and Lumley, J. L. (1972). *A first course in turbulence* (Cambridge, MA: MIT Press).

Termini, D. (2019). Turbulent mixing and dispersion mechanisms over flexible and dense vegetation. *Acta Geophysica* 67 (7), 961–970. doi: 10.1007/s11600-019-00272-8

Thielicke, W., and Stamhuis, E. J. (2014). PIVlab – towards user-friendly, affordable and accurate digital particle image velocimetry in MATLAB. *J. Open Res. Software* 2, 1-10. doi: 10.5334/jors.bl

Tinoco, R. O., and Coco, G. (2016). A laboratory study on sediment resuspension within arrays of rigid cylinders. *Adv. Water Resour.* 92, 1–9. doi: 10.1016/j.advwatres.2016.04.003

Tseng, C.-Y., and Tinoco, R. O. (2020). A model to predict surface gas transfer rate in streams based on turbulence production by aquatic vegetation. *Adv. Water Resour.* 143, 1-18. doi: 10.1016/j.advwatres.2020.103666

Vargas-Luna, A., Crosato, A., and Uijttewaal, W. S. J. (2015). Effects of vegetation on flow and sediment transport: Comparative analyses and validation of predicting models. *Earth Surface Processes Landforms* 40 (2), 157–176. doi: 10.1002/esp.3633

Veelen, T., Fairchild, T., Reeve, D. E., and Karunarathna, H. (2020). Experimental study on vegetation flexibility as control parameter for wave damping and velocity structure. *Coast. Eng.* 157, 103648. doi: 10.1016/j.coastaleng.2020.103648

Wang, H., Cong, P., Zhu, Z., Zhang, W., Ai, Y., and Huai, W.-x. (2022). Analysis of environmental dispersion in wetland flows with floating vegetation islands. *J. Hydrology* 606 (1), 127369. doi: 10.1016/j.jhydrol.2021.127359

Waycott, M., Duarte, C. M., Carruthers, T. J. B., Orth, R. J., Dennison, W., Olyarnik, S. V., et al. (2009). Accelerating loss of seagrass across the globe threatens coastal ecosystems. *Proc. Natl. Acad. Sci.* 106 (30), 12377–12381. doi: 10.1073/pnas.0905620106

Wilcock, R. J., Champion, P. D., Nagels, J., and Croker, G. F. (1999). The influence of aquatic macrophytes on the hydraulic and physico-chemical properties of a new Zealand lowland stream. *Hydrobiologia* 416 (1), 203–214. doi: 10.1023/A:1003837231848

Wilson, J. D. (1988). A second-order closure model for flow through vegetation. *Boundary-Layer Meteorology* 42 (4), 371–392. doi: 10.1007/BF00121591

Xu, Y., and Nepf, H. M. (2020). Measured and predicted turbulent kinetic energy in flow through emergent vegetation with real plant morphology. *Water Resour. Res.* 56 (12), e2020WR027892. doi: 10.1029/2020WR027892

Yang, J., Chung, H., and Nepf, H. M. (2016). The onset of sediment transport in vegetated channels predicted by turbulent kinetic energy. *Geophysical Res. Lett.*, 43 (21), 11, 261–11, 268. doi: 10.1002/2016GL071092

Yang, J., and Nepf, H. M. (2019). Impact of vegetation on bed load transport rate and bedform characteristics. *Water Resour. Res.* 55, 1-16. doi: 10.1029/2018WR024404

Zhang, J., Lei, J., Huai, W., and Nepf, H. M. (2020a). Turbulence and particle deposition under steady flow along a submerged seagrass meadow. *J. Geophysical Research: Oceans* 125, e2019JC015985. doi: 10.1029/2019JC015985

Zhang, S., Liu, Y., Wang, Z., and Li, G. (2019). Effect of flexible vegetation lodging on overland runoff resistance. *Water Environ. J.* 34 (3), 1–9. doi: 10.1111/wej.12529

Zhang, Y., Tang, C., and Nepf, H. M. (2018). Turbulent kinetic energy in submerged model canopies under oscillatory flow. *Water Resour. Res.* 54, 1734–1750. doi: 10.1002/2017WR021732

Zhang, Y., Wang, P., Cheng, J., Wang, W.-J., Zeng, L., and Wang, B. (2020b). Drag coefficient of emergent flexible vegetation in steady nonuniform flow. *Water Resour. Res.* 56 (8), e2020WR027613. doi: 10.1029/2020WR027613

Zimmerman, R. C. (2003). A biooptical model of irradiance distribution and photosynthesis in seagrass canopies. *Limnology Oceanography 48(1 Part* 2), 568–585. doi: 10.4319/lo.2003.48.1_part_2.0568

frontiers | Frontiers in Marine Science

TYPE Original Research
PUBLISHED 12 January 2023
DOI 10.3389/fmars.2022.1123067

OPEN ACCESS

EDITED BY
Yi Pan,
Hohai University, China

REVIEWED BY
Hongshuai Qi,
State Oceanic Administration, China
Shihao Liu,
East China Normal University, China

*CORRESPONDENCE
Jie Liu
liujie@fio.org.cn
Ping Li
liping@fio.org.cn

SPECIALTY SECTION
This article was submitted to Coastal Ocean Processes, a section of the journal Frontiers in Marine Science

RECEIVED 13 December 2022
ACCEPTED 27 December 2022
PUBLISHED 12 January 2023

CITATION
Gao W, Du J, Gao S, Xu Y, Li B, Wei X, Zhang Z, Liu J and Li P (2023) Shoreline change due to global climate change and human activity at the Shandong Peninsula from 2007 to 2020.
Front. Mar. Sci. 9:1123067.
doi: 10.3389/fmars.2022.1123067

Shoreline change due to global climate change and human activity at the Shandong Peninsula from 2007 to 2020

Wei Gao[1,2], Jun Du[1], Shan Gao[1,2], Yuanqin Xu[1,2], Bing Li[3], Xia Wei[4], Zhuoli Zhang[4], Jie Liu[1,2]* and Ping Li[1,2]*

[1]Key Laboratory of Marine Geology and Metallogeny, First Institute of Oceanography, Ministry of Natural Resources (MNR), Qingdao, China, [2]Laboratory for Marine Geology, Pilot National Laboratory for Marine Science and Technology (Qingdao), Qingdao, China, [3]Island Research Center, Ministry of Natural Resources (MNR), Pingtan, China, [4]College of Marine Geosciences, Ocean University of China, Qingdao, China

In this study, how shoreline change responses to global climate change and human activity at the Shandong Peninsula was quantified by analyzing shoreline locations, inshore erosion/accretion rates, and sandy beach profiles for 2007–2020. During the study period, the total shoreline length decreased from 3345.55 km to 3310.18 km, whereas the natural shoreline decreased by 25.41%. As a dominant shore type, the artificial shoreline increased by 827.89 km. Human activities, such as land reclamation and harbor construction, have caused continuous shoreline advance, resulting in a net land increase of 672.40 km^2. However, natural shores (e.g., sandy shore) receded at an average annual rate of –1.0 m due to ongoing erosion. The inshore waters of the Shandong Peninsula were largely sedimentary as erosion occurred only at a few hotspots. Therefore, seaward sediment deposition dominated the erosion/accretion trends of the inshore areas of the peninsula. However, global climate change and human activities have exacerbated the erosion caused by sea level rise. Specifically, the climate change caused absolute sea level rise and increasing frequency of extreme weather events, whereas the human activity dominated the transport and supply of sediment in the coastal zone. In the short term, the shoreline of the Shandong Peninsula continues to advance toward the sea due to the growing artificial shoreline. However, this disrupts the balance between sediment supply and marine energies in the coastal zone, and the system then rebalance itself by eroding unprotected natural shores. In the long term, main shoreline evolution trends depend on global climate change and sea level rise which plays a decisive role in shoreline retreat in the Shandong Peninsula.

KEYWORDS

global climate change, human activity, shoreline change, coastal erosion, sea level rise

1 Introduction

The coastal zone is the interface where spatiotemporally complex and dynamic exchanges of matter and energy most intensely occur among the hydrosphere, lithosphere, biosphere, and atmosphere (Fraser et al., 2017)Therefore, the coastal zone has long been the focus of studies on land–sea interactions (Temmerman et al., 2013; Williams et al., 2018). Coastal zones also experience the greatest degree of overlap among urbanization, industry, wind, and solar power generation, and various exploration of national resources (Nicholls, 2004; Davenport and Davenport, 2006). For these reasons, they are one of the hotspots in the world for socioeconomic development (Barbier et al., 2011). Overall, the multiple governing factors of the coastal zone (e.g., sediment supply, the hydrodynamic environment, and the interaction zone) mutually interact constraining or facilitating each other *via* various mechanisms (Yates et al., 2009). If the equilibrium between sediment supply and the hydrodynamic environment is disrupted, the interaction zone either retreats or advances to establish a new equilibrium (Ranasinghe and Stive, 2009 and Ranasinghe, 2016). The consequent changes in the land-side boundary of the interaction zone then manifest as shoreline change. Some of these processes have been in action over millennia but slow, whereas others have been recent but fast (Fred and Andrew, 1996). Thus, shoreline change depends on both natural and anthropogenic factors. The former includes sea level, wave action, tidal currents, storm surges, and changes in the supply of terrigenous sediment (Esteves et al., 2002; Cai et al., 2009; Nerem et al., 2018; Flor-Blanco et al., 2021). The latter includes human-induced disturbances, such as land reclamation, harbor construction, the damming of rivers that drain into the sea, sand mining, and beach maintenance projects (Anthony et al., 2015; Warrick et al., 2019; Grottoli et al., 2020; Pan et al., 2022). Due to global climate change (especially sea level rise) and the increasing intensity and scale of human-induced disturbances in the coastal zone (Nicholls and Cazenave, 2010), coastal zone systems are now experiencing large and rapid changes in their governing factors or overall patterns (Meinshausen et al., 2011). The rapid increase in artificial shorelines and shoreline control projects has caused anthropogenic factors to dominate shoreline change (Chu et al., 2020), with its severe consequences for coastal geo-environments and ecosystems (McGranahan et al., 2007; Mentaschi et al., 2018).

The warming of oceans across the globe has reduced the decadal average Arctic sea-ice extent to its lowest level since 1850. Furthermore, virtually all glaciers around the world are in retreat, and the rate of ice cap melting during 2010–2019 was four times than that during 1992–1999. Sea level rise since 1900 due to warming-driven ocean thermal expansion (Ehlert and Zickfeld, 2018; Widlansky et al., 2020) and glacier/ice cap melting (Alley et al., 2005) are already greater than that in any century over the past 3,000 years. In addition, it may be unlikely that this trend will reverse in the next century or millennium. This rapid increase in global sea level threatens to "sandwich" coastal regions (Zhang et al., 2004).

China has a long shoreline and large swathes of coast, which have had a long history of development and exploitation. As the shoreline of China had been stable or advancing toward the sea until the end of the 1950s, in the past, most coastal geomorphologists focused on the mitigation of siltation-induced problems. This changed during the end of the 1950s and the beginning of the 1960s. First, sandy beaches and shorelines began to erode; the sedimentary regime of major river deltas (e.g., the Yellow River and Yangtze River deltas) then experienced gradual transitions from rapid accretion to widespread erosion (Hou et al., 2016). Since then, erosion-induced shoreline retreat has become the main trend in the coastal regions of China (Luo et al., 2015).

The Shandong Peninsula is surrounded by the Bohai sea and the Yellow sea, its northern side faces the Liaodong Peninsula across the Bohai Strait, whereas its eastern side faces Korea across the Yellow Sea. The shoreline of Shandong is connected to Hebei in the north by the Dakou River estuary and Suzhou Province in the south through the Xiuzhen River estuary. From north to south, this shoreline passes through seven prefecture-level coastal cities, Binzhou, Dongying, Weifang, Yantai, Weihai, Qingdao, and Rizhao. With a length of 3,345 km, it is the 3rd longest shoreline in China and accounts for 18% of total shoreline length of China. The shoreline of the Shandong Peninsula is quite diverse as it includes rocky, sandy, silty, estuary, and artificial shores (Xu et al., 2009). Due to their geographic location and topography, coastal regions of Shandong are frequently affected by typhoons and cold front storms. In particular, Laizhou Bay and Bohai Bay are infamous for the severity and frequency of their storm surges. Although there are hundreds of rivers that flow into the sea from the Zhangweixin River that borders Hubei in the north and the Xiuzhen River bordering Suzhou in the south, most of these rivers are seasonal mountain streams. Therefore, runoff and sediment load from the Yellow River account for the vast majority of runoff and sediment load to Shandong. As Shandong has the third longest shoreline in China and diverse shore types, the intensification of coastal development and exploitation has resulted in drastic shoreline change (Gracia et al., 2018) and major changes in shore type (Yin et al., 2018) (Figure 1). As Shandong is a major marine economy, rapid development of its marine economy combined with natural factors have led to intense changes in its coastal environment (Xue et al., 2009), which also accelerate shoreline change. Thus, Shandong Peninsula is an ideal site for studies about the patterns and mechanisms of shoreline change (Li G. et al., 2013; Hegde and Akshaya, 2015). In this study, we analyzed the shoreline data of the Shandong Peninsula from 2007 to 2020, to characterize and quantify the behaviors and mechanisms of shoreline change in the face of global climate change and human disturbances.

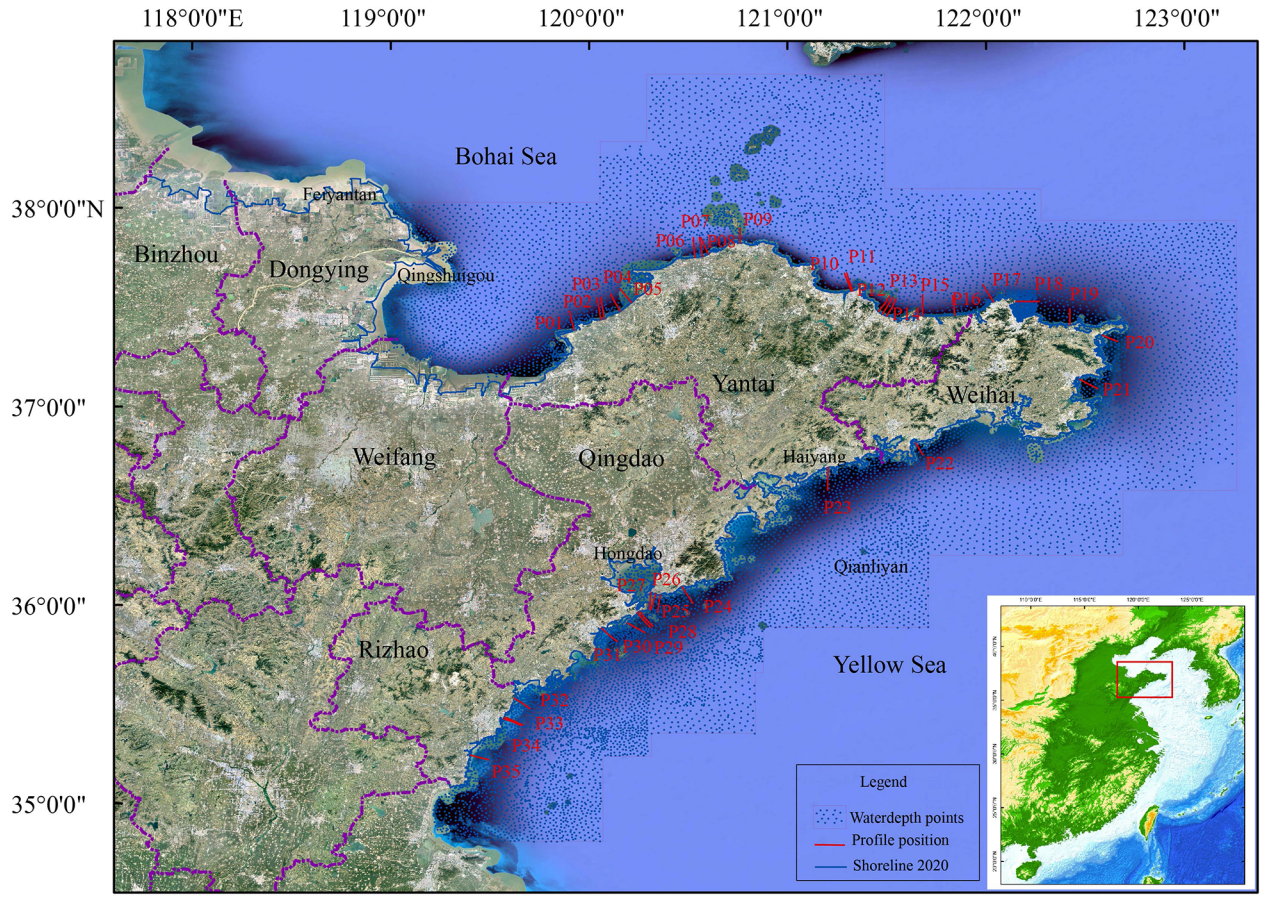

FIGURE 1
Location and satellite image of the Shandong Peninsula.

2 Data sources and methodology

2.1 Shoreline data and extraction

Satellite remote sensing is the most efficient way to quantify shoreline changes over large spaces and long timescales. In this study, images taken by the Ziyuan-3 Earth observation satellite were preprocessed and then fed into ArcGIS to extract and classify shoreline data. The multispectral data includes 4 bands of blue, green, red and near-infrared, with spatial resolution of 5.8m, the spatial resolution of panchromatic data and multispectral data is 2.1m (Dong et al., 2019). To classify and locate the various shore types (e.g., rocky, sandy, silty, estuary, or artificial), remote sensing indices based on color, texture, and feature adjacency were created based on the features of the coastal zone in satellite images and field surveys. These indices were then used for shore classification in synthesized false-color images constructed by combining the near infrared, red, and green bands (Zhang et al., 2021). The average high-water line was defined as the shoreline which the artificial and rocky shoreline were easy to identify. The sandy and silty shoreline were significantly affected by the tide, and the result of shoreline was generally the instantaneous waterline at the time of the remote sensing image acquisition, so it was necessary to determine the location of shoreline according to the correction of tide level at the time of satellite imaging (Yin et al., 2022). The shoreline in 2007 was the historical data, and part of the shoreline in 2020 was identified by remote sensing images taken from January to May of 2020, these remote sensing images were all calibrated by field measurement, and the error was limited to about 5m after the comparison between interpretation and actual measurement. In addition, an aerial drone (DJI Matrice 600 Pro hexacopter) was used to capture aerial images. Preliminary field surveys were conducted in advance to determine the range for drone observation. The drone was flown during the day according to predetermined routes at an altitude of 150 m, during the neap tide. Ground control points (five per km) were set up to facilitate calibration during the post-processing stage. Comparison of the control points with the datum points showed that the post-processed drone images had a horizontal precision >0.05 m and an elevation precision of 0.10 m. Finally, manual surveys were

conducted at complex and typical shore sections, to determine and calibrate the interpreted shoreline location, in orders to ensure that the current state and historical changes in the shoreline were calculated accurately.

2.2 Analysis of land area change

In this study, land area change is identified as the change in coastal land area caused by changes in shoreline position. If the shoreline moves toward the sea (shoreline advancement), land area increases; if the shoreline moves toward the land (shoreline retreatment), land area decreases. Therefore, if the net change in coastal land area is positive, the shoreline is advancing toward the sea as a whole; otherwise, the shoreline is receding due to erosion. Land area changes were calculated by superimposing the shoreline from two different periods in ArcGIS and then performing a topology analysis to obtain polygons that represent the differences between these shorelines and their land areas. The nature of each polygon was then ascertained (i.e., whether it represents an increase or decrease in land area). Finally, the increases and decreases in land area were tallied to ascertain the net change in land area.

2.3 Analysis of shoreline change: the baseline method

Shoreline change was quantified using the Digital Shoreline Analysis System (DSAS) (Thieler et al., 2009; Himmelstoss et al, 2018). First, the buffer method was used to create a baseline that was roughly parallel to the shoreline. The shorelines from different periods were made to lie on the same side of the baseline. Equally separated perpendicular transects (transect (i)) were then drawn on the baseline so that the distance between two shorelines on a transect represented the shoreline change between their corresponding time points. The rate of shoreline change for a given period can be calculated by using a variety of models. In this study, the end point rate (EPR) method of Crowell et al. (1993) was used for this purpose (Figure 2), where the rate of shoreline change was defined as the perpendicular distance between two shorelines divided by their time difference. The sampling interval was 200 m, and a total of 10 819 transects were generated after multiple rounds of smoothing, fitting, and adjustment. EPR was estimated as follows:

$$EPR_{m(i,j)} = \frac{D_{mj} - D_{mi}}{T}$$

ere $EPR_{m(i,j)}$ are the rates of change in shorelines with i and j on the m-th transect; D_{mi} and D_{mj} are the distances between the baseline and the intersections of shorelines with i and j on the m-th transect, respectively; T is the time difference between i and j. The change rate (m/a) may be negative or positive values, which represent erosion and accretion respectively. A value of 0 indicates that the position of the shoreline remains unchanged. The thresholds for erosive, stable, and accreting shorelines are EPR ≤ −0.5 m/a, −0.5 m/a > EPR< 0.5 m/a, and EPR ≥ 0.5 m/a, respectively.

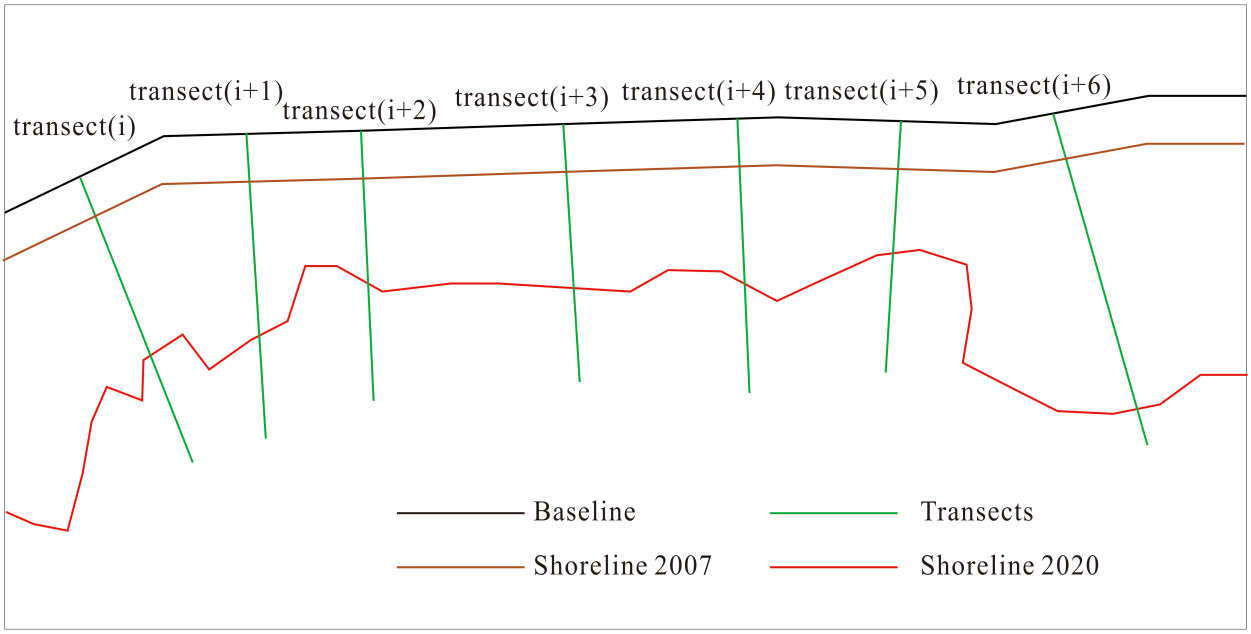

FIGURE 2
Schema of the analysis of shoreline change by baseline method.

2.4 Erosion and accretion in inshore waters

Water depth data for 2007–2020 were standardized to the WGS84 coordinate frame, using ArcGIS, and the digital elevation model (DEM) was constructed using kriging and the TIN-to-raster method. Cross-validation was performed to ensure consistency between DEM and actual terrain. To characterize accretion/erosion in the inshore waters of the Shandong Peninsula, the differences between the 2007 and 2020 DEMs were extracted, and the cut-fill tool was used to obtain the accretion and erosion parameters (e.g., the areas of erosion/accretion, and net accreted/eroded volumes).

2.5 Sandy beach profile changes

In 2020, how beach changes in the profile view were evaluated in 25 typical sandy beaches at Shandong Peninsula by comparing the 2010–2020 profiles to the baseline profile in 2010 so as to quantify the erosion of sandy shorelines over the past 10 years. At shore segments where the changes in the sandy shoreline or a part of the shoreline were small, 35 beach elevation monitoring profiles were set up along the shoreline transect. The geodetic coordinates and elevation data of these sections were sampled at specific periods, using a high precision real-time differential positioning technique based on the Continuously Operating Reference Station (CORS) system. A map of beach profile changes was constructed, and the beach elevation changes were used to identify the trends of beach profile and shoreline change in the Shandong Peninsula.

3 Results

3.1 Shore-type changes

The total shoreline length of Shandong in 2007 was 3345.55 km, with artificial, rocky, sandy, silty, and estuarine shores accounting for 1292.23 km (38.62%), 888.55 km (26.56%), 759.08 km (22.69%), 401.57 km (12.00%), and 4.13 km (0.12%), respectively. In total, natural shoreline retention was 61.37%. The total shoreline length of Shandong in 2020 was 3310.18 km, with artificial, rocky, sandy, silty, and estuarine shores accounting for 2120.12 km (64.05%), 513.43 km (15.51%), 342.59 km (10.35%), 323.47 km (9.77%), and 10.56 km (0.32%), respectively. Natural shoreline retention was only 35.96%.

During 2007–2020, the total shoreline of Shandong decreased by 35.37 km to 3310.18 km, which corresponded to an annual change rate of −2.72 km/a. The decreases in rocky, sandy, and silty shorelines were 565.08 km, 245.65 km, and 58.98 km, equivalent to annual change rates of −43.47 km/a, −18.90 km/a, and −4.54 km/a, respectively. Artificial and estuary shorelines increased by 827.89 km and 6.43 km (change rates of 63.68 km/a and 0.49 km/a, respectively). During 2007–2020, not only did artificial shore account for the largest proportion of Shandong's shoreline, but also it was the fastest growing shore type (Figure 3). Natural shoreline retention decreased by 25.41%.

3.2 Rates of shoreline and land area changes

Analysis of shoreline change at the 10 819 transects revealed that the average rate of shoreline change in Shandong during 2008–2020 was 13.86 m/a, indicating an overall shoreline advancement (Figure 4). The 1,047 transects (9.68%) showed shoreline retreatment, with an average rate of −11.71 m/a. These transects were mainly located at sandy and silty shores. The largest retreat occurred near the Diaokou River mouth (northern part of the modern Yellow River delta), where the rate of shoreline retreatment was −142.32 m/a (2). The 3,033 transects (28.03%) showed shoreline advancement, with an average rate of 46.68 m/a. These transects were mainly located at newly constructed artificial shores and silty shores at large estuaries (1, 3–9) (Figure 5), such as the shores of Hongdao Island in Jiaozhou Bay (7) and the Qingshuigou channel of Yellow River (3). The 6,739 transects (62.29%) were stable, and the majority of these transects were located at artificial and rocky shores, such as the rocky shores of Laoshan District in Qingdao City and some artificial shores.

The land area changes that corresponded to advancement and recession were 694.67 km^2 and 22.27 km^2, respectively, which amounted to a net increase of 672.40 km^2 and a rate of land area change of 51.72 km^2/a. The largest increase in land area occurred at the northern part of Jiaozhou Bay in Qingdao City, mainly due to land reclamation to join Hongdao Island to the mainland (7) (in Figure 6). Shoreline retreatment mainly occurred near the Feiyan Beach, at the northern part of the Yellow River delta (2) in (Figure 6); this was caused by the diversion of the Yellow River away from the Diaokou course, which led to continuous erosion in this area.

3.3 Inshore erosion and accretion

The inshore area of the Shandong Peninsula was accretionary overall, and the isobaths of the accretionary zones also exhibited a significant seaward advancement (Figure 7). Accretion was most intense in the north but somewhat less

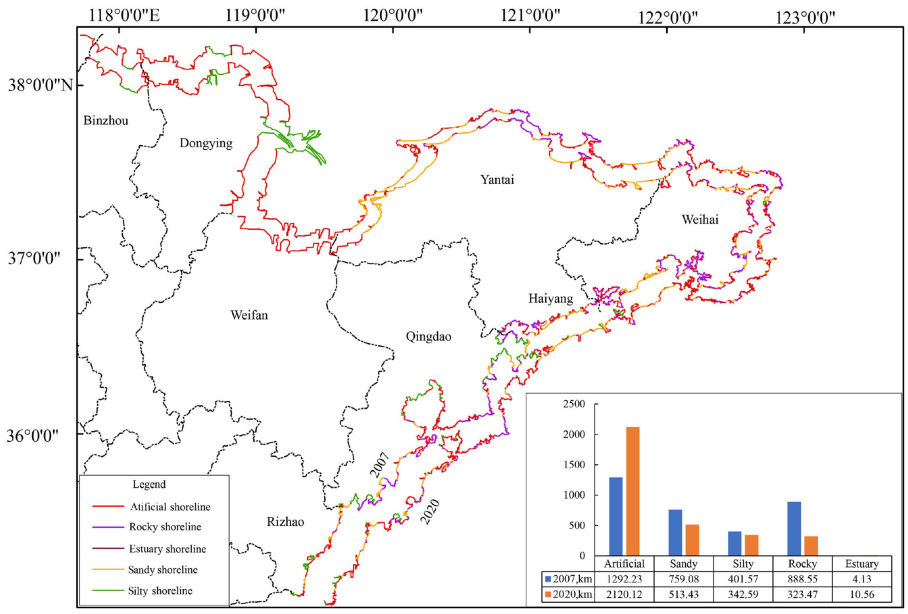

FIGURE 3
Type-classified shoreline lengths of Shandong in 2007 and 2020.

pronounced in the east and south as there were many areas that were in equilibrium in those regions. The areas that were in equilibrium did not exhibit considerable changes in their underwater terrain. The inshore area with the widest area of accretion and with the largest amount of accretion was the western side of Laizhou Bay, which showed an area of accretion of 6.59×10^8 m^2, a volume of accretion of 3.8×10^8 m^3, and a net volume of accretion of 2.13×10^8 m^3. The area with the highest accretion values was the inshore area of Chengshantou, with a maximum accretion value of 17.9 m. Inshore erosion only occurred in hotspots. These hotspots were mainly located near artificial coastal structures, such as harbors, or areas with strong hydrodynamics where they occur alongside accretion zones. The largest area of erosion was located between Taozi Bay and Yangma Island, where the volume of erosion was 0.10×10^8 m^3 (Table 1).

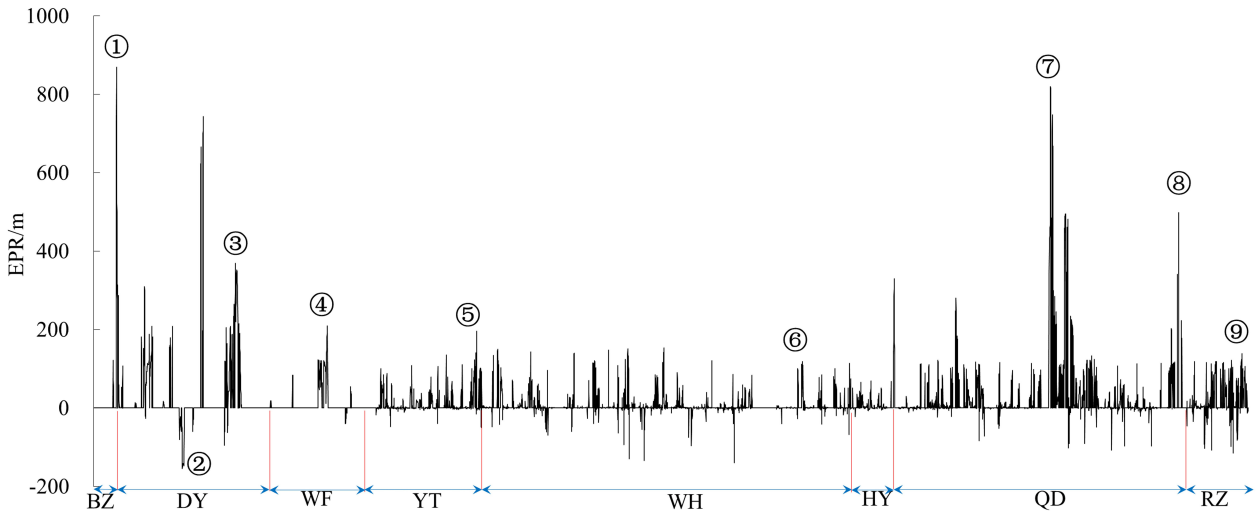

FIGURE 4
Shoreline changes in the Shandong Peninsula from 2007 to 2020.

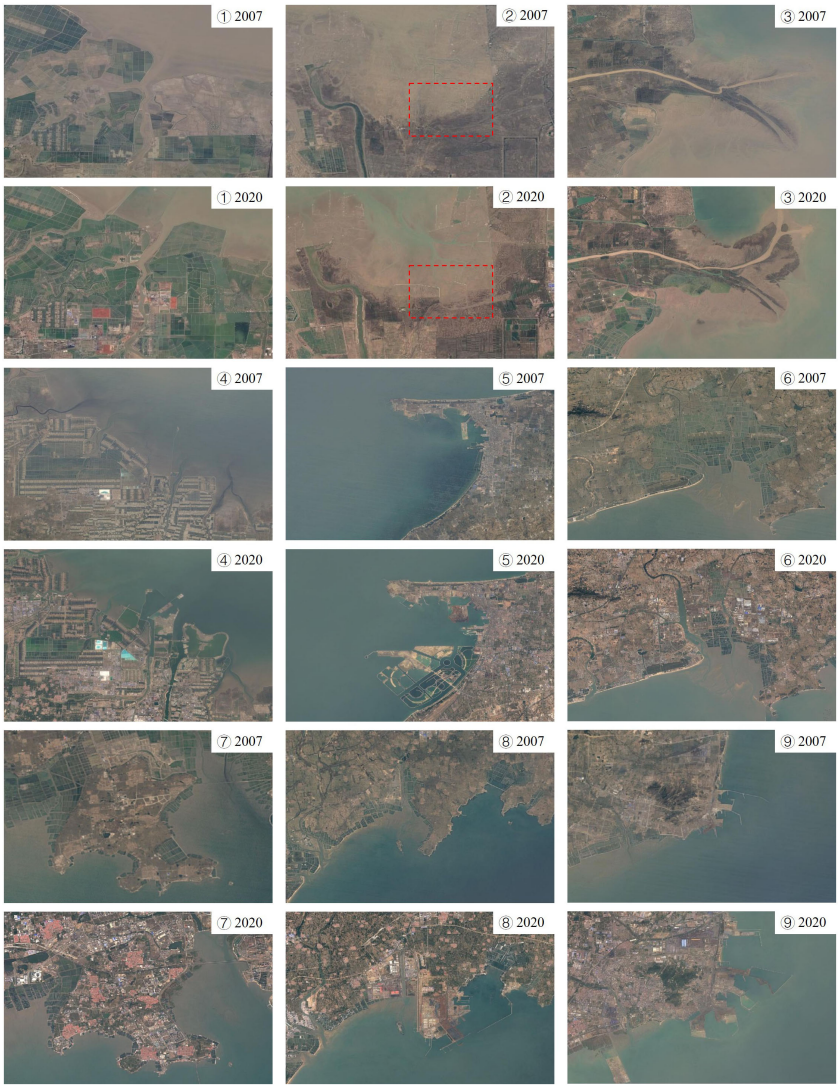

FIGURE 5
Remote sensing images showing typical examples of shoreline change for the period of 2007–2020.

3.4 Changes in sandy shorelines

Although Shandong has many beaches that have been accretionary since the Holocene, they are eroded to date. According to a survey in 2010, the shoreline of the Shandong Peninsula had 123 beaches with a cumulative length of 366 km (approximately accounting for 1/9 of the total shoreline of the peninsula). Among the 25 typical sandy beaches, 19 beaches were eroded between 2010 and 2020. Only 5 beaches were accretionary, and 1 beach was stable. Their rates of retreat were approximately −1.0 m/a, and the rate of vertical erosion varied between −0.06 m/a and −0.10 m/a. 76% of the sandy beaches in Shandong were eroded, indicating that they were predominantly erosive (Table 2).

4 Discussion

4.1 Shoreline change in association with global climate change

4.1.1 Effects of sea level rise

Based on the extensive spatiotemporal observations of the global climate system and numerous indicators, there is little ambiguity that global warming is ongoing. Sea level rise has accelerated over the past 25 years in response to the global warming. Coastal sea levels around China also rise with accelerated rates over the last four decades, and the risk posed by sea level rise to coastal regions in China is amplified by the rapid urbanization. The coastal sea levels of China rise at a rate of

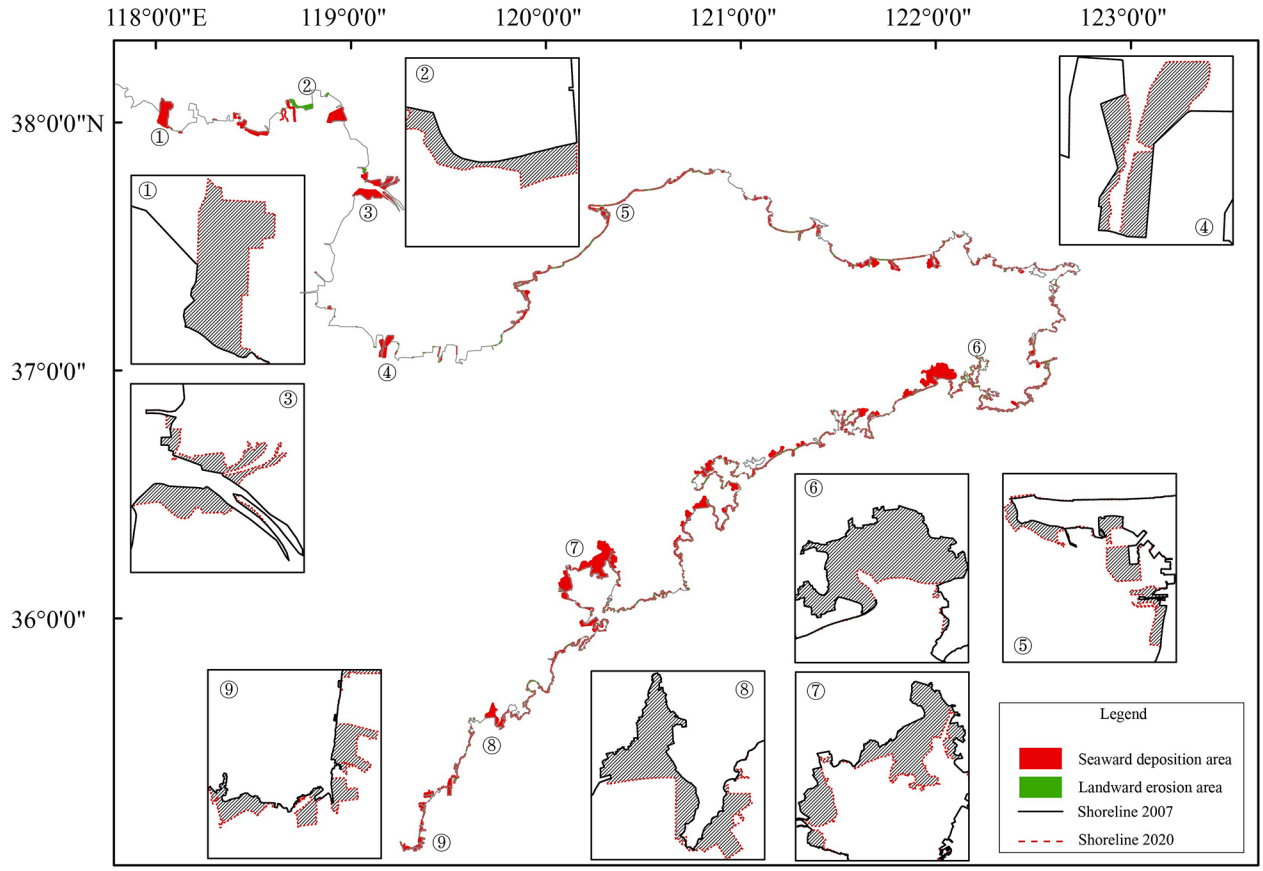

FIGURE 6
Land area changes in the Shandong Peninsula from 2007 to 2020.

3.4 mm/a, higher than the global average. Furthermore, the average coastal sea level of China over the past decade is at its highest level in the last 40 years. Although shoreline change is driven by many factors, there is a direct relation between shoreline change and sea level change (Athanasiou et al., 2020). On the shoreline of the Shandong Peninsula, stabilized artificial shores, rocky shores, and estuaries (whose topography is mainly determined by riverine sediment) are generally insensitive to sea level change. However, sandy shores are the most fragile type of shore as their topography and morphology are extremely prone to sea level change (Castelle et al., 2018). Therefore, the behaviors of the sandy shoreline can serve as an accurate indicator of ecosystem responses to sea level rise. Bruun's rule can be used to detect the shoreline retreatment due to sea level rise (Bruun, 1988). However, Bruun's rule does not account for a variety of factors, including longshore transport and other sources of sediment (Cooper and Pilkey, 2004; Mariotti and Hein, 2022). Nonetheless, it still remains an adequate "rule of thumb" for the analysis of the effects of sea level rise on shoreline change. Bruun's rule is expressed as follows:

$$R = \frac{L}{B + h} S$$

where R is the distance of shoreline retreatment due to sea level rise; h is the depth of closure; L is the horizontal distance between the shoreline and h; B is the dune height above sea level; and S is the sea level rise. Note that $\tan \theta = (B + h)/L$, where θ is the slope of the beach.

According to the field measurements, the slope of the shoreline position varied between 3° and 10° in the Shandong Peninsula. Therefore, $\tan \theta = 0.05 - 0.18$. Since $S = 3.4$ mm/a, Bruun's law gave R values of 0.02–0.07 m. Given that the sandy shoreline had an average recession rate of 1.0 m/a, it may be estimated that the recession caused by sea level rise was relatively small. Hence, sea level rise has only played a very small role in the shoreline changes in the Shandong Peninsula.

4.1.2 Effects of extreme weather

In addition to sea level rises, global warming also increased the frequency and intensity of extreme weather events (e.g.,

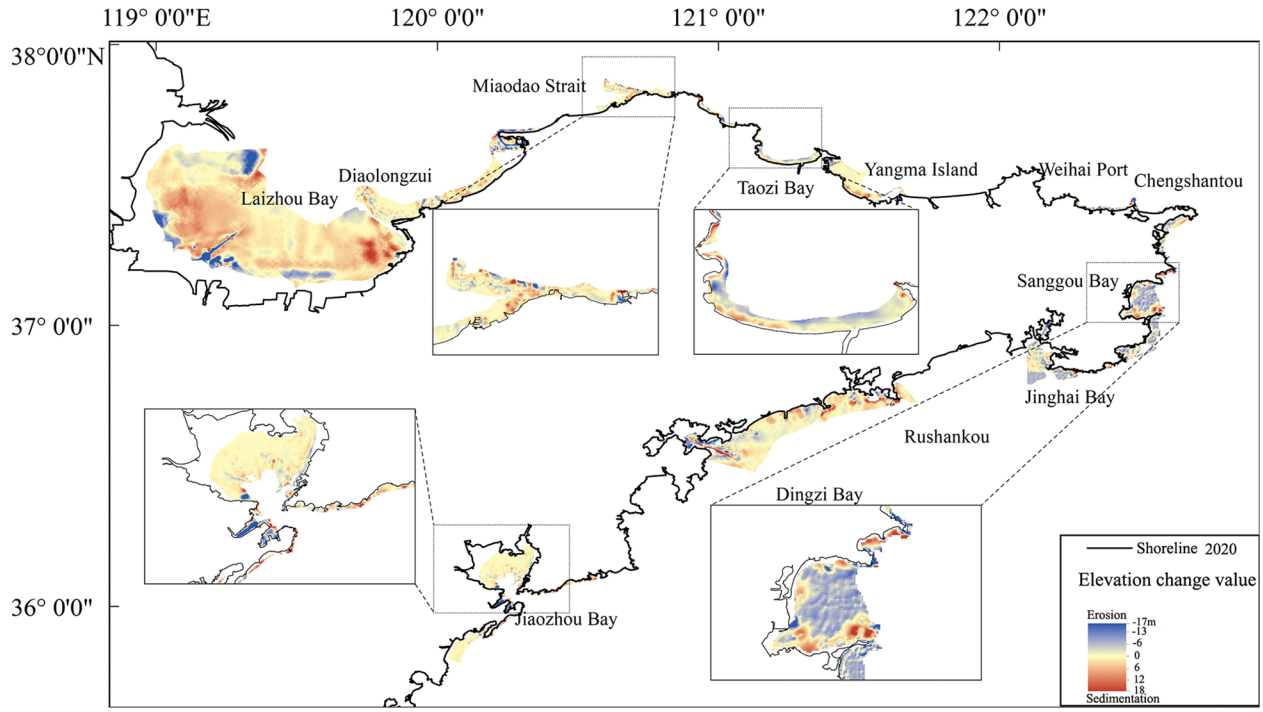

FIGURE 7
Map of erosion and accretion in the inshore waters of Shandong for the period of 2007–2020.

tropical typhoons and storms). Global warming increased the latitudinal temperature gradient between the Western Pacific and Central and Eastern Pacific, which has amplified the vertical shear and relative turbulence of Pacific Northwest windstorms. This, in turn, has affected the spatiotemporal patterns of tropical cyclone activity in the Northwest pacific and brought the entirety of the cyclone lifecycle closer to East Asia. In this regard, the frequency and intensity of tropical cyclones likely further increase in the future (Gu et al., 2016). As the Shandong Peninsula is surrounded on three sides by the sea and has a long and winding shoreline, its shoreline is highly susceptible to hydrological and climatic extremes. Furthermore, an average of 1.1 typhoons made landfall in Shandong each year. Cyclone-induced waves are among the most significant drivers of beach morphology changes (Qi et al., 2010). Storm surges, which can overlap with tidal processes, also play a significant role in

TABLE 1 State of erosion/accretion in typical inshore areas.

Research area	Scouring volume/ $\times10^8m^3$	Silting volume/ $\times10^8m^3$	Net sedimentation volume/ $\times10^8m^3$	Siltation rate/ $\times10^8m^3*a^{-1}$
West Laizhou Bay	1.67	3.8	2.13	0.152
East Laizhou Bay	0.18	1.63	1.46	0.103
Diaolongzui to Miaodao Strait	2.02	2.57	0.56	0.043
Luanjiakou Port to Taozi Bay	0.74	0.97	0.23	0.019
Taozi Bay to Yangma Island	0.83	0.72	-0.10	-0.007
Weihai Port to Jinghai Bay	0.94	2.55	1.62	0.019
Rushankou to Dingzi Bay	1.13	2.91	1.78	0.148
Jiaozhou Bay	0.76	1.34	0.57	0.115

10.3389/fmars.2022.1123067

TABLE 2 Erosion of sandy shores on the Shandong Peninsula.

Shore number	Profile number	Slope at the shoreline position (°)	Distance of shoreline retreatment (m)	Rate of recession (m/a)	Change in beach profile elevation (m)	Rate of vertical erosion (m/a)
1	P01	5.2	/	/	-0.9	-0.10
2	P02	6.3	-3.4	-0.38	-0.4	-0.04
	P03	/	-11.2	-1.24	/	/
3	P04	3.5	-7	-0.8	-1.3	-0.14
	P05	7.1	/	/	-1.4	-0.16
4	P06	10.5	-11	-1.22	-2.2	-0.24
	P07	4.4	45.3	5.03	5	0.56
	P08	2.3	31.3	3.48	2.3	0.26
5	P09	2.5	/	/	1.2	0.13
6	P10	8.3	2	0.22	-0.95	-0.11
	P11	8.5	-4.0	-0.44	-0.55	-0.06
7	P12	3.5	/	/	-0.5	-0.06
	P13	2.9	-5.0	-0.56	-0.8	-0.09
	P14	10.2	/	/	0.7	0.08
8	P15	5.2	10	1.1	-0.5	-0.06
	P16	4.6	3.0	0.3	-0.4	-0.04
9	P17	8.2	-12.0	-1.2	-0.9	-0.09
10	P18	6.0	3.0	0.3	0.6	0.06
11	P19	3.5	-8.0	-0.8	/	/
12	P20	8.0	-4.0	-0.4	0.7	0.07
13	P21	6.5	/	/	-0.6	-0.06
14	P22	3.6	/	/	1.5	0.15
15	P23	9.1	-7	-0.7	-1.0	-0.10
16	P24	1.8	-12	-1.33	-0.7	-0.08
17	P25	1.5	0	0	0	0
18	P26	3.6	/	/	-0.3	-0.03
19	P27	6.2	/	/	-0.2	-0.02
20	P28	3.0	-10	-1.1	0.7	0.08
	P29	3.2	-9.0	-1.0	-0.8	-0.09
21	P30	2.3	/	/	-0.3	-0.03
22	P31	6.5	-10	-1.1	-0.7	-0.08
23	P32	1.5	-14	-1.56	-1.0	-0.10
24	P33	4.0	/	/	-0.5	-0.06
	P34	9.0	/	/	0.3	0.03
25	P35	7.9	/	/	1.0	0.11

shoreline change. Therefore, we studied the beach profile of Wanmi Beach in Haiyang City after Typhoon Lekima passed over Shandong in August 2019, to analyze the effects of extreme weather events on the shoreline (Robinet et al., 2018).

According to tidal data from Qianli Yan station, situated near Haiyang, the average and maximum surge heights when Typhoon Lekima passed through were > 50 cm and 75 cm, respectively. Based on the path of Typhoon Lekima, it was deduced that the typhoon's counter clockwise rotation intensified the impact of southeasterly winds on Wanmi Beach and caused onshore winds to dominate during the typhoon. The typhoon created waves directly struck the beach and caused severe erosion. During the typhoon incident, the storm surge combined with the high tide induced rapid rise in water level, which severely eroded the upper part and foreshore of the beach face. The increase in water level also lifted the underwater surface of the beach, which reduced beach seepage and caused large amounts of beach sediment to be washed into inshore waters. Therefore, typhoons often cause severe beach erosion in a very short time. In the monitored beach area, the shoreline retreated greatly after the typhoon, up to distances greater than 10 m. It was estimated that the passage of Typhoon Lekima caused 2.43×10^4 m^3 of erosion (Gao et al., 2020), this is almost equal to the cumulative erosion that occurred over an entire year under normal hydrodynamic conditions as the erosion at Wanmi Beach between 2018 and 2019 was 2.48×10^4 m^3. Although the beach recovered after the typhoon, the damage caused to the foreshore and coastal dunes could be permanent or take a long time to be mitigated; this is one of the major causes of sandy shoreline retreatment in this region. Therefore, even against a backdrop of widespread erosion in sandy shorelines, extreme weather events, such as typhoons, are gradually becoming the important cause of shoreline retreatment in natural shores (e.g., unstable sandy shores).

4.2 Shoreline change in association with human activities

Evolution of the coastal zone in history has proven to be jointly controlled by marine, terrestrial, and atmospheric factors. More recently, however, human activities have also begun to affect the coastal zone. Since the industrial revolution, human-induced influences on the coastal zone have exceeded natural ones in terms of intensity, extent, and rate. Thus, human activities can be considered as "a third driving force" that is inferior only to the Sun and the Earth's internal energy (Xu et al., 2014). Due to the rapid development of coastal economies on the Shandong Peninsula, the degree of shoreline exploitation, which can be represented by the length of artificial shoreline, has increased. The proportion of artificial shoreline increased from 38.63% in 2007 to 64.04% in 2020.

Due to the seaward sediment load of the Yellow River, the shores on the northwestern part of the Shandong Peninsula (Binzhou, Dongying, and Weifang) are dominated by silty shores. The remainder of the shoreline (Yantai, Weihai, Qingdao, and Rizhao) alternates between rocky and sandy shores. Silty shores have shallow inshore waters and flat tidelands, and their dominant human activities are land reclamations, such as farming (Binzhou and Dongying) and salt evaporation ponds (Weifang). As these activities cause the shoreline to advance toward the sea in parallel with the original shoreline, they only cause small changes in shoreline length even when the land area is expanded greatly. Rocky shores have deep inshore waters and are relatively stable (Swirad et al., 2020). As these shores are an important part of the Binhai Scenic Area, the rocky shores in and around this area are generally well-preserved. These deep inshore waters are also conducive to the development of harbors, which are intensifying at an accelerating pace. Particularly, in various places such as Qingdao and Rizhao, rocky shores were converted to harbors and factories (i.e., artificial shore), which in turn cause the shoreline to advance toward the sea (Figure 8). As sandy shores are valued for their scenic characteristics, they are mainly used as tourist attractions. Therefore, the sandy shoreline mainly consists of preserved natural shoreline and artificially stabilized shoreline. However, the equilibrium between sediment sources and the hydrodynamic environment in the coastal zone has been disrupted by the continuous advancement of other shore types, which causes shoreline retreatment and vertical erosion at sandy shores. The artificial diversion of the Yellow River from the Diaokou course to the Qingshuigou course in 1976 caused sediment accretion around the river mouth, as well as advancement of nearby shorelines toward the sea. Shoreline retreatment is extremely severe at the Feiyan Beach (northern part of the Yellow River Delta) due to the loss of sediment supply from the Yellow River and the intense hydrodynamic actions of the Bohai Sea (Zhang et al., 2016; Zhang et al., 2019).

Shore type is a major constraint for developments in the coastal zone as it may either facilitate or restrict the development of the local marine economy. This works both ways as the development of the coastal zone and marine economy are also important factors for the rate of shoreline change. Up to the date of this study, at Binzhou, Dongying, and Weifang, the shoreline advanced toward the sea at rates of 182.28 m/a, 143.45 m/a, and 99.22 m/a, respectively. At Yantai, Weihai, Qingdao, and Rizhao, the rates of shoreline advancement were 24.58 m/a, 20.88 m/a, 63.99 m/a, and 41.06 m/a, respectively. The rates of shoreline advancement and land area increase were significantly higher at silty shores than other shore types (Figure 9). This may be attributed to two causes: (1) The economies of Yantai, Weihai, Qingdao, and Rizhao are well-developed, and their shorelines were developed and stabilized before the beginning of the study period. However, shoreline advancement still occurred at a few

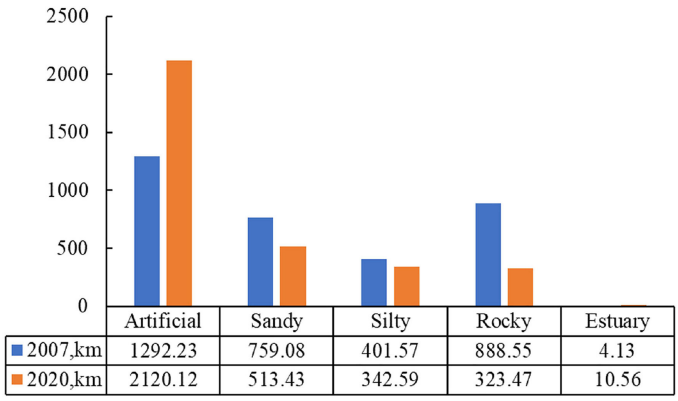

	Artificial	Sandy	Silty	Rocky	Estuary
2007,km	1292.23	759.08	401.57	888.55	4.13
2020,km	2120.12	513.43	342.59	323.47	10.56

FIGURE 8
Shoreline changes at the coastal cities of Shandong. BZ, Binzhou; DY, Dongying; WF, Weifang; YT, Yantai; WH, Weihai; QD, Qingdao; and RZ, Rizhao. See the locations of the shorelines in Figure 1.

sections of the shoreline (e.g., Hongdao Island and Longkou) due to urban expansion. (2) The shorelines of Binzhou, Dongying, and Weifang are dominated by tidelands and with small populations, and they were formed by intense land reclamations in recent years. As the artificial shoreline continues to expand, meandering natural shorelines are gradually replaced by straight and regular artificial shorelines, which may, over time, shorten the shoreline of the Shandong Peninsula. However, the development trends in this region indicated that further greater expanses of coastal ecosystems are required for human activities, thus indicating shoreline advancement as the most dominant trend in the near future.

4.3 Future trends of shoreline change

Globally, due to sea level rise and the intensified artificial impact on coastal and watershed areas, pertinent risks of coastal

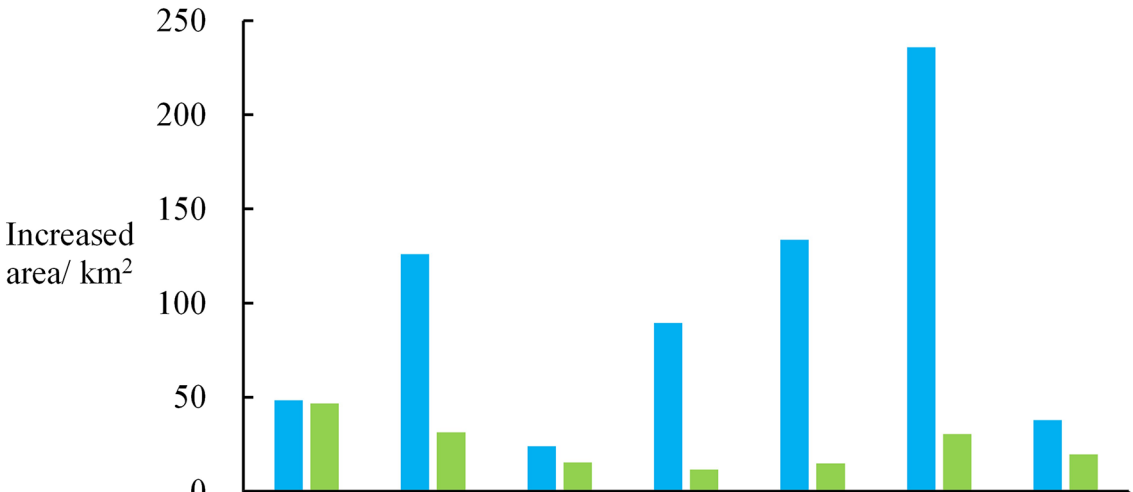

	BZ	DY	WF	YT	WH	QD	RZ
Increased area	48	126	24	89	134	236	38
Increased area/km*100	47	31	15	12	15	30	20

FIGURE 9
Coastal land area changes at the coastal cities of Shandong. BZ, Binzhou; DY, Dongying; WF, Weifang; YT, Yantai; WH, Weihai; QD, Qingdao; and RZ, Rizhao. See the locations of the shorelines in Figure 1.

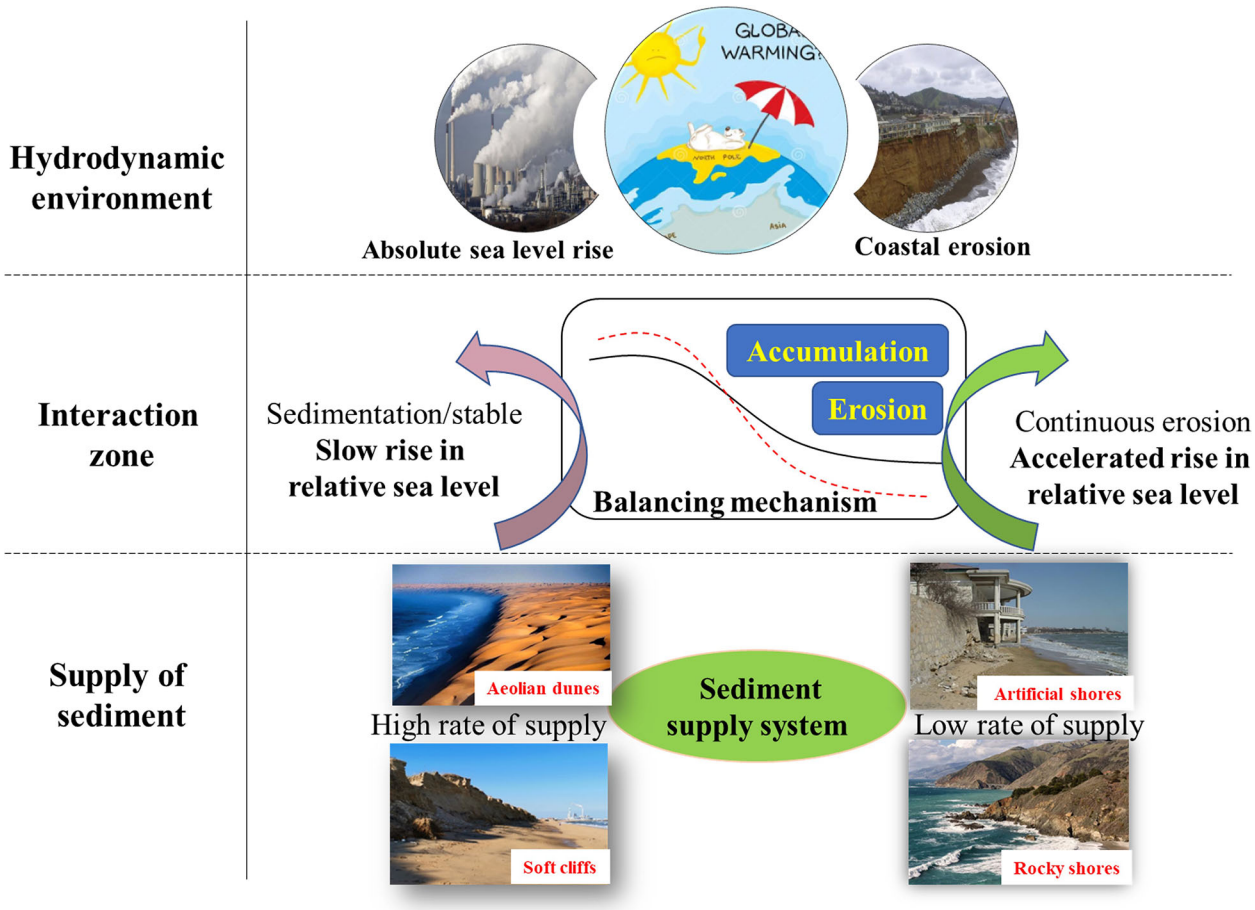

FIGURE 10
Balancing between the supply of sediment and hydrodynamic environment in the coastal zone.

geohazards significantly increased. Of the three elements that govern the coastal zone (supply of sediment, hydrodynamic environment, and interaction zone), it is the balance between sediment supply and marine energies that determines the stability of the shore. However, global climate change is driving absolute sea level rises and an increasing frequency and severity of climatic and hydrological extremes (Oddo et al., 2020). This in turn increases the potency of coastal hydrodynamics, thus exacerbating coastal erosion (Harley et al., 2017). Human activities have altered the transport and supply of sediment to the coastal zone, which amplified erosion caused by sea level rise. The synchronous relationship between coastal sediment accumulation and hydrodynamic changes is the key to understanding how the supply of sediment and marine energies constrain each other (Figure 10) as well as the trends of shoreline change. From 2007 to 2020, the inshore area of the Shandong Peninsula was dominated by sedimentation due to the deposition of riverine input and erosion only occurred in hotspots. As the riverine input decreased, eroded coastal materials became a larger part of the seaward sediment load. At shores with aeolian dunes or soft soil cliffs, a high rate of sediment supply ensues, thus slowing down relative rises in sea level (Cooper et al., 2020). Conversely, the low rate of sediment supply at rocky and artificial shores exacerbates relative sea level rises. At shores stabilized by artificial structures, vertical beach erosion dominates if there is no space for shoreline retreat.

In the short term, human activities exert fast-acting and intense effects on the shoreline. For example, land reclamation, harbor construction, sand mining from coastal zone (Wang et al., 2021), and shoreline stabilization quickly and directly (or indirectly) alter the modality of sediment transport and seaward sediment loads and then disrupt the balance between the supply of sediment and hydrodynamic environment. Although it is not possible for hydrodynamic forces to break through fortified artificial shores, other shores in their vicinity are eroded, in particular, shores made of soft and loose materials, such as sandy and silty shores. This results in shoreline retreat and vertical beach erosion at those shores. In addition, sand mining activities have decreased significantly, but the coastal erosion caused by it lasts for a long time (Jonah et al., 2017).

Unlike sea level rise, coastal erosion responses to human activity are temporally rapid and spatially localized (Nourdi et al., 2021). For example, the construction of a groin at Foshou Bay in Rizhao City in 1970 impeded the NNE-to-SSW transport of sediment. This led to rapid sedimentation on the northern side of the jetty and erosion on the southern beach, which disappeared after 4 years. Guancaowang Village, downstream from Foshou Bay, also suffered from severe erosion (Figure 11). The construction of Port Gangluan in the northern suburbs of Longkou impeded longshore transport in the SW direction, with severe shore erosion and retreat in the downstream. Between 2003 and 2020, the maximum erosion-induced shoreline retreat was 56 m (Figure 11) (Li B. et al., 2013). After the environmental changes caused by human activity have stabilized, coastal erosion equilibrates after a long period of time. The Feiyan Beach took 40 years to reach stabilization status after the Yellow River was diverted away from the Diaokou course, following successive periods of gradually weakening erosion (Chen et al., 2005). Between 2007 and 2020, the coastal land area of the Shandong Peninsula increased by 672.40 km^2, mainly from artificial land reclamations and some land forming in the Yellow River delta. The rate of natural shoreline retreat was only 22.27 km^2. Owing to the large difference between shoreline advancement and recession in the Shandong Peninsula, its coastal zone is experiencing a severe imbalance between sediment supply and the hydrodynamic environment. Therefore, the unprotected shorelines of this region are at disproportionate risk of severe erosion since a long time.

In the long term, sea level rise caused by global climate change is most likely to define the trends of shoreline evolution. Temperature rise drives the thermal expansion of the sea and accelerates ice cap and glacier melting, thus boosting the rise in global average sea level. As this trend is irreversible on the century-to-millennium scale, the peril of coastal erosion continues to loom over coastal regions across the globe. The coastal sea level of China is predicted to rise by 68–170 mm in 2050 (China Sea Level Bulletin, 2021). Given the uncertainty in the effects of ice cap melting, several scenarios were predicted; in the high scenario, global sea level rise may reach 2 m by 2100 and 5 m by 2150. The corresponding retreat of sandy shorelines (in the extreme scenario) may reach 3.4 m (Figure 12), 40 m (Figure 12), and 100 m (Figure 12) by 2050, 2100, and 2150, respectively (Vousdoukas et al., 2020). Shoreline retreatment further increases at silty shores. On the decadal scale, the shoreline retreatment caused by sea level rise is small relative to that caused by human activities. On the century scale or greater, however, sea level rise exerts disastrous effects on the shoreline. After the ice caps have fully melted, the northern plains of the Shandong Peninsula will be submerged, and the continuous erosion of sandy shores on the southern and eastern sides of the peninsula will ultimately conjoin the Yellow and Bohai seas. The Shandong Peninsula will thus be transformed into an island (Figure 12).

5 Conclusion

Between 2007 and 2020, the shoreline of the Shandong Peninsula decreased by 35.37 km, but the length of artificial shoreline increased by 827.89 km, which is continuously

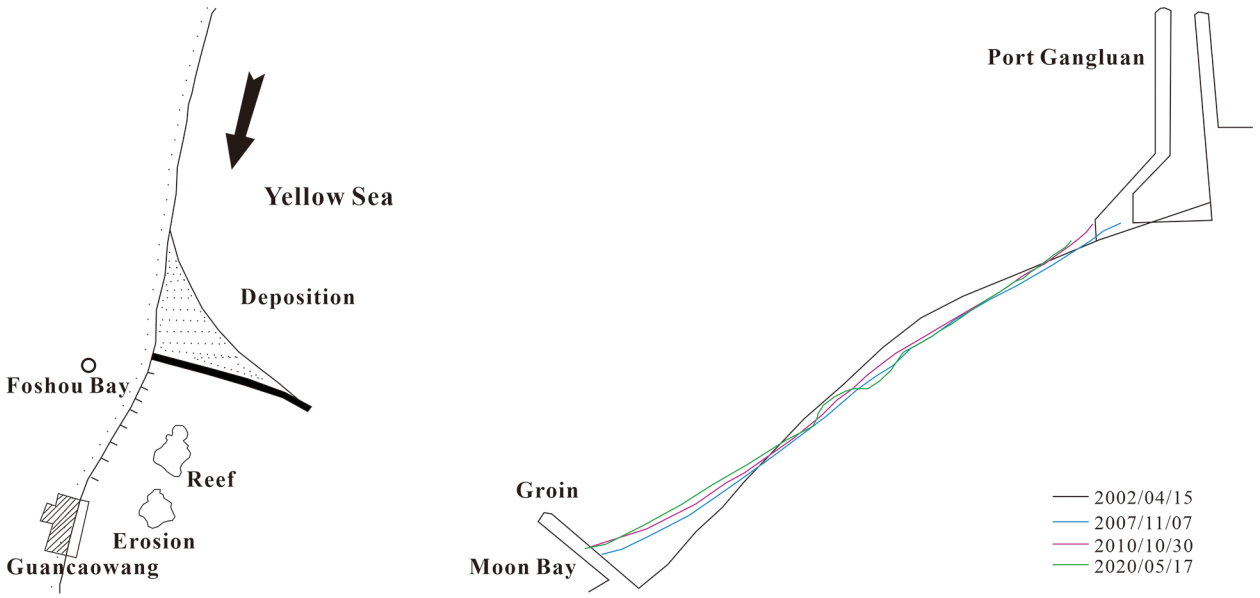

FIGURE 11
Effects of human activities on shoreline change.

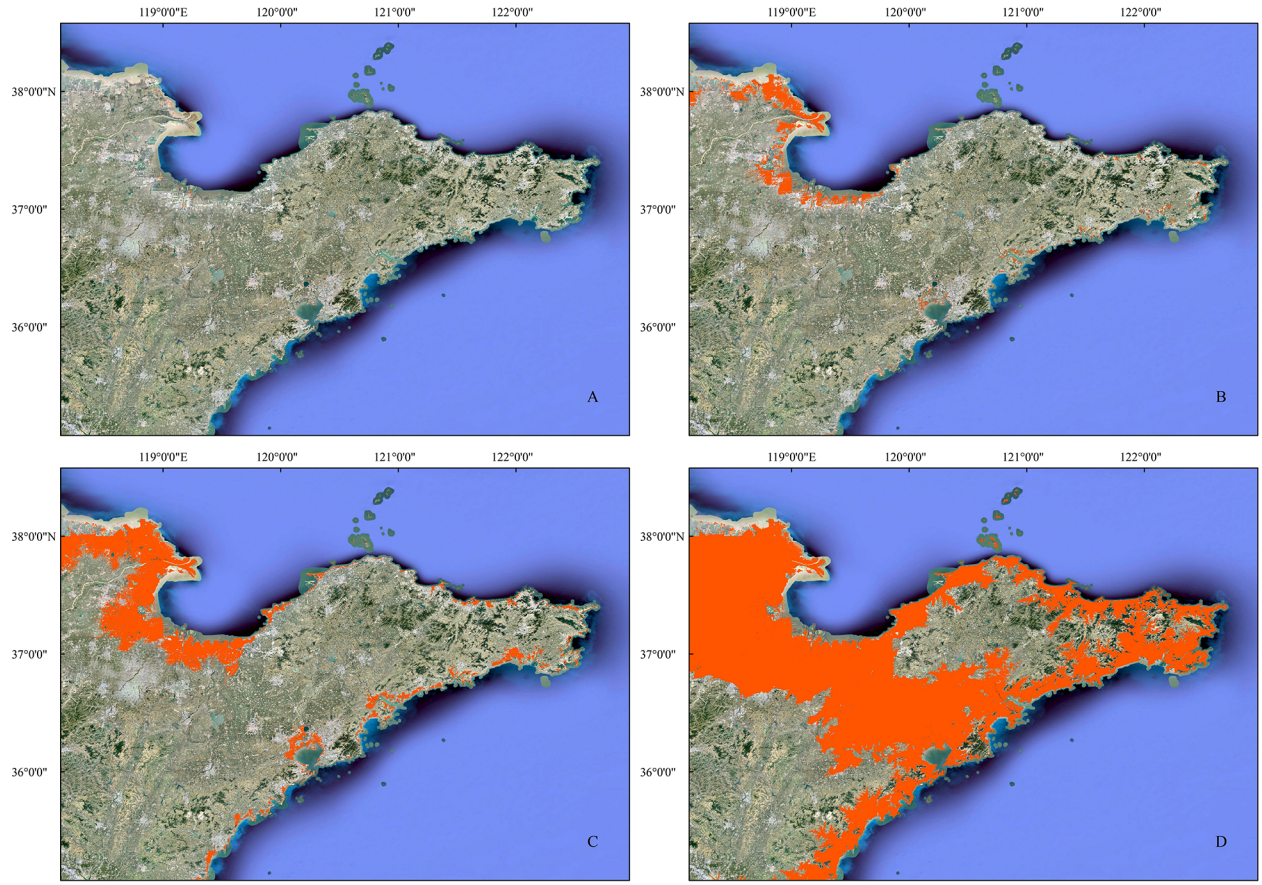

FIGURE 12
The areas of the Shandong Peninsula that will be submerged due to sea level rise **(A)**: 2050; **(B)**: 2100; **(C)**: 2150; and **(D)**: after all ice caps were melted.

increasing at an accelerated pace. Within the same period, natural shoreline retention decreased by 25.41%. The net increase in land area was 672.40 km^2; in addition to natural accretion in the estuaries of large rivers, this was mainly caused by human-induced disturbances, such as land reclamation and harbor construction. Shoreline shortening was mainly caused by the replacement of meandering natural shores with straight and regularly shaped artificial shorelines. Currently, shoreline evolution in the study area was dominated by shoreline advancement due to the development of the coastal zone.

Among the three governing factors of the coastal zone (i.e., the supply of sediment, hydrodynamic environment, and interaction zone), shore stability mainly depends on the balance between sediment supplies and marine energies. In the short term, shoreline evolution is dominated by human activities, and the effects of sea level rise over the last decade have been relatively small. In the long term, however, shoreline evolution will be dominated by global climate change; on time scales in the centuries or greater, sea level rise will be the dominant effect in shoreline evolution. Human-driven shoreline advancement is causing shoreline retreat and beach erosion at the unprotected natural shores of the Shandong Peninsula. Unless preventive and mitigative measures are implemented at the required rate, the Shandong Peninsula will eventually become an island after its low-lying areas have been submerged by sea level rise.

Data availability statement

The original contributions presented in the study are included in the article/supplementary material. Further inquiries can be directed to the corresponding authors.

Author contributions

WG, PL, JD, and JL contributed to conception and design of the study. ZZ, XW, and BL organized the database. WG, SG, ZZ, XW, and BL performed the statistical analysis. WG wrote the

first draft of the manuscript. PL and JL wrote sections of the manuscript. All authors contributed to the article and approved the submitted version.

Funding

This study is supported by the National Key Research and Development Program of China (Grant No. 2022YFC3106104), the Shandong Provincial Natural Science Foundation, China (Grant No. ZR2021MD098), the Marine S&T Fund of Shandong Province for Pilot National Laboratory for Marine Science and Technology (Qingdao) (Grant No.2018SDKJ0503-3), the NSFC-Shandong Joint Fund for Marine Science Research Centers (Grant No. U1606401), and the Ocean Public Welfare Scientific Research Project (Grant No.201005010).

Conflict of interest

The authors declare that the research was conducted in the absence of any commercial or financial relationships that could be construed as a potential conflict of interest.

Publisher's note

References

Alley, R. B., Clark, P. U., Huybrechts, P., and Joughin, I. (2005). Ice-sheet and sea-level changes. *Science.* 5747, 456–460. doi: 10.1126/science.111461

Anthony, E. J., Brunier, G., Besset, M., Goichot, M., Dussouillez, P., and Nguyen, V. L. (2015). Linking rapid erosion of the Mekong river delta to human activities. *Sci. Rep.* 5, 1–12. doi: 10.1038/srep14745

Athanasiou, P., van Dongeren, A., Giardino, A., Vousdoukas, M. I., Ranasinghe, R., and Kwadijk, J. (2020). Uncertainties in projections of sandy beach erosion due to sea level rise: An analysis at the European scale. *Sci. Rep.* 10, 1–14. doi: 10.1038/s41598-020-68576-0

Barbier, E. B., Hacker, S. D., Kennedy, C., Koch, E. W., Stier, A. C., and Silliman, B. R. (2011). The value of estuarine and coastal ecosystem services. *Ecol. Monogr.* 2, 169–193. doi: 10.1890/10-1510.1

Bruun, P. (1988). The bruun rule of erosion by sea-level rise: a discussion on large-scale two-and three-dimensional usages. *J. Coastal. Res.* 4, 627–648.

Cai, F., Su, X., Liu, J., Li, B., and Lei, G. (2009). Coastal erosion in China under the condition of global climate change and measures for its prevention. *Prog. Nat. Sci.* 4, 415–426. doi: 10.1016/j.pnsc.2008.05.034

Castelle, B., Guillot, B., Marieu, V., Chaumillon, E., Hanquiez, V., Bujan, S., et al. (2018). Spatial and temporal patterns of shoreline change of a 280-km high-energy disrupted sandy coast from 1950 to 2014: SW France. *Estuar. Coast. Shelf.* S. 200, 212–223. doi: 10.1016/j.ecss.2017.11.005

Chen, S., Zhang, G., Chen, X., Zhang, J., and Xu, C. (2005). Coastal erosion feature and mechanism at feiyantan in the yellow river delta. *Mar. Geology Quaternary Geology.* 3, 9–14. doi: 10.16562/j.cnki.0256-1492.2005.03.002

Chu, L., Oloo, F., Sudmanns, M., Tiede, D., Hölbling, D., Blaschke, T., et al. (2020). Monitoring long-term shoreline dynamics and human activities in the hangzhou bay, China, combining daytime and nighttime EO data. *Big Earth Data.* 3, 242–264. doi: 10.1080/20964471.2020.1740491

Cooper, J. A. G., Masselink, G., Coco, G., Short, A. D., Castelle, B., Rogers, K., et al. (2020). Sandy beaches can survive sea-level rise. *Nat. Clim. Change.* 11, 993–995. doi: 10.1038/s41558-020-00934-2

Cooper, J. A. G., and Pilkey, O. H. (2004). Sea-Level rise and shoreline retreat: time to abandon the bruun rule. *Global. Planet. Change.* 3-4, 157–171. doi: 10.1016/j.gloplacha.2004.07.001

Crowell, M., Leatherman, S. P., and Buckley, M. K. (1993). Shoreline change rate analysis: long term versus short term data. *Shore Beach.* 2, 13–20.

Davenport, J., and Davenport, J. L. (2006). The impact of tourism and personal leisure transport on coastal environments: a review. *Estuar. Coast. Shelf.* S. 1-2, 280–292. doi: 10.1016/j.ecss.2005.11.026

Dong, Z., Fu, D., Liu, D., Yu, G., and Zhang, X. (2019). Study on the extraction of waterline with different landforms based on ZY-3 remote sensing images. *Hydrographic surveying charting.* 2, 34–39. doi: 10.3969/j.issn.1671-3044.2019.02.008

Ehlert, D., and Zickfeld, K. (2018). Irreversible ocean thermal expansion under carbon dioxide removal. *Earth. Syst. Dynam.* 1, 197–210. doi: 10.5194/esd-9-197-2018

Esteves, L. S., Toldo, E. E., Dillenburg, S. R., and Tomazelli, L. J. (2002). Long- and short-term coastal erosion in southern Brazil. *J. Coastal. Res.* 36, 273–282. doi: 10.2112/1551-5036-36.sp1.273

Flor-Blanco, G., Alcántara-Carrió, J., Jackson, D. W. T., Flor, G., and Flores-Soriano, C. (2021). Coastal erosion in NW Spain: Recent patterns under extreme storm wave events. *Geomorphology.* 387, 107767. doi: 10.1016/j.geomorph.2021.107767

Fraser, C., Bernatchez, P., and Dugas, S. (2017). Development of a GIS coastal land-use planning tool for coastal erosion adaptation based on the exposure of buildings and infrastructure to coastal erosion, québec, Canada. *Geomat. Nat. Haz. Risk.* 2, 1103–1125. doi: 10.1080/19475705.2017.1294114

Fred, E. C., and Andrew, M. (1996). Defining and interpreting shoreline change. *Ocean. Coast. Manage.* 3, 129–151. doi: 10.1016/S0964-5691(96)00059-2

Gao, W., Li, P., Gao, S., Tian, Z., Li, B., and Liu, J. (2020). Response process of the haiyang beach evolution to typhoon lekima in Shandong province. *HaiyangXuebao* 11, 88–99. doi: 10.3969/j.issn.0253–4193.2020.11.009

Gracia, A., Rangel-Buitrago, N., Oakley, J. A., and Williams, A. T. (2018). Use of ecosystems in coastal erosion management. *Ocean. Coast. Manage.* 156, 277–289. doi: 10.1016/j.ocecoaman.2017.07.009

Grottoli, E., Cilli, S., Ciavola, P., and Armaroli, C. (2020). Sedimentation at river mouths bounded by coastal structures: A case study along the Emilia-romagna coastline, Italy. *J. Coastal. Res.* 95 (SI), 505–510. doi: 10.2112/SI95-098.1

Gu, C., Kang, J., Yan, G., and Chen, Z. (2016). Spatial and temporal variability of Northwest Pacific tropical cyclone activity in a global warming scenario. *J. Trop. Meteorol.* S1, 15–23. doi: 10.16555/j.1006-8775.2016.S1.002

Harley, M. D., Turner, I. L., Kinsela, M. A., Middleton, J. H., Mumford, P. J., Splinter, K. D., et al. (2017). Extreme coastal erosion enhanced by anomalous extratropical storm wave direction. *Sci. Rep.* 7, 1–9. doi: 10.1038/s41598-017-05792-1

Hegde, A. V., and Akshaya, B. J. (2015). Shoreline transformation study of karnataka coast: geospatial approach. *Aquat. Procedia.* 4, 151–156. doi: 10.1016/j.aqpro.2015.02.021

Himmelstoss, E. A., Henderson, R. E., Kratzmann, M. G., and Farris, A. S. (2018). Digital shoreline analysis system (DSAS) version 5.0 user guide: U.S. *Geological Survey Open-File Rep.* 2018–1179, 110 p. doi: 10.3133/ofr20181179

Hou, X., Wu, T., Hou, W., Chen, Q., Wang, Y., and Yu, L. (2016). Characteristics of coastline changes in mainland China since the early 1940s. *Sci. China. Earth. Sci.* 9, 1791–1802. doi: 10.1007/s11430-016-5317-5

Jonah, F. E., Adams, O., Aheto, D. W., Jonah, R. E., and Mensah, E. A. (2017). Coastal zone management challenges in Ghana: issues associated with coastal sediment mining. *J. Coast. Conserv.* 21, 343–353. doi: 10.1007/s11852-017-0511-y

Li, G., Gong, L., Yang, J., Ding, D., Li, B., Cao, L., et al. (2013). Beach erosion along the coast of Shandong province and protection countermeasures. *Mar. Geology Quaternary Geology*. 5, 35–45. doi: 10.3724/SP.J.1140.2013.05035

Li, B., Zhuang, Z., Cao, L., and Du, F. (2013). Countermeasures against coastal erosion for protection of the sandy coast in Shandong province. *Mar. Geology Frontiers*. 5, 47–54. doi: 10.16028/j.1009-2722.2013.05.006

Luo, S., Cai, F., Liu, H., Lei, G., Qi, H., and Su, X. (2015). Adaptive measures adopted for risk reduction of coastal erosion in the people's republic of China. *Ocean. Coast. Manage.* 103, 134–145. doi: 10.1016/j.ocecoaman.2014.08.008

Mariotti, G., and Hein, C. J. (2022). Lag in response of coastal barrier-island retreat to sea-level rise. *Nat. Geosci.* 15, 633–638. doi: 10.1038/s41561-022-00980-9

McGranahan, G., Balk, D., and Anderson, B. (2007). The rising tide: assessing the risks of climate change and human settlements in low elevation coastal zones. *Environ. Urban.* 1, 17–37. doi: 10.1177/0956247807076960

Meinshausen, M., Smith, S. J., Calvin, K., Daniel, J. S., Kainuma, M. L., Lamarque, J. F., et al. (2011). The RCP greenhouse gas concentrations and their extensions from 1765 to 2300. *Climatic Change.* 1, 213–241. doi: 10.1007/s10584-011-0156-z

Mentaschi, L., Vousdoukas, M. I., Pekel, J. F., Voukouvalas, E., and Feyen, L. (2018). Global long-term observations of coastal erosion and accretion. *Sci. Rep.* 8, 1–11. doi: 10.1038/s41598-018-30904-w

Nerem, R. S., Beckley, B. D., Fasullo, J. T., Hamlington, B. D., Masters, D., and Mitchum, G. T. (2018). Climate-change–driven accelerated sea-level rise detected in the altimeter era. *Proc. Natl. Acad. Sci.* 9, 2022–2025. doi: 10.1073/pnas.1717312115

Nicholls, R. J. (2004). Coastal flooding and wetland loss in the 21st century: changes under the SRES climate and socio-economic scenarios. *Global. Environ. Chang.* 1, 69–86. doi: 10.1016/j.gloenvcha.2003.10.007

Nicholls, R. J., and Cazenave, A. (2010). Sea-Level rise and its impact on coastal zones. *Science.* 5985, 1517–1520. doi: 10.1126/science.1185782

Nourdi, N. F., Raphael, O., Grégoire, A. O., Rudant, J. P., and Minette, T. E. (2021). Seasonal to decadal scale shoreline changes along the cameroonian coastline, bay of bonn To 2020). *Reg. Stud. Mar. Sci.* 81, 101798. doi: 10.1016/j.rsma.2021.101798

Oddo, P. C., Lee, B. S., Garner, G. G., Srikrishnan, V., Reed, P. M., Forest, C. E., et al. (2020). Deep uncertainties in sea-level rise and storm surge projections: Implications for coastal flood risk management. *Risk. Anal.* 1, 153–168. doi: 10.1111/risa.12888

Pan, Y., Yin, S., Chen, Y. P., Yang, Y. B., Xu, C. Y., and Xu, Z. S. (2022). An experimental study on the evolution of a submerged berm under the effects of regular waves in low-energy conditions. *Coast. Eng.* 176, 104169. doi: 10.1016/j.coastaleng.2022.104169

Qi, H., Cai, F., Lei, G., Cao, H., and Shi, F. (2010). The response of three main beach types to tropical storms in south China. *Mar. Geol.* 1-4, 244–254. doi: 10.1016/j.margeo.2010.06.005

Ranasinghe, R. (2016). Assessing climate change impacts on open sandy coasts: A review. *Earth-Sci. Rev.* 160, 320–332. doi: 10.1016/j.earscirev.2016.07.011

Ranasinghe, R., and Stive, M. J. (2009). Rising seas and retreating coastlines. *Climatic Change.* 3, 465–468. doi: 10.1007/s10584-009-9593-3

Robinet, A., Idier, D., Castelle, B., and Marieu, V. (2018). A reduced-complexity shoreline change model combining longshore and cross-shore processes: The LX-shore model. *Environ. Modell. Software* 109, 1–16. doi: 10.1016/j.envsoft.2018.08.010

Swirad, Z. M., Rosser, N. J., Brain, M. J., Rood, D. H., Hurst, M. D., Wilcken, K. M., et al. (2020). Cosmogenic exposure dating reveals limited long-term variability in erosion of a rocky coastline. *Nat. Commun.* 1, 1–9. doi: 10.1038/s41467-020-17611-9

Temmerman, S., Meire, P., Bouma, T. J., Herman, P. M., Ysebaert, T., and De Vriend, H. J. (2013). Ecosystem-based coastal defence in the face of global change. *Nature.* 7478, 79–83. doi: 10.1038/nature12859

Thieler, E. R., Himmelstoss, E. A., Zichichi, J. L., and Ergul, A. (2009). The Digital Shoreline Analysis System (DSAS) version 4.0-an ArcGIS extension for calculating shoreline change. *US Geological Survey*. 2008-1278. doi: 10.3133/ofr20081278

Vousdoukas, M. I., Ranasinghe, R., Mentaschi, L., Plomaritis, T. A., Athanasiou, P., Luijendijk, A., et al. (2020). Sandy coastlines under threat of erosion. *Nat. Clim. Change.* 3, 260–263. doi: 10.1038/s41558-020-0697-0

Wang, Y., Tian, Z., Li, X., and Sun, H. (2021). Coastal erosion mechanism and its prevention in haiyang. *Mar. Sci.* 12, 18–30. doi: 10.11759/hykx20210202001

Warrick, J. A., Stevens, A. W., Miller, I. M., Harrison, S. R., Ritchie, A. C., and Gelfenbaum, G. (2019). World's largest dam removal reverses coastal erosion. *Sci. Rep.* 9, 1–12. doi: 10.1038/s41598-019-50387-7

Widlansky, M. J., Long, X., and Schloesser, F. (2020). Increase in sea level variability with ocean warming associated with the nonlinear thermal expansion of seawater. *Commun. Earth Environment.* 1, 1–12. doi: 10.1038/s43247-020-0008-8

Williams, A. T., Rangel-Buitrago, N., Pranzini, E., and Anfuso, G. (2018). The management of coastal erosion. *Ocean. Coast. Manage.* 156, 4–20. doi: 10.1016/j.ocecoaman.2017.03.022

Xue, Z., Feng, A., Yin, P., and Xia, D. (2009). Coastal erosion induced by human activities: A northwest bohai Sea case study. *J. Coastal. Res.* 3, 723–733. doi: 10.2112/07-0959.1

Xu, L., Li, J., Li, W., Zhao, S., Yuan, Q., Wang, M., et al. (2014). Progress in impact of human activities on coastal resource and environment. *J. Nanjing Normal Univ. (Natural Sci. Edition)* 3, 124–131. doi: 10.3969/j.issn.1001-4616.2014.03.023

Xu, X., Peng, H., Xu, Q., Xiao, H., and Benoit, G. (2009). Land changes and conflicts coordination in coastal urbanization: a case study of the Shandong peninsula in China. *Coast. Manage.* 1, 54–69. doi: 10.1080/08920750802612788

Yates, M. L., Guza, R. T., and O'reilly, W. C. (2009). Equilibrium shoreline response: Observations and modeling. *J. Geophys. Res-Oceans.* 114 (C09014), 1–16. doi: 10.1029/2009JC005359

Yin, P., Duan, X. Y., Gao, F., Li, M. N., Lü, S. H., Qiu, J. D., et al. (2018). Coastal erosion in Shandong of China: status and protection challenges. *China. Geol.* 4, 512–521. doi: 10.31035/cg2018073

Yin, H., Qi, H., Cai, F., Zhang, C. H., Liu, G., Zhao, S. H., et al. (2022). Sandy coastline fine extraction and correction method based on high resolution image. *HaiyangXuebao.* 4, 143–152. doi: 10.12284/hyxb2022084

Zhang, K., Douglas, B. C., and Leatherman, S. P. (2004). Global warming and coastal erosion. *Climatic Change.* 1, 41–58. doi: 10.1023/B:CLIM.0000024690.32682.48

Zhang, X., Lu, K., Yin, P., and Zhu, L. (2019). Current and future mudflat losses in the southern huanghe delta due to coastal hard structures and shoreline retreat. *Coast. Eng.* 152, 103530. doi: 10.1016/j.coastaleng.2019.103530

Zhang, X., Tan, X., Hu, R., Zhu, L., Wu, C., and Yang, Z. (2021). Using a transect-focused approach to interpret satellite images and analyze shoreline evolution in haiyang beach, China. *Mar. Geol.* 438, 1–16. doi: 10.1016/j.margeo.2021.106526

Zhang, X., Zhang, Y., Ji, Y., Zhang, Y., and Yang, Z. (2016). Shoreline change of the northern yellow river (Huanghe) delta after the latest deltaic course shift in 1976 and its influence factors. *J. Coastal. Res.* 74 (10074), 48–58. doi: 10.2112/SI74-005.1

frontiers | Frontiers in Marine Science

TYPE Original Research
PUBLISHED 12 January 2023
DOI 10.3389/fmars.2022.1073345

OPEN ACCESS

EDITED BY
Yi Pan,
Hohai University, China

REVIEWED BY
Shuxue Liu,
Dalian University of Technology, China
Zhiyao Song,
Nanjing Normal University, China
Gang Wang,
Hohai University, China

*CORRESPONDENCE
Zijun Zhou
charlebilly@163.com

SPECIALTY SECTION
This article was submitted to Coastal Ocean Processes, a section of the journal Frontiers in Marine Science

RECEIVED 18 October 2022
ACCEPTED 09 December 2022
PUBLISHED 12 January 2023

CITATION
Zhou Z, Sun Z, Zhou Y, Zuo Q, Wang H, Chen Y and Huang F (2023) Laboratory study of the combined wave and surge overtopping-induced normal stress on dike.
Front. Mar. Sci. 9:1073345.
doi: 10.3389/fmars.2022.1073345

Laboratory study of the combined wave and surge overtopping-induced normal stress on dike

Zijun Zhou[1,2]*, Zhongbing Sun[1,2], Yiren Zhou[1,2], Qihua Zuo[1,2], Hongchuan Wang[1,2], Yongping Chen[1,3] and Feiyang Huang[1,3]

[1]State Key Laboratory of Hydrology-Water Resources and Hydraulic Engineering, Nanjing Hydraulic Research Institute, Nanjing, China, [2]Nanjing Hydraulic Research Institute, Nanjing, China, [3]College of Harbor, Coastal and Offshore Engineering, Hohai University, Nanjing, China

Normal stress on dikes is one of the most critical parameters for a sound dike design. With more rapidly rising sea levels due to global warming, dikes are seriously threatened by overtopping induced by the combination of wave and storm surge. Compared with wave overtopping on positive freeboard, the curling breaking wave on dikes induced by the combined wave and surge overtopping may destroy the weakly protected dike crest and landward slope. Thus, in order to prevent severe damage to dikes, it is necessary to fully understand the normal stress induced by the combined wave and surge overtopping. In this paper, physical model tests were carried out to study the normal stress on dike induced by the combined wave and surge overtopping. Two characteristics of normal stress on dike were observed. The spatial distribution of normal stress on dike was also analyzed. It was found that the Weibull distribution can be used to effectively describe the statistical distribution of peak normal stresses. Furthermore, by curve fitting of the laboratory measured data, the Weibull factors on the part of the crest and the upper part of the landward slope were obtained.

KEYWORDS

dike, combined wave and surge overtopping, normal stress, weibull distribution, physical model

1 Introduction

The normal stress on dikes is one of the most critical parameters in their design. In conventional dikes, the dike crest is normally higher than the sea level (positive freeboard), and the seaward slope is also well protected with an armor layer and is able to withstand strong wave impacts. Several previous studies have focused on the normal stress (wave pressure) induced by waves on the seaward slope under positive

freeboard (e.g., Hattori et al., 1994; Jensen et al., 2014; Zhou et al., 2020; Celi et al., 2021; Pan et al., 2022; Raby et al., 2022). These studies found that the large value of normal stress often occurs when the breaking wave swashes directly against the seaward slope (Hattori et al., 1994).

With more rapidly rising sea levels due to global warming (IPCC, 2012), there is a serious threat to dikes induced by the combined wave and surge overtopping (i.e., wave overtopping under negative freeboard) (Hughes, 2008). For example, during Hurricane Katrina in 2005, the combined wave and surge overtopping caused more than 50 breaches of dikes in New Orleans (ASCE Hurricane Katrina External Review Panel, 2007). Compared with the threat induced by wave overtopping on positive freeboard, the curling breaking wave on dikes induced by the combined wave and surge overtopping may cause more severe damage on the less protected, vulnerable dike crest and landward slope, although they are paved with grass or gravel.

After Hurricane Katrina, many hydraulic parameters, such as the average overtopping discharge, the individual wave overtopping volumes, flow velocity, flow thickness, turbulent kinetic energy, and the shear stress of the combined wave and surge overtopping, have been investigated and thoroughly studied (e.g., Reeve et al., 2008; Hughes and Nadal, 2009; Hughes and Nadal, 2009; Hughes et al., 2011; Li et al., 2012; Pan et al., 2012; Pan et al., 2013a; Pan et al., 2013b; Yuan et al., 2014; Pan et al., 2015; EurOtop, 2017; Pan et al., 2020). Despite this, the normal stress on the dike crest and the landward slope has been seldom discussed and is still not well understood. This is because, under a high value of negative freeboard, the overtopping flow of the combined wave and surge is similar to the surge-only overflow, which passes the dike crest smoothly and causes high shear stress along the dike, the normal stress being small enough to be neglected. However, under a lower value of negative freeboard (Pan et al., 2020), the overtopping flow of the combined wave and surge is similar to the wave-only overtopping flow. The curling breaking wave may be generated and swashed downward directly against the dike crest or on the landward slope. In this case, a large normal stress is exerted on the dike crest or on the landward slope. Consequently, neglecting this extra normal stress in the design of dikes may potentially compromise the dike stability or cause dike breaching. Therefore, the study of the normal stress on dikes induced by the combined wave and surge overtopping is essential.

In this paper, physical model tests were conducted to investigate the normal stress on dike induced by the combined wave and surge overtopping. At the same time, the average overtopping discharges were accurately measured and compared with those from several existing theoretical and experimental formulas. From the measured time series of the normal stresses on dike, two characteristics (i.e., abrupt and gradual change) were observed. These were consonant with the two wave passing patterns (i.e., breaking or smooth passing). Furthermore, the spatial distribution of the normal stress on dike was analyzed. The statistical distribution of the peak normal stress was effectively expressed by the Weibull distribution. Additionally, the Weibull factors, respectively on the dike crest and on the upper part of the landward slope, were calculated by curve fitting of the laboratory measured data.

2 Laboratory experiment setup

Physical model tests were carried out in the wave flume (175 m long, 1.8 m wide, and 1.8 m deep) at the River and Harbor Engineering Department of Nanjing Hydraulic Research Institute, China (Figure 1). The wave flume was equipped with a blade-type wave maker.

FIGURE 1
Photo of the wave flume.

A trapezoidal dike cross-section was designed with a geometry scale of 1:10 normal model. The whole layout of the experiment is shown in Figure 2. A long 1:100 approach slope, following a 1:10 transition slope, was connected to the bottom of the flume in the front of the model. The distance between the tested dike cross-section to the wave maker was 42.0 m. The crest of the tested dike cross-section was 0.925 m above the bottom of the wave flume (0.325 m above the top of the 1:10 slope), while the width of the dike crest was 0.257 m in model scale. The seaward slope of the dike model section was 1:4.25, while the landward slope was 1:3. Three plastic plates were respectively installed on the seaward slope, the crest, and the landward slope. The bottom of the flume was equipped with a bidirectional circulating pump, which was used to provide a return flow in order to counterbalance the mean overtopping due to the combined wave and surge, as shown in Figure 2.

Seven wave gauges, G1–G7, were placed near the toe of the seaward slope (Figure 2). From the measured time series of wave heights, the incident and reflected wave heights were calculated *via* a three-point method. The measuring frequency of the wave gauge was 100 Hz.

The average overtopping discharge was measured at the inside of the tested section by collecting the overtopping water (over a width of 0.1 m) *via* an overtopping chute (a lifting device was installed in the front of the chute, which enables placing and removing the chute from the dike crest quickly) into the overtopping box (equipped with two large pumps). A larger pump (pump A) was connected with a Φ10-cm steel pipe to the back of the wave flume, and a flow meter was placed on the steel pipe. A smaller pump (pump B) was connected with a plastic pipe to a bucket that is constantly weighed on a balance. Pump C was used to pump the water from the bucket to the wave flume in order to keep the water level unchanged in the wave flume during the test (see Figure 3).

At the beginning of the test, the chute was lifted under the surge-only overflow condition. When the wave reached the dike, the chute was placed down on the dike crest and timing was started. In smaller discharge test cases ($R_c > -0.06$ m), pump B was used to pump the water from the overtopping box into the bucket and then a balance was used to weigh the water. In larger discharge test cases ($R_c \leq -0.06$ m), pump A was opened and a flow meter was used to measure the discharge. At the end of wave making, we lifted the chute and stopped timing to measure the total water volume or the discharge during this period. Using this process, the average discharge was obtained.

As shown in Figure 4, the normal stress on the dike was measured by 15 pressure gauges, P1–P15, of which five were evenly distributed on the dike crest (the interval was 0.043 m in model scale) and 10 were located on the landward slope (the interval was 0.075 m in model scale). The measuring frequency

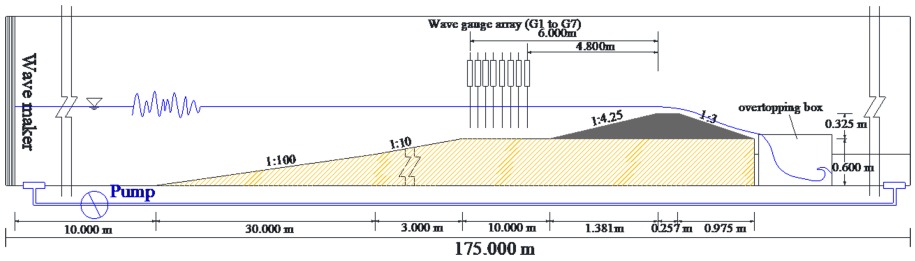

FIGURE 2
Profile view of the wave flume.

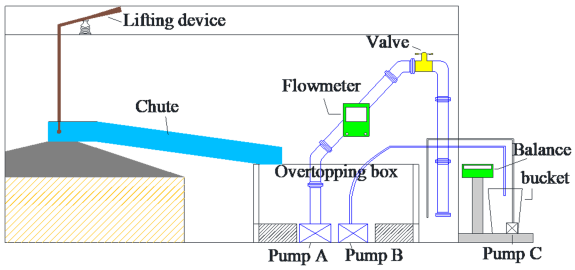

FIGURE 3
Overtopping collection system.

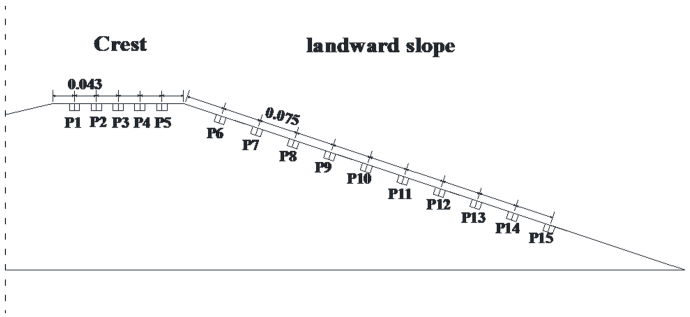

FIGURE 4
Layout of the pressure gauges.

of the pressure gauge was 100 Hz. The collected pressure data were filtered to remove unwanted higher- or lower-frequency oscillations.

In this test, the incident waves were generated according to the JONSWAP (Joint North Sea Wave Project) spectrum. A total of 15 unique wave conditions are listed in Table 1. Each test lasted for 480 s. This gave about 140 waves for tests with the longest peak wave periods.

3 Average discharge of the combination of wave and surge

Understanding the average discharge is the first step to understanding the normal stresses on dikes induced by the combined wave and surge overtopping. In this section, the measured average discharge in the test was compared with those of the existing average discharge formulas.

TABLE 1 Test cases of the physical model tests.

Test cases	Prototype-scale parameters		
	R_c (m)	H_{m0} (m)	T_p (s)
Trial 11	−0.30	1.03	4.11
Trial 12	−0.30	1.05	4.74
Trial 13	−0.30	1.03	6.32
Trial 14	−0.30	1.05	9.49
Trial 15	−0.30	1.37	4.74
Trial 21	−0.60	1.04	4.11
Trial 22	−0.60	1.08	4.74
Trial 23	−0.60	1.02	6.32
Trial 24	−0.60	1.05	9.49
Trial 25	−0.60	1.51	4.74
Trial 31	−0.90	1.00	4.11
Trial 32	−0.90	0.98	4.74
Trial 33	−0.90	0.97	6.32
Trial 34	−0.90	1.05	9.49
Trial 35	−0.90	1.52	4.74

R_c, freeboard; H_{m0}, wave height; T_p, wave period.

3.1 Existing average discharge formulas of the combination of wave and surge

Several formulas had been obtained from previous studies to estimate the average discharge of the combined wave and surge overtopping (e.g., Reeve et al., 2008; Hughes and Nadal, 2009; EurOtop, 2017).

In EurOtop (2017), the average overtopping discharge of the combined wave and surge overtopping can be calculated as:

$$q_{ws} = q_s + q_w \tag{1}$$

The average discharge was divided into two parts: surge-only overflow (q_s) and wave overtopping (q_w) with zero freeboard. The surge-only overflow (q_s) part was calculated as follows (e.g., Henderson, 1966):

$$q_s = \left(\frac{2}{3}\right)^{3/2} \sqrt{g} h_1^{3/2} \tag{2}$$

where g is the gravity acceleration and h_1 ($-R_c$) is the upstream head.

The wave overtopping (q_w) part was calculated as follows (e.g., Schüttrumpf et al., 2001):

$$\frac{q_w}{\sqrt{gH_{m0}^3}} = 0.0537\xi_{m-1,0}\ \xi_{m-1,0<2.0} \tag{3}$$

$$\frac{q_w}{\sqrt{gH_{m0}^3}} = \left(0.0136 - \frac{0.226}{\xi_{mm-1,0}^3}\right)\xi_{m-1,0>2.0} \tag{4}$$

where H_{m0} is the significant wave height based on the wave spectrum and $\xi_{m\text{-}1,0}$ is the breaking parameter based on the deepwater wavelength and mean energy period. It should be noted that Eqs. 3, 4 show no relationship with relative freeboard because they are only applicable for cases with zero freeboard.

In Reeve et al. (2008), the average overtopping discharge formula was obtained using a numerical wave flume model, which can be calculated as:

$$Q_R = \frac{q_{ws}}{\sqrt{gH_s^3}}\frac{\sqrt{\tan\alpha}}{\xi_p} = 0.051\exp\left(-1.98\frac{R_c}{H_s\xi_p}\right) \text{ for breaking waves} \tag{5}$$

$$Q_R = \frac{q_{ws}}{\sqrt{gH_s^3}} = 0.233\exp\left(-1.29\frac{R_c}{H_s}\right) \text{ for non-breaking waves} \tag{6}$$

where ξ_p is the breaking parameter based on the deep-water wavelength and peak energy period. The value of freeboard (R_c) should be entered as a negative number.

In Hughes and Nadal (2009), the average overtopping discharge formula was obtained by a laboratory study on a wave flume with a prototype-to-model length scale of 25:1. The formula related to the dimensionless overtopping discharge and the relative freeboard can be described as:

$$\frac{q_{ws}}{\sqrt{gH_{m0}^3}} = 0.034 + 0.53\left(\frac{-R_c}{H_{m0}}\right)^{1.58} \tag{7}$$

It should be noted that the wave period is not related to the average overtopping discharge, according to the conclusion of Hughes and Nadal (2009).

3.2 Analysis of the average overtopping discharge

Table 2 lists the average overtopping discharge values measured in this test. Figure 5 shows the dimensionless average discharge *versus* the relative freeboard for all 15 tests. The calculation results using the formulas of EurOtop (2017), Reeve et al. (2008), and Hughes and Nadal (2009) are also compared in Figure 5. The fitting curve of the Hughes and Nadal (2009) formula (Eq. 7) is shown in Figure 5. The data points calculated using the formulas of EurOtop (2017) (Eq. 1) and Reeve et al. (2008) (Eqs. 5, 6) were based on the wave conditions in this test.

As shown in Figure 5, the data points from the tests were consistent with the calculation results of the formula of EurOtop (2017) in cases of very low absolute values of negative relative freeboard ($-0.4 \le R_c/H_{m0} < 0$) and showed good fit with the formula of Hughes and Nadal (2009) in cases of higher absolute values of negative relative freeboard ($R_c/H_{m0} < -0.4$). However, all of the data points from the tests were smaller than those of the method of Reeve et al. (2008).

Li et al., 2012 concluded that the relative freeboard reflects the proportional relationship between the surge-only overflow and the wave-only overtopping in the combination of surge and wave. Figure 6 shows the ratio of q_{ws}/q_s *versus* the relative negative freeboard. For higher absolute values of relative freeboard, the average discharge of the combined wave and surge overtopping (q_{ws}) was almost equal to the discharge of the surge-only overflow (q_s). This indicates that the hydraulic parameters such as wave period and gradient of seaward slope may not be related to the average overtopping discharge under higher absolute values of negative relative freeboard. However, these hydraulic parameters were still considered in Eq. 1 EurOtop, 2017), whose estimates were larger under higher absolute values of relative freeboard.

On the other hand, for lower absolute values of relative freeboard, the average overtopping discharge of the combined wave and surge overtopping (q_{ws}) was slightly bigger than that of the surge-only overflow discharge (q_s). This indicates that, when the relative freeboard approaches zero, the wave is more influential in the average discharge of the combined wave and surge overtopping. Thus, the hydraulic parameters such as wave period and gradient of seaward slope still have obvious influences on the discharge under lower absolute values of negative relative freeboard. However, these hydraulic

10.3389/fmars.2022.1073345

TABLE 2 Measured average overtopping discharge.

Test cases	Hydraulic parameters		Average discharge	
	H_{m0} (m)	T_p (s)	q_s (m^3/s/m)	q_{ws} (m^3/s/m)
Freeboard: R_c = −0.3 m				
Trial 11	1.03	4.11	0.280	0.418
Trial 12	1.05	4.74	0.280	0.455
Trial 13	1.03	6.32	0.280	0.475
Trial 14	1.05	9.49	0.280	0.503
Trial 15	1.37	4.74	0.280	0.598
Freeboard: R_c = −0.6 m				
Trial 21	1.04	4.11	0.792	0.847
Trial 22	1.08	4.74	0.792	0.849
Trial 23	1.02	6.32	0.792	0.871
Trial 24	1.05	9.49	0.792	0.897
Trial 25	1.51	4.74	0.792	0.952
Freeboard: R_c = −0.9 m				
Trial 31	1.00	4.11	1.454	1.449
Trial 32	0.98	4.74	1.454	1.443
Trial 33	0.97	6.32	1.454	1.422
Trial 34	1.05	9.49	1.454	1.459
Trial 35	1.52	4.74	1.454	1.470

R_c, freeboard; H_{m0}, wave height; T_p, wave period; q_s, surge-only overflow; q_{ws}, wave overtopping.

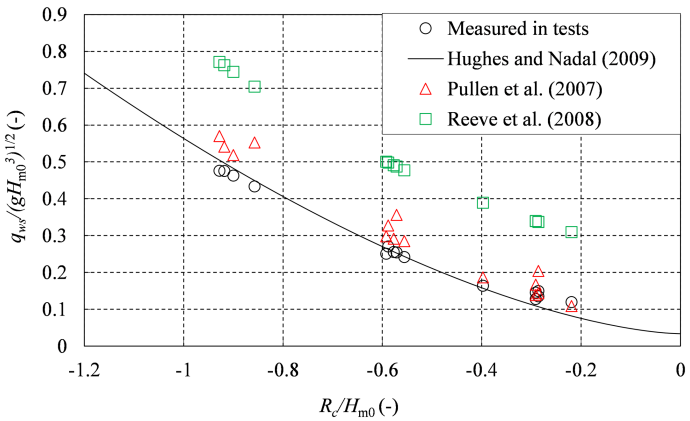

FIGURE 5
Dimensionless average discharge *versus* relative freeboard.

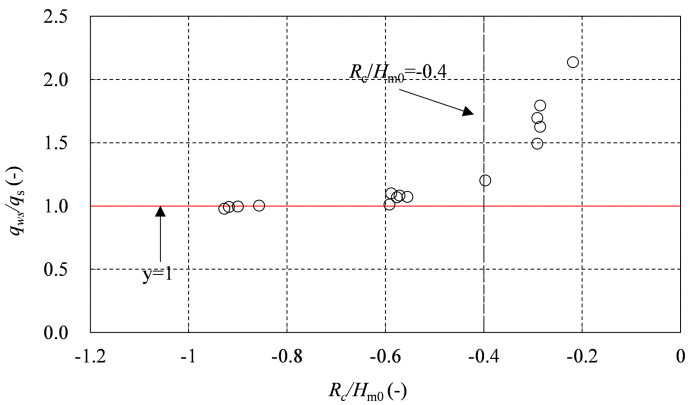

FIGURE 6
q_{ws}/q_s *versus* the relative negative freeboard.

parameters were neglected in the formula of Hughes and Nadal (2009), which led to the unsatisfactory performance of Eq. 7 (Hughes and Nadal, 2009) in cases of lower absolute values of negative relative freeboard ($-0.4 \leq R_c/H_{m0} < 0$).

Therefore, Eq. 7 (Hughes and Nadal, 2009) can be used to calculate the average discharge of the combined wave and surge overtopping in cases of higher absolute values of negative relative freeboard ($R_c/H_{m0} < -0.4$), while Eq. 1 (EurOtop, 2017) can be used to calculate the average discharge of the combined wave and surge overtopping in cases of lower absolute values of negative relative freeboard ($-0.4 \leq R_c/H_{m0} < 0$).

4 Normal stress

This section analyzes the characteristic and spatial distributions of normal stress on the dike induced by the combined wave and surge overtopping. The Weibull distribution was used to represent the statistical distribution of peak normal stress.

4.1 Time series analysis

The time series of normal stress measured using a pressure gauge was used to analyze the characteristics of normal stress along the dike. Figure 7 gives two examples of the time series of normal stress measured by pressure gauge P1 on the front of the dike crest from trial 13 ($R_c = -0.3$ m, $H_{m0} = 1.03$ m, $T_p = 6.32$ s) and trial 33 ($R_c = -0.9$ m, $H_{m0} = 0.97$ m, $T_p = 6.32$ s). The values have been converted to the prototype scale according to a length scale of 10. Figure 7A displays the sharp increase of the normal stress at about 709, 734, and 742 s (as circled in Figure 8A), and much greater than that induced by the surge-only overflow (blue line). The sharp increase of normal stress (referred to as abrupt change) indicates that the dike withstands an impulsive downward-flushing flow directly. As shown in Figure 7B, the normal stress increased slowly (referred to as gradual change), which is the order of the static pressure due to the wave elevation. As Pan et al. (2015) pointed out, breaking passing (plunging breaks on the crest or the landward slope) and smooth passing (waves passing without a breaker) of waves are the two passing patterns in the combination of wave and surge. In cases of lower absolute values of negative freeboard ($R_c = -0.3$ m), the main wave passing pattern is breaking passing, with the downward-flushing flow directly impacting the dike crest and the upper part of the landward slope and the normal stress characterized by abrupt change. In cases of medium absolute values of negative freeboard ($R_c = -0.6$m), both wave passing patterns are possible, with the downward-flushing flow mainly impacting the upper part of the landward slope, the normal stress on the dike crest characterized by gradual change, and the normal stress on the upper part of the landward slope characterized by abrupt change. In cases of higher absolute values of negative freeboard ($R_c = -0.9$m), the main wave passing pattern was smooth passing, and the normal stress on the dike was characterized by gradual change.

4.2 Spatial distribution of normal stress

Figure 8 shows six examples of the spatial distribution of 1% relative normal stress, $p_{1\%}^*$ (since the number of waves in this test was about 140, 1% normal stress can be regarded as the maximum value), along the dike with different values of freeboard (R_c), wave height (H_{m0}), and wave period (T_p). The dimensionless parameter 1% relative normal stress, $p_{1\%}^*$ ($p_{1\%}$ denotes that the normal stress level exceeds by 1% of the measured normal stress time series), in this figure is defined as $p_{1\%}^* = p_{1\%}/\gamma H_{m0}$, where γ is the water-specific weight, B is the

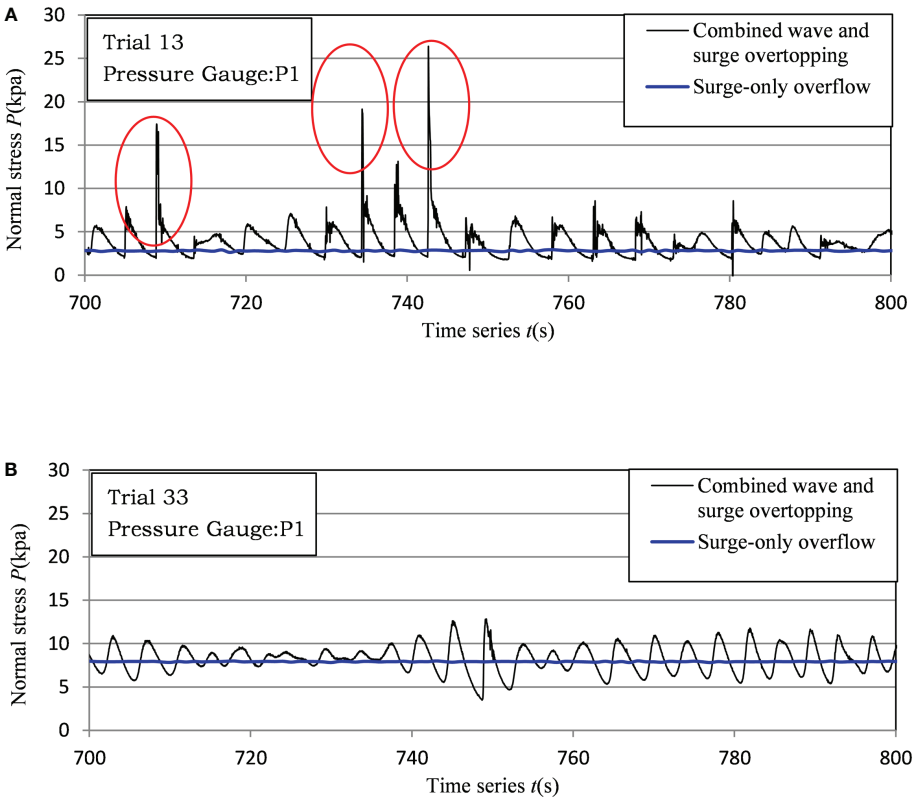

FIGURE 7
Samples of normal stresses time series at P1 on the dike crest: **(A)** abruptly change; **(B)** gradually change.

width of the dike crest, and x is the projection length of the measuring point on the horizontal line (see Figure 9).

It can be seen from Figures 8A, B that, under cases of lower absolute values of negative freeboard (R_c = −0.3 m), the 1% relative normal stress ($p_{1\%}$*) on the dike crest ($0 \le x/B < 1$) was large ($p_{1\%}$* was approximately 3). The maximum normal stress at different measurement points changed significantly, and the location where the maximum normal stress occurred moved back along the dike crest with the wave period increase. Obviously, the $p_{1\%}$* on the upper part of the landward slope ($1 \le x/B < 2.1$) was large ($p_{1\%}$* was approximately 2–3), with the maximum normal stress increasing significantly with the increase of the wave period and the location where the maximum normal stress generally occurring at pressure gauges P7–P9 ($1.5 < x/B < 2.1$). The $p_{1\%}$* on the lower part of the landward slope ($x/B \ge 2.1$) was smaller and gradually decreased along the landward slope.

It is also apparent from Figures 8C, D that, in cases of medium absolute values of negative freeboard (R_c = −0.6m), the $p_{1\%}$* on the dike crest ($0 \le x/B < 1$) was relatively small ($p_{1\%}$* was approximately 2). The maximum normal stress at different measurement points changed little. The $p_{1\%}$* on the upper part of the landward slope ($1 \le x/B < 2.1$) was larger than that on the dike crest ($p_{1\%}$* was approximately 2.5), with the maximum normal stress increasing slightly with the increase of the wave period and the location where the maximum normal stress generally occurring at pressure gauges P7–P9 ($1.5 < x/B < 2.1$). The $p_{1\%}$* on the lower part of the landward slope ($x/B \ge 2.1$) was smaller and gradually decreased along the landward slope.

Finally, Figures 8E, F show that, in cases of higher absolute values of negative freeboard (R_c = −0.9 m), the spatial distribution trend of the normal stress along the dike was similar to that of the surge-only overflow, the $p_{1\%}$* being relatively small and the maximum normal stress occurring at the dike crest. According to the findings detailed in *Section 4.1*, normal stress was caused by the static pressure under higher absolute values of negative freeboard; thus, the normal stress on the dike crest increased slightly due to the larger wave height (Figure 8F), and there was no obvious correspondence with the wave period.

In summary, in the combined wave and surge overtopping, the normal stress caused by the downward-flushing flow impact under lower absolute values of negative freeboard was larger than that caused by the static pressure along the dike due to the wave elevation under higher absolute values of negative

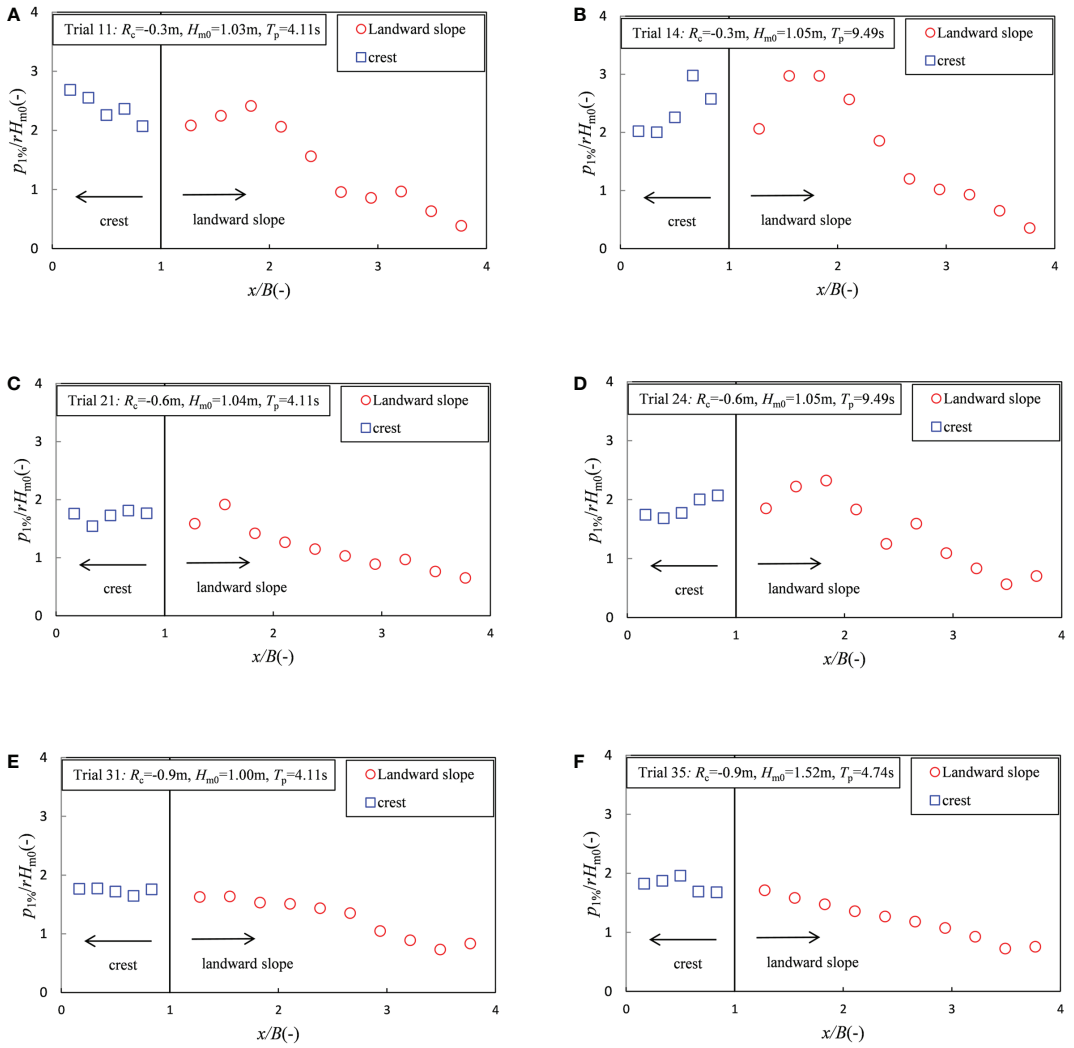

FIGURE 8
Spatial distribution of the relative normal stress along the dike. **(A)** Small wave period (R_c = −0.3m). **(B)** Large wave period (R_c = −0.3m). **(C)** Small wave period (R_c = −0.6m). **(D)** Large wave period (R_c = −0.6m). **(E)** Small wave height (R_c = −0.9m). **(F)** Large wave height (R_c = −0.9m).

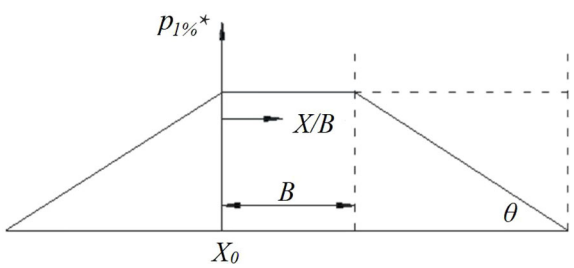

FIGURE 9
Coordinates of the relative normal stress variation along the dike.

freeboard. Moreover, the normal stress occurring at the dike crest ($0 \le x/B < 1$) and the upper part of the landward slope ($1 \le x/B < 2.1$) was larger than that at the lower part of the landward slope ($x/B \ge 2.1$).

4.3 Statistical distribution of normal stress

The values obtained from statistical distribution can be used for the probabilistic calculations of structures. In the present analysis, the two-parameter Weibull distribution was proposed to represent the statistical distribution of the peak value of relative normal stress ($p^{\star} = p/\gamma H_{m0}$) measured by all the pressure gauges (P1–P15). The distribution can be written as follows:

$$P_{p^*} = P(p_i^* \le p^*) = 1 - \exp[-(\frac{p^*}{a_p})^{b_p}] \quad (8)$$

where P_{p^*} is the probability of the peak value of the relative normal stress per wave p_i^* being less than or equal to p^*, a_p is the scale factor, and b_p is the shape factor.

The findings in *Sections 4.1* and *4.2* indicate that the normal stress induced by the combination of wave and surge overtopping expresses different characteristics (an abrupt or gradual change) on the dike crest and the upper and lower parts of the landward slope, thus, three examples of the Weibull distribution of the peak relative normal stress (semi-logarithmic ordinate) on the dike crest. The upper and lower parts of the landward slope are shown in Figure 10. Figure 10A shows an example of a mediocre fit from trial 21 (R_c = −0.6 m, H_{m0} = 1.05 m, T_p = 9.49 s) measured by pressure gauge P2 on the dike crest. Figure 10B shows an example of a good fit from trial 11 (R_c = −0.3 m, H_{m0} = 1.00 m, T_p = 4.11 s) measured by pressure gauge P7 on the upper part of the landward slope. Figure 10C shows an example of a poor fit from trial 21 (R_c = −0.6 m, H_{m0} = 1.04 m, T_p = 4.11 s) measured by pressure gauge P14 on the lower part of the landward slope.

In general, the fitting degrees between the test data measured by pressure gauges P1–P9 (dike crest and upper part of the landward slope) and the Weibull distribution were between the two cases shown in Figures 10A, B. Figure 10C shows that the fitting degrees between the test data measured by pressure gauges P10–P15 (lower part of the landward slope) and the Weibull distribution were poor. This is due to the fact that the flow thickness along the lower part of the landward slope was very small, and the normal stress caused by the static pressure was also very small. When the peak relative normal stress (p_i^*) becomes too small, the Weibull distribution may no longer be applicable. It should be mentioned that the determination of the maximum value of normal stress required for the stability of the structure is key to the dike design. The findings in *Section 4.2* show that the normal stress occurring at the dike crest and the upper part of landward slope was obviously larger than that at the lower part of the landward slope; thus, this paper mainly focused on the normal stress on the dike crest and the upper part of the landward slope induced by the combined wave and surge overtopping.

The plots revealed that the freeboard (R_c), wave height (H_{m0}), and the wave period (T_p) closely controlled the scale of the cumulative probability distribution and were also closely related to the average overtopping discharge (q_{ws}). Figure 11 plots the scale factors a_{pc} on the dike crest and a_{ps} on the upper part of the landward slope *versus* the dimensionless overtopping discharge $[q_{ws}/m0_3^{*0.5}]$.

It can be seen from Figure 11A that, with the increase of $q_{ws}/m0_3^{*0.5}$, the scale factor a_{pc} on the dike crest first decreased slightly and then remained stable. This may be explained by the fact that the scale factor a_{pc} reflects the values of the average peak relative normal stress; when the $q_{ws}/m0_3^{*0.5}$ is relatively small, with most of the waves passing the dike crest with a breaking passing pattern, the average peak normal stress is relatively large, which gives larger a_{pc} values. A comparison of pressure gauges P1–P5 indicated that the values of a_{pc} had no apparent regularity during each test case. The solid line is a best-fit empirical equation for the datasets given by the following equation:

$$a_{pc} = 78.6 \exp\left(-35.5 \frac{q_{ws}}{(gH_{m0}{}^3)^{0.5}}\right) + 1.36 \quad (9)$$

It can be seen from Figure 11B that, with the increase of $q_{ws}/m0_3^{*0.5}$, the scale factor a_{ps} on the upper part of the landward slope first decreased slightly and then remained stable. The three points at pressure gauge P7 from trial 22, trial 23, and trial 24 with a freeboard of −0.6 m tended to be greater than the average trend. Such deviation might be due to the effect of the combination of the downward-flushing flow impact and static pressure. A comparison of pressure gauges P6–P9 indicated that the values of a_{ps} had no apparent regularity during each test. The solid line is a best-fit empirical equation for the datasets given by the following equation:

$$a_{ps} = 22.3 \exp\left(-28.28 \frac{q_{ws}}{(gH_{m0}{}^3)^{0.5}}\right) + 0.65 \quad (10)$$

Figure 12 plots the shape factors b_{pc} on the dike crest and b_{ps} on the upper part of the landward slope *versus* the dimensionless overtopping discharge $[q_{ws}/m0_3^{*0.5}]$.It can be seen from Figure 12A that the shape factor b_{pc} on the dike crest increased with increasing $q_{ws}/m0_3^{*0.5}$. A comparison of pressure gauges P1–P5 indicated that the values of b_{pc} were nearly the same at these pressure gauges during each test. One data point at pressure gauge P3 from trial 25 tended to be greater than the average trend. Such deviation might be due to the H_{m0} (H_{m0} = 1.51m) being relatively large in this test case. The solid line is the best-fit empirical equation for the datasets given by the following equation:

$$b_{pc} = 29.6 \frac{q_{ws}}{(gH_{m0}{}^3)^{0.5}} + 1.9 \quad (11)$$

It can be seen from Figure 12B that the shape factor b_{ps} on the upper part of the landward slope increased with increasing $q_{ws}/m0_3^{*}{}^3)^{0.5}$. A comparison of pressure gauges P6–P9 indicated that the values of b_{ps} were nearly the same at these pressure gauges during each test case. The solid line is the best-fit empirical equation for the datasets given by the following equation:

$$b_{ps} = 15.3 \frac{q_{ws}}{(gH_{m0}{}^3)^{0.5}} + 5.4 \quad (12)$$

The values of the scale factor a_p and the shape factor b_p can be used to calculate the maximum value of the Weibull distribution as (Pan et al., 2015):

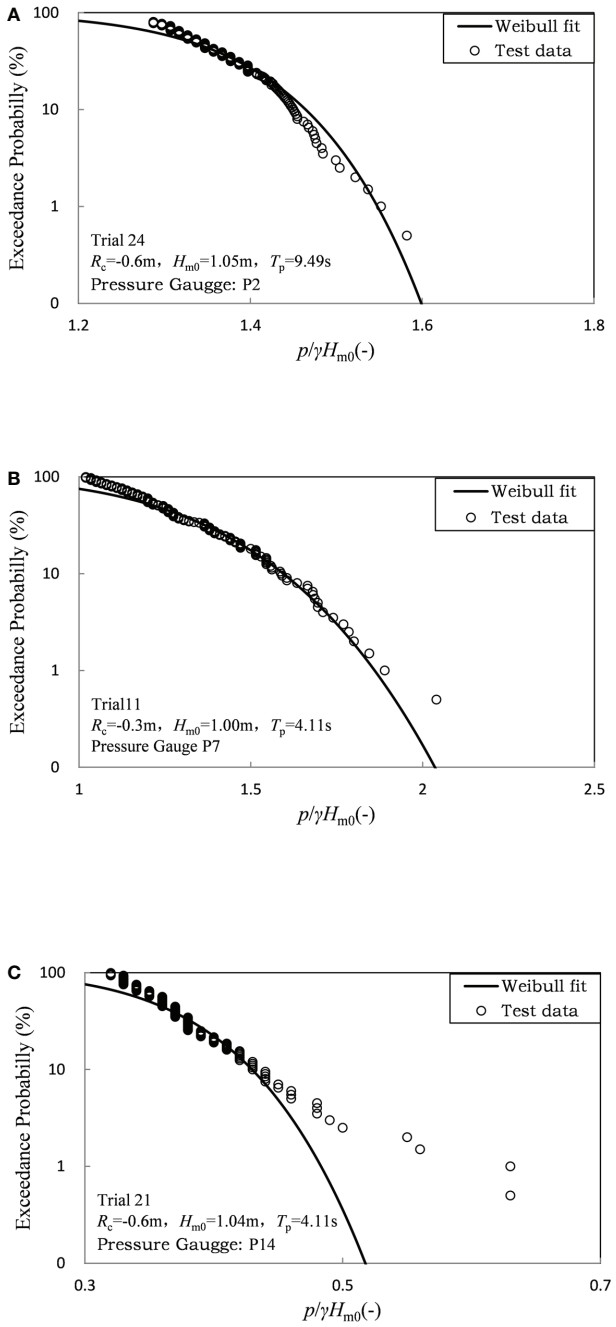

FIGURE 10
Example of the best fits of the Weibull distribution to the peak value of normal stress. **(A)** Example of a mediocre fit from trial 21 (pressure gauge P2). **(B)** Example of a good fit from trial 11 (pressure gauge P7). **(C)** Example of a poor fit from trial 21 (pressure gauge P14).

$$p_{max} = a_p(\ln(N+1))^{1/b_p} \quad (13)$$

where N is the peak normal stress number. From Eqs. 9–12, the scale factor a_p and the shape factor b_p were calculated for all test cases. Then, Eq. 13 was used to estimate the maximum normal stress. Comparisons between the estimated and measured values for the maximum normal stress on the dike crest and upper part of the landward slope are shown in Figure 13. A better prediction can be found for the maximum normal stress on the dike crest, as shown in Figure 13A. The estimation of maximum normal stress on the upper part of the landward slope was mediocre, but reasonable, as shown in Figure 13B. The data showed a good

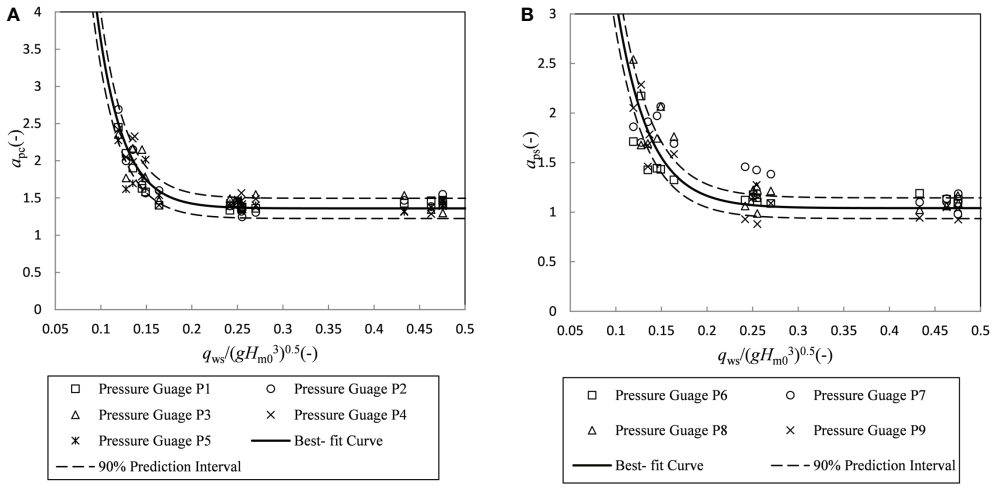

FIGURE 11
Best-fit equations for Weibull factor a_p: **(A)** on the crest; **(B)** on the upper part of landward slope.

trend, but the data points were scattered because of the limited wave numbers and the randomness of the maximum value in limited cases.

5 Conclusions

this paper, the normal stress on a trapezoidal dike cross-section induced by the combined wave and surge overtopping was analyzed using laboratory measurements. The existing average overtopping discharge formulas were compared. The characteristics of normal stress on the dike were obtained based on the analyses of the time series and spatial distribution of normal stress. Two empirical equations were proposed to represent the statistical distribution of peak normal stress. The main conclusions are discussed below.

For higher absolute values of relative freeboard ($R_c/H_{m0} < -0.4$), the average overtopping discharge of the combined wave and surge overtopping was close to the surge-only overflow discharge. For lower absolute values of relative freeboard, the average overtopping discharge of the combined wave and surge overtopping (q_{ws}) was slightly higher than the

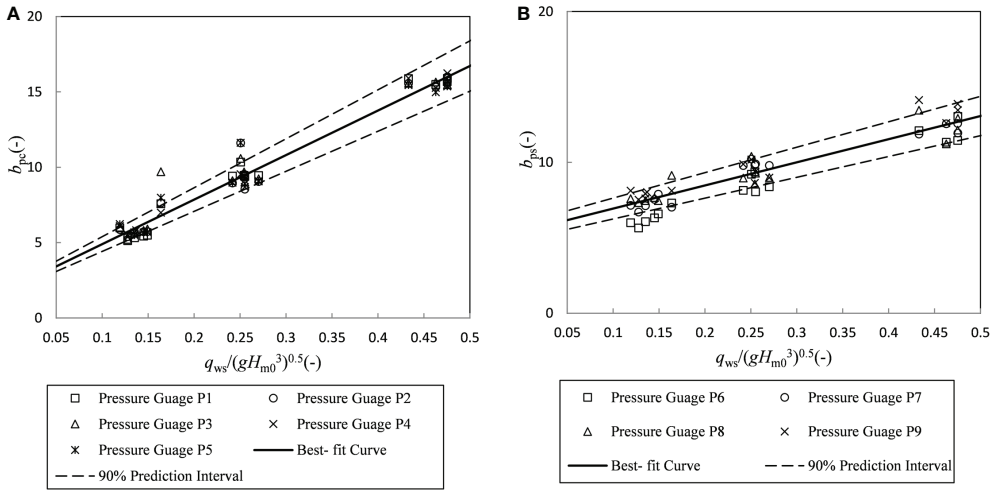

FIGURE 12
Best-fit equations for Weibull factor b_p: **(A)** on the crest; **(B)** on the upper part of landward slope.

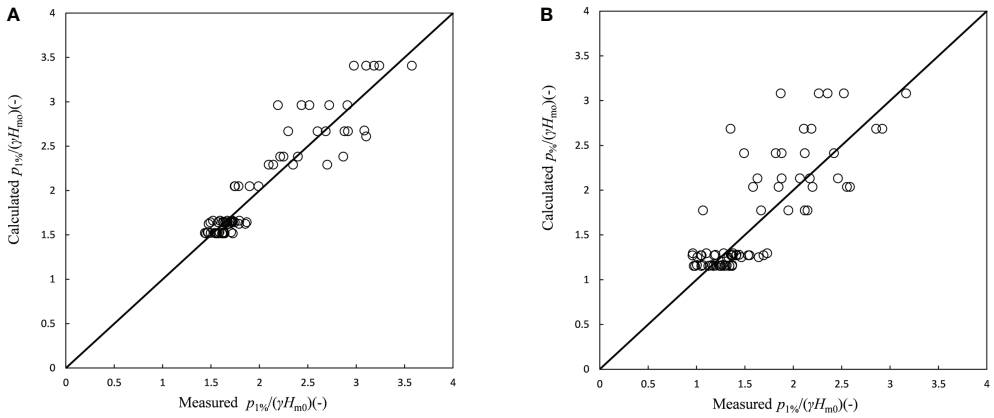

FIGURE 13
Comparison of measured and calculated maximum normal stress: **(A)** on the dike crest; **(B)** on the upper part of landward slope.

surge-only overflow discharge (q_s). Equation 7 (Hughes and Nadal, 2009) can be used to calculate the average discharge of the combined wave and surge overtopping in cases of higher absolute values of negative relative freeboard ($R_c/H_{m0} < -0.4$), while Eq. 1 (EurOtop, 2017) can be used to calculate the average discharge of the combined wave and surge overtopping in cases of lower absolute values of negative relative freeboard ($-0.4 \le R_c/H_{m0} < 0$).

Two characteristics of normal stress can be observed during the tests: a) the abrupt change caused by the downward-flushing flow directly impacting the dike and b) the gradual change caused by the static pressure. In cases of lower absolute values of negative freeboard ($R_c = -0.3$ m), the normal stress on the dike was characterized by abrupt change. In cases of medium absolute values of negative freeboard ($R_c = -0.6$ m), the normal stress on dike crest ($0 \le x/B < 1$) was characterized by gradual change, while the normal stress on the upper part of the landward slope ($1 \le x/B < 2.1$) was characterized by abrupt change. Under higher absolute values of negative freeboard ($R_c = -0.9$ m), the normal stress on the dike was characterized by gradual change. Moreover, analysis of the spatial distribution of normal stress on the dike revealed that the normal stress occurring at the dike crest ($0 \le x/B < 1$) and the upper part of the landward slope ($1 \le x/B < 2.1$) was apparently larger than that occurring at the lower part of the landward slope ($x/B \ge 2.1$).

The two-parameter Weibull distribution shown by Eq. 8 was used to represent the statistical distribution of the peak normal stress. Equations 9, 11 described the calculations used to estimate the scale factor a_{pc} and the shape factor b_{pc} on the part of the dike crest. On the other hand, the calculations given in Eqs. 10, 12 were used to estimate the scale factor a_{ps} and the shape factor b_{ps} on the upper part of the landward slope. The maximum normal stress can be estimated using the calculated Weibull factors a_p and b_p. The calculated maximum normal stress on the dike crest fitted the measurements well, while that on the upper part of the landward slope was mediocre, but was acceptable.

This paper provided better knowledge on the normal stress on dike induced by the combination of wave and surge overtopping. The conclusions presented in this paper are only suitable for dikes with a slope gradient of 1:4.25, and the equations may not be applicable for dikes with a different slope gradient.

Data availability statement

The original contributions presented in the study are included in the article/Supplementary Material. Further inquiries can be directed to the corresponding author.

Author contributions

ZZ: Conceptualization, methodology, software, writing—original draft, and writing—review and editing. ZS: Formal analysis, validation, visualization, and data curation. YZ: Writing—review and editing, and methodology. QZ and YC: Methodology. HW: Software. FH: Data curation. All authors contributed to the article and approved the submitted version.

Funding

We sincerely thank the fundings support from the National Natural Science Foundation of China (no. 51979098) and Fundamental Research Funds for Central Public Welfare Research Institutes (no. Y222010) and Jiangsu Funding Program for Excellent Postdoctoral Talent (no. 2022ZB10).

Conflict of interest

The authors declare that the research was conducted in the absence of any commercial or financial relationships that could be construed as a potential conflict of interest.

Publisher's note

All claims expressed in this article are solely those of the authors and do not necessarily represent those of their affiliated organizations, or those of the publisher, the editors and the reviewers. Any product that may be evaluated in this article, or claim that may be made by its manufacturer, is not guaranteed or endorsed by the publisher.

Supplementary material

The Supplementary Material for this article can be found online at: https://www.frontiersin.org/articles/10.3389/fmars.2022.1073345/full#supplementary-material

References

ASCE Hurricane Katrina External Review Panel (2007). *The new Orleans hurricane protection system: What went wrong and why?* (Reston, Virginia: American Society of Civil Engineers), 92.

Celi, D., Pasquali, D., Fischione, P., Nucci, C., and Rision, M. (2021). Wave-induced dynamic pressure under rubble mound breakwaters with submerged berm: An experimental and numerical study. *Coast. Eng.* 170, 104014. doi: 10.1016/j.coastaleng.2021.104014

EurOtop (2017). Manual on wave overtopping of sea defences and related structure. *An overtopping manual largely based on European research, but for worldwide application*. J. W. Van der Meer, N. W.H. Allsop, T. Bruce, J. De Rouck, A. Kortenhaus, T. Pullen, et al. Available at: www.overtopping-manual.com.

Hattori, M., , Arami, A., and , Yui, T. (1994). Wave impact pressure on vertical walls under breaking waves of various types. *Coast. Eng.* 22, 79–114. doi: 10.1016/0378-3839(94)90049-3

Henderson, F. M. (1966). *Open channel flow* (New York: MacMillian Publishing Co.).

Hughes, S. A. (2008). "Levee overtopping design guidance: what we know and what we need," in *Proceedings of the solutions to coastal disasters congress* (Turtle Bay, Oahu, Hawaii: ASCE), 867–880.

Hughes, S. A., and Nadal, N. C. (2009). Laboratory study of combined wave overtopping and storm surge overflow of a levee. *Coast. Eng.* 56 (2009), 244–259. doi: 10.1016/j.coastaleng.2008.09.005

Hughes, S. A., Shaw, J. M., and Howard, I. L. (2011). Earthen levee shear stress estimates for combined wave overtopping and surge overflow. *J. Wat Port Coast. Ocean Eng. ASCE* 138 (3), 267–273. doi: 10.13140/RG.2.2.21298.63681

IPCC (2012). "Managing the risks of extreme events and disasters to advance climate change adaptation," in *A special report of working Groups I and Ⅱ of the intergovernmental panel on climate Chang* (Cambridge, UK, and New York, NY, USA: Cambridge University Press), 582p.

Jensen, B., Christensen, E. D., and , Mutlu Sumer, B. (2014). Pressure-induced forces and shear stresses on rubble mound breakwater armour layers in regular waves. *Coast. Eng.* 91, 60–75. doi: 10.1016/j.coastaleng.2014.05.003

Li, L., Pan, Y., Amini, F., and Kuang, C. P. (2012). Full scale laboratory study of combined wave and surge overtopping of a levee with RCC strengthening system. *Ocean Eng.* 54 (1), 70–86. doi: 10.1016/j.oceaneng.2012.07.021

Pan, Y., Kuang, C. P., Li, L., and Amini, F. (2015). Full-scale laboratory study on distribution of individual wave overtopping volumes over a levee under negative freeboard. *Coast. Eng.* 97, 11–20. doi: 10.1016/j.coastaleng.2014.12.007

Pan, Y., Li, L., Amini, F., and Kuang, C. (2012). Full scale HPTRM strengthened levee testing under combined wave and surge overtopping conditions: Overtopping hydraulics, shear stress and erosion analysis. *J. Coast. Res* 29 (1), 182–200. doi: 10.2112/JCOASTRES-D-12-00010.1

Pan, Y., Li, L., Amini, F., and Kuang, C. P. (2013a). Full-scale HPTRM-strengthened levee testing under combined wave and surge overtopping conditions: overtopping hydraulics, shear stress, and erosion analysis. *J. Coast. Res.* 29 (1), 182–200. doi: 10.2112/JCOASTRES-D-12-00010.1

Pan, Y., Li, L., Amini, F., and Kuang, C. P. (2013b). Influence of three levee-strengthening systems on overtopping hydraulic parameters and hydraulic equivalency analysis between steady and intermittent overtopping. *J. Wat Port Coast. Ocean Eng.* 139 (4), 256–266. doi: 10.1061/(ASCE)WW.1943-5460.0000179

Pan, Y., Yin, S., Chen, Y. P., Yang, Y. B., Xu, C. Y., and Xu, Z. S. (2022). An experimental study on the evolution of a shoreface nourishment under the effects of regular waves in low-energy conditions. *Coast. Eng.* 176, 104169. doi: 10.1016/j.coastaleng.2022.104169

Pan, Y., Zhou, Z. J., and Chen, Y. P. (2020). An analysis of the downward-flushing flow on the crest of a levee under combined wave and surge overtopping. *Coast. Eng.* 158, 103701. doi: 10.1016/j.coastaleng.2020.103701

Raby, A., Bullock, G., Jonathan, P., Randell, D., and Whittaker, C. (2022). On wave impact pressure variability. *Coast. Eng* 177104168 doi: 10.1016/j.coastaleng.2022.104168

Reeve, D. E., Soliman, A., and Lin, P. Z. (2008). Numerical study of combined overflow and wave overtopping over a smooth impermeable seawall. *Coast. Eng.* 55 (2), 155–166. doi: 10.1016/j.coastaleng.2007.09.008

Schüttrumpf, H., Möller, J., Oumeraci, H., Grüne, J., and Weissmann, R. (2005). Effects of natural sea states on wave overtopping of seadikes [C]. *Proceedings Waves 2001, Conference*, 1565–1574.

Yuan, S. Y., Li, L., Amini, F., and Tang, H. W. (2014). Turbulence measurement of combined wave and surge overtopping over a full scale HPTRM strengthened levee. *J. Wat Coast. Ocean Eng.* 140, 04014014. doi: 10.1061/(ASCE)WW.1943-5460.0000230

Zhou, Z. J., Chen, Y. P., Pan, Y., Shen, Y. S., and Gan, M. (2020). Wave-induced uplift pressure on berm revetment with seabee slope. *Coast. Eng. J* 62 (4), 527–539. doi: 10.1080/21664250.2020.1816527

frontiers | Frontiers in Marine Science

TYPE Original Research
PUBLISHED 12 January 2023
DOI 10.3389/fmars.2022.1045335

OPEN ACCESS

EDITED BY
Zeng Zhou,
Hohai University, China

REVIEWED BY
Shaotong Zhang,
Ocean University of China, China
Yang Yang,
Nanjing Normal University, China

*CORRESPONDENCE
Shuguang Liu
liusgliu@tongji.edu.cn

SPECIALTY SECTION
This article was submitted to Coastal Ocean Processes, a section of the journal Frontiers in Marine Science

RECEIVED 15 September 2022
ACCEPTED 05 December 2022
PUBLISHED 12 January 2023

CITATION
Shen Q, Zhu Q, Liu S, Lou S, Wu H, Zhu Z, Xu B and Yuan R (2023) Sedimentation of cohesive sediments at the subtidal flat affected by wind wave in high turbidity estuary. *Front. Mar. Sci.* 9:1045335. doi: 10.3389/fmars.2022.1045335

Sedimentation of cohesive sediments at the subtidal flat affected by wind wave in high turbidity estuary

Qi Shen[1], Qin Zhu[2], Shuguang Liu[3]*, Sha Lou[3], Hualin Wu[1], Zhenchang Zhu[2], Bin Xu[1] and Rui Yuan[4]

[1]Key Laboratory of Estuarine and Coastal Project, Ministry of Transport, Shanghai Estuarine and Coastal Science Research Center, Shanghai, China, [2]Research Centre of Ecology & Environment for Coastal Areas and Deep Sea, Southern Marine Science and Engineering Guangdong Laboratory (Guangzhou), Guangzhou, China, [3]Department of Hydraulic Engineering, Tongji University, Shanghai, China, [4]Department of Ocean Science and Engineering, Shanghai Maritime University, Shanghai, China

Sedimentation is an important mechanism to mitigate the shrinking of tidal flat and to restore its ecological function by means of sand or mud nourishment. To explore the sedimentation of cohesive sediments, a seabed tripod observation system was deployed at the subtidal region of the Hengsha Shoal adjacent to the turbidity maximum zone of the Yangtze Estuary for 11 days. The results showed that the fine sediment with the median grain size around 8 mm occupied the whole water column. The seabed was in relative equilibrium state with the fluctuation of bed level smaller than 16 mm during the moderate wind condition while the seabed experienced a rapid erosion of 38mm and a successive intensive accretion of 68mm during the process of wind wave and swell. The bottom hydrodynamic at 0.3mab during the bed accretion was stronger than that during the bed erosion. The deposition process of cohesive sediments can be better described by the simultaneous deposition paradigm than that by the exclusive deposition paradigm according to the direct data-model comparison of the bed level changes, especially during the impact of fluid mud. Three possible reasons for the better performance of the simultaneous deposition paradigm were proposed. The first possibility is that the fine suspended sediments do maintain a continuous contact with the sediment bed since the direct bed level changes during our observation period has been well reproduced by the simultaneous deposition paradigm. The second possibility is the SSC-induced turbulence damping which facilitates the fine sediment settling in the form of cohesive sediment flocs, indicating the settling of sediments can't be judged by the critical shear stress for deposition just based on the single particle grain size. The last possibility is the fluid mud-induced overestimated bed shear stress by using turbulent velocity fluctuation above the fluid mud-water interface, which produces excess sediment erosion waiting to be compensated by the simultaneous deposition paradigm. For practical modeling purposes, modeling under the simultaneous deposition paradigm can give satisfactory

results for the sedimentation of cohesive sediment especially during the impact of wave or swell.

KEYWORDS

sedimentation, cohesive sediments, wave and swell, high turbidity estuary, subtidal flat

1 Introduction

Tidal flat, located at the forefront of the coastal estuary wetland, connects marine, terrestrial as well as freshwater ecosystems. As a key component of estuarine ecosystem, tidal flats provide important ecosystem services such as shoreline stabilization, storm and wave buffering, breeding and nursing ground as well as carbon sink (Costanza et al., 1997; Barbier et al., 2008; Cao et al., 2020; Li et al., 2021; Toniolo et al., 2021; Zhang et al., 2021). However, in recent years, tidal flats are under increasing threat from the anthropogenic interventions (e.g., upstream damming, land reclamations) and climate change (e.g., sea level rises, typhoon). For example, since 1990s, the land area in the Yangtze Estuary has increased by 10% (Zhang et al., 2020) while the growth rate of the subtidal zone of tidal flat, including the Hengsha Shoal which we studied in this paper, has decreased from 6.0 km^2/year (1977-1994) to -6.2 km^2/year (1994-2011) (Du et al., 2016). The weakened buffering capacity of tidal flats affects the estuarine land safety and wetland ecosystem stability (Ma et al., 2019; Kim et al., 2020).

Under these circumstances, sedimentation is an important mechanism to mitigate the shrinking of tidal flat and to restore the ecological function of tidal flat. Some practical approaches have been designed for utilizing sedimentation to prevent the erosion of tidal flats, which include soft solutions such as sand nourishments (Cooke et al., 2012; Van der Werf et al., 2015; Brand et al., 2022) and traditional hard solutions such as dikes, groins and seawalls (Kuang et al., 2019). Recently, some innovative underwater nourishments, which are located at the subtidal regions, such as the channel wall nourishment, the shoreface nourishment and the Mud Motor, have been proposed as a more simplified and economical process of nourishing, but the effect of nourishments on the local morphodynamics is still not well understood (Baptist et al., 2019; Huisman et al., 2019; Brand et al., 2022). Therefore, much more studies should be conducted on the sedimentation of cohesive sediments at the subtidal flat.

Previous studies pay much attention on the profile shape of the tidal flat and its long-term morphodynamics (Kirby, 2000; Yang et al., 2003; Friedrichs, 2011; Liu et al., 2011). Tidal current and wave are the two dominant forces that favor a dynamic equilibrium shore-normal convex-up and concave-up profile of tidal flats respectively (Friedrichs, 2011). The analytical result as well as the *in-situ* observation supports the trends that the net transport of suspended sediment at the tidal flat tends to be landward when being dominated by the tidal energy and to be seaward when being dominated by the wave energy (Janssen-Stelder, 2000; Yang et al., 2003; Friedrichs, 2011), which further contributes to the tidal flat erosion during periods of high waves alternating with tidal flat deposition in the presence of mainly tidal currents (Lee et al., 2004; Yang et al., 2008). Other studies concern about some local features of tidal flat and theirs morphodynamics process such as the development and migration of the tidal creek (Wang et al., 2020; Zhao et al., 2022), the morphodynamics impact of emergent vegetation (Sánchez et al., 2001; Temmerman et al., 2007; Schwarz et al., 2014) and the local sediment dynamics accompanied with its morphological impacts (Zhu et al., 2017; Zhu et al., 2019; Wang et al., 2020). Among theses, efforts have been made over the last two decades to measure the erosion threshold of sediments (see the summary by Hir et al., 2008). Recently, Zhu et al. (2019) highlighted the complexity in predicting the erosion of tidal flat due to needing a number of assumption and simplification and endeavored to evaluate the parameters for erosion rate formulation based on the local observation results.

In contrast to the number of studies on erosion properties, few field investigations have been conducted on sedimentation properties (Azhikodan and Yokoyama, 2018), which is the main concern of this paper. The sedimentation at the tidal flat is related to the sediment characteristics (settling velocity, critical shear stress for deposition), the near bed suspended sediment concentration (SSC) and the deposition paradigm. In coastal sedimentology and morphodynamics, especially for those fine sediment estuaries with median grain size (D50) finer than 63 μm, the settling velocity directly determines the vertical distribution of SSC and near-bed deposition flux (Wan et al., 2015). There are a number of factors controlling fine sediment settling velocity such as SSC, turbulence, temperature, salinity, floc size and density, mineral and organic compositions, biological coatings, and the concentration of positive ions in the suspension (Guan, 2003; Winterwerp and Kesteren, 2004). SSC is regarded as the active scalar of settling velocity and as one of the major determinants of fine sediment settling process (Gratiot et al., 2005; Manning et al., 2010). The fine sediments experiences two distinct settling processes with the increasing SSC, that are the accelerated flocculated settling when the SSC is

below the certain limit and the decelerated hindered settling when the SSC is over this critical value (Whitehouse et al., 2000; Wan et al., 2015). The hindering effects that are observed under quiescent conditions when the concentration exceeds the certain limit (approximately 10 kg/m^3) are reduced in highly turbulent conditions (Gratiot et al., 2005). Meanwhile, the bottom water turbulence will be suppressed if the near-bed high SSC prevails and generates a strong vertical stratification, which prevents the upper high tidal energy from being transferred into the water bottom and impacts the erosion and deposition of bed (Shen et al., 2020; Wu et al., 2022).

The critical shear stress for deposition could be another important factor controlling the sedimentation of tidal flat. In general, the critical shear stress for suspended sediment deposition is smaller than the erosion threshold, such that an intermediate range of bottom shear stresses can exist in which neither erosion nor deposition occurs (Sanford and Halka, 1993). However, the need of the deposition threshold for describing the near-bed deposition flux is still under debate, as there are two different paradigms of the erosion and deposition, the exclusive paradigm and the simultaneous paradigm (Sanford and Halka, 1993; Zhu et al., 2017; Dong et al., 2020). The exclusive paradigm suggests that the deposition in the bed occurs only when the bottom shear stress drops below the deposition threshold. In contrast, the simultaneous paradigm allows the deposition to take place at all times regardless of the deposition threshold. A distinct discrepancy of supporting each deposition paradigms has been found among the results from laboratory experiments (Partheniades, 1986; Lau and Krishnappan, 1994; Ha and Maa, 2009), field measurements (Kranck and Milligan, 1992; Sanford and Halka, 1993) and numerical simulations(Ao et al., 2010; Sanford, 2008; Shen et al., 2018; Dong et al., 2020), as the laboratory measurements often seem to support exclusive paradigm while field data or numerical simulation tend to support continuous deposition or the both respectively. Besides that, in natural environments, the combined effects of physical processes, geochemical properties, and biological activity complicate the determination of the critical shear stress for erosion and deposition (Grabowski et al., 2011), which makes the value of deposition threshold become quite variable (Dong et al., 2020).

Although the above studies broaden our knowledge of the morphodynamics of tidal flats, few attentions have been paid on the morphodynamics at the subtidal region of the tidal flat (Yang et al., 2003) and the sedimentation properties. Yang et al. (2003) had proposed to deem the tidal marshes, unvegetated tidal flats, and adjacent subtidal regions as a coupled system and examined its simultaneous response to storms. Recently, the cross-shore analysis on the turbulence, wave energy and sediment transport in the intertidal and shallow subtidal zones of sand beach system has been received increasing attention (Christensen et al., 2018; Christensen et al., 2019; Savige et al., 2021). Therefore, more efforts should be paid to study the sedimentation at the subtidal region of tide flat not only for enriching our knowledge of the sedimentation properties but also for better utilizing the underwater nourishment to mitigate the shrinking of tidal flat under the threat of global climate change.

In this paper, we set up a field campaign at the subtidal region of the Hengsha Shoal which is located near the estuarine turbidity maximum (ETM) of the Yangtze Estuary, China to study the sedimentation process during the impact of wind wave. Instruments with high vertical and temporal resolutions were deployed to capture the near bed SSC variation and the bed level changes for 11 days. Using the *in-situ* data, we reveal a phenomenon on the sedimentation with extreme high SSC at the subtidal region of the tidal flat under the impact of wave and discuss the performance of different deposition paradigms to estimate the near-bed deposition flux.

The paper is organized as follow. Section 2 gives an overview of the study area. The field campaign is described in Section 3. This section provides the definitions of variables and parameters calculated by the observed data as well. Results are shown in Section 4. The interpretation and discussion of the results follows in Section 5. Conclusions are drawn in Section 6.

2 Study area

In situ observations were conducted at the subtidal region of Hengsha Shoal, located near the ETM of the Yangtze Estuary, China (Figure 1A). The Yangtze Estuary is well-known for the considerable runoff from the Yangtze River, strong tides and high SSC. It has a three-tier bifurcation and four outlets to the East China Sea. They are the North Branch, the North Channel, the North Passage and the South Passage, respectively (Figure 1A). The average tidal range varies from 2.4 to 3.2 m, and the annual average freshwater discharge reaches 28,527 m^3/s with the peak value above 50,000 m^3/s during flooding season (Chen et al., 1999). Semi-diurnal tides and reciprocating tidal currents predominate in this estuary. The fluvial annual mean sediment discharge is approximately 0.486 billion tons before the 1990s (Milliman and Syvitski, 1991) and has been reduced to 0.123 billion tons after the operation of Three Gorges Dam in the Yangtze River in 2013 (Dai et al., 2018). In the Yangtze Estuary, the ETM zone is extremely large on a spatial scale, spreading over the entire mouth zone downstream from the south branch and inside the 10-m isobaths (Han and Lu, 2015). The maximum near-bed SSC at the ETM zone of Yangtze Estuary can reach above 40 kg/m^3 during a tidal cycle (Lin et al., 2021). Controlled by the East Asian monsoon system, southeasterly winds dominate in summer in the Yangtze Estuary, with multi-year averages ranging between 3.5 and 4.5 m/s (Yang et al., 2008).

The Hengsha Shoal is located at the east end of the Hengsha Island, situated at the lower segment of the North Channel (Figure 1A). It is in a tongue-shaped distribution along the west east direction. As the forefront of Hengsha Island, the Hengsha

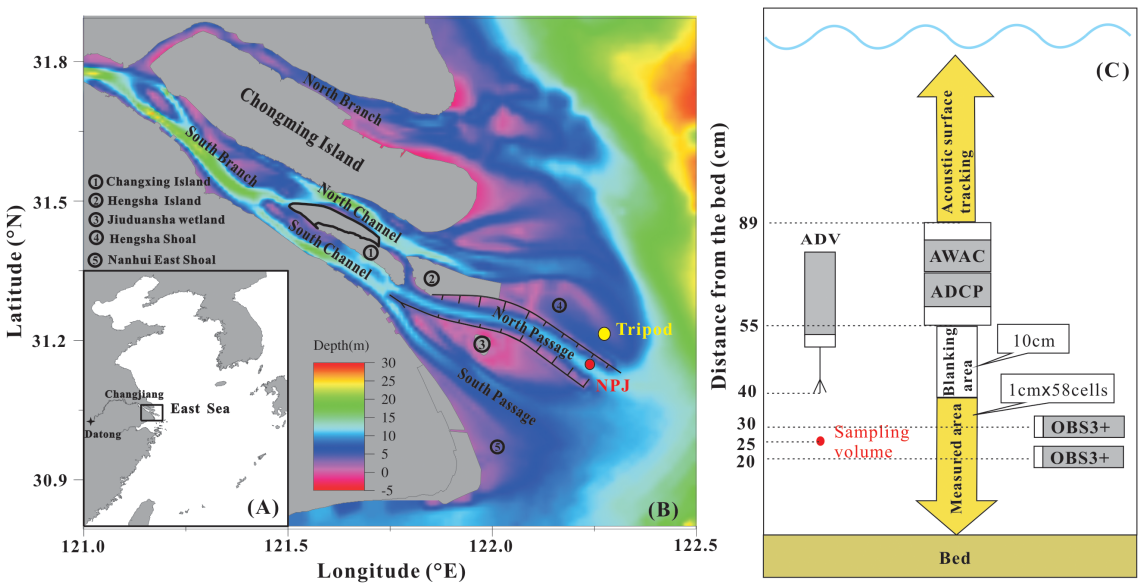

FIGURE 1
(A) Location of Yangtze Estuary. **(B)** Map of the Yangtze Estuary showing the observation sites by means of tripod. **(C)** Schematic representation of instrument deployment and location with respect to the seabed. The AWAC was used to obtain the wave parameters. the ADCP and the OBS3+ were used to measure velocity profiles and turbidity signal respectively. The ADV was deployed for the high-frequency sampling of velocity data at 8 Hz as well as the bed level change.

Shoal is constantly under the impact of wind wave, tidal flow as well as the movement of ETM. After the implementation of the land reclamations in the intertidal zone of Yangtze Estuary, the depth-mean of tidally averaged SSC has been declined and the landward boundary of the ETM zone in the North Channel is moved seaward (Teng et al., 2021). The erosion in the subtidal region of Hengsha Shoal has been accelerated owing to the intertidal reclamations (Du et al., 2016). The bed elevation of our observation site was 4.9m below the mean sea level.

3 Material and methods

3.1 Data collection

Our observations, lasting for 11 days, were carried out from June 21 to July 2, 2019. The bed level changes in association with tides and waves were monitored by the tripod observation system. The tripod was mounted with one wave monitoring instrument, two current monitoring instruments and two water turbidity monitoring instruments (Figure 1B).

The wave height and wave period were collected by the Acoustic Wave and Current Meter (AWAC, Nortek AS, Norway) which tracked the surface fluctuations at a frequency of 2 Hz over a duration of 1024 s, yielding 2048 measurements per burst.

An Acoustic Doppler Current Profile (ADCP, 2.0 MHz high-resolution profiler, Nortek AS, Norway) was used to measure high-resolution 3D current velocity profiles. The burst interval was 4 min. Each velocity profile was the mean value collected at a frequency of 1 Hz over a duration of 30 s. The ADCP was attached to the tripod with the transmitters facing downwards and was located 55 cm above bed (ab). The blanking distance was 10 cm, and the cell size was set to 1 cm.

An Acoustic Doppler Velocimeter (ADV, 6.0 MHz Vector current meter, Nortek AS, Norway) was used to measure three-dimensional turbulent velocities in a 2.65 cm^3 volume of water. The ADV was fixed firmly to a tripod, with the transmitters oriented downwards and the emitter positioned 40 cm ab. The sampled water volume, which was positioned 15 cm in front of the emitter, had a height of 25 cm. the ADV recorded 128 sets at a frequency of 8 Hz, resulting in a 15 second sampling duration every 4 min. The ADV recorded current data was discarded when the number of bad data (signal-to-noise ratio (SNR)< 20 or correlation coefficient (COR)< 70) reached 30% of the whole dataset.

Turbidity in the water column was measured every 4 min by using optical back-scatter sensors (OBS3+, Campbell Scientific, Inc, USA), with the probes positioned 20 cm and 30 cm ab. Turbidity signals from the OBS sensors were converted into SSC values *via* calibration with *in situ* sediment samples. The calibration experiment was carried out in the laboratory. Turbidity dataset was collected with different concentrated

well-mixing water samples obtained by constantly adding sediment from *in-situ* sediment samples to clear water. At the same time, different concentrated water samples were filtered by 0.45-μm filters to obtain SSCs. Regression between SSC and OBS3+ derived turbidity yielded a correlation coefficient of 0.99 (Figure 2). As the regression figure showed that the relationship between turbidity signal strength (counts) and the SSC had two different characters that were the positive relationship and the negative relationship. The turbidity signal strength (counts) was increased with the SSC when the SSC was lower than 10kg/m^3, which presents a positive relationship. While, when the SSC is greater than a certain value, the signal strength decreased dramatically with the increasing SSC, which presents a negative relationship. Due to the impact of extreme high SSC, the acoustic signal strength emitted from the ADCP was absorbed dramatically, which presented a sharp decrease of signal strength. Therefore, the negative relationship was used to estimate the SSC when the abnormal signal strength recorded by the ADCP was found.

The bed level changes were obtained by the ADV's measured distance between its probe to the sea bed (Andersen et al., 2007; Yu et al., 2017; Zhu et al., 2019). The ADV measured the distance between the transmitter and the sediment surface every 4 min with a high accuracy of ±1 mm. The wind velocity and direction were monitored at the NPJ station (Figure 1A).

3.2 Data analysis

3.2.1 Calculation of the bed shear stress

The total bed shear stress due to the combined wave-current action, τ_{cw} (N/m^2), was calculated using the Grant and Madsen (1979) wave–current interaction model:

$$\tau_{cw} = \sqrt{(\tau_w + \tau_c|cos\varphi_{cw}|)^2 + (\tau_c|sin\varphi_{cw}|)^2} \quad (1)$$

in which τ_w (N/m^2) and τ_c (N/m^2) are the wave- and current-induced bed shear stresses, respectively. φ_{cw} (°) is the angle between the current direction φ_c (°) and wave propagation direction φ_w (°). Four separate parameters are required to calculate total bed shear stress, that are τ_w , τ_c , φ_w and φ_c .

The wave-induced bed shear stress, τ_w , was obtained by analyzing surface-elevation monitoring data. Wave parameters (significant wave height H_s and significant wave period (T_s) were derived from the monitored data recorded by AWAC *via* SUV method (Pedersen et al., 2007). At the edge of the wave boundary layer, the peak orbital excursion and peak orbital velocity can be express as:

$$A_\delta = \frac{H_s}{2\sinh(kh)} \quad (2)$$

$$U_\delta = \omega A_\delta = \frac{\pi H_s}{T_s \sinh(kh)} \quad (3)$$

in which k (=$2\pi/L$, $L = (gT_s^2/2\pi)\tanh(kh)$is the wave length) is wave number (m^{-1}), h is water depth (m) and ω is angular velocity (s^{-1}). The time-averaged (over half a wave cycle) bed shear stress due to waves, τ_w (N/m^2), can be expressed as (Van Rijn, 1993):

$$\tau_w = \frac{1}{4}\rho f_w U_\delta^2 \quad (4)$$

in which ρ is the water density, f_w is the friction coefficient (-), which is determined by the diagram of hydraulic regimes of oscillatory flow (Van Rijn, 1993).

$$f_w = \begin{cases} 2Re_w^{-0.5} & , \ laminar \\ 0.09Re_w^{-0.2} & , \ smooth \ \ turbulent \\ min\left[\exp\left(-6 + 5.2r^{-0.19}\right), 0.3\right] & , \ rough \ \ turbulent \end{cases} \quad (5)$$

where $Re_w = \frac{U_\delta A_\delta}{\upsilon}$ (-) and $r = \frac{A_\delta}{k_s}$ (-) are the wave Reynolds number and relative roughness, respectively. k_s (=$2.5d_{50}$) is the Nikuradse roughness where d_{50} is the median grain size of the bed sediment, and υ (m^2/s) is the kinematic viscosity of water.

Since the fluctuating velocities measured in the vertical dimension are assumed not to be contaminated by wave orbital motion (Kim et al., 2000; Andersen et al., 2007), the current-induced bed shear stress, τ_c , was estimated by the variability in turbulent velocity fluctuation in the vertical dimension, $\overline{w_t^2}$, *via* the following equation (Stapleton and Huntley, 1995):

$$\tau_c = 0.19\rho\overline{w_t^2} \quad (6)$$

Because the measured near-bed velocities can be affected by wave motion in tidal areas, wave-turbulence decomposition is

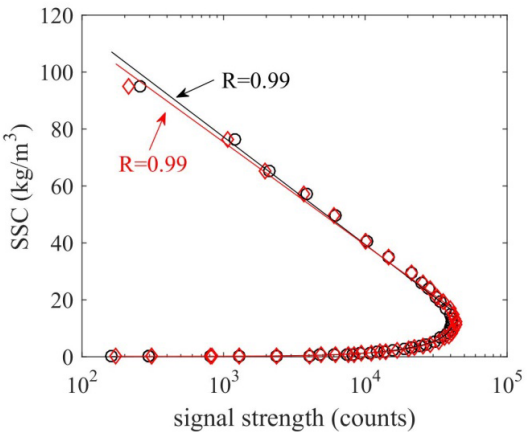

FIGURE 2
Regression relationship between the Obs3+'s signal strength and the SSC.

applied (Zhu et al., 2016). We used the energy spectrum analysis (ESA) approach, which is a technique developed by Soulsby and Humphery (1990) to split the variance without separating the instantaneous time series. The current direction and the wave direction were obtained from the burst-mean velocities and decomposed wave orbital velocities, respectively (Zhu et al., 2016).

3.2.2 Bed level simulation

The bed level variation was determined by the rates of erosion, E, and deposition, D, in kg/m^2/s:

$$\frac{\Delta\eta}{\Delta t} = \frac{1}{\rho_{dry}}(D - E) \tag{7}$$

where $\Delta\eta$ is the bed level variation in the time period Δt , ρ_{dry} (kg/m^3) is the dry density of surficial sediment. The dry density is set to 1400 kg/m^3 in this paper, which is close to the value used by Zhu et al. (2017) in the Yangtze Estuary. The rates of erosion are estimated by the Ariathurai-Partheniades equation (Partheniades, 1965; Ariathurai, 1974):

$$E = M\left(\frac{\tau_{cw}}{\tau_e} - 1\right) \tag{8}$$

where M (kg/m^2/s) is the erosion constant, τ_{cw} (N/m^2) is the total shear stress due to the combined effects of wave and current action, τ_e (N/m^2) is the critical bed shear stress for erosion. The estimate of the erosion threshold remains a challenge since it depends on the grain size distribution (Shields, 1936), the chemical impacts of cohesive sediment (Taki, 2000) and the biological effects (Van Prooijen et al., 2011). Thus, in this paper, the erosion threshold was determined by comparing time series of the bed shear stress and bed level changes in high frequency (Andersen et al., 2007; Verney et al., 2007; Shi et al., 2015; Zhu et al., 2019).

The deposition rate, D, in eq.(7) was derived from the sediment flux at the bed according to the aforementioned two different deposition paradigms:

$$D = c_b\omega_s \qquad \text{(simultaneous paradigm)} \tag{9}$$

or

$$D = \begin{cases} 0, & \tau_{cw} \le \tau_d \\ c_b\omega_s\left(1 - \frac{\tau_{cw}}{\tau_d}\right), & \tau_{cw} \le \tau_d \end{cases} \qquad \text{(exclusive paradigm)} \tag{10}$$

where c_b (kg/m^3) is the near bed suspended sediment concentration, ω_s (m/s) is the group settling velocity of suspended sediment. During the period of accelerated flocculated settling, the group settling velocity of cohesive sediment is strongly dependent on the SSC and can be estimated as:

$$\omega_s = E_1 c_b^{E_2} \tag{11}$$

in which E_1 and E_2 are constants varying among estuaries (Whitehouse et al., 2000). As the sediment concentration is over a certain limit, the process of hindered settling must be accounted for estimating the near bed deposition flux. We followed the formula of Whitehouse et al. (2000) which considered the process of hindered settling.

$$\omega_s = \frac{v}{d_e}\left\{\left[10.36^2 + 1.049\left(1 - C_f\right)^{4.7}D_*^3\right]^{0.5} - 10.36\right\} \tag{12}$$

$d_e = lC^{E_2}/2$,
$l = \left[\frac{19.8\rho\nu\rho_s^{E_2}E_1}{g(\rho_e-\rho)}\right]^{0.5}$,

$$C_f = \frac{(\rho_s - \rho)C}{\rho_e - \rho} \tag{13}$$

where d_e is the effective diameter of a floc increasing with the volume concentration C=c_b/ρ_s , ρ_s is the density of sediment, l is the length-scale, ρ_e =ρ+0.03(ρ_s−ρ) is the effective density of the floc and C_f is the volume concentration of floc. In the Yangtze Estuary, E_1 and E_2 can be set to 0.002 and 1.5, respectively (Zhu et al., 2017).

3.2.3 Gradient Richardson number

The gradient Richardson number (Ri) between 0.2 mab and 0.3 mab is calculated by the ratio of the square buoyancy frequency to the square vertical velocity shear (Dyer, 1986):

$$Ri = \frac{-\frac{g}{\rho_c}\frac{\partial\rho_c}{\partial z}}{\left(\frac{\partial u}{\partial z}\right)^2 + \left(\frac{\partial v}{\partial z}\right)^2} \tag{14}$$

where g is the gravity acceleration (m/s^2), ρ_c=ρ+(1−ρ/ρ_s)·SSC is the SSC-induced density (kg/m^3), z is the height above the seabed. The velocities between 0.2mab and 0.3mab were obtained by the bottom ADCP profiles. The SSC at 0.2mab and 0.3mab was collected by the OBS3+. Based on the linear stability theory, the critical value for active mixing is Ri_c=0.25 . When Ri<0.25 , the flow is unstable and the mixing is enhanced. On the contrary, when Ri>0.25 , the flow is stable and the mixing is suppressed.

4 Results

4.1 Wind and wave

During the 264-h spring-neap tidal cycle, the wind and wave conditions were quite variable (Figures 3A, C). At first, prior to the hours 72 (Phase I, moderate wave), the prevailing wind direction was northeaster and the wind speed was generally moderate. The averaged wind velocity at the NPJ station during this period was 5.2 m/s and the averaged significant wave height (SWH) at the observation site was 0.5 m. During the period from the hours 72 to 120 (Phase II, wind wave), the southeaster wind prevailed and the wind speed was increased rapidly, with the

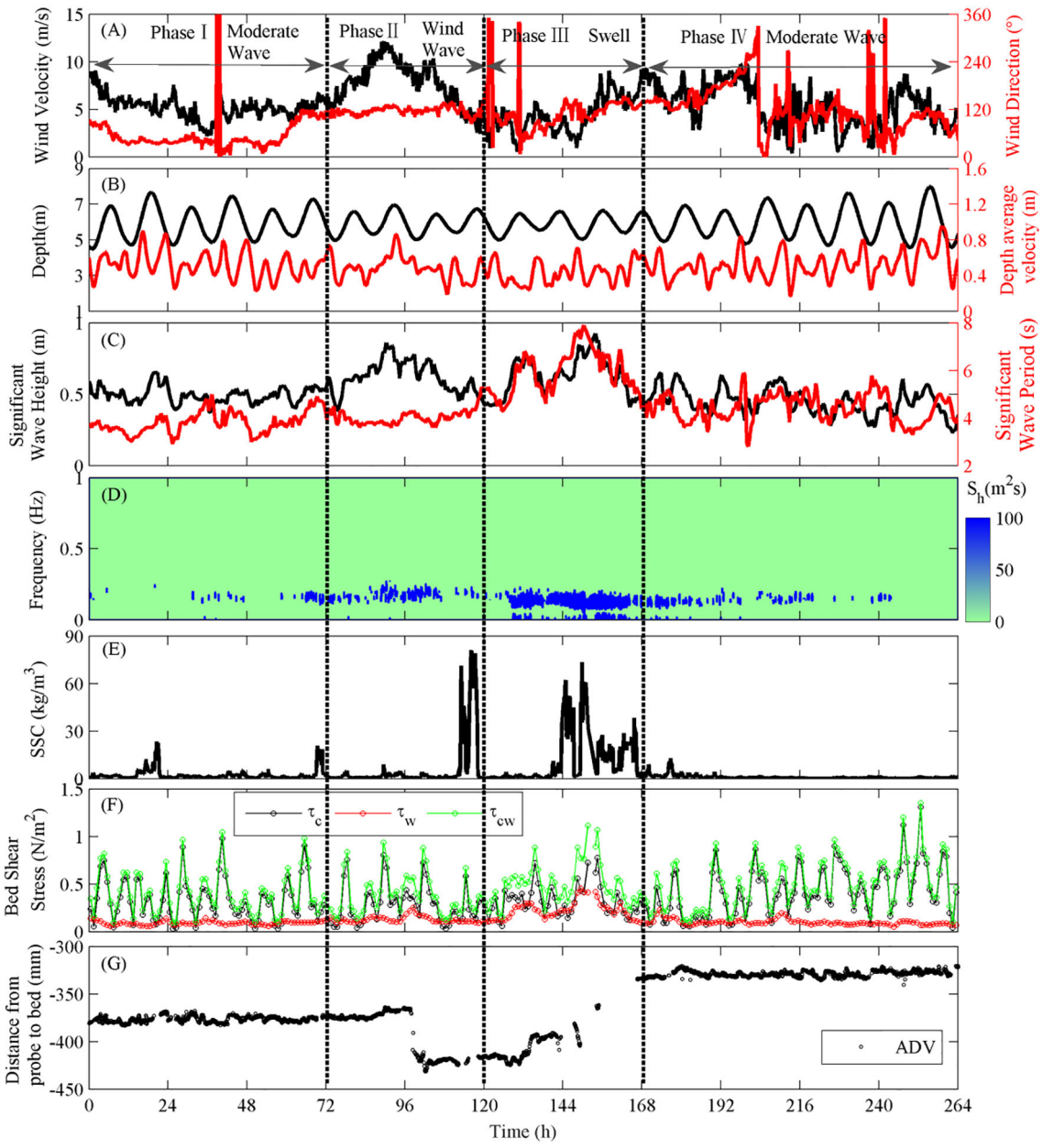

FIGURE 3
Time series of **(A)** wind velocity and direction, **(B)** water depth and depth-averaged current velocity, **(C)** SWH and SWP, **(D)** energy spectra of water level (S_h), **(E)** SSC at 0.2 mab, **(F)** wave/current-induced bed shear stresses (τ_w and τ_c , respectively) and total bed shear stress (τ_{cw}) and **(G)** the bed level changes observed by ADV instrument.

maximum wind speed exceeding 12 m/s. The wind wave was correspondingly intensified, with the SWH increased up to 0.84 m at the observation site. During the period from the hours 120 to 168 (Phase III, swell), the wind speed was back to normal, with the minimum wind velocity being 0.6 m/s and the maximum wind velocity around 9.0 m/s. The averaged wind velocity during this period was 4.3 m/s and the wind direction was somewhat variable. In contrast to the weak wind speed, the wave dynamic was increased dramatically due to the impact of the swell. The strongest wave process was appeared in this field campaign, with the maximum SWH being 0.92 m and the longest significant waver period (SWP) around 8 s. After the impact of swell (Phase IV, hours from 168 to the end, moderate wave), the wind speed remained moderate in general. The wind direction shifted constantly and the wind wave was weak. The averaged wind speed was 5.2 m/s and the averaged SWH at the

observation site was 0.4 m. The SWP during this period was fluctuated around the 4.4 s.

4.2 Tidal current and bed shear stress

During the Phase I, the tide was on the transition from the spring tide into the neap tide. The depth-averaged current velocity at the observation site varied periodically between the 0.23 m/s and 0.9 m/s, with an averaged value of 0.51 m/s during this period (Figure 3B). Due to the moderate wind condition, no clear peak was seen in the water level energy spectrum (Figure 3D), which had also been observed at the intertidal flat of the Yangtze Estuary (Zhu et al., 2016). The wave-induced bed shear stress (τ_w) was negligible, with the value less than 0.15 N/m^2. The averaged total bed shear stress (τ_{cw}) during this period was 0.4 N/m^2 (Figure 3F).

During the Phase II, the tide dynamic became weaker. The depth-averaged current velocity was ranged from 0.19 m/s to 0.86 m/s, with an average value of 0.48 m/s (Figure 3B). In contrast to the weak tidal dynamics, a strong onshore wind prevailed, which generated significant wave dynamic at our observation site. A clear single-peak, occurred at a frequency around 0.18 Hz, was seen in the water level energy spectrum due to the impact of wind wave (Figure 3D). The wave-induced bed shear stress was increased to 0.26 N/m^2, with an averaged value of 0.13 N/m^2 during this period (Figure 3F). The averaged total bed shear stress during this period was 0.38 N/m^2.

During the Phase III, the neap tide dominated and the wild wind calmed down. The depth-averaged current velocity was further decreased, ranging from 0.24 m/s to 0.7 m/s, with an average value of 0.42 m/s (Figure 3B). In contrast to the weak tide and wind, a strong wave process dominated this period due to the impact of the swell. A clear double-peak was found in the water level energy spectrum, of which the energy spectrum covering from 0.07Hz to 0.19 Hz was significantly enhanced (Figure 3D). The wave-induced bed shear stress was further increased to 0.46 N/m^2, with an averaged value of 0.22 N/m^2 during this period, which was stronger than the wave-induced bed shear stress during the Phase II (Figure 3F). The averaged current-induced bed shear stress during this period was 0.32 N/m^2, which was a little greater than the averaged current-induced bed shear stress, around 0.28 N/m^2, during the Phase II (Figure 3F). This phenomenon can be attributed to the extra turbulence increasing τ_c during the impact of wind or wave (Zhu et al., 2016). The averaged total bed shear stress during this period was 0.5 N/m^2.

During the Phase IV, the tide was on the transition from the neap tide into the spring tide and a moderate wind prevailed. The depth-averaged current velocity was ranged from 0.17 m/s to 0.95 m/s, with an average value of 0.5 m/s (Figure 3B). Without the prominent impact of wave, the current-induced bed shear stress was increased in accordance to the tide dynamics (Figure 3F). The averaged total bed shear stress during this period was 0.5 N/m^2.

4.3 Nearbed SSC and bed level changes

The time series of the nearbed SSC monitored at 0.2 mab and the corresponding bed level changes were shown in Figures 3E and G. During the Phase I, the SSC at 0.2 mab was generally lower than 5 kg/m^3, except for the high SSC recorded at the hours 23 and hours 71. The averaged SSC during the flood tide and the ebb tide were 2.5 kg/m^3 and 2.0 kg/m^3 respectively. The averaged flood and ebb velocity was 0.47 m/s and 0.55 m/s,

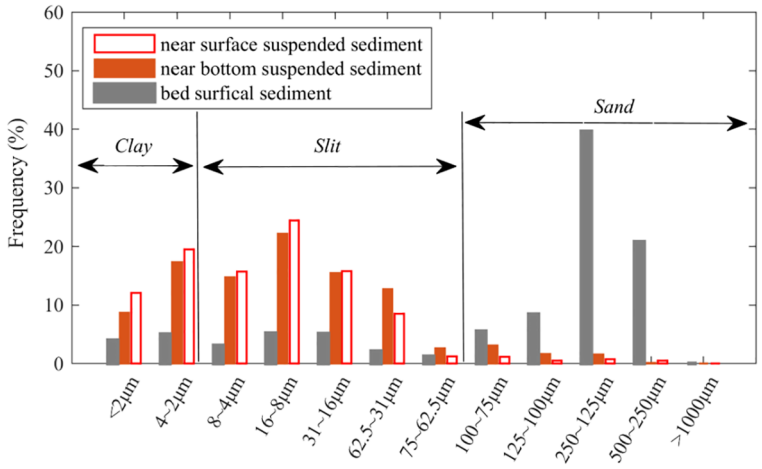

FIGURE 4
Grain size distribution of suspended sediment as well as the bed surficial sediment sampled at the observation site.

respectively. The variation of the SSC at 0.2mab was not in consistence with the variation of the current velocity, which presented the correlation coefficient between the SSC and current velocity lower than 0.2. The lower correlation coefficient indicated that the variation of the SSC at our observation site was not only related to the local sediment resuspension and deposition but also influenced by the advection of the SSC from the nearby ETM zone. This kind of phenomena was also reported in other high turbidity estuary like the Yellow River Delta (Zhang et al., 2022). Recently, Zhang et al. (2021) proposed a multiscale frequency superposition to qualitatively identify the horizontal advection of SSC. During the Phase I, no prominent erosion or deposition of seabed was found, with the bed level fluctuation smaller than 16 mm.

During the Phase II, a strong onshore wind produced a significant increasing of SWH. A prominent erosion of seabed occurred at the hours 96, with the erosion thickness around 38 mm, just when the SWH reached the maximum, which indicated that the wave-induced increase of shear stress triggered the prominent erosion of seabed. However, the corresponding SSC at the hours 96 didn't reached the maximum during this Phase, with the value lower than 1 kg/m^3. The extreme high SSC at 0.2 mab, with the value greater than 70 kg/m^3, was appeared after the hours 108 when the wind wave had been diminished. The extreme high SSC lasting for 5.4 hours induced a slight deposition of seabed with the deposition thickness around 8.4 mm.

The neap tide interacting with the swell dominated the Phase III for two days. In the first day, from the hours 120 to the hours 144, the fluid mud (SSC >10 kg/m^3) was not appeared although the SWH had been increased due to the impact of swell. The average SSC at 0.2 mab during the first day was 2.0 kg/m^3. The bed level was fluctuated slightly during this period, which experienced the swell-induced slight seabed erosion of 8.2 mm from the hours 120 to the hours 130 and the succeeding seabed deposition of 29.8 mm from the hours 130 to the hours 135. The fluid mud appeared at the second day and could almost exist for the whole day except for some short intervals with total 5.75 hours. Due to the absorption of acoustic energy by the fluid mud, the bed level change observed by ADV instrument was missed except for the moments when the fluid mud moved outside our observation site. Thanks to the lower SSC, the ADV captured the trend of bed level variation during and after the impact of fluid mud. According to the measured bed level changes, the rapid seabed deposition of 62 mm during the impact of fluid mud occurred despite of the stronger bed shear stress which was equivalent to the bed shear stress during the Phase II and was stronger than that in the first day during the Phase III.

During the Phase IV, the fluid mud was dissipated and the tidal dynamics was continuously strengthened. Without the impact of wind wave or swell, the SSC at 0.2mab returned to normal and the seabed was in relative equilibrium state with the fluctuation of bed level smaller than 15 mm. The averaged SSC during the flood tide and the ebb tide were 1.17 kg/m^3 and 0.7 kg/m^3 respectively. The bed levels recorded before and after the impact of fluid mud indicated that the fluid mud tended to encourage the bed sedimentation.

4.4 Sediment properties

During a tidal cycle, the median grain size of nearbed suspended sediment varied between 6.6 μm and 10.2 μm, with the average value of 8 μm. Meanwhile, the averaged median grain size of near water surface suspended sediment was 7.9 μm. The grain size distribution of near bottom suspended sediment was quite close to that of near water surface suspended sediment, with a mud (below 62.5μm) content of over 91% (Figure 4). The median grain size of bed surficial sediment at our observation site was 67.3μm, with a mud content of 48% (Figure 4). Therefore, the fine sediment, not only occupying the whole water column but also representing nearly half of bed sediments, could be the major participant in determining the erosion or the deposition of seabed.

By comparing time series of the bed shear stress and bed level changes in high frequency, which had been captured by the ADV instrument, the critical bed shear stress for erosion (τ_e) and deposition (τ_d) was estimated (Andersen et al., 2007). We collected a number of critical bed shear stress, based on the moment when the state of seabed began to shift between the erosion and the deposition. The frequency distribution of the extracted critical bed shear stress during our observation period was shown in Figure 5. The estimated critical bed shear stress for erosion and deposition was 0.15 N/m^2 and 0.13 N/m^2 respectively, after averaging the top three high-frequency values. The critical bed shear stress for deposition was 0.87 times the critical bed shear stress for erosion (τ_d=0.87τ_e). The estimated critical bed shear stresses for erosion and deposition

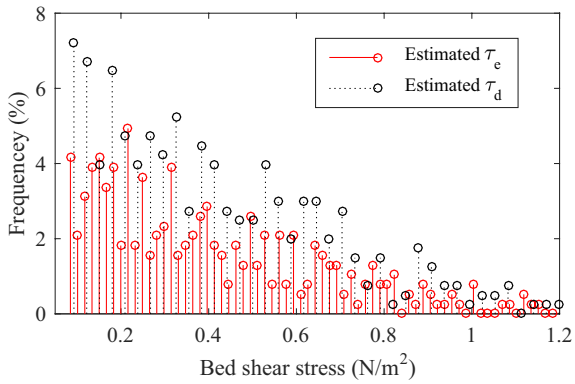

FIGURE 5
Frequency distribution of the estimated critical shear stress for erosion (τ_e) and deposition (τ_d) from the ADV-measured bed level variability.

were therefore applied to describe the bed surficial sediment movement at the subtidal region of Hengsha Shoal.

5 Discussion

5.1 Performance of runs with different deposition model

It's still under debate that whether the critical bed shear stress for deposition (τ_d) should be used to describe the physics of sedimentation even among the results of flume experiments (Partheniades, 1965; Krone, 1993; Winterwerp, 2007). The exclusive paradigm which believes that the sedimentation and erosion can't occur simultaneously in cohesive sediment dynamics was first proposed by Partheniades (1965) according to the experiments carried in a rotating annular flume. In the deposition experiment, the annular flume was set to a specific rotating speed in order to make the mud suspension settle and reach an equilibrium state. After that, the remaining suspension was carefully exchanged with clear water while the flume was maintaining the same speed. It finds that the exchanged water remained clear, which contributes to the conclusion that the erosion does not occur with the deposition. However, in another deposition experiment conducted in a straight flume by using the labeled sediment particles, Krone (1993) found erosion and deposition must occur simultaneously, at least during part of the experiment.

In addition, the indoor experiment can't well represent the unsteady hydrodynamics in estuary (Sanford and Halka, 1993). Therefore, runs with two different deposition models, the exclusive paradigm (Eq. 8,10) and the simultaneous paradigm (Eq. 8,9), for reproducing the bed level changes (Eq. 7) during our observation period were conducted to discuss the physics of sedimentation at the Yangtze Estuary directly. To fulfill this goal, the erosion constant shown in Eq. 8 should be estimated at first. In estuary, it is quite difficult to accurately calculate the erosion constant because it depends on the consolidation of bed, sediment composition, evolution of the sediment under the complex and mixed effects of the physical and biological interaction process. The typical value of this parameter was in the range of 10^{-6} to 10^{-3} kg/m^2/s (Ge et al., 2015). And, according to previous studies (Kuang et al., 2013; Ge et al., 2015; Shen et al., 2018), the erosion rate in the Yangtze Estuary was in the range of 2.5×10^{-6} to 2×10^{-4} kg/m^2/s. Due to the uncertainty of erosion constant, the erosion constants were determined in the range of 10^{-6} to 10^{-3} kg/m^2/s through the process of calibration under two different deposition models during three different phase of our observation period that were the phase of calm wind (Phase I), the phase of wind wave and swell (Phase II and III) and another phase of calm wind (Phase IV) respectively. Meanwhile, the calibrated erosion constant, for example the M_{ex} calibrated under the exclusive deposition model, was also used to predict the bed level changes under the simultaneous deposition model. All the information of running cases and parameter settings was shown in Table 1 and the performances of two different deposition models were shown in Figure 6 and Table 2. During the Phase I and IV, both the simultaneous paradigm and the exclusive paradigm, when using the calibrated erosion constant, could reproduce the relative bed level changes (Figures 6A, C). The RMSEs of case Ex-1 and Sim-1 were both smaller than 6mm (Table 2). However, the trend of this two deposition paradigms showed prominent difference, which showed that the simultaneous deposition paradigm reproduced the trend of the bed level change better than that of the exclusive deposition paradigm (Figures 6A, C). During the Phase II and III, the performance of the exclusive paradigm using the calibrated erosion constant (case Ex-1) was much worse than that of the simultaneous paradigm (case Sim-1), with the RMSE of case Ex-1 around 24.9mm which was bigger than the RMSE of case Sim-1 around 17.5mm (Table 2). Meanwhile, the correlation index of Sim-1and measured bed level change was 0.7 during the Phase II~III, which was quite bigger than the correlation index of Ex-1 with the value of 0.3. The most prominent disagreement between these two deposition paradigms occurred from the hour 144 to the hour 168 when the extreme high concentrated sediment clouds prevailed (Figure 3E). It indicated that the simultaneous deposition

TABLE 1 Simulation codes with different conditions.

Case name	Model	ρ_{dry}(kg/m^3)	τ_e(N/m^2)	τ_d(N/m^2)	M(kg/m^2/s)		
		Phase I ~ IV			PhaseI	PhaseII ~ III	PhaseIV
Ex-1	Eq.(8),(10)	1400	0.15	0.13	1×10^{-6} (calibrated M_{ex})	6.9×10^{-5} (calibrated M_{ex})	2×10^{-4} (calibrated M_{ex})
Sim-1	Eq.(8),(9)	1400	0.15	off	9×10^{-5} (calibrated M_{sim})	2×10^{-4} (calibrated M_{sim})	2×10^{-4} (calibrated M_{sim})
Ex-2	Eq.(8),(10)	1400	0.15	0.13	9×10^{-5} (M_{sim})	2×10^{-4} (M_{sim})	2×10^{-4} (M_{sim})
Sim-2	Eq.(8),(9)	1400	0.15	off	1×10^{-6} (M_{ex})	6.9×10^{-5} (M_{ex})	2×10^{-4} (M_{ex})

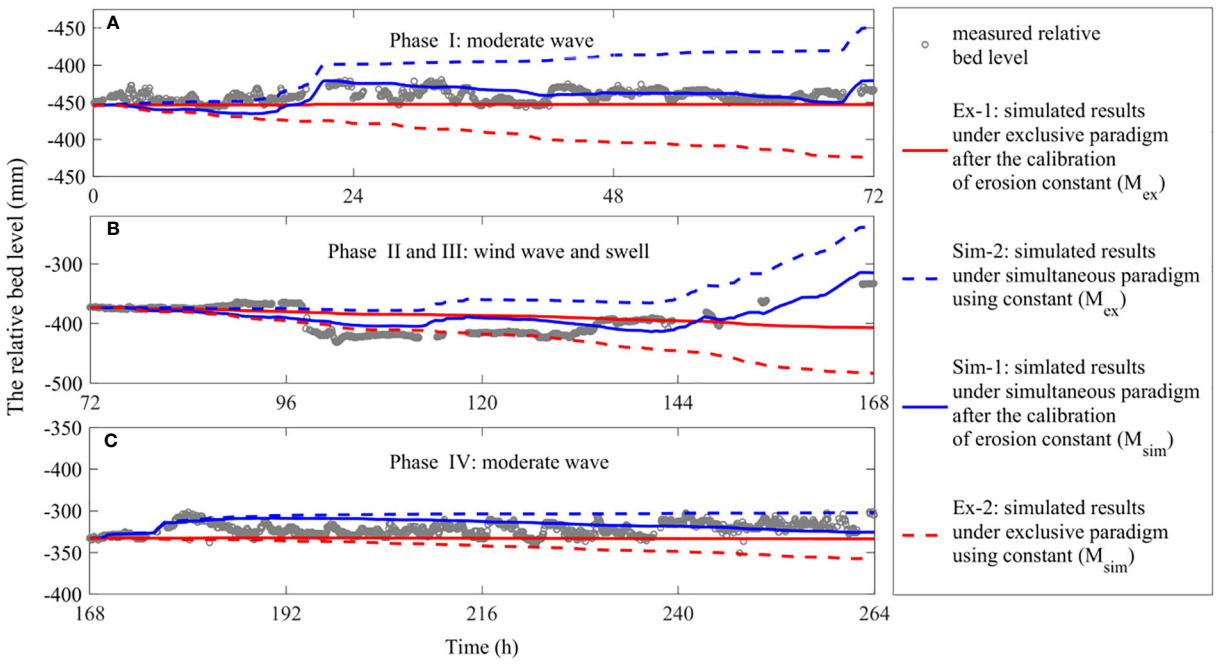

FIGURE 6
Performances of two different deposition paradigms during our observation period (Phase I: **A**, Phase II~III: **B** and Phase IV: **C**).

paradigm worked more efficiently to reproduce the bed level variation when the extreme high concentrated sediment clouds prevailed such as the mud fluid.

Besides that, the results also showed that the erosion constant played a vital role in determining the performance of each deposition models and the erosion constant didn't remain constant during our observation period. The calibrated erosion constant adopted by both the exclusive deposition paradigm and the simultaneous deposition paradigm experienced almost the same changing process. From the Phase I to Phase III, the erosion constant was increased dramatically with the help of the wave (or swell) process (Table 1). The reason for explaining this increasing process can be attributed to the bed liquefaction due to the wave process (Lambrechts et al., 2010; Ren et al., 2020). From the Phase III to the Phase IV, the calibrated erosion constant was increased up to 2×10^{-4} kg/m^2/s under the exclusive deposition paradigm while the calibrated erosion constant under the simultaneous deposition paradigm was remained unchanged, with the value of 2×10^{-4} kg/m^2/s. Due to the poor performance of exclusive deposition paradigm during the Phase II and III (Figure 6B), the calibrated erosion M_{ex} couldn't well represent the erodibility of the sea bed. Therefore, it's more acceptable that the erosion constant (M_{sim}) was nearly unchanged from the Phase III to the Phase IV, according to the results of simultaneous deposition paradigm. The variation of erosion constant is related to the sediment property and the water content (Sanford and Maa, 2001). This unchanged characteristic could be explained by the newly deposited fine sediment whose water content was approximate to that of liquefied surficial sediments during the Phase III.

TABLE 2 Root-mean-square error of simulated results under two different deposition paradigms.

Case name	*RMSE* (mm)		
	Phase I	Phase II~III	Phase IV
Ex-1	5.6	24.9	5.3
Ex-2	21.8	32.3	9.5
Sim-1	4.7	17.5	4.6
Sim-2	18.1	39.2	7.2

5.2 Deposition of cohesive sediments during the impact of swell

Generally, different formulations can be approximately equivalent when they are fit to a limit range of same data (Sanford and Halka, 1993). However, the formulations based on two different deposition paradigms can't reach consensus when reproducing the observed bed level changes during the impact of swell (Phase III, Figure 6B). In response to this problem, a further investigation was carried out to analyze the hydrodynamic and mixing condition during the Phase III of our observation period (Figure 7, Figure 8).

With the help of down looking ADCP instrument (Figure 1C), the time series profiles of current velocity in 30cm above the bed as well as the vertical averaged velocity, which lasted for two tidal cycles, were shown in Figure 7B and Figure 7A respectively. It showed that the tidal dynamics in each tidal cycle were similar. The averaged tidal range was 1.3m during the first tidal cycle of Phase III and the averaged tidal range was 1.4m during the successive tidal cycle (Figure 7A). Meanwhile, the tidal-averaged vertical mean velocity was 0.11m/s and 0.1 m/s during the first and successive tidal cycle respectively (Figure 8). In most time of Phase III, the relatively stronger tidal velocity was stayed at the upper layer, while the velocity close to zero was located near the sea bed (Figure 7B). According to the linear wave theory, the observed swell-induced wave belonged to the shallow-water wave since the estimated wave length ranging from 25m to 52m was much greater than the critical influencing wavelength (= 2 times the water depth). Meanwhile, the breaking wave didn't occur at our observation site because the ratio of the SWH to the water depth was less than 0.2, which was smaller than the critical wave breaking condition (=0.43, Wan et al., 2014) in the Yangtze Estuary. The swell-induced wave dynamic was a little bit enhanced since the

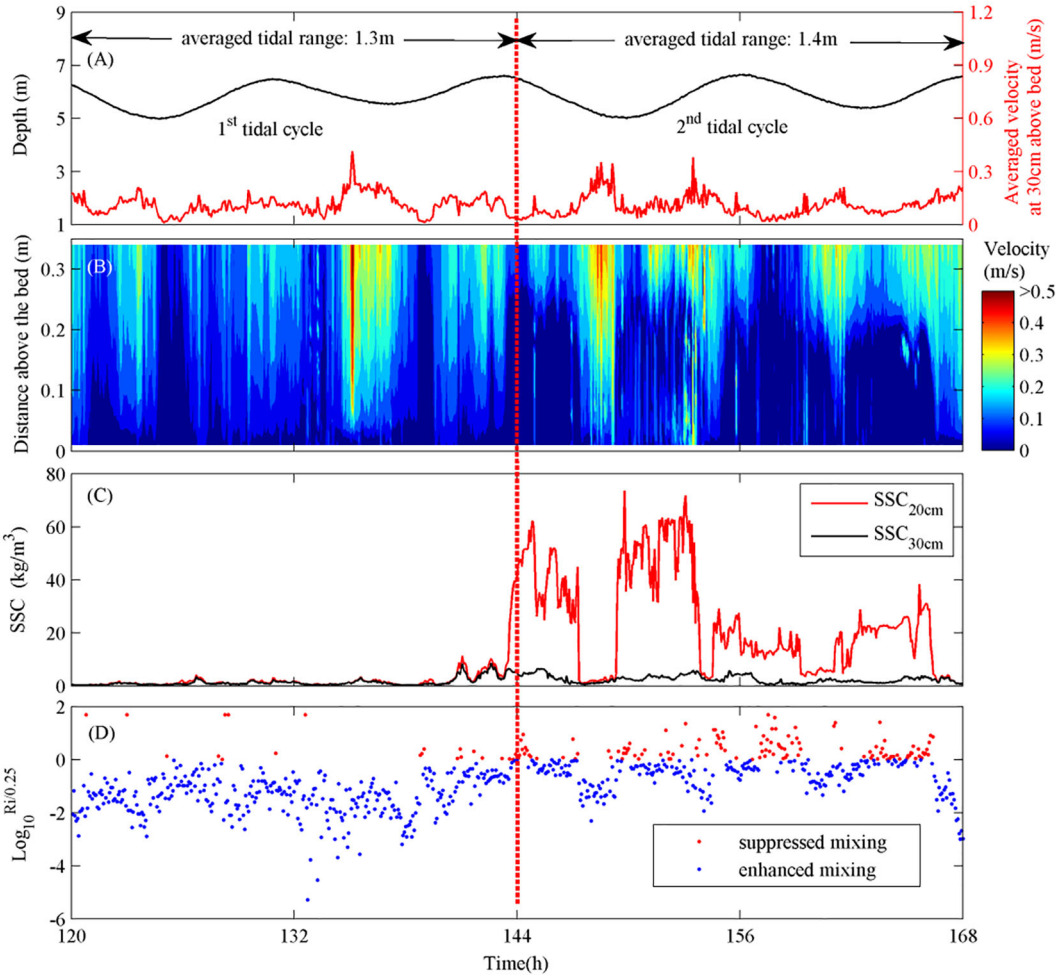

FIGURE 7
The hydrodynamic and mixing condition within 0.3 mab under the impact of fluid mud during our observation period (Phase III), which includes the times series of vertical-averaged velocity within 0.3 mab and the water depth **(A)**, the profiles of current velocity within 0.3 mab **(B)**, the SSC at 0.2 and 0.3 mab **(C)** and the mixing condition within 0.3 mab described by gradient Richardson number **(D)**.

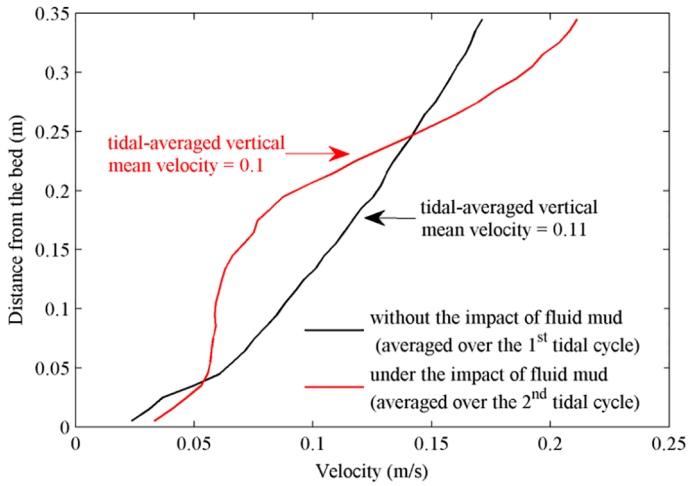

FIGURE 8
The tidal-averaged vertical profile of current velocity during the Phase III of our observation period.

SWH as well the SWP during the second tidal cycle (approximately hours 144 ~ 168, Figure 3F) were greater than those during the first tidal cycle (approximately hours 120 ~ 168, Figure 3F). Therefore, assuming the same tidal dynamic and enhancing wave force are dominated during these two tidal cycles, a relative tendency of bed erosion should be appeared at the successive tidal cycle when compared with the trend of bed variation during the first tidal cycle, which is supposed to be slowing down the rate of bed accretion or triggering the erosion of sea bed. However, the rate of bed accretion during the successive tidal cycle was much greater than that during the first tidal cycle (Figure 3G), indicating that other factor was responsible for the rapid bed accretion during the successive tidal cycle.

Based on the records of two OBS3+ instruments (Figure 1C), the mixing condition near bed was totally different during these two tidal cycles (Figure 7D). During the first tidal cycle, the SSCs at 0.2 mab and 0.3 mab were less than 10 kg/m^3. The vertical difference of SSC between at 0.2 mab and at 0.3mab was negligible, which fostered a well mixing condition near bed (Figure 7D). While during the successive tidal cycle, the vertical difference of SSC between at 0.2 mab and at 0.3 mab was quite obvious owing to the appearance of the near bed fluid mud of which the thickness was less than 0.3m. A stronger SSC-induced vertical stratification was formed and existed almost within the whole successive tidal cycle, which made the mixing condition suppressed near the sea bed. The SSC-induced turbulent damping had been reported at indoors experiment (Li and Gust, 2010) as well as in other field investigations (Shen et al., 2020; Hao et al., 2022), which proposed that the SSC-induced vertical density stratification decreased vertical momentum exchange, prohibited the near bed sediment resuspension and facilitated sediment settling.

Our observation also found that the current velocity above the fluid mud, approximately higher than 0.25 mab, was greater than that without the impact of fluid mud (Figure 8). This phenomenon can be explained by the drag reduction due to the fluid mud suspensions achieved by reduced momentum exchanging and vertical mixing near the upper fluid mud-water interface (Li and Gust, 2010). On the contrary, the near bed current velocity under the impact of fluid mud, located from 0.05mab to 0.2mab, was much smaller than that without the impact of fluid mud (Figure 8). Compared with the flow velocity without the impact of fluid mud, the occurrence of smaller flow velocity under the impact of fluid mud was not only related to the decreased momentum exchanging at the upper water-mud interface but also associated with the increasing viscosity (Qian and Wan, 1983) as well as the change of the rheological behaviors (Wang and Winterwerp, 1992).

Therefore, in despite of the stronger wave dynamics, the rate of bed accretion was increased due to the SSC-induced turbulent damping, the increasing flow viscosity and the rheological behaviors of fluid mud during the second tidal cycle of Phase III.

5.3 Possible reasons for better performance of the simultaneous deposition paradigm

There are three possible reasons for explaining the better performance of the simultaneous deposition paradigm especially during the Phase II and III of our observation period.

The first possibility is that the fine suspended sediments do maintain a continuous contact with the sediment bed according to the results of flume experiment (Mehta and Partheniades, 1975; Krone, 1993; Winterwerp, 2007) and the model simulation (Sanford and Halka, 1993; Sanford, 2008; Dong et al., 2020). Winterwerp (2007) reexamined the original laboratory experiments behind the exclusive erosion and deposition idea (Einstein and Krone, 1962). He noticed that due to the larger time span of the flume experiment, the erosion flux was limited by the availability of erodible material. The experimental results could be equally well reproduced by allowing for continuous deposition but invoking a stochastic bed shear stress and a gradual strengthening of the bed. The so-called critical shear stress for deposition (τ_d) in fact represented the critical shear stress for erosion (τ_e) of freshly deposited sediment (Winterwerp, 2007). Sanford and Halka (1993) simulated the variation of total SSC in Chesapeake Bay under different paradigms of erosion and deposition of mud and pointed out the better performance of the simultaneous deposition paradigm possibly due to the complex *in-situ* field conditions that couldn't be replicated in the laboratory experiments underlying the exclusive paradigm and the relatively weak representation of *in-situ* sediment behavior by a single sediment particle. Compared to the model-data comparison of SSC (Sanford and Halka, 1993; Dong et al., 2020), a more direct model-data comparison of relative bed level change in this paper was further supported the idea that the fine suspended sediments do maintain a continuous contact with the sediment bed in *in-situ* field conditions.

The second possibility is that the near bed high suspended sediment cloud suppresses the momentum exchange and facilitates the forming of cohesive sediment flocs. Since the fine sediments consume the turbulent energy to keep in suspension, the SSC-induced vertical stratification damps the turbulent energy and facilitates the fine sediment settling in the form of cohesive sediment flocs. According to the *in-situ* floc size measurement (Zhu et al., 2022), the floc size at the North Passage of Yangtze Estuary was 24~106μm under different turbulent shear stress, which was an order of magnitude larger than the particle grain size ranging from 5.8 to 10.6μm. The median grain size of nearbed suspended sediment at our observation site was quite close to the particle grain size measured by Zhu et al. (2022) (Figure 4). The critical SSC for maximum flocculation varies over a range of 1~30kg/m^3 (Wu and Wang, 2004; Wan et al., 2015). Therefore, the critical shear stress for deposition of fine sediment particle (τ_d) may not be acceptable to judge the moment of bed accretion since the settling of cohesive sediment flocs could still occur when the bed shear stress is over the critical shear stress for deposition of fine sediment particle (τ_d).

The third possibility is the impact of nearbed high concentrated suspended sediment like fluid mud, which distorted the bottom logarithmic velocity distribution and weakened the bed shear stress. In many practical modelling (Delft Hydraulics, 2003; Lyu and Zhu, 2018; Shen et al., 2018), a logarithmic velocity distribution is used to estimate the bed shear stress since the turbulent bed boundary, usually occupying from several centimeter above bed to 20~30% of water depth, is well developed in nature conditions. Without the impact of fluid mud, the vertical distribution of current velocity 0.3mab fit the logarithmic distribution and the bed shear stress could be estimated by the variability in turbulent velocity fluctuation (Stapleton and Huntley, 1995) (black line, Figure 8). However, the extreme high SSC clouds like fluid mud, with the thickness smaller than 0.3m during our observation, distorted the logarithmic current profile. An overestimated bed shear stress by using turbulent velocity fluctuation at 0.3mab could happen since the current velocity was significantly enhanced above or decreased below the fluid mud-water interface (red line, Figure 8). Compared to the exclusive deposition model, the simultaneous deposition model produced more sediment deposition flux which offset the excessive sediment erosion due to the overestimated bed shear stress especially during the impact of fluid mud. Although a more detailed fluid mud model can be used to simulate the erosion and deposition flux during the impact of fluid mud (Ge et al., 2020), it will be quite complex and time-consuming since an extra fluid mud module should be added to well describe the physical process of fluid mud and the model resolution of vertical grid should be high enough to distinguish the thickness of fluid mud which could be smaller than 30cm during our observation. For practical modeling purposes, modeling under the deposition paradigm can give satisfactory results especially during the impact of wave or swell.

6 Conclusions

264-h spring-neap tidal cycle observation was deployed with a bottom tripod to study the sedimentation of cohesive sediments at the subtidal region of Hengsha Shoal, located near the ETM of the Yangtze Estuary, China. The tripod was mounted with one wave monitoring instrument (AWAC), two current monitoring instruments (ADCP and ADV) and two water turbidity monitoring instruments (OBS3+) in order to collect the information of the wave dynamic, the tidal current, the near bed SSC and the relative bed level changes. The observation period could be divided into four phases according to wind and wave conditions. During the Phase I and IV, a moderate wind prevailed and the tidal dynamic was on the transition between the spring tide and the neap tide. The SSC at 0.2mab was generally lower than 5 kg/m^3 through most of the observation period. The seabed was in relative equilibrium state with the fluctuation of bed level smaller than 16 mm. During the Phase II and III, the neap tidal was accompanied with a significant process of wind wave and swell. A prominent

erosion of sea bed, with the erosion thickness around 38 mm, was achieved at the hours 96 when the wind-wave induced SWH was increased to the maximum and the SSC at 0.2mab was still lower than 1 kg/m^3. In contrast, a rapid seabed deposition of 62 mm from the hours 130 to the hours 135 was observed during the impact of fluid mud although the tidal current and swell-induced wave dynamic was much stronger than that during the erosion of sea bed at the hours 96.

According to the variation of relative bed level, the estimated critical bed shear stress for erosion and deposition was 0.15 N/m^2 and 0.13 N/m^2 respectively. The erosion constant didn't remain unchanged during our observation period. The calibrated erosion constant during the Phase I based on the simultaneous deposition paradigm was 9×10^{-5} kg/m^2/s due to the relatively consolidated surficial sediments while the calibrated erosion constant was increased up to 2×10^{-4} kg/m^2/s due to the impact of wind wave during the Phase II and remain unchanged during the successive tidal cycle (Phase III~IV).

The sedimentation of cohesive sediments at our observation site was analyzed according to the comparison of *in-situ* relative bed level changes to the modeling results under the exclusive and simultaneous deposition paradigms. The results showed that the sedimentation under simultaneous deposition paradigm, which believed that the erosion and deposition of sediment must occur simultaneously, described the relative bed level changes better particularly during the impact of fluid mud. Three possible reasons for the better performance of the simultaneous deposition paradigm were suggested. The first possibility is that the fine suspended sediments do maintain a continuous contact with the sediment bed since not only the indirect variation of SSC came from original laboratory experiments behind the exclusive erosion and deposition idea (Einstein and Krone, 1962) but also the direct bed level changes during our observation period have been well reproduced by the simultaneous deposition paradigm. The second and third possibilities are attributed to the near bed high suspended sediment clouds like fluid mud which suppresses the momentum exchange and distorts the near bed logarithmic velocity distribution. The SSC-induced turbulence damping facilitates the fine sediment settling in the form of cohesive sediment flocs whose size can be an order of magnitude larger than the particle grain size in the Yangtze Estuary, indicating the settling of sediments can't be judged by the critical shear stress for deposition just based on the single particle grain size. Meanwhile, an overestimated bed shear stress by using turbulent velocity fluctuation at 0.3mab could happen since the current velocity was significantly enhanced above or decreased below the fluid mud-water interface. Compared to the exclusive deposition model, the simultaneous deposition model produced more sediment deposition flux to offset the excessive sediment erosion due to the overestimated bed shear stress especially during the impact of fluid mud. For practical modeling purposes, modeling under the deposition paradigm can give satisfactory results especially during the impact of wave or swell.

Data availability statement

The raw data supporting the conclusions of this article will be made available by the authors, without undue reservation.

Author contributions

QS conducted filed observation, conceived the idea, analyzed the data and drafted the manuscript. QZ conceived the idea and analyzed the data. SGL reviewed and edited the manuscript. SL reviewed and edited the manuscript. HW reviewed and edited the manuscript. ZZ analyzed the data and reviewed the manuscript. BX conducted the field observation. RY reviewed and edited the manuscript. All authors contributed to the article and approved the submitted version.

Acknowledgments

Financial support for the study was provided by the National Natural Science Foundation of China (51961145106, U2040204, 51909038) and Shanghai Science and Technology Program Funds (21DZ1201002). We thank the reviewers for their valuable comments and suggestions.

Conflict of interest

The authors declare that the research was conducted in the absence of any commercial or financial relationships that could be construed as a potential conflict of interest.

Publisher's note

References

Andersen, T. J., Fredsoe, J., and Pejrup, M. (2007). In situ estimation of erosion and deposition thresholds by acoustic Doppler velocimeter (ADV). *Estuarine Coast. Shelf Sci.* 75 (3), 327–336. doi: 10.1016/j.ecss.2007.04.039

Ao, C., Wang, Z. B., De Vriend, H. J., and M.J.F., S. (2022). "A process-based approach to sediment transport in the Yangtze estuary," in *Conference on Coastal Engineering*. Shanghai, China: Coastal Engineering Research Council. Available at http://journals.tdl.org/icce/index.php/icce/article/view/1387/pdf_352. accessed date: 20-11-2015.

Ariathurai, C. (1974). *A finite element model for sediment transport in estuaries* (Berkley, USA: University of California).

Azhikodan, G., and Yokoyama, K. (2018). Sediment transport and fluid mud layer formation in the macro-tidal chikugo river estuary during a fortnightly tidal cycle. *Estuarine Coast. Shelf Sci.* 202, 232–245. doi: 10.1016/j.ecss.2018.01.002

Baptist, M. J., Gerkema, T., van Prooijen, B. C., van Maren, D. S., van Regteren, M., Schulz, K., et al. (2019). Beneficial use of dredged sediment to enhance salt marsh development by applying a 'Mud motor'. *Ecol. Eng.* 127, 312–323. doi: 10.1016/j.ecoleng.2018.11.019

Barbier, E. B., Koch, E. W., Silliman, B. R., Hacker, S. D., Wolanski, E., Primavera, J., et al. (2008). Coastal ecosystem-based management with nonlinear ecological functions and values. *Science* 319 (5861), 321–323. doi: 10.1126/science.1150349

Brand, E., Ramaekers, G., and Lodder, Q. (2022). Dutch Experience with sand nourishments for dynamic coastline conservation – an operational overview. *Ocean Coast. Manage.* 217, 106008. doi: 10.1016/j.ocecoaman.2021.106008

Cao, W., Zhou, Y., Li, R., and Li, X. (2020). Mapping changes in coastlines and tidal flats in developing islands using the full time series of landsat images. *Remote Sens. Environ.* 239, 111665. doi: 10.1016/j.rse.2020.111665

Chen, J., Li, D., Chen, B., Hu, F., Zhu, H., and Liu, C. (1999). The processes of dynamic sedimentation in the changjiang estuary. *J. Sea Res.* 41 (1), 129–140. doi: 10.1016/S1385-1101(98)00047-1

Christensen, D. F., Brinkkemper, J., Ruessink, G., and Aagaard, T. (2018). Field observations of turbulence in the intertidal and shallow subtidal zones. *Continental Shelf Res.* 170, 21–32. doi: 10.1016/j.csr.2018.10.002

Christensen, D. F., Brinkkemper, J., Ruessink, G., and Aagaard, T. (2019). Field observations of intra-wave sediment suspension and transport in the intertidal and shallow subtidal zones. *Mar. Geology* 413, 10–26. doi: 10.1016/j.margeo.2019.04.005

Cooke, B. C., Jones, A. R., Goodwin, I. D., and Bishop, M. J. (2012). Nourishment practices on Australian sandy beaches: A review. *J. Environ. Manage.* 113, 319–327. doi: 10.1016/j.jenvman.2012.09.025

Costanza, R., de Arge, R., de Groot, R., Farber, S., Grasso, M., Hannon, B., et al. (1997). The value of the world's ecosystem services and natural capital. *Nature* 387 (6630), 253–260. doi: 10.1038/387253a0

Dai, Z., Mei, X., Darby, S. E., Lou, Y., and Li, W. (2018). Fluvial sediment transfer in the changjiang (Yangtze) river-estuary depositional system. *J. Hydrology* 566, 719–734. doi: 10.1016/j.jhydrol.2018.09.019

Delft Hydraulics (2003). *Delft3D-FLOW: Simulation of multi-dimensional hydrodynamic flows and transport phenomena, including sediments*. (Delft, The Netherlands: WL | delft hydraulics).

Dong, H., Jia, L., He, Z., Yu, M., and Shi, Y. (2020). Application of parameters and paradigms of the erosion and deposition for cohesive sediment transport modelling in the lingdingyang estuary, China. *Appl. Ocean Res.* 94, 101999. doi: 10.1016/j.apor.2019.101999

Du, J.-L., Yang, S.-L., and Feng, H. (2016). Recent human impacts on the morphological evolution of the Yangtze river delta foreland: A review and new perspectives. *Estuarine Coast. Shelf Sci.*, 181, 160–169. doi: 10.1016/j.ecss.2016.08.025

Dyer, K. R. (1986). *Coastal and estuarine sediment dynamics* (Chichester, Sussex (UK: John Wiley and Sons).

Einstein, H. A., and Krone, R. B. (1962). Experiments to determine modes of cohesive sediment transport in salt water. *J. Geophysical Res.* 67 (4), 1451–1461. doi: 10.1029/JZ067i004p01451

Friedrichs, C. T. (2011). "3.06 - tidal flat morphodynamics: A synthesis," in *Treatise on estuarine and coastal science*. Eds. E. Wolanski and D. McLusky (Waltham: Academic Press), 137–170.

Ge, J., Chen, C., Wang, Z. B., Ke, K., Yi, J., and Ding, P. (2020). Dynamic response of the fluid mud to a tropical storm. *J. Geophysical Research: Oceans* 125 (3), e2019JC015419. doi: 10.1029/2019JC015419

Ge, J., Shen, F., Guo, W., Chen, C., and Ding, P. (2015). Estimation of critical shear stress for erosion in the changjiang estuary: A synergy research of observation, GOCI sensing and modeling. *J. Geophysical Research: Oceans* 120 (12), 8439–8465. doi: 10.1002/2015JC010992

Grabowski, R. C., Droppo, I. G., and Wharton, G. (2011). Erodibility of cohesive sediment: The importance of sediment properties. *Earth-Science Rev.* 105 (3), 101–120. doi: 10.1016/j.earscirev.2011.01.008

Grant, W. D., and Madsen, O. S. (1979). Combined wave and current interaction with a rough bottom. *J. Geophysical Research: Oceans* 84 (C4), 1797–1808. doi: 10.1029/JC084iC04p01797

Gratiot, N., Michallet, H., and Mory, M. (2005). On the determination of the settling flux of cohesive sediments in a turbulent fluid. *J. Geophysical Research: Oceans* 110, C06004. doi: 10.1029/2004JC002732

Guan, W. (2003). *Transport and deposition of high-concentration suspension of cohesive sediment in a macrotidal estuary* (Hong Kong: Hong Kong University).

Ha, H. K., and Maa, J. P. Y. (2009). Evaluation of two conflicting paradigms for cohesive sediment deposition. *Mar. Geology* 265 (3), 120–129. doi: 10.1016/j.margeo.2009.07.001

Han, Y. F., and Lu, C. T. (2015). Process research on estuarine turbidity maximum and mouth bar of Yangtze estuary after the improvement works. *Proc. Eng.* 116, 80–87. doi: 10.1016/j.proeng.2015.08.267

Hao, W., Yaping, W., Shu, G., Fei, X., Jieping, T., and Dezhi, C. (2022). Fluid mud dynamics in a tide-dominated estuary: A case study from the Yangtze river. *Continental Shelf Res.* 232, 104623. doi: 10.1016/j.csr.2021.104623

Hir, P. L., Cann, P., Waeles, B., Jestin, H., and Bassoullet, P. (2008). "Chapter 11 erodibility of natural sediments: experiments on sand/mud mixtures from laboratory and field erosion tests," in *Proceedings in marine science*. Eds. T. Kusuda, H. Yamanishi, J. Spearman and J. Z. Gailani (Elsevier), 137–153. doi: 10.1016/S1568-2692(08)80013-7

Huisman, B., Walstra, D.-J., Radermacher, M., De Schipper, M., and Ruessink, G. (2019). Observations and modelling of shoreface nourishment behaviour. *J. Mar. Sci. Eng.* 7, 59. doi: 10.3390/jmse7030059

Janssen-Stelder, B. (2000). The effect of different hydrodynamic conditions on the morphodynamics of a tidal mudflat in the Dutch wadden Sea. *Continental Shelf Res.* 20 (12), 1461–1478. doi: 10.1016/S0278-4343(00)00032-7

Kim, S. C., Friedrichs, C. T., Maa, P. Y., and Wright, L. D. (2000). Estimating bottom stress in tidal boundary layer from acoustic Doppler velocimeter data. *J. Hydraulic Engineering-ASCE* 126 (6), 399–406. doi: 10.1061/(ASCE)0733-9429(2000)126:6(399)

Kim, D., Jo, J., Kim, B., Ryu, J., and Choi, K. (2020). Influence of dike-induced morphologic and sedimentologic changes on the benthic ecosystem in the sheltered tidal flats, saemangeum area, west coast of Korea. *Environ. pollut.* 257, 113507. doi: 10.1016/j.envpol.2019.113507

Kirby, R. (2000). Practical implications of tidal flat shape. *Continental Shelf Res.* 20 (10), 1061–1077. doi: 10.1016/S0278-4343(00)00012-1

Kranck, K., and Milligan, T. G. (1992). Characteristics of suspended particles at an 11-hour anchor station in San Francisco bay, California. *J. Geophysical Research: Oceans* 97 (C7), 11373–11382. doi: 10.1029/92JC00950

Krone, R. B. (1993). "Sedimentation revisited," in *Nearshore and estuarine cohesive sediment transport*. Ed. A. J. Mehta (American Geophysical Union, Coastal and Estuarine Studies), 108–125. doi: 10.1029/CE042p0108

Kuang, C., Liu, X., Gu, J., Guo, Y., Huang, S., Liu, S., et al. (2013). Numerical prediction of medium-term tidal flat evolution in the Yangtze estuary: Impacts of the three gorges project. *Continental Shelf Res.* 52, 12–26. doi: 10.1016/j.csr.2012.10.006

Kuang, C., Mao, X., Gu, J., Niu, H., Ma, Y., Yang, Y., et al. (2019). Morphological processes of two artificial submerged shore-parallel sandbars for beach nourishment in a nearshore zone. *Ocean Coast. Manage.* 179, 104870. doi: 10.1016/j.ocecoaman.2019.104870

Lambrechts, J., Humphrey, C., McKinna, L., Gourge, O., Fabricius, K. E., Mehta, A. J., et al. (2010). Importance of wave-induced bed liquefaction in the fine sediment budget of Cleveland bay, great barrier reef. *Estuarine Coast. Shelf Sci.* 89 (2), 154–162. doi: 10.1016/j.ecss.2010.06.009

Lau, Y., and Krishnappan, B. (1994). Does reentrainment occur during cohesive sediment settling? *J. Hydraulic Eng.* 120 (2), 236–244. doi: 10.1061/(ASCE)0733-9429(1994)120:2(236)

Lee, H. J., Jo, H. R., Chu, Y. S., and Bahk, K. S. (2004). Sediment transport on macrotidal flats in garolim bay, west coast of Korea: significance of wind waves and asymmetry of tidal currents. *Continental Shelf Res.* 24 (7), 821–832. doi: 10.1016/j.csr.2004.01.005

Li, M. Z., and Gust, (2010). Boundary layer dynamics and drag reduction in flows of high cohesive sediment suspensions. *Sedimentology* 47 (1), 71–86. doi: 10.1046/j.1365-3091.2000.00277.x

Li, H., Li, L., Su, F., Wang, T., and Gao, P. (2021). Ecological stability evaluation of tidal flat in coastal estuary: A case study of liaohe estuary wetland, China. *Ecol. Indic.* 130, 108032. doi: 10.1016/j.ecolind.2021.108032

Lin, J., van Prooijen, B. C., Guo, L., Zhu, C., He, Q., and Wang, Z. B. (2021). Regime shifts in the changjiang (Yangtze river) estuary: The role of concentrated benthic suspensions. *Mar. Geology* 433, 106403. doi: 10.1016/j.margeo.2020.106403

Liu, X. J., Gao, S., and Wang, Y. P. (2011). Modeling profile shape evolution for accreting tidal flats composed of mud and sand: A case study of the central jiangsu coast, China. *Continental Shelf Res.* 31 (16), 1750–1760. doi: 10.1016/j.csr.2011.08.002

Lyu, H. H., and Zhu, J. R. (2018). Impact of the bottom drag coefficient on saltwater intrusion in the extremely shallow estuary. *J. Hydrology* 557, 838–850. doi: 10.1016/j.jhydrol.2018.01.010

Ma, T., Li, X., Bai, J., and Cui, B. (2019). Impacts of coastal reclamation on natural wetlands in Large river deltas in China. *Chin. Geographical Sci.* 29 (4), 640–651. doi: 10.1007/s11769-019-1049-8

Manning, A. J., Langston, W. J., and Jonas, P. J. C. (2010). A review of sediment dynamics in the Severn estuary: Influence of flocculation. *Mar. pollut. Bull.* 61 (1), 37–51. doi: 10.1016/j.marpolbul.2009.12.012

Mehta, A. J., and Partheniades, E. (1975). An investigation of the depositional properties of flocculated fine sediments. *J. Hydraulic Res.* 13 (4), 361–381. doi: 10.1080/00221687509499694

Milliman, J., and Syvitski, J. (1991). Geomorphic tectonic control of sediment discharge to ocean – the importance of small mountainous rivers. *J. Geology* 100, 525–544. doi: 10.1086/629606

Partheniades, E. A. (1965). Erosion and deposition of cohesive soils. *Am. Soc. Civil Engineers* 91 (1), 190–192. doi: 10.1061/JYCEAJ.0001165

Partheniades, E. (1986). "A fundamental framework for cohesive sediment dynamics," in *Estuarine cohesive sediment dynamics*. Ed. A. J. Mehta (Berlin: Springer), 219–250.

Pedersen, T., Siegel, E., and Wood, J. (2007). "Directional wave measurements from a subsurface buoy with an acoustic wave and current profiler (AWAC)," in *Proceedings of the Oceans 2007*. (Vancouver, BC: IEEE), 1–10. doi: 10.1109/OCEANS.2007.4449153

Qian, N., and Wan, Z. (1983). *Mechanics of sediment transport* (BeiJing: Science Press), 34–39.

Ren, Y., Xu, G., Xu, X., Zhao, T., and Wang, X. (2020). The initial wave induced failure of silty seabed: Liquefaction or shear failure. *Ocean Eng.* 200, 106990. doi: 10.1016/j.oceaneng.2020.106990

Sánchez, J. M., SanLeon, D. G., and Izco, J. (2001). Primary colonisation of mudflat estuaries by spartina maritima (Curtis) fernald in Northwest Spain: vegetation structure and sediment accretion. *Aquat. Bot.* 69 (1), 15–25. doi: 10.1016/S0304-3770(00)00139-X

Sanford, L. P. (2008). Modeling a dynamically varying mixed sediment bed with erosion, deposition, bioturbation, consolidation, and armoring. *Comput. Geosciences* 34 (10), 1263–1283. doi: 10.1016/j.cageo.2008.02.011

Sanford, L. P., and Halka, J. P. (1993). Assessing the paradigm of mutually exclusive erosion and deposition of mud, with examples from upper Chesapeake bay. *Mar. Geology* 114, 37–57. doi: 10.1016/0025-3227(93)90038-W

Sanford, L. P., and Maa, J. P. Y. (2001). A unified erosion formulation for fine sediments. *Mar. Geology* 179 (1), 9–23. doi: 10.1016/S0025-3227(01)00201-8

Savige, T. R., Kowalczyk, H. E. L., Fellowes, T. E., and Kennedy, D. M. (2021). The role of seaward morphology on wave transformation onto and across a microtidal shore platform. *Continental Shelf Res.* 224, 104472. doi: 10.1016/j.csr.2021.104472

Schwarz, C., Ye, Q. H., van der Wal, D., Zhang, L. Q., Bouma, T., Ysebaert, T., et al. (2014). Impacts of salt marsh plants on tidal channel initiation and inheritance. *J. Geophysical Research: Earth Surface* 119 (2), 385–400. doi: 10.1002/2013JF002900

Shen, Q., Huang, W. R., and Qi, D. M. (2018). Integrated modeling of typhoon damrey's effects on sediment resuspension and transport in the north passage of changjiang estuary, China. *J. Waterway Port Coast. Ocean Eng.* 144 (6), 04018015. doi: 10.1061/(ASCE)WW.1943-5460.0000453

Shen, Q., Huang, W., Wan, Y., Gu, F., and Qi, D. (2020). Observation of the sediment trapping during flood season in the deep-water navigational channel of the changjiang estuary, China. *Estuarine Coast. Shelf Sci.* 237, 106632. doi: 10.1016/j.ecss.2020.106632

Shields, A. (1936). "Application of similarity principles and turbulence research to bed-load movement," in *Mitteilungen der Preussischen Versuchsanstalt fur Wasserbau und Schifbau, Berlin*. eds W. P. Ott and J. C. van Uchelen (Pasadena, CA: California Institute of Technology).

Shi, B. W., Wang, Y. P., Yang, Y., Li, M. J., Li, P., Ni, W. F., et al. (2015). Determination of critical shear stresses for erosion and deposition based on in situ measurements of currents and waves over an intertidal mudflat. *J. Coast. Res.* 31, 1344–1356. doi: 10.2112/JCOASTRES-D-14-00239.1

Soulsby, R. L., and Humphery, J. D. (1990). "Field observations of wave-current interaction at the Sea bed," in *Water wave kinematics*. Eds. A. Tørum and O. T. Gudmestad (Dordrecht: Springer, Netherlands), 413–428.

Stapleton, K. R., and Huntley, D. A. (1995). Seabed stress determinations using the inertial dissipation method and the turbulent kinetic energy method. *Earth Surface Processes Landforms* 20 (9), 807–815. doi: 10.1002/esp.3290200906

Taki, K. (2000). "Critical shear stress for cohesive sediment transport," in *Proceedings in marine science*. Eds. W. H. McAnally and A. J. Mehta (Elsevier), 53–61. doi: 10.1016/S1568-2692(00)80112-6

Temmerman, S., Bouma, T. J., Koppel, J. V. D., Wal, D. V. D., Vries, M. B. D., and Herman, P. M. J. (2007). Vegetation causes channel erosion in a tidal landscape. *Geology* 35 (7), 631–634. doi: 10.1130/G23502A.1

Teng, L., Cheng, H., de Swart, H. E., Dong, P., Li, Z., Li, J., et al. (2021). On the mechanism behind the shift of the turbidity maximum zone in response to reclamations in the Yangtze (Changjiang) estuary, China. *Mar. Geology* 440, 106569. doi: 10.1016/j.margeo.2021.106569

Toniolo, M. A., Seitz, C., and Perillo, G. M. E. (2021). Origin and evolution of tidal depressions in a tidal flat and their role in carbon sequestration in the bahía blanca estuary (Argentina). *Mar. Geology* 436, 106467. doi: 10.1016/j.margeo.2021.106467

Van der Werf, J., Reinders, J., van Rooijen, A., Holzhauer, H., and Ysebaert, T. (2015). Evaluation of a tidal flat sediment nourishment as estuarine management measure. *Ocean Coast. Manage.* 114, 77–87. doi: 10.1016/j.ocecoaman.2015.06.006

Van Prooijen, B. C., Montserrat, F., and Herman, P. M. J. (2011). A process-based model for erosion of macoma balthica-affected mud beds. *Continental Shelf Res.* 31 (6), 527–538. doi: 10.1016/j.csr.2010.12.008

Van Rijn, L. C. (1993). *Principles of sediment transport in rivers, estuaries and coastal seas* (Amsterdam, the Netherlands: Aqua Publication).

Verney, R., Deloffre, J., Brun-Cottan, J. C., and Lafite, R. (2007). The effect of wave-induced turbulence on intertidal mudflats: Impact of boat traffic and wind. *Continental Shelf Res.* 27 (5), 594–612. doi: 10.1016/j.csr.2006.10.005

Wang, X., Sun, J., and Zhao, Z. (2020). Effects of river discharge and tidal meandering on morphological changes in a meso tidal creek. *Estuarine Coast. Shelf Sci.* 234, 106635. doi: 10.1016/j.ecss.2020.106635

Wang, Z. B., and Winterwerp, J. C. (1992). *A model to simulate the transport of fluid mud. tech. rep. Z163, WL | delft hydraulics* (Delft, The Netherlands: WL | delft hydraulics).

Wan, Y., Roelvink, D., Li, W., Qi, D., and Gu, F. (2014). Observation and modeling of the storm-induced fluid mud dynamics in a muddy-estuarine navigational channel. *Geomorphology* 217, 23–36. doi: 10.1016/j.geomorph.2014.03.050

Wan, Y., Wu, H., Roelvink, D., and Gu, F. (2015). Experimental study on fall velocity of fine sediment in the Yangtze estuary, China. *Ocean Eng.* 103, 180–187. doi: 10.1016/j.oceaneng.2015.04.076

Whitehouse, R., Soulsby, R., Roberts, W., H., M., and H.R., W. (2000). *Dynamics of estuarine muds: a manual for practical applications* (London: Thomas Telford Limited).

Winterwerp, J. C. (2007). "On the sedimentation rate of cohesive sediment," in *Proceedings in marine science*. Eds. J. P. Y. Maa, L. P. Sanford and D. H. Schoellhamer (Elsevier), 209–226. doi: 10.1016/S1568-2692(07)80014-3

Winterwerp, J., and Kesteren, W. (2004). *Introduction to the physics of cohesive sediment in the marine* (Amsterdam: Elsevier), 576.

Wu, W., and Wang, S. S. Y. (2004). Depth-averaged 2-d calculation of tidal flow, salinity and cohesive sediment transport in estuaries. *Int. J. Sediment Res.* 19 (3), 172–190. Available at: http://www.cqvip.com/QK/71135X/201107/11055782.html.

Wu, H., Wang, Y. P., Gao Xing, S. F., Tang, J. P., and Chen, D. Z (2022). Fluid mud dynamics in a tide-dominated estuary: A case study from the Yangtze River. *Continental Shelf Res.* 232, 104623.

Yang, S.-L., Friedrichs, C. T., Shi, Z., Ding, P.-X., Zhu, J., and Zhao, Q.-Y. (2003). Morphological response of tidal marshes, flats and channels of the outer Yangtze river mouth to a major storm. *Estuaries* 26 (6), 1416–1425. doi: 10.1007/BF02803650

Yang, S. L., Li, H., Ysebaert, T., Bouma, T. J., Zhang, W. X., Wang, Y. Y., et al. (2008). Spatial and temporal variations in sediment grain size in tidal wetlands, Yangtze delta: On the role of physical and biotic controls. *Estuarine Coast. Shelf Sci.* 77 (4), 657–671. doi: 10.1016/j.ecss.2007.10.024

Yu, Q., Wang, Y., Shi, B., Wang, Y. P., and Gao, S. (2017). Physical and sedimentary processes on the tidal flat of central jiangsu coast, China: Headland induced tidal eddies and benthic fluid mud layers. *Continental Shelf Res.* 133, 26–36. doi: 10.1016/j.csr.2016.12.015

Zhang, Y., Chen, R., and Wang, Y. (2020). Tendency of land reclamation in coastal areas of shanghai from 1998 to 2015. *Land Use Policy* 91, 104370. doi: 10.1016/j.landusepol.2019.104370

Zhang, M., Dai, Z., Bouma, T. J., Bricker, J., Townend, I., Wen, J., et al. (2021). Tidal-flat reclamation aggravates potential risk from storm impacts. *Coast. Eng.* 166, 103868. doi: 10.1016/j.coastaleng.2021.103868

Zhang, S., Nielsen, P., Perrochet, P., and Jia, Y. (2021). Multiscale superposition and decomposition of field-measured suspended sediment concentrations: Implications for extending 1DV models to coastal oceans with advected fine sediments. *J. Geophysical Research: Oceans* 126, e2020JC016474. doi: 10.1029/2020JC016474

Zhang, S. T., Zhang, Y. Q., Xu, J. S., Guo, L., Li, G. X., Jia, Y. G., et al. (2022). In situ observations of hydro-sediment dynamics on the abandoned diaokou lobe of the yellow river delta: Erosion mechanism and rate. *Estuarine Coast. Shelf Sci.* 277, 108065. doi: 10.1016/j.ecss.2022.108065

Zhao, B. X., Liu, Y. X., Wang, L., Liu, Y. C., Sun, C., Fagherazzi, S., et al. (2022). Stability evaluation of tidal flats based on time-series satellite images: A case study of the Jiangsu central coast, China. *Estuarine Coast. Shelf Sci.* 264, 107697.

Zhu, W., Li, J., and Li, W. (2022). Observations of fine sediment flocculation in the turbidity maximum of the changjiang estuary. *J. Sea Res.* 179, 102150. doi: 10.1016/j.seares.2021.102150

Zhu, Q., van Prooijen, B. C., Maan, D. C., Wang, Z. B., Yao, P., Daggers, T., et al. (2019). The heterogeneity of mudflat erodibility. *Geomorphology* 345, 106834. doi: 10.1016/j.geomorph.2019.106834

Zhu, Q., Van Prooijen, B. C., Wang, Z. B., Ma, Y. X., and Yang, S. L. (2016). Bed shear stress estimation on an open intertidal flat using in situ measurements. *Estuar. Coast. Shelf Sci.* 182 (Pt.A), 190–201. doi: 10.1016/j.ecss.2016.08.028

Zhu, Q., van Prooijen, B. C., Wang, Z. B., and Yang, S. L. (2017). Bed-level changes on intertidal wetland in response to waves and tides: A case study from the Yangtze river delta. *Mar. Geology* 385, 160–172. doi: 10.1016/j.margeo.2017.01.003

frontiers | Frontiers in Marine Science

TYPE Original Research
PUBLISHED 19 January 2023
DOI 10.3389/fmars.2023.1097177

OPEN ACCESS

EDITED BY
Sha Lou,
Tongji University, China

REVIEWED BY
Zhong Peng,
East China Normal University, China
Zhenchang Zhu,
Guangdong University of Technology, China

*CORRESPONDENCE
Peng Yao
p.yao@hhu.edu.cn
Peixiong Chen
chenpeixiong@126.com

SPECIALTY SECTION
This article was submitted to Coastal Ocean Processes, a section of the journal Frontiers in Marine Science

RECEIVED 13 November 2022
ACCEPTED 04 January 2023
PUBLISHED 19 January 2023

CITATION
Zhang R, Chen Y, Chen P, Zhou X, Wu B, Chen K, Sun Z and Yao P (2023) Impacts of tidal flat reclamation on suspended sediment dynamics in the tidal-dominated Wenzhou Coast, China.
Front. Mar. Sci. 10:1097177.
doi: 10.3389/fmars.2023.1097177

Impacts of tidal flat reclamation on suspended sediment dynamics in the tidal-dominated Wenzhou Coast, China

Rong Zhang[1,2], Yongping Chen[1,2], Peixiong Chen[3,4,5]*, Xin Zhou[2,4,5], Biying Wu[2], Kehao Chen[3], Zhilin Sun[3] and Peng Yao[1,2,6]*

[1]State Key Laboratory of Hydrology-Water Resources and Hydraulic Engineering, Hohai University, Nanjing, China, [2]College of Harbour, Coastal and Offshore Engineering, Hohai University, Nanjing, China, [3]Ocean College, Zhejiang University, Zhoushan, China, [4]The Second Institute of Oceanography, Ministry of Natural Resources, Hangzhou, China, [5]Key Laboratory of Ocean Space Resource Management Technology, Ministry of Natural Resources, Hangzhou, China, [6]State Key Laboratory of Coastal and Offshore Engineering, Dalian University of Technology, Dalian, China

Reclamation of tidal flats is one of the engineering measures of expanding land area and developing the economy in coastal areas; however, this process disturbs the natural processes of the tidal flat system. Taking the flood-tidal dominant Oufei tidal flat at the Wenzhou coast as a study area, the influences of tidal flat reclamation on tidal and suspended sediment dynamics were comprehensively investigated *via* numerical modeling. Before the reclamation, the Eulerian residual current flows alongshore and the residual sediment transport on-shore in the tidal flat area. The reclamation reduces the tidal flat area, shifting the M4 co-phase line toward the coast and squeezing the flood-dominated area. Consequently, the tidal current is weakened and the suspended sediment concentration (SSC) is reduced, but the residual sediment transport change insignificantly. The residual sediment transport in the Feiyunjiang Estuary is controlled by the tidal pumping effect. The upper estuary shows a net sediment transport landward, while a seaward transport is observed in the lower estuary, which further splits into two circulation outside the estuary. The south Oufei dike construction interferes the northern sediment circulation, resulting in the alteration of local SSC and enhancing landward sediment transport inside the estuary. The methodology and understandings arising from this study could be a good reference for the analysis of suspended sediment transport under tidal flat reclamation effects at other sites.

KEYWORDS

tidal flat reclamation, suspended sediment transport, suspended sediment concentration, tidal asymmetry, tidal waves

1 Introduction

The coastal zone is a transitional land-sea interaction area influenced by oceanic and terrestrial forcing. Since more than one-third of the world's population lives in coastal zones, it is also highly interfered with human activities (Temmerman et al., 2013; Zhu et al., 2020). Tidal flats are a crucial geomorphic unit of the coastal zone and are mainly composed of muddy deposits. Tidal flats can provide a habitat for flora and fauna to protect biodiversity, protect the coasts from storms, and increase the coastal protection capacity (Murray et al., 2019; Zhou et al., 2022). With the progress of society and the development of the economy, the reclamation of upper tidal flats has become the primary engineering method of solving the problem of land scarcity in many coastal cities worldwide, promoting economic development (Sengupta et al., 2018; Chu et al., 2022). In addition, tidal flat reclamation can effectively elevate the low-lying coastal areas which are frequently threatened by sea level rise, flooding, storm surges and other disasters (Goemans and Visser, 1987; Hoeksema, 2007; Chen et al., 2019; Pan et al., 2022). With global climate change and the intensification of human activities, tidal flats are under unprecedented pressure.

The tidal flats mainly serve as sedimentary sinks of fine-grained sediments and are high-frequency areas of land reclamation projects (Pedersen and Bartholdy, 2006; van Maren et al., 2016; Wu et al., 2018). However, tidal flat reclamation can cause a sharp reduction or even loss of sediment sinks. Consequently, the suspended sediment concentration (SSC) may increase in the surrounding channels, bringing siltation. Thus, sediment sinks shift from shallow tidal flats to nearby deep channels due to tidal flat reclamation (van Maren et al., 2016; Gao et al., 2018; Cheng et al., 2020). Meanwhile, in the tidal flat just near the sea dike, the sedimentation rate may be reduced or even turn to erosion due to strengthened tidal current velocity and wave conditions (Zhang and Chen, 2015; Cox et al., 2022). As a result, the tidal flats shift from suspended sediment sink to a source. Due to the differences in engineering designs and dynamic coastal environments, the coastal geomorphological responses to reclamation projects vary in different regions. The variations are related not only to the coastal morphology, geomorphological patterns, and hydrodynamic forces after reclamation, but also to the strength and persistence of the reclamation (Su et al., 2020; Xu et al., 2021).

Regarding tidal flats inside the estuaries, Winterwerp and Wang (2013) and Winterwerp et al. (2013) found that the reclamation of tidal flats and the deepening of navigation channels can change the properties of the original estuaries. Due to the narrowing and deepening of the tidal-dominated estuaries, the original low-turbidity estuaries have been transformed into high-turbidity. The high turbidity estuaries will further reduce the bottom friction, amplifying the upstream tidal waves, and forming an irreversible cycle. van Maren et al. (2016) reported that reclamation projects squeeze the sediment deposition area in the estuary, leading to increased SSC inside the estuary. Under increased tidal waves due to the narrowing and deepening of the estuary, the seaward sediment transport reverses landward, resulting in upstream sedimentation. Xie et al. (2017) found that similar reverse sediment transportation and sedimentation occurred in the upper estuaries in the Qiantang Estuary. They suggested continuous reclamation of the estuarine area was essential in changing sediment transport regimes. For such tidal-dominated estuaries, it is known that reclamation and channel dredging have irreversible effects on estuary evolution (van Maren et al., 2015; Wang et al., 2015). The main mechanisms can be summarized as follows: the superiority of the flood tide is strengthened, the amplitude of the tidal waves is enhanced, the trend of the net sediment transport is changed, and the natural properties of the estuary are affected.

The Oufei tidal flat on the Wenzhou coast in China is located between the Feiyunjiang River estuary and the Oujiang River estuary (Chen et al., 2021) (Figure 1). It is a typical muddy tidal flat with a slow deposition trend, featured by a flood-dominant tide. In the last ten years, due to economic development, a series of reclamation projects have been progressively carried out in the Oufei tidal flat, advancing the shoreline to the sea (Mei et al., 2019; Cai et al., 2021). Different from the reclamation inside the estuary, which may cause the regime shift of the estuary properties, it is unclear on the effects of reclamation on accreting open tidal flats and on the adjacent estuaries.

In this study, we take the Oufei tidal flat as a research site, aiming to explore the impacts of reclamation on suspended sediment dynamics in the tidal-dominated tidal flat and the adjacent estuary. To this end, a numerical model was established to simulate the tidal and sediment dynamics before and after the reclamation. By analysis of the tidal current pattern, SSC distribution, and the residual suspended sediment transport in the study area, the influence mechanism of the reclamation project on the sediment dynamics was identified. Section 2 introduces the study area and the numerical model; Section 3 illustrates the results on tidal and sediment dynamics before and after the reclamation; Section 4 discusses the corresponding mechanisms by analyzing tidal asymmetry and decomposing on net sediment transport; the conclusions are listed in Section 5.

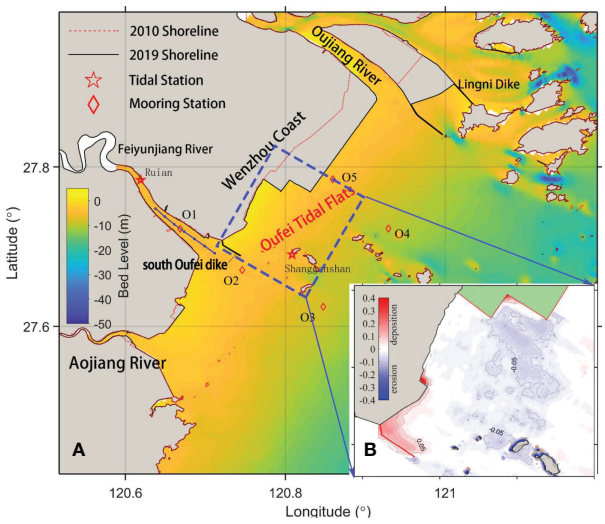

FIGURE 1
(A) Bathymetric map of the Oufei tidal flat area in 2019 and **(B)** morphological changes of Oufei tidal flat between 2010 and 2019 (unit: m/yr). The blue line in **(A)** inside the Feyunjiang River defines six locations (points) used to conduct sediment flux decomposition in Section 4.

2 Materials and methods

2.1 Study area

The Oufei tidal flat is located in the eastern part of the Wenzhou coast. It is characterized by a straight shoreline and an accreting tidal flat (Figure 1). The tides around the Oufei tidal flat region are regular semi-diurnal tides, and the M2 tidal components are dominant (Xu, 2020; Chen et al., 2021). The average tidal range is 4.4 m and can be classified as a macro-tidal area. Influenced by the shape of the local topography, the tidal current in the Oufei tidal flat is mainly reciprocating, with the flood current pointing toward the northwest and the ebb current directing toward the southeast. According to long-term measurements at Nanji Island Oceanographic Station, the waves are mainly wind-waves, with an annual average wave height $H_{1/10}$ of about 1 m.

The Oujiang River and the Feiyunjiang River flow into the sea to the north and the south of the Oufei tidal flat, respectively. The annual average discharge of the Oujiang River is 470 m^3/s, and that of the Feiyunjiang River is 75 m^3/s (Li, 2010). A large amount of sediment from the Yangtze Estuary is transported to the offshore area of the Oufei tidal flat by longshore currents. Subsequently, the local tidal currents and waves push this sediment toward the tidal flats (Chen et al., 2021). The SSC in the Feiyunjiang River Estuary is much higher than in the Oufei tidal flat area, leading to the maximum turbidity zone being located in the estuary.

2.2 Model setup

Based on the open-source Delft3D software, a numerical model that considers both the tidal current and sediment transport in the Oufei tidal flat was constructed. The flow module of the Delft3D software is mainly based on shallow water equations and the Boussinesq assumption for an incompressible fluid. Since the Wenzhou Coast is a macro-tidal-dominated and well-mixed coast, and the Feiyunjiang Estuary is classified as well-mixed at most times of the year according to Simmons's classification method (Jin and Sun, 1992), we apply a depth-averaged (i.e., 2D) way to compute tidal current and sediment transport. More details can be found in the user manual of Delft3D (Deltares, 2011). The suspended sediment transport was calculated using the two-dimensional advection-diffusion equation:

$$\frac{\partial(HS)}{\partial t}+\frac{1}{G_\xi}\frac{\partial(HUS)}{\partial \xi}+\frac{1}{G_\eta}\frac{\partial(HVS)}{\partial \eta} = \frac{1}{G_\xi}\frac{\partial}{\partial \xi}\left(v_s\frac{H}{G_\xi}\frac{\partial S}{\partial \xi}\right)+\frac{1}{G_\eta}\frac{\partial}{\partial \eta}\left(v_s\frac{H}{G_\eta}\frac{\partial S}{\partial \eta}\right)-F_s, \quad (1)$$

where S is the average depth of the SSC (kg/m^3); t is time (s); ξ and η are orthogonal curvilinear coordinates under the Cartesian coordinate system (m); G_ξ and G_η are the Lame coefficients in the coordinate system; U and V are the average velocity components along the water depth (m/s) in directions ξ and η, respectively; ζ is the tidal elevation (m); d is the water depth (m); H = ζ + d is the total water depth (m); v_s is the turbulent diffusion coefficient for suspended sediment (m^2/s); F_s is the sediment exchange item between the sediment bed and water; $F_s = D_b - E_b$; D_b is the sediment deposition flux on the seabed surface; and E_b is the scour flux on the seabed.

The Oufei tidal flat and its adjacent estuaries are dominated by fine sediments. The median grain size of the suspended sediment is around 6 μm (Wu et al., 2015). Therefore, the Partheniades–Krone equation was used to calculate the sediment exchange term between the sediment bed and water. The sedimentation flux (D_b) is:

$$D_b=\begin{cases}\omega_s S_b\left(1-\frac{\tau_{bs}}{\tau_d}\right) & \tau_{bs}\le\tau_d\\ 0 & \tau_{bs}>\tau_d\end{cases}, \quad (2)$$

where ω_s is the sedimentation velocity of the cohesive sediment (m/s); S_b is the sediment concentration (kg/m^3); τ_{bs} is the effective shear stress (N/m^2); and τ_d is the critical deposition shear stress (N/m^2). The erosion flux (E_b) is written as follows:

$$E_b=\begin{cases}M\left(\frac{\tau_{bs}}{\tau_e}-1\right) & \tau_{bs}\ge\tau_e\\ 0 & \tau_{bs}<\tau_e,\end{cases} \quad (3)$$

where τ_e is the critical erosion shear stress (N/m^2); and M is the erosion coefficient related to the sediment properties, which reflects the erosion resistance of the sediment in the seabed.

The domain of the Oufei Model (OM) ranges from 119°E to 124° E and from 32°N to 36.5°N. The entire area was about 200 km×550 km. The total number of grids was 104133. The grid resolution ranges from 30m in the Feiyunjiang River Estuary to 100 in the nearshore area of the Oufei tidal flat. The tidal elevation data were used as the open boundary conditions, provided by the two-dimensional tidal current model of the East China Sea (Su et al., 2015). The shallow water area (i.e., tidal flats) was processed into the moving boundary using the wet-dry boundary condition. According to the grain size analysis of the surface sediments in the Oufei tidal flat conducted by Wu et al. (2015), the bed sediment of the model was set as silt, with a particle size of 8 μm (slightly larger than the suspended sediment size, i.e., 6 μm), a dry density of 500 kg/m^3, a critical starting shear stress of 0.5 Pa, and a settling velocity (flocculation settling velocity) of 2.4 mm/s.

Two cases were set up based on the OM. One uses the shorelines and bathymetric data in 2010 (namely, 2010 model) representing the condition before reclamation. The other uses shorelines and bathymetric data in 2019 (namely, 2019model) to represent the condition after reclamation. The bathymetric data in 2010 and 2019 in the Oufei tidal flat were derived from field surveys, while the nautical charts in the corresponding period were used for Feiyunjiang Estuary and the seaward area. These data were processed to the same vertical datum (i.e., China national height datum 1985). An additional case (caseSL) was setup by keeping the bathymetry the same as in 2010 and the shoreline the same as in 2019, to explore the impacts of shoreline changes.

2.3 Model verification

The calculation time of the pre-reclamation case (that is, the 2010 model) was from October 1, 2010, to November 1, 2010, and the calculation time step was 30 s, which satisfies the stability conditions of the Courant number. During the one-month simulation, the bed

level changes were also simulated. However, the resulting bed level changes were small because the simulation period only covered two spring-neap tidal cycles. Figure 1 shows the distribution of the measurement stations for tidal elevation, velocity and SSC in the Oufei tidal flat in 2010. The tidal elevation, tidal current, and SSC at each station were calculated using the model and were compared with the measured data for verification. Figures 2–4 shows part of model verification results. See Supplementary Materials for details. In Supplementary Materials, the model verification results of 2019model were also listed. The results demonstrate that the calculated values of the tide level, flow velocity, flow direction, and SSC are in good agreement with the measured values, and the errors are within 10%. The errors between simulation and measurement were mainly due to the inaccurate bathymetric data (e.g., the depth near O1 is from the nautical charts), ignorance of waves and winds, complexity in sediment transport modelling. It can be considered that the model can accurately simulate the hydrodynamic and sediment characteristics of the Oufei tidal flat in 2010 and 2019, respectively.

2.4 Data analysis

Based on the validated numerical model (i.e., the 2010 model) of the Oufei tidal flat, the tidal current and sediment transport during one month in 2010 and 2019 were calculated, respectively. The tidal elevation, flow current, SSC, and suspended sediment transport in the study area before and after reclamation were compared and analyzed.

The tidal ratio, $(H_{K_1}+H_{O_1})/H_{M_2}$, in the mouth of the Feiyunjiang River ranges from 0.18 to 0.28, and the sea area is a normal semi-diurnal tidal area. The tidal asymmetry characteristics are mainly generated by the interaction between the semi-diurnal tide (M_2) and the shallow water tide (M_4). Therefore, the harmonic analysis is mainly focused on the M_2 and M_4 sub-tides. The M_4/M_2 amplitude ratio and ($2M_2$–M_4) relative phase parameters defined by Friedrichs and Aubrey (1988) were used to analyze the asymmetry of the tides.

$$A = \frac{H_{M_4}}{H_{M_2}}, \tag{4}$$

$$G = 2\varphi_{M_2} - \varphi_{M_4}, \tag{5}$$

where H_{M_2} and H_{M_4} are the amplitudes of the M_2 and M_4 tides, respectively; and φ_{M_2} and φ_{M_4} are the phase lags of the M_2 and M_4 tides, respectively. The tidal deformation coefficient A is the amplitude ratio of the M_4 tide to the M_2 tide, and the tidal deformation coefficient G is the phase difference between the M_4 tide and M_2 tide. $A > 0.01$ indicates a large deformation during the tidal wave propagation. G represents the dominant relationship between the high and low tides in the tidal asymmetry.

To analyze the characteristics and main factors controlling the residual suspended sediment transport in the study area, the suspended sediment flux decomposition method proposed by Dyer (1997) was adopted to decompose the residual transport rate, $F(kg/(m \cdot s))$, of the suspended sediment during the entire tidal cycle T.

$$\begin{aligned} F &= \frac{1}{T}\int_0^T \int_0^1 hucdzdt \\ &= h_0 u_0 c_0 + c_0 \overline{h_t u_t} + u_0 \overline{h_t c_t} + h_0 \overline{u_t c_t} + \overline{h_t u_t c_t} + h_0 \overline{c_v}\ \ \overline{u_v} + h_0 \overline{c_{vt} u_{vt}} \\ &= T_1 + T_2 + T_3 + T_4 + T_5 + T_6 + T_7, \end{aligned} \tag{6}$$

where h, u and c are the total water depth, tidal current velocity and SSC respectively; T is tidal period; the subscript 0 means the tidal average; the subscript t tidal variation, the subscript v means the vertical variation and the subscript vt denotes the variation over tidal cycle and water depth; overbar means the average over tidal cycle; angled bracket means average over water depth. Totally, suspended

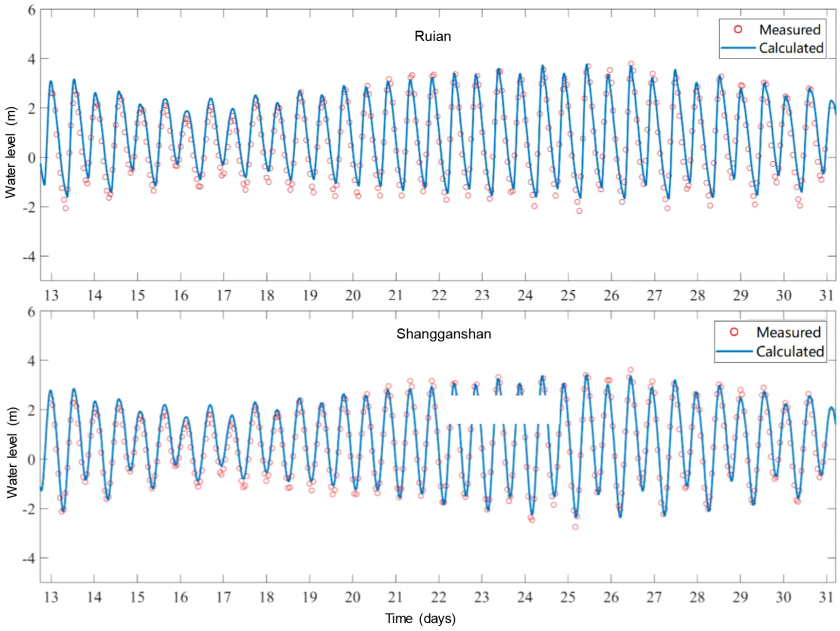

FIGURE 2
Comparison of calculated and measured water levels. The measurement period was from October 13 to October 31, 2010, at the different stations.

10.3389/fmars.2023.1097177

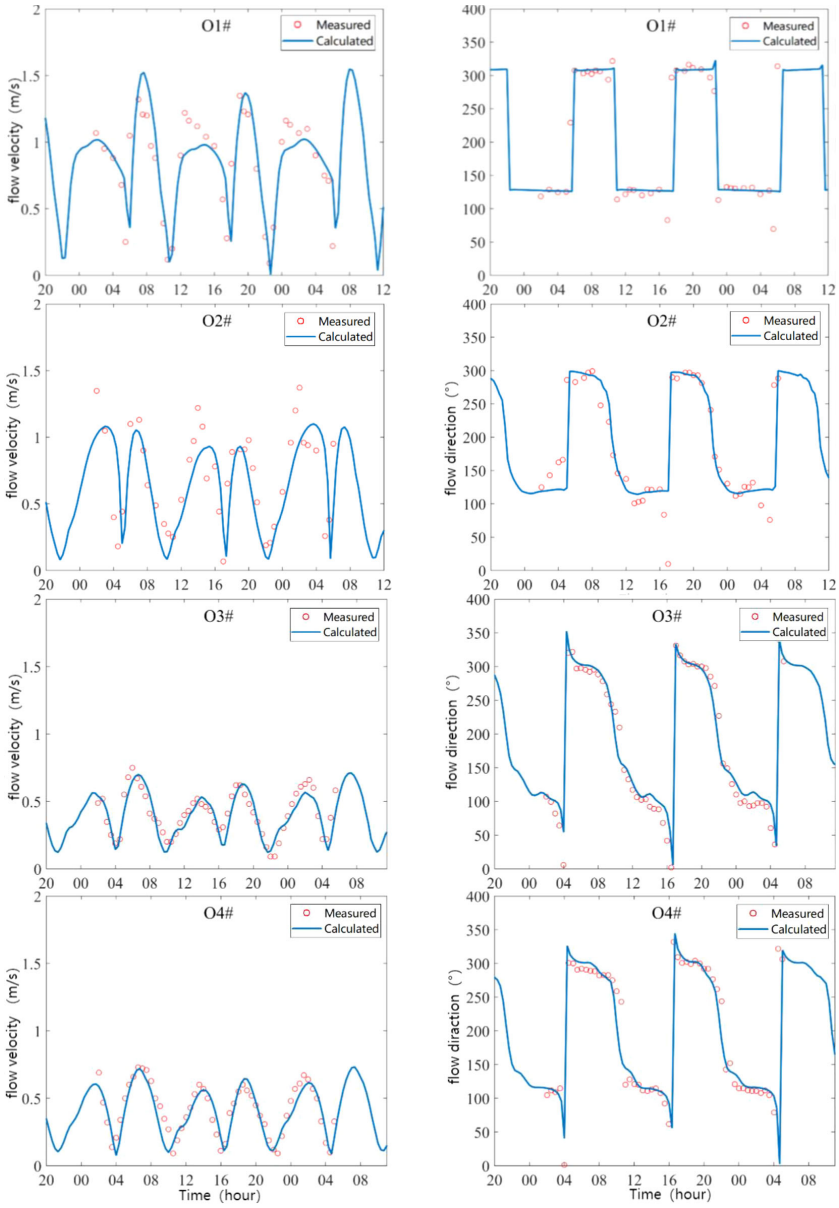

FIGURE 3
Comparison of the simulated and measured flow velocity during spring tide. The measurement period was from October 24 to 25 in 2010.

sediment flux can be decomposed into seven terms. T_1 is the suspended sediment transport term caused by the Eulerian residual current; T_2 is the Stokes drift transport term; and $T_1 + T_2$ is the Lagrange advection transport term. T_3 is caused by the phase difference between the tidal elevation and SSC. T_4 is the phase difference between the tidal current and SSC, which is mainly caused by the sediment settling and erosion lag, and it is also known as the tidal trapping effect. T_5 is the phase difference among the tidal elevation, tidal current, and SSC, which is caused by the settling lag and erosion lag. $T_3 + T_4 + T_5$ is related to the tidal pumping term; T_6 is the gravity circulation term along the vertical direction of the estuary; and T_7 is the difference between the vertical distributions of the velocity and sediment concentration caused by the tidal wave deformation. $T_6 + T_7$ is the residual vertical circulation transport term, which is related to the shear diffusion effect.

3 Results

3.1 Variations of the tidal water level

Figure 5 shows the co-tidal and co-amplitude charts of the M_2 and M_4 tides before and after the tidal flat reclamation. Before the reclamation, the M_2 tide propagated east to west, and the phase lag increased from 34° to 42°. The amplitude increased toward the shore, and the peak was about 2.40 m. The M_2 tidal amplitude in the Oufei tidal flat area increased initially and then decreased from the sea toward the land, and the peak value was about 2.40 m. After the reclamation, the M_2 tidal distribution was the same as before. Influenced by the south Oufei dike, the amplitude of the southern shelter area increased, and the peak amplitude area of 2–2.4 m contracted toward the shore.

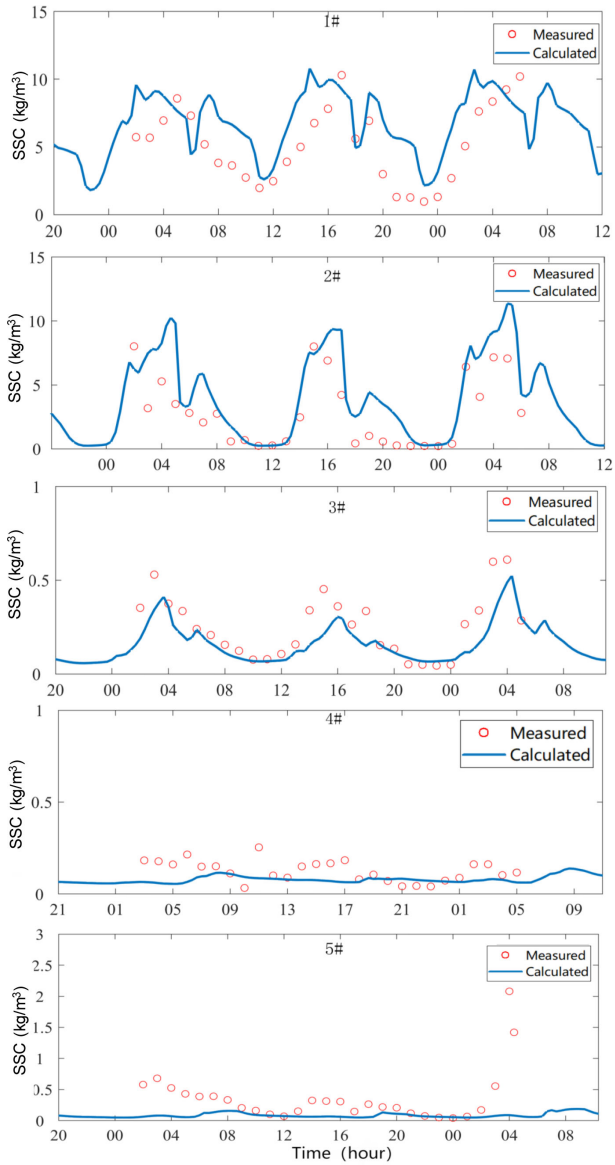

FIGURE 4
Comparison of the simulated and measured SSCs during spring tide. The measurement period was from October 24 to 25 in 2010.

Before the reclamation, the M_4 tidal amplitude gradually increased from the sea toward the land, exhibiting significant shallow water effects. The M_4 tidal amplitude was slightly smaller than the M_2 tidal amplitude, and the peak value was only 0.40 m. The M_4 co-tidal line and amplitude distribution were similar. The co-tidal line is parallel to the coastline, and the 280 -340° co-tidal lines almost coincide, indicating the effects of a sloped topography. After the reclamation, the overall pattern of the M_4 did not change significantly, but each co-tidal line was shifted toward the shore.

3.2 Variations of the tidal current

The tidal current is one of the leading forces shaping the landform of the Wenzhou Coast. Figure 6 shows the differences in the tidal current field between the flooding and ebb peak before and after the reclamation. The reclaimed area is shown in green. From the south of the reclaimed area to the Feiyunjiang Estuary, the flow direction exhibits noticeable deflection after the reclamation.

During flood peak, the tidal current flows perpendicular to the shoreline near the Oufei tidal flat before the reclamation, while the tidal currents change to flow along the artificial shoreline after the reclamation. The maximum flow velocities during flood tide decrease more than 0.4 m/s after the reclamation. The construction of the south Oufei dike blocks part of the water exchange between the tidal flat and the estuary, decreasing flow velocity (~0.4 m/s) near the dike. The dike also prolongs the estuary, enlarging the flow velocity (0.1-0.2 m/s) at the prolonged estuary section, while the flow velocity decreased inside the estuary (0.1 m/s). Furthermore, the flow velocity around the offshore islands varies significantly, up to 0.4 m/s.

During ebb peak, the changes in both flow direction and flow magnitude caused by reclamation, are relatively small compared to flood tide. For example, the ebb flow velocity only reduces as large as 0.4 m/s near the reclaimed dike, while the reduction in the offshore area is not significant. During ebb tide, the south Oufei dike near estuary reduces velocity 0.05-0.1 m/s, which provides sheltering effect on the nearby tidal flat It worth noting that there are also changes in the flow directions and magnitudes near the offshore islands, but these changes are all concentrated in local areas.

The residual current refers to the movement of the remaining water body after the current separates from the cyclical tidal current movement, which is related to the long-term transport direction of the sediment along the coast. The monthly averaged Eulerian residual current distribution in the Oufei tidal flat area before and after reclamation was calculated (Figure 7). Before the reclamation, the tidal flow in the tidal flats area was predominantly in the along-shore direction toward the Feiyunjiang Estuary. There was a strong tongue-shaped residual current spreading from the estuary towards sea. The velocity of the residual current was between 0.04 and 0.12 m/s. Around the offshore islands, there were several clockwise circulations and localized high-velocity areas. The average velocity was 0.07 m/s.

After the reclamation, the residual flow velocity in the southern corner of the reclamation area increased significantly (by 0.12 m/s). There is a circumfluence zone on both sides of the south Oufei dike, and the velocity decreases slightly, while the residual velocity increases locally at the head of the dike and its northern sheltered area, with a maximum increase of 0.06 m/s. In general, due to the reclamation, the distribution of the residual current in the southern corner of the reclamation area and near the south Oufei dike changed greatly, while the impact on the rest of the sea area was not significant.

CaseSL shows the reclamation impacts on velocity magnitude if only changing the shorelines (Figure 8). The obvious velocity variations occur near the reclamation dikes and the changes in velocity magnitude is more significant during ebb (i.e., as large as 0.4 m/s). In the offshore islands area, the velocity variations before and after reclamation are within 0.05 m/s during flood tide, and within 0.1 m/s during ebb. This indicates that the impacts of tidal flat reclamation on velocity is limited around these islands. However, the changes in velocities around the reclamation area and these islands after reclamation may influence the local bathymetric changes. The changes of bathymetry in turn influences the local flow velocity. Hence, the cumulative impact due to the shoreline change still needs further study.

10.3389/fmars.2023.1097177

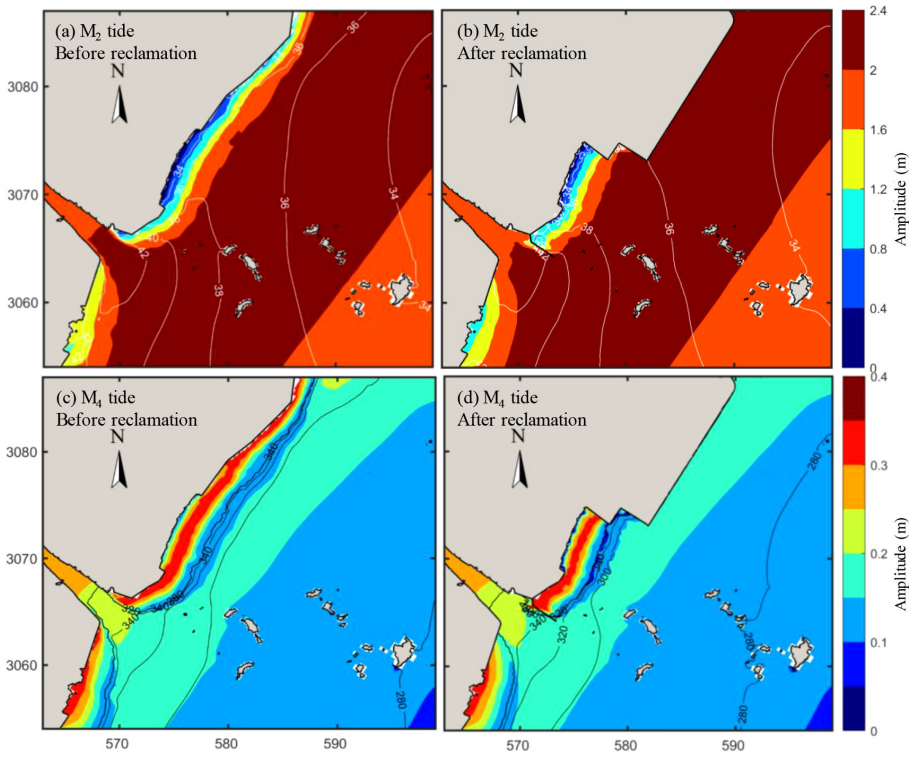

FIGURE 5
Co-tidal and co-amplitude charts before and after reclamation: M2 tidal constituent (a) before reclamation and (b) after reclamation; M4 tidal constituent (c) before reclamation and (d) after reclamation.

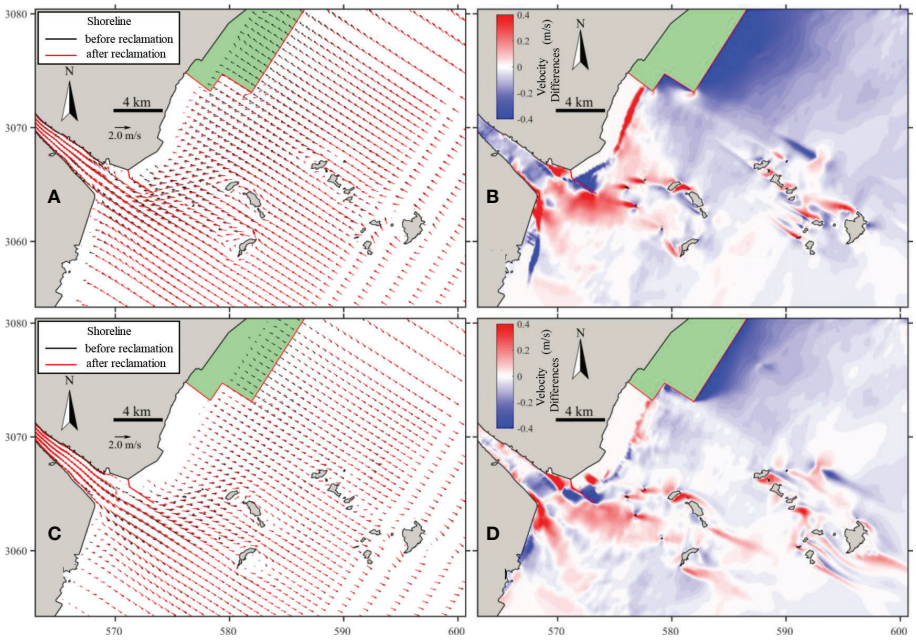

FIGURE 6
Tidal current field during spring tide before and after reclamation. Flow vectors comparisons during **(A)** flood peak and **(C)** ebb peak; Differences in velocity magnitude during **(B)** flood peak and **(D)** ebb peak. The reclamation area is shown in green area and the south Oufei dike is shown in red line near the estuary.

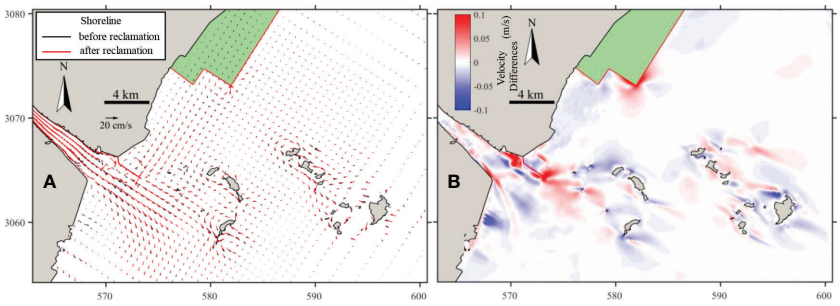

FIGURE 7
Residual tidal current for two spring-neap cycles before and after reclamation. **(A)** Flow vector comparison; **(B)** differences in velocity magnitude.

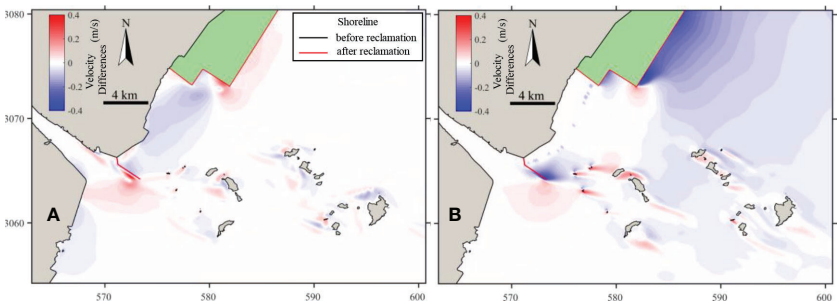

FIGURE 8
Differences in velocity magnitude during **(A)** flood peak and **(B)** ebb peak of spring tide of only changing shorelines (caseSL-2010model). Note that, caseSL keeps the bathymetry as the same, and only the shoreline changes.

3.3 Variations of suspended sediment dynamics

Figures 9A, B show the average SSC distribution over the spring tide before and after the reclamation. The SSC shows a similar distribution pattern before and after the reclamation, i.e., the SSC is high inside the estuary (larger than 14 kg/m^3) and gradually decreases in the seaward direction. Meanwhile, the SSC in the Oufei tidal flat is rather smaller. In the Feiyunjiang Estuary, the average SSC during spring tide decreased after the reclamation, with a maximum reduction value of 4 kg/m^3 (Figure 9C). The SSC in the northern reclaimed area also exhibited an overall decreasing trend, with an average decrease of about 1 kg/m^3. The SSC increases only in the sheltered area of the south Oufei dike and around the offshore islands.

Figure 9D shows the differences in the average SSC in the full spring-neap tidal cycle before and after the reclamation. The overall change in SSC is similar to that of the spring tide, but with a smaller magnitude. That is, the SSC slightly increases by about 0.2 kg/m^3 in the northeast area of the estuary and slightly decreases by about 0.5 kg/m^3 on the southwest side and on both sides of the south Oufei dike.

Figure 10 shows the changes of residual suspended sediment transport in the study area before and after the reclamation. It can be seen from Figure 10A that the suspended sediment was transported toward the tidal flat before the reclamation, resulting in the accreting tidal flat there. Inside the Feiyunjiang Estuary, the sediment transports landward in the upper estuary, whereas it directs seaward in the lower estuary. After the suspended sediment was exported from the estuary, the suspended sediment was divided into two parts, which formed a clockwise circulation to the south and a counterclockwise circulation to the north. The residual sediment was eventually transported to the estuary and the nearshore area.

After the reclamation, the residual sediment transport depicts an along-shore direction instead of on-shore. But the changes in magnitude is too small to be shown in Figure 10B. Inside the estuary the landward and seaward transport still exists, but the separation point moves seaward. This is because the construction of the south Oufei dike extends the estuary, increasing the distance of sediment entering the sea. Thus, the residual sediment transport in the upper estuary is increased, while it is decreased in the lower estuary. Outside the estuary, there are alternating increases and decreases from north to south, with changes in transport magnitude not exceeding 5×10^{-4} m^3/s/m.

In summary, the impact of the northern tidal flat reclamation on the sediment transport is relatively limited, while the construction of the south Oufei dike near the estuary mouth has a significant impact on the direction and strength of the residual sediment transport in and near the estuary.

4 Discussions

4.1 Effects of the tidal flat reclamation on the tidal asymmetry

The Oufei tidal flat is in a slow accreting state and featured by the flood-dominant tide. Since the tide, especially the tidal asymmetry,

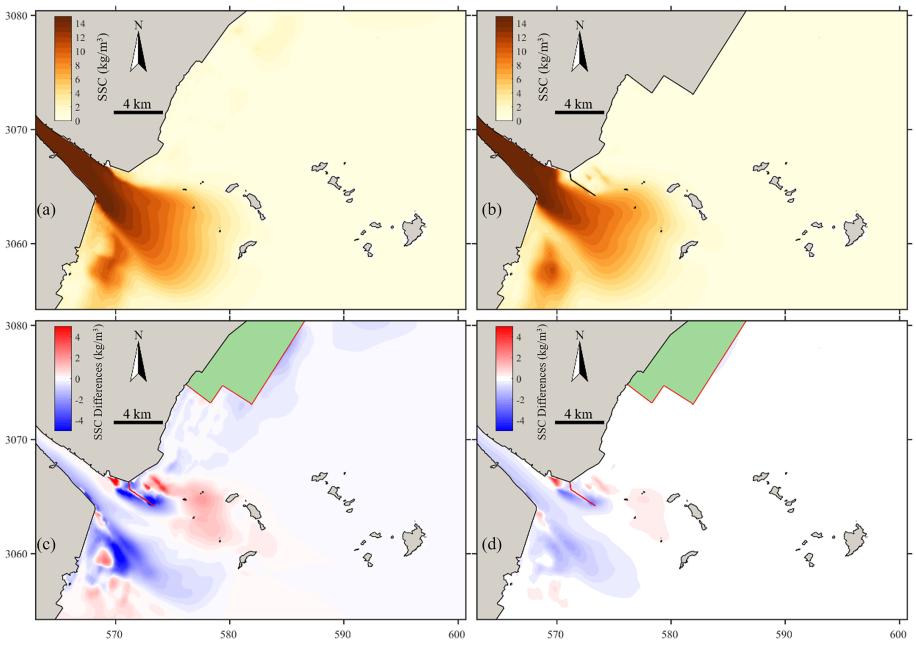

FIGURE 9
Tidal-averaged SSC during the spring tide **(A)** before and **(B)** after the reclamation; and the differences in the tidal-averaged SSC during **(C)** the spring tide and **(D)** a full spring-neap tide cycle before and after the reclamation.

plays a primary role in the morphodynamics of the Oufei tidal flat, it is necessary to investigate the effects of the reclamation influences on the tidal asymmetry.

Figure 11 shows the spatial distribution characteristics of the tidal asymmetry coefficient amplitude ratio (A) and tidal deformation coefficient (G) before and after the reclamation of the Oufei tidal flat. The tidal amplitude ratios A in the nearshore area exceeded the limit of 0.01, indicating that the tidal waves experienced significant deformation under the influences of the topography when they reached the shallow area of the Oufei tidal flat. The amplitude ratio at the mouth of the Feiyunjiang River (0.1–0.2) was smaller than that in the nearshore area of the Oufei tidal flat (0.3–0.6). This indicates that the M_4 tide was more enhanced than the M_2 tide in the nearshore area. After the reclamation, the amplitude ratios in the offshore and nearshore area did not change much. Only the amplitude ratio in the circumfluence zone on the north side of the south Oufei dike increased slightly, while the amplitude ratio in the shelter area on the south side decreased.

Before and after the reclamation, the tidal phase differences in the study area were all between 0° and 180°, confirming that the tidal current during flood tide was larger than the ebb current, and the flood tide duration was shorter than the ebb duration, i.e., the tide asymmetry is flood-dominant. The flood-dominancy gradually increased with decreasing water depth from the sea toward the land. The tidal deformation coefficient G was close to 90°, and the tidal waves tend to exhibit the maximum positive asymmetry. After the reclamation, the contours of the tidal deformation coefficient G shifted toward the shore, indicating that the flood-dominancy was slightly weakened and the sediment transport capacity of the tidal current was weakened, which may be the reason for the decrease in the suspended sediment concentration in this area.

4.2 Effects of the tidal flat reclamation on the suspended sediment transport

To further understand the mechanisms of the suspended sediment transport in the estuary and to identify the effects of the tidal flat reclamation, the residual suspended sediment transport was decomposed into the advection term and the tidal pumping term using the flux decomposition method as mentioned in Section 3. Figure 12 depicts the spatial distribution of flux decomposition before and after the reclamation. In addition, six locations were set along the estuary section (blue line in Figure 1), and the sediment transport rate over tidal cycles and the contribution of each decomposed component at each point were extracted. The results are presented in Figure 13.

Regarding the advection term, there is overall transport toward the sea outside the estuary with a transport rate larger than 0.3 kg/(m · s). The sediment transport is parallel to the tidal flat area with a relatively small magnitude. Outside the estuary, a clockwise transport pattern exists. According to the T1 and T2 terms of each calculation point inside the estuary (Figure 13A), the Eulerian residual current transport term (T1) was toward the sea, whereas the Stokes drift term (T2) was toward the land. The T2 term is comparable to the T1, hindering the upstream transport of the suspended sediment toward the sea. As a result, the advection transport term (T1+T2) of the suspended sediment inside the estuary contributes little to the residual transport of sediment (Figure 13B). Before and after reclamation, the distribution of advection transport terms was slightly reduced except the area around the south Oufei dike (P7).

With respect to the tidal pumping term, it depicts a landward sediment transport in the Oufei tidal flat with a relatively small magnitude. Outside the estuary, there is a seaward sediment transport direction in the middle, while landward sediment transports are distinguishable in the south and north estuary, respectively. Inside

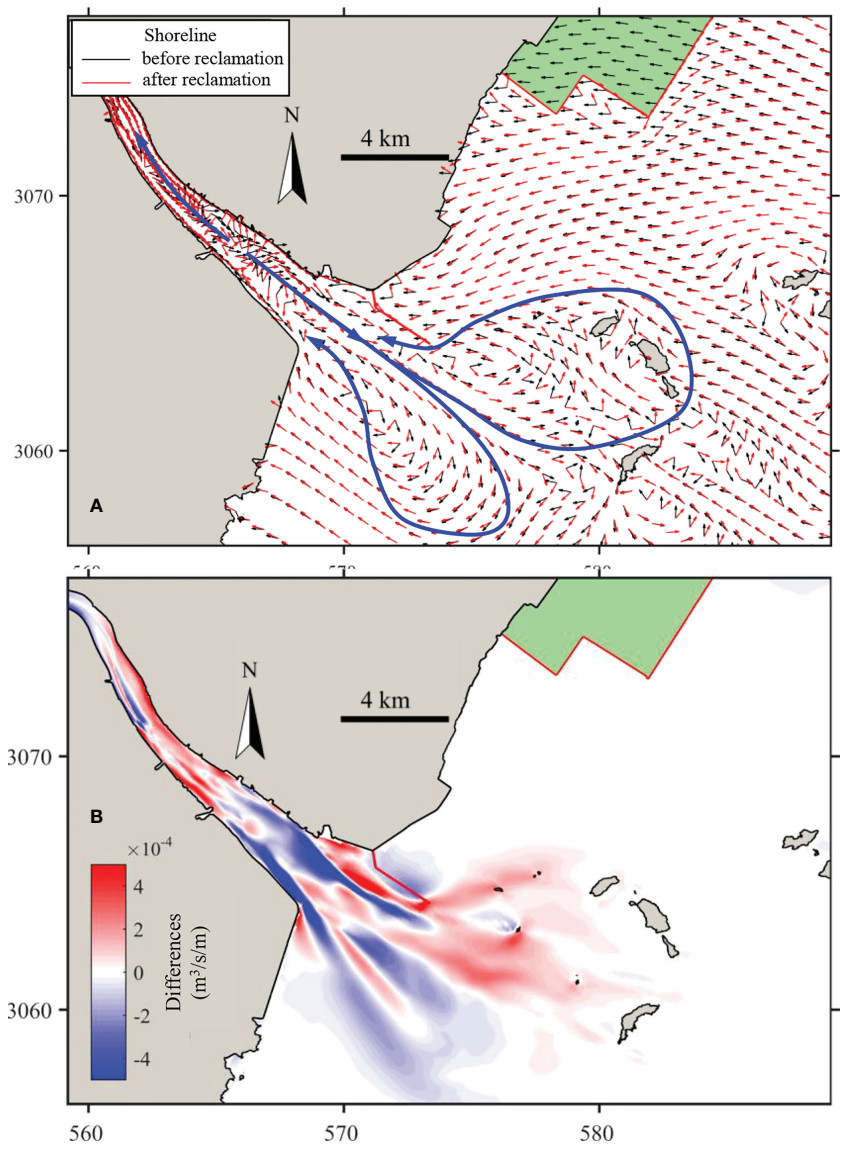

FIGURE 10
Differences in **(A)** residual sediment transport direction and **(B)** magnitude during one month before and after the reclamation.

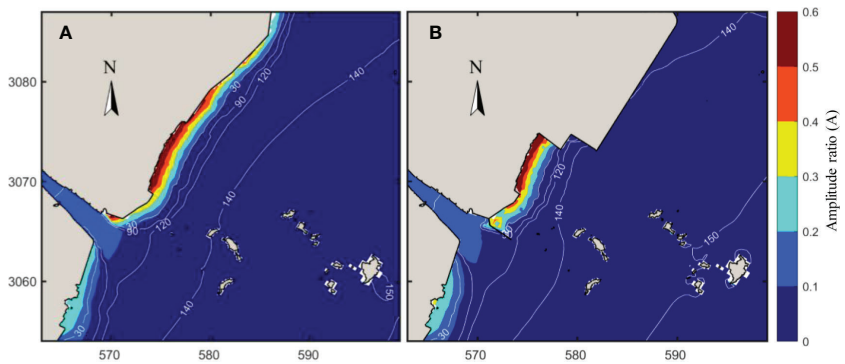

FIGURE 11
Spatial distributions of tidal asymmetry parameters **(A)** before and **(B)** after the reclamation. Note: the background map represents the amplitude ratio **(A)**, and the contour lines represent the phase difference (G).

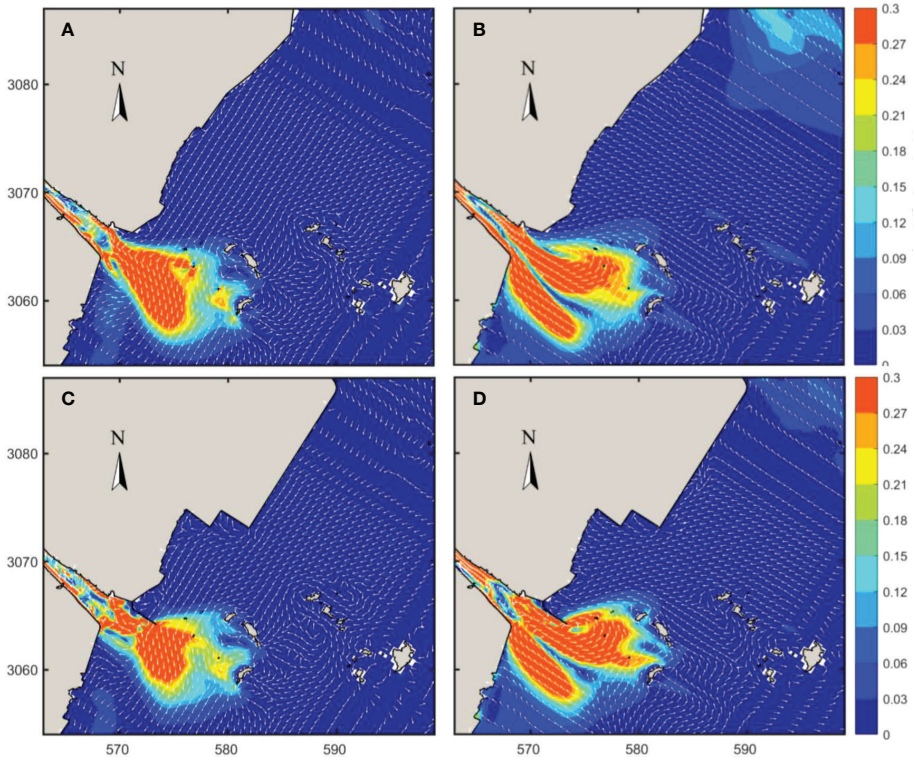

FIGURE 12
Decomposition of the residual suspended sediment transport over a spring-neap tidal cycle **(A, B)** before and **(C, D)** after the reclamation. **(A, C)** Distribution of advection transport term; and **(B, D)** tidal pumping term. The units are kg/m/s.

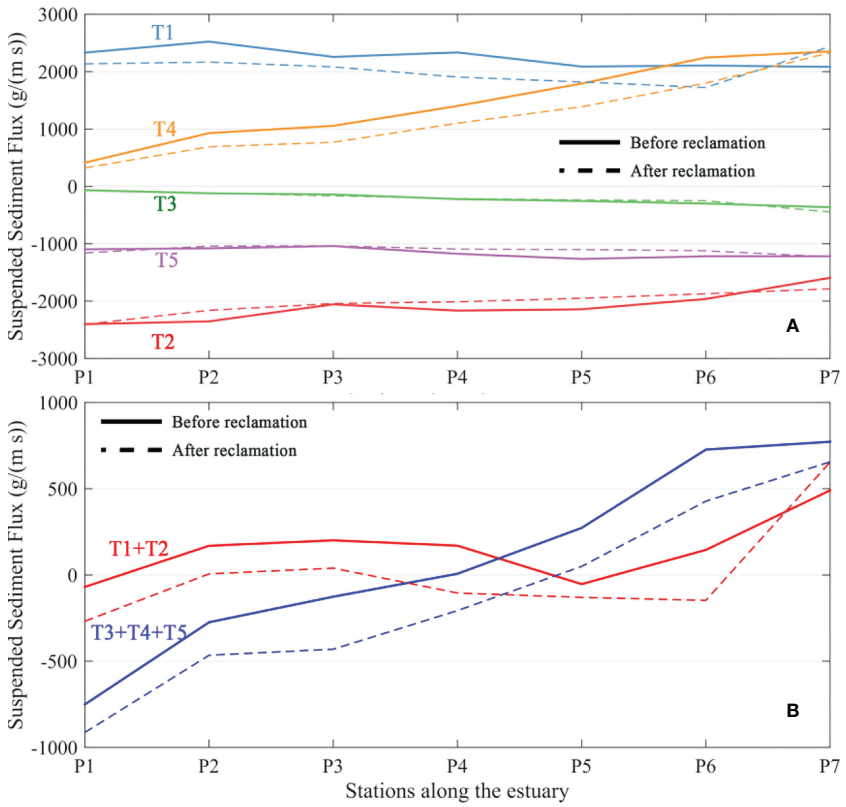

FIGURE 13
Contributions of different decomposition components to suspended sediment flux at different positions in the estuary: **(A)** five decomposition components (T1 to T5); **(B)** advection (T1+T2) and tidal pumping terms (T3+T4+T5). Note that seaward is positive, point 1 is upstream of the estuary, and other points are distributed successively downstream with an interval of 1600 m.

the estuary, the residual sediment is transported landward in the upper part, whereas it directs seaward near the mouth. The tidal pumping induced transport pattern is in line with the overall residual sediment transport shown in Figure 10A, indicating that the tidal pumping term (induced by tidal asymmetry) is the critical factor controlling the sediment transport in the Oufei tidal flat region.

The tidal pumping term inside the Feiyunjiang Estuary shows that the contributions of the T4 and T5 were more significant (Figure 13A). The T4 term points to the sea, and the intensity increases toward the sea. T4 term represents the relationship between the asymmetry of the tidal current and the suspended sediment concentration. That is, the suspended sediment transport caused by the ebb tide is more significant than that caused by the flood tide, resulting in the residual transport of the sediments toward the sea. In addition, the seaward increase in T4 indicates an enhancement of the tidal asymmetry at the mouth. T5 term shows a landward transport, and the intensity slightly increases seaward. T5 term represents the relationship between the tidal elevation asymmetry, the tidal current asymmetry, and the SSC. It reveals that the sediment transport in the mouth is greater at high tide than at low tide, resulting in residual sediment transport toward the land. T4 and T5 terms are in the same magnitude, more or less, leading to the residual sediment transport in opposite directions in the upper and lower estuary (Figure 13B). After the construction of the south Oufei dike, the length of the estuary was extended, strengthening the landward transport.

4.3 Limitations and remarks for future research

Effects of waves on residual sediment transport. There are significant seasonal variations in wave climates. In winter, the most frequent wave is from the NNE to NE direction, while in summer, it is from the E-ESE direction. Moreover, the wave height in winter is more significant than that in summer. The annual average $H_{1/10}$ wave height is about 1 m. Therefore, there would be seasonal differences in sediment transport induced by waves. While both the Oufei tidal flat and the Feiyunjiang Estuary are dominated by the tide, it is still necessary to understand the contribution of the wave on residual sediment transport and the impacts of reclamation in different temporal scales (e.g., tidal cycles, seasonal and annual).

Morphological changes and the contribution of reclamation. Comparing surveyed bathymetries makes it possible to obtain morphological changes in different periods. As shown in Figure 1B, during 2010-2019, the sedimentation mainly occurred in the upper tidal flat and the area sheltered by the south Oufei Dike, while slight erosion (annual mean erosion rate smaller than 0.05m) can be found in the lower tidal flat and seaward areas. Together with the velocity and SSC variations before and after reclamation, the sedimentation near the south Oufei Dike is due to reduced velocity and sediment transport. However, the residual sediment transport variations before and after reclamation in the lower tidal flat area were too small to be recognized. On the one hand, the morphological change was a gradual and feedback process with the tidal current, wave, and sediment transport. On the other hand, reclamation was also gradual in the past decades. The construction of each reclamation dike involves a chain reflection between hydrodynamics, sediment transport, and bed level changes. Hence, it is difficult to accurately reveal morphological change and the contribution of reclamation by comparing only the changes in residual sediment transport between two snap-shot runs. A morphodynamic model should be utilized to understand the contribution of the reclamation on morphological changes.

5 Conclusions

Through numerical modeling, the impacts of tidal flat reclamation on the suspended sediment dynamics in a flood-dominant and accreting coast have been analyzed. The main conclusions are as follows:

(1) In the Oufei tidal flat area, the M_4 tidal amplitude gradually increases from the sea toward the land, enhancing the flood-dominancy in the shallow tidal flat and promoting on-shore sediment transport. The tidal flat reclamation weakens the flood-dominancy near the reclamation area, which leads to a more pronounced tidal current velocity reduction (~0.4 m/s) during flood tide, and reduces the SSC there. But the intensity of the residual transport of the suspended sediment did not change significantly after the reclamation.

(2) In the Feiyunjiang Estuary, the SSC and the residual transport intensity of the suspended sediment in the Feiyunjiang Estuary are controlled by the tidal pumping effect, with the magnitude of ten times greater than that at the Oufei tidal flat. The residual sediment, transport landward in the upper estuary, while seaward transport is distinguishable in the lower estuary. The residual sediment transport depicts two circulation patterns outside the estuary. The south Oufei dike construction interferes the northern sediment circulation, resulting in the alteration of local SSC and enhancing landward sediment transport inside the estuary.

Data availability statement

The original contributions presented in the study are included in the article/Supplementary Material. Further inquiries can be directed to the corresponding authors.

Author contributions

RZ: Conceptualization, methodology, formal analysis, visualization, and writing—original draft. YC: Conceptualization, investigation, and writing—review and editing. PC: Conceptualization and writing—review and editing. XZ: Formal analysis, visualization, and writing—review. BW: Visualization and writing—review and editing. KC: Writing—review and editing. ZS: Writing—review and editing. PY: Conceptualization, methodology, investigation, formal analysis, writing— review and editing. All authors contributed to the article and approved the submitted version.

Funding

This study was supported by grants from the National Natural Science Foundation of China (52201320, 51979076), the Fundamental

Research Funds for the Central Universities of China (B220202078), the Postdoc International Exchange Program of China (YJ20210073), the Scientific Research Fund of the Second Institute of Oceanography, Ministry of Natural Resources, China (JG1801), and the Open Fund of the State Key Laboratory of Coastal and Offshore Engineering (LP2207).

Conflict of interest

The authors declare that the research was conducted in the absence of any commercial or financial relationships that could be construed as a potential conflict of interest.

Publisher's note

Supplementary material

The Supplementary Material for this article can be found online at: https://www.frontiersin.org/articles/10.3389/fmars.2023.1097177/full#supplementary-material

References

Cai, J. X., Pan, G. F., and Chen, P. X. (2021). Analysis of the characteristics and dynamic mechanism of scouring and silting changes in oufei tidal flat before and after the reclamation project. *J. Mar. Sci.* 39 (03), 63–71. doi: 10.3969/j.issn.1001-909X.2021.03.007

Cheng, Z., Jalon-Rójas, I., Wang, X. H., and Liu, Y. (2020). Impacts of land reclamation on sediment transport and sedimentary environment in a macro-tidal estuary. *Estuarine Coast. Shelf Sci.* 242, 106861. doi: 10.1016/j.ecss.2020.106861

Chen, Y., Li, J., Pan, S., Gan, M., Pan, Y., Xie, D., et al. (2019). Joint probability analysis of extreme wave heights and surges along china's coasts. *Ocean Eng.* 177, 97–107. doi: 10.1016/j.oceaneng.2018.12.010

Chen, P., Sun, Z., Zhou, X., Xia, Y., Li, L., He, Z., et al. (2021). Impacts of coastal reclamation on tidal and sediment dynamics in the rui'an coast of China. *Ocean Dynamics* 71, 323–341. doi: 10.1007/s10236-021-01442-3

Chu, N., Yao, P., Ou, S., Wang, H., Yang, H., and Yang, Q. (2022). Response of tidal dynamics to successive land reclamation in the lingding bay over the last century. *Coast. Eng.* 173, 104095. doi: 10.1016/j.coastaleng.2022.104095

Cox, J. R., Leuven, J. R. F. W., Pierik, H. J., van Egmond, M., and Kleinhans, M. G. (2022). Sediment deficit and morphological change of the Rhine–meuse river mouth attributed to multi-millennial anthropogenic impacts. *Continental Shelf Res.* 244, 104766. doi: 10.1016/j.csr.2022.104766

Deltares (2011). *Delft3D-FLOW user manual. 3.15 ed* (Delft, The Netherlands: Deltares (WL).

Dyer, K. R. (1997) *Estuaries: A physical introduction, 2nd edition* (Chichester: JohnWiley and Sons). Available at: http://eu.wiley.com/WileyCDA/WileyTitle/productCd-0471974714.html (Accessed June 27, 2015).

Friedrichs, C. T., and Aubrey, D. G. (1988). Non-linear tidal distortion in shallow well-mixed estuaries: A synthesis. *Estuarine Coast. Shelf Sci.* 27, 521–545. doi: 10.1016/0272-7714(88)90082-0

Gao, G. D., Wang, X. H., Bao, X. W., Song, D., Lin, X. P., and Qiao, L. L. (2018). The impacts of land reclamation on suspended-sediment dynamics in jiaozhou bay, qingdao, China. *Estuarine Coast. Shelf Sci.* 206, 61–75. doi: 10.1016/j.ecss.2017.01.012

Goemans, T., and Visser, T. (1987). The delta project: The Netherlands experience with a megaproject for flood protection. *Technol. Soc.* 9, 97–111. doi: 10.1016/0160-791X(87)90034-0

Hoeksema, R. J. (2007). Three stages in the history of land reclamation in the Netherlands. *Irrigation Drainage* 56, S113–S126. doi: 10.1002/ird.340

Jin, Y. H., and Sun, Z. L. (1992). Mixing characteristics ofsalt water and fresh water in Chinese estuaries. *Acta Geographica Sin.* 47 (2), 165–173.

Li, M. G. (2010). The effect of reclamation in areas between islands in a complex tidal estuary on the hydrodynamic sediment environment. *J. Hydrodynamics Ser. B* 22, 338–350. doi: 10.1016/S1001-6058(09)60063-9

Mei, Y. P., Cai, T. L., Wang, X. K., Xia, X. M., and Jia, J. J. (2019). Evaluation on the suitability of mud flat reclamation based on intertidal morphodynamics. *Mar. Sci. Bull.* 38 (06), 707–718. doi: 10.11840/j.issn.1001-6392.2019.06.013

Murray, N. J., Phinn, S. R., DeWitt, M., Ferrari, R., Johnston, R., Lyons, M. B., et al. (2019). The global distribution and trajectory of tidal flats. *Nature* 565, 222–225. doi: 10.1038/s41586-018-0805-8

Pan, Y., Yin, S., Chen, Y. P., Yang, Y. B., Xu, C. Y., and Xu, Z. S. (2022). An experimental study on the evolution of a submerged berm under the effects of regular waves in low-energy conditions. *Coast. Eng.* 176, 104169. doi: 10.1016/j.coastaleng.2022.104169

Pedersen, J. B. T., and Bartholdy, J. (2006). Budgets for fine-grained sediment in the Danish wadden Sea. *Mar. Geology* 235, 101–117. doi: 10.1016/j.margeo.2006.10.008

Sengupta, D., Chen, R., and Meadows, M. E. (2018). Building beyond land: An overview of coastal land reclamation in 16 global megacities. *Appl. Geogr.* 90, 229–238. doi: 10.1016/j.apgeog.2017.12.015

Su, M., Gong, Z., Yao, P., Pu, J., and Lu, Y. (2020). Investigation on factors of influence on long-term morphodynamic evolution of a multi-outlets estuarine-delta system: A case study of the lingding bay, pearl river delta. *J. Coast. Res.* 95, 664–668. doi: 10.2112/SI95-129.1

Su, M., Yao, P., Wang, Z. B., Zhang, C. K., and Stive, M. J. F. (2015). Tidal wave propagation in the yellow Sea. *Coast. Eng. J.* 57, 1550008-1-155008–29. doi: 10.1142/S0578563415500084

Temmerman, S., Meire, P., Bouma, T. J., Herman, P. M. J., Ysebaert, T., and De Vriend, H. J. (2013). Ecosystem-based coastal defence in the face of global change. *Nature* 504, 79–83. doi: 10.1038/nature12859

van Maren, D. S., Oost, A. P., Wang, Z. B., and Vos, P. C. (2016). The effect of land reclamations and sediment extraction on the suspended sediment concentration in the ems estuary. *Mar. Geol.* 376, 147–157. doi: 10.1016/j.margeo.2016.03.007

van Maren, D. S., Winterwerp, J. C., and Vroom, J. (2015). Fine sediment transport into the hyper-turbid lower ems river: the role of channel deepening and sediment-induced drag reduction. *Ocean Dyn.* 65, 589–605. doi: 10.1007/s10236-015-0821-2

Wang, Z. B., Van Maren, D. S., Ding, P. X., Yang, S. L., Van Prooijen, B. C., De Vet, P. L. M., et al. (2015). Human impacts on morphodynamic thresholds in estuarine systems. *Cont. Shelf Res.* 111, Part B, 174–183. doi: 10.1016/j.csr.2015.08.009

Winterwerp, J. C., and Wang, Z. B. (2013). Man-induced regime shifts in small estuaries–I: theory. *Ocean Dynamics* 63, 1279–1292. doi: 10.1007/s10236-013-0662-9

Winterwerp, J. C., Wang, Z. B., Braeckel, A.v., Holland, G.v., and Kösters, F. (2013). Man-induced regime shifts in small estuaries–II: A comparison of rivers. *Ocean Dynamics* 63, 1293–1306. doi: 10.1007/s10236-013-0663-8

Wu, C. S., Huang, S.c., Luo, X. X., Mu, J. B., and Zhao, X. (2015). Characteristics of surface sediment grain size in oufei tidal flat and adjacent sea area and hydrodynamic responses. *Mar. Sci. Bull.* 34 (04), 399–406. doi: 10.11840/j.issn.1001-6392.2015.04.006

Wu, Z., Milliman, J. D., Zhao, D., Cao, Z., Zhou, J., and Zhou, C. (2018). Geomorphologic changes in the lower pearl river delta 1850–2015, largely due to human activity. *Geomorphology* 314, 42–54. doi: 10.1016/j.geomorph.2018.05.001

Xie, D., Pan, C., Wu, X., Gao, S., and Wang, Z. B. (2017). Local human activities overwhelm decreased sediment supply from the changjiang river: Continued rapid accumulation in the hangzhou bay-qiantang estuary system. *Mar. Geol.* 392, 66–77. doi: 10.1016/j.margeo.2017.08.013

Xu, H. (2020). Numerical study on the impact of sanjiangkou reclamation in wenzhou on coastal hydrodynamics. *Dalian Univ. Technol.*

Xu, C., Zhou, C., Ma, K., Wang, P., and Yue, X. (2021). Response of water environment to land reclamation in jiaozhou bay, China over the last 150 years. *Front. Mar. Sci.* 8. doi: 10.3389/fmars.2021.750288

Zhang, C. K., and Chen, X. D. (2015). Offshore environmental changes and countermeasures in response to large-scale tidal flat reclamation. *J. Hohai Univ. (Natural Sciences)* 43 (5), 424–430. doi: 10.3876/j.issn.1000-1980.2015.05.006

Zhou, Z., Wu, Y., Fan, D., Wu, G., Luo, F., Yao, P., et al. (2022). Sediment sorting and bedding dynamics of tidal flat wetlands: Modeling the signature of storms. *J. Hydrology* 610, 127913. doi: 10.1016/j.jhydrol.2022.127913

Zhu, Z., Vuik, V., Visser, P. J., Soens, T., van Wesenbeeck, B., van de Koppel, J., et al. (2020). Historic storms and the hidden value of coastal wetlands for nature-based flood defence. *Nat. Sustain* 3, 853–862. doi: 10.1038/s41893-020-0556-z

frontiers | Frontiers in Marine Science

TYPE Original Research
PUBLISHED 20 January 2023
DOI 10.3389/fmars.2023.1109146

OPEN ACCESS

EDITED BY
Sha Lou,
Tongji University, China

REVIEWED BY
Aijun Wang,
Ministry of Natural Resources, China
Qing Xu,
Ocean University of China, China

*CORRESPONDENCE
Huan Li
anuolihuan@163.com

SPECIALTY SECTION
This article was submitted to Coastal Ocean Processes, a section of the journal Frontiers in Marine Science

RECEIVED 27 November 2022
ACCEPTED 04 January 2023
PUBLISHED 20 January 2023

CITATION
Zhang N, Li H, Zhang J, Chen J, Wu H and Gong Z (2023) Study of the spatial and temporal distributions of tidal flat surface sediment based on multitemporal remote sensing.
Front. Mar. Sci. 10:1109146.
doi: 10.3389/fmars.2023.1109146

Study of the spatial and temporal distributions of tidal flat surface sediment based on multitemporal remote sensing

Nan Zhang[1,2,3], Huan Li[2,3]*, Jiabao Zhang[3], Jiayin Chen[3], Hongbo Wu[2] and Zheng Gong[1,2,3]

[1]State Key Laboratory of Hydrology-Water Resources and Hydraulic Engineering,Hohai University, Nanjing, China, [2]Jiangsu Key Laboratory of Coast Ocean Resources Development and Environment Security, Hohai University, Nanjing, China, [3]Field Scientific Observation and Research Station of Ministry of Education for Tidal Flat Ecosystem in the Jiangsu Radial Sand Ridge Region, Hohai University, Nanjing, China

Introduction: The ecological environment of tidal flats often changes due to tidal erosion and sedimentation. The distribution of tidal flat surface sediment is a natural reflection of the changes in the external dynamic environment, the spatial and temporal distribution pattern is of great significance.

Methods: In this study, the output structure of traditional convolutional neural network is combined with BP neural network. Meanwhile, four phases of Sentinel-2 multispectral images were collected and combined with field data from the Doulonggang tidal flat in Jiangsu Province, China, to construct the sediment composition inversion model.

Results: The inversion accuracy was higher than 80% compared with the measured results. According to the inversion result, from 2017 to 2022, the surface sediment particle size of the tidal flat in Jiangsu varied seasonally and was coarse in summer and fine in winter. Additionally, the sediment composition tended to coarsen, showing an interannual change trend of increasing sand content and decreasing clay and silt contents.

Discussion: The above change of the sedimentary environment of the tidal flat may be caused by the decrease of fine grained sediment deposition, the introduction of exotic vegetation, the global sea level rise and the influence of human activities.

KEYWORDS

Jiangsu tidal flat, sediment component content, satellite remote sensing, multitemporal, convolutional neutral network

1 Introduction

A tidal flat is an important low-lying coastal landform located at the junction of sea and land. Such flats are widely distributed on the eastern coast of China, the western and southeastern coasts of Britain, the western coast of the Netherlands, the northwestern coast of the United States and the western coast of France (Dalrymple et al., 1992; Li et al., 2022). The tidal flat in China starts in Liaoning Province in the north and ends at the coast of Guangxi in the south. The tidal flat is 4000 km long, and the Jiangsu tidal flat within this coastal zone is the longest in China (Baoguo et al., 1997). The Jiangsu tidal flat is 888.9 km long, and it starts from the Xiuzhen estuary to the north of the Yangtze estuary. The Jiangsu tidal flat has a strong carbon sink capacity and plays an extremely essential role in improving coastal protection, protecting biodiversity and improving the social and economic value of Jiangsu (Liu et al., 2020).

However, tidal flats are among the regions most sensitive to global environmental change. In recent years, issues related to the vulnerability of the ecological environment of tidal flats have been reported many times (Kirwan and Megonigal, 2013; Temmerman and Kirwan, 2015; Murray et al., 2019; Schuerch et al., 2019). Global climate change and high-intensity tidal flat resource development have led to a sharp decline in the size of tidal flat wetlands in China. Between 1950 and 2000, the area of the tidal flat in the Yellow Sea decreased by approximately 50-80% (Murray et al., 2014). From 1985 to 2015, the tidal flat area of the Yangtze River estuary decreased by approximately 36% (Chen et al., 2016). Currently, the Jiangsu tidal flat also faces serious erosion issues (Yu and Zou, 2013). The distribution characteristics of tidal flat sediment components are very sensitive to the erosion of the external dynamic environment. Studying the evolution of tidal flat erosion and deposition can better alert people of the erosion risk of tidal flats in the future.

Understanding the characteristics of the sediment composition distribution is often of high value for decision-making, planning, and the construction of geo-morphodynamic models (Cabezas-Rabadán et al., 2021). However, the tidal flat environment is very complex, and it is very difficult to sample due to the abundance of inaccessible muddy surfaces. Although the accuracy of *in situ* observations of sediment components is relatively high (Wang and Ke, 1997; Jia et al., 2006; Gong et al., 2017), observations are difficult to obtain over large areas. Insufficient field data may lead to the oversimplification of the particle size distribution and hinder the prediction and modelling of tidal flat erosion and deposition trends (Buscombe et al., 2014). In view of the above problems, airborne and spaceborne remote sensing are used to map the clay content and intertidal grain size distribution (Rainey et al., 2003), the inverse contents of sand, silt and clay (Castillo et al., 2011) and different sediment types (Adam et al., 2008) to facilitate data acquisition. Additionally, various types of hyperspectral, multispectral and microwave satellite data are used to classify sediment types in intertidal zones (Yates et al., 1993), and inverse particle size parameters can be determined. The use of these data has been demonstrated in Germany (Jung et al., 2015), Italy (Pitarch et al., 2019), South Korea (Park, 2019), China's Yangtze River estuary and East China Sea (Nasiha et al., 2019), the Jiangsu coast (Zhang et al., 2015) and other areas. Some scholars have also generated classification maps of tidal flat surface sediment (Fairley et al., 2018; Kim et al., 2019) through UAV remote sensing, which can improve the application of optical instruments in tidal flat research.

In the past, spectral methods were rarely used to obtain the properties of sediment in tidal flats due to the relatively low accuracy of results when building sediment composition inversion models. Moreover, most models can only be effectively applied in a specific single region at a given time, and generality is difficult to confirm at different spatial and temporal scales. In recent years, with advances in deep learning theory and computing power (Smirnov et al., 2014), convolutional neural network technology has achieved good results in a large number of remote sensing image recognition and classification tasks, such as slope detection (Ghorbanzadeh et al., 2019), wetland extraction (Mahdianpari et al., 2018), ship detection (Geng et al., 2021) and chlorophyll content inversion (Jin et al., 2021). In addition, some scholars applied convolutional neural networks to quantify the grain size on pebble beaches, and the verification result R^2 reached 0.75 (Soloy et al., 2020). The above results show that convolutional neural networks have strong abstraction and generalization abilities and can identify the important features in remote sensing data. Moreover, such networks can be further applied to assess the distribution of sediment components in different historical periods and enhance the understanding on dynamic geomorphic processes. Thus, this approach has important value for developing dynamic geomorphic models of tidal flats.

The purpose of this study is to establish an inversion model of the tidal flat surface sediment composition by improving the convolutional neural network method and to use Sentinel-2 remote sensing imagery to obtain the spatial and temporal distributions of the sediment composition. The specific objectives are as follows: (1) establish and evaluate the applicability of convolutional neural network technology in the inversion of tidal flat sediment components, (2) obtain the spatial distribution characteristics of the sediment components of the Jiangsu Doulonggang tidal flat from 2017 to 2022 and (3) analyse and discuss the seasonal variations and interannual evolution of the sediment components of the Jiangsu Doulonggang tidal flat.

2 Materials and methods

2.1 Study area

In this study, the Doulonggang tidal flat was selected as the study area (Figure 1) to monitor the change in muddy tidal flats. Due to frequent changes in nearshore erosion and deposition, this area is the most typical muddy tidal flat in Jiangsu Province, China, which reflects the complex characteristics of mixed sand, silty sand, sandy silt, clayey silt, silt and other tidal flat sediment types (Wang and Ke, 1997). The Doulonggang tidal flat is located in Dafeng District, Yancheng city, which is in central-eastern Jiangsu Province, with an average width of 3-4 km, a slope of 0.01-0.03%, an irregular semidiurnal tide and a tidal range of 2-4 m near the shore (Dai et al., 2019).

2.2 Sediment collection and analysis

2.2.1 Tidal flat sediment sampling

To ensure that the intertidal zone was always exposed during tidal flat sediment sampling and did not affect the normal progress of the sampling work, four periods of low tide on December 4, 2017 (42

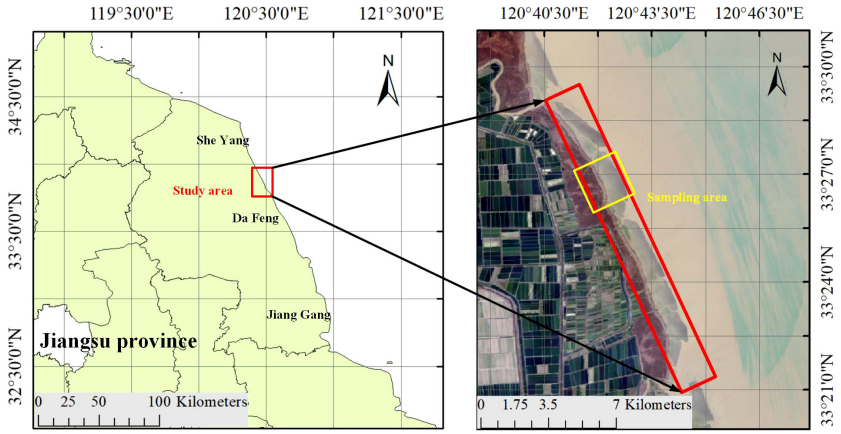

FIGURE 1
Monitoring and Study Area of Sediment Grain Size Change.

sediment samples were collected), October 19, 2018 (140 sediment samples were collected), June 11, 2019 (108 sediment samples were collected), and November 3, 2019 (45 sediment samples were collected) were selected. Field sampling was performed at the Doulonggang tidal flat. The surface sediment (<3 cm) on the tidal flat was sampled, placed into a prenumbered sampling bag and sealed. As shown in Figure 2, 335 samples were obtained from this tidal flat sediment sampling.

2.2.2 Analysis of tidal flat sediment composition

A Mastersizer 3000 Laser Diffraction Particle Size Analyser was used to analyse the component content of sediment samples. The measuring range is 0.01-3500 μm. The relative error of repeated measurements of the same sample is less than 3%, which can be considered highly accurate (Choi et al., 2016).

After removing the carbonate in the sediment with hydrochloric acid and removing the organic matter in the sediment with hydrogen peroxide, the collected sample was divided into three suspensions. Each prepared soil particle suspension was analysed with the Mastersizer 3000 Laser Diffraction Particle Size Analyser to ensure that the shading was within the appropriate range. Three groups of particle size distribution tests were conducted, and the values of the three groups of tests were averaged to obtain the particle size distribution of the sample. According to the definitions of gravel, sand, silty sand and clay, the particle size distribution of the samples was divided, and the boundaries were 2 mm, 1/16 mm (0.0625 mm) and 1/256 mm (0.0039 mm), respectively. Finally, through statistical analysis, the proportions of gravel, sand, silt and clay in the sample were determined, the sediment component content was obtained, and the sediment was classified according to the Folk Triangle Sediment Classification Method (Folk et al., 1970).

2.3 Acquisition and preprocessing of multispectral remote sensing data

The multispectral remote sensing data used in this study were Sentinel-2 imagery from the European Space Agency. Sentinel-2 consists of two satellites, Sentinel-2A and Sentinel-2B, which were launched on June 23, 2015, and March 7, 2017, respectively (Duan et al., 2022). The unique dual-satellite remote sensing mode used by these satellites can obtain data through the same sensor, greatly improving the temporal resolution of the imagery. Data from wave bands B_2 (wavelength 458-523 nm), B_3 (wavelength 543-578 nm), B_4 (wavelength 650-680 nm) and B_8 (wavelength 785-900 nm), all with a spatial resolution of 10 m, were downloaded. The data can be downloaded for free on the Copernicus Open Access Hub (https://scihub.copernicus.eu/).

As shown in Table 1, eight Sentinel-2 images with no or little cloud cover were selected for this study. Sen2Cor is the processor for Sentinel-2 product generation and formatting. It corrects Sentinel-2 Level-1C products for atmospheric scattering and absorbance,

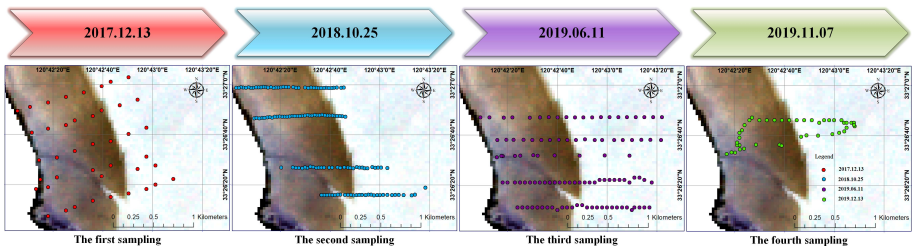

FIGURE 2
Location of Field Sampling Points in the Study Area.

TABLE 1 Sediment sampling and remote sensing imaging times.

Serial Number	Sampling Time	Remote Sensing Imaging Time	Time Interval (Day)	Sampling Tide Level	Remote Sensing Imaging Tide Level
1	2017.12.04	2017.12.20	16	Spring Tide	Spring Tide
2	2018.10.19	2018.10.31	12	Neap Tide	Neap Tide
3	2019.06.11	2019.05.29	13	Neap Tide	Neap Tide
4	2019.11.03	2019.11.15	12	Mid-tide	Mid-tide
5	/	2020.06.02	/	/	Neap Tide
6	/	2021.05.08	/	/	Spring Tide
7	/	2021.11.24	/	/	Mid-tide
8	/	2022.08.21	/	/	Neap Tide

delivering a Level-2A product (Pancorbo et al., 2021). In this study, after atmospheric correction (Bernardo et al., 2017) of the images by Sen2Cor_v2.8.0, the vegetation and water bodies in the tidal flat area were removed through supervised classification and threshold segmentation (Abbaszadeh et al., 2019), and the bare flat image was obtained for subsequent analysis. The imaging time and sampling time of Phases 1-4 were quasi-synchronous, and the images were mainly used to build training samples and establish a surface sediment inversion model. The images from Phases 5-8 were used for the inversion model application to obtain the spatial and temporal distributions of surface sediment components.

2.4 Normalization of multitemporal remote sensing data

Normalization is an important part of any multitemporal remote sensing inversion approach. Although radiance is generally used a reference after radiation correction, pre-processed images are often still incomparable due to different observation geometries and meteorological conditions during data collection. Normalization can make the features have the same metric scale,significantly affecting the applicability of inversion models (Paolini et al., 2007).

In this study, a statistics-based correction method was adopted for relative radiance correction (Li et al., 2014). Z score normalization was first conducted for each band according to the mean radiation value and standard variance of Sentinel-2 images of the study area in each period. Next, the radiation values of images in each period were converted to comparable relative values. Then, according to the mean and standard deviation of radiance for the reference image, the radiance of each band of the corrected image was projected to the domain consistent with the reference image. In this study, the image data from the first period (December 20, 2017) were selected to establish the reference image. The specific radiance correction equation is

$$g_d = \frac{g_r - u_r}{\sigma_r} \times \sigma_f + u_f \quad (1)$$

In equation (1), g_d is the pixel radiation value after correction of the source image; u_f and σ_f are the mean and standard deviation of radiance for the reference image, respectively; and gr, u_r, and σ_r are the pixel radiation, mean radiance and standard deviation of radiance for the source image, respectively.

2.5 Construction of the sediment composition inversion model

The sediment particles on the surface of a tidal flat are small, and the texture characteristics are not always obvious. The relationship between the content of a component and remote sensing spectral reflectance is very complicated. The convolutional neural network (CNN) can effectively reduce the complexity of parameters, and it has significant advantages for deep structures. Thus, CNNs are commonly used in deep learning, and their application scope is gradually expanding (Smirnov et al., 2014). However, most CNN structures are used for image classification, and they cannot be directly used to build inversion models. Therefore, the BP-CNN algorithm was improved in this study, and the adjustment content is shown in Figure 3.

In the BP-CNN structure, the convolution layer is moved around the input image through the convolution kernel and accumulates the product of the convolution kernel and image values to identify the characteristics of the input object. Pooling layers can compress the features of convolution, reduce the complexity of the convolution operation and ensure that the image features do not change due to rotation, translation, expansion, etc. In this study, the convolution layer and pooling layer in the convolutional network structure were used as feature extractors without modification.

In the network output, the fully connected layer does not classify the images but analyses the correlation between the feature values and the sediment component contents. Here, a back-propagation neural network was introduced to determine the optimal weight (lowest RMSE) for each feature by testing the correlation variation between the feature value and sediment component content. According to the prediction results, the network backpropagated the error to each layer of the network and updated the parameters according to the difference between the actual value and the predicted value to achieve promising training results.

Sediment samples and matched remote sensing images were used to generate training sets. The sample data from the first three imaging periods were randomly divided into a training set and a verification

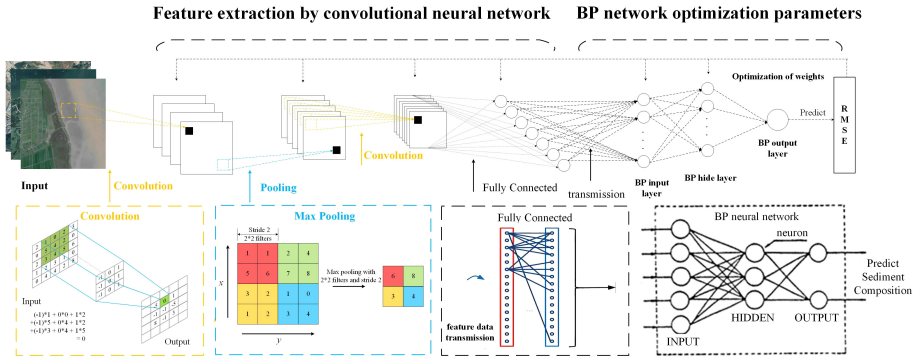

FIGURE 3
Structure of the Sediment Inversion Model.

set at a ratio of 3:1. The training set was input into the sediment composition inversion model for training, and the accuracy of the model was evaluated using the verification set. After completing the training, the fourth phase of sample data was used to evaluate the accuracy and transferability of the model in retrieving tidal flat sediment components,and compared this article methods with stepwise linear regression, SVM regression, BP neural network and convolutional neural network.

3 Results and discussion

3.1 Particle size distribution analysis

The surface sediment of the tidal flat in the study area is mainly fine sediment, with almost no gravel. Therefore, the sediment was classified based on the Folk Triangle Gravel-Free Sediment Classification Method. As shown in Figure 4, the surface sediment types of the Doulonggang tidal flat are mainly silty sand (zS), sandy silt (sZ) and silt (Z), of which sandy silt (sZ) is the most widely distributed.

As shown in Table 2, from 2017 to 2019, the clay content in the Doulonggang tidal flat was always low, with an average content of approximately 2%. The silt content was relatively high, accounting for approximately 45-85% of the sediment composition across the main part of the study area. The sand content was at a medium level, accounting for 10-50% of the sediment composition. The median sediment particle size D_{50} in the study area ranged from 8 μm to 80 μm, and the average median particle size was approximately 60 μm.

3.2 Establishment of a remote sensing inversion model for sediment composition

The training set was input into the adjusted BP-CNN for training, and the training accuracy of the set observation model was verified(Phase 1-3). As shown in Figures 5A–C, the prediction accuracy R^2 of the model for clay, silt and sand was 0.75. The root mean square error (RMSE) for clay was lower than 2.4, and the RMSEs for silt and sand were lower than 6.0.

After debugging the model, the sample data for Phase 4 were used to further evaluate the model. As shown in Figures 5D–F, the R^2 of the validation group reached 0.74, and the RMSE was not significantly different from that for the training validation set. Additionally, the mean absolute error (MAE) of the two inspections was no greater than 1.05 for clay and 6.5 for silt and sand. The mean absolute percentage error (MAPE) of silt and sand was less than 30%, and the MAPE of clay was approximately 50%. The proposed method is compared with the traditional method based on the same verification set in Table 3. The results show that the BP-CNN method can accurately identify the relative relationship among each sediment component, and the inversion model displays good accuracy and transferability.

3.3 Inversion results for the surface sediment composition

To clearly assess the changes in the distribution of the surface sediment components of the Doulonggang tidal flat in recent years, the sediment inversion model was applied to eight phases of Sentinel-2 (Table 1) data during the period of 2017-2022.

3.3.1 Inversion diagram of the surface sediment component contents in the Doulonggang tidal flat

Figure 6 shows the change in sediment composition in the Doulonggang tidal flat from 2017 to 2022 based on the developed BP-CNN. According to the inversion results, the sediment in the study area was mainly silty sand, followed by sand and then clay, which was consistent with the measured results above.

1. As shown in Figures 6A–H, the clay in the study area was mainly distributed along the front edge of the salt marsh. The clay content only slightly increased in summer and remained relatively low in other periods.
2. As shown in Figures 6I–P, the silt content in the study area was relatively high, and silt was mainly distributed from the front edge of the salt marsh to the intertidal zone. The content ranged from 45% to 85% and was low in summer and relatively high in winter.
3. As shown in Figures 6Q–X, the sand in the study area was mainly distributed in the subtidal zone, near the water border, and the content near the shore was relatively low. The seasonal

10.3389/fmars.2023.1109146

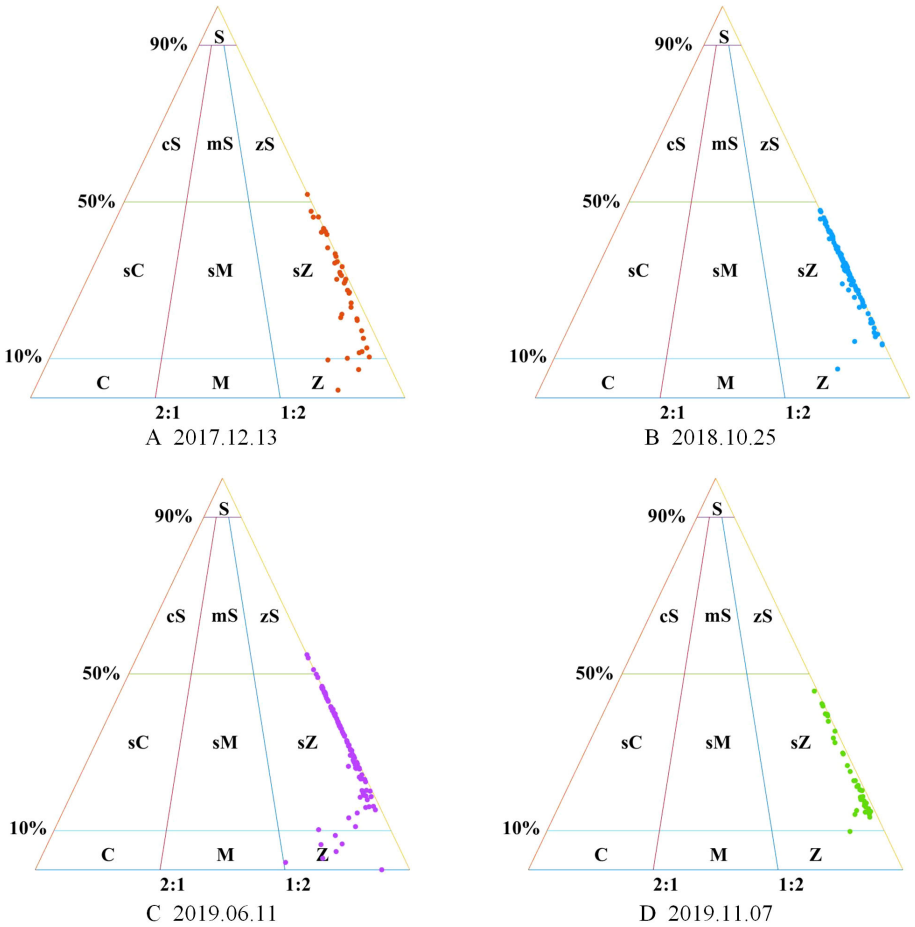

FIGURE 4
According to Folk Classification Theory, 335 Samples Obtained from Field Research were used for Particle Size Analysis.

variation in the sand content was opposite that for silt, with a low content in winter and a high content in summer.

In general, the grain sizes of mud and sand in the study area trend from fine to coarse from land to sea and have coarsened in recent years.

3.3.2 Distribution characteristics of surface sediment components in different seasons and years

We calculated the average of the inversion content of sediment components in the study area in different periods and observed the corresponding evolution trend. The results are shown in Figure 7. The

TABLE 2 Particle size distribution of the surface sediments at different time stages in the Doulonggang tidal flat.

Sampling Time	Number of Samples	Statistical Parameters	Clay (%)	Slit (%)	Sand (%)	D_{50} (μm)
2017.12.04	42	Mean Value	3.02	68.57	28.41	56.66
		Range	0.00-16.91	47.96-85.23	1.97-51.94	16.07-76.37
2018.10.19	140	Mean Value	1.20	66.32	33.08	64.29
		Range	0.00-15.61	52.13-85.87	7.36-47.87	26.10-74.43
2019.6.11	108	Mean Value	2.24	66.53	31.22	61.02
		Range	0.00-32.22	45.10-92.50	0.02-54.90	8.18-78.30
2019.11.03	45	Mean Value	1.83	74.74	23.44	56.88
		Range	0.35-9.25	53.52-85.33	9.79-45.62	37.40-71.81

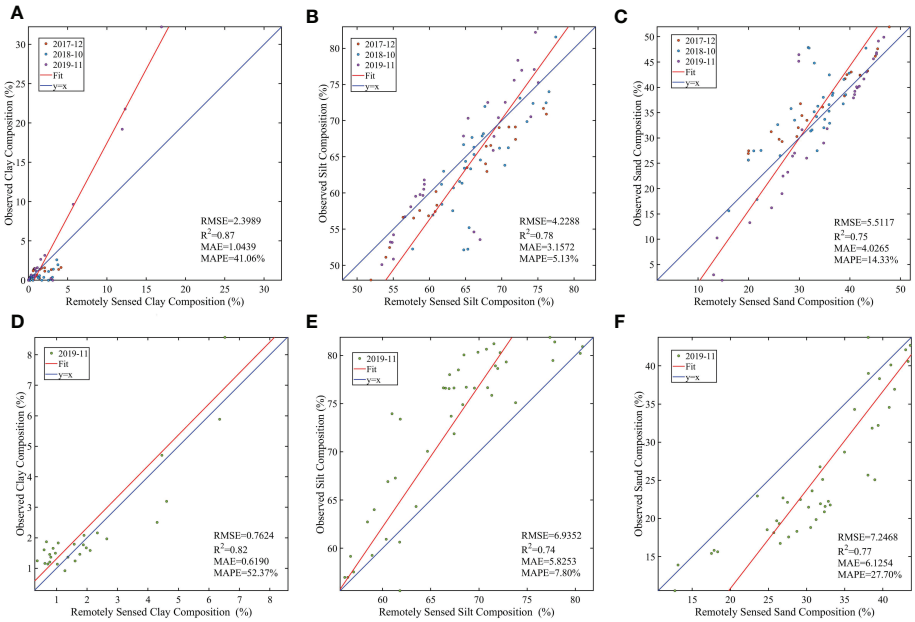

FIGURE 5
Accuracy of the Sediment Composition Inversion Model used in the BP-CNN Model. **(A–C)** show the training accuracy of the model for clay, silt and sand(Phase 1-3). **(D–F)**, show the validation accuracy for clay, silt and sand (Phase 4). The accuracy of the model prediction results was higher than 80%.

grain size distribution of the surface sediment in the Doulonggang tidal flat area was variable at different time intervals. Because the clay content was very small, only the seasonal and interannual spatial and temporal changes for sand and silt are discussed.

The grain size of the surface sediment in the study area exhibited a seasonal variation pattern of coarse in summer and fine in winter. This phenomenon is consistent with *in situ* observations (Gong et al., 2017) and the results simulated by hydrodynamic models (Jia et al., 2006; Gong et al., 2017; Zhu et al., 2022). The seasonal variation of tidal flat particle size is highly correlated with the tidal range: (1) The tidal flat range in Jiangsu in summer is large,and the silt content in summer declined. For example, the silt content on November 24, 2021, was significantly higher than that on May 8, 2021, and August 21, 2022. (2) In winter, the tidal range of Jiangsu tidal flat is small, the silt content rebounded, but the reduction in summer was greater than the increase in winter. Overall, the silt content in the study area is declining. However, the sand content displays the opposite pattern. The sand content in the intertidal middle zone and lower zone is low in winter and high in summer.

The particle size of the surface sediment increased slowly year to year, as follows: (1) From 2017 to 2022, the surface mud and silt of the Doulonggang tidal flat were eroded to varying degrees. The loss of silt in the intertidal zone was the most severe, and the distribution range of near-shore silt declined over time. Although the silt content increased in the winters of 2019 and 2021, the silt content decreased considerably overall. (2) Moreover, the sand content in the intertidal zone increased

TABLE 3 The accuracy of different methods in tidal flat sediment composition inversion.

Model	Data Category	Clay		Silt		Sand	
		R^2	RMSE	R^2	RMSE	R^2	RMSE
Stepwise Linear Regression	Phases 1-3	0.410	3.890	0.360	9.835	0.589	6.891
	Phase 4	0.544	1.151	0.298	10.157	0.325	10.041
SVM Regression	Phases 1-3	0.661	3.152	0.521	8.023	0.722	6.163
	Phase 4	0.486	1.414	0.640	7.872	0.674	8.230
BP Neural Network	Phases 1-3	0.640	3.278	0.659	7.467	0.774	5.252
	Phase 4	0.462	1.584	0.828	5.480	0.632	8.410
Convolutional Neural Network	Phases 1-3	0.904	1.777	0.762	4.797	0.731	5.972
	Phase 4	0.738	0.926	0.704	7.280	0.771	7.173
This article model(BP-CNN)	Phases 1-3	0.870	2.399	0.780	4.229	0.750	5.512
	Phase 4	0.820	0.762	0.740	6.935	0.770	7.247

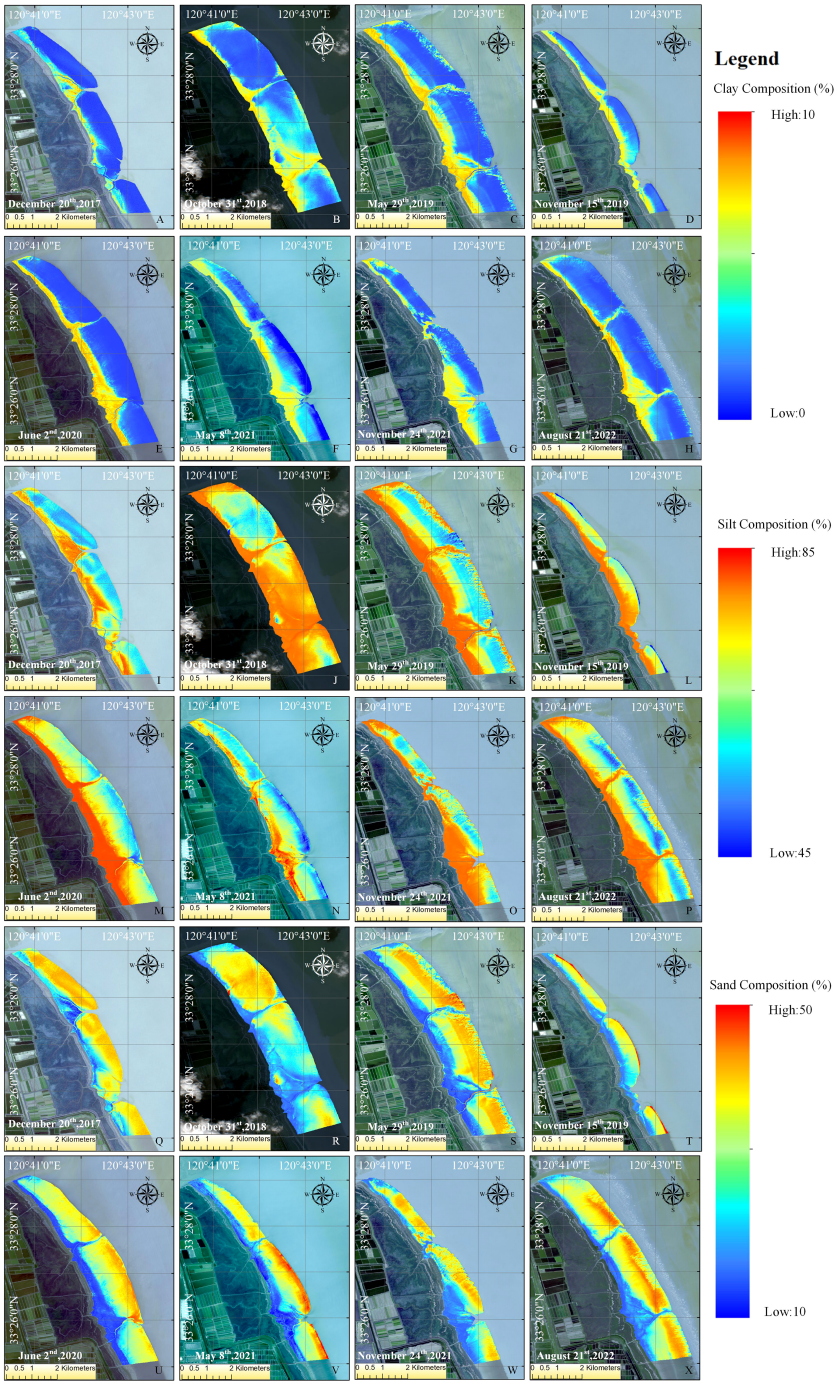

FIGURE 6
Inversion Diagram of the Sediment Component Contents in the Tidal Flat from 2017 to 2022 based on the BP-CNN Model Results. **(A–H)**, **(I–P)**, and **(Q–X)**, respectively show the spatial distribution of clay,silt and sand from 2017 to 2022. The sediment in the study area was mainly silty sand, followed by sand and then clay.

rapidly, and the distribution range expanded. The sediment on the tidal flat surface coarsened over time. The sand content in the study area decreased in winter and increased slowly in other seasons. Overall, the sand content increased each year.

In general, from 2017 to 2022, the sand content of the Jiangsu tidal flat increased, the clay and silt contents decreased, the sediment type gradually changed to sandy silt (sZ), and the sediment particle size gradually coarsened. Tidal flat development and evolution are often very complex. From the perspective of sediment sources, the sediment in the study area comes from the southward transport of waste erosion materials from the Yellow River Delta. The construction of coastal seawalls in Jiangsu may affect the hydrodynamic balance of the original tidal flat, causing reflection interference within the seawall and weakening the energy of tidal flat entering the tidal current. As a result, the sediment transported from the seawall with relatively fine particle size is more likely to be silted in the seawall, while deposition outside the seawall is relatively slow. Therefore, fine sediment particles are gradually lost.

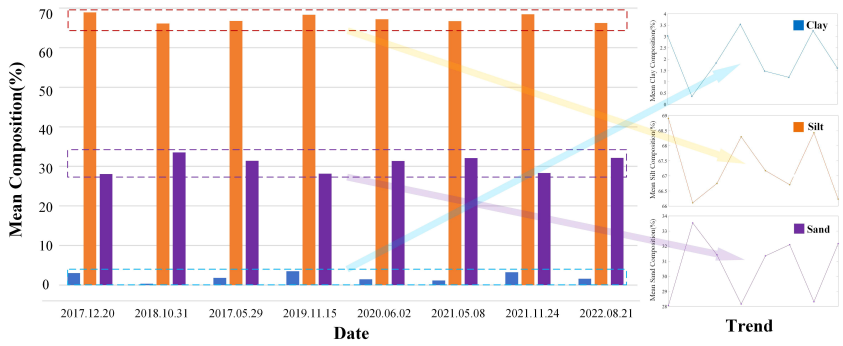

FIGURE 7
Evolution Trend of the Average Contents of Sediment Components in the Doulonggang Tidal Flat from 2017 to 2022.

Meanwhile, according to the inversion results, we observed that the sediment particle size is finer in the Spartina zone, while the sediment particle size increases obviously in subtidal zone. This may be because Spartina trap too much sediment, resulting in weakened siltation in other places, making the tidal flat coarser. At the same time, in recent years, the global sea level has risen due to the greenhouse effect, and ocean dynamic conditions have been strengthened, which has intensified the ability of currents to erode sediment (Ji and Jiang, 1994). Therefore, the grain size of tidal flat sediments has coarsened. In addition, the sedimentary environment of tidal flats may change under the influence of human activities (Zhang and Feng, 2011), such as vegetation introduction, reclamation and dike construction (Dethier et al., 2022; Pan et al., 2022), as well as port engineering, which ultimately lead to changes in the tidal flat in Jiangsu.

4 Conclusion

In this study, the Doulonggang tidal flat in Jiangsu Province was selected as the study area, and a remote sensing inversion method for determining tidal flat sediment components was investigated. Based on Sentinel-2 imagery, the distribution of surface sediment components was inversely estimated. The research conclusions are as follows:

1. Considering the complex relationship between the contents of surface sediment components and the remote sensing spectral reflectance for tidal flat areas, the traditional CNN was improved. An inversion model for determining the contents of surface sediment components (sand, silt, and clay) was built, achieving an average R^2 of 0.75. Based on measured values, the accuracy of the model prediction results was higher than 80%, indicating that Sentinel-2 remote sensing data can be used for the fine-scale inversion of sediment components.
2. The spatial distribution characteristics of surface sediments such as clay, silt and sand in the Doulonggang tidal flat were described. The surface sediment characteristics varied seasonally from coarse in summer to fine in winter. The phenomenon of the gradual coarsening of the sediment grain size in the Jiangsu tidal flat from 2017 to 2022 was analysed. The interannual variation in surface sediment fluctuated, and the magnitude of variations gradually increased year to year.
3. The error in BP-CNN model-based inversion was mainly due to the limited number of samples and the mismatch between imagery dates and survey data collection dates, thus limiting the model inversion accuracy. It is suggested to further analyse and predict the mechanism of sediment coarsening by applying dynamic numerical simulation technology.

Data availability statement

The original contributions presented in the study are included in the article/Supplementary material. Further inquiries can be directed to the corresponding author.

Author contributions

NZ: Conceptualization, Methodology, Software, Investigation, Visualization, and Writing – Original Draft. HL: Supervision, Writing, Reviewing and Editing, Funding Acquisition. JZ: Supervision, Funding Acquisition. JC: Supervision, Funding Acquisition. HW: Software, Validation. ZG: Supervision, Funding Acquisition. All authors contributed to the article and approved the submitted version.

Funding

This work was supported in part by National Key R&D Program of China under Grant 2022YFC3106204, in part by the China National Funds for Distinguished Young Scientists under Grant 51925905, in part by the National Natural Science Foundation of China under Grant 41976156, in part by the Marine Science and Technology Innovation Project of Jiangsu Province under Grant JSZRHYKJ202214, and in part by the Carbon Peak Carbon Neutral Science and Technology Innovation Projects of Jiangsu Province under Grant BK20220020.

Acknowledgments

The authors would like to thank Xiaowei Yue, Yunhua Shu, and Liu Wei, for their assistance in sample collection and sediment composition experiment. The authors also extremely grateful to Wanpeng Yue, Fuzheng Xia, Xiquan Chen, Fei Zhu,and Tianyu Li, who have kindly provided assistance and companionship in the course of preparing this paper.

Conflict of interest

The authors declare that the research was conducted in the absence of any commercial or financial relationships that could be construed as a potential conflict of interest.

Publisher's note

All claims expressed in this article are solely those of the authors and do not necessarily represent those of their affiliated organizations, or those of the publisher, the editors and the reviewers. Any product that may be evaluated in this article, or claim that may be made by its manufacturer, is not guaranteed or endorsed by the publisher.

Supplementary material

The Supplementary Material for this article can be found online at: https://www.frontiersin.org/articles/10.3389/fmars.2023.1109146/full#supplementary-material

References

Abbaszadeh, M., Mahdavi, R., and Rezai, M. (2019). Assessment of sedimentation process in flood water spreading system using IRS (P5) and supervised classification algorithms (case study: Dahandar plain, minab city, south of iran). remote sens. *Appl. Soc Environ.* 16, 100269. doi: 10.1016/j.rsase.2019.100269

Adam, S., De Backer, A., Degraer, S., Monbaliu, J., Toorman, E. A., and Vincx, M. (2008). Sediment characterization of intertidal mudflats using remote sensing. *Proc. Mar. Sci.* 9, 109–124. doi: 10.1016/S1568-2692(08)80011-3

Baoguo, Y., Ying, W., and Dakui, Z. (1997). THE TIDAL FLAT RESOURCE OF CHINA. *J. OF Natural Resour.* 12, 307–316. doi: 10.11849/zrzyxb.1997.04.003

Bernardo, N., Watanabe, F., Rodrigues, T., and Alcântara, E. (2017). Atmospheric correction issues for retrieving total suspended matter concentrations in inland waters using OLI/Landsat-8 image. *Adv. Space Res* 59, 2335–2348. doi: 10.1016/j.asr.2017.02.017

Buscombe, D., Rubin, D. M., Lacy, J. R., Storlazzi, C. D., Hatcher, G., Chezar, H., et al. (2014). Autonomous bed-sediment imaging-systems for revealing temporal variability of grain size. *Limnol. Oceanogr. Methods* 12, 390–406. doi: 10.4319/lom.2014.12.390

Cabezas-Rabadán, C., Pardo-Pascual, J. E., and Palomar-Vázquez, J. (2021). Characterizing the relationship between the sediment grain size and the shoreline variability defined from sentinel-2 derived shorelines. *Remote Sens.* 13, 2829. doi: 10.3390/rs13142829

Castillo, E., Pereda, R., Luis, J. M., Medina, R., and Viguri, J. (2011). Sediment grain size estimation using airborne remote sensing, field sampling, and robust statistic. environ. *Monit. Assess.* 181, 431–444. doi: 10.1007/s10661-010-1839-z

Chen, Y., Dong, J., Xiao, X., Zhang, M., Tian, B., Zhou, Y., et al. (2016). Land claim and loss of tidal flats in the Yangtze estuary. *Sci. Rep.* 6, 24018. doi: 10.1038/srep24018

Choi, T. J., Park, J. Y., and Choi, J. Y. (2016). Partitioning of grain-size component populations in bimodal sediments. *J. Coast. Res.* 75, 1322–1326. doi: 10.2112/si75-265.1

Dai, W., Li, H., Gong, Z., Zhang, C., and Zhou, Z. (2019). Application of unmanned aerial vehicle technology in geomorphological evolution of tidal flat. *Adv. Water Sci.* 30, 359–372. doi: 10.14042/j.cnki.32.1309.2019.03.006

Dalrymple, R. W., Zaitlin, B. A., and Boyd, R. (1992). Estuarine facies models; conceptual basis and stratigraphic implications. *J. Sediment. Res.* 62, 1130–1146. doi: 10.1306/D4267A69-2B26-11D7-8648000102C1865D

Dethier, E. N., Renshaw, C. E., and Magilligan, F. J. (2022). Rapid changes to global river suspended sediment flux by humans. *Science* 376, 1447–1452. doi: 10.1126/science.abn7980

Duan, Z., Chu, S., Cheng, L., Ji, C., Li, M., and Shen, W. (2022). Satellite-derived bathymetry using landsat-8 and sentinel-2A images: assessment of atmospheric correction algorithms and depth derivation models in shallow waters. *Opt. Express* 30, 3238–3261. doi: 10.1364/OE.444557

Fairley, I., Mendzil, A., Togneri, M., and Reeve, D. (2018). The use of unmanned aerial systems to map intertidal sediment. *Remote Sens.* 10, 1918. doi: 10.3390/rs10121918

Folk, R. L., Andrews, P. B., and Lewis, D. W. (1970). Detrital sedimentary rock classification and nomenclature for use in new Zealand. *N. Z. J. Geol. Geophys.* 13, 937–968. doi: 10.1080/00288306.1970.10418211

Geng, X., Shi, L., Yang, J., Li, P., Zhao, L., Sun, W., et al. (2021). Ship detection and feature visualization analysis based on lightweight CNN in VH and VV polarization images. *Remote Sens.* 13, 1184. doi: 10.3390/rs13061184

Ghorbanzadeh, O., Blaschke, T., Gholamnia, K., Meena, S., Tiede, D., and Aryal, J. (2019). Evaluation of different machine learning methods and deep-learning convolutional neural networks for landslide detection. *Remote Sens.* 11, 196. doi: 10.3390/rs11020196

Gong, Z., Jin, C., Zhang, C., Zhou, Z., Zhang, Q., and Li, H. (2017). Temporal and spatial morphological variations along a cross-shore intertidal profile, jiangsu, China. *Cont. Shelf Res.* 144, 1–9. doi: 10.1016/j.csr.2017.06.009

Jia, J., Wang, Y., Gao, S., Wang, A., and Li, Z. (2006). Interpreting grain-size trends associated with bedload transport on the intertidal flats at dafeng, central jiangsu coast. *Chin. Sci. Bull.* 51, 341–351. doi: 10.1007/s11434-006-0341-z

Ji, Z., and Jiang, Z. (1994). Impacts of sea level rise on coastal erosion in the changjiang river delta and north jiangsu coastal plain. *Chin. Geogr. Sci.* 4, 310–321. doi: 10.1007/BF02664369

Jin, D., Lee, E., Kwon, K., and Kim, T. (2021). A deep learning model using satellite ocean color and hydrodynamic model to estimate chlorophyll-a concentration. *Remote Sens* 13, 2003. doi: 10.3390/rs13102003

Jung, R., Adolph, W., Ehlers, M., and Farke, H. (2015). A multi-sensor approach for detecting the different land covers of tidal flats in the German wadden sea — a case study at norderney. *Remote Sens. Environ.* 170, 188–202. doi: 10.1016/j.rse.2015.09.018

Kim, K. L., Kim, B. J., Lee, Y. K., and Ryu, J. H. (2019). Generation of a large-scale surface sediment classification map using unmanned aerial vehicle (UAV) data: a case study at the hwang-do tidal flat, Korea. *Remote Sens.* 11, 229. doi: 10.3390/rs11030229

Kirwan, M. L., and Megonigal, J. P. (2013). Tidal wetland stability in the face of human impacts and sea-level rise. *Nature* 504, 53–60. doi: 10.1038/nature12856

Li, W., Sun, K., and Zhang, H. (2014). Algorithm for relative radiometric consistency process of remote sensing images based on object-oriented smoothing and contourlet transforms. *J. Appl. Remote Sens.* 8, 83607. doi: 10.1117/1.Jrs.8.083607

Liu, R., Pu, L., Zhu, M., Huang, S., and Jiang, Y. (2020). Coastal resource-environmental carrying capacity assessment: a comprehensive and trade-off analysis of the case study in jiangsu coastal zone, eastern China. *Ocean Coast. Manage.* 186, 105092. doi: 10.1016/j.ocecoaman.2020.105092

Li, T., Zhang, G., Wang, S., Mao, C., Tang, Z., and Rao, W. (2022). The isotopic composition of organic carbon, nitrogen and provenance of organic matter in surface sediment from the jiangsu tidal flat, southwestern yellow sea. *Mar. pollut. Bull.* 182, 114010. doi: 10.1016/j.marpolbul.2022.114010

Mahdianpari, M., Salehi, B., Rezaee, M., Mohammadimanesh, F., and Zhang, Y. (2018). Very deep convolutional neural networks for complex land cover mapping using multispectral remote sensing imagery. *Remote Sens.* 10, 1119. doi: 10.3390/rs10071119

Murray, N. J., Clemens, R. S., Phinn, S. R., Possingham, H. P., and Fuller, R. A. (2014). Tracking the rapid loss of tidal wetlands in the yellow sea. *Front. Ecol. Environ.* 12, 267–272. doi: 10.1890/130260

Murray, N. J., Phinn, S. R., DeWitt, M., Ferrari, R., Johnston, R., Lyons, M. B., et al. (2019). The global distribution and trajectory of tidal flats. *Nature* 565, 222–225. doi: 10.1038/s41586-018-0805-8

Nasiha, H. J., Shanmugam, P., and Sundaravadivelu, R. (2019). Estimation of sediment settling velocity in estuarine and coastal waters using optical remote sensing data. *Adv. Space Res.* 63, 3473–3488. doi: 10.1016/j.asr.2019.02.023

Pancorbo, J. L., Lamb, B. T., Quemada, M., Hively, W. D., Gonzalez-Fernandez, I., and Molina, I. (2021). Sentinel-2 and WorldView-3 atmospheric correction and signal normalization based on ground-truth spectroradiometric measurements. *ISPRS J. Photogramm. Remote Sens.* 173, 166–180. doi: 10.1016/j.isprsjprs.2021.01.009

Pan, Y., Yin, S., Chen, Y. P., Yang, Y. B., Xu, C. Y., and Xu, Z. S. (2022). An experimental study on the evolution of a submerged berm under the effects of regular waves in low-energy conditions. *Coast. Eng.* 176, 104169. doi: 10.1016/j.coastaleng.2022.104169

Paolini, L., Grings, F., Sobrino, J. A., Muñoz, J. C. J., and Karszenbaum, H. (2007). Radiometric correction effects in landsat multi-date/multi-sensor change detection studies. *Int. J. Remote Sens.* 27, 685–704. doi: 10.1080/01431160500183057

Park, N. W. (2019). Geostatistical integration of field measurements and multi-sensor remote sensing images for spatial prediction of grain size of intertidal surface sediments. *J. Coast. Res.* 90, 190. doi: 10.2112/si90-023.1

Pitarch, J., Falcini, F., Nardin, W., Brando, V. E., Di Cicco, A., and Marullo, S. (2019). Linking flow-stream variability to grain size distribution of suspended sediment from a satellite-based analysis of the Tiber river plume (Tyrrhenian sea). *Sci. Rep.* 9, 19729. doi: 10.1038/s41598-019-56409-8

Rainey, M. P., Tyler, A. N., Gilvear, D. J., Bryant, R. G., and McDonald, P. (2003). Mapping intertidal estuarine sediment grain size distributions through airborne remote sensing. *Remote Sens. Environ.* 86, 480–490. doi: 10.1016/s0034-4257(03)00126-3

Schuerch, M., Spencer, T., Temmerman, S., Kirwan, M. L., Wolff, C., Lincke, D., et al. (2019). Author correction: Future response of global coastal wetlands to sea-level rise. *Nature* 569, E8. doi: 10.1038/s41586-019-1205-4

Smirnov, E. A., Timoshenko, D. M., and Andrianov, S. N. (2014). Comparison of regularization methods for ImageNet classification with deep convolutional neural networks. *AASRI Proc.* 6, 89–94. doi: 10.1016/j.aasri.2014.05.013

Soloy, A., Turki, I., Fournier, M., Costa, S., Peuziat, B., and Lecoq, N. (2020). A deep learning-based method for quantifying and mapping the grain size on pebble beaches. *Remote Sens.* 12, 3659. doi: 10.3390/rs12213659

Temmerman, S., and Kirwan, M. L. (2015). Building land with a rising sea. *Science* 349, 588–589. doi: 10.1126/science.aac8312

Wang, X., and Ke, X. (1997). Grain-size characteristics of the extant tidal flat sediments along the jiangsu coast, China. *Sediment. Geol.* 112, 105–122. doi: 10.1016/S0037-0738(97)00026-2

Yates, M. G., Jones, A. R., McGrorty, S., and Goss-Custard, J. D. (1993). The use of satellite imagery to determine the distribution of intertidal surface sediments of the wash, England. *Estuar. Coast. Shelf Sci.* 36, 333–344. doi: 10.1006/ecss.1993.1020

Yu, W. J., and Zou, X. Q. (2013). The research on the farmer households' economic behavior and sustainable utilization issues in tidal flat of jiangsu province. *Adv. Sci. Lett.* 19, 1819–1822. doi: 10.1166/asl.2013.4573

Zhang, C., and Feng, X. (2011). Natural and human-induced effects on grain size of surface sediments along the lianyungang muddy coast, China. *Chin. J. Oceanol. Limnol.* 29, 387–397. doi: 10.1007/s00343-011-0007-9

Zhang, Y., Huang, Z., Chen, C., He, Y., and Jiang, T. (2015). Particle size distribution of river-suspended sediments determined by *in situ* measured remote-sensing reflectance. *Appl. Opt.* 54, 6367–6376. doi: 10.1364/AO.54.006367

Zhu, S., Chen, Y., Yan, W., Xing, F., Li, R., Li, M., et al. (2022). The hummocky patches and associated sediment dynamics over an accretional intertidal flat. *Front. Earth Sci.* 10. doi: 10.3389/feart.2022.908351

frontiers | Frontiers in Marine Science

TYPE Original Research
PUBLISHED 24 January 2023
DOI 10.3389/fmars.2023.1113494

OPEN ACCESS

EDITED BY
Yi Pan,
Hohai University, China

REVIEWED BY
Chi Zhang,
Hohai University, China
Shaohua Zhao,
MNR, China

*CORRESPONDENCE
Shentang Dou
doushentang@126.com
Weiqi Dai
vickey_hhu@163.com

SPECIALTY SECTION
This article was submitted to Coastal Ocean Processes, a section of the journal Frontiers in Marine Science

RECEIVED 01 December 2022
ACCEPTED 09 January 2023
PUBLISHED 24 January 2023

CITATION
Wu Y, Dou S, Fan Y, Yu S and Dai W (2023) Research on the influential characteristics of asymmetric wind fields on typhoon waves.
Front. Mar. Sci. 10:1113494.
doi: 10.3389/fmars.2023.1113494

Research on the influential characteristics of asymmetric wind fields on typhoon waves

Yan Wu[1], Shentang Dou[1*], Yaoshen Fan[1], Shoubing Yu[1,2] and Weiqi Dai[1*]

[1]Key Laboratory of Yellow River Channel and Estuary Regulation of the Ministry of Water Resources, Yellow River Institute of Hydraulic Research, Zhengzhou, China, [2]State Key Laboratory of Estuarine and Coastal Research, Faculty of Earth Science, East China Normal University, Shanghai, China

The East China Sea is an ocean region with frequent typhoons, typhoons are also the main reason for inducing typhoon waves. The complexity of typhoon waves is closely related to the complexity of typhoon wind field. In previous studies, symmetrical wind field models or superimposed wind field models were usually used to simulate typhoon waves. However, the actual wind fields are asymmetric, and the asymmetry is affected by many factors. Therefore, three wind field models are used to simulate the wind field of Typhoon Muifa that moved through the East China Sea. Moreover, the abovementioned wind field models are used to drive the third-generation wave model SWAN to simulate the wave field and wave spectrum of Typhoon Muifa. Studies show that the values generated by the asymmetric wind field model are most consistent with the actual measurement data. This is especially the case if the typhoon center is closer to the station. The accuracy of the typhoon waves simulated using the asymmetric wind field model is better than that of the other two wind field models. The asymmetric wind field can reflect the asymmetric characteristics of the typhoon well. The substantial wave heights on the right side of typhoon's path are substantially higher than those on the left side of path. Additionally, the maximum wave spectral density and total energy of waves as simulated by the asymmetric wind field are both larger than those of the other two wind field models. Thus, the asymmetric wind field model is more suitable for the numerical simulation of typhoon waves in the East China Sea.

KEYWORDS

Typhoon Muifa, wind model, typhoon waves, asymmetry, SWAN model, East China Sea

1 Introduction

A typhoon is a severe tropical cyclone that is one of the most destructive weather systems in geophysical environments (Chen et al., 2019). The threat of typhoons to social interests, property, and public safety in coastal areas has become more and more prominent due to the intensification of global climate change and the increase in the coastal population

(Ambinakudige and Khanal, 2010; Walsh et al., 2016; Cui and Caracoglia, 2016; Walsh et al., 2019; Pan et al., 2022). The oceanic response to typhoons is the strongest air-sea interaction, involving complex processes from weather to climate timescales, from local to global spatial scales, and from dynamics and thermodynamics to multiple environmental variables (Lee and Chen, 2012; Ge et al., 2017; Dai et al., 2018; Ma et al., 2019; Wu et al., 2019; Wu et al., 2020; Li et al., 2022).

Using the original equations to calculate the typhoon pressure field and wind field need to be improved due to a lack of accuracy in the initial conditions and the boundary conditions (Zhang et al., 2010). Therefore, efficient and straightforward parametric typhoon field models have been widely used. Previous studies often use the circularly symmetrical pressure field model to solve the gradient wind according to the cyclone constant wind principle (Myers, 1954; Jelesnianski, 1965; Holland, 1980; Miyamoto et al., 2014) or to superimpose the circularly symmetrical wind field model and the traveling wind field model to form a superimposed wind field model (Miyazaki, 1961; Jelesnianski, 1966; Ueno, 1981). However, the circular symmetrical wind field model does not consider the asymmetry of the typhoon, and the superimposed wind field model only considers the asymmetry of the typhoon caused by the ambient airflow. Yet, the actual asymmetric features of the typhoon are more complicated due to the influence of various factors such as the underlying surface, Coriolis force, and ambient temperature (Xie et al., 2006). At the same time, the data released by National Oceanic and Atmospheric Administration show that typhoons are asymmetric. Yoshizumi (1968) and Bell and Ray (2004) also propose that the actual structure of the typhoon is asymmetric, with the maximum wind possibly located in the rear-right quadrant or the front-right quadrant. Diagnosing an asymmetric system is helpful for accurately assessing coastal risk (Lin and Chavas, 2012). Typhoon data reported by the Joint Typhoon Warning Center also show that typhoons have different scales in each quadrant; especially, the wind radii in the northeast and southwest quadrants are very different.

The wind field, as a driving factor, plays an important role in the simulation of typhoon waves. With the improvement of the accuracy requirements for typhoon waves in forecasting and post-forecasting modes, constructing a more accurate typhoon wind field model has become an important research topic (Rogers et al., 2007; Wang et al., 2020). This study introduces the Holland circular symmetric wind field model, superimposes the Holland wind field model and the moving wind field model to form a superimposed wind field model, and introduces an improved four-quadrant asymmetric wind field model based on the Holland model. Moreover, the three wind field models are modified by introducing a correction factor to make them more suitable for the numerical simulation of typhoon in the East China Sea. Referring to the radial extent of the 34-, 50-, and 64-kt winds in the four quadrants (northeast, southeast, southwest, and northwest), this study use the above three wind field models to simulate the wind field distribution of Typhoon Muifa, and compare the simulated results of the three wind field. Meanwhile, some numerical wave models have been adopted to simulate typhoon waves (Tajima et al., 2016a; Tajima et al., 2016b; Akpinar et al., 2016; Mao et al., 2016; Nikishova et al., 2017; Kutupoğlu et al., 2018; Vieira et al., 2020). In this study, three wind fields were used to drive the third-generation wave model, SWAN. The numerical simulation of wave field and wave spectrum of Typhoon Muifa was carried out to evaluate the effect of typhoon asymmetry on the energy distribution inside the waves and finally select a wind field model that can more accurately simulate typhoon waves in the East China Sea.

2 Model description and numerical experiments

2.1 Wind field model

2.1.1 Key parameter-radius of maximum wind

The radius of maximum wind is an important parameter that characterizes the scale of the typhoon, and it is also a key parameter to describe the wind field (Jiang et al., 2008; Fang and Lin, 2013). The radius of the maximum wind refers to the distance between the typhoon center and the maximum wind speed zone of the typhoon, and it directly affects the overall wind speed distribution (Lin and Fang, 2013). Therefore, an accurate radius of maximum wind is important for improving the calculation accuracy of the typhoon wind field and the simulation effect of the wave field.

Previous research efforts have investigated the parameterized calculation scheme of the radius of maximum wind. Kato (2005) conducted a statistical analysis of typhoons along the coast of Japan and pointed out that the radius of maximum wind and the central pressure of the typhoon are linearly distributed. Willoughby and Rahn (2004) conducted a statistical analysis of typhoon data from 1977 to 2000 released by the National Oceanic and Atmospheric Administration and concluded that the radius of maximum wind is linearly distributed with the central latitude of the typhoon.

Studies have shown that the central pressure of the typhoon characterizes the intensity of the typhoon. The central latitude of a typhoon reflects the geographical location of typhoon and the local temperature. The moving velocity of typhoon's center is affected to a large extent by the synoptic-scale and upper-tropospheric height field that are linked to the large-scale background wind field. These three factors have a certain influence on the radius of maximum wind. This study statistically analyzes typhoon data released by the Joint Typhoon Warning Center (http://www.metoc.navy.mil/jtwc/jtwc.html) in the Northwest Pacific from 2002 to 2020, and the relationship between the radii of the 34-, 50-, and 64-kt winds and its influencing factors are shown in Figure 1.

It can be seen from Figure 1A that the radial extent of the 34-, 50-, and 64-kt winds in four quadrants decrease with an increased central pressure difference of typhoon. This is because the central pressure difference of the typhoon reflects its strength. With the increase of the central pressure difference, the typhoon intensity increases, the suction effect and vortex motion increase, each wind circle is closer to the typhoon center, and the wind speed radii of each wind circle decreases. Figure 1B shows that the radial extent of the 34-, 50-, and 64-kt winds in the four quadrants increase along with the increasing latitude of the typhoon center, but when the latitude is greater than

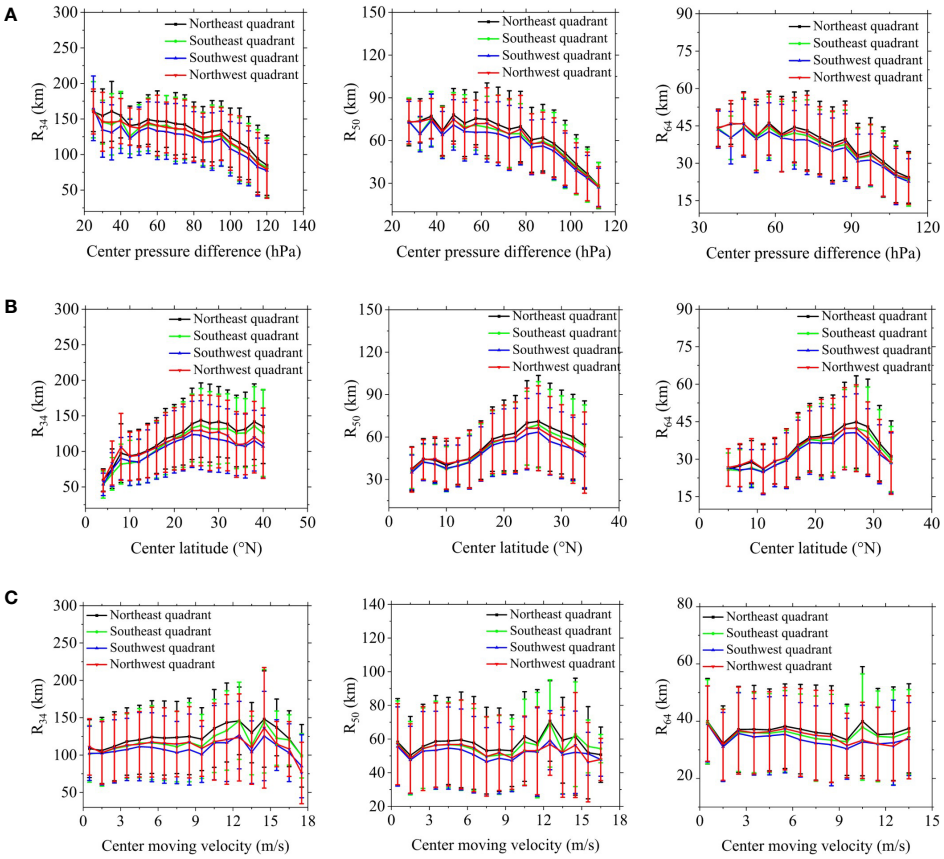

FIGURE 1
Distribution map of the radii of wind and: **(A)** the central pressure difference of the typhoon, **(B)** the central latitude of the typhoon, **(C)** the central moving velocity of the typhoon.

25°, the radial extent of the 34-, 50-, and 64-kt winds in four quadrants decrease with the increase of the latitude of the typhoon center. This is because the geographical latitude mainly reflects the local environmental temperature; as the latitude increases, the ambient temperature changes, but when the latitude is poleward of 25°N, due to the influence of the subtropical high pressure, the ambient surface pressure rises and the typhoon central pressure difference increases, making the central pressure difference the dominant factor, resulting in a decrease in the radial extent of the 34-, 50-, and 64-kt winds in all four quadrants. At the same time, Figure 1C shows that the influence of the central moving velocity of the typhoon on the radial extent of the 34-, 50-, and 64-kt winds in four quadrants is not prominent and can be ignored.

2.1.2 Symmetric wind field model

From the perspective of the construction of the typhoon wind field, people often use a circular symmetrical pressure field model, that is, first use a theoretical model, empirical formulas, or semi-theoretical and semi-empirical model to construct the pressure distribution in the typhoon area, and then use the gradient wind equations or geostrophic wind equation to obtain the wind field distribution in the typhoon area (Fujita, 1952; Myers, 1954; Jelesnianski, 1965; Holland, 1980). The most commonly used model is the Holland circular symmetric pressure wind field model, which is expressed as

$$P_{(r)} = P_c + (P_n - P_c)\exp^{-(R_{\max}/r)^B} \quad (1)$$

where $P_{(r)}$ is the surface pressure at a distance of r from the typhoon center; r the distance from the center of the typhoon; P_c the typhoon central surface pressure; P_n the ambient surface pressure; $R_{\max}$ the radius of maximum wind; B a hurricane-shape parameter (Vickery and Wadhera, 2008). From Eq. (2), the initial value of B can be determined by using $V_{\max}$, P_n, and P_c:

$$B = \frac{V_{\max}^2 \rho e}{P_n - P_c} \quad (2)$$

where $V_{\max}$ is the hurricane's maximum wind speed; the air density; e = 2.7183.

The gradient wind is given by the pressure field via the cyclone wind principle:

$$V_{(r)} = \left[\frac{B}{\rho}\left(\frac{R_{\max}}{r}\right)^B (P_n - P_c)\exp^{-(R_{\max}/r)^B} + \left(\frac{rf}{2}\right)^2\right]^{1/2} - \frac{rf}{2} \quad (3)$$

where $V_{(r)}$ is the velocity at a distance r from the hurricane center; f is the Coriolis parameter.

The correction for the gradient wind speed of the model to obtain the gradient wind speed at 10 m on the sea surface is given by:

$$V = c_1 V_{(r)} \begin{bmatrix} -\sin(\theta+\beta) \\ \cos(\theta+\beta) \end{bmatrix} \quad (4)$$

where V is the corrected wind speed; c_1 is a correction factor, and its value depend on the location of typhoon, by conducting tests of many typhoon cases in the East China Sea, c_1 in this region is set as 0.9; θ the angle between the calculated point and the x-axis; β the angle between the gradient wind and the sea-surface wind.

2.1.3 Superimposed wind field model

Since actual typhoons are often asymmetrical, various asymmetric wind field models have been proposed to better describe the actual wind field (Pan et al., 2016). The previous asymmetric wind field model considered the impact of a typhoon moving asymmetrically, that is, superimposing the symmetrical wind field model with the moving wind field model. This method can involve the asymmetrical typhoon wind field caused by ambient airflow. Miyazaki (1961) introduced a moving wind field mod

$$V_t = V_f e^{-\pi r/R_G} \quad (5)$$

where V_t is the moving speed of typhoon; V_f is the moving speed of typhoon center; R_G is the environmental scale, set to 500 km in this article.

Synthesize the gradient wind field with the moving wind field to obtain a superimposed wind field:

$$V_M = c_1 V_{(r)} \begin{bmatrix} -\sin(\theta+\beta) \\ \cos(\theta+\beta) \end{bmatrix} + c_2 V_t \quad (6)$$

where V_M is the wind speed of the superimposed wind field; c_1 and c_2 are the correction factors: c_1 has the same value as Eq. (4) and is set as 0.9. c_2 is set as 0.5.

2.1.4 Asymmetric wind field

Typhoons are affected by many factors, such as the underlying surface, Coriolis force, and ambient temperature, making the actual asymmetry of typhoons more complicated (Olfateh et al., 2017). Therefore, Xie et al. (2006) incorporated the National Hurricane Center forecast guidance into the Holland model. R_{max} is modified to become a function of the azimuthal angle (θ):

$$R_{\max(\theta)} = P_1\theta^4 + P_2\theta^3 + P_3\theta^2 + P_4\theta + P_5 \quad (7)$$

where $R_{max(\theta)}$ is calculated by Eq. (3), when the value of $V_{(r)}$ and r are given; $P_1 \sim P_5$ the coefficients of the fourth-order polynomial are obtained by a polynomial curve fitting of the R_{max} value.

Upon substituting, the $R_{max(\theta)}$ obtained by Eq. (7) into the following equation, can obtain the four-quadrant asymmetric wind field:

$$V_{(r,\theta)} = c_1 [R_{\max}(\theta)/\bar{R}_{\max}]^{B/2} V_r \begin{bmatrix} -\sin(\theta+\beta) \\ \cos(\theta+\beta) \end{bmatrix} \quad (8)$$

where $V_{(r,\theta)}$ is the wind speed of the asymmetric wind field; c_1 is the correction factors, and it has the same value as Eq. (4) and is set as 0.9; R_{max} is the mean value of the radius of maximum wind. Because R_{max} is different in each azimuth, the calculated wind field is asymmetric.

2.2 Wave model

SWAN is a third-generation wave model for obtaining realistic estimates of wave parameters in coastal areas, lakes, and estuaries from the given wind, bottom, and current conditions (Booij et al., 1999; Rogers et al., 2003). However, SWAN can be used on any scale relevant to wind-generated surface gravity waves. The model is based on the wave action balance equation with sources and sinks:

$$\frac{\partial N}{\partial t} + \frac{\partial c_\lambda N}{\partial \lambda} + \frac{1}{\cos\varphi}\frac{\partial c_\varphi \cos\varphi N}{\partial \varphi} + \frac{\partial c_\sigma N}{\partial \sigma} + \frac{\partial c_\theta N}{\partial \theta} = \frac{S}{\sigma} \quad (9)$$

$$N(\sigma,\theta) = E(\sigma,\theta)/\sigma \quad (10)$$

where N is the momentum spectral density; E the energy spectral density; t the time; λ the longitude; φ the latitude; σ the frequency; θ the direction of propagation; c_λ, c_σ and c_θ are the propagation speeds of the dynamic spectral density in the λ, σ and θ direction.

2.3 Computational experiments

The simulation results of three different calculation schemes are used to compare and analyze the simulation effects of varying wind field models on wind field, wave field, and wave spectrum, which include:

(1) Run 1(T1): using the symmetrical wind field model to simulate the wind field and drive SWAN to simulate the wave field and wave spectrum.

(2) Run 2(T2): using a superimposed wind field model to simulate the wind field and drive SWAN to simulate the wave field and wave spectrum.

(3) Run 3(T3): using an asymmetric wind field model to simulate the wind field and drive SWAN to simulate the wave field and wave spectrum.

3 Study area and data sources

3.1 Study area

Typhoons frequently occur in the Northwest Pacific (Guo et al., 2016). Typhoons generated in the Northwest Pacific account for about 35% of the total number of typhoons worldwide each year. Most typhoons in the Northwest Pacific will eventually land after passing through the East China Sea or South China Sea. Many typhoons passing through the South China Sea will first pass through the Philippine Islands. Therefore, their strength will be weakened and their internal structure will change before they land due to the effect of the underlying surface. However, the East China

Sea is relatively wide, and typhoons passing through this area are less affected by underlying surface. Therefore, typhoons passing through the East China Sea were selected for this study.

3.2 Typhoon path data

Because the asymmetry of the typhoon will increase due to the influence of the underlying surface and other factors when it makes landfall, this study chose to use Typhoon Muifa, which passed through the East China Sea before making landfall. Super Typhoon Muifa was generated in the Northwest Pacific Ocean on 24 July 2011. It assembled in the eastern Philippines on 29 July and moved slowly to the west and then turned to the north and continued to move through the East China Sea, making landfall on the Korean Peninsula before dying out in Jilin Province. The path data of Muifa was sourced from the Joint Typhoon Warning Center and contains the date, time, latitude, longitude, maximum sustained wind speed (V_{max}), typhoon central pressure (P_c), wind circle speed (V), wind speed radius of the four quadrants under the wind circle speed (R_{ne}, R_{se}, R_{sw}, R_{nw}), ambient surface pressure (P_n), and the radius of maximum wind (R_{max}). The time resolution of the typhoon-path data from Joint Typhoon Warning Center is six hours.

3.3 Buoy data

To validate the model forecast of the wind and wave time change processes, the wind and wave fields computed with the asymmetric wind field model (T3) were compared with those produced using the superimposed wind field model (T2), symmetrical wind field model (T1), and buoy observations. The buoy data was from the QF207 buoy station (124.1°E, 29.05°N). The QF207 buoy station is located in the East China Sea, close to the path of Super Typhoon Muifa, and records the wind and wave data during the typhoon. The location of the QF207 buoy station and the typhoon's path are shown in Figure 2.

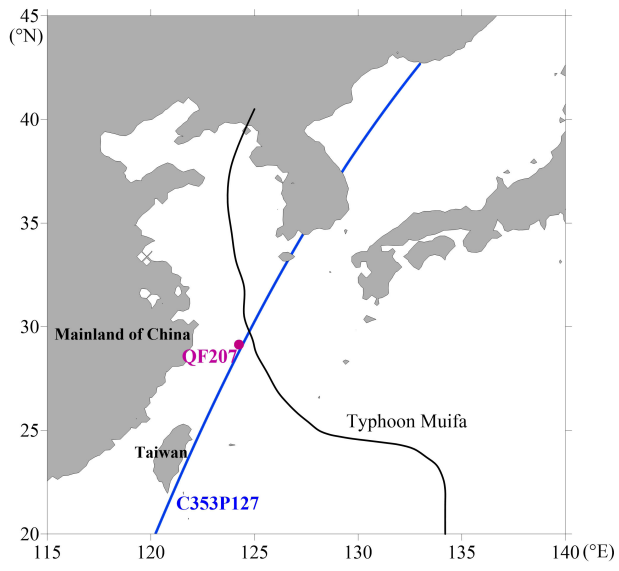

FIGURE 2
The location of the QF207 buoy station, satellite orbit and the typhoon path.

3.4 Satellite data

To validate the model forecast of the wind and wave space change process, the wind field and wave field computed with the asymmetric wind field model (T3) were compared with those produced using the superimposed wind field model (T2), symmetrical wind field model (T1) and satellite observations. The satellite data came from the C353P127 orbit of the Jason-1 satellite.

The Jason-1 satellite data is released by the AVISO website. The satellite is a marine terrain satellite developed by the French National Space Research Center (CNES) and the National Aeronautics and Space Administration (NASA). It is mainly used to measure the topography and sea level of the ocean surface. Each satellite is equipped with a radar altimeter and a microwave radiometer, which can observe the average sea level, sea-surface wind speed, sea-surface significant wave height, and other data. Its sea-level height observation accuracy is 4.2 cm, the spherical observation accuracy can reach 25 cm. The orbit of the Jason1 satellite is in a circular orbit with an operating altitude of 1336 km, which can effectively reduce the influence of the Earth's gravitational field and atmospheric drag on the observation. The satellite's orbital inclination is 66° and the orbital scanning spatial coverage is 66.03°S~66.03°N, which can cover 90% of the global ocean area. The time needed to complete one earth orbit in 9.9156 days, fully considering the impact of temporal and spatial resolution and tidal aliasing. The satellite orbit and typhoon path are shown in Figure 2.

4 Results and discussion

4.1 Wind field

To show the difference between the three wind field models in simulating wind speed, the T1~T3 scheme was applied to the East China Sea. The wind speed simulation results of Muifa and the

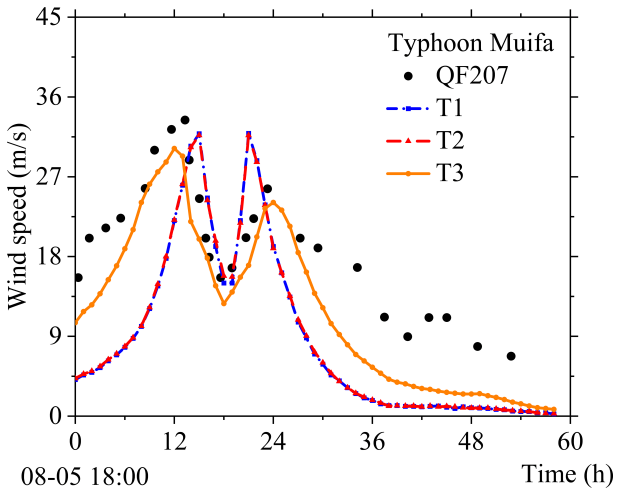

FIGURE 3
The modeled and buoy station observed wind speed.

measured results of the QF207 buoy station are shown in Figure 3, and the comparison results of the simulated wind field value of Typhoon Muifa and the actual measured value of the buoy station are shown in Table 1.

It can be seen from Figure 3 that the variation trend of the simulated wind speed time change process of each scheme is in good agreement with that measured by the buoy station. However, the simulation effect of the asymmetric wind field T3 on the wind speed is closer to the actual measured wind speed than the superimposed wind field T2 and the circular symmetric wind field T1. This is because the typhoon has asymmetric characteristics, and the asymmetric wind field can better reflect the actual typhoon. The simulation results of the superimposed wind field T2 and the circular symmetrical wind field T1 are not much different. This is because the asymmetric characteristics of the typhoon are not only affected by the movement of the typhoon but also affected by various factors such as environment, topography, and underlying surfaces (Olfateh et al., 2017).

The resultant simulated wind speed of Typhoon Muifa, given in Table 1, shows that the average wind speed error and the root mean square error of wind speed in the T3 scheme are reduced compared with the T1 and T2 schemes. Among them, the root mean square error of wind speed is reduced by 45.70% and 46.08% compared with T1 and T2, corresponding to a root mean square error of only 5.37 m/s. At the same time, during the developmental stage of Typhoon Muifa, the correlation between the simulated wind speed value of the T3 scheme and the actual wind speed value at the buoy station was the best, and the correlation coefficient reached 0.96, which was significantly higher than the other two schemes.

To show the spatial distribution characteristics of the typhoon wind field constructed by the above three wind field models, the wind speed and wind direction simulation results of Muifa and the measured results of the C353P127 orbit of Jason-1 satellite are shown in Figure 4 and the comparison results of the simulated wind field value of Typhoon Muifa and the actual measured value of the satellite are shown in Table 2.

The results in Figure 4 show that because the satellite scanning zone crosses the typhoon center area, the satellite-measured wind field presents prominent asymmetrical characteristics, that is, the typhoon center wind speed is very low, and the wind speed on the right side of the typhoon wind field is significantly higher than that on the left side. At this time, the asymmetric wind field T3 can well reflect the asymmetric characteristics of the typhoon, in contrast, the superimposed wind field T2 does not show the asymmetric characteristics of the typhoon clearly, the circular symmetric wind field T1 does not show the asymmetric characteristics of the typhoon.

In the simulation of the wind direction process of Typhoon Muifa, the three wind field models that simulated the wind direction process line almost the same, which is in good agreement with the actual wind direction as measured by the satellite at the center of the typhoon, and gradually changes with the change of latitude. However, in the peripheral area of the typhoon, there are differences between the simulated wind direction values of the three wind field models and the actual measured value of the satellite. This is because the typhoon's periphery is mainly affected by the environmental wind, so a single typhoon wind field model cannot simulate the wind process well (Shen et al., 2016).

It can be seen from Table 2 that when the satellite scanning zone C353P127 passes through the center of Typhoon Muifa, the asymmetric wind field in T3 is significantly correlated with the measured wind field compared to the circular symmetric wind field in T1 and the superimposed wind field in T2. The root mean square error of wind speed in T3 is reduced by 45.99% and 45.38% compared with T1 and T2. It can be seen that the asymmetric wind field can better depict the characteristics of wind speed distribution in the typhoon center area.

4.2 Wave field

4.2.1 Typhoon wave calculation effect

Using the above three wind field models to drive the third-generation wave model SWAN to simulate the spatiotemporal changes of the significant wave heights of the typhoon in the East China Sea, we used the measured data from the buoy stations and satellites to compare the effects of different wind field models on the calculation results of the space and time distributions of the waves. For the verification of the calculated typhoon waves within the time range, the results of the typhoon wave-time-change process, as simulated using the wind field model and the measured results of the QF207 buoy station are shown in Figure 5A. For the verification of the calculated effect of the typhoon waves within space, the results of the typhoon wave-space change process, as simulated using the wind field model, and the measured results of the C353P127 orbit of Jason-1 satellite are shown in Figure 5B.

It can be seen from Figure 5A that the three wind field models can all reflect the wave change trend. In the simulation of the time change process of the wave heights of Typhoon Muifa, T1 and T2 both

TABLE 1 Wind speed simulation and buoy station measured values.

Typhoon	Buoy station	Wind field model	V_{max}(m/s)		V(m/s)		V_{max} error (m/s)	V error (m/s)	Correlation coefficient	RMSE of wind speed (m/s)
			Measured	Calculated	Measured	Calculated				
Muifa	QF207	T1	33.38	31.81	18.94	12.74	1.57	-6.20	0.71	9.89
		T2	33.38	31.73	18.94	12.81	-1.65	-6.13	0.70	9.96
		T3	33.38	30.26	18.94	14.25	-3.12	-4.68	0.96	5.37

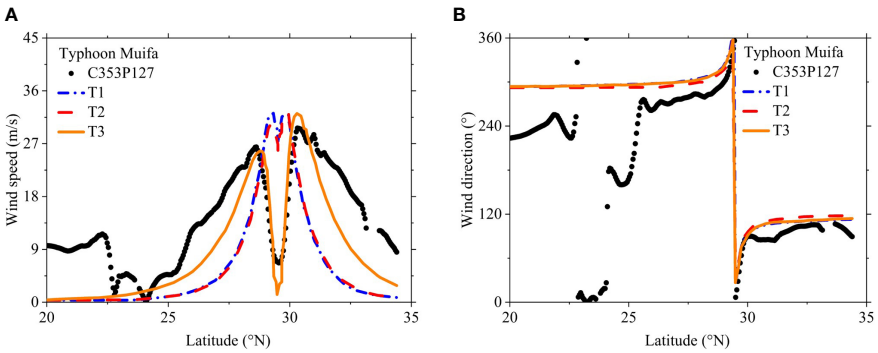

FIGURE 4
The modeled and satellite observed: **(A)** wind speed, **(B)** wind direction.

underestimated the significant wave heights. In the simulation of the maximum wave height near the buoy station, the simulated value of the asymmetric wind field T3 is more consistent with the measured value, and it can more accurately simulate the significant wave height in the central area of the typhoon.

Figure 5B shows that the change trend of the simulated value of the significant wave height of each wind field model is basically the same as the measured value on the satellite orbit. The deviation between the simulated value of the average wave height of each wind field model and the measured value on the satellite orbit is small, and the three wind field models can show the average level of the significant wave height distribution on the satellite scanning zone. However, the asymmetric wind field of T3 is more accurate in the simulation of the change trend of significant wave heights, especially the simulation of the maximum value of the significant wave height of the typhoon waves, which can more accurately describe the extreme value distribution of the typhoon waves within the satellite scanning zone.

4.2.2 Wave field simulation effect

To further demonstrate the influence of three different wind field models on the distribution characteristics of the wave fields, the wave fields simulated using the three wind field models at 1200 UTC 3 August 2011, 1800 UTC 4 August 2011, 0000 UTC 6 August 2011, as Typhoon Muifa passed through the East China Sea are shown in Figures 6–8.

The simulation results in Figures 6–8 show that the wave field exhibits prominent asymmetric characteristics during the typhoon's movement. At 1200 UTC 3 August and 1800 UTC 4 August, the wave fields simulated using the three wind fields show asymmetric characteristics of the maximum significant wave height in the northwest quadrant and the minimum significant wave height in the southeast quadrant. At 0000 UTC 6 August, the wave fields simulated using the three wind fields show the asymmetric characteristics of the maximum significant wave height in the northeast quadrant and the minimum significant wave height in the southeast quadrant. The three typical time points all show that the wave height on the right side of the typhoon's path is significantly higher than the wave height on the left side, forming a crescent-shaped wave height contour distribution on the right side. Meanwhile, the significant wave height of the typhoon simulated using the asymmetric wind field at three typical time points is the largest, reaching above 11 m at 1200 UTC 3 August and 1800 UTC 4 August, above 10 m at 0000 UTC 6 August, which are about 2 m higher than the significant wave height simulated using the circular symmetrical wind field and the superimposed wind field. At the same time, the distribution range of the large wave area simulated using the asymmetric wind field is more extensive than that of the other two wind fields.

4.2.3 Influence range of typhoon waves

The typhoon wind field is the primary energy source of typhoon waves, so there is a clear correlation between the two (Ou et al., 2002). To explore the distribution characteristics and influence range of the extreme value of wind field and wave field simulated using each wind field model, the maximum wind speed field and maximum wave height field during the period of Typhoon Muifa passing through the East China Sea are shown in Figure 9.

Figures 9A, C, E show the simulation of the maximum wind speed field. During the typhoon transit, the maximum wind speed contour simulated using the circular symmetric wind field model shows a symmetrical belt-like distribution centered on the typhoon's path and

TABLE 2 Wind speed simulation and Jason-1 satellite measured value.

Typhoon	The orbit of Jason-1 satellite	Wind field model	V_{max}(m/s)		V(m/s)		V_{max} error (m/s)	V error (m/s)	Correlation coefficient	RMSE of wind speed (m/s)
			Measured	Calculated	Measured	Calculated				
Muifa	QF207	T1	29.66	31.82	13.93	6.61	2.16	-7.32	0.46	11.72
		T2	29.66	32.14	13.93	6.50	2.48	-7.43	0.47	11.59
		T3	29.66	32.02	13.93	9.23	2.36	-4.70	0.89	6.33

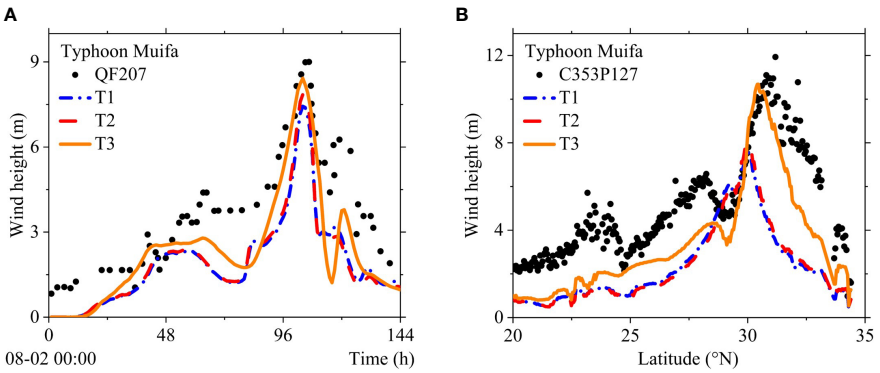

FIGURE 5
Typhoon waves: **(A)** the modeled and buoy station observed, **(B)** the modeled and satellite observed.

spreads from the symmetrical center area to both sides and gradually decreases (Figure 9A). The maximum wind speed contours simulated using the superimposed wind field model shows an asymmetrical belt-like distribution centered on the typhoon's path, but the asymmetry is weak (Figure 9C). In contrast, the maximum wind speed contour simulated using the asymmetric wind field model shows an asymmetrical belt-like distribution centered on the typhoon's path, and the asymmetric features are prominent. The maximum wind speed on the right side of path is higher than that on the left side. At the same time, the typhoon's high wind area, as simulated using the asymmetric wind field model, has a wide distribution range (Figure 9E).

For the simulation of the maximum wave height field, Figures 9B, D, F show that the maximum wave height fields simulated using the three typhoon wind field models all show an asymmetrical belt-like distribution centered on the typhoon's path. Among them, the wave field simulated using the asymmetric wind field model has the strongest asymmetry, that is, the maximum wave height on the right side of typhoon moving path is about 2 m higher than that on the left side of movement path (Figure 9F). However, the maximum wave height simulated using the circular symmetric wind field model (Figure 9B) and superimposed wind field model (Figure 9D) on the right side of typhoon moving path is only about 1 m higher than that on the left side of movement path. Therefore,

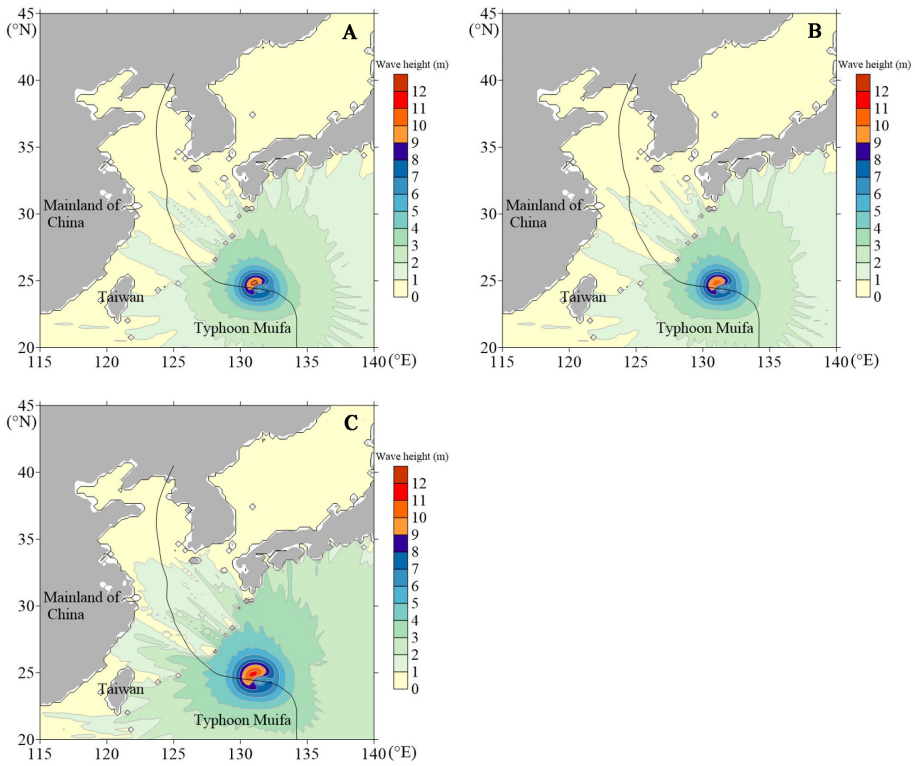

FIGURE 6
Distribution map of the wave field of Typhoon Muifa at 1200 UTC 3 August 2011: **(A)** symmetrical wind field, **(B)** superimposed wind field, **(C)** asymmetric wind field.

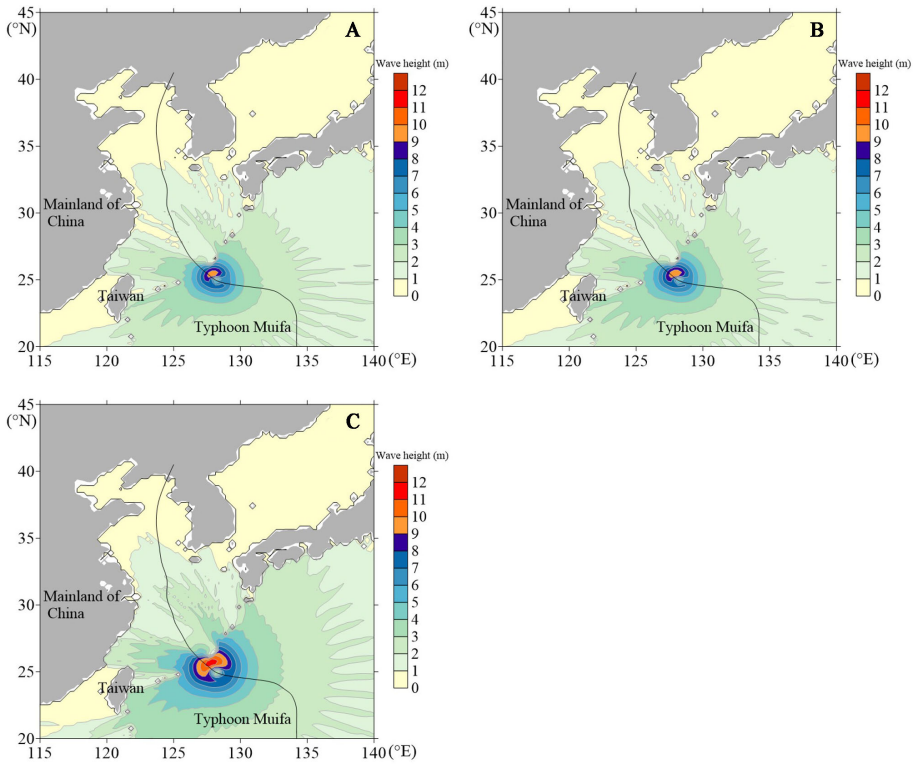

FIGURE 7
Distribution map of the wave field of Typhoon Muifa at 1800 UTC 4 August 2011: **(A)** symmetrical wind field, **(B)** superimposed wind field, **(C)** asymmetric wind field.

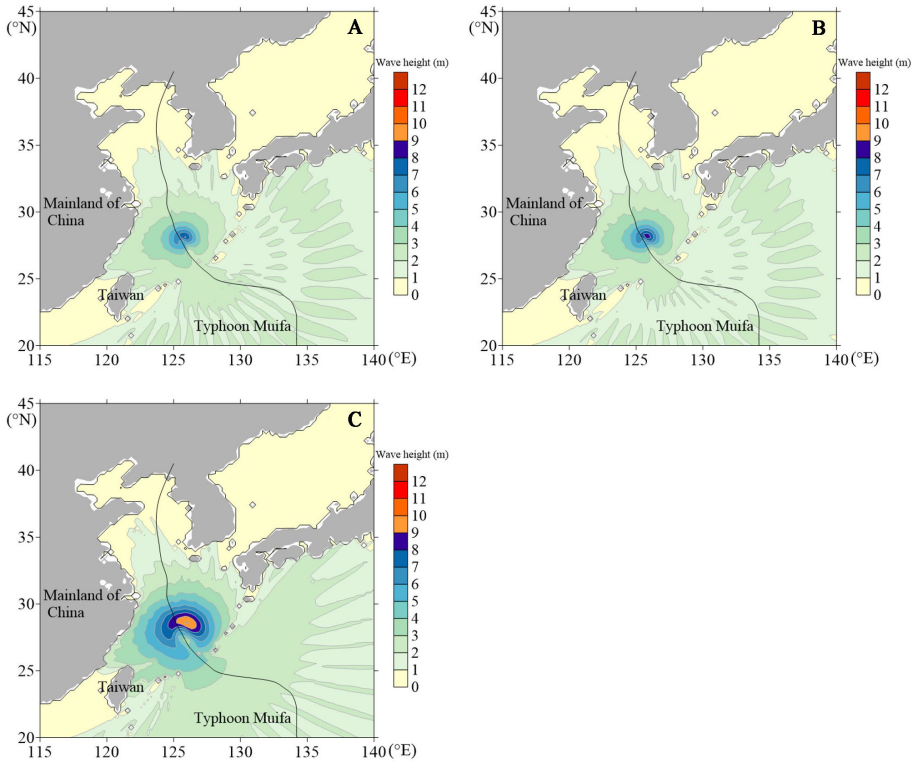

FIGURE 8
Distribution map of the wave field of Typhoon Muifa at 0000 UTC 6 August 2011: **(A)** symmetrical wind field, **(B)** superimposed wind field, **(C)** asymmetric wind field.

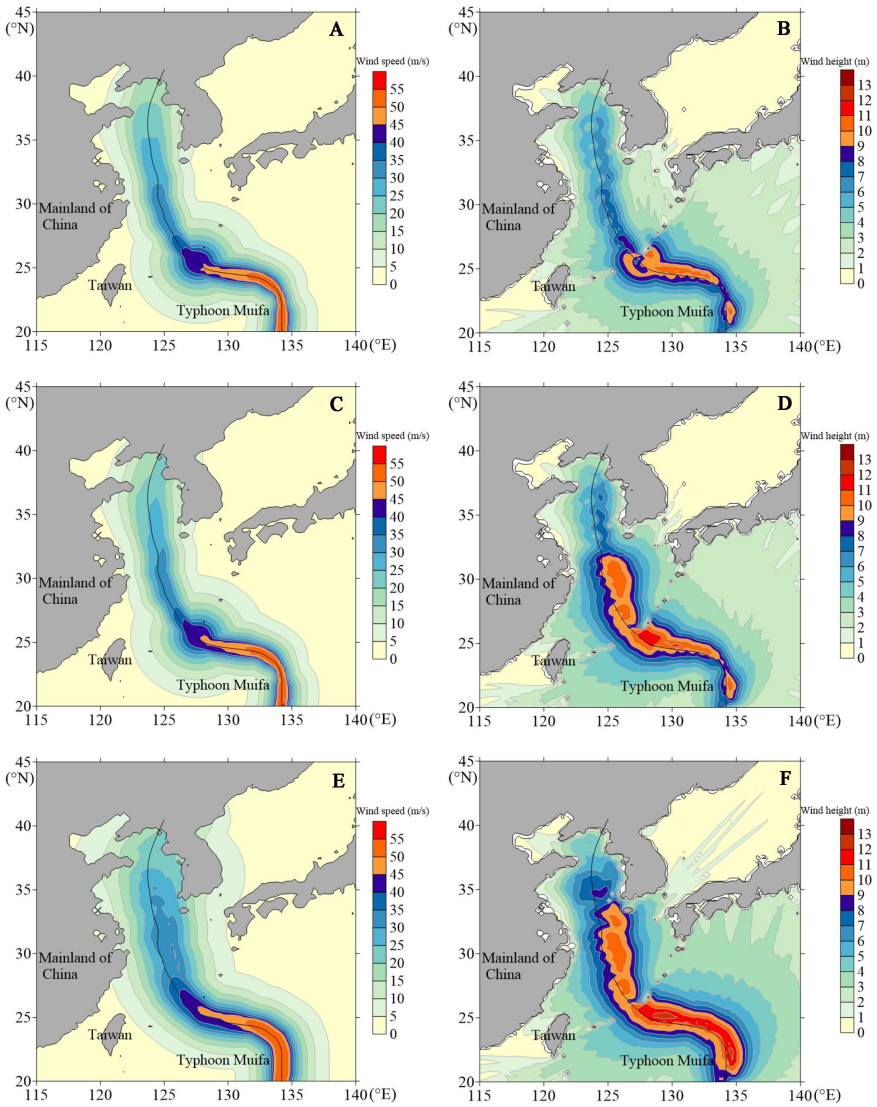

FIGURE 9
Distribution maps of the maximum wind speed field and maximum wave height field of Typhoon Muifa: **(A)** wind speed of symmetrical wind field, **(B)** wave height of symmetrical wind field, **(C)** wind speed of superimposed wind field, **(D)** wave height of superimposed wind field, **(E)** wind speed of asymmetric wind field, **(F)** wave height of asymmetric wind field.

the asymmetric characteristics of the maximum wave height field simulated using the asymmetric wind field model are substantially higher than the other two wind field models. The asymmetric wind field model can more accurately describe the actual wave field characteristics in typhoons.

The maximum wind speed and wave height fields also have a certain correlation. Since the maximum wind speed field simulated using the circular symmetric wind field model is symmetrically distributed, the maximum wave height field simulated using this model has the weakest asymmetry; the maximum wind speed field simulated using the asymmetric wind field model is asymmetrically distributed, so the maximum wave height field simulated using this model has the strongest asymmetry. At the same time, the 10 m/s wind speed affected area in the maximum wind speed contour map basically corresponds to the 5-m wave effect area in the maximum wave height contour map, and the distribution trends of wind speed and wave height are basically the same within the two affected areas.

4.3 Wave spectrum

Wave spectrum analysis is based on the composition waves analysis method, which determines the distribution of wave energy concerning the composition waves of each frequency (Wan et al., 2020). The wave spectrum reflects the distribution characteristics of each frequency component wave, which contains comprehensive information on the wave motions. Analysis of the wave spectrum of Typhoon Muifa, as simulated using the three wind field models, shows the influence of the asymmetric wind field on the energy distribution inside the waves. The simulated value of the wave spectrum of each wind field model during the period of Typhoon Muifa passing the QF207 buoy station is shown in Figure 10. The comparison results of the wave spectral density peak of each wind field model are shown in Table 3.

It can be seen from Figure 10 and Table 3 that during the typhoon passage through the buoy station, the wave spectral density simulated

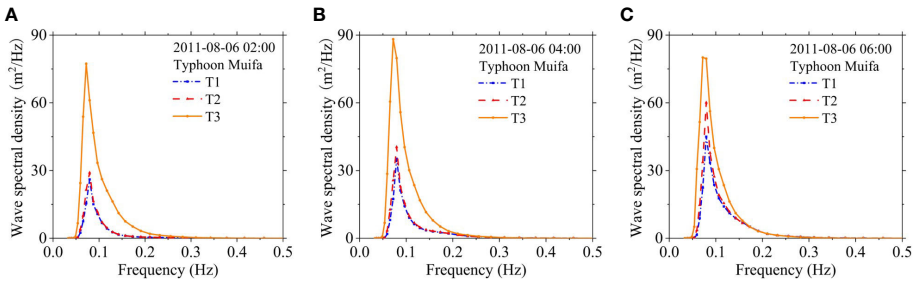

FIGURE 10
Wave spectrum during Typhoon Muifa passing QF207 buoy station: **(A)** 0200 UTC 6 August 2011, **(B)** 0400 UTC 6 August 2011, **(C)** 0600 UTC 6 August 2011.

TABLE 3 Comparison of wave spectral density of various wind fields during Typhoon Muifa passing by the buoy station.

Typhoon	Buoy station	Time	Wave spectral density peak (m^2/Hz)		
			T1	T2	T3
Muifa	QF207	0200 UTC 6 August 2011	26.06	29.07	77.33
		0400 UTC 6 August 2011	35.19	40.46	88.20
		0600 UTC 6 August 2011	45.01	60.13	80.08

by each scheme shows a trend of first increasing and then decreasing with the increase of wave spectral frequency. The wave spectral density is close to zero when the frequency is less than 0.05 Hz and more than 0.25 Hz. At the same time, the simulation results of the three wind field models show that the wave spectral density simulation effect of the asymmetric wind field model at the QF207 buoy station is significantly different from the other two wind field models. The wave spectral density peak simulated using the asymmetric wind field model is the largest, and the area enclosed by the wave spectral density curve and the abscissa is also the largest. This shows that the total energy of the waves simulated using the asymmetric wind field model is larger than that of the other two wind field models, and the intensity of the generated typhoon waves is also greater.

4.4 Potential applications

The asymmetric wind field model can improve the accuracy of post-forecasting of typhoon that moved through the East China Sea and more accurately estimate the typhoon waves and wave fields caused by it. At the same time, simulation of accurate typhoon waves will help to obtain a wealth of ocean wave databases and provide a reference for the construction of ocean engineering and the development of coastal resources.

In addition, the actual typhoon wind field is also affected by the peripheral environmental factors. In the future, methods for integrating the background wind and asymmetric wind field model can be considered to discuss and analyze the typhoon wind field and the wave field caused by it.

5 Conclusions

Through the statistical analysis of the wind radii issued by the Joint Typhoon Warning Center, this study investigated the asymmetric characteristics of a typhoon. Based on the third-generation ocean wave model SWAN, this study constructs three numerical calculation models for typhoon waves in the East China Sea based on three wind field models, the circular symmetric wind field model, the superimposed wind field model, and the asymmetric wind field model. These three models are applied to Typhoon Muifa to explore the difference in the simulation effects of each model and the accuracy of wave simulation, as well as the influence of asymmetric wind fields on the distribution characteristics of typhoon waves.

The asymmetric wind field model predicts the wind speed and wave change processes in time and space more reasonably, as the simulation results are more consistent with the measured results. This is especially the case regarding the simulation of wind speed near the typhoon's center, where the simulation results of the asymmetric wind field model are significantly better than the circular symmetrical wind field model and the superimposed wind field model. Furthermore, the asymmetric field model has a higher calculation accuracy for peak wave heights and presents a more accurate simulation of asymmetric features at the typhoon's center. It is evident that the asymmetric wind field model most accurately reflects the actual wind speed and wave characteristics.

The influence of the asymmetric wind field model on the wave field is mainly reflected by the following findings. 1) The asymmetry of the wave field simulated using the asymmetric wind field model is obviously more potent than that of the other two wind field models; 2) its asymmetric characteristics are mainly reflected in wave heights on the right side of the typhoon's path that are significantly higher than that on the left side of the movement path; 3) at the same time, the

peak value of the wave spectrum density simulated using the asymmetric wind field model is the largest, and the total energy and intensity of the simulated waves are obviously larger than the other two wind field models. The asymmetric wind field can effectively simulate the asymmetric characteristics of the energy distribution within the waves.

This study makes the case that the actual wind fields have typical asymmetric characteristics, and the asymmetric wind field model can more accurately simulate the asymmetric characteristics of typhoons that moved through the East China Sea.

Data availability statement

The original contributions presented in the study are included in the article/supplementary material. Further inquiries can be directed to the corresponding authors.

Author contributions

YW wrote the original manuscript. SD contributed to conception and design of the study. YF revised the manuscript. SY provided project administration and funding acquisition. WD analyzed the results. All authors contributed to the manuscript and approved the submitted version.

Funding

This work was supported by the Open Research Fund of State Key Laboratory of Estuarine and Coastal Research (SKLEC-KF202111), State Key Program of National Natural Science Foundation of China (NO. U2243207), National Natural Science Foundation of China (No. 52079056), Science and Technology Development Fund of the Yellow River Institute of Hydraulic Research (No. 202210) and Basic Scientific Research of YRIHR (HKY-JBYW-2020-06, HKY-JBYW-2020-11, HKY-JBYW-2022-05).

Conflict of interest

The authors declare that the research was conducted in the absence of any commercial or financial relationships that could be construed as a potential conflict of interest.

Publisher's note

All claims expressed in this article are solely those of the authors and do not necessarily represent those of their affiliated organizations, or those of the publisher, the editors and the reviewers. Any product that may be evaluated in this article, or claim that may be made by its manufacturer, is not guaranteed or endorsed by the publisher.

References

Akpinar, A., Bingolbali, B., and van Vledder, G. P. (2016). Wind and wave characteristics in the black Sea based on the SWAN wave model forced with the CFSR winds. *Ocean Engineering.* 126 (1), 276–298. doi: 10.1016/j.oceaneng.2016.09.026

Ambinakudige, S., and Khanal, S. (2010). Assessment of impacts of hurricane Katrina on net primary productivity in Mississippi. *Earth Interact.* 14 (14), 1–12. doi: 10.1175/2010EI292.1

Bell, K., and Ray, P. S. (2004). North Atlantic hurricanes 1977-99: surface hurricane-force wind radii. *Monthly Weather Review.* 132 (5), 1167–1189. doi: 10.1175/1520-0493(2004)1322.0.CO;2

Booij, N., Ris, R. C., and Holthuijsen, L. H. (1999). A third-generation wave model for coastal regions 1. model description and validation. *J. Geophysical Res.* 104 (C4), 7649–7666. doi: 10.1029/98JC02622

Chen, Y. R., Chen, L. H., Zhang, H., and Gong, W. P. (2019). Effects of wave-current interaction on the pearl iver estuary during typhoon hato. *Estuar. Coast. Shelf Science.* 228 (15), 1–15. doi: 10.1016/j.ecss.2019.106364

Cui, W., and Caracoglia, L. (2016). Exploring hurricane wind speed along US Atlantic coast in warming climate and effects on predictions of structural damage and intervention costs. *Eng. Structures* 122, 209–225. doi: 10.1016/j.engstruct.2016.05.003

Dai, Z. J., Fagherazzi, S., Gao, S., Mei, X. F., Ge, Z. P., and Wei, W. (2018). Scaling properties of estuarine beaches. *Mar. Geology.* 404, 130–136. doi: 10.1016/j.margeo.2018.07.011

Fang, W. H., and Lin, W. (2013). A review on typhoon wind field modeling for disaster risk assessment. *Prog. Geography.* 32 (6), 852–867. doi: 10.11820/dlkxjz.2013.06.002

Fujita, T. (1952). Pressure distribution within typhoon. *Geophysical Magazine.* 23, 15–28.

Ge, Z. P., Dai, Z. J., Pang, W. H., Li, S. S., Wei, W., Mei, X. F., et al. (2017). LIDAR-based detection of the post-typhoon recovery of a meso-macro-tidal beach in the beibu gulf, China. *Mar. Geology.* 391, 127–143. doi: 10.1016/j.margeo.2017.08.008

Guo, R., Cao, X. G., and Weng, Y. Y. (2016). An analysis on tropical cyclones' source region and interdecadal variation feature in Western north pacific (WNP). *Climate Change Res. Letters.* 05 (4), 209–216. doi: 10.12677/CCRL.2016.54026

Holland, G. J. (1980). An analytic model of the wind and pressure profiles in hurricanes. *Monthly Weather Review.* 108 (8), 1212–1218. doi: 10.1175/1520-0493(1980)108<1212:AAMOTW>2.0.CO;2

Jelesnianski, C. P. (1965). Numerical calculation of storm tides induced by a tropical storm impinging on a continental shelf. *Monthly Weather Review.* 93 (6), 83–88. doi: 10.1175/1520-0493(1993)0932.3.CO;2

Jelesnianski, C. P. (1966). Numerical computations of storm surges without bottom stress. *Monthly Weather Review.* 94 (6), 740–752. doi: 10.1175/1520-0493(1966)094<0379:ncossw>2.3.co;2

Jiang, Z. H., Hua, F., and Qu, P. (2008). A new scheme for adjusting the tropical cyclone parameters. *Adv. Mar. Science.* 26 (1), 1–7. doi: 10.3969/j.issn.1671-6647.2008.01.001

Kato, F. (2005). *Study on risk assessment of storm surge flood* (Tokyo: National Institute for Land and Infrastructure Management).

Kutupoğlu, V., Çakmak, R. E., Akpinar, A., and van Vledder, G. P. (2018). Setup and evaluation of a SWAN wind wave model for the Sea of marmara. *Ocean Engineering.* 165, 450–464. doi: 10.1016/j.oceaneng.2018.07.053

Lee, C. Y., and Chen, S. S. (2012). Symmetric and asymmetric structures of hurricane boundary layer in coupled atmosphere-wave-ocean models and observations. *J. Atmospheric ences.* 69 (12), 3576–3594. doi: 10.1175/jas-d-12-046.1

Lin, N., and Chavas, D. (2012). On hurricane parametric wind and applications in storm surge modeling. *J. Geophysical Res. Atmospheres* 117, 1–19. doi: 10.1029/2011JD017126

Lin, W., and Fang, W. H. (2013). Regional characteristics of Holland b parameter in typhoon wind field model for Northwest pacific. *Trop. Geogr.* 33 (2), 124–132. doi: 10.13284/j.cnki.rddl.002331

Li, Y., Zhang, C., Song, J. C., Chi, S. H., Zhao, S. H., Qi, H. S., et al. (2022). Tide-modulated wave characteristics and breaking regimes in the intertidal zone of a dissipative beach. *Ocean Engineering.* 266, 113055. doi: 10.1016/j.oceaneng.2022.113055

Ma, B. B., Dai, Z. J., Pang, W. H., Ge, Z. P., Li, S. S., Mei, X. F., et al. (2019). Dramatic typhoon-induced variability in the grain size characteristics of sediments at a meso-macrotidal beach. *Cont Shelf Res.* 191, 1–9. doi: 10.1016/j.csr.2019.104006

Mao, M. H., van der Westhuysen, A. J., Xia, M., Schwab, D. J., and Chawla, A. (2016). Modeling wind waves from deep to shallow waters in lake Michigan using unstructured SWAN. *J. Geophysical Research: Oceans.* 121 (6), 1–30. doi: 10.1002/2015JC011340

Miyamoto, Y., Satoh, M., Tomita, H., Oouchi, K., Yamada, Y., Kodama, C., et al. (2014). Gradient wind balance in tropical cyclones in high-resolution global experiments. *Monthly Weather Review.* 142 (5), 1908–1926. doi: 10.1175/MWR-D-13-00115.1

Miyazaki, M. (1961). Theoretical investigations of typhoon surges along the Japanese coast. *Oceanographical Magazine.* 13 (2), 103–118. doi: 10.1016/0022-3115(71)90106-1

Myers, V. A. (1954). Characteristics of united states hurricanes pertinent to levee design for lake Okeechobee, Florida. *Hydrometeorol.rep.u.s.weather Bur.* 32, 38–50.

Nikishova, A., Kalyuzhnaya, A., Boukhanovsky, A., and Hoekstra, A. (2017). Uncertainty quantification and sensitivity analysis applied to the wind wave model SWAN. *Environ. Model. Software* 95, 344–357. doi: 10.1016/j.envsoft.2017.06.030

Olfateh, M., Callaghan, D. P., Nielsen, P., and Baldock, T. E. (2017). Tropical cyclone wind field asymmetry-development and evaluation of a new parametric model. *J. Geophysical Res.* 122 (1), 458–469. doi: 10.1002/2016jc012237

Ou, S. H., Liau, J. M., Hsu, T. W., and Tzang, S. Y. (2002). Simulating typhoon waves by SWAN wave model in coastal waters of Taiwan. *Ocean Engineering.* 29 (8), 947–971. doi: 10.1016/S0029-8018(01)00049-X

Pan, Y., Chen, Y. P., Xia, J., and Ding, X. L. (2016). Improvement of wind field hind casts for tropical cyclones. *Water Sci. Engineering.* 9 (1), 58–66. doi: 10.1016/j.wse.2016.02.002

Pan, Y., Yin, S., Chen, Y. P., Yang, Y. B., Xu, C. Y., and Xu, Z. S. (2022). An experimental study on the evolution of a submerged berm under the effects of regular waves in low-energy conditions. *Coast. Engineering.* 176, 104169. doi: 10.1016/j.coastaleng.2022.104169

Rogers, W. E., Kaihatu, J. M., Hsu, L., Jensen, R. E., Dykes, J. D., and Holland, K. T. (2007). Forecasting and hindcasting waves with the SWAN model in the southern California bight. *Coast. Engineering.* 54 (1), 1–15. doi: 10.1016/j.coastaleng.2006.06.011

Rogers, W. E., Wang, P. A., and Wang, D. W. (2003). Investigation of wave growth and decay in the SWAN model: three regional-scale applications. *J. Phys. Oceanogr.* 33 (2), 366–389. doi: 10.1175/1520-0485(2003)0332.0.CO;2

Shen, X. W., Chen, G. P., Yan, S. C., Xu, Y. F., and Zhou, Y. (2016). Offshore wave parameter analysis of different return periods under the effect of combined wind field. *Mar. Forecasts.* 33 (5), 41–47. doi: 10.11737/j.issn.1003-0239.2016.05.005

Tajima, Y., Gunasekara, K. H., Shimozono, T., and Cruz, E. C. (2016). Study on locally varying inundation characteristics induced by super typhoon haiyan. part 1: dynamic behavior of storm surge and waves around San Pedro bay. *Coast. Eng. J.* 58 (1), 26–54. doi: 10.1142/S0578563416400027

Tajima, Y., Shimozono, T., Gunasekara, K. H., and Cruz, E. C. (2016). Study on locally varying inundation characteristics induced by super typhoon haiyan. part 2: deformation of storm waves on the beach with fringing reef along the east coast of Eastern samar. *Coast. Eng. J.* 58 (1), 55–78. doi: 10.1142/S0578563416400039

Ueno, T. (1981). Numerical computations of the storm surges in tosa bay. *J. Oceanogr.* 37 (2), 61–73. doi: 10.1007/bf02072559

Vickery, P. J., and Wadhera, D. (2008). Statistical models of Holland pressure profile parameter and radius to maximum winds of hurricanes from flight-level pressure and h*wind data. *J. Appl. Meteorol. Climatol.* 47 (10), 2497–2517. doi: 10.1175/2008JAMC1837.1

Vieira, F., Cavalcante, G., and Campos, E. (2020). Analysis of wave climate and trends in a semienclosed basin (Persian gulf) using a validated SWAN model. *Ocean Engineering.* 196 (15), 1–12. doi: 10.1016/j.oceaneng.2019.106821

Walsh, K. J. E., Camargo, S. J., Knutson, T. R., Kossin, J., and Patricola, C. (2019). Tropical cyclones and climate change. *Trop. Cyclone Res. Review.* 8 (4), 240–250. doi: 10.1016/j.tcrr.2020.01.004

Walsh, K. J. E., Mcbride, J. L., Klotzbach, P. J., Balachandran, S., and Sugi, M. (2016). Tropical cyclones and climate change. *Wiley Interdiscip. Reviews: Climate Change* 7 (1), 65–89. doi: 10.1002/wcc.371

Wang, L. Q., Zhang, Z. Z., Liang, B. C., Lee, D. Y., and Luo, S. Y. (2020). An efficient method for simulating typhoon waves based on a modified Holland vortex model. *J. Mar. Sci. Engineering.* 8 (3), 177–197. doi: 10.3390/jmse8030177

Wan, Y., Wan, L., and Dai, Y. S. (2020). Ocean wave spectrum inversion method and its sea trial experimental verification based on RADARSAT-2 SAR data. *Res. Explor. Laboratory* 39 (07), 16–19+27.

Willoughby, H. E., and Rahn, M. E. (2004). Parametric representation of the primary hurricane vortex. part I: observations and evaluation of the holland (1980) model. *Monthly Weather Review.* 132 (12), 3033–3048. doi: 10.1175/MWR2831.1

Wu, Z. Y., Chen, J., Jiang, C. B., Liu, X. J., Deng, B., Qu, K., et al. (2020). Numerical investigation of typhoon kai-tak 1213) using a mesoscale coupled WRF-ROMS model. part II: wave effects. *Ocean Engineering*. 196 (15), 1–14. doi: 10.1016/j.oceaneng.2019.106805

Wu, Z. Y., Jiang, C. B., Deng, B., Long, Y. N., Qu, K., and Liu, X. J. (2019). Numerical investigation of typhoon kai-tak 1213) using a mesoscale coupled WRF-ROMS model. *Ocean Engineering.* 175 (1), 1–15. doi: 10.1016/j.oceaneng.2019.01.053

Xie, L., Bao, S. W., Pietrafesa, L. J., Foley, K., and Fuentes, M. (2006). A real-time hurricane surface wind forecasting model: Formulation and verification. *Monthly Weather Review.* 134 (5), 1355–1370. doi: 10.1175/MWR3126.1

Yoshizumi, S. (1968). On the asymmetry of wind distribution in the lower layer in typhoon. *J. Meteorological Soc. Japan* 46 (3), 153–159. doi: 10.2151/jmsj1965.46.3_153

Zhang, Q. H., Wei, Q., and Chen, L. S. (2010). Impact of landfalling tropical cyclones in mainland China. *Sci. China Earth Sci.* 53 (10), 1559–1564. doi: 10.1007/s11430-010-4034-8

frontiers | Frontiers in Marine Science

TYPE Original Research
PUBLISHED 02 February 2023
DOI 10.3389/fmars.2023.1075683

OPEN ACCESS

EDITED BY
Yi Pan,
Hohai University, China

REVIEWED BY
Beatrice M.S. Giambastiani,
University of Bologna, Italy
José Pinho,
University of Minho, Portugal

*CORRESPONDENCE
Constantinos Matsoukis
cm262@stir.ac.uk

SPECIALTY SECTION
This article was submitted to Coastal Ocean Processes, a section of the journal Frontiers in Marine Science

RECEIVED 20 October 2022
ACCEPTED 10 January 2023
PUBLISHED 02 February 2023

CITATION
Matsoukis C, Amoudry LO, Bricheno L and Leonardi N (2023) Investigating how river flow regimes impact on river delta salinization through idealized modeling. *Front. Mar. Sci.* 10:1075683. doi: 10.3389/fmars.2023.1075683

Investigating how river flow regimes impact on river delta salinization through idealized modeling

Constantinos Matsoukis[1,3]*, Laurent O. Amoudry[2], Lucy Bricheno[2] and Nicoletta Leonardi[1]

[1]Department of Geography and Planning, School of Environmental Sciences, University of Liverpool, Liverpool, United Kingdom, [2]National Oceanography Centre, Liverpool, United Kingdom, [3]Department of Biological and Environmental Sciences, Faculty of Natural Sciences, University of Stirling, Stirling, United Kingdom

Introduction: Excessive salinity can harm ecosystems and compromise the various anthropogenic activities that take place in river deltas. The issue of salinization is expected to exacerbate due to natural and/or anthropogenic climate change. Water regulations are required to secure a sufficient water supply in conditions of limited water volume availability. Research is ongoing in seek of the optimum flow distribution establishing longer lasting and fresher conditions in deltas.

Methods: In this study a three–dimensional (3D) numerical model built for an idealized delta configuration was utilized to investigate how different river discharge annual distributions affect saltwater in deltas. Five simulations were carried out by implementing annual distributions of equal water volume but different shape.

Results: The results showed that peak flow magnitude, time of occurrence and the length of a hydrograph's tails can be important parameters affecting stratification, freshwater residence, and renewal times. Hydrographs of small flow range and light tails were the most successful in keeping the delta and its trunk channel fresher for longer periods. Salinity distributions showed a slower response to decreasing rather than increasing river discharges. An increase in the flow rate can result in salinity standards demanded for certain activities (e.g., farming, irrigation etc.) in much shorter times. On the other hand, hydrographs with heavy tails can push the salt intrusion limit further away and be more efficient in mixing the water column. However, they present low freshwater residence and high-water renewal times.

Discussion: These results provide strong indications that it is possible to improve the freshwater conditions in deltas without seeking for additional water resources but by modifying the water distribution. The main outcomes of this work may be able to support and assist coastal scientists and stakeholders dealing with the management of freshwater resources in river deltas across the world.

KEYWORDS

river deltas, salt intrusion, idealized modeling, flow regimes, water management

1 Introduction

Rising sea level and decreasing streamflow threaten water resourcing and freshwater availability by causing an upstream intrusion of the saltwater zone (Gornitz, 1991; Bhuiyan and Dutta, 2012; Hong and Shen, 2012; Hong et al., 2020; Bricheno et al., 2021). Saltwater intrusion (SI) is much exacerbated in low lying areas such as deltas (Zhou et al., 2017). SI is a serious problem that affects households, agriculture, irrigation and industry (Allison, 1964; Smedema and Shiati, 2002; Zhang et al., 2011) because rivers and aquifers contaminated by high salinity decrease freshwater storage and water quality (Gornitz, 1991). In addition, SI reduces soil fertility resulting in low crops yield (Bhuiyan and Dutta, 2012), threatens vegetation and freshwater species with limited salinity tolerance (Visser et al., 2012; White et al., 2019), increases plants mortality (Kaplan et al., 2010; Bhuiyan and Dutta, 2012) and affects human health (Sarwar, 2005; Rahman et al., 2019).

Many deltas face already the consequences of saltwater intrusion including the Mekong in Vietnam (Nguyen and Savenije, 2006; Trieu and Phong, 2015; Eslami et al., 2019) the Ganges-Brahmaputra in Bangladesh (Nobi and Das Gupta, 1997; Bhuiyan and Dutta, 2012; Rahman, 2015; Yang et al., 2015; Bricheno et al., 2016; Sherin, 2020; Bricheno et al., 2021), the Mississippi in the Gulf of Mexico (Holm and Sasser, 2001; Day et al., 2005; Das et al., 2012), the Yangtze in China (Chen et al., 2001; Hu and Ding, 2009; Dai et al., 2011; Qiu and Zhu, 2015), the Pearl River (Liu et al., 2019; Hong et al., 2020) and the Nile Delta (Frihy, 2003). Unfortunately, limitations in water supply come along with an increase in water demand because of population growth, economic development, and land use changes (Phan et al., 2018).

Sustainable water management and enhanced water conservation practices are necessary for the available water supply to meet with the future demand (Dawadi and Ahmad, 2013). These practices often rely on the assumption that salt intrusion reduces as river discharge increases (Garvine et al., 1992; Gong and Shen, 2011). In the absence of tides or other driving mechanisms (i.e., atmospheric or oceanic forcing) the river discharge dominates the salinity distribution (Valle-Levinson and Wilson, 1994; Wong, 1995; Monismith et al., 2002). During the 20th century, water management relied on technical and engineering solutions (Ha et al., 2018). The so called 'hard-path' approach consisted of dams, aqueducts, pipelines and complex treatment plants (Gleick, 2003). However, this type of solutions often comes with a cost. For example, tens of millions of people have been displaced by their homes due to water related projects (Adams, 2000) while the freshwater flows reaching many deltas are not adequate anymore and this has several consequences for the local environment and population (Gleick, 2003). Recently, the need for more adaptive management to sustain freshwater resources has been identified (Ha et al., 2018; Zevenbergen et al., 2018). A 'soft-path' approach for water is now promoted that would include regulatory policies for better use of existing water resources than seeking for additional ones (Gleick, 2002). In this context, an efficient water usage is preferred with equitable distribution and sustainable system operation over time while local communities should be also included in water management decisions (Gleick, 2002; Gleick, 2003). Within this concept, the problem of saltwater intrusion in deltas could probably be mitigated by an efficient water management of a catchment's freshwater availability instead of resorting to technical solutions. This could be achieved for example by storing a certain amount of water that is available during a wet season and supply it during the next dry season when the demand for freshwater is higher. Coastal reservoirs -water storage structures constructed at a river estuary or other coastal area to store fresh water and control water resources- have already been constructed in China, South Korea, Hong Kong and Singapore (Yuan and Wu, 2020; Tabarestani and Fouladfar, 2021). These structures are constructed near the coast, in natural river basins and have a smaller environmental footprint compared to other technical solutions (Sitharam et al., 2020). An additional advantage is that they could be used for the generation of tidal renewable energy assisting further into the development of sustainable and environmentally friendly infrastructure (Sitharam et al., 2020). Independent of a hard or soft path, the main management strategy is to affect river discharge, which is likely to cause changes to the annual hydrograph. Such changes are also expected to occur as a consequence of natural climate variability and anthropogenic climate change (Deser et al., 2012; Zhang and Delworth, 2018). Possible effects to deltas' salinity distribution from these changes need to be assessed. Even though salinity response to changes in river discharges has been studied extensively in estuaries (Garvine et al., 1992; Wong, 1995; Uncles and Stephens, 1996; MacCready, 1999; Chen et al., 2000; Monismith et al., 2002; Bowen, 2003; Banas et al., 2004; Chen, 2004; Hetland and Geyer, 2004; Brockway et al., 2006; Liu et al., 2007; Lerczak et al., 2009; Gong and Shen, 2011; Wei et al., 2016) it is still unclear if and how this changes in the presence of a channelized network.

The present study investigates the effect of various annual flow distributions of equal water volume on the salt intrusion. The paper tries to answer questions such as: 1) how salinity responds to flow changes, 2) what is the impact on salinity from changes in hydrographs' shape 3) which flow distribution cause the maximum increase of mixing in the delta and 4) which flow regime ensures fresher water conditions for the longest period and to what extent.

The answer to the last question derives from measuring flushing and residence times that are useful tools to assess the efficacy and adequacy of a certain flow distribution for averting the salt intrusion (Choi and Lee, 2004; Sámano et al., 2012). Flushing time (FT) is defined as the time required for the cumulative freshwater inflow to equal the amount of freshwater originally present in the region (Dyer 1973; Sheldon and Alber, 2002). The simplest and most common method for the FT calculation is the freshwater fraction in which the freshwater volume is divided by the freshwater input (Dyer 1973; Fischer et al., 1979; Williams, 1986). A difficulty on the determination of the freshwater volume and input arises in the case of unsteady flow and tidal conditions. Many researchers implemented the method by taking averages over a certain period (Pilson 1985; Christian et al., 1991; Balls, 1994; Lebo et al., 1994; Eyre and Twigg, 1997; Alber and Sheldon, 1999; Hagy, et al., 2000; Huang and Spaulding, 2002; Sheldon and Alber, 2002; Huang, 2007). Alber and Sheldon (1999) proposed a specific technique to determine the appropriate averaging period of the river discharge by assuming that this should be equal or very close to the flushing time itself. They tested their method in Georgia Estuaries. Whereas the FT is a unique value representative of

an entire water body, the residence time (RT) is a measure of spatial variation (Choi and Lee, 2004; Sámano et al., 2012). It is defined as the remaining time that a particle will spend in a defined region after first arriving at some starting location (Zimmerman, 1976;Sheldon and Alber, 2002). Therefore, the RT is applied within a restricted geographical area such as an estuary, a water basin or a box model (Hagy et al., 2000; Sheldon and Alber, 2022; Sámano et al., 2012).

In this study, the concept of RT is adapted to measure the time that the water remains fresh within the delta. This requires a definition of what exactly fresh water is which is usually case dependent. There are salinity standards for execution of certain activities and survival of vegetation species and aquatic life. For instance, salinity in the water has to be at least less than 1 PSU for it to be potable (Ahmed and Rahman (2000); Sarwar (2005); Dasgupta et al. (2015)) and crop yields can be severely affected if salinity is more than 4 PSU (Clarke et al., 2015). Some aquatic organisms (e.g. phytoplankton, larvae fish, shrimps, smelt etc.) and vegetation (e.g. Sagittaria Latifolia, Sagittaria Lancifolia, phragmites australis) species do not survive in environments with more than 2 PSU salinity (Jassby et al., 1995; Visser et al., 2012; Hutton et al., 2016; White et al., 2019; Wang et al., 2020). In particular, the location of the 2-PSU bottom isohaline has been found to have significant statistical relationships with many estuarine resources (e.g., phytoplankton, larvae fish, shrimps, smelt etc.) (Jassby et al., 1995; Hutton et al., 2016). It is also a threshold for freshwater wetlands conversion to brackish marsh (Conner et al., 1997; Wang et al., 2020). Therefore, the location of 2 PSU isohaline has been established as a salt intrusion measure in many similar studies (Schubel, 1992; Monismith et al., 1996; Monismith et al., 2002; Herbold and Vendlinkski, 2012; Andrews et al., 2017). In this context, a freshwater RT in this study is determined to be the time that the salinity remains below 2 PSU.

For the purposes of this study, a 3D numerical model for an idealized delta configuration is built in Delft3D. Idealization is chosen with the consideration that idealized (or exploratory) models can offer simpler and better explanations of certain behaviors in systems involving many interacting processes (Murray, 2002). In this approach, some parameters are intentionally omitted (e.g., tides and/or waves) and only the core causal factors (e.g., river discharge) are retained (Weisberg, 2007). Idealized studies have the advantage of reducing the complexity that is found in real systems and provide a better physical insight on the effect of a certain variable in a physical phenomenon isolated from others. Therefore, the use of idealized models aims to reveal the direct impact of external forcing factors in a system's variable separately for each one of them. In this paper, five simulations with different flow distributions are carried out. The implemented hydrographs follow typical distributions similar to some that can be often found in real deltas. The paper aspires to provide answers through the idealized modeling for a more sustainable use of freshwater resources in deltaic systems.

2 Methods

2.1 Model setup

Matsoukis et al. (2022) built a 3D model with an idealized delta configuration to investigate the impact of tidal level changes in a static delta's salinity neglecting morphological changes. The same model is used in this paper. The model –that was built in Delft3D (Deltares, 2014)- uses a structured rectangular grid with dimensions of 20 km to 22 km. The grid resolution varies from 50 m to 200 m in the X direction and between 20 m and 100 m in the Y direction of a Cartesian co-ordinate system. The delta was built by implementing a high and constant river discharge of 3000 m^3/s in an initially uniform bathymetry. The flow enters in the domain through an inlet of 1.3 km length and 380 m width. Erosion and sedimentation caused by the river discharge resulted in the delta bathymetry that can be seen in Figure 1F. The delta covers an area of 4.8 km x 8 km. A bed slope of 0.5^0 has been imposed 10 km downstream of the river boundary so that the water depth reaches 30 m at the offshore boundary. The full model's bathymetry can be seen in the Supplementary Material. To note that results analysis shown in this paper includes only the delta area as it is presented in Figure 1F and excludes the deeper offshore area outside of it as the focus is restricted only within the delta limits. The model's bathymetry remains constant during the simulations and there is no sediment input. Bed level changes are not considered so that the impact of flow distributions on the salinity is isolated from any morphological effects. The vertical resolution consists of eight sigma layers. Higher numbers of vertical layers were considered too. However, it was found that the increase of vertical layers had only a quantitative and not qualitative impact on the results. The main conclusions for each paper's section remained unaffected, probably due to the relatively shallow water depths. Considering that this is an idealized study where the actual magnitude values are not so important, it was decided then to keep the vertical resolution equal to 8 layers to satisfy computational efficiency limitations for a full year study. The default Delft3D values for horizontal diffusion and viscosity are introduced in the model equal to 10 m^2/s and 1 m^2/s respectively that were found to be the optimum for model's performance and stability. A relatively large diffusion coefficient is justified for large scale applications where estuarine physics apply. In addition, diffusion can vary a lot when seasonal flows for a one-year simulation period are implemented as they may cause substantial salinity changes in the vertical (Monismith et al., 1996). The vertical diffusion is fully modelled by the κ-ϵ turbulence closure model. A spatially constant Chezy coefficient (45 $m^{1/2}/s^{-1}$) is implemented to account for bed roughness in accordance with what has been used in other idealized delta studies with Delft3D (Edmonds and Sligerland, 2010; Leonardi et al., 2013; Caldwell and Edmonds, 2014; Burpee et al., 2015; Liu et al., 2020). A cyclic implicit numerical scheme is used, and the time step is 30 seconds being the optimum value for both model stability and computational time. Further details on the model's parameters and the process of bathymetry development can be found in the Supplementary Material (S1).

2.2 Hydrodynamic forcing

The model is forced with an annual river flow distribution. Five simulations are setup with hydrographs of equal water volume but different shape each time. This is achieved by implementing the Beta (B) function to an original hydrograph and obtain five beta distributions. The Po delta flow distribution for 2009 (Montanari, 2012) is used as the original hydrograph to build the five idealized

ones. The use of the 2009 Po delta hydrograph does not imply any resemblance with the idealized delta and is chosen merely as a guide. To build a beta distribution the following equation is used (Yue et al., 2002):

$$B\ (\alpha,\beta) = \int_0^1 x^{\alpha-1}\ (1-x)^{\beta-1} dx \qquad (1)$$

$$0 < x < 1;\ \ \alpha,\quad \beta > 0$$

Where B is the probability density function, x is the probability of occurrence of each daily flow taken equal to 1/365 for an annual distribution. The shape parameters α and β determine the shape of the hydrograph. The normalized probability distribution is then converted to a flow distribution by multiplying by the annual water volume of the original hydrograph (Po Delta in 2009). Consequently, the five idealized hydrographs contain the same water volume with the original one. However, the size of the idealized delta is much smaller than the Po delta and the implementation of the original flow range causes stability issues in the model. Therefore, the hydrographs are reduced by the river cross-sections' ratio between the real (Po Delta) and the idealized delta. The produced hydrographs can be seen in panels a-e of Figure 1. Table 1 presents the basic statistic parameters for each beta distribution. Equal shape parameters result into symmetric hydrographs (Figures 1A-C) and the higher their value the higher the peak is. When α is smaller than β a left skewed hydrograph occurs (Figure 1D). The hydrograph exhibits right skewness when β is smaller than α (Figure 1E).

The five hydrographs in Figure 1 can be qualitatively classified based on their shape and the tails of each distribution as: 1) Platykurtic (light tails and low peak), 2) Mesokurtic (relatively light tails and medium peak), 3) Leptokurtic (heavy tails and high peak), 4) Left skewed (long tail on the right) and 5) Right skewed (long tail on the left). All of them correspond to seasonal regimes with a pronounced wet season (Hansford et al., 2020). The distinction between heavy and light tails in this paper is defined as follows: heavy tails indicate distributions with larger probability of getting an outlier (e.g., leptokurtic) and light tails indicate distributions that go to zero faster than the exponential distribution (e.g., platykurtic) (Bryson, 1974; Glen, 2016).

Small scale discharge events have been purposefully neglected in the five hydrographs that all have smooth shapes. The use of irregular shapes would add into complexity – in contrast to the benefits of a simplified and idealized approach- and would hinder the extraction of concrete conclusions on the effects of hydrographs shape. However, an indication of potential transient peaks effects and larger flow amplitudes can be given if comparing results between the three symmetric distributions.

Annual flow distributions with shapes close to the hydrographs of Figure 1 are recorded often in many real deltas. For example, left skewed hydrographs (Figure 1D) were reported in deltas located at the Gulf of Mexico including the Wax Lake Delta in the years between 2006 and 2010 (Shaw et al., 2013) and the Mississippi Delta between 1993 and 2012 (Kolker et al., 2018). Based on large data records from internet data bases and national agencies, Latrubesse et al. (2005) showed that the Mekong and the Ganges-Brahmaputra river catchments develop usually right skewed annual hydrographs (Figure 1E). The Yangtze delta sees its peak flow often in the middle of the year at some time during the wet season that occurs between May and September (Birkinshaw et al., 2017). Such flow distributions are similar to that of Figure 1C and have been reported in the years between 1996 and 2005 (Lai et al., 2014; Birkinshaw et al., 2017) in the Yangtze Delta. In addition, when Hansford et al. (2020) averaged daily flow data for one year between 1978-2009 in the Parana Delta (Argentina), they detected an annual flow hydrograph very similar to a platykurtic distribution (Figure 1A). Finally, mesokurtic hydrographs as the one in Figure 1B have been observed in the Colorado and Nile deltas. Averaged annual hydrographs for the 1950-1993 period in the Colorado (Pitlick and

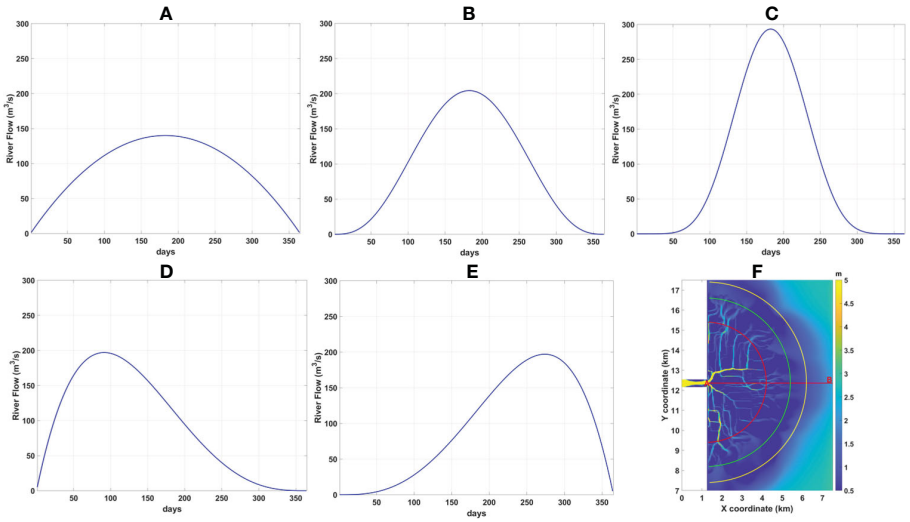

FIGURE 1
The hydrographs implemented in the model: **(A)** Platykurtic **(B)** Mesokurtic **(C)** Leptokurtic **(D)** Left Skewed and **(E)** Right Skewed flow distribution for one year. **(F)** The delta bathymetry. The red line AB measures the 6km distance from the river mouth (point A) corresponding to the length of the salt intrusion curve displayed in Figure 2B. The colored semicircles with their centre at point A and radius 3km (red), 4.2km (green) and 5km (yellow) visualize the cross sections over which salinity is averaged for the results analysis in sections 3.1, 3.2 and 3.4.

TABLE 1 Statistical parameters for each hydrograph type.

Scenario	Shape parameters	Kurtosis	Qmax (m^3/s)	Qmean (m^3/s)
Platykurtic	$\alpha = \beta = 2$	2.14	140	93
Mesokurtic	$\alpha = \beta = 4$	2.45	204	93
Leptokurtic	$\alpha = \beta = 8$	2.68	293	93
Left Skewed	$\alpha = 2\ \beta = 4$	2.62	197	93
Right Skewed	$\alpha = 4\ \beta = 2$	2.62	197	93

Cress, 2000) and flow distributions at several stations in the Nile (Eldardiry and Hossain, 2019) confirm this. The averaged over the years 1984-1996 annual hydrograph in the Niger Delta also exhibited a mesokurtic hydrograph shape (Lienou et al., 2010).

2.3 Boundary conditions

A zero-water level is implemented at the offshore boundary while the Riemann condition (in the form of a zero-velocity variant) applies in the lateral boundaries. Fresh water is assumed at the upstream river boundary and seawater salinity (30PSU) at the offshore and lateral boundaries. Special care was taken at the lateral (north and south) boundaries so that the freshwater plume is not clamped by the imposed seawater salinity but is allowed to spread radially with no boundary effects. This is possible to do in Delft3D by setting the horizontal diffusion equal to zero only at the two last grid lines along these two boundaries. In this way, the model is allowed to calculate its own salinities close to the boundaries unaffected of the imposed 30 PSU.

2.4 Initial conditions

A spin-up simulation precedes each time to get a dynamic equilibrium for salinity to be introduced as initial conditions. A uniform salinity equal to 30 PSU is implemented in the model except for the river upstream boundary where zero salinity is imposed. It is decided to spin-up the model with the initial flow of each hydrograph in Figure 1. These are very small but non-zero values and this reduces the time required to reach a dynamic equilibrium. This means that the simulations start in dry season (low flows) conditions. The river flow in the spin-up model is constant and the simulation is stopped after 30 days when steady state conditions are reached in all cases. The full model setup is summarized in Table 2.

2.5 Assumptions and limitations

The goal of the study is to assess the effects of flow regimes on the salinity distribution isolated from any other effects (i.e., tides and waves). Therefore, the delta's idealized bathymetry has been developed after a morphological simulation where no tidal forcing is considered and subsequently no tides are included in the five simulations of different annual flow distributions. This decision is taken on the grounds that a different morphology would be required if tides were included as it is known that tides have a strong influence together with river discharges on deltas' morphology depending on their range (Galloway, 1975). Even though this may compromise the applicability of the results, the present bathymetry retains many typical and common delta features such as the erosion in front of the river mouth and the downstream shallowing and widening of the channels (Hori and Saito, 2007; Lamb et al., 2012). In addition, the idealized delta exhibits bathymetric irregularities with deeper channels on the left of the delta apex (looking seaward) and shallower right of it. Due to the presence of such common and special features of deltas morphology, the model can capture bathymetric effects on the salinity horizontal and vertical distribution that would have not been uncovered if a more simplified bathymetry had been implemented. This is crucial because the role of bathymetry on salinity distribution is important as it has been identified in previous studies as well (Sridevi et al., 2015; Wei et al., 2017; Matsoukis et al., 2022). In addition, the world's deltas are reported to be in a continuous state of transition regarding their dynamic morphological equilibrium due to natural climate change and human activities and thus such irregularities may not be uncommon (Hoitink et al., 2017).

Matsoukis et al. (2022) identified these irregularities as the cause of asymmetries in the salinity distribution between delta areas especially during low flow seasons. They then neglected Coriolis force on this basis to avoid an extra source of asymmetry in the model, something that is adopted in this work as well with the same justification. Nevertheless, this omission is not expected to have remarkable impact on the results in this specific case. Buoyant plumes may become geostrophic dominated only beyond the near-field region (Horner-Devine et al., 2015) where momentum balance is yet mainly dominated by barotropic and baroclinic pressure gradients, frictional stresses, and flow acceleration (McCabe et al., 2009). But specifically in deltas, freshwater plumes are formed at the channels outlets and interact with each other (Yuan et al., 2011; Horner-Devine et al., 2015) to form larger scale ones. This goes beyond the focus area in this study as depicted in Figure 1F where Coriolis force effects would be minimal. Likewise, wind forcing is usually considered of second order in the near-field region (Kakoulaki et al., 2014) although there are recent indications that plume dynamics may be more sensitive to winds than previously assumed (Kakoulaki et al., 2014; Kastner, 2018; Spicer et al., 2022). Despite this, the wind effects on the plume's orientation, spreading, thickness and mixing and their subsequent impact on flushing, residence times and stratification have not been considered in this case. The reason is that

TABLE 2 Summary of the main model setup parameters.

Vertical resolution	8 layers
Time step	30 seconds
Horizontal diffusion	10 m^2/s
Horizontal viscosity	1 m^2/s
Vertical diffusion	κ-ϵ turbulence scheme
Roughness	Chezy coefficient (45 $m^{1/2}/s^{-1}$)
Lateral flow boundaries	Riemann invariant (0 m/s)
Offshore flow boundary	Water Level (0 m)
River flow boundary	Time series of daily river discharges for one year
Lateral boundaries salinity	30 PSU
Offshore boundary salinity boundaries	30 PSU
River boundary salinity	0 PSU
Initial flow conditions	Water Level (0 m)
Initial salinity conditions	Spatial variation input file after a spin-up simulation starting with uniform 30 PSU salinity

the wind acts intermittently and in much smaller time scales compared to the annual flow distributions of the current setup and the direct effect of the latter would not be discernible.

The above simplifications would indicate that the applicability of this paper's findings might be limited to river dominated deltas or at least deltas with little tidal influence and in medium latitudes. These may include for example deltas in the Gulf of Mexico (Mississippi, Atchafalaya and Wax Lake), Orinoco, the Danube, the Irrawaddy and the Po delta.

However, idealized modeling does not aim to provide specific answers and solutions directly interpretable to real systems. Real case models should be used for such purposes. The level of complexity in real systems is such that non-linear effects cannot always be captured by idealized models where several simplifications are considered. Nonetheless, the advantage of idealized models is that they are more oriented towards a 'knowledge obtaining' and fundamental physical analysis that results in more general and universal conclusions. In that sense, the present work's conclusions can refer to a larger number of deltas than those mentioned in this section and with various hydrodynamic conditions.

2.6 Flushing time calculation

Flushing time (FT) is measured in section 3.6 for each flow regime. The river delta as depicted in Figure 1F is considered for the calculation which is executed based on the 'freshwater fraction method' given by the following equation (Dyer 1973; Alber and Sheldon, 1999):

$$FT = \frac{\sum_i^n \left(\frac{S_{SW} - S_i}{S_{SW}}\right) V_i}{Q_F} \quad (2)$$

For a total number n of grid cells i, V_i and S_i are its volume and salinity respectively. S_{SW} is the sea water salinity (in this case equal to 30 PSU) and Q_F an averaged over a time frame river discharge. The equation assumes a steady state system which can be justified in this case because the flow changes slowly compared to salinity adjustment scales (see also section 4.1). Sheldon and Alber (2006) indicated that equation 2 is more appropriate for systems with high freshwater flow and large salinity differences between an estuary and the ocean which is also true in the present case (especially at high flow seasons). The determination of the appropriate period of averaging for the calculation of Q_F can be a tricky task. In this paper, the Date Specific Method (DSM) is used as introduced by Alber and Sheldon (1999). The method assumes that the averaging period must be equal to the FT. By selecting an observation day as a starting point, the FT is calculated through an iterative process working backwards and stops when its value equals the period over which the river discharge is averaged.

3 Results

3.1 Salinity response to river discharge changes

Previous studies detected a hysteresis on the salinity's temporal response to flow changes in estuaries (Hetland and Geyer, 2004; Savenije, 2005; Chen, 2015). The salinity responds slower to flow decreases than increases. An investigation follows on the existence or not of this hysteresis in the idealized delta for the symmetric and skewed hydrographs in separate. To do this, the salinity is first averaged over depth and over a radial cross-section of 3 km distance from the mouth. Then, this is plotted either in time and/or against the river discharge. The decision to show results for this particular radial section (3 km) for both symmetric and skewed distributions is taken with the consideration that it is probably safer to assess the salinity response in a location with medium influence of the river discharge where the water does not become completely fresh.

This is a somewhat arbitrary decision, but it does not affect much the conclusions. The same analysis but for a section closer to the river (1 km) (available in the Supplementary Material, section S2, Figures S3, S4) shows similar results.

3.1.1 Symmetric hydrographs

Figure 3A displays the mean over depth daily salinity averaged over a radial cross-section of 3 km distance (red semicircle in Figure 1F) from the mouth at every date for the three symmetric distributions. The bottom axis shows the dates of the 1st semester and the corresponding salinity for each day denoted by dotted lines. During the 1st semester the salinity decreases monotonously. The top axis shows the dates of the 2nd semester in reverse order starting from right to the left and the corresponding salinity for each day is denoted by circled lines. During the 2nd semester the salinity increases monotonously. The unique daily values of the river discharge from each one of the three symmetric hydrographs are also added in the plot displayed as continuous lines and with its scale being on the right axis. Due to the symmetry, the dates on the top are projections of the dates on the bottom axis of equal river discharges. Therefore, the points of intersection of a vertical line drawn in Figure 3A with the dotted and circled lines give us the salinity level at days of equal flow.

Figure 3A shows that initially, the order between the three symmetric distributions is as follows:

$S_{leptokurtic} > S_{mesokurtic} > S_{platykurtic}$ because the relationship between the river discharge (Q) magnitude of the three symmetric distributions follows the opposite order $Q_{platykurtic} > Q_{mesokurtic} > Q_{leptokurtic}$. The order between the river discharges changes as the flow increases in the 1st semester and so does that of the salinity. $S_{leptokurtic}$ falls below $S_{platykurtic}$ at first and $S_{mesokurtic}$ a few days later. The dates of the intersection between the salinity curves correspond to the dates of intersection between the flow curves in each case which means that the salinity becomes lower in one simulation when its flow becomes higher than the flow of another simulation.

The opposite procedure takes place at the 2nd semester and as long as the flow decreases. The salinity of the leptokurtic hydrograph becomes higher than the mesokurtic and then than the platykurtic salinity.

Figure 3A indicates that there is a hysteresis on the salinity's response between increasing and decreasing flows. For example, the leptokurtic salinity falls below the platykurtic one in the 1st semester on the 5th of May. This means that the change occurs only 55 days before the peak flow day on the 1st of July. On the contrary, the leptokurtic salinity becomes higher than the platykurtic one in the 2nd semester on the 10th of September. This is 72 days far from the 1st of July (peak flow day) which shows a delay in comparison to the interchange in the 1st semester between the two simulations. Similar conclusions can be drawn when comparing between any couple of simulations.

In addition, it can be seen that there is a time frame in each simulation when the salinity in the 2nd semester is always lower compared to its corresponding date of equal flow in the 1st semester. This indicates that the salinity might not be equal at dates of equal flow depending on whether the flow is increasing or decreasing and whether the peak flow has occurred already or not. However, this effect is not present for very low flows (at the start of the simulation) or very high ones while getting closer to the peak flow day. In this case, the salinity is equal for equal flows independent of increasing or decreasing river discharge.

To get a clearer image of this salinity asymmetry between 1st and 2nd semester, the salinity differences of more than 0.5 PSU between the two semesters are plotted in Figure 3B for each day and each simulation separately. The maximum salinity difference increases with the peak flow magnitude, but the duration of salinity differences decreases with it. For example, differences in salinity between the two semesters can reach 10 PSU in the leptokurtic case but they are present only for approximately 1.5 months. On the contrary, the maximum salinity difference in the platykurtic case is 8 PSU but differences are present for 2.5 months instead.

3.1.2 Skewed hydrographs

The analysis for the two skewed hydrographs is presented in a different manner since the flow range remains the same in both cases. Figure 4 displays the salinity averaged over depth and over the radial cross section 3 km far from the mouth against the river discharge. The left skewed case shows almost equal salinity between the start and the end of the simulation. The long tail covers a period of 9 months with decreasing flows that allows the salinity to recover and return to its initial state. In contrast, the salinity for the right skewed hydrograph is

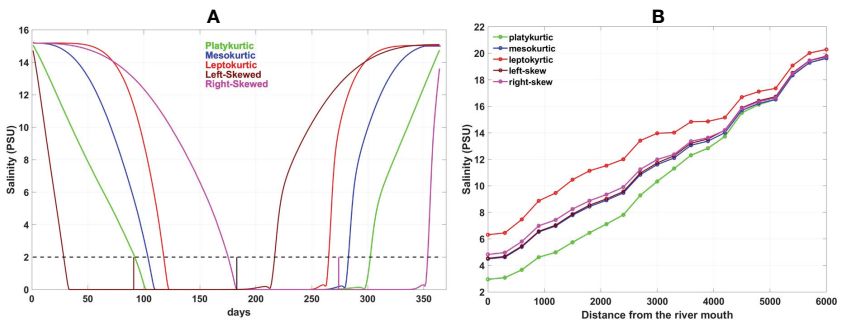

FIGURE 2
(A) Time series of the bottom salinity at the river mouth (point A in Figure 1F). Each colour represents results for a simulation with a different hydrograph. The dashed black line draws the 2 PSU threshold. The short brown, magenta and black vertical lines indicate the time moment of the peak flow on the horizontal axis for the left skewed, right skewed and symmetric distributions equal to 91, 274 and 183 days respectively. **(B)** Annual averages of the mean over depth salinity when averaged radially every 300 m along a distance of 6 km from the river mouth.

about 1 PSU lower at the end of the simulation compared to its initial value. In this case, the simulation ends with the short tail that covers a period of only 3 months with a very sharp flow decrease that does not allow the salinity to recover.

There are indications of a hysteresis in salinity's response to flow changes in Figure 4 as well. Both simulations exhibit a time frame with lower salinity during the decreasing flow periods compared to equal discharges at increasing flow periods. The salinity is lower in the short tail for the right skewed and in the long tail for the left skewed case.

Similar to what is observed in Figure 3A for the symmetric hydrographs, there is a flow range with equal salinity. This occurs during high flow periods. When the flow is between 120 m^3/s and 200 m^3/s the salinity is equal between the two skewed hydrograph simulations. This indicates that for very high flows, the salinity's response is independent of skewness and of increasing or decreasing flows.

The flow range in the short and long tails is equal in both simulations and varies between very low discharges and the peak flow that is close to 200 m^3/s. The short and long tail seem to cause the same level of salinity variation as this fluctuates between 0 PSU and 24 PSU implying that by increasing the flow rate a salinity standard could be achieved in much shorter time.

3.2 Stratification

Changes in the river discharge affect the stratification. Increases in the river discharge usually result in stronger stratification (Monismith et al., 2002; MacCready, 2004; Ralston et al., 2008; Lerczak et al., 2009; Wei et al., 2016) with high top to bottom density differences. Therefore, the influence of the flow distribution on the stratification is measured in this section by taking the difference of the top to bottom layer salinity. To visualize the results, the top to bottom

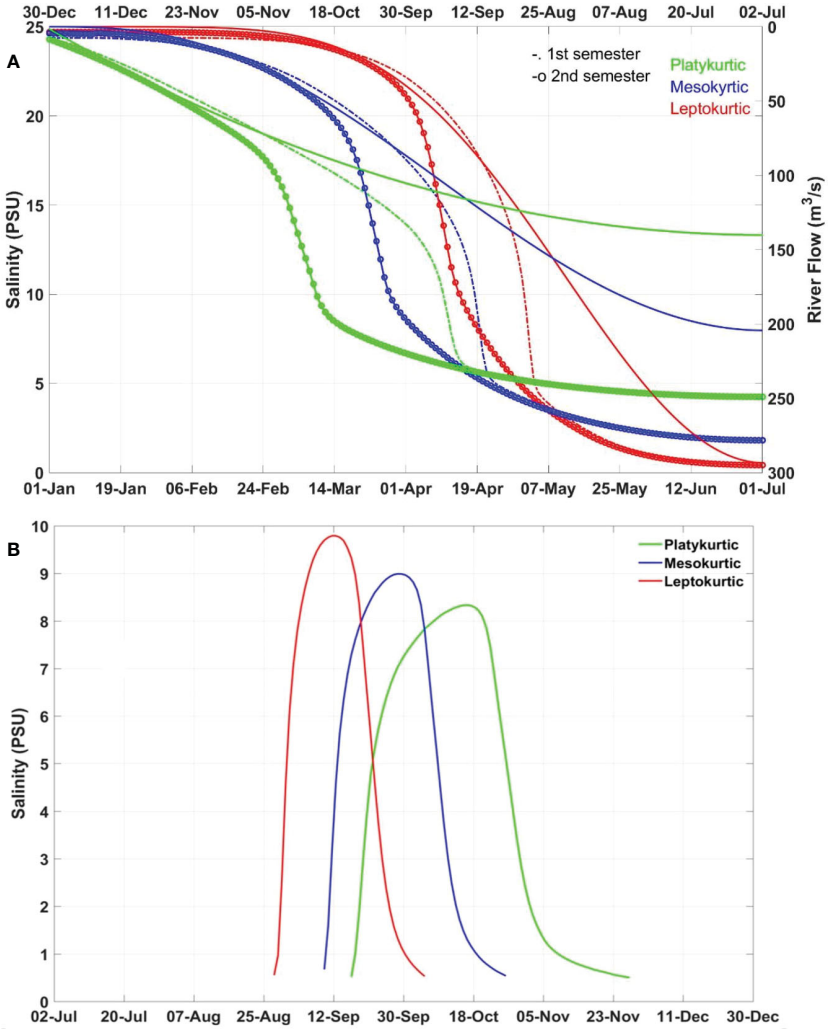

FIGURE 3
(A) A comparison of the mean over depth salinity averaged over a distance of 3 km from the river mouth between the three symmetric distributions. Bottom axis shows the dates of the 1st semester. The dotted lines denote salinity in the 1st semester. Top axis shows the dates of the 2nd semester moving from right to the left. Circled lines denote salinity in the 2nd semester increasing from right to the left. The river discharge of each symmetric distribution is added with continuous lines and with its scale on the right axis. The flow increases from 1st of January until 1st of July following the bottom axis and decreases from 2nd of July until 31 of December following the top axis. **(B)** A timeline of the salinity differences above 0.5 PSU between the 1st and 2nd semester for each symmetric distribution.

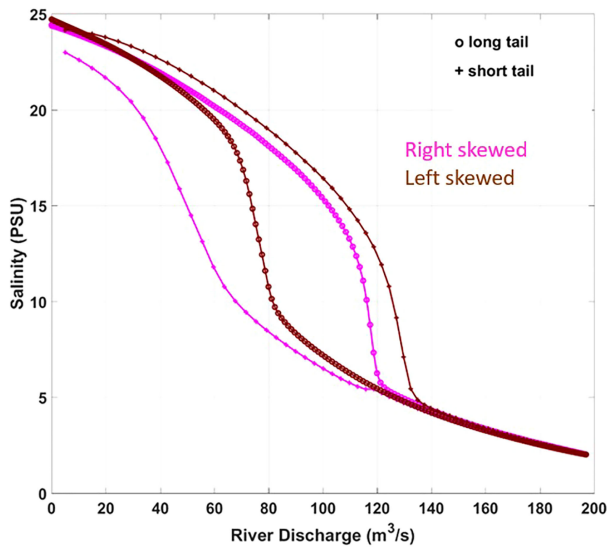

FIGURE 4
The mean over depth salinity averaged over a distance of 3 km far from the river mouth against the river discharge for the two skewed hydrographs. The circles correspond to the dates of the long tail and the crosses to those of the short tail.

salinity differences are averaged over radial cross-sections like it was done in section 3.1. The averaging is done over points in a distance of 3 km and 5 km from the river mouth (red and yellow semicircles in Figure 1F) to compare results between shallow locations in the delta front (i.e. area including delta channels) and deeper ones at the pro-delta (i.e. delta area beyond the channels ends) (Hori and Saito, 2007). The evolution in time of the stratification is presented for both symmetric and skewed flow distributions and for both radial sections in Figure 5.

The shape of the hydrograph does not seem to affect the range of stratification which remains similar between the five cases in each section (3km and 5km). This range is relatively small at the 3 km section (Figures 5A, B) which is the shallower one where mixing occurs under the influence of stronger bottom friction. The three symmetric hydrographs (Figure 5A) show a stratification level that increases initially following the hydrographs shape. For example, the leptokurtic curve demonstrates initially little change in stratification for as long as the low river discharges in the hydrograph's tail (Figure 1C) do not differ much. At the same time, the platykurtic curve demonstrates a sharp increase of stratification in accordance with its hydrograph's sharp flow increase (Figure 1A). As the river discharge increases continuously, it crosses a threshold above which it manages to mix the water column despite the absence of other contributors (e.g., tide-induced mixing). This is usually accompanied by a seaward shift of the salt intrusion length. The level of mixing depends on the level of the peak flow. The higher the peak the lower the stratification is. In that sense, the leptokurtic is the more efficient hydrograph against stratification while the decrease of stratification in the platykurtic is not substantial. The skewed hydrographs (Figure 5B) present similar results. Initially, the stratification increases following the flow increase but it drops when the river discharge is high enough to mix the waters. This occurs earlier in the left skewed case, 40 days after the start of the simulation and during the short tail. It occurs later in the right skewed simulation, 170 days after the start and during the long tail. In both cases, the stratification starts to increase again when the river discharge drops below a threshold value when it is not sufficient to mix the water anymore. After this point and till the end of the simulation, the top to bottom salinity differences follow the flow distribution.

In the deeper waters (5 km radial section, Figures 5C, D), the stratification follows the flow distribution and increases/decreases when the river discharge does increase/decrease too irrespective of the hydrograph shape. Its value reaches its maximum at the time of the peak flow. Accordingly, the higher the peak flow the higher the stratification can become, and this is why the leptokurtic shows the maximum top to bottom salinity difference (17 PSU) and the platykurtic the minimum one (13 PSU). In the same concept, the two skewed simulations (Figure 5D) show an equal maximum stratification occurring though at different time moments following the difference in the position of their peak on the hydrograph.

Changes in the spatial salinity distribution are reflected in Figures 5C, D as spikes, one before and another one after the peak flow. As the flow increases, the freshwater spreads radially in wider areas resulting in more symmetric spatial distributions. An example of a change in the spatial salinity distribution for the platykurtic hydrograph is given in the Supplementary Material (section 7.3). At the moment this change occurs, the rate of stratification increase/decrease in the 1st/2nd semester also changes. The time period between the spike and the peak flow is longer in the 2nd semester when the flow decreases as a result of the slower salinity's response to decreasing than increasing flows.

3.3 Salt intrusion in the inlet

Sustained drought periods may result in salt intrusion inside the river mouth. This is often defined by the location of the 2 PSU bottom isohaline (Schubel, 1993; Monismith et al., 1996; Monismith et al., 2002; Herbold and Vendlinkski, 2012; Andrews et al., 2017). The time that the salinity at the bottom of the river mouth remains below 2 PSU is measured for each simulation with the intention to detect the flow distribution that keeps the river mouth fresh for the most time. Figure 2A shows the level of the bottom salinity at the river mouth (point A in Figure 1F) for the whole simulation period in each case. The five simulations start from a dry season state with very high salinity at the bottom of the mouth meaning that there is salt intrusion in the inlet. The intrusion is averted when the river flows become higher during the wet season. It is identified from Figure 2 that the river discharge at the time the salinity falls below 2 PSU is approximately 100 m^3/s in each case. The rate at which the flow rises in each hydrograph until it reaches this threshold determines the moment that the inlet's salt intrusion disappears first. The earliest this can happen is for the left skewed and the latest for the right skewed hydrograph. The time period that the inlet remains fresh is determined by the hydrographs' tails and the peak flow position. Table 3 displays the total number of days and the days after the peak flow that the bottom salinity at the mouth is less than 2 PSU. The symmetric distributions indicate that the lighter the tails (platykurtic) the longer the inlet is fresh (210 days). The left skewed case, which also shows light tails but for shorter time, exhibits the second longer

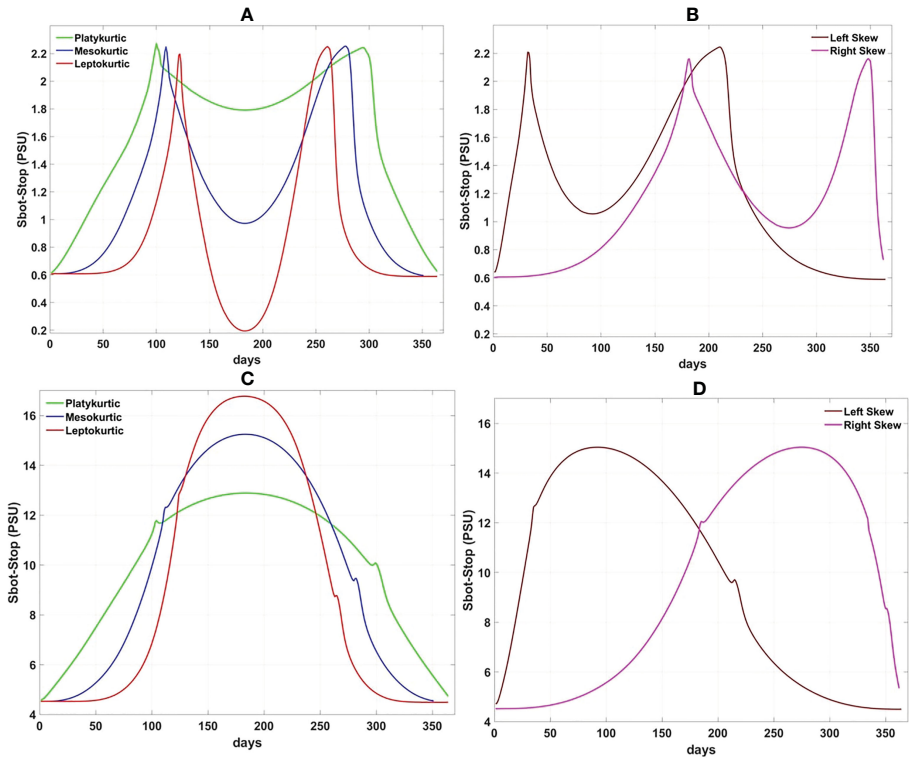

FIGURE 5
(A, B) The evolution in time of the top to bottom layer difference of the radially averaged salinity in a distance 3 km from the mouth in the symmetric and skewed flow distributions respectively. **(C, D)** The evolution in time of the top to bottom layer difference of the radially averaged salinity in a distance 5 km from the mouth in the symmetric and skewed flow distributions respectively.

period (189 days). Being antisymmetric to the left, the right skewed hydrograph keeps the inlet fresh for a long period as well (179 days). However, the fact that its peak occurs much later in time seems to have an effect by cutting out 10 days making it equal to the mesokurtic hydrograph. The minimum duration of all (147 days) corresponds to the leptokurtic as it exhibits the heavier tails of all. The results are slightly different when the time is measured after the peak flow. In this case, the left skewed hydrograph exhibits the longer duration (126 days) with the platykurtic being second now (119 days). This indicates that it might be better to force a peak flow to occur early in the year in order to establish a freshwater system for longer periods. This is further supported by the indication that the right skewed hydrograph manages to keep the bottom salinity at the mouth below 2 PSU only for 80 days, even 2 days less than in the leptokurtic hydrograph.

3.4 Salinity longitudinal distribution

Possible effects of the hydrographs shape on the salinity longitudinal distribution are investigated in this section. In Figure 2B, the mean over depth and annual averages of salinity in the delta are averaged over radial cross sections every 300 m along a distance of 6 km from the river mouth (see cross-section AB in Figure 1F). This technique follows the concept of the salt intrusion curves, often used in other studies to measure cross-sectional salinity averages from the estuary mouth's to its head (Savenije, 1993; Nguyen and Savenije, 2006; Nguyen et al., 2008; Zhang et al., 2011). The annual salinity average at the river mouth is above the 2 PSU threshold in every case. This is probably caused by the long periods of heavy tails (meaning very low flows) at all hydrographs except for the platykurtic one. Having the lightest tails of all, the platykutic case presents the lowest salinity value and closest to the 2 PSU threshold at the river mouth. The spatial salinity distribution in the delta increases gradually downstream. The rate of salinity increase between two successive sections is not constant because in contrast to their length, the depth of the radial cross-sections does not increase monotonously downstream. The shape of the five curves in Figure 2B is very similar and does not seem to be affected by the shape of the hydrograph. A border exists 4.2 km far from the river mouth where downstream of it the salinity is equal between the platykurtic, mesokurtic and the two skewed hydrographs. The green semi-circle in Figure 1F denotes the radial section of 4.2 km. This is located at the border between the delta front and the pro-delta. Upstream of this border, hydrographs with lighter tails (platykurtic) provide a salt intrusion curve of the lowest salinity. Hydrographs with almost equal peaks and flow ranges, such as the left skewed and the mesokurtic provide the exact same spatial salinity distribution in the delta. The salinity in the right skewed is slightly higher than them. A negative effect can be deduced then when moving the peak closer to the end instead of the start of the hydrograph as it causes an increase of salinity. Downstream of the green semicircle, in the absence of the complex channels' bathymetry and in deeper waters (pro-delta), the salt intrusion curve is the same for all cases with the exception of the leptokurtic hydrograph that still shows the highest salinity. It appears then that the salinity in deep areas is less affected by changes in a hydrograph shape.

TABLE 3 The total duration and the time after the peak flow that the bottom salinity is less than 2 PSU at the river mouth.

Case	Total Duration (days)	Duration after the Peak (days)
Platykurtic	210	119
Mesokurtic	179	100
Leptokurtic	147	82
Left Skewed	189	126
Right Skewed	179	80

3.5 Freshwater residence time

Considering the water to be fresh as long as its salinity remains below 2 PSU, its residence time is calculated to determine how long the delta remains fresh in each simulation and to what extent. Figure 6 includes maps of the delta for each simulation displaying the total time in days that the depth averaged salinity remains below 2 PSU. The delta channels borders are delineated in the background (in black colour) to visualize the size of the area that becomes fresh in each case. The cyan color in these maps represents areas that never become fresh (freshwater RT is zero). In every case, the tendency is that the time salinity remains below 2 PSU decreases downstream in long distances from the river mouth. The peak flow seems to be the determinant factor for the extent that becomes fresh. This is almost the same for the mesokurtic (Figure 6B) and the two skewed cases (Figures 6D, E) because their maximum flows are very close (204 m^3/s in the mesokurtic and 197 m^3/s in the skewed hydrographs).

In the symmetric distributions, the delta area that becomes fresh increases with increasing peak flow. Hence, every delta channel becomes fresh when the leptokurtic hydrograph is implemented - with the exception of the two most distant ones at the top left and bottom left corner of the map. On the contrary, a more limited delta area becomes fresh with the platykurtic hydrograph (Figure 6A) compared to the other hydrograph cases. Interestingly though, this case provides the longest freshwater conditions period. The delta is fresh in relatively small or medium distances from the mouth for almost 7 months. The freshwater duration period of a symmetric distribution decreases as the tails of the hydrograph become heavier. Therefore, the maximum time that salinity can be below 2 PSU with the leptokurtic hydrograph is only 5 months (Figure 6C). In the case of the skewed hydrographs the left one (Figure 6D) keeps the delta fresh for more time than the right (Figure 6E) highlighting the importance of its hydrograph slope that shows a rapid flow rise in the 1st semester and an early in time peak discharge. The hydrograph's slope is identified as another crucial factor because the two cases exhibiting the faster rate of flow rise in the 1st semester (platykurtic and right skewed) provided the longer freshwater conditions in the delta.

In the map plots, differences in the duration within certain areas of the delta indicate bathymetry effects. There seems to be a difference of 25 days in the duration between the right and left sides of the inlet (looking seaward) (Figures 6A, B, D). The latter is deeper and thus the higher bottom salinity reduces the duration in comparison to the shallower areas right of the inlet. This difference is more pronounced in the right skewed case (Figure 6E) when the dry season is prolonged and the low freshwater flows do not manage to decrease the salinity in the deeper areas. On the other hand, this separation between deep and shallow areas is not present in the leptokurtic case (Figure 6C) because the peak flow is very high and can distribute symmetrically the fresh water throughout the delta.

3.6 Flushing times

Following the procedure discussed in section 2.6, the FT was measured twice after determining the averaging period first by setting the start at the day of the maximum flow and second at the last day of the simulation. Figure 7A displays the FT for both starting days. The five simulations show comparable results when the maximum flow day is considered the starting point. In this case, the averaging period is only one day because the river flow is so high that replaces immediately the salt with fresh water and so Q_F in equation 2 is also the Q_{max}. Consequently, the FTs are about 1 day and the differences between the five simulations are in the order of a few hours. The order of the FT magnitude between the five hydrographs follows the order of their peaks and the higher the flow the lower the FT is.

If the last day of the simulation is taken as the observation day to determine the averaging period, the differences in the FT between each hydrograph are more significant. The right skewed hydrograph exhibits the lowest FT (4 days) because it contains the highest flows at its end. The symmetric distributions show a progressive decrease of the FT as the hydrographs' tails become lighter. As a result, the leptokurtic hydrograph requires the most time for water renewal (17 days) with the left skewed one demonstrating similar values since its heavy long tail occurs at the end of the simulation.

However, since most of the hydrographs contain very low river discharges at the end of their simulation, it is possible that the average discharge Q_{end} introduced in equation 2 might lead to an underestimation of the FT when the starting date is the last one. For this reason, the calculation of the FT is repeated for this specific case by introducing the median discharge over the averaging period instead of its mean value. Figure 7B provides a comparison between the FTs measured with the median and the average discharge. The outcome is very interesting because even though the relationship of the FTs between the various hydrographs remains the same, the values in some cases are quite different. In the leptokurtic case, the median FT is more than 120 days (4 months) while the average one was just 17 days. Clearly, the average discharge leads to an underestimation for a hydrograph with very heavy tails. Similarly, the left skewed hydrograph that also exhibits heavy tails at the end of the simulation gave a higher median FT (30 days) than its average one

10.3389/fmars.2023.1075683

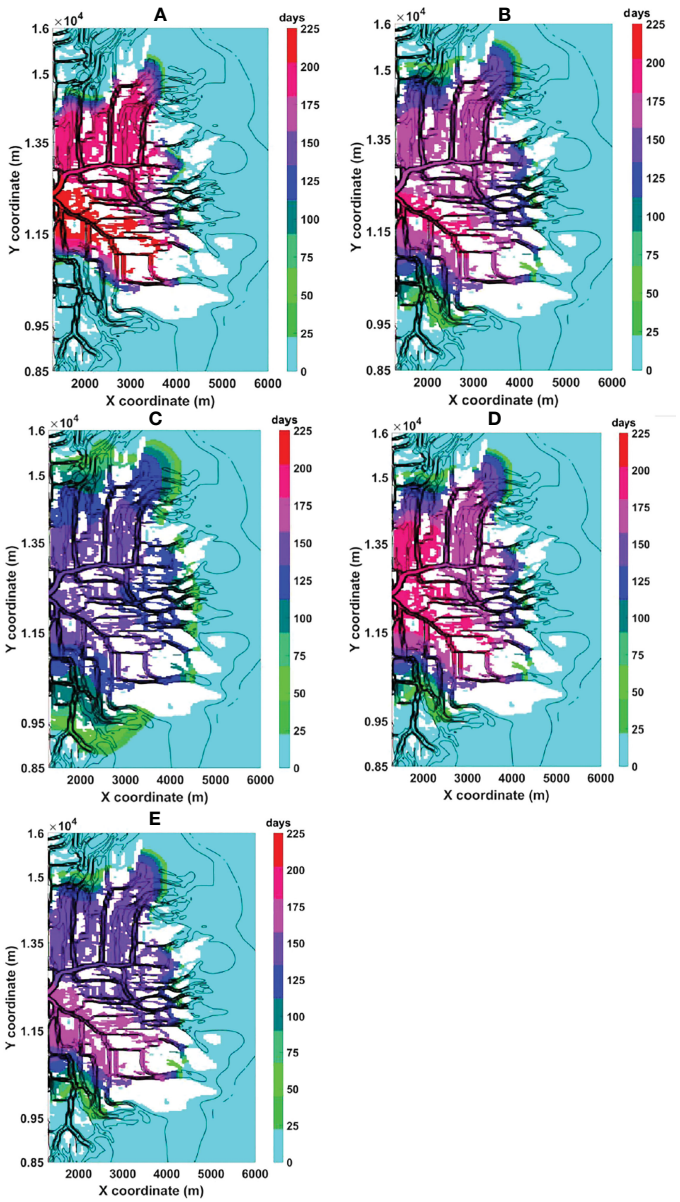

FIGURE 6
The time in days that salinity is less than 2 PSU in the delta for the **(A)** Platykurtic **(B)** Mesokurtic **(C)** Leptokurtic **(D)** Left and **(E)** Right skewed hydrograph cases. The black lines in the background delineate the delta channels. White coloured spaces denote dry areas. The river inlet has been taken out from the maps and the abscissa is set to start at the river mouth. Cyan coloured areas never become fresh.

(17 days). In addition, the median FT uncovers a significant difference of the time required for water renewal between the leptokurtic and the left skewed hydrograph which was not detected when the average discharge was used. The left skewed hydrograph exchanges water 3 months faster than the leptokurtic according to the median FT calculation.

4 Discussion

4.1 Salinity response to river discharges

Results in section 3.1 indicate the existence of an asymmetry in the salinity response to flow changes. The salinity responds slower to decreasing than increasing flow independent of the hydrographs shape. This asymmetry has been identified in several estuarine studies as well (Blanton et al., 2001; Hetland and Geyer, 2004; Savenije, 2005; MacCready, 2007; Uddin and Haque, 2010; Chen, 2015). Savenije (2005) simply stated that the replacement of fresh with saltwater takes more time. Hetland and Geyer (2004) attributed the asymmetry in the estuarine response to the increase of the bottom drag when the flow decreases. The idealized delta presents a complex and asymmetric bathymetry so that it would be reasonable to assume an effect of the bottom drag to the salinity response. For example, Figure 6 shows higher freshwater RT in the shallower parts of the delta for some simulations. However, Figure 3A shows that this asymmetry does not concern periods with very high or very low flows. At these times, the salinity is equal for equal flows between the

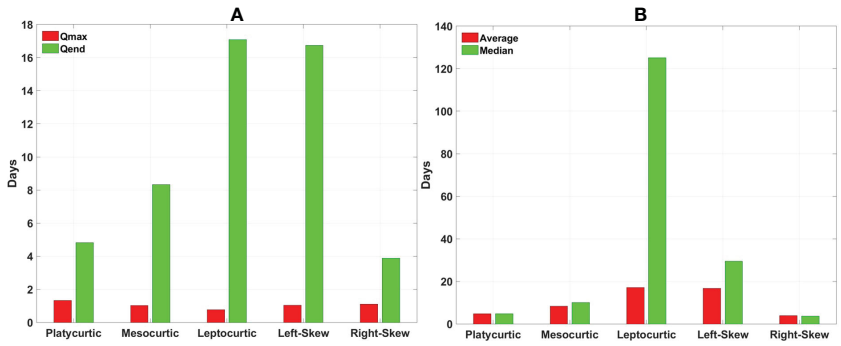

FIGURE 7
The flushing time for each simulation calculated using the Date Specific Method (DSM) to determine the river discharge averaging period. **(A)** Comparison of the flushing time measured with the average river discharge over a period with the starting date at the day of the maximum flow (Qmax, red bars) and the last day of the simulation (Qend, green bars). **(B)** Comparison of the flushing time measured with the average (red bars) and the median (green bars) river discharge over a period with a starting date at the last day of the simulation.

two semesters irrespective of whether the flow increases or decreases. The peak flow magnitude seems to have a strong influence. The higher the peak the shorter the asymmetry period is and the higher the salinity decreases too (Figure 3B). This may refer to the shorter adjustment times to large peaks in estuaries that Chen (2015) reported. In contrast to Hetland and Geyer (2004); Chen (2015) claims that the asymmetry is caused by two other factors: non-linearity of the salt flux and large variations in the river forcing. The results in section 3.1 present a direct dependence of the salinity response timescale to the flow. Monismith (2017) states that this is true only in systems close to steady state although the relationship is not linear. This is most probably true for the present case since the hydrographs of Figure 1 assume slow flow changes and this justifies the direct dependence of salinity response to river discharge observed in the results. In addition, Monismith (2017) examined if it is possible to take advantage of this asymmetry and achieve a specific salinity standard with flow variations of lower freshwater volumes compared to a constant flow for the same time frame. The outcome was that the flow needed to obtain a certain salinity value (e.g., 2 PSU) increases as the period of flow variation increases. Similarly, Figure 6C indicates that to sustain the 2 PSU salinity threshold in its most distant position, higher flow would be required to vary for a longer period. However, this would require an increased freshwater volume compared to that of the five hydrographs.

The response asymmetry of salinity to flow changes can be well detected in the skewed hydrographs too (Figure 4). The effect of high flow periods when the salinity does not vary between increasing or decreasing flows is also present. Most importantly though, the conclusion is that for a given flow range a standard salinity decrease could be achieved in much shorter time if the hydrographs tails become sharper or in other words if the flow rate is increased.

The latter outcome could be much useful in terms of water management as it seems that for a given flow range, the increase of its rate can decrease faster the salinity and improve remarkably the conditions in the delta. The faster rate of flow change (lighter tails) is also what probably makes the platykurtic hydrograph a preferable option compared to the leptokurtic one since it sustains freshwater conditions in the delta for longer periods. This would prolong the period that the various anthropogenic activities could take place safely in the delta even though the leptokurtic hydrograph could achieve larger salinity decrease but for a limited time.

4.2 Drivers of hydrographs shape change and its impact on salinity

Deltas can be found at all latitudes and climatic zones (Roberts et al., 2012). Although not absolute, a hydrograph's shape could be indicative of certain climate zones. Climate change will affect hydrological regimes in the future which can reflect as changes in hydrographs shape. Riverine flow changes result from either natural climate variability (NCV) (Deser et al., 2012) or anthropogenic climate change (ACC) (Zhang and Delworth, 2018). NCV influences riverine floods magnitude and timing (Merz et al., 2014; Francois et al., 2019). Atmospheric processes such as intensified precipitation (Viglione et al., 2016) can increase riverine flood peak discharges (Hall et al., 2014; Zhang et al., 2015). Such increases may result in hydrographs like the leptokurtic in Figure 1C that presents a sharp peak. This type of hydrograph with large differences between maximum and minimum flows is often found in monsoonal climates (Hansford et al., 2020). The results analysis in section 3 indicates that peak flow increases could result in an offshore displacement of the salt intrusion length, freshening of a larger area in the delta, mixing of the water column with freshwater and fast renewal times during this period. However, this positive effect would be only temporary if it is not accompanied by an increase of the streamflow throughout the year and the delta's salinity will shortly recover to its pre-peak flow state. A platykurtic hydrograph that has lower peak but smaller differences between maximum and minimum flows is more successful in retaining the delta fresh for longer periods. Increases of peak flows magnitude with thus similar effects may arise by ACC as well as for example urbanization and land use changes that decrease soil infiltration and weaken the natural buffering effect (Vogel et al., 2011; Prosdocimi et al., 2015; Francois et al., 2019).

Warmer temperatures have led to earlier spring discharges in rivers affected by snowmelt (IPCC, 2007; Matti et al., 2017; Bloschl et al., 2017). The left skewed hydrograph's peak is of similar magnitude to the mesokurtic and the right skewed one but occurs

earlier in time. An earlier occurrence of the same magnitude peak flow shows to have an advantage in terms of keeping the delta and its river mouth fresh for longer periods compared to the two other cases. Despite this, the annual and spatial averaged salinity remains the same between these three cases. Moreover, the earlier spring peak discharge shifts the river runoff away from the summer and the autumn which are the months with the highest water demand and so special consideration should be taken in these conditions (IPCC, 2007). On the other hand, polar warming has caused a delay of winter floods in the North Sea and some sectors in the Meditteranean Coast (Bloschl et al., 2017). In the hydrographs of Figure 1, when the peak flow is positioned late in time (right skewed) the freshwater residence time is much lower compared to other cases of equal peak flow. However, the winter's water renewal time may become faster in this case because of the higher flows during this period.

Rises of temperature, increases of evaporation and warming of the oceans in recent years has intensified droughts that have also become more frequent (IPCC, 2007). In addition, reduction of runoff in many regions is assumed to be the result of a poleward expansion of the subtropical dry zone due to anthropogenic climate warming (Lu et al., 2007; Milly et al., 2008). Conversion of delta regions to arid zones due to sustained drought periods could modify their annual hydrographs into a mesokurtic shape which is the hydrograph type usually met in these zones (Hansford et al., 2020) as is the case for the Colorado and Nile deltas (Day et al., 2021). The effect on salinity would depend mainly on the peak flow change. If the peak flow increases then an offshore displacement of the salt intrusion zone should be expected, a decrease of stratification and freshwater residence times together with a delay in water renewal times. The reverse effects should be expected if the peak flow decreases.

4.3 Effects of flow distribution on stratification

The evolution of stratification in time with flow changes depends a lot on bathymetry. In deep waters, it follows the hydrographs shape consistent with what is reported in many estuarine studies (Monismith et al., 2002; MacCready, 2004; MacCready, 2007; Ralston et al., 2008; Lerczak et al., 2009; Wei et al., 2016). The level of stratification increases with the flow increase so that the leptokurtic hydrograph exhibits the maximum and the platykurtic the minimum top to bottom salinity differences. In shallow waters, the link between the stratification and the hydrograph shape breaks when the river discharge is sufficient to mix completely the water column. This is expected to happen in areas closer to the river mouth where the depth is shallower and the river discharge's influence stronger. This difference of stratification between deep and shallow areas is not surprising and has been reported earlier. For example, Sridevi et al. (2015) observed something similar in the Godavari estuary where the top to bottom salinity differences varied along the estuary due to bathymetric differences. Stratification was higher in deeper stations and lower in the shallow ones. Several conclusions can be drawn considering this result.

If the interest regarding stratification is focused inside the delta and in areas closer to the river mouth, a flow distribution that follows the leptokurtic hydrograph shows several advantages. It presents longer periods with either mixed waters or very low vertical salinity differences compared to the other hydrographs. It should be noted though that during low flow periods, the salinity can be high despite low vertical differences. Special consideration should be taken then concerning the salinity thresholds of different activities taking place in the delta. The two skewed and the mesokurtic hydrographs demonstrate a very similar stratification range in accordance with their flow range. It could be deduced then that the level of stratification may be more sensitive to the peak flow magnitude than its position in the hydrograph.

The range of stratification is much higher in the deeper areas (Figures 5C, D) and that can be explained by the weakening of the bottom friction that leads to stronger stratification (Monismith et al., 1996; Shaha et al., 2012). Stratification may cause anoxic conditions at the bottom layers and low oxygen can have environmental consequences to the aquatic life (Chant, 2012). For example, riverine waters are responsible for recurrent summertime hypoxia at the bottom waters of the river dominated Mississippi Delta (Schiller et al., 2011). It is important to mention the absence of tides in this case because when present they contribute to vertical mixing reducing usually the stratification effects. For instance, active oxygen replenishment from the atmosphere is observed in the macrotidal Scheldt and Chikugo estuaries (Sun et al., 2020). It should be expected then that many of these conclusions could be relatively different in systems with high tide.

The same may apply if future sea level rise (SLR) scenarios are considered. SLR can strengthen the stratification as it is reported for example in the Pearl River Estuary (Hong et al., 2020). Shallower sections may become deep in certain SLR future scenarios, something that would increase stratification and thus require changes to water management to avert the subsequent implications. On the other hand, some recent studies suggest that the SLR effect on SI is often less significant than that of a decrease of upstream flows (Akter, 2019; Bellafiore et al., 2021). Flow seasonality must be considered as well when assessing the SLR effect as this is expected to be stronger during low discharge periods. For instance, in their modeling experiments, Bricheno et al. (2021) found that the SLR effect to SI in the Ganges-Brahmaputra-Ganges delta is enhanced during dry season but counteracted during wet season by an enhanced monsoon. For the same delta, Akter, 2019) identified a local impact to SI from SLR while decreases of the freshwater flow were found to affect the entire region.

4.4 Hydrograph shape effects on water renewal and freshwater residence times

The results of sections 3.5 and 3.6 indicate that each hydrograph type has certain advantages and disadvantages. Therefore, the decision on the selection of an optimum hydrograph regarding water quality should be per case and according to water management demands. The peak flow magnitude and the tails of each hydrograph are important parameters affecting freshwater RT and water renewal time. An incremental increase of the peak flow results in a seaward salt intrusion limit displacement due to the negative correlation between river discharge and salinity (Garvine et al., 1992; Wong, 1995; Liu et al., 2001; Monismith et al., 2002; Liu et al., 2007; Becker et al., 2010). This is reflected in the panels of Figure 6 as an increase of the freshwater area with the peak flow increase. The freshwater area and RT follow an opposite trend. An increase of the peak flow results in an increase of the

freshwater area but decrease of the RT. This is a consequence of the heavier tails that the hydrographs with higher peak flows exhibit. For example, the leptokurtic hydrograph shows the lowest RT because of its sharp peak and the uneven flow distribution throughout the year. For the same reason, the leptokurtic dry season FT is also the maximum one since the freshwater cannot be fast enough replenished in such low flow conditions. Heavy tails cause also the leptokurtic hydrograph to present the maximum annual and space averaged salinity while the platykurtic shows the minimum.

Hydrographs of similar flow range and peak flows (e.g., skewed and mesokurtic) make fresh almost equal areas (Figure 6). However, the RT may vary between them because of bathymetry or the time of the peak flow in the hydrograph. For example, the left skewed hydrograph shows higher RT which indicates positive effect of an early peak river discharge. In contrast, when the peak flow is positioned at the end of the year (right skewness) the RT decreases significantly. In the last case, bathymetric effects are more pronounced because the difference in the RT between shallow and deeper areas is much higher than the two other cases.

Estimations of the water renewal time are important considering the increase in tracers transport times expected in the future for both seasons because of SLR (Hong and Shen, 2012; Chen et al., 2015; Ahn et al., 2018; Hong et al., 2020). Flushing times in estuaries and deltas are also expected to increase for the same cause. FT is known to vary a lot with seasonality (Ensign et al., 2004) and this results in different order of FTs between the five hydrographs during wet and dry season. FT gets shorter values during wet and higher during dry seasons.The critical parameters for the FT are the peak flow in the wet and the hydrographs tails in the dry season. However, the effect of the tails in the second case is much stronger than that of the peak discharges in the first case. The hydrographs shape does not significantly influence the FT during wet seasons. Although the FT decreases with the increase of the peak flow the difference is only within the range of hours. In contrast, the FT increases by days as the tails become heavier. The selection of the statistical river discharge value to be introduced in the freshwater fraction method equation is very important in the case of heavy tails such as those of the leptokurtic and left skewed hydrographs. The use of an average over a period of very low discharges such as those included in hydrographs with heavy tails can decrease the FT and provide an unrealistic estimation of the renewal time (Alber and Sheldon, 1999). The use of the median discharge is proposed instead. Table 4 summarizes the overall conclusions of the study by providing the basic advantages and disadvantages of each flow regime.

5 Conclusions

In this study, the impact of different flow regimes on the salinity distribution in deltaic systems has been investigated. The work is motivated by the need to moderate saltwater intrusion consequences in deltas by better management of existing freshwater resources instead of resorting to expensive and harmful to the environment technical solutions. A 3D numerical model built in Delft3D for an idealized delta configuration was implemented for this purpose. Five test cases were considered, three of them with flow regimes of annual symmetric distribution but different flow range and two others with annual hydrographs of left and right skewness. To avoid complexity that could obscure direct conclusions, the simulations do not consider tides and Coriolis force was neglected. This may compromise the conclusions which might be then most applicable to river dominated deltas with little tidal influence and in medium latitudes.

The results analysis leads to interesting conclusions regarding the impact of various flow regimes on stratification, water renewal, freshwater area extent and residence times. In addition, the salinity response to flow changes has been assessed. It was found that the salinity responds slower to river discharge decreases than increases which is in accordance with what is stated in similar estuarine studies. The effect of flow regimes on stratification and mixing differs between shallow and deep areas in the delta. In deep waters and far from the delta apex, the top to bottom layer salinity difference follows the shape of the hydrograph and increases as the river discharge increases. In this case, leptokurtic and platykurtic hydrographs show the highest and lowest stratification level respectively following the difference in

TABLE 4 A summary of the effects in stratification, flushing and residence times and freshwater areas caused by the main characteristics of the flow regimes under consideration.

Shape	Stratification	Flushing time	Residence Time	Freshwater Areas
Light tails and small differences between high and low flow seasons (e.g., platykurtic, Figure 1A)	Little effectiveness compared to other flow distributions	Very efficient, fast water renewal in both high and low flow season	Water can remain fresh for significantly long periods	Limited size covering only areas close to the delta apex
Heavy tails and large differences between high and low flow seasons (e.g., leptokurtic, Figure 1C)	Full mixing during high flow season in shallow and close to the delta apex areas but strong stratification in deeper delta areas	Very low efficiency, slow water renewal especially during low flow season	Water remains fresh for limited time in most delta areas	Farthest seaward displacement of the saltwater zone, freshwater can cover temporarily the entire delta
Peak flow closer to the start, falling limb on the right (e.g., left skewness, Figure 1D)	Little effectiveness, limited for a short period after the flow crosses a certain threshold and mixes temporarily the water	Slow water renewal especially during low flow season	Water can remain fresh for relatively long periods	Much efficient, can cover wider area than platykurtic but smaller than leptokurtic case
Peak flow closer to the end, rising limb on the left (e.g., right skewness, Figure 1E)	Little effectiveness, limited for a short period after the flow crosses a certain threshold and mixes temporarily the water	Fast water renewal compared to the other cases for both seasons	Water remains fresh for limited time in deep but for longer time in shallow delta areas	Much efficient, can cover wider area than platykurtic but smaller than leptokurtic case

their peak flows. However, the reverse occurs in shallower and closer to the main trunk channel delta areas because the river discharge can mix the water column when crossing a certain flow threshold.

A hydrograph's shape was found to be determinant factor for freshwater areas extent, renewal, and residence times. Platykurtic hydrographs present the maximum freshwater residence times because of their light tails (i.e., sharp flow increase) and small differences between maximum to minimum flow allowing an even water distribution throughout the year. The bathymetry is another crucial parameter as shallow areas remain fresh for longer periods. On the contrary, the extent of freshwater areas is determined by peak flows and therefore a leptokurtic hydrograph results in the farthest seaward displacement of the salt intrusion limit. Finally, the flow regime affects flushing times mainly during low flow periods. Water renewal becomes slower in the case of hydrographs with heavy tails (i.e., long periods with relatively low flows) rendering the leptokurtic hydrograph as the least efficient case. It was also discovered that the median instead of the mean over the averaging period river discharge results in more realistic and valid flushing times when hydrographs with very long low flow periods are considered.

The work in this paper indicates that it is possible to mitigate saltwater intrusion in deltas by applying water supply regulations. Each flow regime demonstrates different benefits for the various parameters under consideration (e.g., freshwater area and residence time) which should be accounted before any decisions for modifying existing hydrographs shape into another type. Nevertheless, the present study focuses on river flow forcing only and thus further research might be needed to determine the impact of other parameters such as for example tide-induced mixing and wind forcing.

Data availability statement

The original contributions presented in the study are publicly available. This data can be found here: https://zenodo.org/record/7373598#.Y9BAq3bP13gdoi:10.5281/zenodo.7373598.

Author contributions

CM: Conceptualization, Methodology, Software, Pre- and Post-processing, Visualization, Formal analysis, Writing, Original draft and reviewed versions preparation. LA: Supervision, reviewing and editing. LB: Supervision, reviewing and editing. NL: Supervision, reviewing and editing. All authors contributed to the article and approved the submitted version.

Funding

The work contained in this paper contains work conducted during a PhD study supported by the Natural Environment Research Council (NERC) EAO Doctoral Training Partnership whose support is gratefully acknowledged. Grant ref NE/L002469/1. Funding support from the School of Environmental Sciences, University of Liverpool are also gratefully acknowledged. For the purpose of Open Access, the author has applied a Creative Commons Attribution (CC BY) license to any Author Accepted Manuscript version arising.

Conflict of interest

The authors declare that the research was conducted in the absence of any commercial or financial relationships that could be construed as a potential conflict of interest.

Publisher's note

Supplementary material

The Supplementary Material for this article can be found online at: https://www.frontiersin.org/articles/10.3389/fmars.2023.1075683/full#supplementary-material

References

Adams, W. (2000). *World commission on dams, dams and development: A new framework for decision-making* Vol. 1 (London: EarthScan), 1–28.

Ahmed, M. F., and Rahman, M. M. (2000). *Water supply and sanitation–rural and low-income urban communities. ITN–bangladesh, center for water supply and waste management, BUET, dhaka, bangladesh with contribution from IRC* (The Netherlands: International Water and Sanitation Center, Delft).

Ahn, D. T., Hoang, L. P., Bui, M. D., and Rutschmann, P.. (2018). Simulating future flows and salinity intrusion using combined one- and two-dimensional hydrodynamic modeling-the case of hau river, Vietnamese Mekong delta. *Water* 10 (7), 1–21. doi: 10.3390/w10070897

Akter, R. (2019). The dominant climate change event for salinity intrusion in the GBM delta. *Climate* 7, 69. doi: 10.3390/cli7050069

Alber, M., and Sheldon, J. E. (1999). Use of a date-specific method to examine variability in the flushing times of Georgia estuaries. *Estuarine Coast. Shelf Sci.* 49 (4), 469–482. doi: 10.1006/ecss.1999.0515

Allison, L. E. (1964). Salinity in relation to irrigation. *Adv. Agron.* 16 (C), 139–180. doi: 10.1016/S0065-2113(08)60023-1

Andrews, S. W., Gross, E. S., and Hutton, P. H.. (2017). Modeling salt intrusion in the San Francisco estuary prior to anthropogenic influence'. *Continental Shelf Research* 146, 58–81. doi: 10.106/j.csr.2017.07.010

Balls, P. W. (1994). 'Nutrient inputs to estuaries from nine scottish east coast rivers; influence of estuarine processes on inputs to the north sea'. *Estuarine Coast. Shelf Sci.* 39, 329–352. doi: 10.1006/ecss.1994.1068

Banas, N. S., Hickey, B. M., MacCready, P., and Newton, J. A.. (2004). Dynamics of willapa bay, Washington: A highly unsteady, partially mixed estuary. *J. Phys. Oceanogr.* 34 (11), 2413–2427. doi: 10.1175/JPO2637.1

Becker, M. L., Luettich, R. A. Jr, and Mallin, M. A.. (2010). Hydrodynamic behavior of the cape fear river and estuarine system: A synthesis and observational investigation of discharge-salinity intrusion relationships. *Estuar. Coast. Shelf Sci.* 88 (3), 407–418. doi: 10.1016/j.ecss.2010.04.022

Bellafiore, D., Ferrarin, C., Maicu, F., Manfe, G., Lorenzetti, G., Umgiesser, G., et al. (2021). Saltwater intrusion in a Mediterranean delta under a changing climate. *J. Geophys. Res.: Oceans* 126, e2020JC016437. doi: 10.1029/2020JC016437

Bhuiyan, M. J. A. N., and Dutta, D. (2012). "Assessing impacts of sea level rise on river salinity in the gorai river network, Bangladesh," in *Estuarine, coastal and shelf science*, vol. 96. (Elsevier Ltd), 219–227. doi: 10.1016/j.ecss.2011.11.005

Birkinshaw, S. J., Guerreiro, S. B., Nicholson, A., Liang, Q., Quinn, P., Zhang, L, et al. (2017). Climate change impacts on Yangtze river discharge at the three gorges dam. *Hydrol. Earth Syst. Sci.* 21 (4), 1911–1927. doi: 10.5194/hess-21-1911-2017

Blanton, J., Alber, M., and Sheldon, J.. (2001). Salinity response of the satilla river estuary to seasonal changes in freshwater discharge. *Proceedings of the 2001 Georgia Water Resources Conference, held March 26-27, 2001, at the University of Georgia*. K. J. Hatcher editor Athens, Georgia: Institute of Ecology, The University of Georgia.

Bloschl, G., Hall, J., Parajka, J., Perdigao, R. A., Merz, B., Arheimer, B., et al. (2017). Changing climate shifts timing of European floods. *Science* 357 (6351), 588–590. doi: 10.1126/science.aan2506

Bowen, M. M. (2003). Salt transport and the time-dependent salt balance of a partially stratified estuary. *J. Geophys. Res.* 108 (C5), 1–15. doi: 10.1029/2001jc001231

Bricheno, L. M., Wolf, J., and Islam, S.. (2016). Tidal intrusion within a mega delta: An unstructured grid modeling approach. *Estuarine Coast. Shelf Sci.* 182, 12–26. doi: 10.1016/j.ecss.2016.09.014

Bricheno, L. M., Wolf, J., and Sun, Y.. (2021). Saline intrusion in the Ganges-Brahmaputra-Meghna megadelta. *Estuarine Coast. Shelf Sci.* 252, 107246. doi: 10.1016/j.ecss.2021.107246

Brockway, R., Bowers, D., Hoguane, A., Dove, V., and Vassele, V.. (2006). A note on salt intrusion in funnel-shaped estuaries: Application to the incomati estuary, Mozambique. *Estuarine Coast. Shelf Sci.* 66 (1–2), 1–5. doi: 10.1016/j.ecss.2005.07.014

Bryson, M. (1974). Heavy tailed distributions: Properties and tests. *Technometrics* 16 (1), 61–68. doi: 10.1080/00401706.1974.10489150

Burpee, A. P., Slingerland, R. L., Edmonds, D. A., Parsons, D., Best, J., and Cederberg, J.. (2015). Grain-size controls on the morphology and internal geometry of river-dominated deltas. *J. Sediment. Res.* 85 (6), 699–714. doi: 10.2110/jsr.2015.39

Caldwell, R., and Edmonds, D. A. (2014). The effects of sediment properties on deltaic processes and morphologies: A numerical modeling study. *J. Geophys. Res.* 119 (5), 961–982. doi: 10.1002/2013JF002871.Received

Chant, R. J. (2012). *Interactions between estuaries and coasts: River plumes - their formation, transport, and dispersal, treatise on estuarine and coastal science* (Elsevier Inc). doi: 10.1016/B978-0-12-374711-2.00209-6

Chen, X. J. (2004). Modeling hydrodynamics and salt transport in the alafia river estuary, Florida during may 1999-December 2001. *Estuarine Coast. Shelf Sci.* 61 (3), 477–490. doi: 10.1016/j.ecss.2004.06.012

Chen, W. B., Liu, W. C., and Hsu, M. H. (2015). 'Modeling assessment of a saltwater intrusion and a transport time scale response to sea-level rise in a tidal estuary'. *Environ. Fluid Mech.* 15, 491–514. doi: 10.1007/s10652-014-9367-y

Chen, S. N. (2015). Asymmetric estuarine responses to changes in river forcing: A consequence of nonlinear salt flux. *J. Phys. Oceanogr.* 45 (11), 2836–2847. doi: 10.1175/JPO-D-15-0085.1

Chen, X., Flannery, M. S., and Moore, D. L.. (2000). Response times of salinity in relation to changes in freshwater inflows in the lower hillsborough river, Florida. *Estuaries* 23 (5), 735–742. doi: 10.2307/1352899

Chen, X., Zong, Y., Zhang, E., Xu, J., and Li, S.. (2001). Human impacts on the changjiang (Yangtze) river basin, China, with special reference to the impacts on the dry season water discharges into the sea. *Geomorphology* 41 (2), 111–123. doi: 10.1016/S0169-555X(01)00109-X

Choi, K. W., and Lee, J. H. W. (2004). Numerical determination of flushing time for stratified water bodies. *J. Mar. Syst.* 50, 263–281. doi: 10.106/j.marsys.2004.04.005

Christian, R. R., Boyer, J. N., and Stanley, D. W. 'Multi-year distribution patterns of nutrients within the neuse river estuary. north carolina. *Mar. Ecol. Prog. Ser.* 71, 259–274. https://www.jstor.org/stable/24817298.

Clarke, D., Williams, S., Jahiruddin, M., Parks, K., and Salehin, M.. (2015). Projections of on-farm salinity in coastal Bangladesh. *Environ. Sci.: Process. Impacts R. Soc. Chem.* 17 (6), 1127–1136. doi: 10.1039/c4em00682h

Conner, W. H., McLeod, K.W., and McCarron, J. K. (1997). 'Flooding and salinity effects on growth and survival of four common forested wetland species.'. *Wetland Ecol. Manage.* 5, 99–109.

Dai, Z., Chu, A., Stive, M., Zhang, X., and Yan, H.. (2011). Unusual salinity conditions in the Yangtze estuary in 2006: Impacts of an extreme drought or of the three gorges dam? *Ambio* 40 (5), 496–505. doi: 10.1007/s13280-011-0148-2

Das, A., Justic, D., Inoue, M., Hoda, A., Huang, A., and Park, D. (2012). Impacts of Mississippi river diversions on salinity gradients in a deltaic Louisiana estuary: Ecological and management implications. *Estuarine Coast. Shelf Sci. Elsevier Ltd* 111, 17–26. doi: 10.1016/j.ecss.2012.06.005

Dasgupta, S., Kamal, F.A., Khan, Z. H., Choudhury, S., and Nishat, A.. (2015). River salinity and climate change: Evidence from coastal Bangladesh. *World Sci. Ref. Asia World Econ.*, 205–242. doi: 10.1142/9789814578622_0031

Dawadi, S., and Ahmad, S. (2013). Evaluating the impact of demand-side management on water resources under changing climatic conditions and increasing population. *J. Environ. Manage. Elsevier Ltd* 114, 261–275. doi: 10.1016/j.jenvman.2012.10.015

Day, J. W., Barras, J., Clairian, E., Johnston, J., Justic, D., Kemp, G. P., et al. (2005). Implications of global climatic change and energy cost and availability for the restoration of the Mississippi delta. *Ecol. Eng.* 24 (4 SPEC. ISS.), 253–265. doi: 10.1016/j.ecoleng.2004.11.015

Day, J., Goodman, R., Chen, Z., Hunter, R., Giosan, L., Wang, Y., et al. (2021). Deltas in Arid environments. *Water* 13 (12), 1677 (Switzerland: Water). doi: 10.3390/w13121677

Deltares (2014). Delft3D-flow: Simulation of multi-dimensional hydrodynamic flows and transport phenomena, including sediments. *User Manual Hydro-Morphodynamics* 3.15, 34158.

Deser, C., Knutti, R., Solomon, S., and Phillips, A.S.. (2012). Communication of the role of natural variability in future north America climate. *Natural Climate Change* 2, 775–779. doi: 10.1038/NCLIMATE1562

Dyer, K. R. (1973). *Estuaries: A physical introduction* (London UK: John Wiley and Sons).

Edmonds, D. A., and Slingerland, R. L. (2010). "Significant effect of sediment cohesion on deltamorphology," in *Nature geoscience*, vol. 3. (Nature Publishing Group), 105–109. doi: 10.1038/ngeo730

Eldardiry, H., and Hossain, F. (2019). Understanding reservoir operating rules in the transboundary nile river basin using macroscale hydrologic modeling with satellite measurements. *J. Hydrometeorol.* 20 (11), 2253–2269. doi: 10.1175/JHM-D-19-0058.1

Ensign, S. H., Halls, J. N., and Mallin, M. A.. (2004). Application of digital bathymetry data in an analysis of flushing times of two large estuaries. *Comput. Geosci.* 30 (5), 501–511. doi: 10.1016/j.cageo.2004.03.015

Eslami, S., Hoekstra, P., Trung, N. N., Kantoush, S. A., Doan, V. B., Do, D. D, et al. (2019). Tidal amplification and salt intrusion in the Mekong delta driven by anthropogenic sediment starvation. *Sci. Rep.* 9 (1), 1–10. doi: 10.1038/s41598-019-55018-9

Eyre, B., and Twigg, C. (1997). 'Nutrient behaviour during post-flood recovery of the richmond river estuary northern NSW. *Australia'. Estuarine Coast. Shelf Sci.* 44 (3), 311–326. doi: 10.1006/ecss.1996.0124

Fischer, H. B., List, E. J., Imberger, J., Koh, R. C. Y., and Brooks, N. H. (1979). *Mixing in inland and coastal waters* (New York: Academic Press).

Francois, B., Schlef, K. E., Wi, S., and Borwn, C. M.. (2019). Design considerations for riverine floods in a changing climate – a review. *J. Hydrol.* 547, 557–573. doi: 10.1016/j.jhydrol.2019.04.068

Frihy, O. E. (2003). The nile delta-Alexandria coast: Vulnerability to sea-level rise, consequences and adaptation. *Mitigation Adapt. Strat. Global Change* 8 (2), 115–138. doi: 10.1023/A:1026015824714

Galloway, W. E. (1975). "Process framework for describing the morphologic and stratigraphic evolution of deltaic depositional systems," in *Deltas: Model for exploration* (Houston Geological Society), p.87–p.98.

Garvine, R. W., McCarthy, R. K., and Wong, K.. (1992). The axial salinity distribution in the delaware estuary and its weak response to river discharge. *Estuarine Coast. Shelf Sci.* 35 (2), 157–165. doi: 10.1016/S0272-7714(05)80110-6

Gleick, P. H. (2002). Soft paths water. *Nature* 418 (July), 2002.

Gleick, P. H. (2003). Global freshwater resources: Soft-path solutions for the 21st century. *Science* 302 (5650), 1524–1528. doi: 10.1126/science.1089967

Glen, S. (2016). "Heavy Tailed Distribution & Light Tailed Distribution: Definition & Examples," in *From StatisticsHowTo.com: Elementary Statistics for the rest of us*! Available at: https://www.statisticshowto.com/heavy-tailed-distribution/.

Gong, W., and Shen, J. (2011). "The response of salt intrusion to changes in river discharge and tidal mixing during the dry season in the modaomen estuary, China," in *Continental shelf research*, vol. 31. (Elsevier), 769–788. doi: 10.1016/j.csr.2011.01.011

Gornitz, V. (1991). Global coastal hazards from future sea level rise. *Palaeogeogr. Palaeoclimatol. Palaeoecol.* 89 (4), 379–398. doi: 10.1016/0031-0182(91)90173-O

Ha, T. P., Dieperink, C., Tri, V. P. D, Otter, H. S., and Hoekstra, P.. (2018). Governance conditions for adaptive freshwater management in the Vietnamese Mekong delta. *J. Hydrol.* 557, 116–127. doi: 10.1016/j.jhydrol.2017.12.024

Hagy, J. D., Boynton, W. R., and Sanford, L. P. (2000). 'Estimation of net physical transport and hydraulic residence times for a coastal plain estuary using box models'. *Estuaries* 23 (3), 328–340. doi: 10.2307/1353325

Hall, J., et al. (2014). Understanding flood regime changes in Europe: a state-of-the-art assessment. *Hydrol. Earth Syst. Sci.* 18, 2735–2772. doi: 10.5194/hess-18-2735-2014

Hansford, M. R., Plink-Bjorklund, P., and Jones, E. R.. (2020). "Global quantitative analyses of river discharge variability and hydrograph shape with respect to climate types," in *Earth-science reviews*, vol. 200. (Elsevier), 102977. doi: 10.1016/j.earscirev.2019.102977

Herbold,, and Vendlinkski, (2012). Modeling estuarine habitat in the bay delta, unifying one and three dimensional approaches to modeling X2 and the low salinity zone. *Tech. Workshop Estuary Habitat.*

Hetland, R. D., and Geyer, W. R. (2004). An idealized study of the structure of long, partially mixed estuaries. *J. Phys. Oceanogr.* 34 (12), 2677–2691. doi: 10.1175/JPO2646.1

Hoitink, A. J. F., Wang, Z. B., Vermeulen, B., Huismans, Y., and Kastner, K.. (2017). Tidal controls on river delta morphology. *Nat. geosci.* 10, 637–645. doi: 10.1038/NGEO3000

Holm, J., and Sasser, C. E. (2001). Differential salinity response between two Mississippi river subdeltas: Implications for changes in plant composition. *Estuaries* 24 (1), 78–89. doi: 10.2307/1352815

Hong, B., Liu, Z., Shen, J., Wu, H., Gong, W., Xu, H., et al. (2020). "Potential physical impacts of sea-level rise on the pearl river estuary, China," in *Journal of marine systems*, vol. 201. (Elsevier), 103245. doi: 10.1016/j.jmarsys.2019.103245

Hong, B., and Shen, J. (2012). "Responses of estuarine salinity and transport processes to potential future sea-level rise in the Chesapeake bay," in *Estuarine, coastal and shelf science*, vol. 104–105. (Elsevier Ltd), 33–45. doi: 10.1016/j.ecss.2012.03.014

Hori, K., and Saito, Y. (2007). "Classification, architecture and evolution of Large-river deltas," in *Large Rivers: Geomorphology and management*. Ed. A. Gupta (John Wiley & Sons Ltd), 75–96.

Horner-Devine, A. R., Hetland, R. D., and MacDonald, D. G.. (2015). Mixing and transport in coastal river plumes. *Annu. Rev. Fluid Mech.* 47, 569–594. doi: 10.1146/annurev-fluid-010313-141408

Hu, K., and Ding, P. (2009). The effect of deep waterway constructions on hydrodynamics and salinities in Yangtze estuary, China. *J. Coast. Res.* SPEC. ISSUE 56), 961–965.

Huang, W. (2007). Hydrodynamic modeling of flushing time in a small estuary of north bay, florida, USA. *Estuarine Coast. Shelf Sci.* 74 (4), 722–731. doi: 10.1016/j.ecss.2007.05.016

Huang, W., and Spaulding, M. (2002). 'Modelling residence-time response to freshwater input in apalachicola bay, florida, USA'. *Hydrological Processes* 16 (15), 3051–3064. doi: 10.1002/hyp.1088

Hutton, P. H., Rath, S. J., Chen, L., Ungs, M. J., and Roy, S. B.. (2016). Nine decades of salinity observations in the San Francisco bay and delta: Modeling and trend evaluations. *J. Water Resour. Plann. Manage.* 142 (3), 1–11. doi: 10.1061/(ASCE)WR.1943-5452.0000617

IPCC (2007). "Climate change 2007: Impacts, adaptation and vulnerability," in *Contribution of working group II to the fourth assessment report of the intergovernmental panel on climate change*, vol. ch1.3 . Eds. M. L. Parry, O. F. Canziani, J. P. Palutikof, P. J. v. d. Linden and C. E. Hanson (Cambridge, UK: Cambridge University Press), pp.85–pp111.

Jassby, A. D., Kimmerer, W. J., Monismith, S. G., Armor, C., Cloern, J. E., and Powell, T. M.. (1995). Isohaline position as a habitat indicator for estuarine populations. *Ecol. Appl.* 5 (1), 272–289. doi: 10.2307/1942069

Kakoulaki, G., MacDonald, D., and Horner-Devine, A. R.. (2014). The role of wind in the near field and midfield of a river plume. *Geophys.Res. Lett.* 41, 5132–5138. doi: 10.1002/2014GL060606

Kaplan, D., Munoz-Carpena, R., Wan, Y., Hedgepeth, M., Zheng, F., Roberts, R., et al. (2010). Linking river, floodplain, and vadose zone hydrology to improve restoration of a coastal river affected by saltwater intrusion. *J. Environ. Qual.* 39 (5), 1570–1584. doi: 10.2134/jeq2009.0375

Kastner, S. E. (2018). The influence of wind and waves on spreading and mixing in the Fraser river plume. *J. Geophys. Res.: Oceans* 123, 6818–6840. doi: 10.1029/2018JC013765

Kolker, A., et al. (2018) *The impacts of the Mississippi river and its delta on the oceanography, ecology and economy of the gulf of Mexico Large marine ecosystem*. Available at: http://mississippiriverdelta.org/files/2018/08/Known-Impacts-of-the-Mississippi-River.pdf.

Lai, X., Lai, X., Huang, Q., Zhang, Y., and Jiang, J.. (2014). Impact of lake inflow and the Yangtze River flow alterations on water levels in Poyang Lake,China. *Lake Reserv. Manage.* 30 (4), 321–330. doi: 10.1080/10402381.2014.928390

Lamb, M. P., Nittrouer, J. A., Mohrig, D., and Shaw, J.. (2012). Backwater and river plume controls on scour upstream of river mouths: implications for fluvio-deltaic morphodynamics. *J. Geophys. Res.* 117, F01002. doi: 10.1029/2011JF002079

Latrubesse, E. M., Stevaux, J., and Sinha, R.. (2005). Tropical rivers. *Geomorphology* 70 (3-4 SPEC. ISS.), 187–206. doi: 10.1016/j.geomorph.2005.02.005

Lebo, M. E., Sharp, J. H., and Cifuentes, L. A. (1994). 'Contribution of river phosphate variations to apparent reactivity estimated from phosphate-salinity diagrams'. *Estuarine Coast. Shelf Sci.* 39, 583–594. doi: 10.1016/S0272-7714(06)80011-9

Leonardi, N., Canestrelli, A., Sun, T., and Fagherazzi, S.. (2013). Effect of tides on mouth bar morphology and hydrodynamics. *J. Geophys. Res.: Oceans* 118 (9), 4169–4183. doi: 10.1002/jgrc.20302

Lerczak, J. A., Geyer, W. R., and Ralston, D. K.. (2009). The temporal response of the length of a partially stratified estuary to changes in river flow and tidal amplitude. *J. Phys. Oceanogr.* 39 (4), 915–933. doi: 10.1175/2008JPO3933.1

Lienou, G., Mahe, G., Dieulin, C., Paturel, J. E., Bamba, F., Sighomnou, D., et al. (2010). "The river Niger water availability: Facing future needs and climate change," in *Global change: facing risks and threats to water resources: Proceedings of the sixth world FRIEND conference*, vol. 340. (Wallingford: AISH).

Liu, W. C., Hsu, M. H., Kuo, A. Y., and Kuo, J. T.. (2001). The influence of river discharge on salinity intrusion in the tanshui estuary, Taiwan. *J. Coast. Res.* 17 (3), 544–552.

Liu, W. C., Chen, W. B., Cheng, R. T., Hsu, M. H., and Kuo, A. Y.. (2007). Modeling the influence of river discharge on salt intrusion and residual circulation in danshuei river estuary, Taiwan. *Cont. Shelf Res.* 27 (7), 900–921. doi: 10.1016/j.csr.2006.12.005

Liu, B., Peng, S., Liao, Y., and Wang, H.. (2019). "The characteristics and causes of increasingly severe saltwater intrusion in pearl river estuary," in *Estuarine, coastal and shelf science*, vol. 220. (Elsevier), 54–63. doi: 10.1016/j.ecss.2019.02.041

Liu, Y., Chen, H., Wang, J., Yang, S., and Chen, A.. (2020). Numerical simulation for the effects of waves and grain size on deltaic processes and morphologies. *Open Geosci.* 12 (1), 1286–1301. doi: 10.1515/geo-2020-0196

Lu, J., Vecchi, G. A., and Reichler, T.. (2007). Expansion of the Hadley cell under global warming. *Geophys. Res. Lett.* 34, L06805. doi: 10.1029/2006GL028443

MacCready, P. (1999). Estuarine adjustment to changes in river flow and tidal mixing. *J. Phys. Oceanogr.* 29 (4), 708–726. doi: 10.1175/1520-0485(1999)029<0708:EATCIR>2.0.CO;2

MacCready, P. (2004). Toward a unified theory of tidally-averaged estuarine salinity structure. *Estuaries* 27 (4), 561–570. doi: 10.1007/BF02907644

MacCready, P. (2007). Estuarine adjustment. *J. Phys. Oceanogr.* 37 (8), 2133–2145. doi: 10.1175/JPO3082.1

Monismith, S. G. (2017). An integral model of unsteady salinity intrusion in estuaries. *J. Hydraulic Res.* 55 (3), 392–408. doi: 10.1080/00221686.2016.1274682

Matsoukis, C., Amoudry, L. O., Bricheno, L. M., and Leonardi, N.. (2022). Numerical investigation of river discharge and tidal variation impact on salinity intrusion in a generic river delta through idealized modelling. *Estuaries Coasts* 46, 57–83. doi: 10.1007/s12237-022-01109-2

Matti, B., Dahlke, H. E., Dieppois, B., Lawler, D. M., and Lyon, S. W.. (2017). Flood seasonality across Scandinavia – evidence of a shifting hydrograph? *Hydrol. Process.* 31, 4354–4370. doi: 10.1002/hyp.11365

McCabe, R. M., MacCready, P., and Hickey, B. M.. (2009). Ebb tide dynamics and spreading of a large river plume. *J. Phys. Oceanogr.* 39, 2839–2856.

Merz, B., Aerts, J., Arnbjerg-Nielsen, K., Baldi, M., Becker, A., Bichet, A., et al. (2014). Floods and climate: emerging perspectives for flood risk assessment and management. *Natural Hazards Earth Syst. Sci.* 14, 1921–1942. doi: 10.5194/nhess-14-1921-2014

Milly, P. C. D., Betancourt, J., Falkenmark, M., Hirsch, R. M., Kundzewicz, Z. W., Lettenmaier, D. P., Stouffer, R., et al. (2008). Stationarity is dead: Whiter water management? *Science* 319, 573–574. doi: 10.1126/science.11519

Monismith, S. G., Burau, J. R., and Stacey, M. T. (1996). Stratification dynamics and gravitational circulation in northern San Francisco Bay. In: *San Francisco Bay: The Ecosystem* edited by T. Hollibaugh Washington, D. C.: Am. Assoc. for the Advance. of Sci., pp. 123–153.

Monismith, S. G., Kimmerer, W., Burau, J. R., and Stacey, M. T.. (2002). Structure and flow-induced variability of the subtidal salinity field in northern San Francisco bay. *J. Phys. Oceanogr.* 32 (11), 3003–3019. doi: 10.1175/1520-0485(2002)032<3003:SAFIVO>2.0.CO;2

Montanari, A. (2012). Hydrology of the po river: Looking for changing patterns in river discharge. *Hydrol. Earth Syst. Sci.* 16 (10), 3739–3747. doi: 10.5194/hess-16-3739-2012

Murray, A. B. (2002). Seeking explanation affects numerical modeling strategies. *Eos* 83 (38), 418–419. doi: 10.1029/2002EO000304

Nguyen, A. D., Savenije, H. H. G., Pham, D. N., and Tang, D. T.. (2008). "Using salt intrusion measurements to determine the freshwater discharge distribution over the branches of a multi-channel estuary: The Mekong delta case," in *Estuarine, coastal and shelf science*, vol. 77. , 433–445. doi: 10.1016/j.ecss.2007.10.010

Nguyen, A. D., and Savenije, H. H. G. (2006). Hydrology and earth system sciences salt intrusion in multi-channel estuaries: a case study in the Mekong delta, Vietnam. *Hydrol. Earth Syst. Sci.* 10, 743–754. doi: 10.5194/hess-10-743-2006

Nobi, N., and Das Gupta, A. (1997). Simulation of regional flow and salinity intrusion in an integrated stream-aquifer system in coastal region: Southwest region of Bangladesh. *Ground Water* 35 (5), 786–796. doi: 10.1111/j.1745-6584.1997.tb00147.x

Phan, T. D., Smart, J. C. R., Sahin, O., Capon, S. J., and Hadwen, W. L.. (2018). Assessment of the vulnerability of a coastal freshwater system to climatic and non-climatic changes: A system dynamics approach. *J. Cleaner Prod.* 183, 940–955. doi: 10.1016/j.jclepro.2018.02.169

Pilson, M. E. Q. (1985). 'On the residence time of water in narragansett bay'. *Estuaries* 8, 2–14.

Pitlick, J., and Cress, R. (2000). *Longitudinal trends in channel characteristics of the Colorado river and implications for food-web dynamics* (Grand Junction, Colorado: U.S. Fish and Wildlife Serv.)

Prosdocimi, I., Kjeldsen, T. R., and Miller, J. D.. (2015). 'Detection and attribution of urbanization effect on flood extremes using nonstationary flood-frequency models. *Water Resour. Res.* 51, 4244–4262. doi: 10.1002/2015WR017065

Qiu, C., and Zhu, J. (2015). Assessing the influence of Sea level rise on salt transport processes and estuarine circulation in the changjiang river estuary. *J. Coast. Res.* 31 (3), 661–670. doi: 10.2112/JCOASTRES-D-13-00138.1

Rahman, M. D. M, Mustafi, M. A. A., Islam, A. F.M.T, and Mohammad, N. (2014). The effect of rainfall, temperature and humidity on saline in the southern area of Bangladesh. *Journal of Biology, Agriculture and Healthcare* 4 (22), 58–61.

Rahman, M. M., Penny, G., Mondal, M. S., Zaman, M. H., Kryston, A., Salehin, M., et al. (2019). "Salinization in large river deltas: Drivers, impacts and socio-hydrological feedbacks," in *Water security*, vol. 6. (Elsevier), 100024. doi: 10.1016/j.wasec.2019.100024

Ralston, D. K., Geyer, W. R., and Lerczal, J. A.. (2008). Subtidal salinity and velocity in the Hudson river estuary: Observations and modeling. *J. Phys. Oceanogr.* 38 (4), 753–770. doi: 10.1175/2007JPO3808.1

Roberts, H. H, Weimer, P., and Slatt, R. M.. (2012). *River deltas, regional geology and tectonics* (Elsevier B.V), 490–511. doi: 10.1016/B978-0-444-53042-4.00017-0

Sámano, M. L., Barcena, J. F., Garcia, A., Gomez, A. G., Alvarez, C., and Revilla, J. A. (2012). Flushing time as a descriptor for heavily modified water bodies classification and management: Application to the huelva harbour. *J. Environ. Manage.* 107, 37–44. doi: 10.1016/j.jenvman.2012.04.022

Sarwar, M. G. M. (2005). *Impacts of Sea level rise on the coastal zone of Bangladesh* ((Masters Programme in environmental science). (Sweden: Lund University).

Savenije, H. H. G. (1993). Predictive model for salt intrusion in estuaries. *J. Hydrol.* 148 (1–4), 203–218. doi: 10.1016/0022-1694(93)90260-G

Savenije, H. H. G. (2005). *Salinity and tides in alluvial estuaries* (Delft University of Technology), 8.

Schiller, R. V., Kourafalou, V. H., Hogan, P., and Walker, N. D. (2011). The dynamics of the mississippi river plume: Impact of topography, wind and offshore forcing on the fate of plume waters. *J. Geophysical Research: Oceans* 116 (6), 1–22. doi: 10.1029/2010JC006883

Schubel, J. R. (1992). Managing freshwater discharge to the San Francisco Bay/Sacramento San Joaquin delta estuary the scientific basis for an estuarine standard. In *Conclusions and recommendations of members of the scientific,policy, and management communities of the bay/delta estuary*. United States Environmental Protection Agency.

Shaha, D. C., Cho, Y. K., Kim, T. W., and Valle-Levinson, A.. (2012). Spatio-temporal variation of flushing time in the sumjin river estuary. *Terrestrial Atmos. Ocean. Sci.* 23 (1), 119–130. doi: 10.3319/TAO.2011.08.22.01(Hy

Shaw, J. B., Mohrig, D., and Whitman, S. K.. (2013). The morphology and evolution of channels on the wax lake delta, Louisiana, USA. *J. Geophys. Res.: Earth Surf.* 118 (3), 1562–1584. doi: 10.1002/jgrf.20123

Sheldon, J. E., and Alber, M. (2006). The calculation of estuarine turnover times using freshwater fraction and tidal prism models: A critical evaluation. *Estuaries Coasts* 29 (1), 133–146. doi: 10.1007/BF02784705

Sheldon, J. E., and Alber, M. (2002). A comparison of residence time calculations using simple compartment models of the altamaha river estuary, georgia. *Estuaries* 25 (68), 1304–1317.

Sherin, V. R. (2020). "Recent salinity intrusion in the Bengal delta: Observations and possible causes," in *Continental shelf research*, vol. 202. (Elsevier Ltd), 104142. doi: 10.1016/j.csr.2020.104142

Sitharam, T. G., Yang, S. Q., Falconer, R., Sivakumar, R., Jones, B., Kolathayar, S., et al. (2020). *Sustainable water resource development using coastal reservoirs*. Matthew Deans Butterworth-Heinemann.

Smedema, L. K., and Shiati, K. (2002). Irrigation and salinity: A perspective review of the salinity hazards of irrigation development in the arid zone. *Irrig. Drain. Syst.* 16 (2), 161–174. doi: 10.1023/A:1016008417327

Spicer, P., Cole, K. L., Huguenard, K., MacDonald, D. G., and Whitney, M.. (2022). Wind effects on near- and midfield mixing in tidally pulsed river plumes. *J. Geophys. Res.: Oceans* 127, e2022JC018462. doi: 10.1029/2022JC018462

Sridevi, B., Sarma, V. V. S. S., Murty, T. V. R., Sadhuram, Y., Reddym, N. P. C., and Vijayakumar, K.. (2015). Variability in stratification and flushing times of the gautami–godavari estuary, India. *J. Earth Syst. Sci.* 124 (5), 993–1003. doi: 10.1007/s12040-015-0594-5

Sun, J., Liu, L., Lin, J., Lin, B., and Zhao, H. (2020). Vertical water renewal in a large estuary and implications for water quality. *Sci. Total Environ.* 710, 1–12. doi: 10.1016/j.scitotenv.2019.135593

Tabarestani, M. K., and Fouladfar, H. (2021). Numerical modeling of salinity changes in the desalination stage of a coastal reservoir. *J. Hydraul* 16 (3), 69–83. doi: 10.30482/JHYD.2021.281280.152110.30482/JHYD.2021.281280.1521

Trieu, T. T. N., and Phong, N. T. (2015). The impact of climate change on salinity intrusion and pangasius (Pangasianodon hypophthalmus) farming in the Mekong delta, Vietnam. *Aquacult. Int.* 23 (2), 523–534. doi: 10.1007/s10499-014-9833-z

Uddin, M., and Haque, A. (2010). Salinity response in southwest coastal region of Bangladesh due to hydraulic and hydrologic parameters. *Int. J. Sustain. Agric. Technol.* 6 (3), 1–7.

Uncles, R. J., and Stephens, J. A. (1996). Salt intrusion in the Tweed estuary. *Estuarine Coast. Shelf Sci.* 43 (3), 271–293. doi: 10.1006/ecss.1996.0070

Valle-Levinson, A., and Wilson, R. E. (1994). Effects of sill processes and tidal forcing on exchange in eastern long island sound. *J. Geophys. Res.* 99 (C6), 12667–12681. doi: 10.1029/94jc00721

Viglione, A., Merz, B., Dung, N. V. D., Parajka, J., Nester, T., and Bloschl, G.. (2016). Attribution of regional flood changes based on scaling fingerprints. *Water Resour. Res.* 52 (7), 5322–5340. doi: 10.1002/2016WR019036

Visser, J. M., Day, J. W., Battaglia, L. L, Shaffer, G. P., and Hester, M. W.. (2012). "Mississippi River Delta Wetlands," in *book:Wetland Habitats of North America Ecology and Conservation Concerns* Edition *1st*, ch.5. D. Batzer and A. Baldwin Editors. University of California Press, 63–74. doi: 10.1525/9780520951419-007

Vogel, R. M., Yaindl, C., and Walter, M.. (2011). Nonstationarity: flood magnification and recurrence reduction factors in the united states. *J. Am. Water Resour. Assoc.* 47 (3), 464–474. doi: 10.1111/j.1752-1688.2011.00541.x

Wang, H., Krauss, K. W., Noe, G. B., Stagg, C. L., Swarzenski, C. M., Duberstein, A. A., et al. (2020). Modeling soil porewater salinity response to drought in tidal freshwater forested wetlands. *J. Geophys. Res.: Biogeosci.* 125 (2). doi: 10.1029/2018JG004996

Wei, X., Schramkowski, P., and Schuttelaars, H. M.. (2016). Salt dynamics in well-mixed estuaries: Importance of advection by tides. *J. Phys. Oceanogr.* 46 (5), 1457–1475. doi: 10.1175/JPO-D-15-0045.1

Wei, X., Kumar, M., and Schuttelaars, H. M.. (2017). Three-dimensional salt dynamics in well-mixed estuaries: Influence of estuarine convergence, Coriolis and bathymetry. *J. Phys. Oceanogr.* 47, 1843–1871. doi: 10.1175/JPO-D-16-0247.1

Weisberg, M. (2007). Three kinds of idealization. *J. Philosophy* 104 (12), 639–659. doi: 10.5840/jphil20071041240

Williams, B. L. (1986). Flushing time calculations for the upper waitemata harbour, new zealand. *New Z. J. Mar. Freshw. Res.* 20 (3), 455–465. doi: 10.1080/00288330.1986.9516165

White, E. D., Meselhe, E., Reed, D., Renfro, A., Snider, N. P., and Wang, Y.. (2019). Mitigating the effects of sea-level rise on estuaries of the Mississippi delta plain using river diversions. *Water* 11 (10), 2028. doi: 10.3390/w11102028

Wong, K. C. (1995). On the relationship between long-term salinity variations and river discharge in the middle reach of the delaware estuary. *J. Geophys. Res.: Oceans* 100 (C10), 20,705–20,713. doi: 10.1029/95JC01406

Yang, Y. C. E., Ray, P. A., Brown, C. M., Khalil, A. F., and Yu, W. H.. (2015). Estimation of flood damage functions for river basin planning: a case study in Bangladesh. *Natural Hazards* 75 (3), 2773–2791. doi: 10.1007/s11069-014-1459-y

Yuan, Y., Avener, M. E., and Horner-Devine, A. R.. (2011). A two-color optical method for determining layer thickness in two interacting buoyant plumes. *Exp. .Fluids* 50, 235–1245. doi: 10.1007/s00348-010-0969-y

Yuan, J. Z., and Wu, C. (2020). "Insights into the design and development of shanghai coastal reservoirs," in *Sustainable water resource development using coastal reservoirs* (Elsevier Inc), 97–110. doi: 10.1016/b978-0-12-818002-0.00006-x

Yue, S., Ouarda, T. B. M., Bobee, B., Legendre, P., and Bruneau, P.. (2002). Approach for describing statistical properties of flood hydrograph. *J. Hydrol. Eng.* 7 (2), 147–153. doi: 10.1061/(ASCE)1084-0699(2002)7:2(147

Zevenbergen, C., et al. (2018). Adaptive delta management: a comparison between the Netherlands and Bangladesh delta program. *Int. J. River Basin Manage. Taylor Francis* 16 (3), 299–305. doi: 10.1080/15715124.2018.1433185

Zhang, H., and Delworth, T. L. (2018). Robustness of anthropogenically forced decadal precipitation changes projected for the 21st century. *Nat. Commun.* doi: 10.1038/s41467-018-03611-3

Zhang, E., Savenije, H. H. G., Wu, H., Kong, Y., and Zhu, J.. (2011). "Analytical solution for salt intrusion in the Yangtze estuary, China," in *Estuarine, coastal and shelf science*, vol. 91. (Elsevier Ltd), 492–501. doi: 10.1016/j.ecss.2010.11.008

Zhang, Q., Gu, X., Singh, V. P., Xiao, M., and Chen, X.. (2015). 'Evaluation of flood frequency under non-stationarity resulting from climate indices and reservoir indices in the East river basin, China. *J. Hydrol.* 527, 565–575. doi: 10.1016/j.jhydrol.2015.05.029

Zhou, X., et al. (2017). "Prospective scenarios of the saltwater intrusion in an estuary under climate change context using Bayesian neural networks," in *Stochastic environmental research and risk assessment*, vol. 31. (Berlin Heidelberg: Springer), 981–991. doi: 10.1007/s00477-017-1399-7

Zimmerman, J. T. F. (1976). Mixing and flushing of tidal embayments in the western dutch wadden sea part i: Distribution of salinity and calculation of mixing time scales. *Netherlands J. Sea Res.* 10 (2), 149–191. doi: 10.1016/0077-7579(76)90013-2

frontiers | Frontiers in Marine Science

TYPE Original Research
PUBLISHED 06 February 2023
DOI 10.3389/fmars.2023.1105112

OPEN ACCESS

EDITED BY
Wei-Bo Chen,
National Science and Technology Center for Disaster Reduction(NCDR), Taiwan

REVIEWED BY
Peter M.J. Herman,
Delft University of Technology, Netherlands
Pankaj Raushan,
Indian Institute of Engineering Science and Technology, Shibpur, India

*CORRESPONDENCE
Sha Lou
lousha@tongji.edu.cn

SPECIALTY SECTION
This article was submitted to Coastal Ocean Processes, a section of the journal Frontiers in Marine Science

RECEIVED 22 November 2022
ACCEPTED 24 January 2023
PUBLISHED 06 February 2023

CITATION
Lou S, Chen X, Zhou S, Ma G, Liu S, Radnaeva LD, Nikitina E and Fedorova IV (2023) Numerical study of sediment suspension affected by rigid cylinders under unidirectional and combined wave–current flows. *Front. Mar. Sci.* 10:1105112. doi: 10.3389/fmars.2023.1105112

Numerical study of sediment suspension affected by rigid cylinders under unidirectional and combined wave–current flows

Sha Lou[1,2]*, Xiaolan Chen[1], Shengyu Zhou[1], Gangfeng Ma[3], Shuguang Liu[1,2], Larisa Dorzhievna Radnaeva[4], Elena Nikitina[4] and Irina Viktorovna Fedorova[5]

[1]Department of Hydraulic Engineering, Tongji University, Shanghai, China, [2]Key Laboratory of Yangtze River Water Environment, Ministry of Education, Tongji University, Shanghai, China, [3]Department of Civil and Environmental Engineering, Old Dominion University, Norfolk, VA, United States, [4]Laboratory of Chemistry of Natural Systems, Baikal Institute of Nature Management of Siberian Branch of the Russian Academy of Sciences, Ulan-Ude, Russia, [5]Institute of Earth Sciences, Saint Petersburg State University, St Petersburg, Russia

Sediment transport modeling for flows with cylinders is very challenging owing to the complicated flow–cylinder–sediment interactions, especially under the combined wave-current flows. In this paper, an improved formulation for incipient sediment suspension considering the effect of cylinder density (i.e., solid volume fraction) is employed to simulate the bottom sediment flux in the flow with cylinders. The proposed model is calibrated and validated using laboratory measurements under unidirectional and combined wave-current flows in previous studies. It is proved that the effects of cylinders on sediment suspension can be accounted for through a modified critical Shields number, and the proposed model is capable of simulating sediment suspension under both unidirectional and combined wave–current flows reasonably well with the average the coefficients of determination and model skills greater than 0.8 and 0.64.

KEYWORDS

sediment suspension, modified critical Shields number, cylinder, unidirectional flows, combined wave–current flows

1 Introduction

In estuarine and coastal areas, various types of flows involving cylinders exist. These cylinders, such as aquatic vegetation in wetlands (mangrove, reed, and seaweed/kelp), masts in aquafarm for laver or oysters, and piles foundations of offshore windfarms, can significantly affect flow structure (Nepf and Vivoni, 2000; Nepf, 2012; Lou et al., 2018), wave propagation (Moller et al., 1999; Mendez and Losada, 2004; Augustin et al., 2009), and turbulence development (Nepf, 1999; Ghisalberti and Nepf, 2002; Neumeier, 2007). The cylinders reduce mean flow and convert mean kinetic energy to turbulent kinetic energy (*TKE*), which have great influence on sediment suspension and transport (Balke et al., 2012; Ros et al., 2014). Furthermore, waves and currents usually coexist in coastal zones. Wave-current interactions play an important role in coastal ocean dynamics and nearshore sediment transport (Van Hoften and Karaki, 1976). With the presence of cylinders, sediment suspension under the combined wave-current flow become more complicated, which makes it more difficult to simulate sediment transport in flow with cylinders.

Field observations indicated that the presence of cylinders reduced resuspension and promoted particle retention, for example, studies in Lake Hiidenvesi (Horppila and Nurminen, 2003) and Lake Taihu (Zhu et al., 2015). On the other hand, laboratory studies provided contrary results and showed that sediment resuspension was enhanced in the flows with cylinders comparing to bare bed condition (Tinoco and Coco, 2016; Tinoco and Coco, 2018; Lou et al., 2022). These contrasting findings reflected the influence of cylinders on the flow at two scales: array- and stem- scales (Zhang and Nepf, 2019). In the field, the expanse of cylinders (e.g. the length of region covered by vegetation in wetlands in the order of hundred meters) can lead to the damping of flow and sediment resuspension in the array-scale. In the laboratory, the cylinders enhance sediment resuspension due to stem-generated turbulence. It is found out that cylinder density significantly affects the incipient motion of the sediment (Tinoco and Coco, 2016; Tinoco and Coco, 2018; Tang et al., 2019; Yang and Nepf, 2019). Although the flow velocity is significantly damped with dense cylinders, the amount of sediment lifted into suspension increases owing to the increasing turbulent kinetic energy under unidirectional currents (Tinoco and Coco, 2016; Yang and Nepf, 2019) and oscillatory flows (Ros et al., 2014; Tang et al., 2019). The incipient velocity of sediment motion decreases within cylinder canopy (Tang et al., 2013; Yang et al., 2016; Tinoco and Coco, 2018).

Although field investigations and experimental studies provide a certain basis for the establishment of numerical models, sediment transport modeling for flows with cylinders is more challenging owing to complicated flow–cylinder–sediment interactions. Sediment suspension determined by the bottom sediment flux was related to the turbulent flow structure altered by cylinders. Lopez and Garcia (1998) established a two-equation turbulence model to determine the mean flow and turbulence structure of open channels through cylinders and used this model to estimate sediment transport processes, assuming that the average sediment deposition near the bed and the entrainment rate were in equilibrium. A three-dimensional turbulence model was proposed by Liu and Shen (2008) by introducing cylinder density and drag force into the control equations of flow in the presence of cylinders, and an empirical relation proposed by Van Rijn (1984) was employed to solve the sediment transport equations in flow affected by the cylinders. With an enhanced Manning's roughness coefficient and cylinder-induced drag force representing the effect of the cylinders on flow, sediment flux was computed with the formula of Van Rijn (1993), disregarding the effect of the cylinders on sediment suspension (Hu et al., 2018). The equilibrium sediment transport rates by Wu's formula (Wu and Wang, 2007) were used for bed load, and the suspended sediment flux was modeled by bed shear stress estimated from mean flow velocity with the cylinder effects implemented by additional terms of the cylinder drag and water volume reduction caused by the cylinders (He et al., 2017). A similar method was used in a sediment transport model established by Ma et al. (2013), in which the sediment flux was computed by bed shear stress estimated from mean flow velocity with cylinder effects implemented by additional terms of the cylinder drag. However, in flow with cylinders, the generation of turbulence in the wakes of cylinders exceeds that associated with bed shear, such that the previously used bare bed sediment transport models based on bed shear stress need to be improved to better describe sediment suspension affected by cylinders.

In our previous work (Lou et al., 2021), a vegetated flow and sediment transport model was developed for investigating flow–cylinder(vegetation)–sediment interactions. In the model, the vegetation-induced turbulence was simulated by an improved k-ϵ turbulence closure, in which shear and stem-scale wake turbulent kinetic energies were solved separately due to the different length scales of turbulence in vegetated flow. It simulated both unidirectional and oscillatory flows as well as turbulence structures reasonably well. However, one of the disadvantages of the model was that it included more coefficients for calibration compared to traditional k-ϵ turbulence closure, which introduced uncertainties to model results and restrained its applications.

In this paper, we propose a modified critical Shields number to account for the effects of cylinders on bottom sediment suspension, which will be implemented into the Non-Hydrostatic WAVE (NHWAVE) model (Ma et al., 2012). Purpose of the proposed model is to simplify the numerical simulation of sediment transport in flow with cylinders. With fewer parameters, the sediment initiation can be identified and simulated, which aims to simplify the numerical simulation of sediment transport in flow with cylinders, especially for the combined wave-current flow. In the proposed model, the modified critical Shields number affected by cylinders is determined by the cylinder features (solid volume fraction of cylinders ϕ and the cylinder induced-drag coefficient) and the bottom drag coefficient, and the traditional k-ϵ turbulence closure with a cylinder-induced turbulence production term including both shear and stem-scale turbulence is adopted. The model will be validated by using the experimental measurements collected in a wave-current flume at Tongji University in our previous study (Chen et al., 2020; Lou et al., 2022) and a dataset presented by Lu (2008). The performance of the model will be evaluated by computing the model skill (M_S), the determination coefficient (R^2) and the Root Mean Square Error (*RMSE*). Effects of cylinder densities on sediment suspension will be analyzed and the interactions between flow–cylinder–sediment will be examined. The main purpose of this paper is to study sediment suspension mechanisms affected by cylinders under both

unidirectional and the combined wave-current flows, and to estimate the accuracy of mathematical descriptions of the bottom sediment flux considering the effects of cylinders on sediment suspension threshold condition.

2 Model formulations

The hydrodynamic and sediment transport model in this study is based on the Non-Hydrostatic WAVE (NHWAVE) model, which was originally developed by Ma et al. (2012). It has been well validated and widely applied to study coastal wave processes, including wave/flow–cylinder–sediment interactions (Ma et al., 2013; Ma et al., 2015; Wu et al., 2016).

2.1 NHWAVE model

The vegetation module in NHWAVE is based on the Volume-averaged and Reynolds-averaged Navier-Stokes equations. The effects of the cylinders on the mean flow were modeled by drag forces in the momentum equations. This treatment has been proven successful in simulating turbulent structures in vegetated flows by other modeling efforts (Sheng et al., 2012; Wu et al., 2016). The governing equations, numerical schemes, and boundary conditions were introduced in Ma et al., 2013; Ma et al. (2012). The drag force is given by

$$F_v = \frac{1}{2} C_D a u_i |u| \tag{1}$$

where C_D is the cylinder drag coefficient, a is the frontal area of cylinders per unit volume, u is the velocity vector.

A nonlinear k–ϵ turbulence model was implemented in the NHWAVE model to simulate turbulent flows. According to Nepf (1999), the large-scale mean kinetic energy is converted to small-scale turbulent kinetic energy in flows with cylinders, and turbulent diffusivity is reduced owing to a downward shift in turbulent-length scale. In the NHWAVE model, these processes were modeled by introducing a cylinder-induced turbulence production term, P_v, in the k–ϵ equations (Ma et al., 2012; Ma et al., 2013). The modified k–ϵ equations are written as

$$\begin{aligned} &\frac{\partial Dk}{\partial t} + \nabla \cdot (Duk) = \nabla \cdot [D(\upsilon + \frac{\upsilon_t}{\sigma_k}) \nabla k] \\ &+ D(P_S + P_b + C_{fk} P_v - \epsilon) \end{aligned} \tag{2}$$

$$\begin{aligned} &\frac{\partial D\epsilon}{\partial t} + \nabla \cdot (Du\epsilon) = \nabla \cdot [D(\upsilon + \frac{\upsilon_t}{\sigma_\epsilon}) \nabla \epsilon] + \\ &\frac{\epsilon}{k} D(C_{1\epsilon}(P_S + C_{3\epsilon} P_b + C_{f\epsilon} P_v) - C_{2\epsilon}\epsilon) \end{aligned} \tag{3}$$

$$P_v = \frac{1}{2} C_D \lambda |u|^3 \tag{4}$$

$$\upsilon_t = C_\mu \frac{k^2}{\epsilon} \tag{5}$$

where k is the turbulence kinetic energy; ϵ is the energy dissipation; D is the total water depth; P_s and P_b are shear and buoyancy productions, respectively; υ_t is the turbulent eddy viscosity and υ is the kinematic water viscosity; σ_k(=1.0), σ_ϵ(=1.3), $C_{1\epsilon}$(=1.44), $C_{2\epsilon}$(=1.92), and C_μ(=0.09) are empirical coefficients (Rodi, 1987); the coefficient $C_{3\epsilon}$ is selected as zero for a stably stratified water column (Snyder and Hsu, 2011); C_{fk}(=1.0) and $C_{f\epsilon}$(=1.33) are drag-related coefficients based on Lopez and Garcia (1998).

2.2 Sediment transport model

To study sediment dynamics in flows with cylinders, suspended sediment concentration was computed from the advection–diffusion equation formulated in σ coordinates in the NHWAVE model (Ma et al., 2015).

$$\begin{aligned} &\frac{\partial DC}{\partial t} + \frac{\partial DuC}{\partial x} + \frac{\partial DvC}{\partial y} + \frac{\partial(\omega - \omega_s)C}{\partial \sigma} = \frac{\partial}{\partial x}[D(\upsilon + \frac{\upsilon_t}{\sigma_h})\frac{\partial C}{\partial x}] \\ &+ \frac{\partial}{\partial y}[D(\upsilon + \frac{\upsilon_t}{\sigma_h})\frac{\partial C}{\partial y}] + \frac{1}{D}\frac{\partial}{\partial \sigma}[(\upsilon + \frac{\upsilon_t}{\sigma_v})\frac{\partial C}{\partial \sigma}] \end{aligned} \tag{6}$$

where C is the suspended sediment concentration; ω_s is the sediment settling velocity; σ_h and σ_v are the horizontal and vertical Schmidt numbers of the sediment, respectively. To solve the sediment transport equation, a no-flux boundary condition was employed at the free surface.

$$(\upsilon + \frac{\upsilon_t}{\sigma_h})\frac{1}{D}\frac{\partial C}{\partial \sigma} + \omega_s C = 0 \tag{7}$$

At the bottom, the mass exchange of the suspended sediment was considered by the erosion and deposition fluxes:

$$(\upsilon + \frac{\upsilon_t}{\sigma_h})\frac{1}{D}\frac{\partial C}{\partial \sigma} + \omega_s C = E - D \tag{8}$$

where E and D are sediment fluxes for erosion and deposition, respectively.

For non-cohesive sediments, a pickup function (Van Rijn, 1984) is typically used to simulate the fluxes, expressed as

$$\begin{aligned} &E - D = 0.00033 \cdot D_{50}^{0.8} \cdot \rho_s \cdot (\tfrac{\rho_s - \rho}{\rho})^{0.6} \cdot \\ &g^{06} \cdot \upsilon^{-0.2} \cdot (\tfrac{\psi - \psi_c}{\psi_c})^{1.5} \end{aligned} \tag{9}$$

where D_{50} is the median grain size, ρ_s is the sediment density, ρ is the water density, ψ is the Shields number given by

$$\psi = \frac{\tau_b}{(\rho_s - \rho) g D_{50}} \tag{10}$$

where τ_b is the bottom shear stress, ψ_c is the critical Shields number for incipient sediment motion.

For the combined wave–current flow, the bottom shear stress τ_b is expressed as τ_b^{wc}, calculated using Eq. (11) considering the nonlinear interactions between waves and currents (Soulsby, 1995; Soulsby, 1997).

$$\frac{\tau_b^{wc}}{\tau_b^c} = 1 + 1.2(\frac{\tau_b^w}{\tau_b^w + \tau_b^c})^{3.2} \tag{11}$$

where f_w is the wave friction coefficient, f_w=1.39$(A/z_0)^{-0.52}$, in which $A = \frac{U_w T}{2\pi}$, $z_0 = \frac{2.5 D_{50}}{30}$, T is the wave period, and U_w is the velocity at the wave boundary layer. τ_b^c is the bottom shear stress under the unidirectional flow, calculated by

$$\tau_b^c = c_d \rho U_c |U_c| \tag{12}$$

where c_d is the bottom friction coefficient, and U_c is the mean velocity near the bottom. τ_b^{wc} is the bottom shear stress under a pure wave condition, computed as

$$\tau_b^w = \frac{1}{2}\rho f_w U_w^2 \tag{13}$$

In a flow without cylinders, the critical Shields number, ψ_c, is considered to be a constant which is related to the sediment characteristics, which can be calculated by

$$\psi_c = 0.15(S^*)^{-0.3} + 0.045\exp[-35(S^*)^{-0.59}] \tag{14}$$

with the dimensionless viscosity $S^* = \frac{\sqrt{[(\rho_s/\rho)-1]gD_{50}^3}}{\mu/\rho}$.

However, it has been reported that the incipient velocity decreases under both unidirectional flows and wave conditions affected by cylinders (Tang et al., 2013; Ros et al., 2014; Tang et al., 2019). The turbulence, instead of mean flow, determines sediment resuspension through arrays of rigid vegetation (Tinoco and Coco, 2016; Yang et al., 2016; Tinoco and Coco, 2018). Hence, the sediment transport models based on bed shear stress developed for bare bed do not work well for flows with cylinders.

Based on experimental measurements, Tinoco and Coco (2016) proposed a function to estimate the critical Shields number for unidirectional flow with cylinders (Eq. 15), which was modified for wave conditions (Eq. 16) in Tinoco and Coco (2018) based on the study in Yang et al. (2016). These functions were obtained under the conditions of vegetation solid volume fraction Φ=0.008-0.079, and stem Reynolds number R_{ed}=200-20000 for unidirectional flow, and wave period T=2.5s, wave height H=0.01–0.10m under wave conditions.

$$\frac{\psi_{c,\phi}}{\psi_{c,0}} = e^{-37\phi} \tag{15}$$

$$\frac{\psi_{c,\phi}}{\psi_{c,0}} = \frac{1}{1 + 0.9\cdot\phi^{2/3}\cdot C_D^{2/3}/c_b} \tag{16}$$

where $\psi_{c,0}$ is the critical Shields number in the flows without cylinders, $\psi_{c,\phi}$ is the modified critical Shields number affected by cylinders, and ϕ is the solid volume fraction of cylinders.

Ratios of obstructed to unobstructed critical Shields values in the flows with cylinders using Eq. 15 and Eq. 16 are displayed in Figure 1. It is shown that the values of $\psi_{c,\phi}/\psi_{c,0}$ are approximately the same when the solid volume fraction ϕ is smaller than 0.03.

To demonstrate the effects of cylinders on sediment suspension, numerical simulations were also carried out using the traditional critical Shield number without cylinders (Eq. 14). The predicted suspended sediment concentrations from the improved model (Eq. 15 and 16) and the traditional model (Eq. 14) under both unidirectional and combined wave–current flows were compared.

2.3 Assessment of model performance

The developed model was validated using the experimental measurements, and the model performance was assessed by calculating the model skill (M_S), the coefficient of determination (R^2) and the Root Mean Square Error ($RMSE$). The model skill (Wilmott, 1981) describes the degree to which the measured deviations about the measured mean correspond to the simulated deviations about the measured mean, as shown in Eq. 17. Perfect agreement between the model results and measurements yields M_S of 1.0 whereas complete disagreement yields M_S of 0.

$$M_S = 1 - \frac{\sum_{i=1}^{I}|X_S - X_M|^2}{\sum_{i=1}^{I}(|X_S - \overline{X_M}| + |X_M - \overline{X_M}|)^2} \tag{17}$$

where X_S and X_M are simulated and measured variables being compared, $\overline{X_M}$ is its sample mean, I is the number of the data.

The coefficient of determination (R^2) is a number that indicates how well the data fit a statistical model (Gao et al., 2018). The coefficient of determination for a linear regression model with one independent variable is given by

$$R^2 = \left[\frac{1}{N}\cdot\frac{\sum_{i=1}^{N}(|X_S - \overline{X_S}|\cdot|X_M - \overline{X_M}|)}{\sigma_{X_S}\cdot\sigma_{X_M}}\right]^2 \tag{18}$$

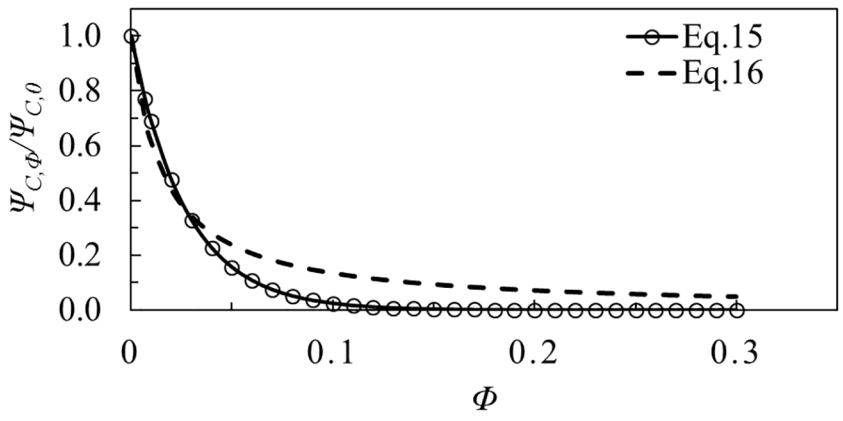

FIGURE 1
Ratios of obstructed to unobstructed critical Shields values in the flow with cylinders.

where σ_{xs} is the standard deviation of X_S, and σ_{X_M} is the standard deviation of X_M. A R^2 of 1 indicates that the regression line perfectly fits the data, while a R^2 of 0 indicates that the line does not fit the data at all.

The root mean square error (*RMSE*), which is a typical metric for measuring the differences between samples and estimators, was also calculated as an additional assessment for the vertically varying density case.

3 Model calibration and validation

To evaluate the performance of NHWAVE with the improved sediment transport model, a number of experimental datasets were chosen for model calibration and validation. Experiments in our previous studies (Chen et al., 2020; Lou et al., 2022) were adopted to calibrate the model, including conditions of unidirectional flow (Test 1) and combined wave-current flows (Test 2-4). Another dataset collected in the experiments of sediment suspension under directional flow affected by rigid submerged cylinders (Lu, 2008) was used to further validate the model, which has also been applied to validate the model in Li et al. (2020). The hydraulic conditions and characteristics of cylinders in these experiments were listed in Tables 1-3. The cylinders were arrayed regularly in the experiments.

To reproduce the vegetated flow in the experiments, the computational domain was discretized by 64 cells in the streamwise direction with intervals of 0.1 m and 50 vertical layers. Periodic boundary conditions were imposed at the streamwise boundaries (Ma et al., 2013). The flow was driven by an external pressure gradient

TABLE 1 Hydrodynamic conditions in experiments conducted by Chen et al. (2020) and Lou et al. (2022) .

Run number	Hydrodynamic state	Hydrodynamic parameters	Water depths
Test 1	Unidirectional currents	Q = 140 L/s	0.8 m
Test 2	Combined wave–current flows	Combination of Test 1 and wave (H = 0.06 m, T = 1.8 s)	0.8 m
Test 3		Combination of Test 1 and wave (H = 0.08 m, T = 1.8 s)	0.8 m
Test 4		Combination of Test 1 and wave (H = 0.10 m, T = 1.8 s)	0.8 m

H: wave height; T: wave period; Q: discharge.

TABLE 2 Cylinder configurations in experiments conducted by Chen et al. (2020) and Lou et al. (2022).

Cases	Diameter d (mm)	Height h_v (m)	Stem number	Density n (stems/m^2)	Solid volume fraction ϕ
Case-a	8	0.4 (uniform heights and vertically uniform density)	806	168	0.008
Case-b			1599	333	0.017
Case-c*		0.2; 0.4; 0.6; 0.8 (four cylinder heights causing the vertically varying density)	369	333 ($0 \le z \le 0.2$) 256 ($0.2 < z \le 0.4$) 166 ($0.6 < z \le 0.8$) 77 ($0.4 < z \le 0.6$)	0.017 ($0 \le z \le 0.2$) 0.013 ($0.2 < z \le 0.4$) 0.008 ($0.4 < z \le 0.6$) 0.004 ($0.6 < z \le 0.8$)
			431		
			430		
			369		

*Total stem number in Case-c is 1599, which is the same with that in Case-b.

TABLE 3 Hydrodynamic conditions and cylinder configurations in experiments conducted by Lu (2008).

Run number	Discharge Q (L/s)	Water depths (m)	Cylinder Diameter d (mm)	Cylinder Height h_v (m)	Density n (stems/m^2)	Solid volume fraction ϕ
C15-1	21.00	0.15	6	0.06	2000	0.023
C15-2	19.07		6	0.06	1000	0.011
C18-1	26.50	0.18	6	0.06	2000	0.019
C18-2	23.83		6	0.06	1000	0.009
C24-1	30.67	0.24	6	0.06	2000	0.014
C24-2	29.55		6	0.06	1000	0.007
C30-1	38.80	0.30	6	0.06	2000	0.011
C30-2	36.42		6	0.06	1000	0.006

determined by the flow condition in the laboratory. The time step was adjusted during the simulation based on the stability restriction. Cylinder-induced bulk drag coefficient C_D is a key parameter for the simulation of flows with cylinders, which is also the main parameter of model calibration. According to laboratory studies, the value of C_D increases with cylinder density and decreases with the increasing stem Reynolds number (Tinoco and Cowen, 2013; Ni, 2014; Lou et al., 2018; Yang and Nepf, 2019), In this study, empirical equations proposed by Tanino and Nepf (2008); Sonnenwald et al. (2019) and Ghisalberti and Nepf (2004) were adopted to estimate this coefficient.

3.1 Calibrations

Datasets in experiments in our previous studies (Chen et al., 2020; Lou et al., 2022) were adopted to calibrate the model, including conditions of unidirectional flow (Test 1) and combined wave-current flows (Test 2-4).

In these simulations, the range of C_D was calculated as 0.3–1.5 using the empirical equations (Ghisalberti and Nepf, 2004; Tanino and Nepf, 2008; Sonnenwald et al., 2019). For sediment simulations, the median grain size of 0.16 mm was used, and the settling velocity ω_s was selected as 0.002 m/s computed by the equation of Soulsby (1997). The critical Shields parameter was taken as 0.03 for flows without cylinders, calculated using the equation in Guo (2002). The modified critical Shields parameters for flows with cylinders were calculated using Eqs. 15 and 16, and the values of 0.02, 0.0145, and 0.02–0.026 were obtained for the sparse (Case-a with uniform cylinder height), dense (Case-b with uniform cylinder height), and vertically varying cylinder density (Case-c with different cylinder heights) cases.

3.1.1 Unidirectional flow (Test 1)

The measured mean flow, *TKE*, and suspended sediment concentration under a unidirectional flow (Test 1) were adopted to validate the established model. Figure 2 shows the comparisons of measured and simulated mean flow velocities affected by cylinders. The data were measured within cylinders by Chen et al. (2020). The simulated results generally agreed with the measurements. The results showed better agreements in Cases-a and b with vertically uniform cylinder density (uniform cylinder heights), with both the model skills and R^2 values larger than 0.95. The simulated mean velocity in Case-a was greater than that in Case-b, in accordance with the measurements. The computed mean velocity in Case-c was relatively lower than the measurement, indicating that the cylinder-induced drag force was larger in the simulation than that in the measurements. In Case-c, the average model skills and R^2 values were relatively low with the values smaller than 0.5, while the average *RMSE* value as an additional assessment was 0.06, which indicated acceptable model accuracy. The simulated results of mean velocities proved that the gradient of mean velocity was much smaller in Case-c with vertically varying cylinder density than that in case with uniform density.

Under a unidirectional flow, the mean velocity was reduced significantly in the cylinder region. Cylinder density significantly affected the mean velocity. The *U* in Case-b with a higher cylinder density was slightly smaller than that in Case-a; the *U* in Case-c with vertically varying cylinder density was higher near the bottom and lower in the upper layer than that in Cases-a and b with uniform density. The gradient of mean velocity in Case-c was much smaller than that in Cases-a and b. In Case-c, some cylinders had a height of the water depth, thereby resulting in a more uniform vertical distribution of the mean velocity. The distributions of mean velocity in all the cases have shown a turbulent boundary-layer profile, which was due to the small canopy drag compared with the bed drag with the cylinder mainly contributing to the bed roughness.

The simulated *TKE* normalized by friction velocity u^* are compared with the measured data in Figure 3, assuming that the lowest grid and measurement points near the bottom fall in the logarithmic velocity profile. Generally, the agreements between simulations and measurements were acceptable in Cases-a and b with

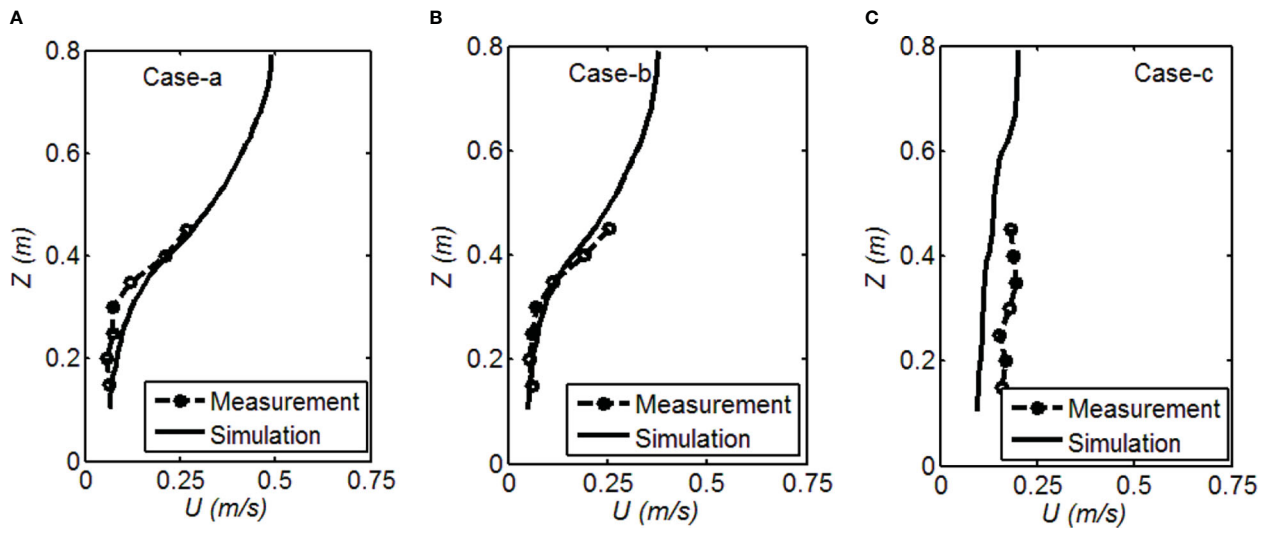

FIGURE 2
Comparisons of measured and simulated mean velocities in Test 1: **(A)** Case-a, **(B)** Case-b, **(C)** Case-c.

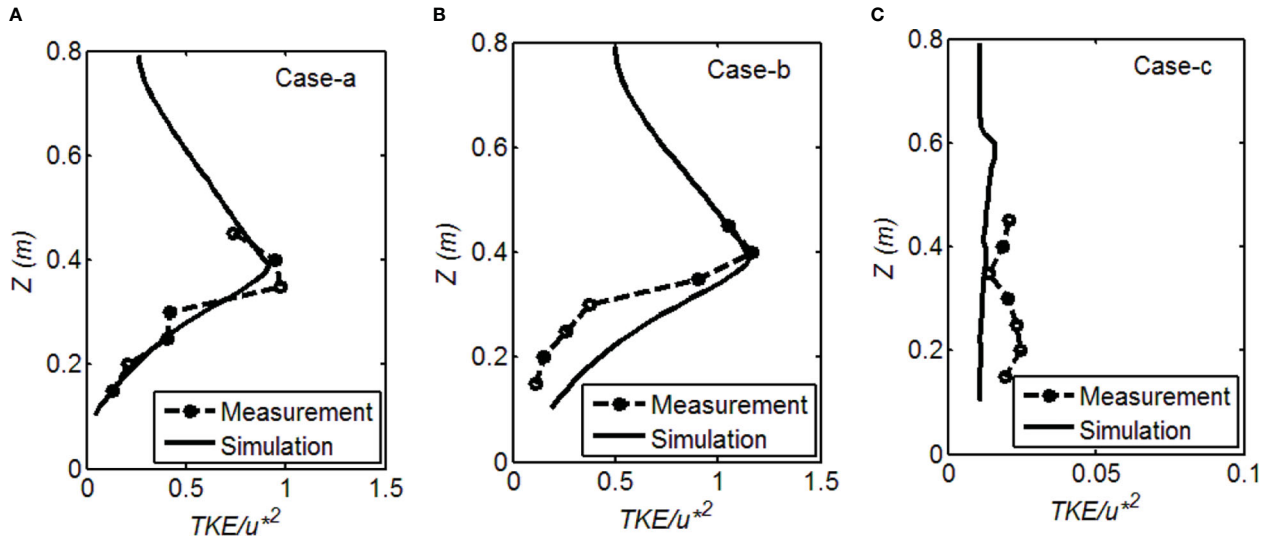

FIGURE 3
Comparisons of measured and simulated TKEs in Test 1: **(A)** Case-a, **(B)** Case-b, **(C)** Case-c.

uniform cylinder density (both the model skills and R^2 values were larger than 0.90). The model could effectively simulate the *TKE* peak around the cylinder top in the cases with uniform cylinder density. Under the unidirectional condition, the gradually increasing of *TKE* from the cylinder top to the bottom was found in both measurement and simulation. The largest values of *TKE* occurred near the cylinder top due to the shear stress caused by the great velocity gradient. Relatively larger deviations occurred in Case-b near the bottom, where the simulations were greater than the measurements. The results implied that cylinder-induced turbulence production was lower in the measurements than that in the simulations in Case-b. In the laboratory experiments, the equipment (ADV) in the measurement was set up among the cylinders, which cannot catch all of the small stem-scale turbulence in the case with dense cylinders. The *TKE* values in Case-c were much lower than those in Cases-a and b. Affected by the vertically varying cylinder density, the turbulence was relatively higher around the layer interfaces under unidirectional currents, i.e. z =0.2, 0.4 and 0.6 m, where cylinder density varies abruptly and strong shear was produced. The simulated vertical profile of *TKE* showed an extremely small gradient in Case-c, consistent with the measurements. However, the simulated *TKE* value was relatively lower than the measured data in Case-c with the model skills and R^2 values lower than 0.3 and *RMSE* of 0.02. In the simulation, the peaks of *TKE* value at z =0.4 and 0.6 m were reproduced, while that at z =0.2 m was absent compared with measured data. In Case-c, turbulence was produced by both the multi-shear layers due to the different cylinder heights and the stem-scale turbulence. The *TKE* value affected by the vertically varying cylinder density was complicate especially near the bottom (z=0.2 m), which could not be well resolved in the simulation.

Under the unidirectional flow (Test 1), the largest values of turbulent kinetic energy (*TKE*) occurred around the cylinder top in cases a and b owing to strong shear turbulence. Affected by the submerged cylinders, the discontinuity in drag appearing at the top of the cylinders generated a region of shear resembling a free shear layer near the top of the canopy, which resulted in higher *TKE* values around the canopy top and relatively lower near the bottom. The maximum value of *TKE* was higher in Case-b than that in Case-a, which was consistent with the results of (Nepf, 1999), that dense cylinders generate stronger shear and greater array-scale turbulence near the cylinder top, but large-scale shear eddies are constrained in the upper layer. In Case-c with vertically varying cylinder density, the vertical distribution of the *TKE* showed more than one reflection point. The varying cylinder heights in Case-c yielded multiple shear layers throughout the water column (0.2–0.6 m), resulting in a higher turbulence near the bottom than that in case with uniform density.

The comparisons of the vertical distributions of measured and simulated sediment concentrations for Cases-a, b and c in Test 1 are shown in Figure 4. The simulation results from the improved and the traditional sediment transport model were both compared with the measured data. The computed suspended sediment concentrations using the improved sediment transport model matched relatively well with the measurements, especially near the bottom layer (z<0.2m). The model skills were 0.85–0.88 and R^2 was 0.8–0.88 in the three cases. The near-bed suspended sediment concentration can directly reflect the level of sediment suspension. The simulated sediment concentrations near bottom were in good agreement with the measurements, which proved that the proposed model can reproduce sediment suspension affected by cylinders based on the modified critical Shield number. However, the suspended sediment concentrations in the upper layer of water column were underestimated in Case-c. In Case-c, the simulated values of mean velocity and *TKE* were relatively smaller than the measurements, resulting in smaller bottom shear stress and diffusivity in the simulation. To better simulate the sediment concentration in the upper layer, the vegetation-induced turbulence including shear and stem-scale wake turbulent kinetic energies should be both considered in the future simulation. Sediment concentrations from the traditional sediment transport model were much lower than the measurements, and there was even no sediment suspension in Case-b and Case-c. Due to the higher cylinder densities in Case-b

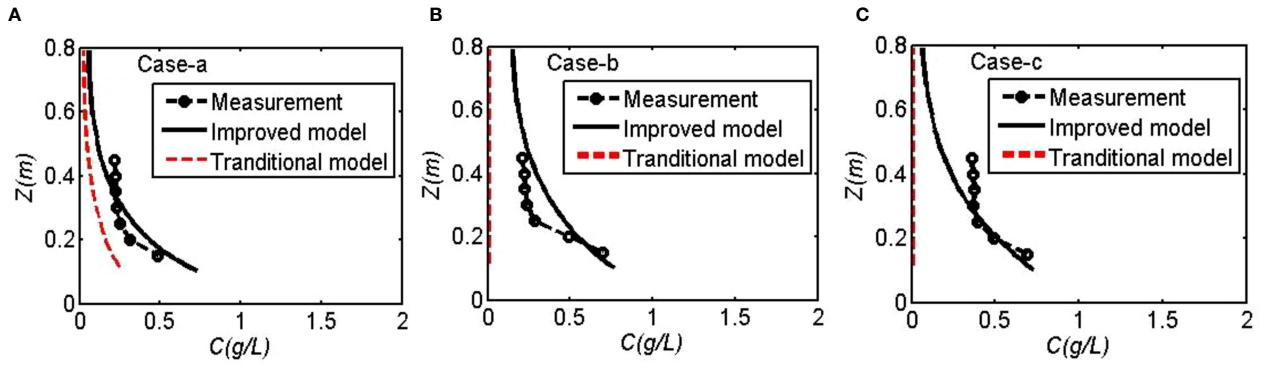

FIGURE 4
Comparisons of measured and simulated sediment concentrations in Test 1: **(A)** Case-a, **(B)** Case-b, **(C)** Case-c.

and Case-c, the flow velocities were damped severely, which resulted in small bed shear stress and the underestimation of sediment suspension using the traditional sediment transport model.

Comparing the sediment concentrations in Case-a with sparse cylinders and Case-b with dense cylinders, it was found that the sediment concentrations increased with the growing cylinder density, especially near the bottom, which agreed well with the results in Tinoco and Coco, 2018; Tinoco and Coco, 2016). It was also proved that the bottom sediment suspension was mainly contributed by the turbulence generated around cylinder stems. In other words, the incipient motion velocity decreased with the increasing cylinder density in flows with cylinders. The sediment concentrations were higher in Case-b and Case-c than that in Case-a under a unidirectional flow (Test 1). Although the solid volume fractions were the same near the bottom in these cases, the vertically varying cylinder density promoted sediment suspension due to higher turbulence near the bottom than that in case with uniform density.

3.1.2 Combined wave-current flows (Tests 2-4)

To further validate the sediment model, experimental data from Tests 2, 3, and 4 were used to simulate sediment suspension in combined wave-current flows. Figures 5–7 show that the computed suspended sediment concentrations using the improved sediment transport model agreed with the measurements near the bottom, while some deviations appeared in the upper layer, where the simulated sediment concentrations were smaller than the measured data. The model skills were 0.83–0.85, 0.66–0.88, and 0.54–0.73 in Tests 2, 3, and 4, respectively (Table 4). The R^2 values were 0.84–0.88, 0.84–0.88, and 0.84–0.89 in Tests 2, 3, and 4, respectively (Table 4). The sediment concentration increased gradually with the growing wave height. Higher wave height induced larger bed shear stress, which enhanced bottom sediment flux and sediment suspension. More suspended sediment was kept stay in the upper layer by the relatively larger turbulent kinetic energy due to higher wave height. Using the modified Shields number given in Eqs. 15 and 16, the model could predict sediment suspension near bottom under combined wave–current flows with a certain accuracy. Due to the similar reason as in Test 1, the suspended sediment concentrations in the upper layer of water column were also underestimated in the combined wave-current flows, especially in Case-c. Affected by cylinders with vertically varying density, the sediment simulation was more difficult due to the complicate turbulence in both canopy- and stem- scale. On the contrary, the sediment suspension was significantly underestimated using the traditional sediment transport model. It is necessary to consider the cylinder effects on the threshold condition of sediment suspension in the flows with cylinders.

Comparing the results in Cases-a and b, it was clear that the suspended sediment concentration increased with cylinder density, indicative of the effects of cylinders on suspended sediment transport in stem scale. Although the stem numbers were the same in Case-b and Case-c, the sediment distributions were slightly different. In Case-

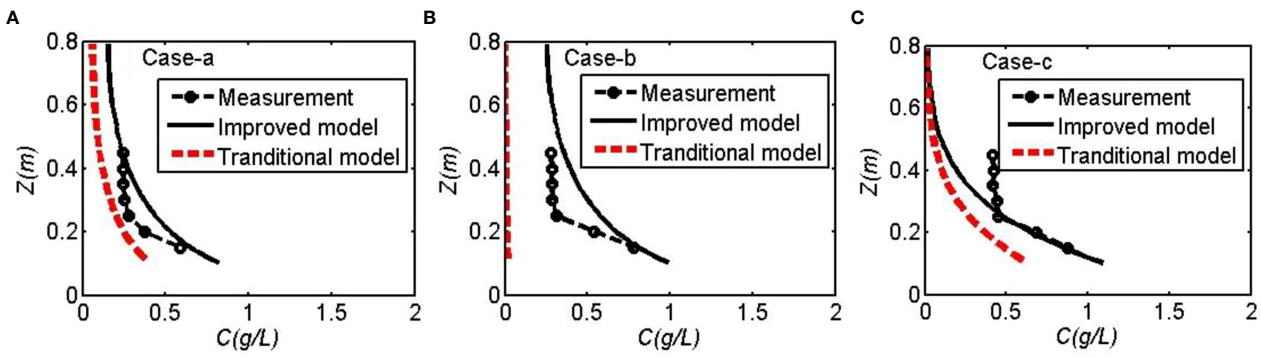

FIGURE 5
Measured and simulated sediment concentrations in Test 2: **(A)** Case-a, **(B)** Case-b, **(C)** Case-c.

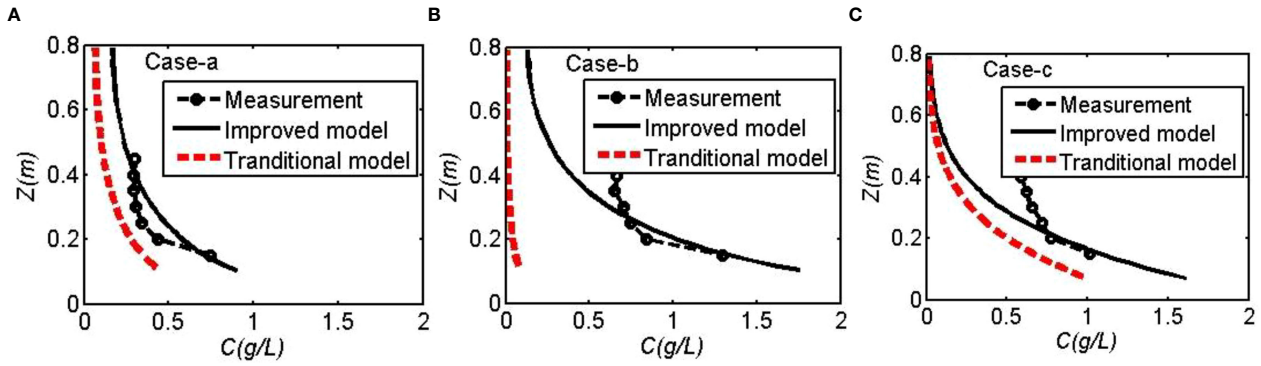

FIGURE 6
Measured and simulated sediment concentrations in Test 3: **(A)** Case-a, **(B)** Case-b, **(C)** Case-c.

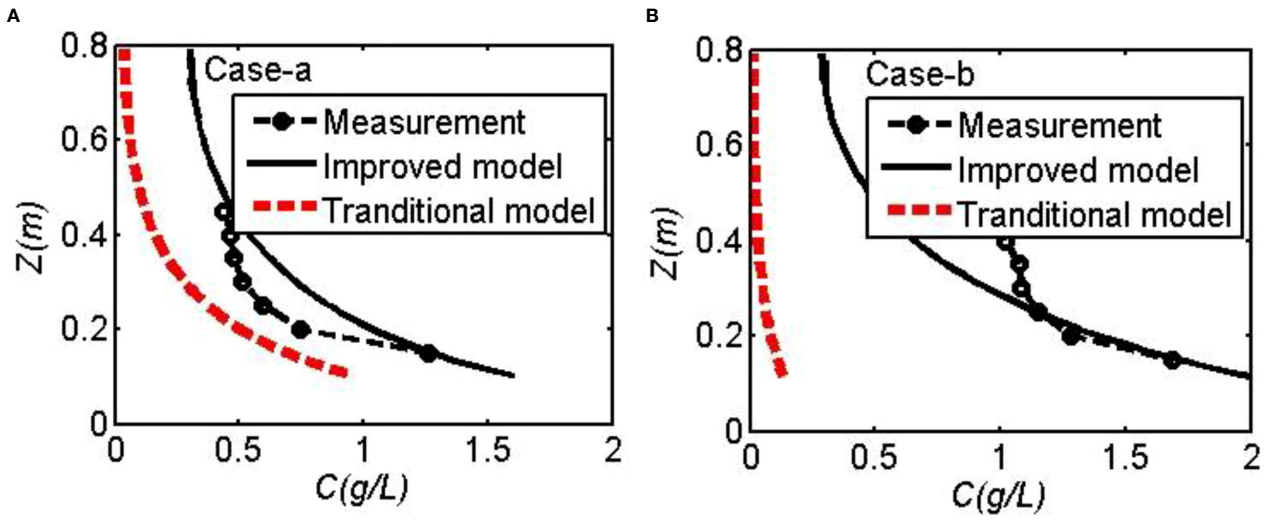

FIGURE 7
Measured and simulated sediment concentrations in Test 4: **(A)** Case-a, **(B)** Case-b.

TABLE 4 Accuracy of model calibrations and validations.

Calibrations	With uniform cylinder density		With vertically varying cylinder density		
	R^2	M_S	R^2	M_S	*RMSE*
Test 1	0.82-0.97	0.88-0.97	0.30-0.80	0.20-0.88	0.02-0.08
Test 2	0.84-0.87	0.83-0.96	0.88	0.88	0.15
Test 3	0.84-0.89	0.65-0.92	0.88	0.87	0.17
Test 4	0.84-0.89	0.54-0.73	–	–	–

Validations	With uniform cylinder density	
	R^2	M_S
C15-1	0.93-0.97	0.93-0.98
C15-2	0.92-0.98	0.94-0.98
C18-1	0.93-0.98	0.97-0.98
C18-2	0.95-0.99	0.95-0.98
C24-1	0.97-0.98	0.95-0.98
C24-2	0.97-0.99	0.88-0.98
C30-1	0.96-0.98	0.91-0.98
C30-2	0.96-0.99	0.68-0.98

10.3389/fmars.2023.1105112

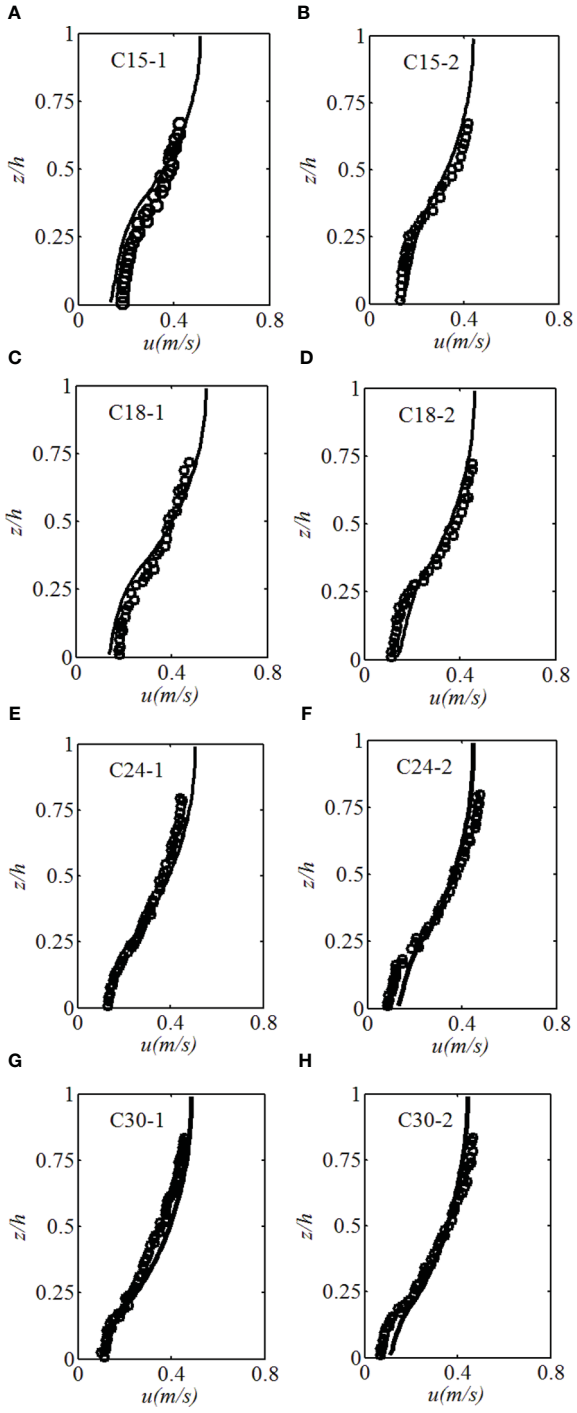

FIGURE 8
Comparisons of measured and simulated mean velocities in tests carried out by Lu (2008): **(A)** C15-1, **(B)** C15-2, **(C)** C18-1, **(D)** C18-2, **(E)** C24-1, **(F)** C24-2, **(G)** C30-1, **(H)** C30-2.

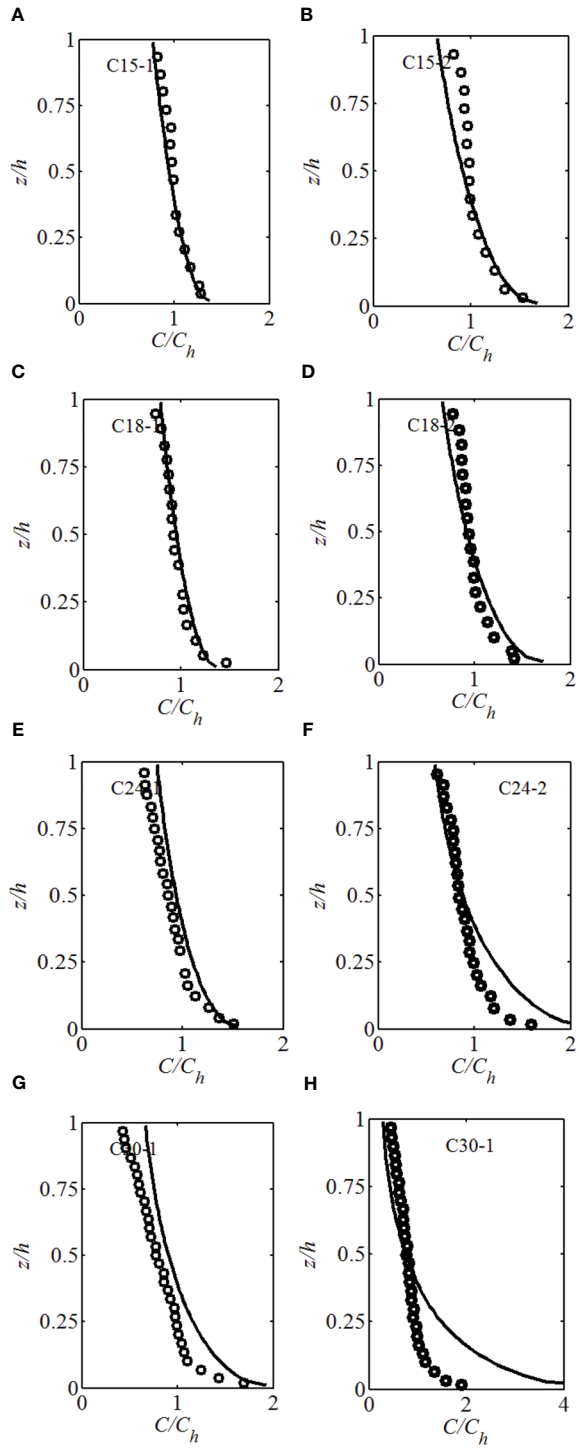

FIGURE 9
Comparisons of measured and simulated sediment concentrations normalized by the concentrations at cylinder top (C_h) in tests carried out by Lu (2008): **(A)** C15-1, **(B)** C15-2, **(C)** C18-1, **(D)** C18-2, **(E)** C24-1, **(F)** C24-2, **(G)** C30-1, **(H)** C30-2.

c, which was affected by vertically varying cylinder density, the array-scale turbulence caused by both the multi-shear layers and stem-scale turbulence affected sediment suspension. The imposed waves increased sediment suspension compared to the results under different hydrodynamic conditions. The co-occurring waves greatly enhanced bottom shear stress and promoted sediment suspension, and the sediment concentration was found to be increased with the growing wave height, especially near the bottom. In the upper layer (z>0.2m), there were clear deviations between the measured and simulated data. The sediment concentration near the bottom was mainly controlled by the bottom sediment flux, while it was determined by turbulent diffusivity in the upper layer.

3.2 Validations

The proposed model was further verified using another experimental dataset by Lu (2008), which has also been applied to validate the model in Li et al. (2020). The material of sediment particles used in the experiments (Lu, 2008) was plastic with the median grain size of 0.217 mm and sediment density of 1.082 g/cm^3. The C_D values were 0.6–0.7 in the simulations according to the empirical equations (Lou et al., 2021). The settling velocity ω_s was 0.0047 m/s based on the experimental measurements (Lu, 2008; Li et al., 2020). The critical Shields parameter was calculated as 0.035 for flows without cylinder using the equation in Guo (2002). The modified critical Shields parameters for flows with cylinders were in the range of 0.02-0.03 calculated using Eq. (15).

To validate the proposed model, model results were compared with experimental datasets in 8 tests (Table 3). Figure 8 shows the comparisons of measured and simulated mean velocities. There was a good correlation between measured and predicted values with both the model skills and R^2 values larger than 0.93 (Table 4). Deviations between model results and experimental data were found at z/h<0.25 in tests C24-2 and at z/h<0.2 in C30-2. Larger values of flow velocity in the simulations were caused by the underestimation of C_D.

Figure 9 presents the comparisons of measured and simulated sediment concentrations normalized by the concentration at the cylinder height (C_h). The simulated results matched with the measured data in tests C15-1, C15-2, C18-1 and C18-2 with the averaged model skill and R^2 value of 0.96 and 0.94. Relatively larger deviations occurred in tests C24-1 (model skill of 0.95) and C30-1 (model skill of 0.91), while obvious disagreements were found in C24-2 (model skill of 0.88) and C30-2 (model skill of 0.68). The simulated concentration was greater than the measured data especially near the bottom, which was greatly affect by the sediment suspension processes. In tests C24-1, C24-2, C30-1 and C30-2, the cylinder density was relatively low. The cylinder densities (ϕ) in tests C24-2 and C30-2 were both less than 0.01 (0.006 and 0.007, respectively). It was found that the proposed sediment transport model was less accurate in cases with small cylinder density (ϕ<0.01).

4 Rationale and limitations of the proposed model

The traditional sediment transport model for bare bed (Eq. 14) without the consideration of cylinders was modified to reproduce the processes of sediment suspension affected by cylinders. Sediment flux near bed was calculated based on a modified critical Shields number due to the presence of cylinders in the improved model (Eqs. 15 and 16). This improvement allowed to capture the strong influence of cylinders on sediment suspension due to the cylinder induced turbulence. This proposed model can be simply used to simulate sediment suspension affected by cylinders in both unidirectional and the combined wave-current flows under similar conditions as the Eqs. 15 and 16 deduced. However, it was found from the model verifications that better agreements between simulations and measurements were observed in cases with uniform density cylinders. Sediment suspension affected by vertically varying density cylinders should be further studied considering the combined influences of shear and stem-scale wake turbulent kinetic energies.

5 Conclusions

Numerical simulations on sediment suspension affected by cylinders under unidirectional and combined wave–current flows were presented. A sediment transport model with a modified critical Shields number considering cylinder density (solid volume fraction ϕ) proposed by Tinoco and Coco (2016) was employed to simulate sediment suspension in the flows with cylinders. Results demonstrated that the improved model could reasonably reproduce sediment suspension in the flows with cylinders, while the sediment transport model with the traditional critical Shields number failed to capture sediment suspension in the cylinder canopy. Numerical simulations showed that denser cylinders and larger wave heights resulted in stronger sediment suspensions. The stem-scale turbulence induced by cylinders and enhanced bed shear stress by waves greatly promoted sediment suspension. Flow–cylinder–sediment interactions are complex and require more investigations, and the proposed sediment transport model should be further validated using field observations.

Data availability statement

The raw data supporting the conclusions of this article will be made available by the authors, without undue reservation.

Author contributions

SL: Conceptualization, Methodology, Writing – original draft, Funding acquisition. XC: Conceptualization, Methodology, Data analysis. SZ: Conceptualization, Methodology, Editing and analysis. GM: Writing – review and editing. SLi: Conceptualization, Project administration. LR: Formula derivation and theoretical analysis. EN: Formula derivation and theoretical analysis, Formal analysis. IF: Conceptualization, Writing – review and editing. All authors contributed to the article and approved the submitted version.

Funding

This work was sponsored by the National Natural Science Foundation of China (42072281), Shanghai Science and Technology Innovation Action Plan (20230742500, 22ZR1464200, 22230712900), the Fundamental Research Funds for the Central Universities (22120210576), and Top Discipline Plan of Shanghai Universities-Class I (2022-3-YB-03).

Conflict of interest

The authors declare that the research was conducted in the absence of any commercial or financial relationships that could be construed as a potential conflict of interest.

Publisher's note

References

Augustin, L. N., Irish, J. L., and Lynett, P. (2009). Laboratory and numerical studies of wave damping by emergent and near-emergent wetland vegetation. *Coast. Eng.* 56 (3), 332–340. doi: 10.1016/j.coastaleng.2008.09.004

Balke, T., Klaassen, P. C., Garbutt, A., van der Wal, D., Herman, P. M. J., and Bouma, T. J. (2012). Conditional outcome of ecosystem engineering: A case study on tussocks of the salt marsh pioneer spartina anglica. *Geomorphology* 153, 232–238. doi: 10.1016/j.geomorph.2012.03.002

Chen, M., Lou, S., Liu, S. G., Ma, G. F., Liu, H. Z., Zhong, G. H., et al. (2020). Velocity and turbulence affected by submerged rigid vegetation under waves, currents and combined wave-current flows. *Coast. Eng.* 159, 103727. doi: 10.1016/j.coastaleng.2020.103727

Gao, T., Wang, Y., Pang, Y., Chen, Q., and Tang, Y. (2018). A time-efficient CFD approach for hydrodynamic coefficient determination and model simplification of submarine. *Ocean Eng.* 154, 16–26. doi: 10.1016/j.oceaneng.2018.02.003

Ghisalberti, M., and Nepf, H. M. (2002). Mixing layers and coherent structures in vegetated aquatic flows. *J. Geophysical Research-Oceans* 107 (C2), 3-1-3-11. doi: 10.1029/2001JC000871

Ghisalberti, M., and Nepf, H. M. (2004). The limited growth of vegetated shear layers. *Water Resour. Res.* 40, (7), 3-1-3-11. doi: 10.1029/2003WR002776

Guo, J. K. (2002). Hunter rouse and shields diagram. *Adv. Hydraulic Water Eng.* 1-2, 1096–1098. doi: 10.1142/9789812776969_0200

He, Z., Wu, T., Weng, H., Hu, P., and Wu, G. (2017). Numerical simulation of dam-break flow and bed change considering the vegetation effects. *Int. J. Sediment Res.* 32 (1), 105–120. doi: 10.1016/j.ijsrc.2015.04.004

Horppila, J., and Nurminen, L. (2003). Effects of submerged macrophytes on sediment resuspension and internal phosphorus loading in lake hiidenvesi (southern Finland). *Water Res.* 37 (18), 4468–4474. doi: 10.1016/S0043-1354(03)00405-6

Hu, K., Chen, Q., Wang, H., Hartig, E. K., and Orton, P. M. (2018). Numerical modeling of salt marsh morphological change induced by hurricane sandy. *Coast. Eng.* 132, 63–81. doi: 10.1016/j.coastaleng.2017.11.001

Liu, C., and Shen, Y. M. (2008). Flow structure and sediment transport with impacts of aquatic vegetation. *J. Hydrodynamics* 20 (4), 461–468. doi: 10.1016/S1001-6058(08)60081-5

Li, D., Yang, Z., Zhu, Z., Guo, M., Gao, W., and Sun, Z. (2020). Estimating the distribution of suspended sediment concentration in submerged vegetation flow based on gravitational theory. *J. Hydrology* 587, 124921. doi: 10.1016/j.jhydrol.2020.124921

Lopez, F., and Garcia, M. (1998). Open-channel flow through simulated vegetation: Suspended sediment transport modeling. *Water Resour. Res.* 34 (9), 2341–2352. doi: 10.1029/98WR01922

Lou, S., Chen, M., Ma, G., Liu, S., and Wang, H. (2022). Sediment suspension affected by submerged rigid vegetation under waves, currents and combined wave–current flows. *Coast. Eng.* 173, 104082. doi: 10.1016/j.coastaleng.2022.104082

Lou, S., Chen, M., Ma, G., Liu, S., and Zhong, G. (2018). Laboratory study of the effect of vertically varying vegetation density on waves, currents and wave-current interactions. *Appl. Ocean Res.* 79, 74–87. doi: 10.1016/j.apor.2018.07.012

Lou, S., Chen, M., Ma, G., Liu, S., and Zhong, G. (2021). Modelling of stem-scale turbulence and sediment suspension in vegetated flow. *J. Hydraulic Res.* 59, 355–377 doi: 10.1080/00221686.2020.1780491

Lu, S. (2008). *Experimental study on distribution law of suspended sediment in water flow of rigid plants (in Chinese)* (China: Hohai University). doi: 10.7666/d.y1268411

Ma, G., Han, Y., Niroomandi, A., Lou, S., and Liu, S. (2015). Numerical study of sediment transport on a tidal flat with a patch of vegetation. *Ocean Dynamics* 65 (2), 203–222. doi: 10.1007/s10236-014-0804-8

Ma, G., Kirby, J. T., Su, S., Figlus, J., and Shi, F. (2013). Numerical study of turbulence and wave damping induced by vegetation canopies. *Coast. Eng.* 80, 68–78. doi: 10.1016/j.coastaleng.2013.05.007

Ma, G., Shi, F., and Kirby, J. T. (2012). Shock-capturing non-hydrostatic model for fully dispersive surface wave processes. *Ocean Model.* 43-44, 22–35. doi: 10.1016/j.ocemod.2011.12.002

Mendez, F. J., and Losada, I. J. (2004). An empirical model to estimate the propagation of random breaking and nonbreaking waves over vegetation fields. *Coast. Eng.* 51 (2), 103–118. doi: 10.1016/j.coastaleng.2003.11.003

Moller, I., Spencer, T., French, J. R., Leggett, D. J., and Dixon, M. (1999). Wave transformation over salt marshes: A field and numerical modelling study from north Norfolk, England. *Estuar. Coast. Shelf Sci.* 49 (3), 411–426. doi: 10.1006/ecss.1999.0509

Nepf, H. M. (1999). Drag, turbulence, and diffusion in flow through emergent vegetation. *Water Resour. Res.* 35 (2), 479–489. doi: 10.1029/1998WR900069

Nepf, H. M. (2012). Flow and transport in regions with aquatic vegetation. *Annu. Rev. Fluid Mechanics* 44, 123–142. doi: 10.1146/annurev-fluid-120710-101048

Nepf, H. M., and Vivoni, E. R. (2000). Flow structure in depth-limited, vegetated flow. *J. Geophysical Research-Oceans* 105 (C12), 28547–28557. doi: 10.1029/2000JC900145

Neumeier, U. (2007). Velocity and turbulence variations at the edge of saltmarshes. *Continental Shelf Res.* 27 (8), 1046–1059. doi: 10.1016/j.csr.2005.07.009

Ni, Y. (2014). *Laboratory investigations on the drag coefficient of cylinder subjected to wave motion* (The Netherlands: Master thesis from Delft University of Technology). 10.2001.

Rodi, W. (1987). Examples of calculation methods for flow and mixing in stratified fluids. *J. Geophysical Research-Oceans* 92 (C5), 5305–5328. doi: 10.1029/JC092iC05p05305

Ros, A., Colomer, J., Serra, T., Pujol, D., Soler, M., and Casamitjana, X. (2014). Experimental observations on sediment resuspension within submerged model canopies under oscillatory flow. *Continental Shelf Res.* 91, 220–231. doi: 10.1016/j.csr.2014.10.004

Sheng, Y. P., Lapetina, A., and Ma, G. (2012). The reduction of storm surge by vegetation canopies: Three-dimensional simulations. *Geophysical Res. Lett.* 39, L20601. doi: 10.1029/2012GL053577

Snyder, P. J., and Hsu, T. J. (2011). A numerical investigation of convective sedimentation. *J. Geophysical Research-Oceans* 116, C09024. doi: 10.1029/2010JC006792

Sonnenwald, F., Stovin, V., and Guymer, I. (2019). Estimating drag coefficient for arrays of rigid cylinders representing emergent vegetation. *J. Hydraulic Res.* 57 (4), 591–597. doi: 10.1080/00221686.2018.1494050

Soulsby, R. L. (1995). *Bed shear-stresses due to combined waves and currents, section 4.5 in advances in coastal, morphodynamics*. Ed. M. J. F. Stive (Delft: Delft Hydraulics).

Soulsby, R. L. (1997). *Dynamics of marine sands* (Thomas Telford, London: A manual for practical applications).

Tang, C., Lei, J., and Nepf, H. M. (2019). Impact of vegetation-generated turbulence on the critical, near-bed, wave-velocity for sediment resuspension. *Water Resour. Res.* 55 (7), 5904–5917. doi: 10.1029/2018WR024335

Tang, H., Wang, H., Liang, D. F., Lv, S. Q., and Yan, J. (2013). Incipient motion of sediment in the presence of emergent rigid vegetation. *J. Hydro-environment Res.* 7, 202–208. doi: 10.1016/j.jher.2012.11.002

Tanino, Y., and Nepf, H. M. (2008). Laboratory investigation of mean drag in a random array of rigid, emergent cylinders. *J. Hydraulic Eng.* 134 (1), 34–41. doi: 10.1061/(ASCE)0733-9429(2008)134:1(34)

Tinoco, R. O., and Coco, G. (2016). A laboratory study on sediment resuspension within arrays of rigid cylinders. *Adv. Water Resour.* 92, 1–9. doi: 10.1016/j.advwatres.2016.04.003

Tinoco, R. O., and Coco, G. (2018). Turbulence as the main driver of resuspension in oscillatory flow through vegetation. *J. Geophysical Research-Earth Surface* 123 (5), 891–904. doi: 10.1002/2017JF004504

Tinoco, R. O., and Cowen, E. A. (2013). The direct and indirect measurement of boundary stress and drag on individual and complex arrays of elements. *Experiments fluids* 54 (4), 1509–1522. doi: 10.1007/s00348-013-1509-3

Van Hoften, J. D. A., and Karaki, S. (1976). Interaction of waves and a turbulent current. *Proc. Int. Conf. Coast. Eng. Proceedings of the 15th International Conference on Coastal Engineering ASCE New York*, 404–422. doi: 10.9753/icce.v15.22

Van Rijn, L. C. (1984). Sediment transport, part II: Suspended load transport. *J. Hydraulic Engineering-ASCE* 110 (11), 1613–1641. doi: 10.1061/(ASCE)0733-9429(1984)110:11(1613)

Van Rijn, L. C. (1993). *Principles of sediment transport in rivers, estuaries, and coastal seas* (The Netherlands: Aqua Publications).

Wilmott, C. J. (1981). On the validation of models. *Phys. Geogr.* 2 (2), 184–194. doi: 10.1080/02723646.1981.10642213

Wu, W., Ma, G., and Cox, D. T. (2016). Modeling wave attenuation induced by the vertical density variations of vegetation. *Coast. Eng.* 112, 17–27. doi: 10.1016/j.coastaleng.2016.02.004

Wu, W., and Wang, S. S. Y. (2007). One-dimensional modeling of dam-break flow over movable beds. *J. Hydraulic Eng.* 133 (1), 48–58. doi: 10.1061/(ASCE)0733-9429(2007)133:1(48)

Yang, J. Q., Chung, H., and Nepf, H. M. (2016). The onset of sediment transport in vegetated channels predicted by turbulent kinetic energy. *Geophys. Res. Lett.* 43, 11,261–11,268. doi: 10.1002/2016GL071092

Yang, J. Q., and Nepf, H. M. (2019). Impact of vegetation on bed load transport rate and bedform characteristics. *Water Resour. Res.* 55 (7), 6109–6124. doi: 10.1029/2018WR024404

Zhang, Y., and Nepf, H. (2019). Wave-driven sediment resuspension within a model eelgrass meadow. *J. Geophysical Research: Earth Surface* 124, 1035–1053. doi: 10.1029/2018JF004984

Zhu, M., Zhu, G., Nurminen, L., Wu, T., Deng, J., Zhang, Y., et al. (2015). The influence of macrophytes on sediment resuspension and the effect of associated nutrients in a shallow and large lake. (Lake Taihu, China) *PloS One* 10 (6), e0127915. doi: 10.1371/journal.pone.0127915

frontiers | Frontiers in Marine Science

TYPE Original Research
PUBLISHED 17 February 2023
DOI 10.3389/fmars.2023.1121833

OPEN ACCESS

EDITED BY
Sha Lou,
Tongji University, China

REVIEWED BY
Guoxiang Wu,
Ocean University of China, China
Fan Xu,
East China Normal University, China

*CORRESPONDENCE
Zhenshan Xu
zsxu2006@hhu.edu.cn

SPECIALTY SECTION
This article was submitted to Coastal Ocean Processes, a section of the journal Frontiers in Marine Science

RECEIVED 12 December 2022
ACCEPTED 06 January 2023
PUBLISHED 17 February 2023

CITATION
Xu Z, Xu C, Wang G, Zhang J and Chen Y (2023) Laboratory study on movement characteristics of a river plume using particle image velocimetry. *Front. Mar. Sci.* 10:1121833. doi: 10.3389/fmars.2023.1121833

Laboratory study on movement characteristics of a river plume using particle image velocimetry

Zhenshan Xu[1]*, Chiyuan Xu[1], Gang Wang[2], Jiabo Zhang[2] and Yongping Chen[1]

[1]College of Harbor, Coastal and Offshore Engineering, Hohai University, Nanjing, Jiangsu, China, [2]Marine Ecological Restoration and Smart Ocean Engineering Research Center of Hebei Province, Marine Ceological Resources Survey Center of Hebei Province, Qinhuangdao, Hebei, China

Rivers are important passages for land-based materials transported to the sea, such as fresh water, sediment, pollutants, and nutrients. River discharge with land-based materials will form a river plume with a buoyancy flow. The river plume is subject to the interaction between nearshore runoff with seawater. In this study, the movement characteristics of the river plume are investigated based on particle image velocimetry (PIV) and the dye tracing method. It is found that the change of flow rate and environmental water density will shape the river plume pattern in both the plan view and the side view. The combined effect of flow rate and environmental water density could be described by the Froude number. The river plume has a free surface in the x-z plane and the horizontal velocity of the plume can be fitted with a 1/2 Gaussian distribution curve. The change of flow rate has little effect on the type of plume thickness curve, while the increase of environmental water density will change the thickness curve type of the river plume. The stable thickness of the river plume increases with the increase of the Froude number. The maximum value of turbulent kinetic energy is located in the middle layer, and the increase of the flow rate or the density difference leads to the increase in the turbulent kinetic energy.

KEYWORDS

river plume, dye tracing, particle image velocimetry, flow field, turbulent kinetic energy

1 Introduction

Rivers are important passages for land-based materials transported to the sea. Lots of fresh water, sediment, pollutants, and nutrients are discharged into the adjacent sea area through estuaries. Land-based materials will directly affect the near-shore water environment and the aquatic ecological conditions. The impact area and the impact extent of land-based materials carried by rivers are primarily affected by the hydrodynamics of the river discharged into the sea. From the perspective of coastal environmental hydraulics, the discharge of rivers with land-based materials will form a river plume with a buoyancy flow. The river plume is the interaction between the nearshore runoff with the seawater (Cameron and Pritchard, 1963).

River plume has several characteristics that distinguishes it from pipe flow. The spatial scale of a river plume is much larger than that of a pipe flow. The river plume has a free surface and will move above the ambient water due to buoyancy. Similar to the jet or plume flow formed *via* a pipe, the movement and transport of river plume is driven by the momentum of the river and the dynamic conditions of the environmental water. Therefore, there are two main types of factors affecting the mixing and transport of river plume. One is the parameters related to the river plume itself, such as the flow rate, the estuary width, and the angle between river plume and coastline. The other is the parameters related to the environmental water, such as the water depth, the tidal current, and the wave. Due to the huge kinetic energy contained in the runoff, an interface of the upper freshwater layer and the lower salt water layer is formed. The interface shear is quite strong, resulting in the lower low-momentum and high-salinity water being swept and mixed by the upper flow (Garvine, 1975). At the same time, the various substances carried by the runoff, especially the pollutants and nutrients suspended in it, are also mixed and diluted by the mixing of freshwater with salt water.

Over the past decades, many researchers have conducted various studies on the river plume and analyzed the salinity change, the front structure, and dynamic process affected by it through field measurement data and the numerical simulation method. For example, Lentz (2004) developed a scale analysis theory to distinguish the features related to the river plume such as flow type, structure, and propagation velocity. Horner-Devine et al., (2009) provides a conceptual summary of the interaction between recirculated buoyancy flow and tides by cruise data. The tide modifies the structure of the plume in the region near the river mouth. The tidal plume flows over the top of the re-circulating plume and is typically bounded by strong fronts that may penetrate well below the re-circulating plume water and eventually spawn internal waves that mix the re-circulating plume further. In addition to the tide, the dynamic action of environmental fluid also includes wind and wave. The influence mechanism of wind on the mixing of estuarine plumes is different from that of tidal current. The wind increases the turbulence intensity on the surface of the flow, thereby enhancing the mixing effect of river plumes and ambient fluid. The wind also generates wind-driven flow on the surface of the water, affecting the movement track of river plumes (Nezlin and DiGiacomo, 2005; Feddersen et al., 2016; Rijnsburger et al., 2018; Qu and Hetland 2019). The impact of waves on river plumes is mainly that the frontal incoming waves increase the broadening of river plumes (Nardin et al., 2013).

However, the field observation of a river plume has certain limitations, which cannot accurately realize the motion observation of all water masses within a certain range. Therefore, laboratory experiments are required as a supplement to conduct more targeted research on the structure and movement characteristics of a river plume. Yuan et al. (2011, Yuan and Horner-Devine 2013) compared the river plume in the laboratory with and without lateral limits and found that lateral spreading dramatically modifies the plume structure. The spreading plume layer consists of approximately linear density and velocity profiles that extend to the surface, whereas the channelized plume profiles are uniform near the surface. Yuan et al. (2018) studied the influence of periodically changing flow on coastal buoyancy flow through the laboratory rotating platform. It was found that the bulge geometry oscillates between a circular plume structure that extends mainly in the offshore direction, and a compressed plume structure that extends mainly in the alongshore direction. The oscillations result in periodic variations in the width and depth of the bulge and the incidence angle formed where the bulge flow re-attaches with the coastal wall.

Despite meaningful results from previous research, laboratory investigations of river plume are still insufficient. The effect of the buoyancy and the flow rate on the movement characteristics of the river plume has been less studied. In fact, the difference in density between the upper and lower fluid layers has a great influence on the change of fluid turbulence intensity and velocity. The mixing process and movement characteristics of a river plume under the effect of different buoyancy and the plume flow rate are comprehensively studied using particle image velocimetry (PIV) technology. The main contents of this paper are organized as follows. In Section 2, the experimental setup and PIV measuring system are briefly described. The results, including the river plume qualitative description, the river plume quantitative flow field, Gaussian distribution of horizontal velocity, the river plume thickness, and the turbulent kinetic energy of the river plume, are presented in Section 3. Finally, conclusions are summarized in Section 4.

2 Methodology

2.1 Experimental setup

As shown in Figure 1, the experiment was conducted in a rectangular tank (1.5m long, 0.6m wide, and 0.5m deep). The rectangular tank was made with transparent acrylic plates with a good light transmission. The river plume was discharged from the right side of the rectangular tank, and the left side was designed with extra length as a buffer to reduce the backflow. The source of the river plume is a constant water tank located 3.0m above the rectangular tank, which is connected to a rectangular channel through a pipe. The center of the river mouth water surface was defined as the origin of the Cartesian coordinate. x positive direction is right, representing the onshore coordinates; z positive direction is upward, representing vertical coordinates; y is alongshore coordinate. The mouth of the rectangular channel is submerged in the environmental water. The width of the rectangular channel is 5 cm and the slope is 0.16.

Two stages of experiment were designed in this study: the qualitative and the quantitative measurement. In the qualitative experiment, the plume was stained with dye, and two cameras were set above and in front of the rectangular tank, similar to the work of Pan et al. (2022). As a result, the planar view of the plume movement at the x-y plane and the side view at the x-z plane were captured. For quantitative experiments, the velocity of the plume movement at the x-z plane was recorded by the PIV system. The size of the field of view (FOV) was 35 cm × 12 cm.

2.2 PIV system and post-processing

The PIV system consists of a high-speed camera with 2-Gigabyte-memory storage and a continuous laser with a wavelength of 532nm.

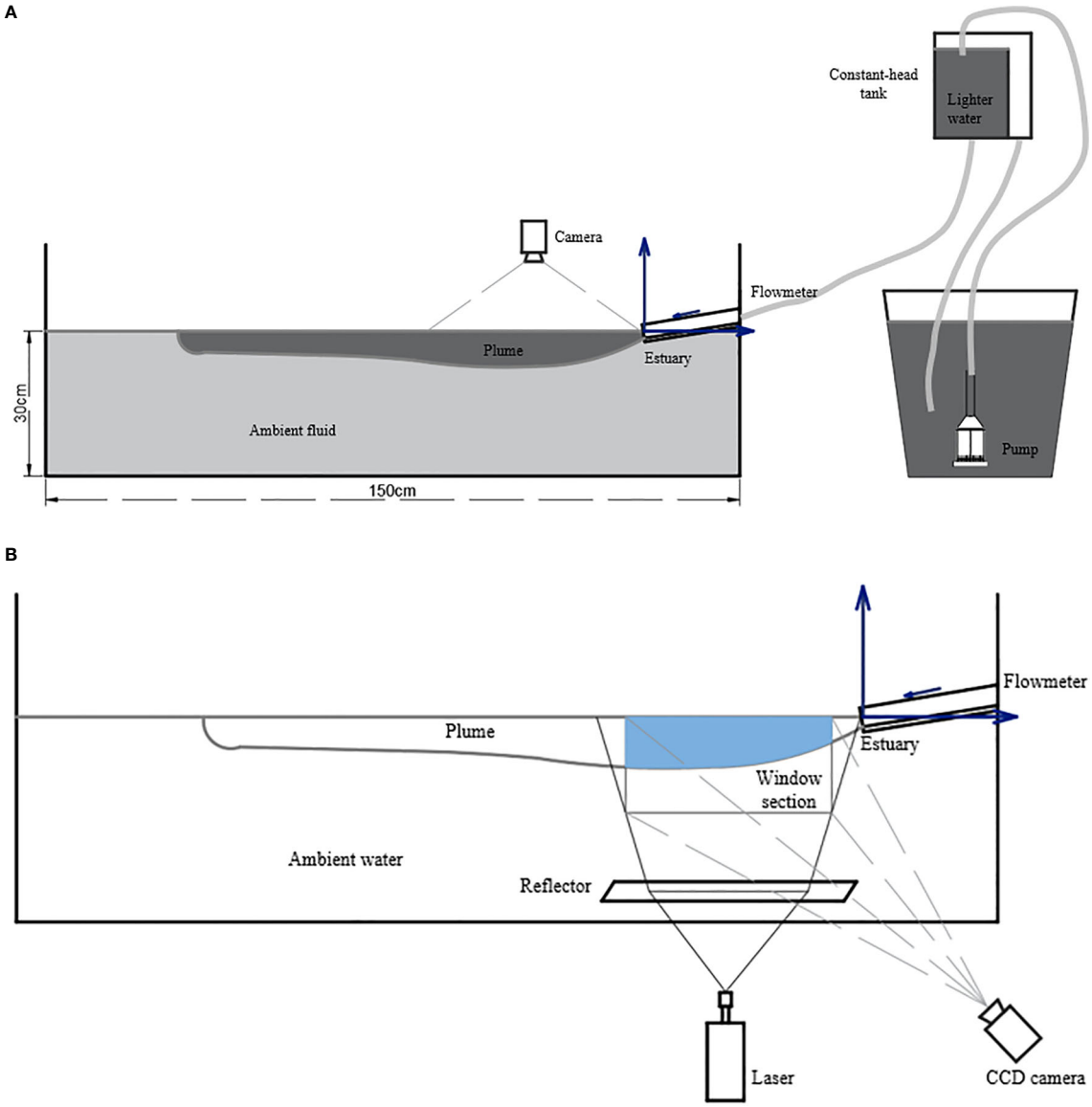

FIGURE 1
Diagram of the experimental setup: qualitative plan-view experiment **(A)** and qualitative and quantitative side-view experiment **(B)**.

The resolution of the high-speed camera is 2048 × 2048 pixels. The camera framing rate was set to 200fps. The output power of the MGL-W-532 solid state laser was set to 8W. In the experiment, the incident light of the laser was parallel to the rectangular tank bottom and then was reflected by a plane mirror which had an angle of 45° with the bottom. As a result, the laser light could pass vertically upwards through the central axis of the river plume. The thickness of the laser light was about 2mm. Hence, the river plume was illuminated by the laser light. At the same time, tracer particles with a diameter of 50μm were added into the river plume.

A multi-grid interrogation method, which can increase the spatial and temporal resolution of flow field (Hsieh, 2008; Hsieh et al., 2016), was used in the post-processing stage. The multi-grid interrogation method consisted of three different interrogation window sizes: 32×32 pixels, 16×16 pixels, and 8×8 pixels. All passes adopted a 50% overlap between adjacent sub-windows. In traditional PIV image processing, a fixed time interval is usually used to calculate flow field. But if the velocity gradient is large (i.e., jet), adopting a fixed-time interval will inevitably result in bias error when calculating relatively small velocities. By adopting the multi-time interval method, the aforementioned bias error can be reduced. Four different time intervals (1, 3, 9, and 21) were used in this method; the most suitable time interval would be selected to reduce errors in the post-processing stage. Details of this multi-time interval algorithm can be found in Hsieh et al. (2016).

2.3 Experimental cases

In this study, nine cases of river plume were carried out for both the qualitative dyeing experiments and the velocity measurements. The specific parameters of the experimental cases are shown in Table 1. The effects of the buoyancy change and the flow rate on the movement characteristics of the river plume were examined.

TABLE 1 The parameters of the experiments.

expt	Q_0(Lpm)	ρ_0 (g/cm^3)	g_0'	U_0(cm/s)	Fr_i	Re
ND-1	1.50	0.9997	0.49	3.00	1.92	7634
ND-2	2.00	0.9997	0.49	3.80	2.43	9670
ND-3	2.50	0.9997	0.49	4.90	3.13	12469
HD-1	1.50	1.0030	3.72	2.90	0.67	7404
HD-2	2.00	1.0030	3.72	3.80	0.88	9702
HD-3	2.50	1.0030	3.72	5.10	1.18	13021
ED-1	1.50	1.0060	6.63	3.10	0.54	7938
ED-2	2.00	1.0060	6.63	4.00	0.69	10243
ED-3	2.50	1.0060	6.63	5.10	0.89	12548

The initial velocity of the plume could be calculated by using the initial flow rate. The reduced gravitational acceleration was used to describe the effect of different buoyancies. Hence, the Froude number Fr_i, which is the ratio of inertial force to the buoyancy, could be described as

$$g_0' = \frac{\rho_0 - \rho}{\rho_0} g \tag{1}$$

Where ρ_0 is the density of ambient fluid, ρ is the density of inflow, and g is gravitational acceleration,

$$Fr_i = \frac{U_0}{\sqrt{g_0' H_0}} \tag{2}$$

Where U_0, g_0', and H_0 represent the velocity, reduced gravity, and the maximum depth of river plume inflow. The Reynolds number of each case is also listed in Table 1.

$$\mathrm{Re} = \frac{\rho U_0 H_0}{\mu} \tag{3}$$

Where μ represents the dynamic viscosity of the water.

In these cases, Fr_i ranges from 0.54 to 3.13. If $Fr_i > 1$, the flow is supercritical and if $Fr_i < 1$ the flow is subcritical. Re ranges from 7404 to 13021, indicating that the flow of each case is turbulent.

3 Result and discussion

3.1 Qualitative description of river plume

River plume generally enters the ocean from a channel with a certain gradient. In this study, the slope is set to 0.16. The dynamic processes of a river plume movement could be divided into the near-field process and the far-field process. In the near-field area, the initial velocity of the river plume causes the velocity shear and turbulence mixing with the sea water, and the density difference between the river plume and the sea water will cause a lateral expansion of the plume. In the far-field of the plume, the thickness of the plume tends to be stable and the mixing between the two water layers is weakened. The plan view and side view of the river plume in the qualitative experiments are illustrated in Figures 2, 3. All sets of the views were captured when the river plume was steady.

Figure 2 shows the qualitative description for cases ND-1, ND-2, and ND-3. The Froude number Fr_i of these three cases are larger than those in other cases; ND-3 is the largest of all groups and the flow is supercritical. For the plan view of these three cases, the river plume appears as jet-like currents with large offshore velocities and begins to show the tendency to expand laterally after maintaining the jet-like state. The change of plume shape caused by the increase of initial velocity shows that the lateral diffusion trend of plume decreases slightly within the observation range.

For the side view of these three cases, it is found that the plume maintains a steady state with a relatively constant thickness after a certain downward intrusion at the estuary. The stable thickness of the river plume in case ND-1 is obviously smaller than that in case ND-2 and case ND-3, and the stable thickness of the river plume in ND-3 is slightly greater than that in case ND-2. Comparing the pattern of mixing between the river plume and the ambient fluid, the mixing in case ND-1 is the weakest blending, and the interface between the river plume and the ambient fluid was the smoothest and most stable in the three cases. The mixing between the river plume and the ambient fluid in case ND-2 and case ND-3 at the interface was significantly stronger. The Kelvin–Helmholtz instability at the interface was more obvious in the two cases. In the observation of qualitative experiments, it is found that a more obvious vortex is formed when the front of the river plume interacts with the ambient fluid.

Figure 3 is the plan view and side view of the river plume at three ambient fluid densities at a flow rate of 2.5 LPM, namely case ND-3, case HD-3, and case ED-3. Among the three cases, ND-3 has the largest Fr_i, followed by Fr_i of HD-3, with Fr_i of ED-3 being the smallest.

In the sets of plan view, unlike case ND-3(high Fr_i) which shows a strong jet-like state, flows of case HD-3 and case ED-3 only maintain the offshore direction at the central axis and within a certain width, while the edge of the plume shows a clear lateral spread trend. In other words, the alongshore movement of the two plumes are significantly stronger than that in case ND-3. The higher the ambient fluid density

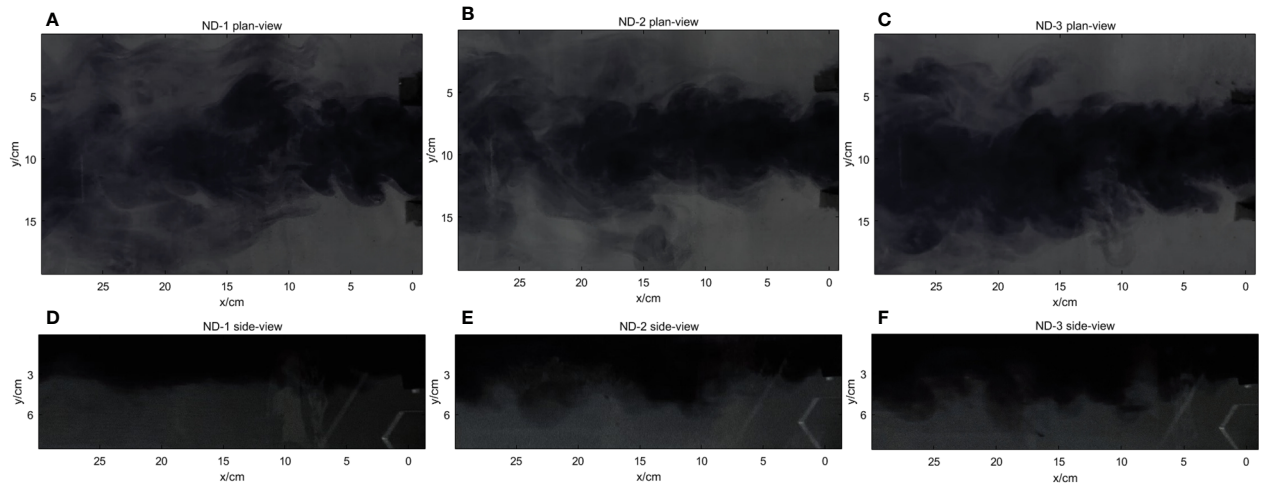

FIGURE 2
Plan and side view of plume with an ambient water density of 0.9997g/cm^3: plan-view of Case ND-1,ND-2 and ND-3 **(A–C)**,side-view of Case ND-1,ND-2 and ND-3 **(D–F)**.

is, the more obvious the lateral spread trend of the river plume is, and the river plume shape changes from a "trumpet" shape to "fan" shape.

In the sets of side views, the plume pattern of case HD-3 and case ED-3 are quite similar and differ greatly from case ND-3, and the Kelvin–Helmholtz instability at the interface gradually decreases with the increase of the ambient fluid density. That is to say, the increasing of the ambient fluid density limits the mixing at the interface between the river plume and the ambient fluid.

3.2 Flow field of river plume

The flow field of the river plume in all cases is shown in Figure 4. It is obvious that the flow field of the river plume is distributed with the maximum velocity at the surface layer. The velocity decreases gradually along the downward water depth, and the velocity of each layer of the river plume decreases gradually along the entrance toward the offshore direction. With the increase of the flow rate, the overall velocity of the river plume increases (the average surface velocities of HD-1, HD-2, and HD-3 are 2.2, 3.4, and 4.7 cm/s respectively); the high velocity range of plume also increases, while the low velocity range changes a little.

Due to the slope of the rectangular channel being 0.16, in case ND-2 and case ND-3, the direction of velocity vectors at the middle and bottom layer presents a downward direction deviating from the horizontal in the near mouth, but after moving for a distance under the buoyancy effect (relatively smaller than in HD and ED groups), they gradually change to deviating from the horizontal to the upward direction.

For the plume in case HD and ED groups, their velocity vectors all deviate from the horizontal upward direction near the river mouth. After moving to the surface, the velocity vector turns to the horizontal direction. It indicates that the buoyancy effect on the plume is obviously greater than the effect of its inertial force in these cases,

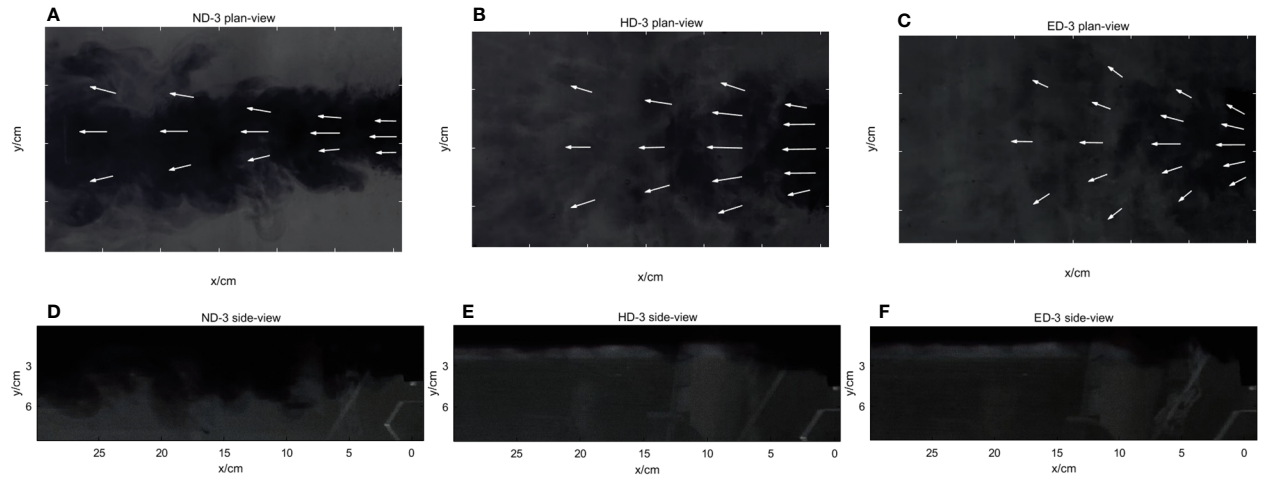

FIGURE 3
Plan and side view of plume with the flow rate of 2.5lpm: plan-view of Case ND-3, HD-3 and ED-3 **(A–C)**,side-view of Case ND-3, HD-3 and ED-3 **(D–F)**.

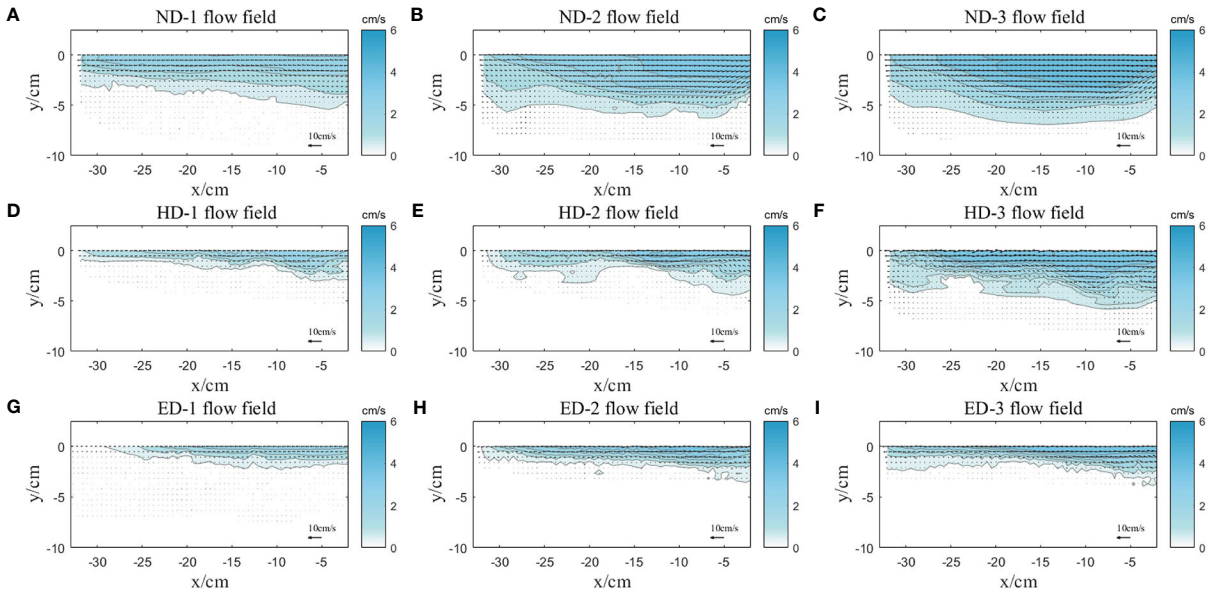

FIGURE 4
Flow field of the river plume in all cases: Case ND-1 **(A)**, Case ND-2 **(B)**, Case ND-3 **(C)**,Case HD-1 **(D)**, Case HD-2 **(E)**, Case HD-3 **(F)**, Case ED-1 **(G)**, Case ED-2 **(H)** and Case ED-3 **(I)**.

and it is consistent with the phenomena in the plan view of Figure 3. Under the action of buoyancy, the flow in the lower layer gradually rises to the surface, and the fluid that was originally on the surface of the plume is pushed to two flanks.

3.3 Gaussian distribution of horizontal velocity

Zhao et al. (2019) fitted the vertical velocity of the vertically discharged buoyant flow with a Gaussian distribution curve and the vertical velocity in different water depths conforms to the curve well. The horizontal velocity distribution along the water depth of the river plume in this study also follows the Gaussian distribution well. The river plume has a free surface in the x-z plane, and the surface velocity is maximum. Therefore, this paper selects half of the Gaussian distribution to fit the horizontal velocity of the river plume and uses the axis of the Gaussian distribution to correspond to the horizontal velocity of the free surface, obtaining a good fitting effect. Yuan et al. (2018) used the variance of Gaussian distribution to define the width of plume in plan-view ($b=C\sigma$). According to the experimental observation and freshwater conservation, C was set to 4, which was consistent with the width of buoyancy flow. In this study, we use C=2.2 to represent the horizontal velocity distribution width of each section because half of the Gaussian distribution was fitted with the data.

Figure 5 shows the fitting result of the horizontal velocity of each section for case ND-1, case ND-2, and case ND-3. The horizontal velocity of each section in the three cases increases significantly with the increase of flow rate and decreases with the increase of offshore distance. The distribution width of horizontal velocity also decreases along the river plume movement direction.

Figure 6 shows the fitting result of the horizontal velocity of each section for case ND-3, case HD-3, and case ED-3 under the condition that the plume flow rate is 2.5 LPM. The horizontal velocities of each section in the three groups change a little with the density of the environmental fluid, while the distribution width of the horizontal velocities change greatly. The increase of environmental fluid density reduces the width of horizontal velocity distribution at the same location, but each section still conforms well to the Gaussian distribution.

3.4 Thickness of the river plume

The water depth where the horizontal velocity drops to 1/e of the surface velocity is defined as the plume thickness in this study, which is similar to the definition of the half-width with a free jet. Starting from the maximum thickness location, the thickness scatter points of the river plume on each section were fitted with different types of curve, as shown in Figure 7.

For the cases in the ND group, the densities of environmental water are the same. The thickness change along the river plume movement direction is similar in these cases, and the curve types do not change. All of them in these three cases are the inverse tangent function type, and the increase of flow rate only causes the change of parameter A1. The thickness in case ND-2 and case ND-3 increases first and then decreases along the river plume movement direction, and the decreasing of the flow rate makes the thickness curve tend to be flat. For the cases in the D-3 group, the change of the

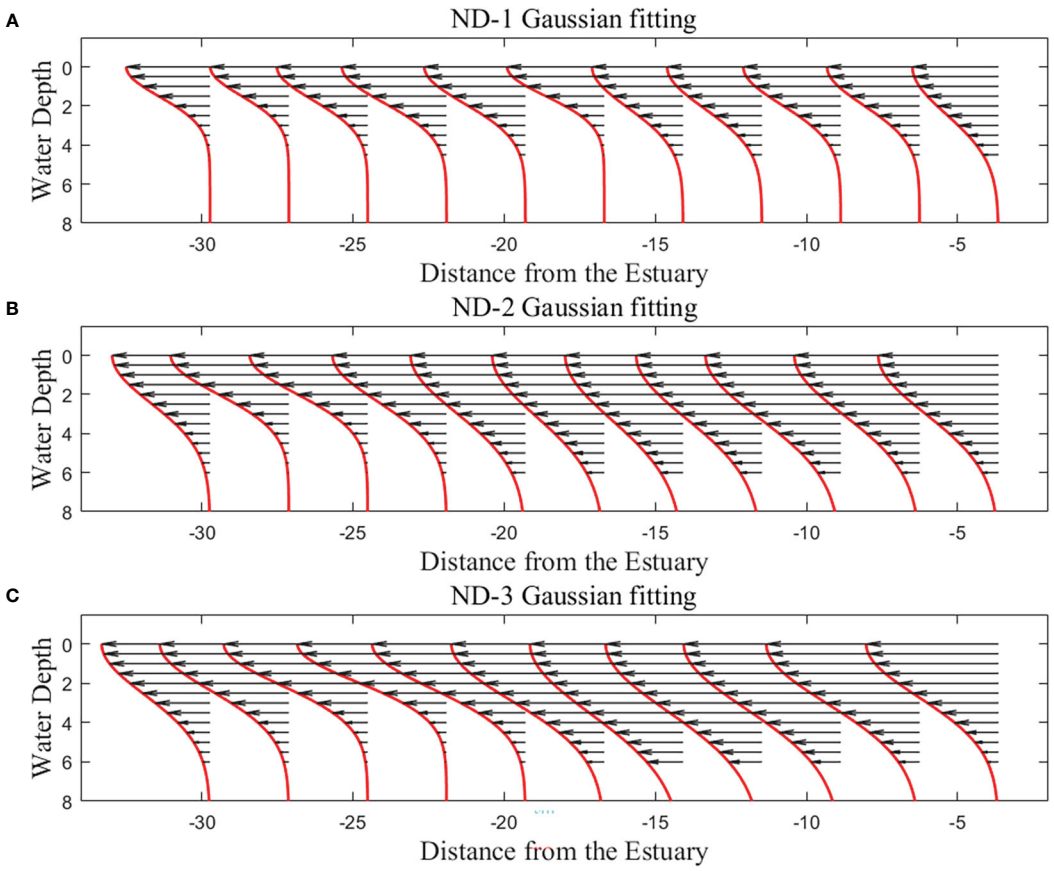

FIGURE 5
Gaussian distribution of horizontal velocity of ND groups: Case ND-1 **(A)**, Case ND-2 **(B)** and Case ND-3 **(C)**.

environmental water density causes a great change in the shape of the thickness curve. The shape of the thickness curve changes from an inverse tangent curve to a log curve with the increase of the environmental water density. The thickness curves of case HD-3 and case ED-3 are in the form of log curves. Compared with case HD-3, the environmental water density in case ED-3 is higher, resulting in the maximum thickness of plumes being smaller, the stable thickness being smaller, and the decreasing rate of the thickness from the maximum thickness to the stable thickness being significantly smaller.

Under the effects of the buoyancy and the inertial force, the upper and lower layer of water shear with each other and the plume thickness changes along the river plume direction. Figure 8 shows the relationship between the thickness of river plume after reaching stability with the Froude number Fr_i. The Froude number of case ED and HD groups is relatively small, and the stable thickness of the river plume will be small. The scattered points lie in the lower left corner. The Froude number of case ND group is relatively large, and as a result the stable thickness of river plume is also large. An obvious linear relationship could be found between the stable thickness of the river plume with the Froude number. It indicates that the Froude number is a key parameter to describe the behaviors of the river plume.

3.5 Turbulent kinetic energy

Turbulent kinetic energy is an important parameter reflecting the turbulent characteristics of river plume. Turbulent kinetic energy is defined as follows:

$$\mathrm{k} = \frac{1}{2}(u_i'^2 + v_i'^2) \tag{4}$$

$$u_i' = u_i - \bar{u}_i \tag{5}$$

$$k_{Ui} = \frac{1}{2}\frac{\sum_{i=1}^{n} u_i'^2}{n} = \frac{1}{2}\frac{\sum_{i=1}^{n}(u_i - \bar{u}_i)^2}{n} \tag{6}$$

$$k_{Vi} = \frac{1}{2}\frac{\sum_{i=1}^{n} v_i'^2}{n} = \frac{1}{2}\frac{\sum_{i=1}^{n}(v_i - \bar{v}_i)^2}{n} \tag{7}$$

Where, k is turbulent kinetic energy and u_i' is the fluctuating velocity, defined as the D-value of velocity u_i and average speed $\bar{u}_i$. Therefore, the turbulent kinetic energy at the measuring point is $k_i = k_{Ui} + k_{Vi}$.

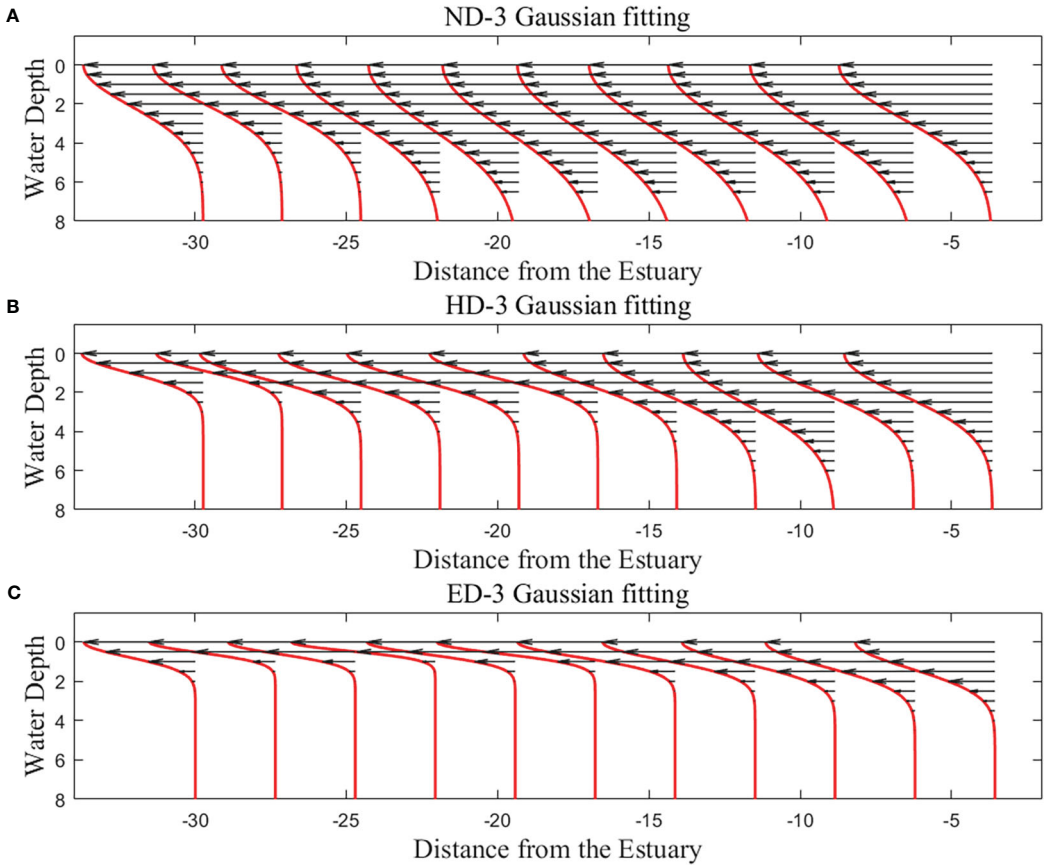

FIGURE 6
Gaussian distribution of horizontal velocity of D-3 groups: Case ND-3 **(A)**, Case HD-3 **(B)** and Case ED-3 **(C)**.

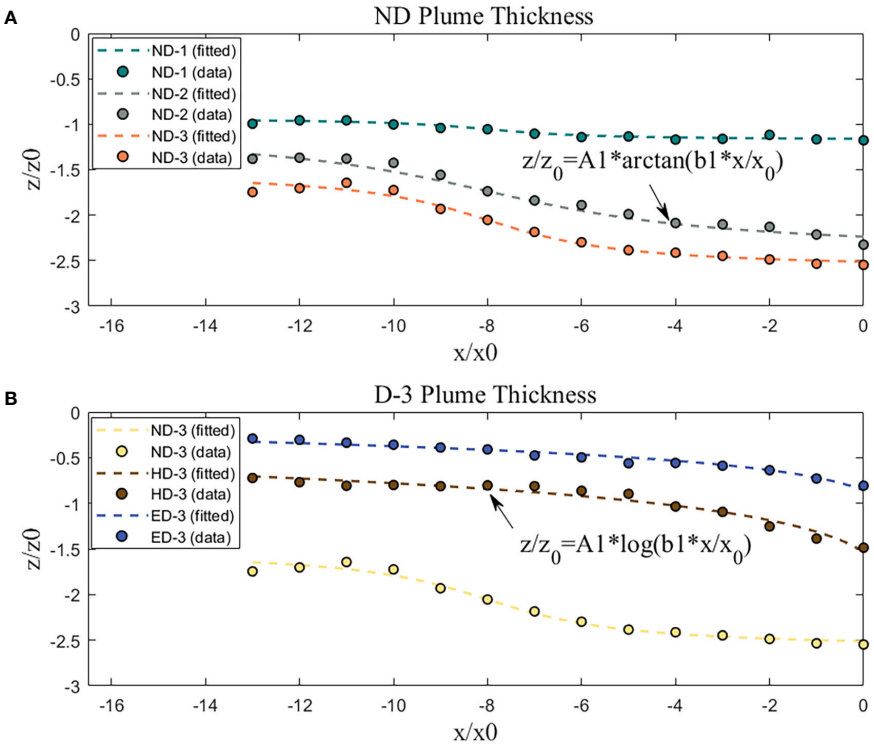

FIGURE 7
Thickness of river plume in different cases: ND group **(A)** and D3 group **(B)**.

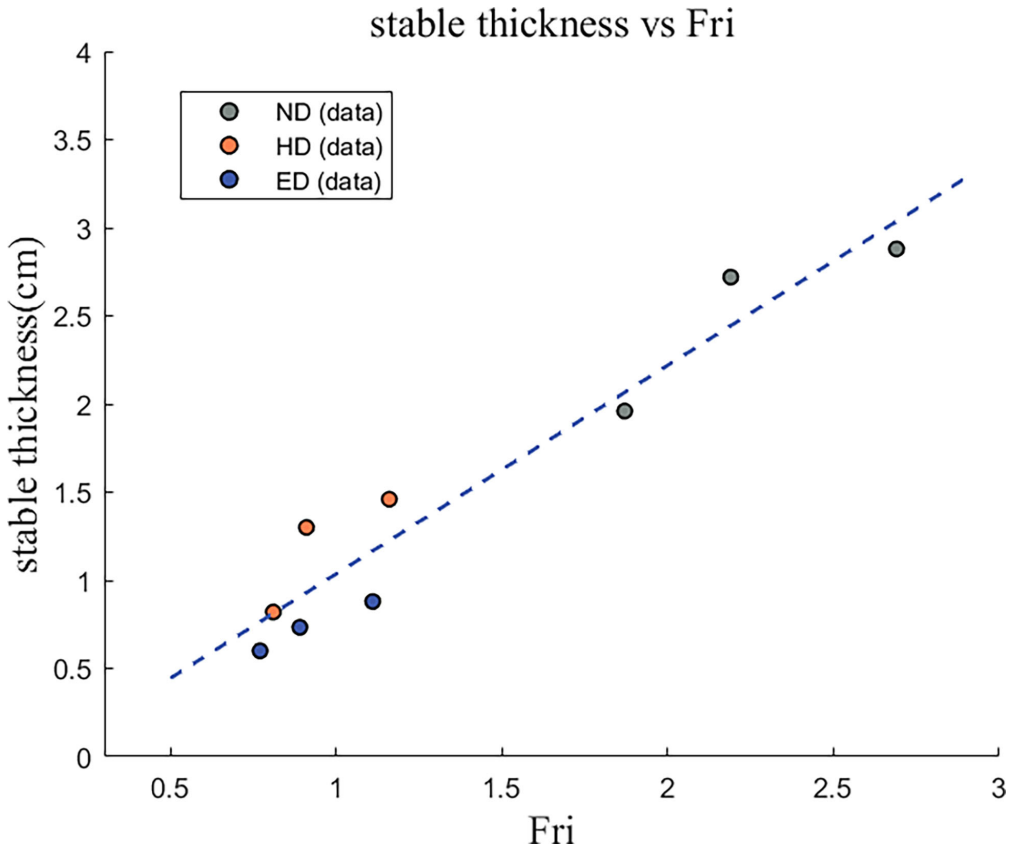

FIGURE 8
The relationship between the stable thickness and the Froude number.

In the flow field, the turbulent kinetic energy k_i is used to represent the velocity fluctuating energy, that is, if the turbulent kinetic energy at a certain position is higher, there will be greater velocity fluctuating, and more energy transfer and dissipation.

We chose the section where the plume thickness is the largest as an example. The distribution of turbulent kinetic energy along the water depth in such a section was drawn in Figure 9. It is obvious that the increase of flow rate will cause the increase of turbulent kinetic energy. In each case, the maximum value of turbulent kinetic energy is located in the middle layer, and the turbulent kinetic energy gradually increases from the surface to the middle layer and then decreases to the bottom. The turbulent kinetic energy of the surface layer is obviously smaller than that of the middle layer. At the bottom boundary of the plume, the mixing of plume makes the velocity in this area reduce significantly. The increase of environmental water density will also enhance the turbulent kinetic energy. MacDonald and Geyer (2004) measured the velocities at three passes at the estuarine front in Fraser River, and the distribution shape of TKE production is quite similar to this study. TKE of the pass with higher salinity is significantly larger, and the peak is also closer to the upper layer. The results here verify the distribution pattern of TKE, and show the change of TKE under the influence of environmental water density and flow rate. A higher TKE production implies that the mixing between the river plume and the ocean will be increased and will enhance the exchange of substances.

4 Conclusions

In this study, the mixing process and movement characteristics of a river plume under the effect of different buoyancies and the plume flow rates are comprehensively studied using particle image velocimetry (PIV) technology. The main conclusions are summarized as follows.

(1) The change of flow rate and environmental water density will shape the river plume pattern in both the plan view and the side view. The combined effect of flow rate and environmental water density could be described by the Froude number.

(2) The river plume has a free surface in the x-z plane and the horizontal velocity of the plume could be fitted with a 1/2 Gaussian distribution curve.

(3) The thickness of the river plume increases with the increase of flow rate, and the increase in the density of ambient water changes the shape of the plume thickness curve from an

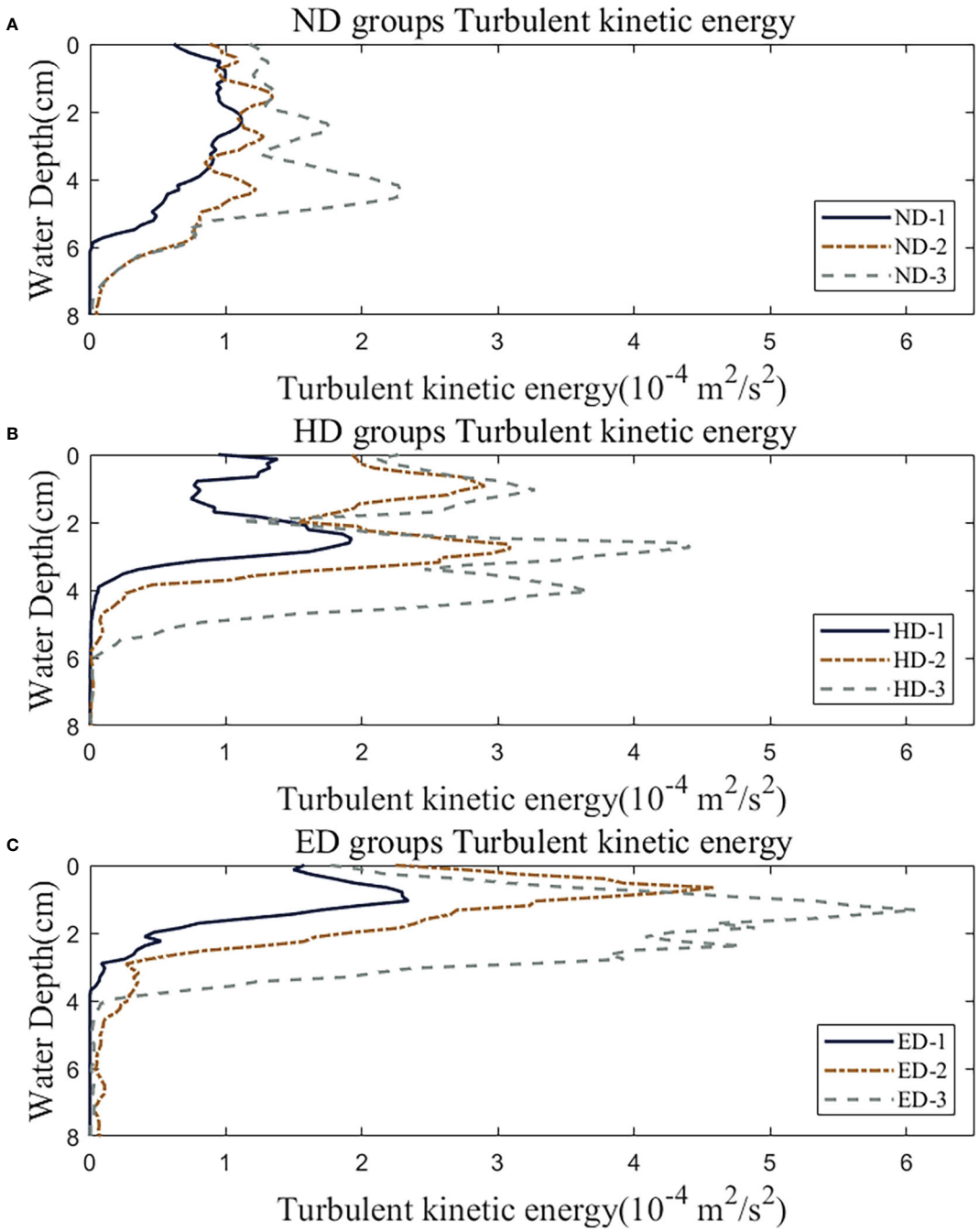

FIGURE 9
Turbulent kinetic energy at the maximum thickness section: ND group **(A)**, HD group **(B)** and ED group **(C)**.

arctan-type to log-type. The stable thickness of the river plume increases with the increase of the Froude number.

(4) The maximum value of turbulent kinetic energy is located in the middle layer, and the increase of the flow rate or the density difference leads to the increase in the turbulent kinetic energy.

Data availability statement

The original contributions presented in the study are included in the article/supplementary material. Further inquiries can be directed to the corresponding author.

Author contributions

ZX: conceptualization, methodology, formal analysis, and writing—review and editing. CX: experiment, and writing—original draft. GW: formal analysis and writing—review and editing. JZ: formal analysis, visualization, and writing—review. YC: writing—review and editing. All authors contributed to the article and approved the submitted version.

Funding

We are sincerely grateful for the support from the Key Research and Development Program of Hebei Province (21373302D), Marine Ecological Restoration and Smart Ocean Engineering Research Center of Hebei Province (HBMESO2308) and the National Natural Science Foundation of China (51979076).

Conflict of interest

The authors declare that the research was conducted in the absence of any commercial or financial relationships that could be construed as a potential conflict of interest.

Publisher's note

References

Cameron, W. M., and Pritchard, D. W. (1963). "Estuaries," in *The Sea*, vol. 2 . Ed. M. N. Hill (New York: Wiley), 306–324.

Feddersen, F., Olabarrieta, M., Guza, R. T., Winters, D., Raubenheimer, B., and Elgar, S. (2016). Observations and modeling of a tidal inlet dye tracer plume. *J. Geophys. Res.: Oceans* 121 (10), 7819–7844. doi: 10.1002/2016JC011922

Garvine, R. W. (1975). The distribution of salinity and temperature in the Connecticut river estuary. *J. Geophys. Res.* 80 (9), 1176–1183. doi: 10.1029/JC080i009p01176

Horner-Devine, A. R., Jay, D. A., Orton, P. M., and Spahn, E. Y. (2009). A conceptual model of the strongly tidal Columbia river plume. *J. Mar. Syst.* 78 (3), 460–475. doi: 10.1016/j.jmarsys.2008.11.025

Hsieh, S. C. (2008). *Establishment of high time-resolved PIV system with application to the characteristics of a near wake flow behind a circular cylinder* (Taiwan: National Chung Hsing University).

Hsieh, S. C., Low, Y. M., and Chiew, Y. M. (2016). Flow characteristics around a circular cylinder subjected to vortex-induced vibration near a plane boundary. *J. Fluids Structures* 65, 257–277. doi: 10.1016/j.jfluidstructs.2016.06.007

Lentz, S. (2004). The response of buoyant coastal plumes to upwelling-favorable winds. *J. Phys. oceanogr.* 34 (11), 2458–2469. doi: 10.1175/JPO2647.1

MacDonald, D. G., and Geyer, W. R. (2004). Turbulent energy production and entrainment at a highly stratified estuarine front. *J. Geophys. Res.: Oceans* 109, C05004. doi: 10.1029/2003JC002094

Nardin, W., Mariotti, G., Edmonds, D. A., Guercio, R., and Fagherazzi, S. (2013). Growth of river mouth bars in sheltered bays in the presence of frontal waves. *J. Geophys. Res.: Earth Surface* 118, 872–886. doi: 10.1002/jgrf.20057

Nezlin, N. P., and DiGiacomo, P. M. (2005). Satellite ocean color observations of stormwater runoff plumes along the San Pedro shelf (southern California) during 1997-2003. *Continental Shelf Res.* 25, 1692–1711. doi: 10.1016/j.csr.2005.05.001

Pan, Y., Yin, S., Chen, Y. P., Yang, Y. B., Xu, C. Y., and Xu, Z. S. (2022). An experimental study on the evolution of a submerged berm under the effects of regular waves in low-energy conditions. *Coast. Eng.* 176, 104169. doi: 10.1016/j.coastaleng.2022.104169

Qu, L., and Hetland, R. D. (2019). Temporal resolution of windforcing required for river plumesimulations. *J. Geophys. Res.: Oceans* 124, 1459–1473. doi: 10.1029/2018JC014593.

Rijnsburger, S., Flores, R. P., Pietrzak, J. D., Horner-Devine, A. R., and Souza, A. J. (2018). The influence of tide and wind on the propagation of fronts in a shallow river plume. *J. Geophys. Res.: Oceans* 123, 5426–5442. doi: 10.1029/2017JC013422

Yuan, Y., Avener, M. E., and Horner-Devine, A. R. (2011). A two-color optical method for determining layer thickness in two interacting buoyant plumes. *Experiments fluids* 50 (5), 1235–1245. doi: 10.1007/s00348-010-0969-y

Yuan, Y., and Horner-Devine, A. R. (2013). Laboratory investigation of the impact of lateral spreading on buoyancy flux in a river plume. *J. Phys. Oceanogr.* 43 (12), 2588–2610. doi: 10.1175/JPO-D-12-0117.1

Yuan, Y., Horner-Devine, A. R., Avener, M., and Bevan, S. (2018). The role of periodically varying discharge on river plume structure and transport. *Continental Shelf Res.* 158, 15–25. doi: 10.1016/j.csr.2018.02.009

Zhao, L., Zhang, W., He, Z., Tan, L., and Jiang, H. (2019). The process of mass transport for a buoyant plume in linearly stratified environment. *J. Shanghai Jiaotong Univ.* 53 (04), 473–479. doi: 10.16183/j.cnki.jsjtu.2019.04.012

frontiers | Frontiers in Marine Science

TYPE Original Research
PUBLISHED 01 March 2023
DOI 10.3389/fmars.2023.1143925

OPEN ACCESS

EDITED BY
Yi Pan,
Hohai University, China

REVIEWED BY
Yupeng Ren,
Ocean University of China, China
Chunyang Xu,
Hohai University, China

*CORRESPONDENCE
Zhe Huang
huangzhe1829@tju.edu.cn
Yuchuan Bai
ychbai@tju.edu.cn

SPECIALTY SECTION
This article was submitted to Coastal Ocean Processes, a section of the journal Frontiers in Marine Science

RECEIVED 13 January 2023
ACCEPTED 01 February 2023
PUBLISHED 01 March 2023

CITATION
Wang G, Feng X, Zhang J, Huang Z, Bai Y, Song W and Xu H (2023) A numerical study on the responses of coastal water quality to river runoff after heavy rainfall in the case of a complex coastline with two artificial islands.
Front. Mar. Sci. 10:1143925.
doi: 10.3389/fmars.2023.1143925

A numerical study on the responses of coastal water quality to river runoff after heavy rainfall in the case of a complex coastline with two artificial islands

Gang Wang[1,2,3], Xin Feng[2,3], Jiabo Zhang[2,3], Zhe Huang[1,3]*, Yuchuan Bai[1,3]*, Wei Song[4] and Haijue Xu[1]

[1]State Key Laboratory of Hydraulic Engineering Simulation and Safety, Tianjin University, Tianjin, China, [2]The Eighth Geological Brigade of Hebei Bureau of Geology and Mineral Resources Exploration, Qinhuangdao, China, [3]Marine Ecological Restoration and Smart Ocean Engineering Research Center of Hebei Province, Qinhuangdao, China, [4]Key Laboratory of Marine Eco-Environmental Science and Technology, First Institute of Oceanography, Ministry of Natural Resources, Qingdao, China

Heavy rainfall causes large volumes of freshwater and nutrient salts to flow from rivers into the sea. This leads to major changes in the ecological environment of estuarine waters in a short period of time. The responses of the estuarine hydro-environment become more complex with the concentrated construction of artificial structures, which is a major cause of marine ecological disasters. This paper considers the Tang Estuary in Qinhuangdao, where artificial structures (e.g., ports, artificial islands, and bridges) are concentrated, as a prototype with the weak tidal dynamic environment. A nested prototype of hydrodynamics and water quality was established using a Delft3D model, with coupled waves and flows. The model was used to simulate the spatial and ephemeral characteristics of the short-term responses of ecological environmental factors, such as dissolved inorganic nitrogen (DIN), nitrate-nitrogen (i.e., NO_3-N), ammonium-nitrogen (NH_4-N), and orthophosphate (i.e., PO_4-P), to an episode of heavy rainfall in August 2022. The results showed that concentrations of DIN and NO_3-N in the source areas remain high after the flooding process. The concentration recovered to normal values approximately 5.5 days after the flooding process. In contrast, NH_4-N and PO_4-P showed a response with ephemeral correspondence with the flooding process, and concentration recovery took only approximately 1 day. This paper proposes two short-term response modes of pollutant diffusion, which provide help in exploring the role of hydro-environmental changes in offshore algal hazards and the effect of permeable buildings on pollutant dispersion. This additionally provides possibilities with the forecasting of red tide and green tide, and for their prevention in the future.

KEYWORDS

heavy rainfall, river runoff, coastal water quality, land-based pollutants, artificial islands

1 Introduction

The Bohai Sea accounts for only 1.6% of China's national sea area but receives 32.2% of the country's pollutants (Zhang et al., 2006). Monitoring data show that land input dominates in terms of the sources of marine pollutants in the Bohai Sea, accounting for more than 80% of pollution, and 95% of these land-based pollutants are discharged from several estuaries (Zhao and Kong, 2000; Liu, 2010; Luan et al., 2016; Liu et al., 2017). Affected by monsoon and human activities, it is not obvious how pollutants are concentrated to discharge into the Bohai Sea along with land stream at the wet season, even in several short flood discharge processes with heavy rainfall. This land-based pollution leads to seawater eutrophication, which can increase the chances of ecological disasters in ecologically sensitive areas, such as red tides and green tides in the inner bay and coastlines near urban areas (Fletcher, 1996; Lappalainen and Ponni, 2000; Han et al., 2003; Pedersen and Borum, 2010). They may also cause jellyfish blooms as a result of estuarine eutrophication and an increase in small zooplankton and artificial structures (Lucas et al., 2012; Riisgard and Hoffmann, 2012; Makabe et al., 2014; Gu et al., 2017).

Qinhuangdao is located on the west coast of the Bohai Bay at an M2 amphidromic point in the open sea, with a small tidal range and weak tidal current. Affected by intense human activities, its coastline utilization patterns are diversely distributed. Ports, aquaculture, sand beaches, artificial islands, and primitive tidal flats are alternately distributed along the coastline. In recent years, its coastal waters have been more significantly affected by river pollutants flowing into the sea and have been seriously threatened by ecological disasters such as red tide, green tide, and jellyfish blooms. In particular, more attention should be paid to the Golden Dream Bay area, because this is located in the middle of the coastline of Qinhuangdao and its capacity for water exchange and pollutant transport is weakened by structures such as artificial islands, docks, and bridges (Kuang et al., 2015; Pan et al., 2018; Kuang et al., 2019; Pan et al., 2020; Kuang et al., 2021; Pan et al., 2022). Divided by the prismatic island in the estuary, a large amount of flood discharge sediment enters the Golden Dream Bay (Sheng et al., 2016). According to monitoring data, there were 43 red tide disasters in the Qinhuangdao sea area between 2001 and 2014 (Zhai et al., 2016), and 24 red tide disasters between 2015 and 2022. The occurrence of red tide disasters led to the deterioration of the water environment and damaged the aquaculture. Some toxic red tides even seriously threatened human lives and property. For example, the brown tide caused by *Aureococcus anophagefferens* began to appear in 2009 and occurred every year until 2014. During the period of the brown tide, the concentration of dissolved organic nitrogen (DON) was more than five times that of dissolved inorganic nitrogen (DIN) (Zhou et al., 2023). A higher DON concentration and lower levels of inorganic nutrients are suitable conditions for the growth of brown tide algae, whereas lower DIN limits the growth of brown tide algae (Zhang QC. et al., 2020). Another example is the seafood poisoning incident in 2016. This was mainly caused by the toxic species *Alexandrium catenella* (Yu et al., 2021; Tang et al., 2022a). Surficial sediments sampled in the area showed a decreasing trend from northeast to southwest (Tang et al,. 2022b). These ecological disasters are closely related to the levels of nitrogen (N) and phosphorus (P) in the water (Conley, 2000). These elements mainly come from river discharge, especially during periods of extreme rainfall, when the flow of rivers into the sea increases sharply (Meybeck, 1982).

Since 2015, large-scale algal blooms have occurred in the coastal area of Qinhuangdao Golden Dream Bay from April to September every year. The green tide in Qinhuangdao is of local origin and has different origins and development patterns than that of the Yellow Sea (Han et al., 2019). It has a significant positive correlation with the biomass of attached and floating *Pistia stratiotes*. The concentration of nitrate-nitrogen (i.e., NO_3-N) is the most important factor affecting the abundance of micro-propagules (Han et al., 2022). As a starting point, it is proposed that the outbreak of green tide in this area may be related to the eutrophication of estuarine waters and the weakening of regional hydrodynamics caused by the construction of artificial islands (Song et al., 2019). Research on the combination of green tide algae and micro- and nano-phytoplankton suggests that dissolved organic nitrogen (DON) and dissolved organic phosphorus (DOP) will promote biodiversity and the growth of micro- and nano-phytoplankton, and that low levels of dissolved inorganic phosphorus (DIP) will inhibit growth. In a sea environment with a suitable temperature and high concentrations of dissolved organic nitrogen (DON) and N/P, the outbreak of green tide algae will accelerate the transformation of the micro- and nano-phytoplankton community from dominant diatom species to dominant dinoflagellate species (Zhang et al., 2022).

Although there have been some studies conducted on the sea area near the Tang Estuary, a main entrance of drained river flow affecting the Golden Dream Bay, these have focused on the hydrodynamic effect of a single artificial island or an artificial island group. Researchers have not studied the hydrodynamics and pollutant diffusion in the sea area under the influence of the full set of relevant conditions (consisting of the artificial island group, wharf, island bridge, and coastal bathing beach) during flood water flow, which is often the key factor leading to a high degree of short-term eutrophication and short-term outbreaks of ecological disasters in the sea area. Considering the influence of diverse human activities, such as the construction of artificial islands and island bridges, Delft3D was adopted to establish a wave–current coupling hydrodynamic and water quality model using a three-layer nested structure grid for a heavy rainfall and flooding process in August 2022. The spatial and temporal response characteristics of the pollutant discharge process from the Tang River and the ecological environment of the estuary were examined.

2 Materials and methods

Delft3D is among the most advanced of the two-dimensional and three-dimensional hydrodynamics and water quality modeling systems available worldwide; it was developed by Delft Hydraulics (Deltares, formerly WL|Delft Hydraulics, Delft, the Netherlands). A three-scale nested grid was established, using Delft3D, to simulate the hydrodynamics (i.e., tidal current field, wave field), temperature–salinity field, and water quality in the Bohai Sea, Qinhuangdao coastal area, and the Tang Estuary. The results of the numerical model can

provide a basic background on the dynamic field and nutrient environment field for the study of biological growth and forecasting of ecological disasters in the Qinhuangdao coastal area.

2.1 Area and mesh

The finite volume method (FVM) and a structured grid were used to solve the two-dimensional shallow water equation, which mainly considered the tidal and wave action driven by the outer sea boundary and the wind field. For different water depth and sediment conditions, the bottom friction coefficient was introduced, and the dry and wet grid conditions were considered in the nearshore area. In order to describe the flow field and water level process, a triple-nested grid model was established, with the large regional scope of the Bohai Sea, medium regional scope of Qinhuangdao, and fine regional scope of the Tang Estuary (Figure 1). The number of nodes in each of the three scales of model was 249 × 315, 245 × 206, and 372 × 491, respectively. The corresponding grid resolutions were 1500 m, 350 m, and 15 m, respectively. The Dalian–Yantai line was treated as the outer boundary of the Bohai Sea, with water-level superimposition of the static pressure and the astronomical tide. The tide-level data were calculated *via* the tide wave model NAOTIDE, a data set of tide forecast, in the adjacent areas of Japan; the resulting data were verified by comparing them with tide-level data from the tide gauge station in the Bohai Sea. The tidal level and velocity process of the middle-level Qinhuangdao model was provided by the Bohai Sea model. The land boundary of the middle-level model was defined by 11 river estuaries, which were controlled by the measured monthly average runoff of these rivers. The tidal level and flow velocity of the Tang Estuary model were provided by the Qinhuangdao model. The land boundary of the fine-level model was defined by two river estuaries, the Tang River and its tributary Xiaotang River, which were controlled by measured flow velocity.

The model parameters comprised time step, Courant number [Courant–Friedrichs–Lewy (CFL) number], horizontal eddy viscosity coefficient, bed friction, and Coriolis force. The time steps of the triple-scale model were set at 30 s, 15 s, and 3.75–7.5 s. A CFL number below 0.8 was maintained by controlling the time step employed in different ranges, which can effectively solve the problem of model instability. The Manning number was 0.0163 $s/m^{1/3}$, in accordance with the bottom sediment particle size and water depth. The values of the horizontal eddy viscosity coefficient and the horizontal eddy diffusion coefficient were dependent on the grid size; these were set to 15 m^2/s and 100 m^2/s, respectively, in both the Bohai Sea model and the Qinhuangdao model, and to 1 m^2/s and 10 m^2/s, respectively, in the Tang Estuary model. The Coriolis force was determined by the latitude of the model region.

2.2 The hydrodynamic model

The governing equations are:

$$\frac{\partial h}{\partial t} + \frac{\partial hu}{\partial t} + \frac{\partial hv}{\partial y} = hS$$

$$\frac{\partial hu}{\partial t} + \frac{\partial hu^2}{\partial x} + \frac{\partial hvu}{\partial y} = fvh - gh\frac{\partial \eta}{\partial x} + \frac{\tau_{sx} - \tau_{bx}}{\rho} + \frac{\partial}{\partial x}(hT_{xx}) + \frac{\partial}{\partial y}(hT_{xy}) + hu_sS$$

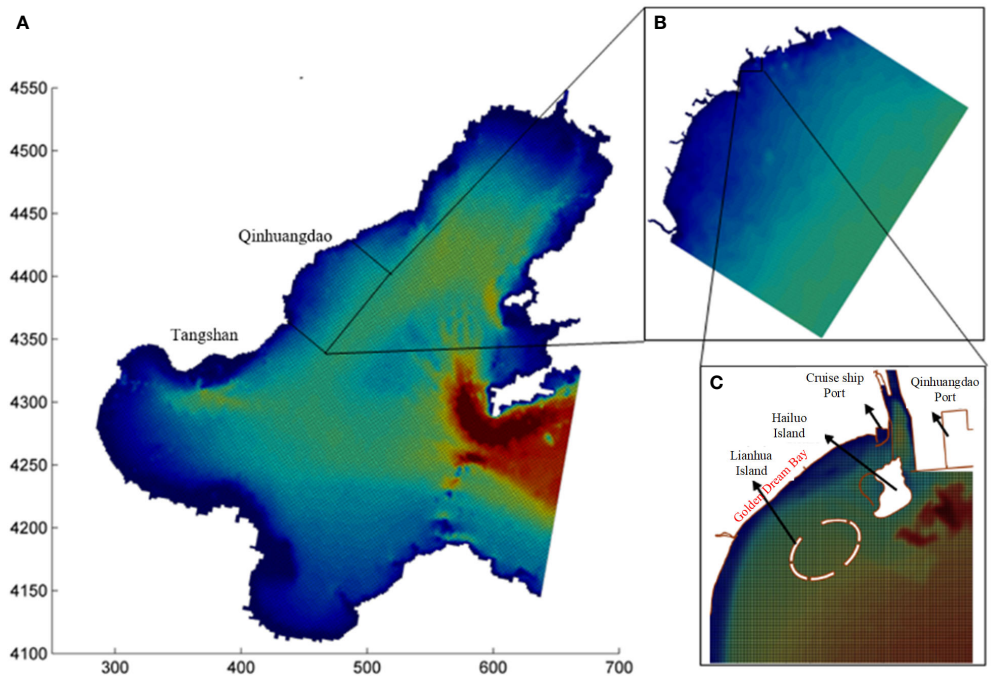

FIGURE 1
Area and mesh of the nested model: **(A)** the Bohai Sea, **(B)** the Qinhuangdao Coastal area, and **(C)** the Tang Estuary.

$$\frac{\partial hv}{\partial t} + \frac{\partial hv^2}{\partial y} + \frac{\partial hvu}{\partial x} = fuh - gh\frac{\partial \eta}{\partial y} + \frac{\tau_{sy} - \tau_{by}}{\rho} + \frac{\partial}{\partial x}(hT_{xy}) + \frac{\partial}{\partial y}(hT_{yy}) + hv_sS$$

where η is the water level, h is the total water depth, d is the static water depth, and $h = \eta + d$; t is time; u and v are the average velocity along water depth in the x and y directions, respectively; g is the acceleration of gravity; $f = 2\Omega sin\phi$ is the Coriolis force coefficient (Ω being the rotation rate of the Earth, and ϕ the geographic latitude); ρ is the density of the water; τ_{sx} and τ_{sy} represent wind stress in the x and y directions, respectively; τ_{Bx} and τ_{By} represent the bottom friction in the x and y directions, respectively; S is the source (sink) item; and u_s and v_s are the velocity components of the source (sink). The lateral stress term T_{ij} includes viscosity and turbulence.

2.3 The water quality model

The Delft3D water quality model can simulate sediment transport and water quality processes in large and medium-scale areas. The water quality model includes the convection–diffusion equation and a large standard equation library, corresponding to the selected material type, and the point source and area source of pollution diffusion processes. Coupled with the hydrodynamic results, the water quality model can calculate the dynamic distribution of concentrations of related materials and their derivatives in the water and sediment layers.

The two-dimensional transport equation is given in the form of convection diffusion, as follows:

$$\frac{\partial hT}{\partial t} + \frac{\partial huT}{\partial x} + \frac{\partial hvT}{\partial y} = hF_T + hH + hT_sS,$$

$$\frac{\partial hs}{\partial t} + \frac{\partial hus}{\partial x} + \frac{\partial hvs}{\partial y} = fF_s + hS_sS,$$

where T and s are the depth-averaged temperature and salinity, respectively; T_s and s_s are the horizontal diffusion terms for temperature and salinity, respectively; F_T and F_s are the source terms for temperature and salinity, respectively; and H indicates the source term for heat exchange between seawater and air.

The boundary conditions are important for the prediction of water quality during the period of heavy rain. Based on data from the online monitoring stations of the Tanghe River and Xiaotanghe River on terrestrial pollutants, the boundary conditions for the model concerning current speed and water quality were set as shown in Table 1.

2.4 Model verification

2.4.1 Verification of hydrodynamics

Verification of the tide and wave data were considered in the hydrodynamic model. Nine stations were designated for tide verification, including Yantai, Bayuquan, Jinzhou Port, Qinhuangdao, Jingtang Port, and Tanggu in the Bohai Sea (shown in Figure 2). Based on the time of occurrence of the extreme weather (heavy rainfall), the tide level data for 15 July to 15 August 2022 were collected from each of these gauge stations. The empirical data were harmonically analyzed as the measured value of the astronomical tide for comparison with the calculated values. Wave monitoring data for the period of 1 July to 1 September 2022 were also collected from each buoy in Qinhuangdao for validation of the model results. The error between the calculated value and the measured value was analyzed to evaluate the accuracy of the model and verify the reliability of the model for the coastal waters of Qinhuangdao.

TABLE 1 Boundary condition settings of the model.

Station	Time	Current (m/s)	NH_4-N (mg/L)	NO_3-N (mg/L)	PO_4-P (mg/L)
Tang River	18/8/2022 20:00:00	−0.01	0.10	2.39	0.02
	19/8/2022 00:00:00	−2.57	0.43	1.91	0.01
	19/8/2022 04:00:00	−4.29	0.33	1.80	0.03
	19/8/2022 08:00:00	−1.61	0.34	3.22	0.04
	19/8/2022 12:00:00	−0.78	0.30	3.93	0.03
	19/8/2022 16:00:00	−0.59	0.33	4.55	0.05
	19/8/2022 20:00:00	−0.36	0.25	5.03	0.04
Xiaotang River	18/8/2022 20:00:00	−0.23	0.69	5.49	0.08
	19/8/2022 00:00:00	−2.34	1.05	2.31	0.18
	19/8/2022 04:00:00	−1.94	0.59	1.81	0.16
	19/8/2022 08:00:00	−1.13	0.43	6.70	0.12
	19/8/2022 12:00:00	−0.68	0.45	5.87	0.13
	19/8/2022 16:00:00	−0.58	0.42	5.83	0.15
	19/8/2022 20:00:00	−0.42	0.43	6.72	0.13

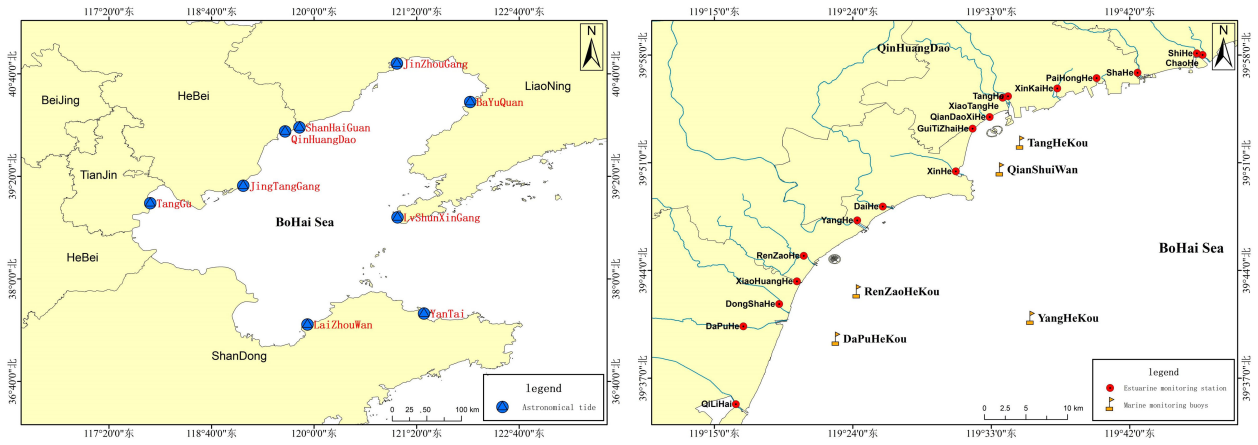

FIGURE 2
Gauge stations used for verification of the numerical model.

In order to obtain a better evaluation criterion than the common method, which uses the correlation coefficient and standard deviation, the Willmott statistical method was used to evaluate the simulation results of the model, as follows:

$$skill = 1 - \frac{\sum_{i=1}^{N}|M-D|^2}{\sum_{i=1}^{N}(|M-\bar{D}|+D-\bar{D}|)^2}$$

The Willmott statistical method takes into account the correlation between the deviation between the measured value D and the measured average value $\bar{D}$, and the deviation between the calculated value M and the measured average value $\bar{D}$. The resulting skill value ranges from 0 to 1. A value of 1 means that the result is completely consistent with the measured value; a value of 0.65–1 represents an excellent corroboration, 0.5–0.65 represents a very good corroboration, 0.2–0.5 represents a good corroboration, and 0–0.2 represents a poor corroboration.

As shown in Table 2, tide level verification indicated excellent model skill, with skill values of more than 0.86 at all the gauge stations; this proves that the model simulation values were in good agreement with the measured values. Verification of the tidal current and wave simulation values indicated that these were good, with skill values of more than 0.4 for selected ocean observation buoys.

As shown in Figure 3, the model can simulate the propagation of tidal waves in the Bohai Sea. Data plotted with dots represent the astronomical tides at typical tidal stations, whereas the black line represents the calculation results for tide amplitude and tide phase.

TABLE 2 Hydrodynamic model evaluation.

Variable	Time	Station	Skill	Performance
Tidal level	15 July–15 August 2011	Yantai	0.95	Excellent
		Lvshunxingang	0.98	Excellent
		Bayuquan	0.99	Excellent
		Jinzhougang	0.99	Excellent
		Shanhaiguan	0.94	Excellent
		Qinhuangdao	0.92	Excellent
		Jingtanggang	0.97	Excellent
		Tanggu	0.98	Excellent
Speed	29 July–1 August 2022 and 12 August–15 August 2022	Yanghekou	0.54	very good
Direction	18 July–23 July 2022	Yanghekou	0.48	good
Effective wave height	1 July–24 August 2022	Tanghekou	0.56	very good
		Yanghekou	0.45	good
		Renzaohekou	0.45	good
		Dapuhekou	0.48	good

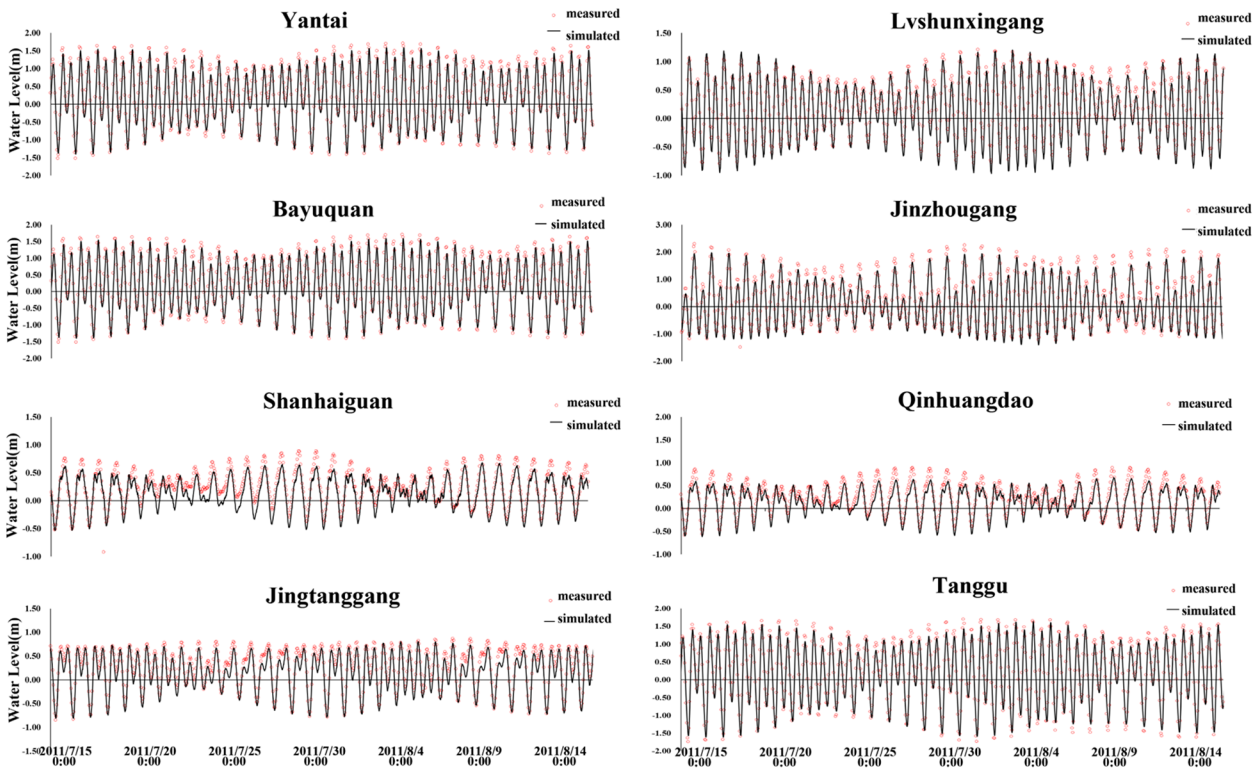

FIGURE 3
Verification of tidal level.

The calculated values are in good agreement with the predicted values for amplitude and phase. Figures 4, 5 show that the simulation results for velocity and wave height were also acceptable.

2.4.2 Water quality verification

Three concentration parameters were used to evaluate the water quality: nitrate-nitrogen, ammonium-nitrogen, and ortho-phosphate (NO_3-N, NH_4-N, and PO_4-P, respectively). These parameters have a significant impact on the growth of algae, and their verification is shown in Figure 6. The data were obtained during the period 15–31 August 2022 at the water quality and nutrient observation buoy in Qinhuangdao coastal waters (shown in Figure 2).

As illustrated, the simulated results fit well with the measured ones, with skill values for NO_3^-, NH_4^+, and PO_4^{-3} of 0.96, 0.93, and 0.93, respectively. The simulated values were very close to the measured values, and can be used to provide the basic background in terms of

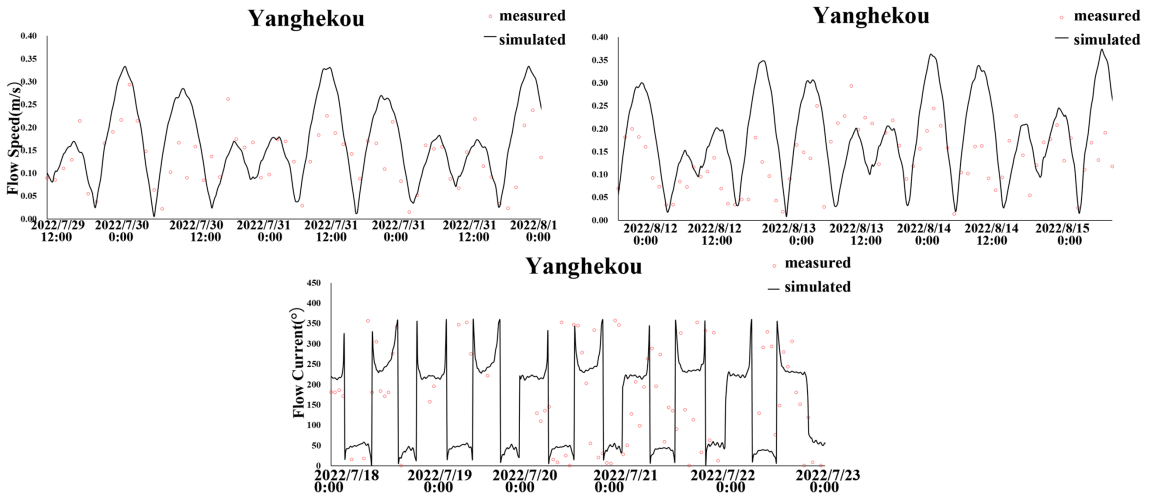

FIGURE 4
Verification of flow velocity.

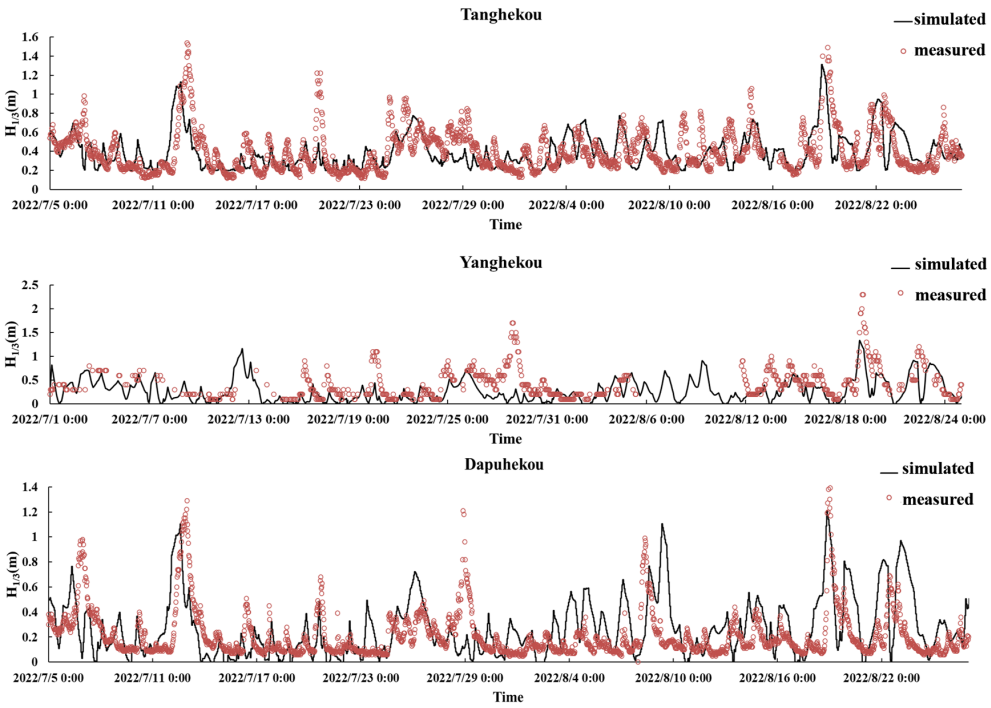

FIGURE 5
Verification of wave height.

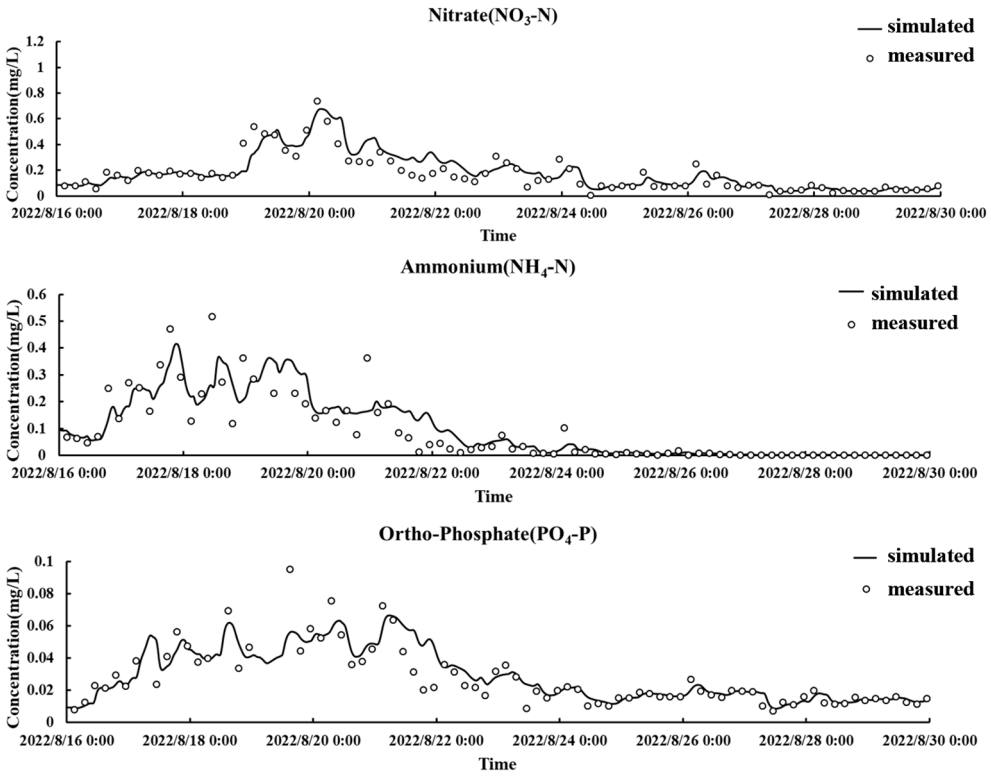

FIGURE 6
Water quality verification.

the dynamic field and environmental field for the study of the warning signs and forecasting of ecological disasters in Qinhuangdao coastal waters.

3 Results

3.1 Discharge of riverine pollutants into the sea as a result of heavy rainfall

In this study, data on the water quality and riverine discharge of the Tang River were collected from the online marine ecological monitoring station at intervals of 4 h. Figure 7 shows the changes in concentration of pollutants during the flood discharge of the Tang River. On the night of 18 August 2022, the riverine discharge of the Tang River into the sea increased rapidly owing to heavy rainfall. At 04:00 on 19 August, the discharge reached its maximum level of 295.4 m^3/s. The discharge then decreased rapidly to 48.6 m^3/s by 12:00,, until 08:00 on 20 August, when the discharge returned to the same magnitude as before the rainfall. At this time, the concentrations of pollutants, as indexed by measures such as chemical oxygen demand (COD), dissolved inorganic nitrogen (DIN), and dissolved total nitrogen (DTN), fell to pre-rainfall levels, and the flooding process ended. As can be seen in Figure 7, the water quality of the Tang River changed as a corroboration of the period of rainfall. The overall pollutant concentrations were all higher than before the rainfall. Different pollutants exhibited different responses; among these, COD and NH_4-N rose and fell consistently with the flow discharge. The concentration of COD reached a maximum value of 37.293 mg/L at 04:00 on 19 August and then decreased rapidly, while NH_4-N reached a maximum concentration of 0.427 mg/L at 0:00 on 19 August and then slowly fluctuated downward. The concentrations of DIN, DTN, and NO_3-N decreased slightly at first, then increased gradually, and gradually stabilized. The concentration of DTP gradually increased during the flooding process and then stabilized at approximately 0.11 mg/L. Finally, the concentrations of PO_4-P and

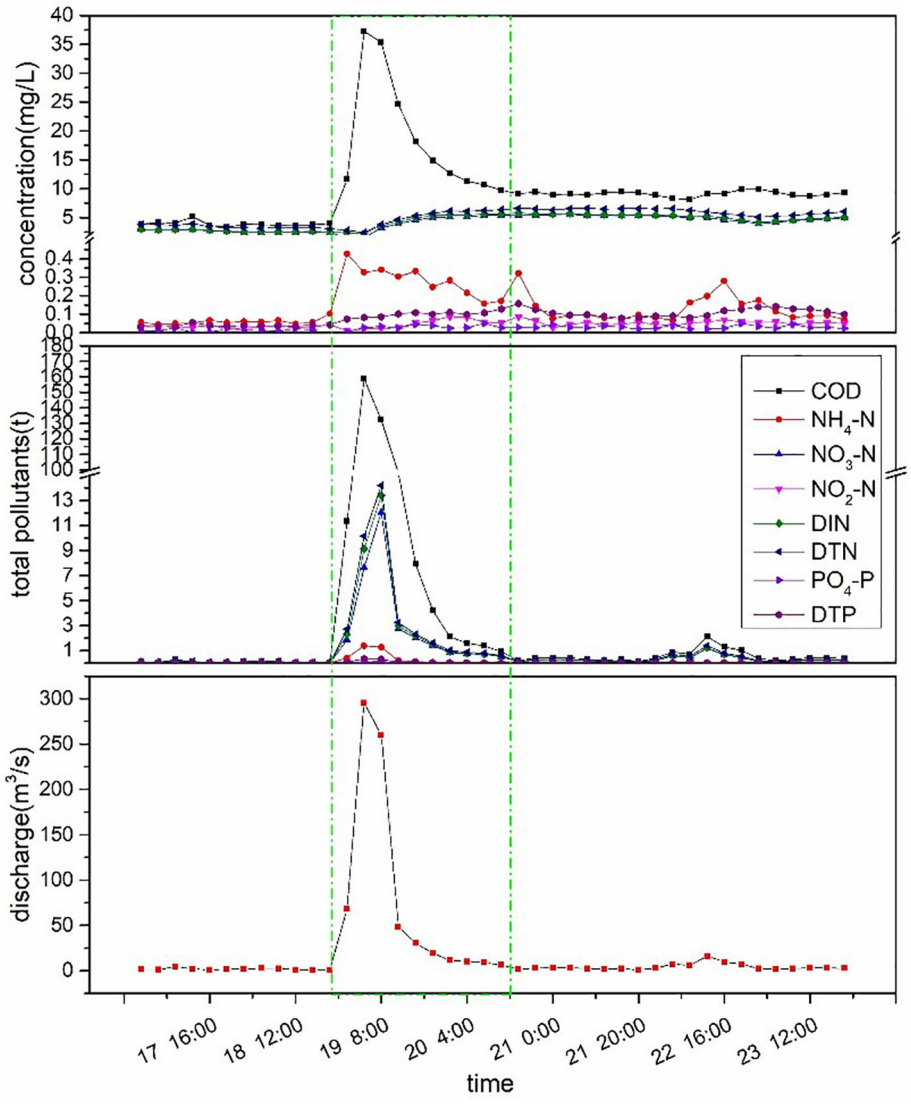

FIGURE 7
Flooding process of the Tang River caused by heavy rainfall in August 2022. DIN: dissolved inorganic nitrogen.

NO_2-N exhibited a fluctuating tendency to increase. The monitoring data indicated that during the flooding process, the changes in the total amount of each pollutant were mainly determined by the flow discharged, given these consistent trends. The total flux of flood water was 1098.86×10^5 m^3; the total amount of DIN discharged into the sea was 37.97 t, mainly consisting of 30.84 t of NO_3-N and 3.21 t of DON. The total amount of DTP discharged into the sea was 0.96 t, consisting of 0.64 t of DOP and 0.32 t of PO_4-P. Finally, the overall ratio of nitrogen to phosphorus in the discharged flood water was approximately 48:1.

3.2 Hydrodynamic responses

As a result of the flood water flow induced by the period of heavy rainfall, the coastal hydrodynamics in the Tang Estuary were significantly changed (shown in Figure 8). The flow velocity in the west coastal area of the Tang River channel was relatively higher. In the east coastal area, vortexes of varying sizes were formed by the blocking of the discharging flow by Hailuo Island, the port breakwater, and the Tongdao Bridge. The discharging flow was divided into two component currents by Hailuo Island. Current A moved southwest along the shore under the Tongdao Bridge to reach the Golden Dream Bay, causing a 180° transition of the tidal flow on the landward side of Lianhua Island. Current B moved offshore along the channel between Hailuo Island and the port breakwater, where the hydrodynamics on the seaward side of the island underwent no significant changes. With the increasing discharge from the Tang River into the sea, the vortexes on the east coast became larger with decreased number. Meanwhile, the current flow velocity on both sides of Hailuo Island increased significantly, with a larger influencing range. Current A, constrained by the tourist port breakwater and Hailuo Island, formed a clockwise vortex in the Golden Dream Bay, and current B began to affect the external area on the southeast side of Hailuo Island. At 03:00 on August 19, the flood water reached the maximum range of the hydrodynamic environment. The two vortexes on the east side of the Tang River channel and the west side of the port breakwater became much larger. The impact of current A significantly exceeded the landward shelter area of the two islands, where the flow velocity near the islands was higher and gradually decreased landwards. The hydrodynamics on the seaward side of the two islands were mainly influenced by current B, which changed its direction in the area southeast of Hailuo Island and flowed southwest along the seaward side of the two islands. The velocity gradually decreased, and the current was deflected at the southwest end of

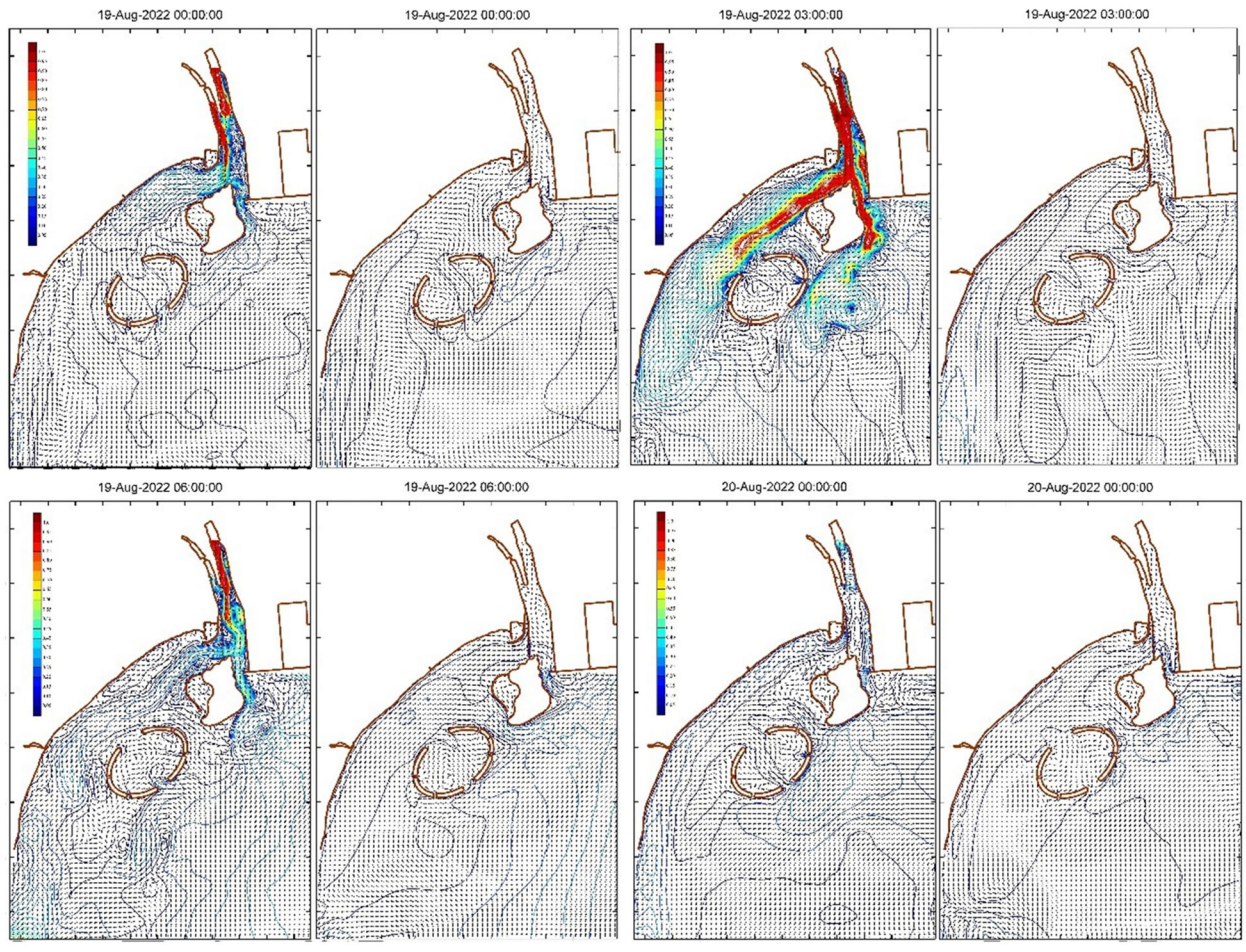

FIGURE 8
Hydrodynamic responses caused by heavy rainfall in August 2022.

Lianhua Island under the influence of open sea dynamics. With the gradual reduction of the flow discharge, the effects on the hydrodynamics in the Tang Estuary were also gradually weakened. At 06:00 on 19 August, because of the significantly weakened state of current A on the land side of the islands, a larger vortex formed under interaction with the falling tide. With the continuous reduction of the discharging flow of the Tang River, the hydrodynamics became more complex owing to the joint action of the runoff flow and the tide in the Tang Estuary. After 11:00 on 19 August, the hydrodynamics in the Tang Estuary were mainly determined by the rising or falling tide. At 18:00 on 19 August, the hydrodynamics on the sea side of the islands were in complete accordance with the rising and falling tide, while the runoff flow was only visible from the land side of the islands and was mainly limited to the river channel.

3.3 Pollutant migration and dispersion during flood discharge

The flooding of the Tang River drained a large quantity of pollutants into the sea and ocean. This paper presents a simulation of the migration and dispersion processes of the major inorganic nutrients (DIN, NO_3-N, NH_4-N, and PO_4-P) that damage the marine ecological environment. Following this simulation, the responses of the water environment to the pollutants draining out were then investigated.

The overall changes of the concentrations of DIN and NO_3-N were found to have broadly the same distribution, as shown in Figures 9, 10. At 00:00 on 19 August, the water from the upstream river rapidly entered the estuary channel, at which time the concentrations of DIN and NO_3-N also increased rapidly. The concentrations of DIN and NO_3-N at the river mouth were greater than 3 mg/L and 2 mg/L, respectively. The concentrations on the landward side of Hailuo Island and in the sea area on the side of the port breakwater decreased gradually from the Tang Estuary to the outer sea. Owing to the dramatic increase in flood water flow into the sea, the scope of influence of DIN and NO_3-N was enhanced. At 01:00 on 19 August, the concentrations of DIN and NO_3-N on the landward side of Hailuo Island and Lianhua Island were greater than 2 mg/L and 1.5 mg/L, respectively, while the concentrations on the seaward side began to increase. At 03:00, the concentrations of DIN and NO_3-N were greater on the landward side of the islands than on the seaward side; there was a gradual decrease in concentration from the shore to the sea. The concentrations showed a trend of decreasing from the Tang Estuary along both sides of the coast. The areas of maximum concentration of DIN and NO_3-N in the Golden Dream Bay coincided with the vortex area formed by the hydrodynamics at this time. At 06:00 on 19 August, the concentrations of DIN and NO_3-N began to gradually increase again. Influenced by the flood water flow and tidal power, the dispersion of DIN and NO_3-N migration increased on the landward side of the islands, while decreasing on the

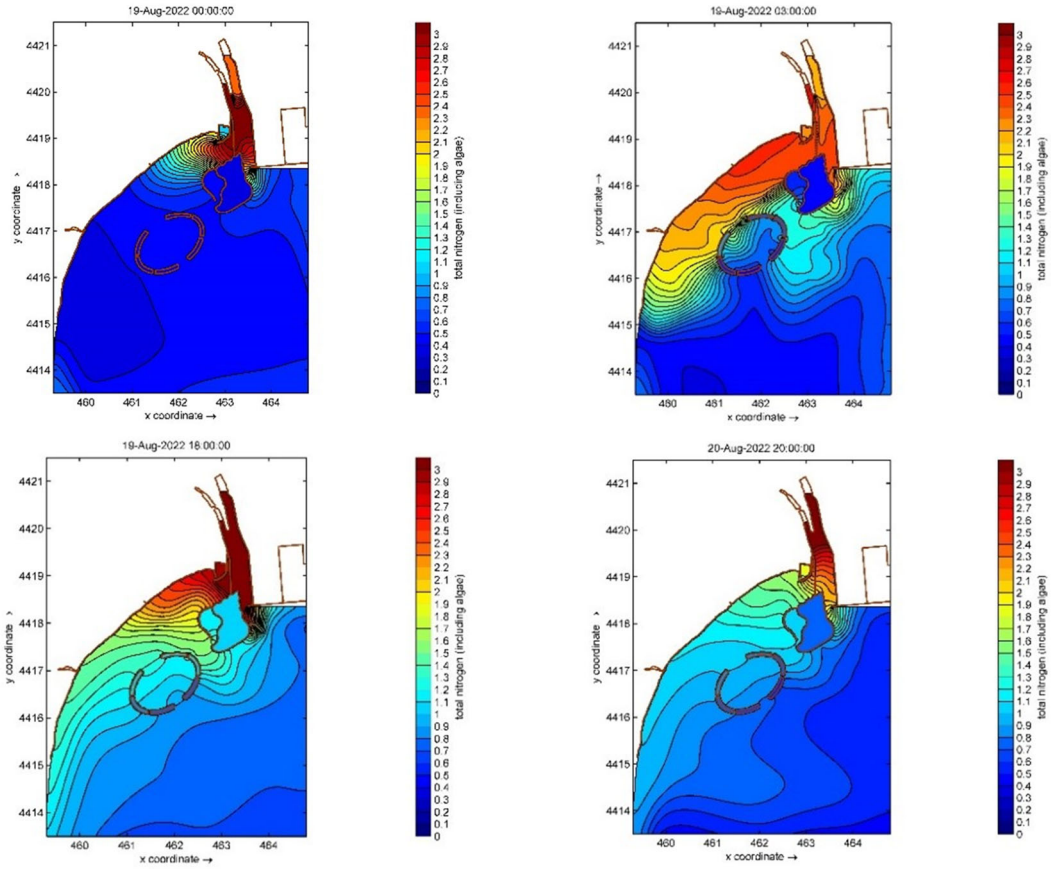

FIGURE 9
The process of diffusion of dissolved inorganic nitrogen (DIN) in the Tang Estuary caused by heavy rainfall in August 2022.

seaward side. The range of high DIN and NO_3-N concentration was affected by the reduction in the flood water flow, with a gradual decrease in their distribution. By 18:00 on 19 August, the concentrations of DIN and NO_3-N on the landward side of the islands and in the area between the two islands were greater than 1 mg/L and 0.8 mg/L, respectively. The high concentrations of DIN and NO_3-N were mainly concentrated in the river channel at the estuary. After this point, the concentrations around the islands began to gradually decrease. At 00:00 on August 20, the concentrations outside the islands had essentially dropped to their pre-flooding levels. With the further reduction of the runoff flow, the influence of tides increased to form a high concentration in source area of DIN and NO_3-N at the river mouth. At this point, the dynamics of migration were dominated by the tidal power rather than the flood water flow. By 16:00 on 20 August, the effects of the Tang River flooding had almost entirely disappeared. At 10:00 on 25 August, the high concentrations of DIN and NO_3-N in the source area had returned to pre-flood levels under the influence of tidal currents. Following this flooding process, the impact of DIN and NO_3-N discharging into the sea lasted for approximately 6.5 days.

The pollutants NH_4-N and PO_4-P were mainly discharged from the Xiaotang River, a tributary of the Tang River. The overall characteristics of the discharge of these pollutants differed from those of the discharge of DIN and NO_3-N (shown in Figures 11 and 12). During the initial stage of flooding, the concentrations of these pollutants in the main channel of the upper Tang River were low. In contrast, concentrations in the Xiaotang River were very high, causing a rapid increase in the estuary, with concentrations of NH4-N and PO4-P greater than 0.4 mg/L, and 0.06 mg/L,respectively. At 01:00 on 19 August, the flood water flow in the main channel increased rapidly, and the concentrations of NH_4-N and PO_4-P in the estuary decreased. The concentrations on the landward side of the two islands and the seaward side of Hailuo Island increased rapidly. At 03:00 on 19 August, the pollutants on the landward side of the two islands migrated continuously in a southwesterly direction, with concentrations on the landward side significantly greater than those on the seaward side. Subsequently, the concentrations of the pollutants decreased continuously. At 06:00 on 19 August, the concentrations of NH_4-N and PO_4-P in the river channel decreased rapidly to 0.035 mg/L, and 0.035 mg/L, respectively. The contours of these concentrations were broadly the same as the coastal direction. In the direction normal to the shoreline, the concentrations showed a trend of gradually decreasing, and migrated and spread out to the sea under the influence of the tidal power. By 00:00 on 20 August, the concentrations were broadly the same as the baseline ocean values. The total duration of the diffusion process was approximately 1 day.

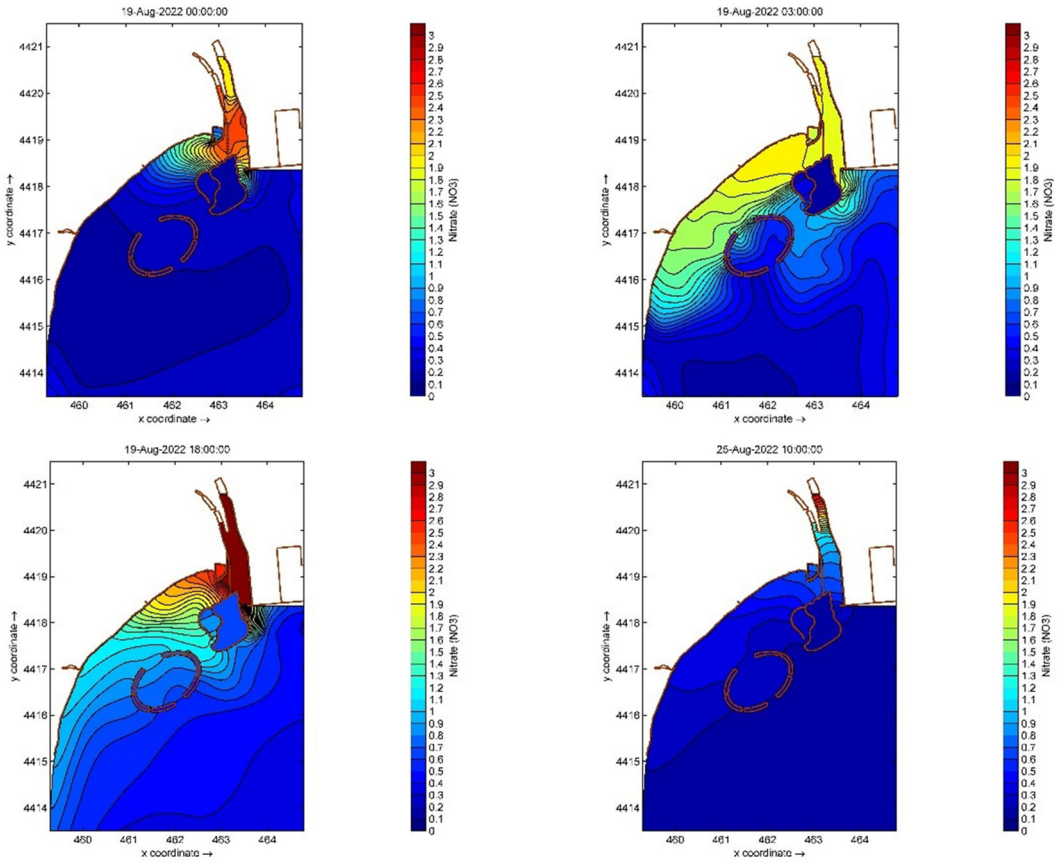

FIGURE 10
Nitrate-nitrogen (NO_3-N) diffusion process in the Tang Estuary caused by heavy rainfall in August 2022.

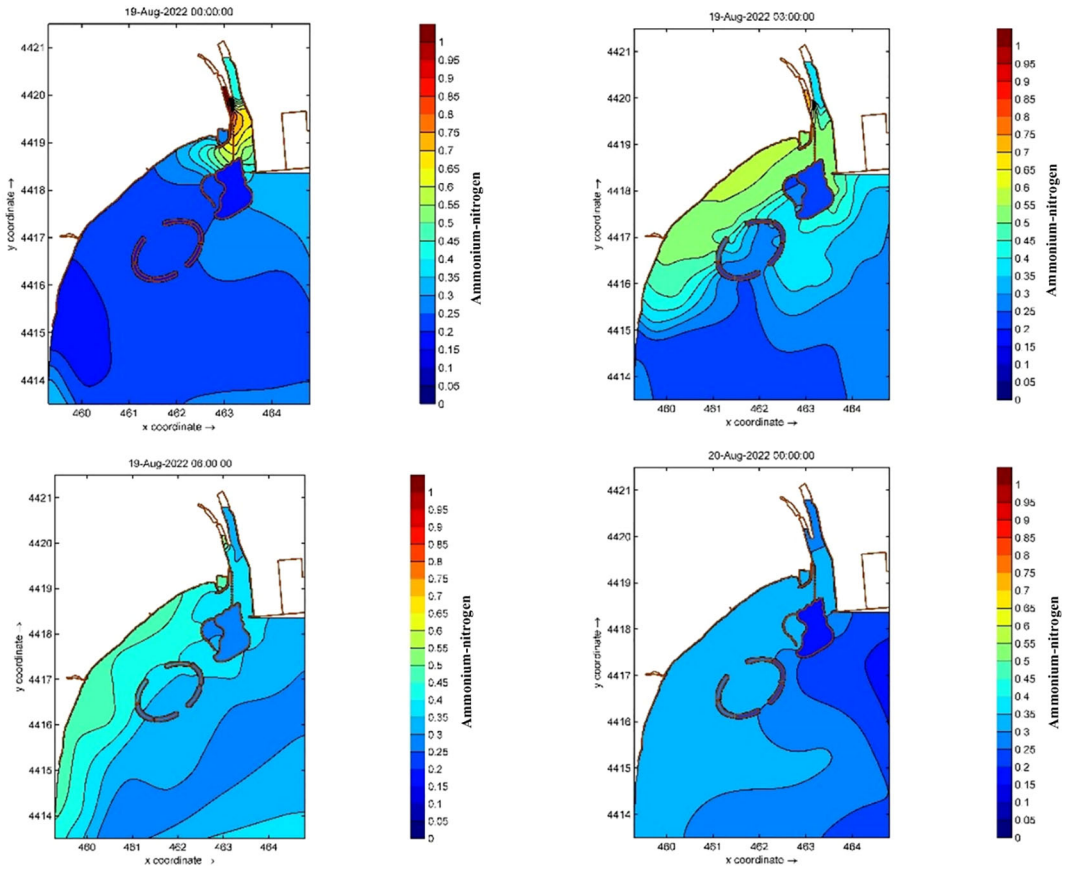

FIGURE 11
The process of diffusion of NH_4-N in the Tang Estuary caused by heavy rainfall in August 2022.

4 Discussion

4.1 Response modes for pollutant discharge into the sea

Under weak tidal dynamics, the short-term responses of pollution discharge into the sea can be roughly divided into two modes according to the formation of high concentrations in the source area, namely "rapid migration by the flood water flow + diffusion of a high concentration in the source area" and "rapid migration by the flood water flow + diffusion by the tide".

In this study, the diffusion patterns of DIN and NO_3-N were found to follow the first mode. During the stage of rapid migration by the flood water flow, the coastal area is mainly influenced by the flood flow of the river (Gu et al., 2017). Pollutants migrate rapidly with the flood water flow, and the concentration shows a trend of an initial high level, followed by a decrease, and then an increase again. This trend is related to the heavy rainfall and upstream pollutant release process (Kuang et al., 2015). During the stage in which the flood waters fall, pollutant diffusion enters the second stage, characterized by diffusion of the high concentration in the source area by tidal power. In this case, owing to the presence of complex artificial constructions, the estuary forms a relatively closed area meaning that the pollutant concentration in the area is high (Makabe et al., 2014; Kuang et al., 2019), forming a pollutant source area. This pollutant source area becomes another fixed pollutant source, slowly diffused under tidal power. The diffusion time of this pollutant source is much longer than the rapid migration occurring in the case of the flooding current, with the ratio of the durations of the two stages being approximately 1:5.5.

In contrast, the diffusion patterns of NH_4-N and PO_4-P were found to follow the second stage. At the early stage of flooding, high concentrations can be found in the flooding water. Under the action of the flood water flow, the pollution rapidly migrates and disperses in the coastal area, with the concentrations gradually decreasing or fluctuating slightly (Cao et al., 2017). With the decreasing flood flow, the pollutant dispersion process shifts to become dominated by tidal power, at which point the concentrations are essentially returning to pre-flooding levels, without forming an obvious "high concentration in the source area". With the further reduction of the flood water flow, the impact on these pollutants gradually ceases entirely.

As shown in Table 1, according to the field observations, NH_4-N and PO_4-P mainly come from the Xiaotang River, a tributary of the Tang River. When the small runoff from the Xiaotang River carries these pollutants into the Tang River, the large flow of the main stem disperses the concentration of these pollutants. With the concentration diluted, the pollutants are more easily carried away by the main stem to discharge into the sea. Therefore, a high concentration cannot form in the source area. In contrast, NO_3-N

comes from both the main stem of the Tang River and the Xiaotang River. The inflow of the Xiaotang River leads to a further increase in NO_3-N concentration in the estuary. Moreover, with the continuous water supply, the concentration of the pollutant in the estuary cannot easily be dissipated. Thus, a high concentration can form in the source area.

4.2 Responses in the form of eco-toxicogenic algal disaster

Studies have shown that most harmful algal blooms in coastal waters around the world are related to eutrophication (Fletcher, 1996; Valiela et al., 1997; Anderson et al., 2002; Heisler et al., 2008). Ecological disasters such as red and green tides occur frequently on the coast of Qinhuangdao. The growth of the causative algae is closely related to the pollutant diffusion, hydrodynamics, and meteorology of the Tang River (Cao et al., 2017; Han et al., 2019; Song et al., 2019; Zhang WL. et al., 2020; Han et al., 2022; He et al., 2022).

The Golden Dream Bay is the main area of Qinhuangdao where ecological disasters such as red and green tides occur (Kuang et al., 2021; Han et al., 2022). Figure 13 shows the changes in biomass of red tide and green tide algae species before and after the period of heavy rainfall examined here. The biomass of these species in the Golden Dream Bay decreased sharply during the rapid migration stage of the flooding current, although the concentration of nutrients (i.e., N and P) increased rapidly. This was caused by the high velocity of the flood water flow, which destroyed the habitat of the algal species that produce red and green tides (Han et al., 2019). With the gradual weakening of the flood water flow, the biomass of algae increased dramatically under the suitable environmental conditions of tidal power and high concentrations of nutrients (Pedersen and Borum, 2010). The high-concentration source area serves as an additional source of nutrient salts and prolongs the time span of the local eutrophication. These high-concentration nutrient salts also provide a continuous source of growth and reproduction of biomass for red tide and green tides. It can be concluded that this is one of the main reasons why ecological disasters such as red and green tides often occur 1–5 days after heavy rainfall.

4.3 The influence of the Tongdao Bridge on coastal water quality

The ecological environment of the bay area near the estuary is very vulnerable to flooding of the river. During the flooding caused by heavy rainfall, the river not only brings a large amount of pollutants into the sea, but also carries a large amount of land-based waste material, which accumulates on the bay beach and damages the beach's usability for bathing.

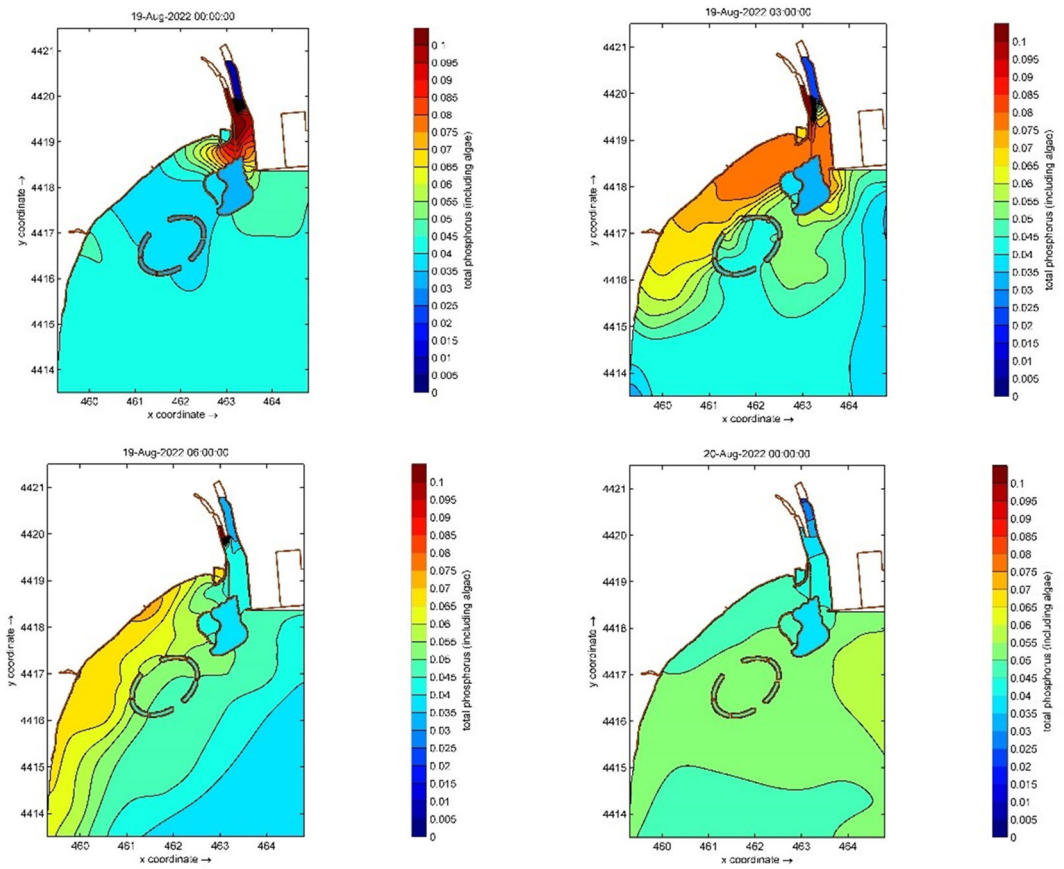

FIGURE 12
The process of diffusion of PO_4-P in the Tang Estuary caused by heavy rainfall in August 2022.

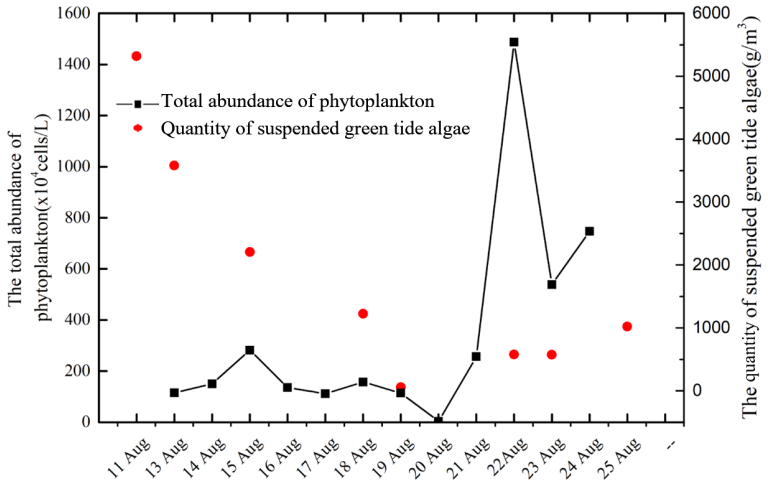

FIGURE 13
Changes in red tide and green tide biomass in August 2022.

From the hydrodynamic simulation, it can be seen that, in the Tang Estuary, the overall hydrodynamic conditions are weakened by the fact that the Tongdao Bridge reduces the cross-section area between Hailuo Island and the mainland. This reduces the diffusion rate of pollutants from the river (Kuang et al., 2019). The bridge may negatively affect the water quality of the Golden Dream Bay bathing beach under conventional ocean dynamics (Sheng et al., 2016). During short-term flooding of the Tang River, a large amount of land-based waste material may be deposited on the bathing beach adjacent to the path of the flood water under the bridge. The presence of the bridge leads to the accumulation of a large amount of land-based waste material, such as plant stalks, dead grass, domestic waste, and farming nets, on the Golden Dream Bay beach. The reduction in the water-crossing area by the bridge may play a certain beneficial role in maintenance of the water quality and in interdiction of the accumulation land-based waste material on the Golden Dream Bay bathing beach. At the same time, the bridge exerts a certain flow-guiding effect, so that some of the land-based pollutants and garbage drain into the sea through the channel between the Hailuo Island and Qinhuangdao Port breakwaters. On the basis of future hydrodynamics calculations, the construction of movable sluice gates under the bridge could be considered. The sluice gates could provide scientifically calculated and reasoned control over the water-crossing section of the bridge during the early rapid migration stage of the influx of flood water, so that the flood water could be directed into the channel between Hailuo Island and Qinhuangdao Port. This measure could reduce the pressures on the ecological environment, such as poor water quality and the presence of land-based waste material in the Golden Dream Bay.

5 Conclusions

The main objective of this study was to investigate the hydro-environmental responses of a weak tidal estuary to heavy rainfall, based on the analysis of field observation data and a numerical simulation. The modes of response to pollutant discharge, eco-toxicogenic algal disasters, and effects of permeable buildings on pollutant dispersion have been discussed. The main conclusions can be summarized as follows:

1. The quality of the discharging water was altered by the heavy rainfall. Overall pollutant concentrations were all higher than those occurring before the rainfall, but each pollutant responded with different changes. The trends in COD and NH_4-N concentrations were broadly the same as those in the flood water flow. The concentrations of DIN, DTN, and NO_3-N all decreased slightly, then gradually increased, and finally stabilized. The concentrations of PO_4-P and NO_2-N showed a lightly fluctuating trend toward increasing.

2. The hydrodynamic simulations showed that the flood water flow induced by heavy rainfall caused significant changes in the hydro-environment in the Tang Estuary. The coastal flow velocity increased on the west side of the river channel. Multi-scale vortexes were formed on the east side. As the flooding flow increased, the nearshore flow velocity further increased, and the vortexes became larger with decreased number.

3. The concentrations of typical pollutants in the estuary were closely related to the river flooding process. The concentrations of DIN and NO_3-N increased rapidly with the flooding. The diffusion of these two pollutants was very limited because of their high concentration in the source area. Normalization of these concentrations lagged behind the flooding process by approximately 5.5 days. In contrast, the diffusion of NH_4-N and PO_4-P occurred significantly more quickly because of the origination of these pollutants from the tributary and the fact that a high concentration did not accumulate in the source area.

4. Two short-term response modes for pollutant diffusion have been proposed. The two modes provide a viewpoint for exploration the role of changes in the hydro-environment in terms of offshore algal hazards and the effects of permanent structures on pollutant dispersion.

Data availability statement

The original contributions presented in the study are included in the article/supplementary material. Further inquiries can be directed to the corresponding authors.

Author contributions

GW: investigation, methodology, and writing of the original draft. XF: investigation, methodology, and validation. JZ: funding acquisition, resources, and supervision. ZH: funding acquisition, supervision, visualization, and writing of the original draft. YB: conceptualization and supervision. WS: resources. HX: writing of the original draft. All authors contributed to the article and approved the submitted version.

Funding

This work is supported by the National Key R&D Program of China (2019YFC1407905), the Key R&D Program of Hebei Province (21373302D), the National Natural Science Foundation of China (No. 52109097), and the Opening Fund of State Key Laboratory of Hydraulic Engineering Simulation and Safety (HESS-2226).

Acknowledgments

The author would like to thank Hebei Marine Environment Laboratory for the observed data for verification.

Conflict of interest

The authors declare that the research was conducted in the absence of any commercial or financial relationships that could be construed as a potential conflict of interest.

Publisher's note

References

Anderson, D. M., Glibert, P. M., and Burkholder, J. M. (2002). Harmful algal blooms and eutrophication: Nutrient sources, composition, and consequences. *Estuaries* 25, 704–726. doi: 10.1007/BF02804901

Cao, X. H., Yu, Z. M., Song, X. X., Yuan, Y. Q., Wu, Z. X., and He, L. Y. (2017). Pollution and discharge from tributaries to the Sea along qinhuangdao Coast:Impact on the bioactive elements related to brown tide outbreak. *Oceanol Et Limnol Sin.* 48 (5), 970–981. doi: 10.11693/hyhz20170300077

Conley, D. J. (2000). Biogeochemical nutrient cycles and nutrient management strategies. *Hydrobiologia* 410, 87–96. doi: 10.1023/A:1003784504005

Fletcher, R. L. (1996). "The occurrence of "green tides", a review," in *Marine benthic vegetation: recent changes and the effects of eutrophication*. Eds. W. Schramm and P. H. Nienhuis (Berlin: Springer-Verlag), 7–43.

Gu, J., Hu, C. F., Li, Z. Y., Kuang, C. P., Zhang, Y. F., et al. (2017). Coupling simulation and analysis of hydrodynamics and water quality in qinhuangdao rivers and coastal waters. *Mar. Sci.* 41 (2), 1–11. doi: 10.11759/hykx20160815001

Han, H. B., Li, Y., Ma, X. J., Song, W., Wang, Z. L., and Zhang, X. L.. (2022). Factors influencing the spatial and temporal distributions of green algaemicro-propagules in the coastal waters of jinmenghaiwan, qinhuangdao, China. *Mar. pollut. Bull* 175, 113328. doi: 10.1016/j.marpolbul.2022.113328

Han, H. B., Song, W., Wang, Z. L., Ding, D. W., Yuan, C., Zhang, X. L., et al. (2019). Distribution of green algae micropropagules and their function in the formation of the green tides in the coast of qinhuangdao, the bohai Sea, China. *Acta Oceanol Sin.* 38 (8), 72–77. doi: 10.1007/s13131-018-1278-1

Han, X. R., Wang, X. L., Sun, X., Shi, X., , Y., Zhu, C. J., Zhang, C. S., et al. (2003). Nutrient distribution and its relationship with occurrence of red tide in coastal area of East China Sea. *Chin. J. Appl. Ecol.* 14 (7), 1097–1101. doi: 10.13287/j.1001-9332.2003.0245

He, Y. K., Chen, Z. Y., Feng, X., Wang, G. Y., Wang, G., and Zhang, J. B. (2022). Daily samples revealing shift in phytoplankton community and its environmental drivers during summer in qinhuangdao coastal area, China. *Water* 14, 1625. doi: 10.3390/w14101625

Heisler, J., Glibertm, P. M., Burkholder, J. M., Anderson, D., Cochlan, W., Dennison, W., et al. (2008). Eutrophication and harmful algal blooms: A scientific consensus. *Harmful Algae* 8, 3–13. doi: 10.1016/j.hal.2008.08.006

Kuang, C. P., Hu, C. F., Mao, X. D., and Gu, J.. (2015). Numerical simulation of hydrodynamics and pollutant transport in qinhuangdao coastal water in the flood season. *J. Tongji Univ. (Natural Science)* 43 (9), 1355–1366.

Kuang, C. P., Wang, D., Zhao, F., Liu, H. X., and Zhu, L. (2021). Temporal and spatial distribution characteristics of water environmental factors in jinmeng bay and its adjacent waters. *J. Tongji Univ. (Natural Science)* 49 (6), 880–890. doi: 10.11908/j.issn.0253-374x.21008

Kuang, C. P., Yu, L. L., Gu, J., Dong, Z. C., Song, H. L., Zhu, L., et al. (2019). Influences of artificial island on water exchange of jinmeng bay. *China Environ. Sci* 39 (2), 757–767. doi: 10.19674/j.cnki.issn1000-6923.2019.0093

Lappalainen, A., and Ponni, J. (2000). Eutrophication and recreational fishing on the Finnish coast of the gulf of Finland, a mail survey. *Fish Manag Ecol.* 7, 323–335. doi: 10.1046/j.1365-2400.2000.007004323.x

Liu, X. H. (2010). Analysis on environment situation of coastal areas of bohai Sea. *Environ. Prot. Sci.* 36 (1), 14–18. doi: 10.16803/j.cnki.issn.1004-6216.2010.01.005

Liu, J., Liu, L. S., and Zheng, B. H. (2017). Problems and countermeasures of water environmental management in estuaries. *Res. Environ. Sci.* 30 (5), 645–653. doi: 10.13198/j.issn.1001-6929.2017.02.28

Luan, W. X., Wang, H., and Kang, M. J. (2016). *Study on the integrated zoning and control of pollution pressure in bohai rim region* (Beijing: Ocean Press).

Lucas, C. H., Graham, W. M., and Widmer, C. (2012). Jellyfish life histories: Role of polyps in forming and maintaining scyphomedusa populations. *Adv. Mar. Biol.* 63, 133–96. doi: 10.1016/B978-0-12-394282-1.00003-X

Makabe, R., Furukawa, R., Takao, M., and Uye, S.. (2014). Marine artificial structures as amplifiers of aurelia aurita s.l. blooms: a case study of a newly installed floating pier. *J. Oceanogr* 70, 447–455. doi: 10.1007/s10872-014-0249-1

Meybeck, M. (1982). Carbon, nitrogen, and phosphorus transport by world rivers. *Am. J. Sci.* 282, 401–450. doi: 10.2475/ajs.282.4.401

Pan, Y., Kuang, C. P., Chen, Y. P., Yin, S., Yang, Y. B., and Yang, Y. X.. (2018). A comparison of the performance of submerged and detached artificial headlands in a beach nourishment project. *Ocean Eng* 159, 295–304. doi: 10.1016/j.oceaneng.2018.04.038

Pan, Y., Yin, S., Chen, Y. P., Yang, Y. B., Xu, C.Y., and Xu, Z. S. (2022). An experimental study on the evolution of a submerged berm under the effects of regular waves in low-energy conditions. *Coast. Eng* 176, 104169. doi: 10.1016/j.coastaleng.2022.104169

Pan, Y., Zhou, Z. J., and Chen, Y. P. (2020). An analysis of the downward-flushing flow on the crest of a levee under combined wave and surge overtopping. *Coast. Eng.* 158, 103701. doi: 10.1016/j.coastaleng.2020.103701

Pedersen, M. F., and Borum, J. (2010). Nutrient control of estuarine mac-roalgae: growth strategy and the balance between nitrogen requirements and uptake. *Mar. Ecol-Prog Ser.* 1), 5–9. doi: 10.3354/meps161155

Riisgard, H. U., and Hoffmann, E. (2012). From fish to jellyfish in the eutrophicated limfjorden (Denmark). *Estuaries Coasts* 35, 701–713. doi: 10.1007/s12237-012-9480-4

Sheng, T. H., Sun, D. M., and Zhang, Y. (2016). Analysis of artificial island construction influences on individual flood erosion and deposition in estuary. *J. Waterway Harbor* 37 (1), 18–26.

Song, W., Wang, Z. L., Li, Y., and Zhang, X. L.. (2019). Tracking the original source of the green tides in the bohai Sea, China. *Estuarine Coast. Shelf Sci* 219, 354–362. doi: 10.1016/j.ecss.2019.02.036

Tang, W. J., Geng, H. X., Xi, Y. J., Zhang, Q. C., Tan, X. X., Yu, R.C., et al. (2022b). Mapping the resting cysts of dinoflagellate alexandrium catenella along the coast of qinhuangdao, China. *J. Oceanol Limnol* 40, 2312–2321. doi: 10.1007/s00343-022-2190-2

Tang, W. J., Lin, Z. R., Zhang, Q. C., Geng, H. X., Sun, H. X., Tang, X. X., et al. (2022a). An investigation on bloom dynamics of alexandrium catenella and a. pacificum and toxin accumulation in shellfish along the coast of qinhuangdao, China. *Mar. pollut. Bull* 183, 114058. doi: 10.1016/j.marpolbul.2022.114058

Valiela, I., McClelland, J., Hauxwell, J., Behr, P. J., Hersh, D., and Foreman, K. (1997). Macroalgal blooms in shallow estuaries: controls and ecophysiological and ecosystem consequences. *Limnol Oceanogr* 42, 1105–1118. doi: doi: 10.4319/lo.1997.42.5_part_2.1105

Yu, R. C., Zhang, Q. C., Liu, Y., Chen, Z. F., Geng, H. X., Dai, L., et al. (2021). The dinoflagellate alexandrium catenella producing only carbamate toxins may account for the seafood poisonings in qinhuangdao, China. *Harmful Algae* 103, 101980. doi: 10.1016/j.hal.2021.101980

Zhai, W. K., Xu, Z. Z., and Zhang, J. (2016). Analysis on characteristics of red tide disaster in hebei coastal waters. *Mar. Environ. Sci.* 35 (2), 243–251. doi: 10.13634/j.cnki.mes.2016.02.015

Zhang, W. Q., Han, H. B., and Qiu, L. M. (2022). Variations in nano- and pico-eukaryotic phytoplankton assemblages in the qinhuangdao green-tide area. *J. Oceanol Limnol* 40, 2446–2461. doi: 10.1007/s00343-022-2198-7

Zhang, W. L., Ma, X., Zhang, Y. F., Zhang, J. L., Zhao, S. L., Li, G. M., et al. (2020). An analysis of red tide characteristics in qinhuangdao coastal seawater. *Trans. Oceanol Limnol* 5, 48–55. doi: 10.13984/j.cnki.cn37-1141.2020.05.007

Zhang, Q. C., Yu, R. C., Zhao, J. Y., Kong, F. Z., Chen, Z. F., Niu, Z., et al. (2020). Distribution of aureococcus anophagefferens in relation to environmental factors and implications for brown tide seed sources in qinhuangdao coastal waters, China. *Harmful Algae* 109, 102015. doi: 10.1016/j.hal.2021.102105

Zhang, Z. H., Zhu, M. Y., Wang, Z. L., and Wang, J.. (2006). Monitoring and managing pollution load in bohai Sea, PR China. *Ocean Coast. Manage.* 49 (9), 706–716. doi: 10.1016/j.ocecoaman.2006.06.005

Zhao, Z. Y., and Kong, L. H. (2000). Environmental status quo and protection countermeasures in bohai marine areas. *Res. Environ. Sci.* 2), 23–27. doi: 10.13198/j.res.2000.02.26.zhaozhy.008

Zhou, Z. X., Kong, F. Z., Zhang, Q. C., Gao, Y., Koch, F., Gobler, C. J., et al. (2023). Brown tides linked to the unique nutrient profile in coastal waters of qinhuangdao, China. *Environ. Res.* 216, 114459. doi: 10.1016/j.envres.2022.114459

frontiers | Frontiers in Marine Science

TYPE Original Research
PUBLISHED 23 March 2023
DOI 10.3389/fmars.2023.1118795

OPEN ACCESS

EDITED BY
Sha Lou,
Tongji University, China

REVIEWED BY
Guoxiang Wu,
Ocean University of China, China
Jishang Xu,
Ocean University of China, China

*CORRESPONDENCE
Chunyan Zhou
cyzhou@hhu.edu.cn

SPECIALTY SECTION
This article was submitted to Coastal Ocean Processes, a section of the journal Frontiers in Marine Science

RECEIVED 08 December 2022
ACCEPTED 13 March 2023
PUBLISHED 23 March 2023

CITATION
Wu Z, Zhou C, Wang P and Fei Z (2023) Responses of tidal dynamic and water exchange capacity to coastline change in the Bohai Sea, China.
Front. Mar. Sci. 10:1118795.
doi: 10.3389/fmars.2023.1118795

Responses of tidal dynamic and water exchange capacity to coastline change in the Bohai Sea, China

Zhengcheng Wu[1], Chunyan Zhou[1*], Peng Wang[2] and Zihao Fei[1]

[1]College of Harbour, Coastal and Offshore Engineering, Hohai University, Nanjing, China, [2]Marine Academy of Zhejiang Province, Hangzhou, China

Bohai Sea (BHS) is a semi-enclosed shallow continental sea in China that has suffered from the deteriorative hydrodynamic environment due to large-scale reclamation. Single-factor simulations of tidal dynamic and material transport under the influence of the coastline changes from 1999 to 2019 in BHS were carried out. The model results showed that the amplitude of M2 tide increased slightly in Liaodong Bay and Bohai Bay, but decreased obviously in Laizhou Bay along with larger reclamation. The amplitude variation of the semi-diurnal constituents (M2, S2) was greater than the diurnal ones (K1, O1). The basin residence time in Liaodong Bay and Laizhou Bay increased by 5.44% and 49.44% from 1999 to 2019, respectively. Runoff of the Huanghe River can shorten the residence time of Laizhou bay while only having little effect on Bohai Bay and Liaodong Bay. The study of the Bohai Sea evolution can provide recommendations for subsequent marine ecological restoration efforts and serve as a reference for the study of other large semi-enclosed bays.

KEYWORDS

Bohai Sea, coastline change, tidal dynamics, tidal prism, land reclamation, water-exchange

1 Introduction

Reclamation changes the coastline and geomorphology of coastal areas and has an obvious impact on the propagation, refraction, reflection and dissipation of bottom energy of gravity waves such as tidal waves and storm surges, thus changing the phase of ocean wave fluctuations and the spatial distribution of energy (Zhu et al., 2016). Large-scale reclamation has alleviated the problem of conflicting urban land use, but the water environment in many bays has suffered some negative effects due to some unregulated engineering construction (Li et al., 2020).

Many researchers have analyzed the water environment changes of bays due to human activities. The construction of sea walls in the Mokpo coastal zone has resulted in a decrease of 43 cm for the extreme low tide and an increase of 60 cm for the extreme high tide. This amplification can cause severe inundation when a typhoon hits (Kang, 1999). Reclamation

significantly altered the morphological characteristics of the Shannon estuary, leading to changes in the physical and hydrodynamics environment of the estuary, and modification of the characteristics of the wetland habitat in the estuary environment (Healy and Hickey, 2002). Liang et al. (2018) investigated the hydro-morphodynamics of Caofeidian channel-shoal along with large-scale reclamation projects from 2003 to 2020. Numerical results indicated that continuous land reclamation caused a continuous loss of tidal sediment volume by reducing the sediment storage capacity of tidal flats.

Bohai Sea is a semi-enclosed shallow continental sea, located within 37°07′N-41°00′N, 117°35′E-121°10′E (Figure 1). The sea is divided into four parts: Bohai Bay, Liaodong Bay, Laizhou Bay and the central BHS. The sea covers an area of 77,000 km^2 with an average depth of 18 m, and 95% of BHS is less than 30 m.

Coastal areas were reclaimed along with rapid economic development in cities surrounding BHS. From 1987 to 2016, the total area of BHS decreased by 1889.51 km^2 and the length of the coastline increased by 1672.16 km (Zhu et al., 2018). The average reclamation rate in BHS is 325 km^2/year, and more than 60% of the total reclamation area is unused land, aquaculture land and saline land (Ding et al., 2019). Zhao and Sun (2013) studied the impact of reclamation on the wave in the Caofeidian region and found that the significant wave height tends to decline by 0.1-0.4 m from 2000 to 2010. Li et al. (2010) used an integrated hydrodynamic-dispersion numerical model to investigate the impact of land reclamation on the water exchange in the coastal area of Tianjin in Bohai Bay. From 1976 to 2011, the tidal system in BHS changed significantly with M2 amplitudes varying up to 20 cm in some areas (Pelling et al., 2013). Jia et al. (2018) predicted the effects of shoreline changes in Bohai Bay and showed that the coastline change weakened the residual currents, resulting in weaker water exchange and poor pollutant-diffusing capacity.

However, there is still a lack of studies on the effects of water environmental degradation in the whole BHS due to reclamation, which is essential for providing a comprehensive reference for future ecological restoration. In this paper, single-factor simulations of the tidal dynamics are performed under the influence of coastline changes in BHS and compare the impact of runoff of the Huanghe River on the water exchange capacity in BHS before and after reclamation. This research explores the response of tidal prism, tidal system and water exchange to large-scale reclamation in BHS from 1999 to 2019, and provides a reference for similar studies of other large semi-enclosed bays with intensive anthropogenic activities.

2 Data and methods

2.1 Coastline data

The coastline was derived from the Chinese mainland shoreline (CLINE) database. The CLINE database consists of a coastline extraction algorithm based on the remote sensing image data from Google Earth Engine, 37 years (1984~2020) of the year-by-year coastline of China and its supporting analysis information. Compared with other coastline databases, the CLINE database has the characteristics of high temporal resolution, lengthy periods, and large spatial coverage for the coastline of mainland China. Reclamation projects in BHS were rare before 2000 and the Chinese government introduced strict control measures to prohibit reclamation in 2018, thereafter the coastline was almost

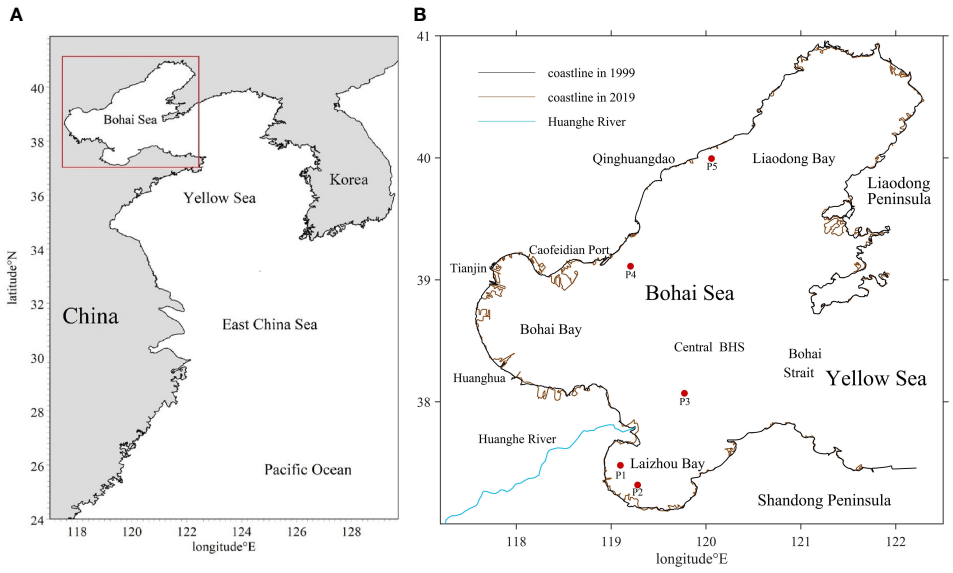

FIGURE 1
(A) Location of Bohai Sea; **(B)** Coastline in 1999 and 2019.

unchanged by human activities. This paper chose the coastline in 1999, 2009 and 2019 to build hydrodynamic models.

2.2 Numerical model

The simulations were performed using the MIKE 21 Flow Model. The momentum equations are the incompressible, Reynolds-averaged form of the Navier–Stokes equations, obeying the Boussinesq assumption and the hypothesis of vertical hydrostatic pressure. The continuity equation is Equation 1, two horizontal momentum equations for the x and y components are Equation 2 and Equation 3, respectively:

$$\frac{\partial h}{\partial t}+\frac{\partial h\bar{u}}{\partial x}+\frac{\partial h\bar{v}}{\partial y}=hS \tag{1}$$

$$\frac{\partial h\bar{u}}{\partial t}+\frac{\partial h\bar{u}^2}{\partial x}+\frac{\partial h\bar{v}\bar{u}}{\partial y}=f\bar{v}h-gh\frac{\partial \eta}{\partial x}-\frac{\tau_{bx}}{\rho_0}$$

$$\frac{1}{\rho_0}\left(\frac{\partial S_{xx}}{\partial x}+\frac{\partial S_{xy}}{\partial y}\right)+\frac{\partial}{\partial x}(hT_{xx})+\frac{\partial}{\partial y}(hT_{xy})+hu_sS \tag{2}$$

$$\frac{\partial h\bar{v}}{\partial t}+\frac{\partial h\overline{uv}}{\partial x}+\frac{\partial h\bar{v}^2}{\partial y}=-f\bar{u}h-gh\frac{\partial \eta}{\partial y}-\frac{\tau_{by}}{\rho_0}-$$

$$\frac{1}{\rho_0}\left(\frac{\partial S_{yx}}{\partial x}+\frac{\partial S_{yy}}{\partial y}\right)+\frac{\partial}{\partial x}(hT_{xy})+\frac{\partial}{\partial y}(hT_{yy})+hv_sS \tag{3}$$

where h is the total water depth, t time, x and y are the Cartesian coordinates, and are depth averages of velocity components in the x and y direction, S is the magnitude of the discharge because of point sources, f is the Coriolis parameter, g is gravitational acceleration, η is surface elevation, ρ_0 is the reference density of water, $\tau_{bx}$and τ_{by} are the components of bottom stress, u_s, v_s are the velocity at which the water is discharged into the ambient water, T_{xy}, T_{xx} and T_{yy} are the lateral stresses.

A transport module was coupled to the Mike21 hydrodynamic model to simulate tracer transport, as Equation 4 and Equation 5 (Bai et al., 2021).

$$\frac{\partial(hC)}{\partial t}+\frac{\partial(\bar{u}hC)}{\partial x}+\frac{\partial(\bar{v}hC)}{\partial y}$$
$$=\frac{\partial}{\partial x}\left(hD_x\frac{\partial C}{\partial x}\right)+\frac{\partial}{\partial y}\left(hD_y\frac{\partial C}{\partial y}\right)-FhC+S \tag{4}$$

$$S=Q_s(C_s-C) \tag{5}$$

where D_x, D_y are the diffusion coefficients in the x and y directions, C is the composite concentration, F is the linear attenuation coefficient, S is the source discharge, Q_s is source-sink term flow, C_s is the concentration at the source-sink.

The open boundary conditions are water levels derived from tide prediction based on the harmonic constants of tide stations at the open boundary. The bottom friction is one of the main factors affecting the calculation accuracy, which is set as a constant Chezy number of 118 after model validation.

2.3 Residence time calculation

Residence time is calculated by the Eulerian definition. A tracer with a concentration of 1 is released in the bay, and the concentration of each grid cell changes under the combined effect of runoff and water exchange outside the bay, and the volume changes with the rise and fall of the tide level. The relative tracer mass (RTM) is given as Equation 6 (Yuan et al., 2021):

$$RTM(t)=\frac{\sum_{i=1}^{n}C_i(t)V_i(t)}{\sum_{i=1}^{n}C_i(t_0)V_i(t_0)} \tag{6}$$

where the subscript i is the number of the grid, C_i is the concentration of grid number i at the time t, V_i is the volume of grid number i at the time t. Due to the initial condition setting, here $C_i(t_0)$=1, so the denominator of Equation 6 is the initial bay volume.

Residence time is the average time that a dissolved or suspended material resides in the bay before it is transported into the open sea (Liu et al., 2011). Basin residence time and local residence time are used to reflect the water exchange capacity of the whole bay and a single grid respectively. The residence time in Zhao et al. (2002) was defined as the time required for the concentration of the passive tracer in a given region to decay to e^{-1} (37%) of the initial value. In this paper, the basin residence time is the moment when the RTM $=e^{-1}$ (37%) after a polynomial fit of the average bay concentration (Figure 2). This calculation method eliminates the effect of tidal action on the variation of the average concentration in the bay by polynomial fitting, thus accurately reflecting the residence time in the bay.

But this method cannot be used to calculate the local residence time. Polynomial fit for each grid is too computationally intensive and the water level of the nearshore area drops substantially at low tide, which will cause a decrease in the number of tracers contained in the grid with decreasing water depth, resulting in a small local residence time. Therefore, the residence time of the grid is the moment when the current concentration of the grid is for the first time less than 37% of the initial concentration.

2.4 Tidal prism calculation

The tidal prism is an essential parameter reflecting the hydrodynamics and water environment of a bay, which is highly

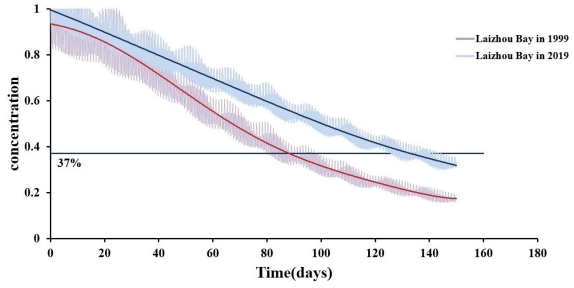

FIGURE 2
Time series of concentration and the polynomial fit in Laizhou Bay.

related to the residence time (Ying et al., 2018). The reduction of the tidal prism will decrease the intensity of water exchange between the bay and the outer sea, and slow down the migration and diffusion of pollutants, thus affecting the self-purification ability of the bay (Fang et al., 2015).

The tidal prism is calculated as the flux of seawater through the boundary section during a high or low tide cycle, and the average of the seawater fluxes in a high tide and low tide period is taken as the tidal prism for the whole tidal cycle. According to this definition, the tidal prism Q is given by:

$$Q = \int_{t_1}^{t_2} (Q_u + Q_v) dt \tag{7}$$

where Q_u and Q_v are the tidal flux through the section per unit time in the x and y directions, t_1 and t_2 are the start and end times of the high tide cycle or low tide cycle, respectively.

2.5 Eulerian tidal residual current calculation

The nonlinear action of tidal currents generates tidal residual currents, thus forming tidal circulation. Although the tidal circulation is relatively weak, the tidal residual current plays an important role in the migration and long-term stable distribution of pollutants in the sea because the Bohai Sea is semi-enclosed and the tide is the main dynamic factor in BHS. Eulerian tidal residual current is defined as the averaged speed at a fixed location during several tidal cycles and calculated according to Equation 8:

$$\begin{aligned} U_E &= \tfrac{1}{nT} \int_{t_0}^{t_0+nt} u(x_0, t) dt \\ V_E &= \frac{1}{nT} \int_{t_0}^{t_0+nt} v(x_0, t) dt \end{aligned} \tag{8}$$

where U_E and V_E are Eulerian average velocities in x and y directions respectively, t_0 is the initial moment of calculation, T is the tidal period, $u(x_0, t)$, $v(x_0, t)$ is the velocity of a fixed point in the x and y directions, n is the number of calculation periods, $N=nT/\Delta t$, Δt is the time step of the numerical simulation. In this paper, the 60 tidal cycles were counted in order to calculate the Eulerian tidal residual current, starting at the highest tidal level of the spring tide and ending at the highest tidal level of the spring tide a month later.

2.6 Model validation

The measured tidal level and current from five stations shown in Figure 1B were used for model validation. Figure 3 shows that the simulated tide levels are in very good match with the observation data. It is shown in Figure 4 that the modeled results of tidal velocity and direction have the same variation pattern with the observation data.

To quantitatively evaluate the accuracy of the hydrodynamic model simulation results, using the statistical method proposed by Willmott (1981) and correlation coefficient (CC) to evaluate simulation results:

$$skill = 1 - \frac{\sum_{i=1}^{N} |X_m - X_s|^2}{\sum_{i=1}^{N} (|X_m - \overline{X_s}| + |X_s - \overline{X_s}|)^2} \tag{9}$$

$$\mathrm{CC} = \frac{\sum (X_s - \overline{X_s})(X_m - \overline{X_m})}{[\sum (X_s - \overline{X_s})^2 \sum (X_m - \overline{X_m})^2]^{1/2}} \tag{10}$$

where X_m is the measured value, X_s is the simulated value, $\overline{X_m}$ and $\overline{X_s}$ are the mean value of the simulated and the measured value, respectively.

The skill value obtained from Equation 9 represents the simulated value deviation from the average of measured values and the CC represents the correlation of two statistical variables, when skill > 0.65 and CC>0.80, it means that the model fits well. The simulated accuracy of tidal currents and tidal level at each observation station can be represented by the skill value and the CC value, as shown in Table 1.

The skill values are larger than 0.95 for the tidal level, while larger than 0.85 for the current speed and direction. The CC is larger than 0.90 for the tidal level, while larger than 0.80 for the current speed and direction, thus the model can reflect the hydrodynamic situation of the whole Bohai Sea.

3 Results and discussion

3.1 Tidal wave

Tidal movement is the most important form of seawater movement in BHS, and the main tides in BHS are O1, K1, M2 and S2, of which the dominant tide is M2. To analyze the changes in the tidal wave system, the same boundary conditions were applied, but with different coastlines in 1999 and 2019, respectively. The simulation results were analyzed by Tide Analysis of Height in Mike21 Toolbox to obtain the amplitude and phase of M2, K1, S2 and O1. The simulation results show that various patterns of semi-diurnal constituents M2 and S2 are similar, but the amplitude of M2 is much larger than that of S2. Diurnal constituents of K1 and O1 have similar variation patterns and amplitudes.

From 1999 to 2019, amplitude of M2 in BHS has changed by -0.222m to 0.760m. It increased slightly in Liaodong Bay and Bohai Bay and decreased obviously in Laizhou Bay with a maximum value of 0.22m. Compared with the other two bays, only the amplitude of the M2 tide in Laizhou Bay was decreased. The reduction of amplitude is most obvious in the western part of Laizhou Bay, and the reduction in some areas is more than 0.04m (Figure 5). The area with a variation of -0.05m to 0.05m accounts for 95.26% of the total area of BHS. The amplitude of diurnal constituents in BHS changed slightly, and the amplitude of K1 changed by -0.023m to 0.243m. The area with the variation of -0.01m to 0.01m accounts for 99.6% of the total area of BHS. The area with decreasing M2 amplitude is larger than the area with increasing amplitude, while the contrary is the case for K1. Overall, the amplitude change range of semi-diurnal constituents was larger than the diurnal ones. The phase change of M2 in Bohai Bay slowed, causing the tidal wave entering from the east to decelerate more slowly, and the phase of M2 in Liaodong Bay barely changed from 1999 to 2019. The cotidal

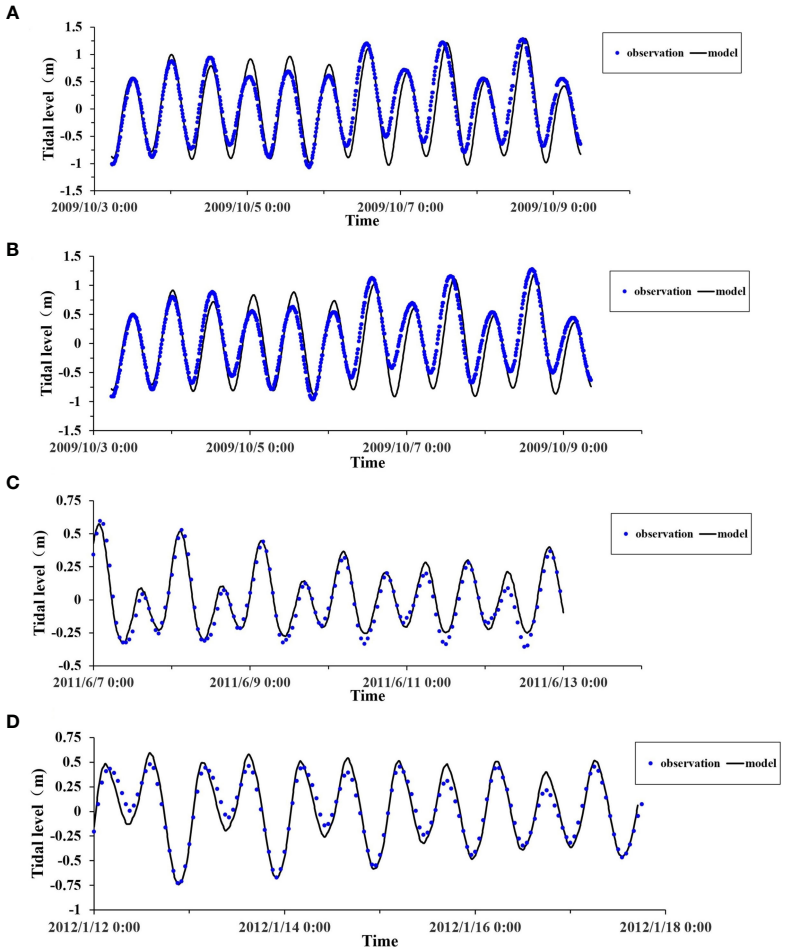

FIGURE 3
Tidal level comparison between model results and measured data at **(A)** Station P_1, **(B)** Station P_2, **(C)** Station P_3, **(D)** Station P_4.

line of K1 in most areas of BHS was deflected counterclockwise, resulting in a slight advance of tide time.

The Yellow River delta is characterized by high sediment load, fast accretion and frequent avulsions. To investigate the influence of the Yellow River Delta evolution on the tidal changes of Laizhou Bay, a case with shoreline only changes near the Yellow River Delta and remain unchanged at other areas was carried out. The results show that the amplitude changes are significant only in the vicinity of the Yellow River Delta, while less than 0.005 m for M2 and less than 0.002 m for K1 in most areas of Laizhou Bay. Therefore, the evolution of the Yellow River Delta is not the dominating factor contributing to tidal changes in the Laizhou Bay (Figures 6A, B).

Figures 6C, D shows that the amphidromic point of M2 near Qinhuangdao migrated 7.73km southwestward, and the amphidromic point near the Huanghe River estuary migrated 9.15 km southeastward. The amphidromic point of K1 in the Bohai Strait migrated 3.71 km southeastward. From the perspective of tidal energy distribution, tidal flats store tidal energy including potential tidal energy and kinetic energy during flood tides and release it during ebb tides. Tidal flats have two functions affecting tidal energy distribution: storage and dissipation. Compared with the tidal energy dissipation caused by bottom friction, the tidal energy storage in the mudflat area is much larger. (Song et al., 2013). The tidal energy stored in the mudflat area will be redistributed in the sea outside the mudflat area due to the reduction of the mudflat area caused by the reclamation, which resulted in the amphidromic point in BHS departing from the coastline (Zhu et al., 2016).

3.2 Residence time

Many seasonal rivers flow into BHS, with a total average annual runoff around 5.0×10^{10} m^3, more than a half comes from the Huanghe River (Ding et al., 2020). In this paper, the impact of the Huanghe River runoff on exchange was investigated in BHS, and the daily average flow of the Huanghe River was obtained from the Huanghe River Conservancy Commission of the Ministry of Water Resources. The simulation duration of Laizhou Bay, Bohai Bay and Liaodong Bay was 5 months, 30 months and 70 months respectively. Hydrodynamic models coupled with the transport module were established for Laizhou Bay and Bohai Bay with and without runoff from the Huanghe River in 1999 and 2019. Liaodong Bay is far away from the Huanghe River estuary, so the influence of

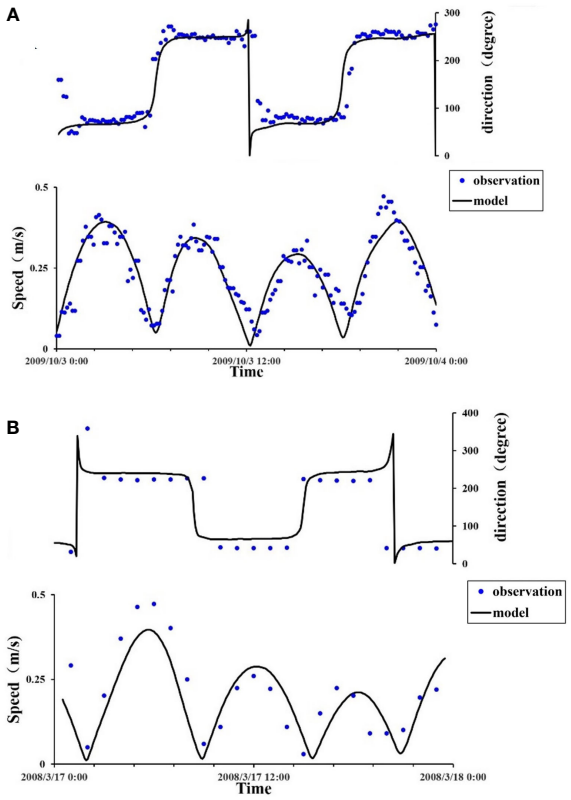

FIGURE 4
Current speed comparison between model results and measured data at **(A)** Station P_2, **(B)** Station P_5.

the Huanghe River runoff on the water exchange in Liaodong Bay was not considered here.

The results showed that the coastline change increased the basin residence time and local residence time in Laizhou Bay, especially in the nearshore waters (Figures 7A1, A3). Basin residence time in Laizhou Bay increased from 89 days in 1999 to 133 days in 2019 and the area with local residence time larger than 140 days increased significantly without considering runoff. Basin residence time in Bohai Bay increased from 466 days in 1999 to 510 days in 2019. The local residence time in the region (a) in the northern part of Bohai Bay decreased from 1999 to 2019 (Figures 7 B1, B3), which was related to the existence of circulation in that area before the construction of Caofeidian Port, impeding the material transport in the northern part of Bohai Bay. After the construction of Caofeidain Port in 2019, the circulation disappeared and Eulerian tidal residual current velocity in the region (a) increased (Figures 8C, D), accelerating the exchange of tracers in the northern part of Bohai Bay with the outer sea, thus leading to a smaller local residence time in the region (a). The local residence time in region (b) in the southern part of Bohai Bay increased from 1999 to 2019 (Figures 7B1, B3), mainly because the Eulerian tidal residual current direction in 2019 obliqued to the north compared to that in 1999, reducing the ability of the tracer to exchange directly with the outer sea, which was probably related to the reclamation shoreward in the southern part of Bohai Bay. The basin residence time in Liaodong Bay is 1894 days in 1999 and 1997 days in 2019, only increase by 5%, which indicates that coastline changes only have little effect on material transport in Liaodong Bay.

Runoff could shorten the basin residence time in Laizhou Bay and Bohai Bay (Table 2). However, the local residence time barely changed in most regions of Bohai Bay and Laizhou Bay with/without the runoff (Figure 7). The main reason is that the calculation methods of basin residence time and local residence time are different as shown in Section 2.3. Under the influence of runoff, the local residence time of Laizhou Bay changed very little and the residence time of Laizhou Bay decreased by 11 days in 1999 and 9 days in 2019, respectively. It indicates that runoff can intensify the oscillation of tracer concentration in the bay with high and low tides, thus affecting the fitted calculated basin residence time. However, the effect of runoff on local residence time is limited to the vicinity of the Huanghe River estuary.

The Eulerian tidal residual current (Figure 8) showed that Laizhou Bay exchanged water with the outer sea through the eastern coast, and the Eulerian residual velocity in this area was relatively large. However, the Eulerian residual velocity at the junction of Bohai Bay and the central BHS was low, leading to seawater containing the tracer staying in the center after flowing out of the bay during the low tide cycle and flowing back into Bohai Bay during the next high tide, so the residence time in Bohai Bay was relatively longer, and the coastline change had a relatively minor impact on the water exchange.

TABLE 1 Skill and CC value at each station.

Items	location	skill	CC
Tidal level	P1	0.95	0.92
	P2	0.95	0.91
	P3	0.98	0.97
	P4	0.98	0.97
Current speed	P2	0.94	0.89
	P5	0.85	0.85
Current direction	P2	0.92	0.9
	P5	0.88	0.82

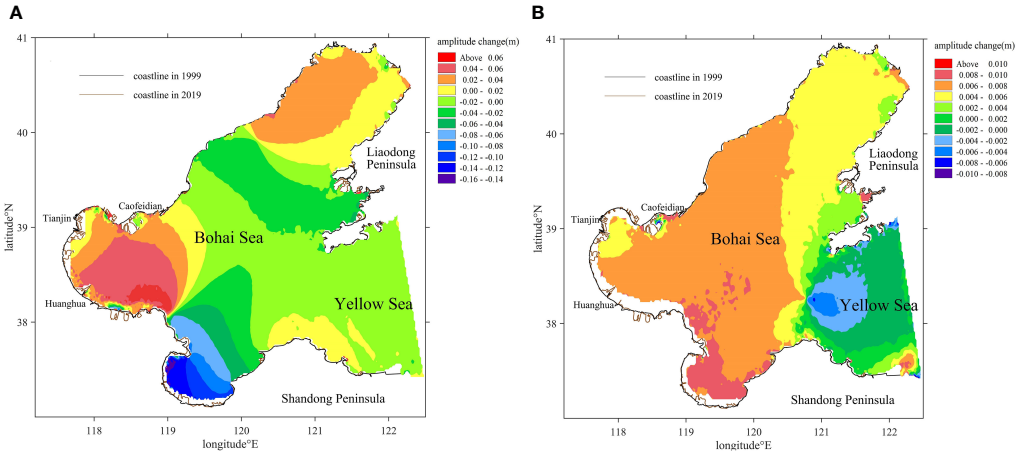

FIGURE 5
Tidal amplitude changes from 1999 to 2019 of **(A)** M2, **(B)** K1.

3.3 Tidal prism

To quantify the influence of the reclamation on the tidal prism of BHS and evaluate the impact of the reclamation on the water exchange capacity of the bay, hydrodynamic models were established to calculate the tidal fluxes in *x* and *y* directions at the boundary sections of three bays from June 1 to August 1. The average tidal prism of the three bays in BHS in 1999, 2009

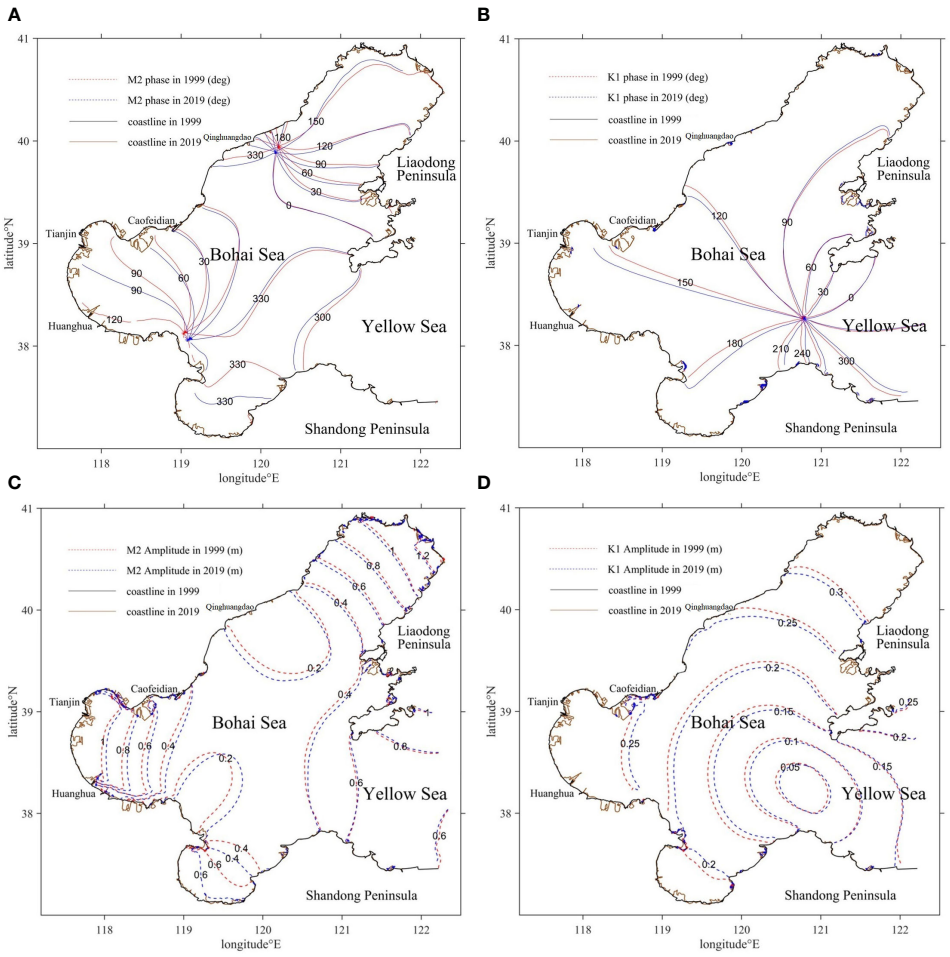

FIGURE 6
M2 and K1 tidal amplitudes and phases. **(A, B)** M2 and K1 tidal phases in 1999 and 2019. **(C, D)** M2 and K1 tidal amplitudes in 1999 and 2019.

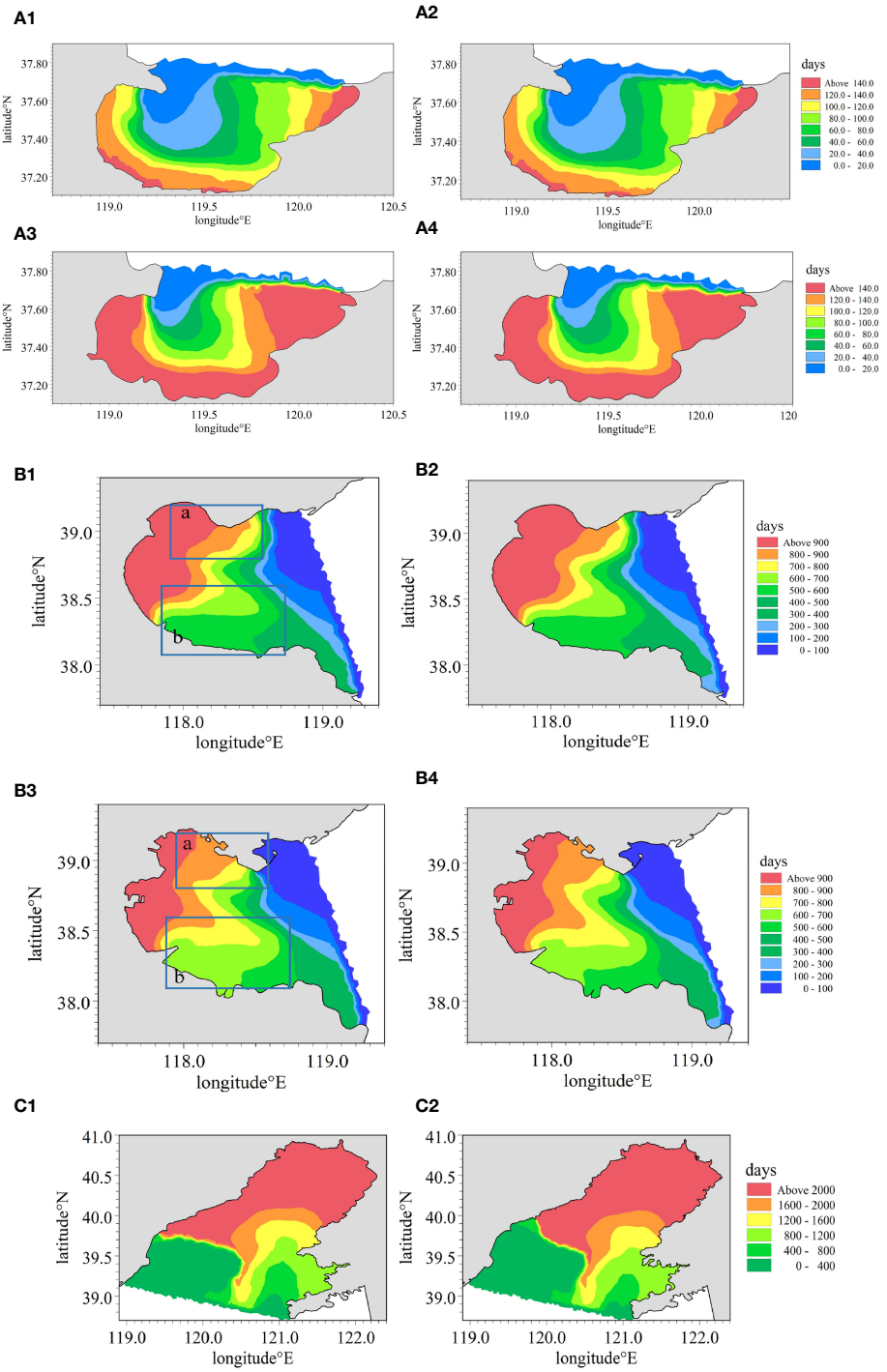

FIGURE 7
Local residence time **(A1)** Bohai Bay in 1999; **(A2)** Bohai Bay under the influence of with runoff in 1999; **(A3)** Bohai Bay in 2019; **(A4)** Bohai Bay with runoff in 2019; **(B1)** Laizhou Bay in 1999; **(B2)** Laizhou Bay with runoff in 1999; **(B3)** Laizhou Bay in 2019; **(B4)** Laizhou Bay with runoff in 2019; **(C1)** Liaodong Bay in 1999; **(C2)** Liaodong Bay in 2019.

and 2019 and its change rate relative to 1999 were listed in Table 3.

In general, the change of prism and residence time in Liaodong Bay was the smallest, and its area decrease was slightly smaller than the other two bays, which indicated that the coastline change in Liaodong Bay had the smallest influence on its water exchange capacity (Tables 2, 3). Therefore, it can be obtained that the water exchange capacity of bays with larger areas is less affected by coastline changes compared to bays with smaller areas. Laizhou Bay has a similar change rate of area with Bohai Bay, but Laizhou Bay has a larger decrease rate of tidal prism than Bohai Bay. The basin residence time increased by 58.97% and 10% respectively for Laizhou Bay and Bohai Bay from 1999 to 2019 without considering the runoff.

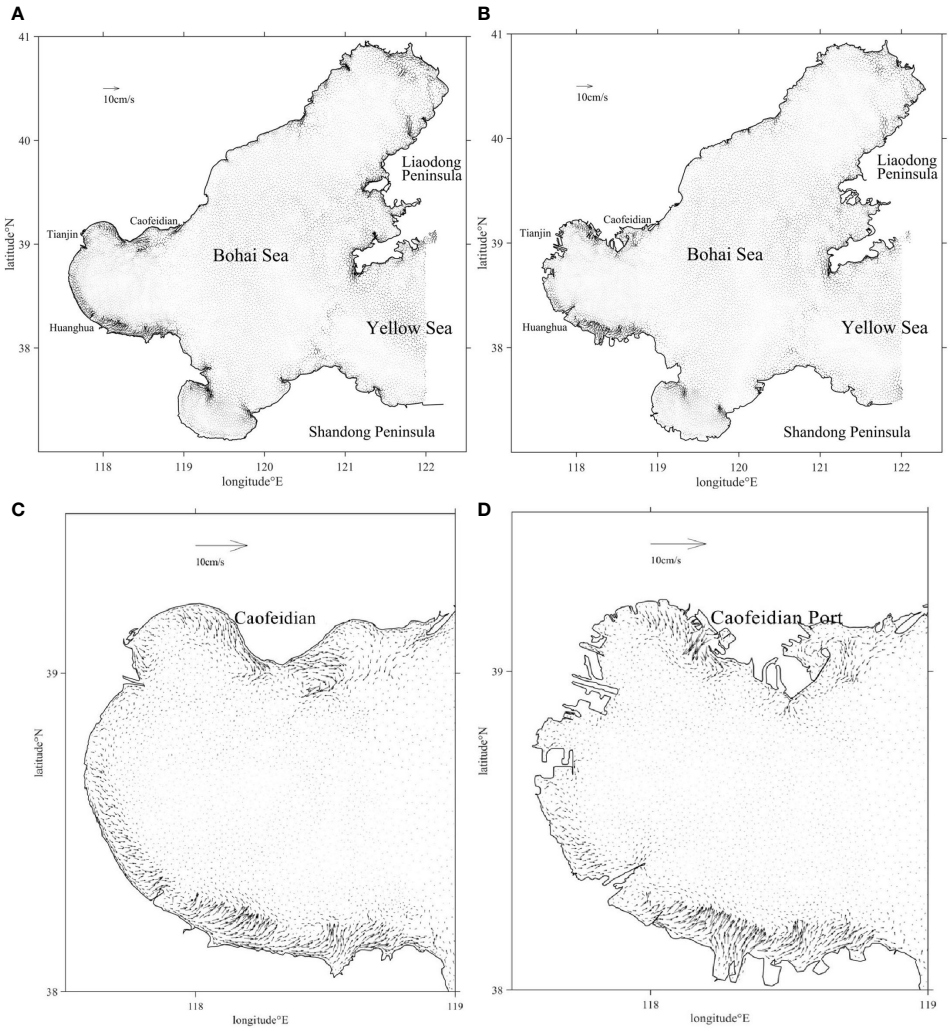

FIGURE 8
Simulated Eulerian tidal residual currents in **(A)** BHS in 1999; **(B)** BHS in 2019; **(C)** Bohai Bay in 1999; **(D)** Bohai Bay in 2019.

4 Conclusions

Large-scale of reclamation has a significant influence on the tidal regime and water exchange capacity in BHS. In this paper, coastline data of BHS in 1999, 2009, and 2019 were used to construct the hydrodynamic model. The model simulation data fit well with the measured data and can be used to study the effects of coastline changes on tidal currents and water exchange in BHS. The model results show that the amplitude of M2 increased slightly in Liaodong Bay and Bohai Bay, and decreased obviously in Laizhou Bay from 1999 to 2019. The amplitude variation of the semi-diurnal constituents (M2, S2) was greater than that of the diurnal ones (K1, O1). The amphidromic point of M2 near Qinhuangdao migrated 7.73km southwestward and the amphidromic point near the Huanghe River estuary migrated 9.15 km southeastward. The amphidromic point of K1 in the Bohai Strait migrated 3.71 km southeastward. Reclamation had weakened the water exchange capacity of BHS, and local residence time and basin residence time

TABLE 2 Basin residence time of the BHS with/without runoff in 1999 and 2019.

Bay	Basin residence time in 1999 with runoff(days) without runoff(days)	Basin residence time in 2019 with runoff(days) without runoff(days)
Laizhou Bay	89 78	133 124
Bohai Bay	466 460	510 506
Liaodong Bay	1894	1997

TABLE 3 Tidal prism and area of the BHS.

Bay	1999 Area(km^2) prism($\times10^{10}m^3$)	2019 Area(km^2) prism($\times10^{10}m^3$)	difference Area(%) prism(%)
Laizhou Bay	6155 0.719	5993 0.663	-2.63 -7.79
Bohai Bay	13179 2.077	12899 2.006	-2.12 -3.42
Liaodong Bay	35373 2.968	34649 2.938	-2.05 -1.01

in three bays had generally increased from 1999 to 2019. Some areas had different change trends due to changes in the Eulerian tidal residual current field. The circulation near Caofeidian Port disappeared with the construction of the port, leading to enhanced water exchange capacity in the northern part of Bohai Bay. With the influence of runoff, the local residence time in Laizhou Bay decreased by 11 days in 1999 and 9 days in 2019, respectively. Runoff only shortened the local residence time near the Huanghe River estuary and did not affect other areas. The research method can provide a reference for the study of other large semi-enclosed bays, and provide suggestions for subsequent marine ecological restoration efforts.

Data availability statement

Publicly available datasets were analyzed in this study. This data can be found here: http://www.coast-hhu.com/?page_id=2547.

Author contributions

ZW ran the numerical model, analyzed the results, and wrote the manuscript draft. CZ designed the numerical experiments and revised the manuscript. PW collected the coastline of BHS. ZF analyzed the coastline data. All authors contributed to the article and approved the submitted version.

Funding

National Natural Science Foundation of China (NSFC) 4160 6042, Fundamental Research Funds for the Central Universities B210202031.

Conflict of interest

The authors declare that the research was conducted in the absence of any commercial or financial relationships that could be construed as a potential conflict of interest.

Publisher's note

All claims expressed in this article are solely those of the authors and do not necessarily represent those of their affiliated organizations, or those of the publisher, the editors and the reviewers. Any product that may be evaluated in this article, or claim that may be made by its manufacturer, is not guaranteed or endorsed by the publisher.

References

Bai, T., Xu, J., Zhang, M., and Chang, C.-M. (2021). Seawater exchange rates for harbors based on the use of MIKE21 coupled with transport and particle tracking models. *J. Coast. Conserv.* 25 (2), 1–10. doi: 10.1007/s11852-021-00815-6

Ding, X., Guo, X., Zhang, C., Yao, X., Liu, S., Shi, J., et al. (2020). Water conservancy project on the huanghe river modifies the seasonal variation of chlorophyll-a in the bohai Sea. *Chemosphere.* 254, 126846. doi: 10.1016/j.chemosphere.2020.126846

Ding, X. S., Shan, X. J., Chen, Y. L., Jin, X. S., and Muhammed, F. R. (2019). Dynamics of shoreline and land reclamation from 1985 to 2015 in the bohai Sea, China. *J. Geographical Sci.* 29 (12), 2031–2046. doi: 10.1007/s11442-019-1703-1

Fang, S., Xie, Y., and Cui, L. (2015). "Analysis of tidal prism evolution and characteristics of the lingdingyang bay at pearl river estuary," in *MATEC Web of Conferences*. (EDP Sciences). 25, 01006. doi: 10.1051/matecconf/20152501006

Healy, M. G., and Hickey, K. R. (2002). Historic land reclamation in the intertidal wetlands of the Shannon estuary, western Ireland. *J. Coast. Res.* 36, 365–373. doi: 10.2112/1551-5036-36.sp1.365

Jia, H., Shen, Y., Su, M., and Yu, C. (2018). Numerical simulation of hydrodynamic and water quality effects of shoreline changes in Bohai Bay. *Front. Earth Sci.* 12, 625-639. doi: 10.1007/s11707-018-0688-x

Kang, J. W. (1999). Changes in tidal characteristics as a result of the construction of Sea-dike/Sea-walls in the mokpo coastal zone in Korea. *Estuarine Coast. Shelf Sci.* 48 (4), 429–438. doi: 10.1006/ecss.1998.0464

Li, F., Ding, D., Chen, Z., Chen, H., Shen, T., Wu, Q., et al. (2020). Change of sea reclamation and the sea-use management policy system in China. *Mar. Policy*. 115, 103861. doi: 10.1016/j.marpol.2020.103861

Li, X., Yuan, D., Sun, J., and Tao, J. H. (2010). "Simulation of land reclamation's effect on the water exchange in tianjin coastal area," in *2010 4th International Conference on Bioinformatics and Biomedical Engineering*. (IEEE), 1–5. doi: 10.1109/icbbe.2010.5517013

Liang, H., Kuang, C., Olabarrieta, M., Song, H., Ma, Y., Dong, Z., et al. (2018). Morphodynamic responses of caofeidian channel-shoal system to sequential large-scale land reclamation. *Continental Shelf Res.* 165, 12–25. doi: 10.1016/j.csr.2018.06.004

Liu, W.-C., Chen, W.-B., and Hsu, M.-H. (2011). Using a three-dimensional particle-tracking model to estimate the residence time and age of water in a tidal estuary. *Comput. Geosci.* 37 (8), 1148–1161. doi: 10.1016/j.cageo.2010.07.007

Pelling, H. E., Uehara, K., and Green, J. A. M. (2013). The impact of rapid coastline changes and sea level rise on the tides in the bohai Sea, China, j. geophys. *Res. Oceans* 118, 3462–3472. doi: 10.1002/jgrc.20258

Song, D., Wang, X. H., Zhu, X., and Bao, X. (2013). Modeling studies of the far-field effects of tidal flat reclamation on tidal dynamics in the East China seas. *Estuarine Coast. Shelf Sci.* 133, 147–160. doi: 10.1016/j.ecss.2013.08.023

Willmott, C. J. (1981). On the validation of models. *Phys. Geogr.* 2, 184. doi: 10.1080/02723646.1981.10642213

Ying, C., Li, R., Li, X., and Liu, Y. (2018). Anthropogenic influences on the tidal prism and water exchange in yueqing bay, zhejiang, China. *J. Coast. Res.* 85, 961–965. doi: 10.2112/si85-193.1

Yuan, Y., Jalón-Rojas, I., and Wang, X. H. (2021). Response of water-exchange capacity to human interventions in jiaozhou bay, China. *Estuar. Coast. Shelf Sci.* 249, 107088. doi: 10.1016/j.ecss.2020.107088

Zhao, X., and Sun, Q. (2013). Influence of reclamation on hydrodynamic environment in bohai bay. *Advanced Mater. Res.* 726-731, 3262–3265. doi: 10.4028/www.scientific.net/amr.726-731.3262

Zhao, L., Wei, H., and Zhao, J. Z. (2002). Numerical study on water exchange in jiaozhou bay. *Chin. J. Oceanol. Limnol.* 33, 23–29.

Zhu, L., Hu, R., Zhu, H., Jiang, S., Xu, Y., and Wang, N. (2018). Modeling studies of tidal dynamics and the associated responses to coastline changes in the bohai Sea, China. *Ocean Dynam.* 68, 1625-1648. doi: 10.1007/s10236-018-1212-2

Zhu, Q., Wang, Y. P., Ni, W., Gao, J., Li, M., Yang, L., et al. (2016). Effects of intertidal reclamation on tides and potential environmental risks: a numerical study for the southern huanghe Sea. *Environ. Earth Sci.* 75 (23), 1-17. doi: 10.1007/s12665-016-6275-0

frontiers | Frontiers in Marine Science

TYPE Original Research
PUBLISHED 27 March 2023
DOI 10.3389/fmars.2023.1101640

OPEN ACCESS

EDITED BY
Juan Jose Munoz-Perez,
University of Cádiz, Spain

REVIEWED BY
Feng Liu,
Sun Yat-sen University, China
Kezhao Fang,
Dalian University of Technology, China

*CORRESPONDENCE
Yi Pan
panyi@hhu.edu.cn

SPECIALTY SECTION
This article was submitted to Coastal Ocean Processes, a section of the journal Frontiers in Marine Science

RECEIVED 18 November 2022
ACCEPTED 16 March 2023
PUBLISHED 27 March 2023

CITATION
Pan Y, Li W, Tan J, Yu P, Chen X and Chen Y (2023) An investigation on the effects of increasing maximum wind speed of tropical cyclones on the return periods of water levels in the sea area of the Yangtze River Delta.
Front. Mar. Sci. 10:1101640.
doi: 10.3389/fmars.2023.1101640

An investigation on the effects of increasing maximum wind speed of tropical cyclones on the return periods of water levels in the sea area of the Yangtze River Delta

Yi Pan[1]*, Weihan Li[1], Jiahui Tan[1], Pubing Yu[2], Xinping Chen[3] and Yongping Chen[1]

[1]College of Harbor, Coastal and Offshore Engineering, Hohai University, Nanjing, Jiangsu, China, [2]Zhejiang Institute of Hydraulics and Estuary, Hangzhou, Zhejiang, China, [3]National Marine Hazard Mitigation Service, Ministry of Natural Resources of the People's Republic of China, Beijing, China

This paper investigates the impact of increasing maximum wind speed of tropical cyclones on the return periods of water levels in the sea area of the Yangtze River Delta. To conduct this study, a series of numerical experiments are performed using historical tropical cyclones that impacted the Yangtze River Delta from 1949 to 2019. The aim is to analyze the effects of global climate change on extreme water levels and the corresponding return periods. To obtain the historical water levels in the sea areas of the Yangtze River Delta, a storm surge model is driven by the selected tropical cyclones. The simulated astronomical tidal levels during the same period are also used. The extreme water levels of different return periods are then calculated. The maximum wind speeds of the selected tropical cyclones are increased by 11% according to the expected amount of increase under global climate change. The extreme water levels of different return periods under this scenario are calculated with the same procedure. The results of the study show that the impact of increasing maximum wind speed of tropical cyclones on the increases of extreme water levels and the decrease of return periods is more significant in the inner area of the estuaries than in the outer areas. Moreover, the responses of the extreme water levels and the corresponding return periods in the Yangtze River Estuary and the Hangzhou Bay show different characteristics. The results of this study provide significant reference value for the management of future coastal disaster prevention and mitigation in the Yangtze River Delta. Furthermore, the methodology used in this study can be applied in other estuaries to investigate the potential impacts of changes in climate and hydrology factors on extreme water levels and the corresponding return periods.

KEYWORDS

return period, extreme water levels, Yangtze River Delta, tropical cyclone, maximum wind speed

1 Introduction

Under the background of global climate change, the maximum wind speed of tropical cyclones and extreme high tide level in coastal areas are likely to increase (IPCC, 2012), which pose a great threat to coastal and estuary areas (e.g., Pan et al., 2013; Pan et al., 2020; Li et al., 2022) and also impact the present return period system based on historical hydrological data. Although some soft shore protection technologies can be used to resist the coastal disasters to some degree (e.g., Temmerman et al., 2013; Pan et al., 2022a), it is necessary to understand the impacts of global climate change on the return period system for the purpose of future coastal disaster prevention and mitigation.

The Yangtze River Delta (YRD) is formed by two estuaries, the Yangtze River Estuary and the Hangzhou Bay (i.e., the Qiantangjiang River Estuary), as seen in Figure 1. It is one of the economic centers of China with dense population and developed commodity economy, and it is often affected by storm surges induced by tropical cyclones. Studies are conducted on the impacts of global climate change on the storm surge induced by tropical cyclones in the Yangtze River Delta (e.g., Wang et al., 2012; Zhao et al., 2014; Feng et al., 2018; Pan and Liu, 2019; Shen et al., 2019) and other estuaries (e.g., Karim and Mimura, 2008; Robins et al., 2016; Yin et al., 2017; Li et al., 2020; Yuan et al., 2022; Zhou et al., 2022). Most of these studies focus on the impacts of climate change on the distribution of extreme storm surge levels in the estuaries. With these studies, a portray of the changes in distribution of extreme storm surge level under climate change can be gained. However, the sea dike risk due to climate change is determined by both the changes in extreme storm surge levels and the original sea dike crest levels, which are determined by historical data and different alone the coast of the estuaries. Therefore, it is necessary to investigate the changes in return periods of water levels due to climate change, to provide reference for future planning of coastal and offshore projects such as sea levees (Pan et al., 2015a; Pan et al., 2015b), harbours (Gao et al., 2020; Wang et al., 2020; Gao et al., 2021), offshore wind power fields (Guan et al., 2019; He et al., 2019), artificial beaches (Pan et al., 2017; Pan et al., 2018; Li et al., 2021; Li et al., 2022), etc.

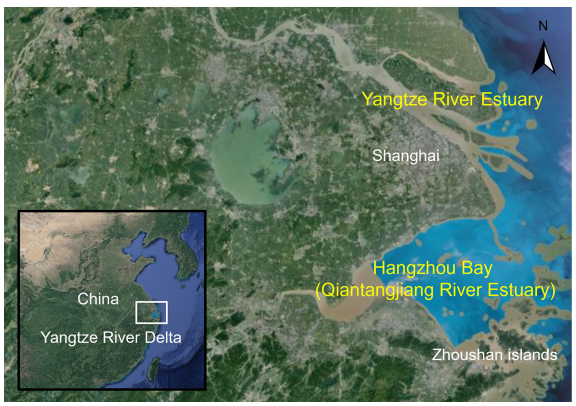

FIGURE 1
The study area: the Yangtze River Delta.

In this paper, the effects of increasing maximum wind speed of tropical cyclones on the return periods of water levels in the sea area of the Yangtze River Delta are investigated *via* a serious of numerical experiments. Although global climate change comes with a serious of effects, e.g., sea level rise, increasing maximum wind speed of tropical cyclones, and changes in the tracks of tropical cyclones, this study only focus on the effects of increasing maximum wind speed of tropical cyclones. Under a hypothesis that the river run-off, astronomical tide, mean sea level, and tracks of tropical cyclones are unchanged, while the maximum wind speeds of tropical cyclones increase in a possible scenario (IPCC, 2012), the effects of increasing maximum wind speed of tropical cyclones on the return periods of water levels in the sea area of the Yangtze River Delta are investigated *via* a numerical model. Based on numerical simulations under different scenarios, the distributions of increase of water levels and decreases of return periods are analyzed and discussed.

2 Methodology

A storm surge model of the Yangtze River Estuary is set up based on the ADCIRC model (e.g., Dietrich et al., 2011) and verified *via* a comparison between the simulated and measured data. With the storm surge model, a two-step numerical study scheme is designed to investigate the possible impact of increasing maximum wind speed of tropical cyclones on the return periods of water levels in the sea area of the Yangtze River Delta. The numerical study scheme is designed based on the hypothesis that the river run-off, astronomical tide, mean sea level, and tracks of tropical cyclones are unchanged, while the maximum wind speeds of tropical cyclones increase in a possible scenario. In the first step, all the tropical cyclones that impact the Yangtze River Delta during 1949 to 2019 are picked out and used to drive the storm surge model. The astronomical tides during 1949 to 2019 are also simulated to provide the maximum annual astronomical tidal levels. With the simulated annual tidal levels (may from either storm surges or astronomical tides), the water levels of different return period are calculated in the sea area of the Yangtze River Delta. In the second step, all the processes in step 1 are repeated except that the tropical cyclones are strengthened according to IPCC (2012), and the water levels of different return periods are calculated accordingly. The new-calculated water levels of different return periods are then compared to the old ones and the impacts of increasing maximum wind speed of tropical cyclones on the spatial distribution of return periods of water levels in the sea area of the Yangtze River Delta are discussed.

2.1 Storm surge model

The storm surge model is set up with ADCIRC model. The ADCIRC model is a shallow-water circulation model that solves for water levels and currents at a range of scales (e.g., Westerink et al.,

2008; Dietrich et al., 2011). The ADCIRC model has been widely used in the numerical studies on storm surge processes around the world (e.g., Parker et al., 2019; Zhang et al., 2020; Shankar and Behera, 2021; Li et al., 2022; Pan et al., 2022b; Wang et al., 2022).

The computational grid and stations used in model verification and data analysis are given in Figure 2. The computational grid covers the sea area of the East China Sea, part of south China sea, and a small part of Pacific Ocean. The total number of computational nodes and elements are 60338 and 112455, respectively. The ocean boundary conditions are provided by the TPXO 7.2 database. In the verification cases, the upper boundary of the Yangtze River is adapted from the measurement at Datong (DT) station, while in the cases for numerical experiments the monthly-averaged run-off discharges are used. Because the runoff of the Qiantang River has little influence on the flow field in Hangzhou Bay, the monthly-averaged runoff of Qiantang River is used for the upper boundary of the Qiantang River in both verification cases and the cases for numerical experiments. A modified Holland model (Holland, 1980; Mattocks and Forbes, 2008; Pan et al., 2016) is used to generate the wind fields according to tropical cyclone tracks. The equation of the wind speed is given as

$$v_{rot} = \sqrt{\frac{B}{\rho_a}\left(\frac{R_{max}}{r}\right)^B (P_n - P_c) exp\left(-\left(\frac{R_{max}}{r}\right)^B\right) + \left(\frac{rf}{2}\right)^2} - \frac{rf}{2} \quad (1)$$

$$B = \frac{((v_r - v_{mc})/W_{PBL})^2}{P_n - P_c} \quad (2)$$

where v_{rot} is the velocity of the rotating storm; P_n is the background surface pressure; P_c is the central surface pressure; ρ_a is the density of air; f is the Coriolis force; B is the hurricane shape parameter, which controls the eye diameter and steepness of the tangential velocity gradient; v_r is the maximum wind speed; v_{mc} is the moving speed of the storm; W_{PBL} is a wind reduction factor, defined at the gradient wind flow level above the influence of the planetary boundary layer (Powell et al., 2003).

The storm surge model is verified by simulating three storm surges that impact the sea area of the Yangtze River Delta significantly. The three simulated storm surges are induced by the tropical cyclones Winnie (9711), Fung-wong (1416) and Lekima (1909) whose tracks are illustrated in Figure 3. Comparisons of simulated and measured water levels at different stations during the three storm surges are plotted in Figure 4. As seen, good agreements can be found between model simulations and observations of water level, indicating that the storm surge model provides satisfactory descriptions of the water levels.

2.2 Numerical study scheme

The tropical cyclones that impact the sea area of the Yangtze River Delta from 1949 to 2019 are firstly picked out. To do this, a circle is made with the center located LCG and the radius of 500 km. All tropical cyclones that moved in this circle area during 1949 to 2019 are considered to have significant impact on the sea area of the

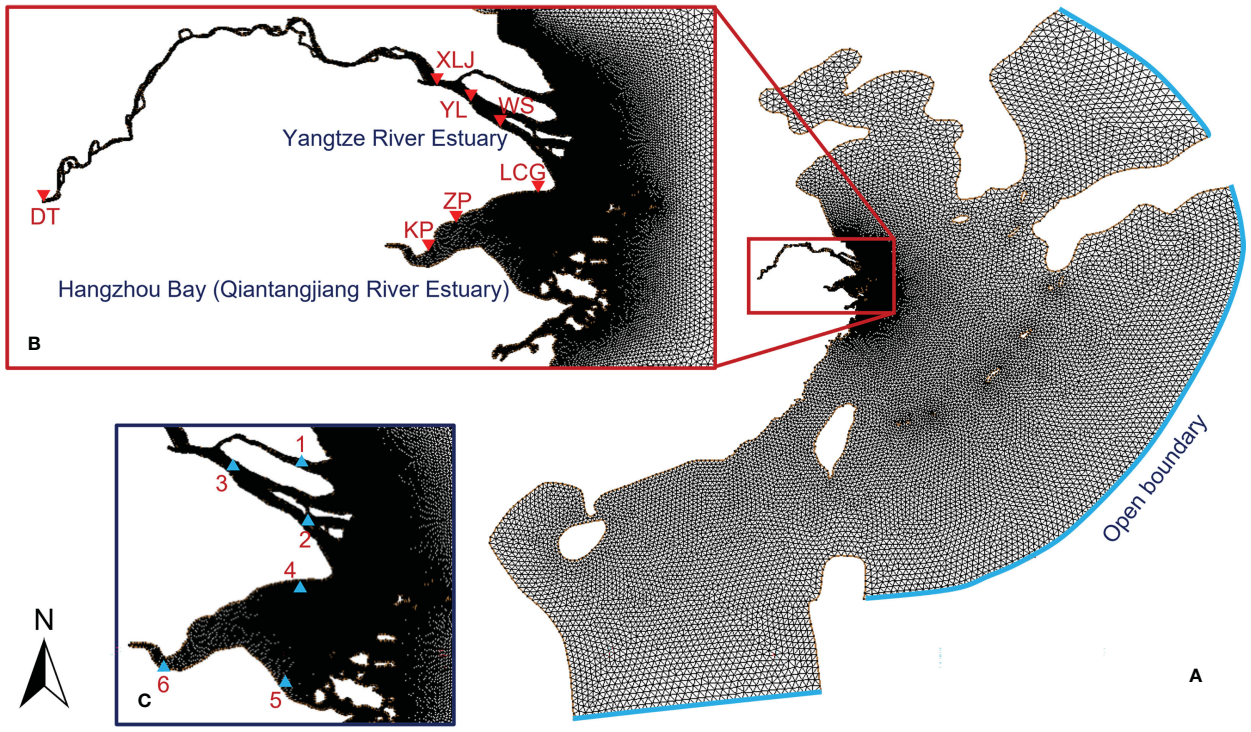

FIGURE 2
Computational grid and stations: **(A)** the computational grid, **(B)** local refinement and stations for model verification and **(C)** stations for data analysis.

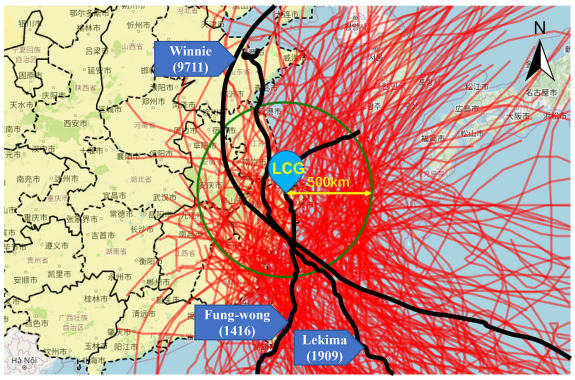

FIGURE 3
The tracks of all selected tropical cyclones that impact the sea area of the Yangtze River Delta and the three tropical cyclones used for model verification.

Yangtze River Delta and a total of 154 tropical cyclones are selected, as seen in Figure 3. The tropical cyclone track data are from the CMA (China Meteorological Administration) Tropical Cyclone Best Track Dataset (Ying et al., 2014; Lu et al., 2021; data available in tcdata.typhoon.org.cn). All the selected tropical cyclones are used to drive the storm surge model to get the water level distributions under the effects of historical tropical cyclones (the cases are referred to as historical cases hereinafter). In addition, the astronomical tides from 1949 to 2019 are also simulated to provide the maximum annual astronomical tidal levels, in case of the annual maximum tidal levels of some years are induced by the highest astronomical tide rather than storm surge (the cases are referred to as astronomical cases hereinafter).

Then the tropical cyclones are enhanced with increased maximum wind speeds and decreased central pressures. According to the special report of IPCC (2012) on extreme events and disasters, the mean maximum wind speed of tropical cyclones may increase 2% to 11% by the end of the 21st century. Based on this, the maximum wind speeds of all selected tropical cyclones are increased according to the upper limit (11%), and the central pressures are deceased accordingly with the empirical relationship

$$V_c = 1.176(1010 - P_c)^{0.87} + 6.5 \quad (3)$$

where V_c is the maximum wind speed, m/s; P_c is the central pressure of a tropical cyclone, hPa. The empirical relationship is extracted according to the relationships between the maximum wind speed and the central pressure of the selected 154 tropical cyclones. It can be seen that the units on the two sides of Equation (1) are not the same. However, because the central pressure of a tropical cyclone has much less influence on the storm surge than the maximum wind speed (usually it is considered that the pressure-induced surge accounts for about 5% of the storm surge), the errors in the center pressure have little influence on the simulated results and a generally reasonable decrease of the central pressure meets the requirement of the numerical study scheme.

The enhanced tropical cyclones are then used to drive the storm surge model to get the water level distributions under the effects of increased maximum wind speed of tropical cyclones (the cases are referred to as enhanced cases hereinafter). The annual maximum tidal levels obtained based on the results of historical cases + the astronomical cases (namely historical scenario) can be labeled as Historical Annual Maximum Tidal Levels (HAMTL), while annual maximum tidal levels obtained based on the results of enhanced cases + the astronomical cases (namely enhance scenario) can be labeled as Enhanced Annual Maximum Tidal Levels (EAMTL).

The two set of annual maximum tidal levels can be used to extract return period information. A theoretical distribution should be chosen firstly. For two reasons, 1) this study focuses on the effects of enhanced tropical cyclones, and 2) the analysis is on all spatial points in the sea area of the Yangtze River Delta for the purpose of spatial comparison, the theoretical distribution needs to meet two requirements: 1) the theoretical distribution can be fitted by only part of the data (in this study the upper part is used to reflect more feature of the extreme high water levels), and 2) the curve-fitting need to be straightforward without manual adjustment. According to the two requirements, the two-parameter Weibull distribution is chosen rather than the Gumbel Probability Distribution (which cannot be fitted by part of the data) and Pearson III Probability Distribution (which has tuning parameters that need manual adjustment). The probability distribution function of two-parameter Weibull distribution is given by

$$P(X \le x) = 1 - exp\left(-\left(\frac{x}{a}\right)^b\right) \quad (4)$$

where P is the probability of the studied variable X being less than or equal to x, a is the scale factor, and b is the shape factor. Because the two-parameter Weibull distribution starts with zero, the X is the difference between the annual maximum tidal levels and the minimum value of the annual maximum tidal levels at each spatial point.

Some samples of the Weibull curve-fitting are given in Figure 5. The curves are fitted with the upper 25% of the annual maximum tidal levels to have a better reflection of the distribution of largest water levels. Using a different theoretical distribution or portion of data might yields different results in detailed values, but the general spatial patterns should be similar. As seen, the Weibull distribution fits well with both the HAMTL and EAMTL, and significant differences can be found between the best fit curves of HAMTL and EAMTL. It can be noticed that in Figure 5D) (station 4) the curve-fitting is moderate, with the middle and lower part of the data have a deviation from the curve. A possible explanation is that the station 4 is close to open sea area and it also influenced little by the Zhoushan islands compared to station 5, so the middle and lower part of the data are more induced by the astronomical tide rather than the storm surge. For all the spatial points in the sea area of the Yangtze River Delta, the Weibull fit is conducted to both the HAMTL and EAMTL. With the best fit curves, the water levels of different return periods under historical and enhanced scenarios can be obtained as the data base for further analysis.

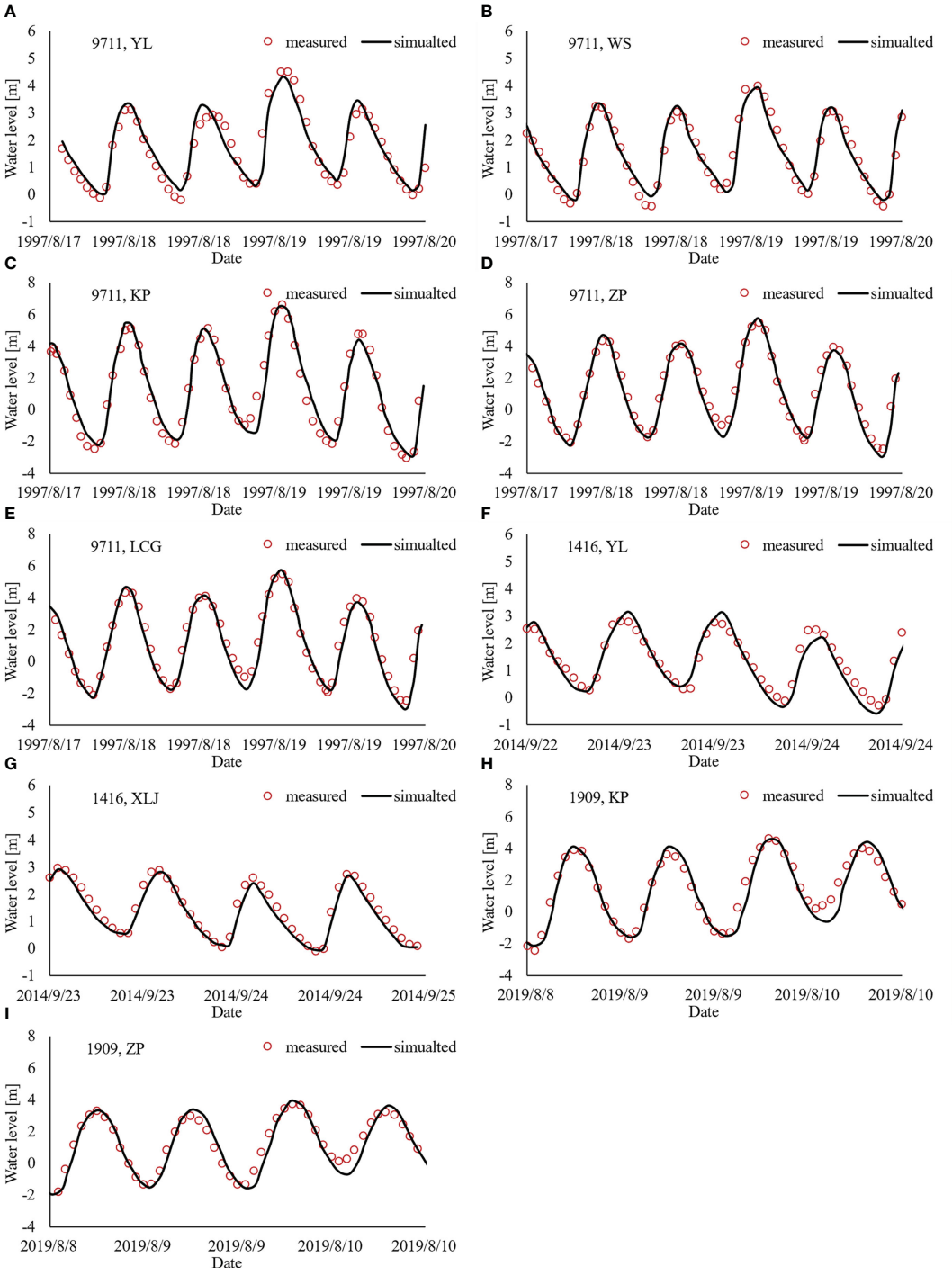

FIGURE 4
Comparisons of simulated and measured water levels at different stations during the tropical cyclones Winnie (9711), Fung-wong (1416) and Lekima (1909). The **(A–F)** respectively correspond to the water levels at YL, WS, ZP, KP and LCG during tropical cyclone Winnie (9711). The **(F)** and **(G)** respectively correspond to the water levels at YL and XLJ during tropical cyclone Fung-wong (1416). The **(H)** and **(I)** respectively correspond to the water levels at KP and ZP during tropical cyclone Lekima (1909). Note: because the measured data are from different sources, different stations are verified in the three storm surge processes.

3 Results and discussion

The differences in extreme water levels (50-year, 100-year, and 200-year return period) between historical and enhanced scenarios are calculated by subtracting the values from the historical scenarios from those from the enhanced scenarios. In this way, the impacts of the increasing maximum wind speed of tropical cyclones on the extreme water levels can be reflected straightforwardly. The distribution of the difference in extreme water levels are illustrated in Figure 6. As seen, under the impact of increased

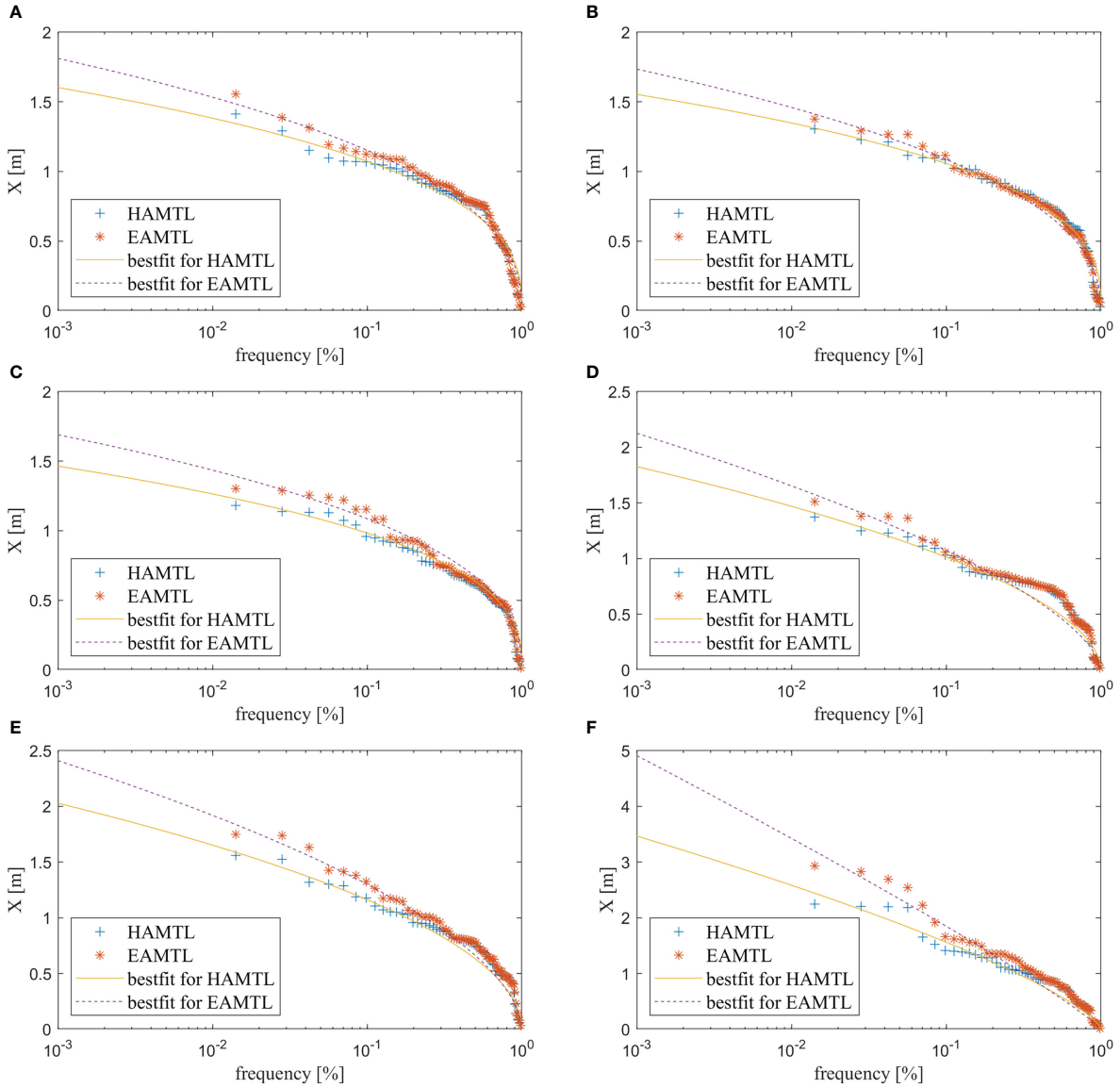

FIGURE 5
Samples of the curve-fitting with HAMTL and EAMTL. The **(A–F)** correspond to the station 1 to station 6 illustrated in Figure 2C.

maximum wind speed, the increase patterns of extreme water levels are majorly controlled by the estuary topography. Generally, the extreme water levels increase more significantly in the inner area than the outer area of the estuary. The increases of the extreme water levels of different return periods increase along the estuary from out sea to the upstream, which applies to both the Yangtze River Estuary and the Hangzhou Bay. A comparison between the two estuaries indicates that the extreme water levels of the Hangzhou Bay are more sensitive to the increase of maximum wind speed of tropical cyclones. At the upstream end of the Yangtze River Estuary (i.e. near the XLJ station in Figure 2) the increase of 200-year water level is about 0.15 m, while at the upstream end of the Hangzhou Bay (i.e. near the station 6 in Figure 2) the value is about 0.4 m. The reason might be the squeezing effect of the horn-shape of the Hangzhou Bay to the storm surge. Noticing that the hypothesis of the numerical study scheme is that the river run-off, astronomical tide, mean sea level, and tracks of tropical cyclones are unchanged, while the maximum wind speeds of tropical cyclones are increased, strictly speaking the changes in extreme water levels are due to the maximum wind speeds of tropical cyclones rather than the climate change. However, the patterns of spatial distributions are of reference significance to the management of future coastal disaster prevention and mitigation.

Except for the increases of the extreme water levels, the decrease of return periods of extreme water levels due to increasing maximum wind speed is also a concerned issue and of great importance to the management of future coastal disaster prevention and mitigation. To calculate the decreases of return periods, the extreme water levels of certain return periods (i.e., 50, 100 and 200 years) are calculated firstly, and then the corresponding return periods of the extreme water levels of certain return periods are calculated based on the simulated results of the enhanced scenarios. The decreases of return periods are then

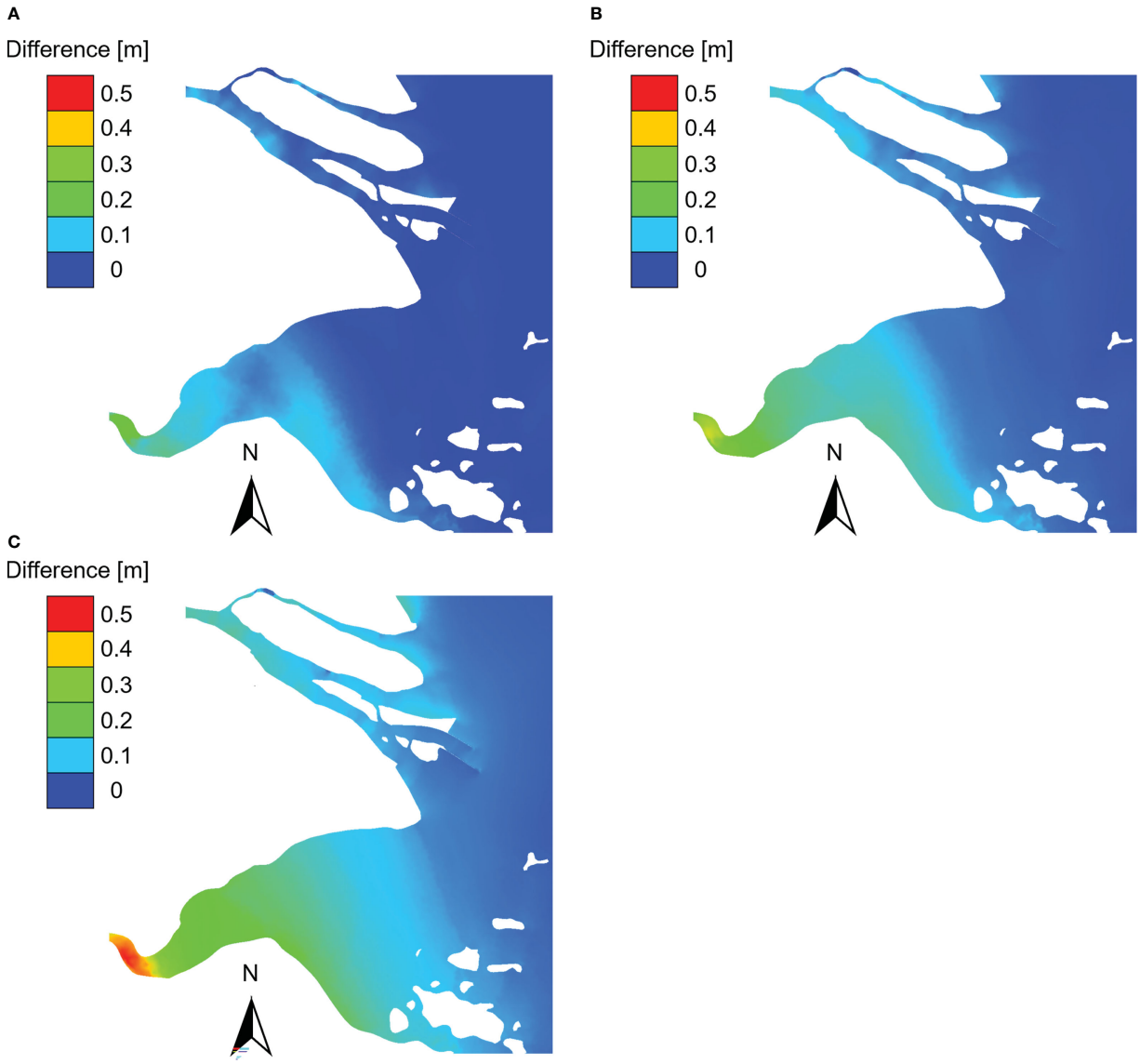

FIGURE 6
The differences in extreme water levels between historical and enhanced scenarios: **(A)** 50-year return period, **(B)** 100-year return period, **(C)** 200-year return period.

calculated by subtracting the new-calculated return periods (based on the enhanced scenarios) from the given ones (based on the historical scenarios) and plotted in Figure 7. It can be seen that the decrease of return periods and increase patterns of extreme water levels have generally similar distributions and some differences in the two estuaries. Under increased maximum wind speed, the return periods decrease more rapidly in the upstream of the estuaries generally. In the sea area out of the estuaries the return periods decrease about 50% (e.g., 25 years for 50-year return period case, 50 years for 100-year return period case, 110 years for 200-year return period case), while in the upper stream ends of the estuaries the return periods decrease about 80% (e.g., 35 years for 50-year return period case, 80 years for 100-year return period case, 170 years for 200-year return period case). A comparison between the two estuaries indicates that, on the contrary of the increase of extreme water levels, the decrease of return periods in the Yangtze River Estuary is more sensitive to increasing maximum wind speed than those of the Hangzhou Bay, the reason of which might be that the extreme water levels are higher in the Hangzhou Bay than those in the Yangtze River Estuary under the same return period. As discussed in preceding paragraph, due to the hypothesis of the study, the changes in extreme water levels are due to the maximum wind speeds of tropical cyclones rather than the climate change. but the patterns of spatial distributions are of reference significance to the management of future coastal disaster prevention and mitigation.

It should also be noticed that all the 154 historical tropical cyclones are strengthened according to the upper limit (11%) of the IPCC (2012) estimation, so the quantitative values of the increases of extreme water levels and the decrease of return periods might be overestimated, but the patterns of spatial distributions are of reference significance.

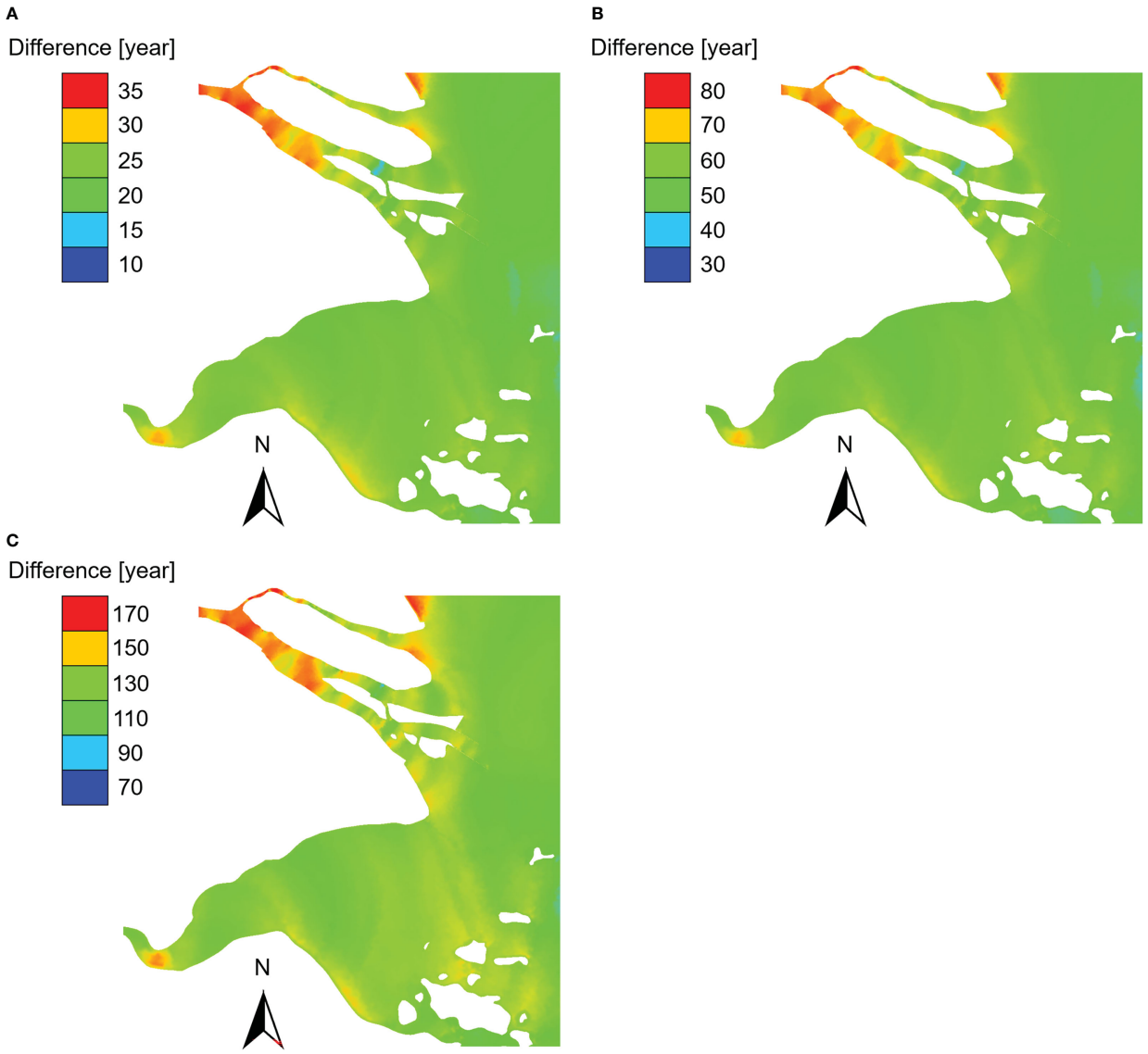

FIGURE 7
The decrease of return periods of extreme water levels of the enhanced scenarios compared to the historical scenarios: **(A)** 50-year return period, **(B)** 100-year return period, **(C)** 200-year return period.

From the points of view of the changes in both extreme water levels and return periods, the inner areas of the estuaries will be under greater pressures from storm surges compared to the open sea areas, which applies to both the Yangtze River Estuary (river-tide dominated) and the Hangzhou Bay (tide dominated). Hence attentions show be paid on the disaster prevention of the inner areas of the estuaries under the background of increasing tropical cyclones.

4 Conclusions

Under the hypothesis that the river run-off, astronomical tide, mean sea level, and tracks of tropical cyclones that affect the Yangtze River Delta are unchanged, while the maximum wind speeds of tropical cyclones increase 11%, the impacts of increasing maximum wind speeds of tropical cyclones on the return periods of water levels in the sea area of the Yangtze River Delta are investigated *via* a series of numerical experiments. The following conclusions can be drawn:

(1) Under the scenario of increased maximum wind speeds of tropical cyclones, the extreme water levels under certain return periods (i.e., 50, 100 and 200 years) increase more significantly in the inner area than the outer area of the estuary. The maximum increases of extreme water level under 50, 100 and 200 years return period are about 0.3, 0.4 and 0.5 m, which appear at the upstream end of the Hangzhou Bay. The extreme water levels in the Hangzhou Bay seems more sensitive to the increase of maximum wind speeds of tropical cyclones, which might be due to the squeezing effect of the horn-shape of the Hangzhou Bay.

(2) Under the scenario of increased maximum wind speeds of tropical cyclones, the decrease of return periods ranges about 10 to

35 years for 50-year return period, 30 to 80 years for 100-year return period, and 70 to 170 years for 200-year return period in the Yangtze River Delta and the sea area out of it. The general patten of the decrease of return periods is similar to that of the increase pattern of extreme water levels, i.e., the changes in the inner areas of the estuaries are more significant than those in the sea areas out of the estuaries. However, the decrease of return periods is less significant in the Hangzhou Bay than that in the Yangtze River Estuaries, which might be due to that the extreme water levels are higher in the Hangzhou Bay themselves.

It should be mentioned that the historical tropical cyclones are strengthened according to the upper limit (11%) of the IPCC (2012) estimation, so the quantitative values of the increases of extreme water levels and the decrease of return periods might be overestimated, but the patterns of spatial distributions are of reference significance to the management of future coastal disaster prevention and mitigation. The methodology can also be used in other estuaries to investigate the potential impacts of changes in climate and hydrology factors on extreme water levels and the corresponding return periods.

Data availability statement

The raw data supporting the conclusions of this article will be made available by the authors, without undue reservation.

Author contributions

Conceptualization and research plan: YP, XC. Numerical Experiments: WL, JT, PY. Data analysis and writing: JT, PY, YC. Review and editing: YP, XC. All authors contributed to the article and approved the submitted version.

Funding

We sincerely thank the supports from the National Natural Science Foundation of China (51979098), the Major Scientific and Technological Project of the Ministry of Water Resources (SKS-2022025) and the Natural Science Foundation of Zhejiang Province (LZ22E090003).

Conflict of interest

The authors declare that the research was conducted in the absence of any commercial or financial relationships that could be construed as a potential conflict of interest.

Publisher's note

All claims expressed in this article are solely those of the authors and do not necessarily represent those of their affiliated organizations, or those of the publisher, the editors and the reviewers. Any product that may be evaluated in this article, or claim that may be made by its manufacturer, is not guaranteed or endorsed by the publisher.

References

Dietrich, J. C., Zijlema, M., Westerink, J. J., Holthuijsen, L. H., Dawson, C., Luettich, R. A. Jr., et al. (2011). Modeling hurricane waves and storm surge using integrally-coupled, scalable computations. *Coast. Eng.* 58 (1), 45–65. doi: 10.1016/j.coastaleng.2010.08.001

Feng, J. L., Li, W. S., Wang, H., Zhang, J. L., and Dong, J. X. (2018). Evaluation of sea level rise and associated responses in hangzhou bay from 1978 to 2017. *Adv. Clim. Change Res.* 9 (4), 227–233. doi: 10.1016/j.accre.2019.01.002

Gao, J., Ma, X., Dong, G., Chen, H., Liu, Q., and Zang, J. (2021). Investigation on the effects of Bragg reflection on harbor oscillations. *Coast. Eng.* 170, 103977. doi: 10.1016/j.coastaleng.2021.103977

Gao, J., Ma, X., Zang, J., Dong, G., Ma, X., Zhu, Y., et al. (2020). Numerical investigation of harbor oscillations induced by focused transient wave groups. *Coast. Eng.* 158, 103670. doi: 10.1016/j.coastaleng.2020.103670

Guan, D., Chiew, Y. M., Melville, B. W., and Zheng, J. (2019). Current-induced scour at monopile foundations subjected to lateral vibrations. *Coast. Eng.* 144, 15–21. doi: 10.1016/j.coastaleng.2018.10.011

He, R., Kaynia, A. M., Zhang, J., Chen, W., and Guo, Z. (2019). Influence of vertical shear stresses due to pile-soil interaction on lateral dynamic responses for offshore monopiles. *Mar. Struct.* 64, 341–359. doi: 10.1016/j.marstruc.2018.11.012

Holland, G. J. (1980). An analytic model of the wind and pressure profiles in hurricanes. *Month. Weather Rev.* 108 (8), 1212–1218. doi: 10.1175/1520-0493(1980)108<1212:AAMOTW>2.0.CO;2

IPCC (2012). *Managing the risks of extreme events and disasters to advance climate change adaptation. a special report of working groups I and II of the intergovernmental panel on climate change* (Cambridge, UK, and New York, NY, USA: Cambridge University Press), 582.

Karim, M. F., and Mimura, N. (2008). Impacts of climate change and sea-level rise on cyclonic storm surge floods in Bangladesh. *Global Environ. Change* 18 (3), 490–500. doi: 10.1016/j.gloenvcha.2008.05.002

Li, Z., Li, S., Hu, P., Mo, D., Li, J., Du, M., et al. (2022). Numerical study of storm surge-induced coastal inundation in laizhou bay, China. *Front. Mar. Sci.* 9, 952406. doi: 10.3389/fmars.2022.952406

Li, M., Zhang, F., Barnes, S., and Wang, X. (2020). Assessing storm surge impacts on coastal inundation due to climate change: Case studies of Baltimore and Dorchester county in Maryland. *Nat. Hazards* 103 (2), 2561–2588. doi: 10.1007/s11069-020-04096-4

Li, Y., Zhang, C., Chen, S., Sui, T., Chen, D., and Qi, H. (2022). Influence of artificial sandbar on nonlinear wave transformation: Experimental investigation and parameterizations. *Ocean Eng.* 257, 111540. doi: 10.1016/j.oceaneng.2022.111540

Li, Y., Zhang, C., Chen, D., Zheng, J., Sun, J., and Wang, P. (2021). Barred beach profile equilibrium investigated with a process-based numerical model. *Cont. Shelf Res.* 222, 104432. doi: 10.1016/j.csr.2021.104432

Lu, X., Yu, H., Ying, M., Zhao, B., Zhang, S., Lin, L., et al. (2021). Western North pacific tropical cyclone database created by the China meteorological administration. *Adv. Atmos. Sci.* 38 (4), 690–699. doi: 10.1007/s00376-020-0211-7

Mattocks, C., and Forbes, C. (2008). A real-time, event-triggered storm surge forecasting system for the state of north Carolina. *Ocean Model.* 25 (3-4), 95–119. doi: 10.1016/j.ocemod.2008.06.008

Pan, Y., Chen, Y. P., Li, J. X., and Ding, X. L. (2016). Improvement of wind field hindcasts for tropical cyclones. *Water Sci. Eng.* 9 (1), 58–66. doi: 10.1016/j.wse.2016.02.002

Pan, Y., Kuang, C. P., Chen, Y. P., Yin, S., Yang, Y. B., Yang, Y. X., et al. (2018). A comparison of the performance of submerged and detached artificial headlands in a beach nourishment project. *Ocean Eng.* 159, 295–304. doi: 10.1016/j.oceaneng.2018.04.038

Pan, Y., Kuang, C. P., Li, L., and Amini, F. (2015a). Full-scale laboratory study on distribution of individual wave overtopping volumes over a levee under negative freeboard. *Coast. Eng.* 97, 11–20. doi: 10.1016/j.coastaleng.2014.12.007

Pan, Y., Kuang, C. P., Zhang, J. B., Chen, Y. P., Mao, X. D., Ma, Y., et al. (2017). Postnourishment evolution of beach profiles in a low-energy sandy beach with a shoreface nourishment. *J. Waterw. Port Coast. Ocean Eng. ASCE* 143 (4), 05017001. doi: 10.1061/(ASCE)WW.1943-5460.0000384

Pan, Y., Li, L., Amini, F., and Kuang, C. P. (2013). Full scale HPTRM strengthened levee testing under combined wave and surge overtopping conditions: Overtopping hydraulics, shear stress and erosion analysis. *J. Coast. Res.* 29 (1), 182–200. doi: 10.2112/JCOASTRES-D-12-00010.1

Pan, Y., Li, L., Amini, F., and Kuang, C. P. (2015b). Overtopping erosion and failure mechanism of earthen levee strengthened by vegetated HPTRM system. *Ocean Eng.* 96, 139–148. doi: 10.1016/j.oceaneng.2014.12.012

Pan, Z. H., and Liu, H. (2019). Extreme storm surge induced coastal inundation in Yangtze estuary regions. *J. Hydrodyn.* 31 (6), 1127–1138. doi: 10.1007/s42241-019-0086-1

Pan, Y., Liu, Y., Chen, Y. P., Xu, Z. S., and Xu, C. Y. (2022b). Probability forecast of storm surge levels in the changjiang estuary induced by tropical cyclones based on the error-estimation ensemble method. *Ocean Eng.* 245, 110524. doi: 10.1016/j.oceaneng.2022.110524

Pan, Y., Yin, S., Chen, Y. P., Yang, Y. B., Xu, C. Y., and Xu, Z. S. (2022a). An experimental study on the evolution of a submerged berm under the effects of regular waves in low-energy conditions. *Coast. Eng.* 176, 104169. doi: 10.1016/j.coastaleng.2022.104169

Pan, Y., Zhou, Z. J., and Chen, Y. P. (2020). An analysis of the downward-flushing flow on the crest of a levee under combined wave and surge overtopping. *Coast. Eng.* 158, 103701. doi: 10.1016/j.coastaleng.2020.103701

Parker, K., Ruggiero, P., Serafin, K. A., and Hill, D. F. (2019). Emulation as an approach for rapid estuarine modeling. *Coast. Eng.* 150, 79–93. doi: 10.1016/j.coastaleng.2019.03.004

Powell, M. D., Vickery, P. J., and Reinhold, T. A. (2003). Reduced drag coefficient for high wind speeds in tropical cyclones. *Nature* 422, 279–283. doi: 10.1038/nature01481

Robins, P. E., Skov, M. W., Lewis, M. J., Giménez, L., Davies, A. G., Malham, S. K., et al. (2016). Impact of climate change on UK estuaries: A review of past trends and potential projections. *Estuar. Coast. Shelf S.* 169, 119–135. doi: 10.1016/j.ecss.2015.12.016

Shankar, C. G., and Behera, M. R. (2021). Numerical analysis on the effect of wave boundary condition in storm wave and surge modeling for a tropical cyclonic condition. *Ocean Eng.* 220, 108371. doi: 10.1016/j.oceaneng.2020.108371

Shen, Y., Deng, G., Xu, Z., and Tang, J. (2019). Effects of sea level rise on storm surge and waves within the Yangtze river estuary. *Front. Earth. Sci.* 13 (2), 303–316. doi: 10.1007/s11707-018-0746-4

Temmerman, S., Meire, P., Bouma, T., Herman, P. M. J., Ysebaert, T., and de Vriend, H. J. (2013). Ecosystem-based coastal defence in the face of global change. *Nature* 504, 79–83. doi: 10.1038/nature12859

Wang, J., Gao, W., Xu, S., and Yu, L. (2012). Evaluation of the combined risk of sea level rise, land subsidence, and storm surges on the coastal areas of shanghai, China. *Climatic Change* 115 (3), 537–558. doi: 10.1007/s10584-012-0468-7

Wang, S., Mu, L., Qin, H., Wang, L., Yao, Z., and Zhao, E. (2022). The utilization of physically based models and GIS techniques for comprehensive risk assessment of storm surge: A case study of huizhou. *Front. Mar. Sci. Coast. Ocean Processes* 9, 939380. doi: 10.3389/fmars.2022.939380

Wang, G., Stanis, Z. E. O. G., Fu, D., Zheng, J., and Gao, J. (2020). An analytical investigation of oscillations within a circular harbor over a conical island. *Ocean Eng.* 195, 106711. doi: 10.1016/j.oceaneng.2019.106711

Westerink, J. J., Luettich, R. A., Feyen, J. C., Atkinson, J. H., Dawson, C., Roberts, H. J., et al. (2008). A basin to channel scale unstructured grid hurricane storm surge model applied to southern Louisiana. *Mon. Weather Rev.* 136 (3), 833–864. doi: 10.1175/2007MWR1946.1

Yin, K., Xu, S., Huang, W., and Xie, Y. (2017). Effects of sea level rise and typhoon intensity on storm surge and waves in pearl river estuary. *Ocean Eng.* 136, 80–93. doi: 10.1016/j.oceaneng.2017.03.016

Ying, M., Zhang, W., Yu, H., Lu, X., Feng, J., Fan, Y., et al. (2014). An overview of the China meteorological administration tropical cyclone database. *J. Atmos. Oceanic Technol.* 31 (2), 287–301. doi: 10.1175/JTECH-D-12-00119.1

Yuan, S. Y., Xu, L., Tang, H. W., Xiao, Y., and Gualtieri, C. (2022). The dynamics of river confluences and their effects on the ecology of aquatic environment: A review. *J. Hydrodyn.* 34, 1–14. doi: 10.1007/s42241-022-0001-z

Zhang, Z., Pan, Y., Yu, P. B., Chen, Y. P., and Yang, Y. Z. (2020). Characteristic of wave-induced setup in the changjiang estuary during typhoon processes. *J. Coast. Res. SI* 95), 1563–1568. doi: 10.2112/SI95-301.1

Zhao, C., Ge, J., and Ding, P. (2014). Impact of sea level rise on storm surges around the changjiang estuary. *J. Coast. Res.* 68, 27–34. doi: 10.2112/SI68-004.1

Zhou, Z., Wu, Y., Fan, D., Wu, G., Luo, F., Yao, P., et al. (2022). Sediment sorting and bedding dynamics of tidal flat wetlands: Modeling the signature of storms. *J. Hydrol.* 610, 127913. doi: 10.1016/j.jhydrol.2022.127913

Frontiers in Marine Science

Explores ocean-based solutions for emerging global challenges

The third most-cited marine and freshwater biology journal, advancing our understanding of marine systems and addressing global challenges including overfishing, pollution, and climate change.

Discover the latest Research Topics

See more →

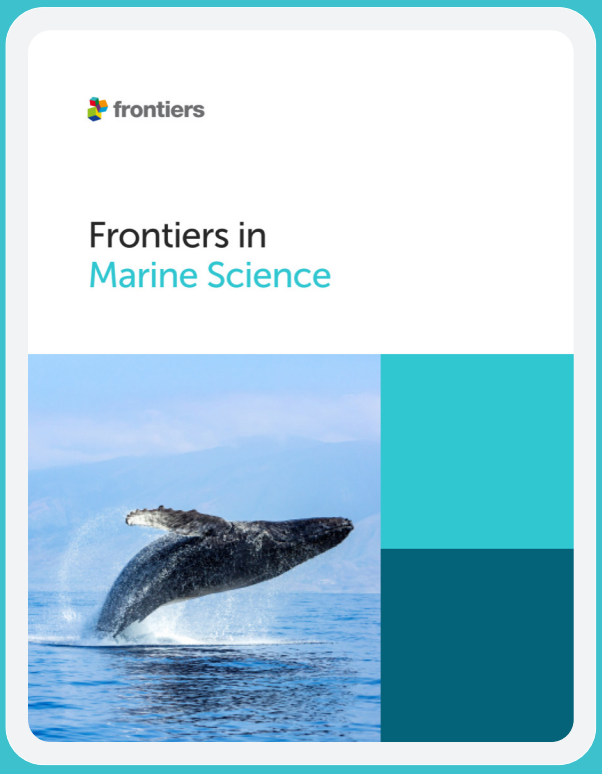

Frontiers

Avenue du Tribunal-Fédéral 34
1005 Lausanne, Switzerland
frontiersin.org

Contact us

+41 (0)21 510 17 00
frontiersin.org/about/contact